Physical and chemical alteration of material from C-Complex asteroids

Laura Elise Jenkins

B.Sc., M.Sc.

(University of Western Ontario)

Submitted in fulfilment of the requirements for the Degree of Doctor of Philosophy

School of Geographical and Earth Sciences,

College of Science and Engineering,

University of Glasgow

Abstract

C-complex asteroids are the parent bodies of carbonaceous chondrite meteorites and are composed of primitive material that was inherited from a molecular cloud, and condensed out of the early solar nebula (e.g., silicates, metal, sulphides, ices, organics). These asteroids have undergone alteration processes and can contain a variety of secondary phases, many of which are volatile bearing (e.g., serpentine, tochilinite, carbonates). It is important to understand the alteration processes experienced by C-complex asteroids and the products produced. C-complex asteroids are important volatile sources in our Solar System that may have delivered water and organics to Earth during its early development. 'Mighei-like' carbonaceous (CM) chondrites have all been aqueously altered and a subset have also undergone subsequent thermal metamorphism (post-hydration heating). Some CM chondrites also contain flattened and aligned chondrules due to deformation. When CM chondrites are exposed to Earth's atmosphere, they experience terrestrial weathering.

To better understand these alteration processes, 13 CM and CM-like chondrites were studied: Allan Hills 83100, Kolang, Lewis Cliff 85311, MacAlpine Hills 88100, Murchison, Murray, Pecora Escarpment (PCA) 02012, PCA 91008, PCA 91084, Shidian, Sutter's Mill, Winchcombe, & Wisconsin Range 91600. These meteorites were investigated using optical petrography, scanning electron microscopy, electron backscattered diffraction, electron microprobe analysis, transmission electron microscopy, Raman spectroscopy, and X-ray diffraction.

The metasomatic mineral, hydroandradite, was found in Kolang and Shidian. This is the first report of meteoritic hydroandradite; it formed from a chemically evolving fluid at >100°C, likely as a product of aqueous alteration. The temperature-timescales of post-hydration heating was investigated through experimentally heating CM chondrite samples as well as by studying naturally heated meteorites. This work established the mechanisms of phase transitions (decomposition of tochilinite, serpentine, calcite, etc.) and the temperatures at which they occur. The temperature-timescales of heating experienced by naturally heated CM chondrites were estimated and found to be quite variable, with temperatures spanning 210-950°C and durations ranging from hours to weeks. The variable timescales experienced indicate that post-hydration heating

was unlikely to have been caused by impact heating; solar heating is the most likely cause. Flattened and aligned chondrules in Kolang were studied to better understand physical deformation occurring on C-complex asteroids. There is a lack of evidence for impacts strong enough to flatten chondrules, indicating that chondrules were non-spherical before accretion. The non-spherical chondrules were aligned subsequently, likely by a mild impact event. The extent of which terrestrial weathering may affect a meteorite's makeup was investigated using the recent CM chondrite fall Winchcombe. Terrestrial calcite, calcium sulphates, and halite were found to have formed rapidly, in the timespan of months, showcasing the reactivity of carbonaceous chondrites under Earth's humid and oxidizing atmosphere.

Various alteration processes experienced by CM and CM-like chondrites, both on their C-complex asteroid parent bodies, and after landing on Earth has been better understood. The reactions and products form these alteration processes have been established.

Table of Contents

List of Tables

List of Figures

Conference Abstracts and Journal Articles Published During this Thesis

Journal Articles

Jenkins, L.E., Lee, M.R., Daly, L., King, A.J., Floyd, C.J., Martin, P-E., Almeida, N.V., and Genge, M.J. (2023) Winchcombe: An Example of Rapid Terrestrial Alteration of a CM Chondrite. *Meteoritics & Planetary Science,* early access.

Lee, M.R., Floyd, C., Martin, P-E., Zhao, Xuchao, Franchi, I.A., **Jenkins, L.E.**, and Griffin, S. (2023) Extended time scales of carbonaceous chondrite aqueous alteration evidenced by a xenolith in LaPaz Icefield 02239 (CM2). *Meteoritics & Planetary Science,* **58**: 672-687.

Genge, M.J., Alesbrook, L., Almeida, N.V, [and 33 others including **Jenkins, L.E.**] (2023) Fusion Crust of Winchcombe Meteorite: A Preserved Record of Atmospheric Entry Processes. *Meteoritics & Planetary Science*

Suttle, M.D., Daly, L., Jones, R.H., [and 39 others, including **Jenkins, L.E.**] (2022) The Winchcombe meteorite – a regolith breccia from a rubble-pile CM chondrite asteroid. *Meteoritics & Planetary Science*

King, A.J., Daly, L., Rowe, H., [and 117 others, including **Jenkins, L.E.**] (2022) The Winchcombe Meteorite, a Unique and Pristine Witness from the Outer Solar System. *Science Advances,* **8:** eabq3925

O'Brien, Á,C., Pickersgill, A., Daly, L., **Jenkins, L.E.,** Floyd, C., Martin, P-E., Hallis, L.J., King, A., and Lee, M.R. (2022) The Winchcombe Meteorite: one year on. *Astronomy & Geophysics,* **63:** 1.21-1.23.

Conference Abstracts

Jenkins, L.E., King, A.J., Lee, M.R., Daly, L., Ignatyev, K., Floyd, C.J., & P-E. M.C. Martin. (2023) The formation of a carlosturanite-like phase during thermal decomposition of serpentine in C-complex asteroids. *86th MetSoc Meeting,* Abstract #6042.

Jenkins, L.E., Lee, M.R., Daly, L., & King, A.J. (2023) Mildly shocked olivine in the Kolang CM chondrite – evidence against petrofabric formation in a single impact. *54th LPSC*, Houston, Texas. Abstract #1526

Jenkins, L.E., Lee, M.R., Daly, L., King, A.J., & Thompson, S.P. (2022) Experimental constraints for impact induced post-hydration heating on C-complex asteroids. *85th MetSoc Meeting,* Abstract #6122

Jenkins, L.E., Lee, M.R., Daly, L., King, A.J., Einsile, J.F., & Salge, T. (2022) Rudashevskyite in the Winchcombe CM chondrite: a sulfide from either nebular condensation or metasomatic alteration. *85th MetSoc Meeting,* Abstract #6123

Genge, M.J., Alesbrook, L.S., Almeida, N.V., [and 31 others, including **Jenkins, L.E.**] (2022) The fusion crust of the Winchcombe meteorite: vigorous degassing during atmospheric entry. *85th MetSoc Meeting,* Abstract #6345

Suttle, M.D., Daly, L., Jones, R.H., [and 35 others, including **Jenkins, L.E.**] (2022) Geologic history of the Winchcombe meteorite – a new CM chondrite fall. *85th MetSoc Meeting,* Abstract #6076

Daly, L., Suttle, M.D., Lee, M.R., [and 38 others, including **Jenkins, L.E.**] (2022) A coordinated approach to investigate the heterogeneity of aqueous alteration at the micro-scale in the Winchcombe meteorite, a CM fall. *85th MetSoc Meeting*, Abstract #6262.

Jenkins, L.E., Lee, M.R., Daly, L., King, A.J., and Li, S. (2022) Calc-silicate metasomatism in CM chondrites Shidian and Kolang: the first report of asteroidal hydroandradite. *53rd LPSC,* Houston, Texas. Abstract #1515

Lee, M.R., Lindgren, P., and **Jenkins, L.E.** (2022) Mg-Fe-Mn carbonates in the carbonaceous chondrites. *53rd LPSC,* Houston, Texas. Abstract #1962.

Jenkins, L.E., Lee, M., Daly, L., and King, A. J. (2021) Comparison of the impact histories of carbonaceous chondrites Murray and MCY 05230. *GAC-MAC 2021,* London, Ontario, Canada

Flemming, R., McCausland, P., Cao, F., Li, Y., **Jenkins, L.E.,** and Newman, J. (2021) Using X-ray diffraction to quantify strain in solids. *GAC-MAC 2021,* London, Ontario, Canada

Jenkins, L.E., Lee, M., Daly, L., King, A.J., and Chung, P. (2021) Post-brecciation chondrule flattening and petrofabric formation in CM chondrite Kolang. *84th MetSoc Meeting,* Abstract #6165

Jenkins, L.E., Lee, M., Daly, L., King, A.J., and Chung, P. (2021) Identification of clasts in CM chondrite fall Kolang with S and Ca. *84th MetSoc Meeting*, Abstract #6161

Lee, M.R., Martin, P.M.C., Floyd, C.J., and **Jenkins, L.** (2021) A xenolith from an early formed parent body in the CM carbonaceous chondrite LaPaz Icefield 02239. *84th MetSoc Meeting,* Abstract #6176

Jenkins, L.E., Lee, M.R, Daly, L., and Li, S. (2021) Fine-grained equant troilite in the CM chondrite Shidian: potential evidence for low temperature post-hydration heating. *52nd LPSC,* Abstract #1204

Jenkins, L.E., Flemming, R.L., Burchell, M., Harriss, K., Peslier, A.H., Christoffersen, R.G., Fritz, J. and Meyer, C. (2019) Creating calibration curves to determine shock pressure in clinopyroxene using lattice strain and strain-related mosaicity. *GSA Annual Meeting 2019*, Phoenix, Arizona. Abstract #240-6

Acknowledgements

Research, by nature, is a collaborative process. During the work of this thesis, I had support from numerous people and organizations that came in varying forms. I am incredibly thankful for this support as I would not have been able to complete this thesis without it. I am thankful to my supervisors for supporting me during my thesis.

I would also like to thank my viva examiners Amanda Owen and Frank Brenker. Their comments and feedback on this thesis, as well as the discussion surrounding it, was quite helpful and has improved this work.

I would like to thank Mendy Ouzillou, Shijie Li, Lawrence Garvie, the Antarctic Search for Meteorites, and the Natural History Museum, London for supplying the meteorite samples used in this work.

Sample preparation is a key part of any laboratory work. I would like to thank Conner Brolly for polishing the sample Kolang for electron backscattered diffraction. I would also like to thank Billy Smith for preparing electron transparent lamellae from select samples. I'd also like to thank Natasha Almeida and Helena Bates for the curation of the Winchcombe meteorite, and Callum Hatch for preparing its polished sections. I would also like to thank Alison McDonald for experimentally heating select samples at the Scottish Universities Environmental Research Centre (SUERC).

Throughout this thesis, I used a variety of laboratory equipment from multiple laboratories. Several people assisted with data collection and maintained laboratory equipment. I would like to thank them for doing so, especially under pandemic conditions wherein laboratory access was limited. These people include Peter Chung, Liene Spruziniece, Stephen Thompson, Konstantin Ignatyev, Sarah Day, Lucy Sanders, Jens Najorka, Claire Wilson, Chris Hayward, Catherine Harrison, Tobias Salge, Rhiannon Heard, Colin How, Cameron Floyd, and Joshua Einsile.

I would also like to thank the Scottish Alliance for Geoscience, Environment, and Society for funding the experimental heating of samples at

SUERC, the collection of transmission electron microscopy data, and the collection of scanning electron microscopy data.

I'd also like to thank Diamond Light Source for allowing my thesis experiments to be conducted at their synchrotron facility. These experiments had the beamtime awards CY29721, SP31815, and CY34715. Some of these experiments required 24-hour monitoring. I would like to thank Pierre-Etienne Martin, Cameron Floyd, and Fahkri Bintang for assisting with this. For one particular experiment, I had to borrow multiple pieces of equipment. I would like to thank Finlay Walton and Zhiyu Lao for lending this equipment, Holly Yu for PAT testing, and Christopher Syme and Ben Russell for advice regarding its use.

Throughout my studies as a Ph.D. student, I required advice from numerous other students, regarding both Ph.D. life as well as with specifics regarding laboratory methods. I would like to thank Sammy Griffin, Cameron Floyd, Pierre-Etienne Martin, Annemarie Pickersgill, Áine O'Brien, Rory Porteous, Fengke Cao, Faisal Khudhur, Robin Haller, and Kang Xie.

I also received tremendous support throughout my studies. I would like to thank both the Planetary Sciences Research Group as well as my colleagues in the Molema PGR office for all of this.

Finally, I'd like to thank my parents. They've been incredibly supportive throughout all my studies and have encouraged me to pursue both science and research in planetary sciences.

Author's declaration

I declare that, except where explicit reference is made to the contribution of others, that this dissertation is the result of my own work and has not been submitted for any other degree at the University of Glasgow or any other institution.

Laura Elise Jenkins

Chapter 1 –CM Chondrites, C-Complex Asteroids, and Alteration

Outside of sample return missions, meteorites and interplanetary dust particles are the only samples of planetary bodies available to study. They most commonly originate from asteroids but can also come from the Moon and Mars (McSween Jr., 1999). These samples offer a wealth of information that can be used to better understand the history of our Solar System and the geological processes occurring on other planetary bodies.

Meteorites can be classified as either chondritic or achondritic. Chondritic meteorites, as the name suggests, are primitive meteorites that contain chondrules, spherules of olivine and pyroxene that formed in the protoplanetary disk in the early Solar System. Chondritic meteorites all come from asteroids. In contrast, achondritic meteorites originate from parent bodies that have undergone melting (McSween Jr., 1999). Most achondrites are igneous in nature, with the potential exception of impact breccias which are arguably sedimentary (McCubbin et al. 2016). These achondrites can come from planets, moons, and the asteroidal remnants of differentiated planetesimals.

Both chondritic and achondritic meteorites can be further divided into classes (Fig. 1.1). For the purposes of this thesis, I will be focusing on chondritic meteorites, however achondrites contain numerous classes (e.g., Martian, ureilites). The most common class of chondritic meteorites are the ordinary chondrites, mainly composed of forsterite ($MgSiO_4$) chondrules set in a glassy or fine-grained matrix (Fig. 1.2) (Weisberg et al. 2006). The Rumuruti-like (R) chondrites are similar to ordinary chondrites in many aspects, however they lack Fe-Ni metal and instead contain an abundance of Fe-rich, Ni-bearing olivine (Weisberg et al. 2006). There are also enstatite chondrites, which tend to contain an abundance of enstatite ($MgSiO_3$) and other Fe-poor silicates, due to their formation under highly reducing conditions (Weisberg et al. 2006). Another relatively common class of chondrite is the carbonaceous chondrites, which are known to contain more refractory elements and phases (Weisberg et al. 2006). There are also many chondrites that do not neatly fit into these classes which are termed ungrouped. Although if enough ungrouped chondrites bearing similarities to each other come to light, more chondrite classes may be defined.

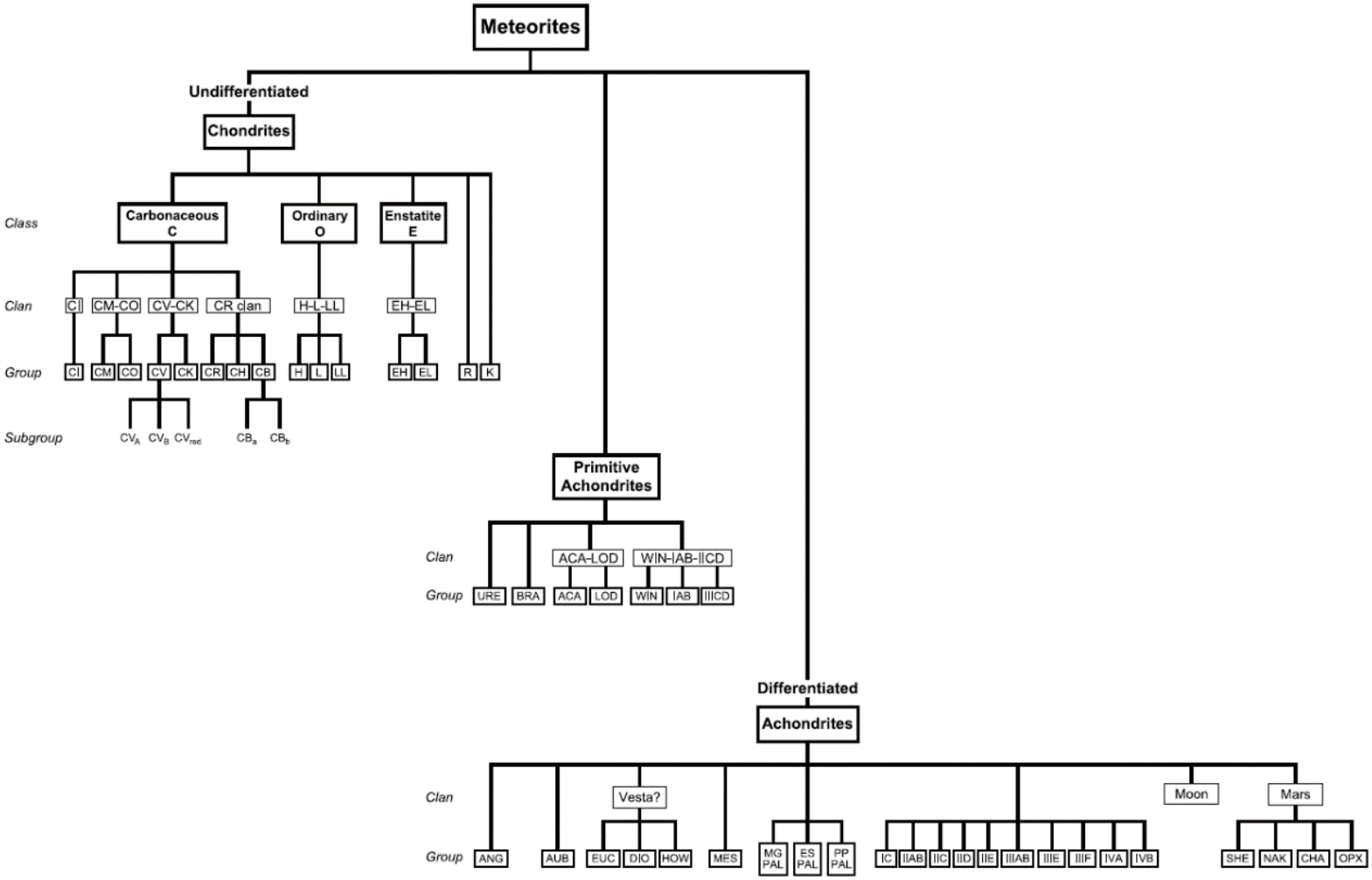

Fig. 1.1. Diagram showing the relationship between different meteorite classes, clans, and groups. Some subgroups are also specified. From Weisberg et al. (2006). Groups established after 2006 are missing (e.g., CY chondrites, Martian regolith breccias).

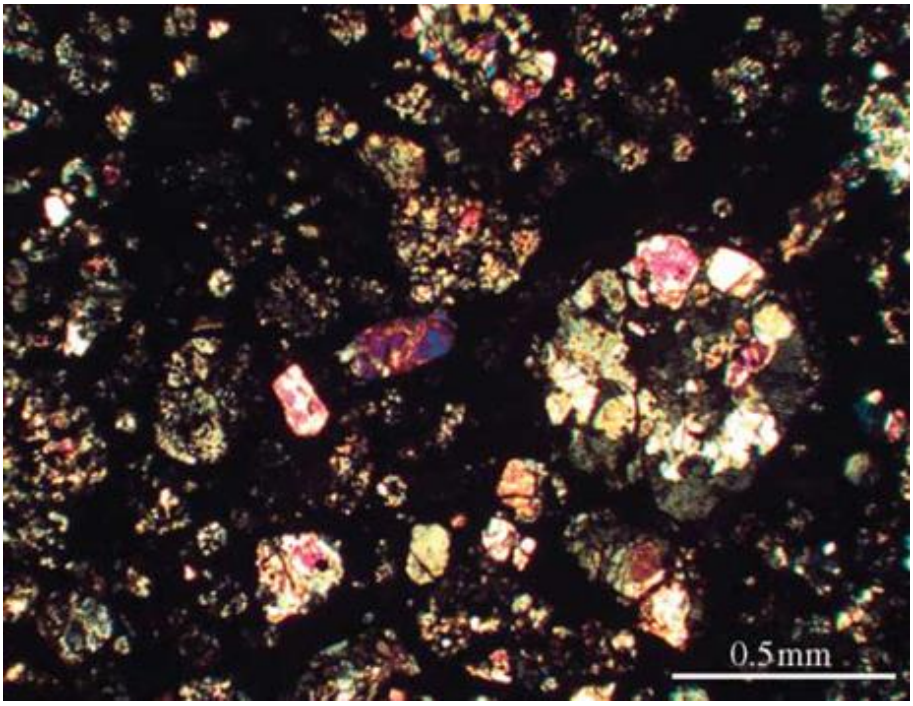

Fig. 1.2. Plane-polarized light image of chondrules in the carbonaceous chondrite Dar al Gani 186. From Sephton (2005).

The carbonaceous chondrite class itself is incredibly variable and its constituent meteorites can be sorted into the following groups: Karoonda-like (CK), Bencubbin-like (CB), ALH 85085-like (CH), Renazzo-like (CR), Vigarano-like (CV), Ornans-like (CO), Mighei-like (CM), Ivuna-like (CI), and Yamato-like (CY) (Weisberg et al. 2006; King et al. 2019a). Each carbonaceous chondrite class has a set of unique petrographic and isotopic characteristics (Weisberg et al. 2006), with bulk oxygen isotopes presenting a method to sort them once their unique petrographic characteristics are accounted for (Fig. 1.3) (Ireland et al. 2020).

The unique petrographic characteristics of each group are as follows. CK chondrites bear similarities to R chondrites in that they lack Fe-Ni metal and contain Fe-bearing olivine, with the addition of abundant Ni-sulphides and magnetite (Fe_3O_4) (Weisberg et al. 2006). CB chondrites are extremely metal rich (60 vol% ≤). CH chondrites are also characterized by a high abundance of metal (~20 vol%), and the relatively small size of their chondrules (≤100 μm). CR chondrites are aqueously altered meteorites that contain unusually large chondrules (~1 mm). CV chondrites are another meteorite group that has experienced minimal alteration that also have large chondrule sizes (~1 mm) (Weisberg et al. 2006). CO chondrites are characterized by the minimal alteration they have experienced, commonly only containing minor amounts of

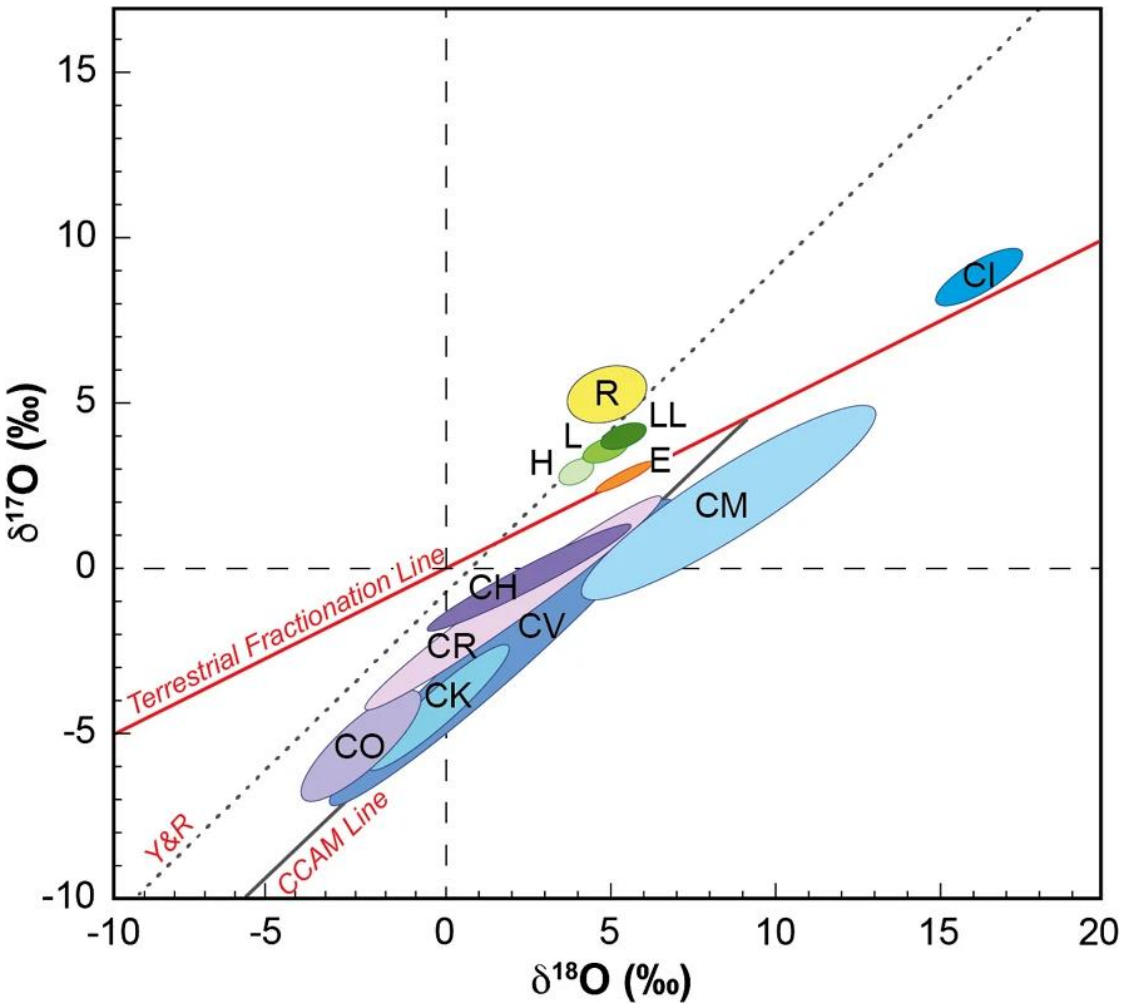

Fig. 1.3. $\delta^{18}O$ versus $\delta^{17}O$ plot for different chondrite groups. $\delta^{18}O$ and $\delta^{17}O$ are relative abundances of the ^{18}O and ^{17}O isotopes to ^{16}O. Terrestrial fractionation line as well as the carbonaceous chondrite anhydrous mineral (CCAM) mixing line are shown for reference. Most carbonaceous chondrite groups (e.g., CV, CK) exist along the CCAM line with the exception of CIs and some CMs. Enstatite chondrites (E) are on the terrestrial fractionation line, while other chondrite groups are above the terrestrial fractionation line. CY chondrites are not included. From Ireland et al. (2020).

metasomatic phases as their secondary minerals (Weisberg et al. 2006). CO chondrites are also known to have small chondrules (~150 μm) and can be distinguished from CV chondrites by such. CM chondrites have been aqueously altered at relatively low temperatures (e.g., 0-240°C; Clayton & Mayeda 1999; Busemann et al. 2007) and contain an abundance of low temperature alteration products, such as tochilinite ($Fe^{2+}_{5-6}(Mg,Fe^{2+})_5S_6(OH)_{10}$), serpentine, sulphides, and calcium carbonate. When CM chondrites do not contain chondrules, their secondary phases often take on their original shape, forming chondrule pseudomorphs (Weisberg et al. 2006; Rubin et al. 2007). CI chondrites have experienced extensive aqueous alteration and can be characterized by their complete lack of chondrules and calcium-aluminium inclusions (CAIs), as well as the abundance of phyllosilicates, carbonates, sulphides, and magnetite

(Weisberg et al. 2006). CY carbonaceous chondrites have experienced extensive aqueous alteration to form abundant hydrous phases (e.g., phyllosilicates, tochilinite), before experiencing post-hydration heating, dehydrating these hydrous phases. The CY chondrites share aspects with both CM and CI chondrites, containing the remnants of tochilinite-cronstedtite intergrowths (TCIs) and magnetite. They also contain chondrules, but few of them (King et al. 2019a; Suttle et al. 2023). There are also carbonaceous chondrites that are ungrouped, either having aspects that do not fit any one group, or a mixture of aspects that can fit it into multiple groups.

Chondritic meteorites are further sorted into petrologic types using the amount of alteration experienced. These petrologic types are based on the Van Schmus & Wood (1967) scale (Fig. 1.4). Initially it was assumed that a highly hydrous meteorite (e.g., a CI1) was completely altered and that a meteorite of petrologic type 3 had experienced thermal metamorphism (Van Schmus & Wood 1967). It is now understood that meteorites that fit into a petrologic type of 3 are unaltered to only mildly altered (Howard et al. 2015). A chondrite that has undergone only thermal metamorphism will have a petrologic type higher than 3 while a chondrite that has undergone only aqueous alteration will have a petrologic type lower than 3 (Howard et al. 2015).

	Petrologic types					
	1	2	3	4	5	6
(i) Homogeneity of olivine and pyroxene compositions	—	Greater than 5% mean deviations		Less than 5% mean deviations to uniform	Uniform	
(ii) Structural state of low-Ca pyroxene	—	Predominately monoclinic		Abundant monoclinic crystals	Orthorhombic	
(iii) Degree of development of secondary feldspar	—	Absent		Predominately as micro-crystalline aggregates		Clear, interstitial grains
(iv) Igneous glass	—	Clear and isotropic primary glass; variable abundance		Turbid if present	Absent	
(v) Metallic minerals (maximum Ni content)	—	(<20%) Taenite absent or very minor	kamacite and taenite present (>20%)			
(vi) Sulfide minerals (average Ni content)	—	>0·5%	<0·5%			
(vii) Overall texture	No chondrules	Very sharply defined chondrules		Well-defined chondrules	Chondrules readily delineated	Poorly defined chondrules
(viii) Texture of matrix	All fine-grained, opaque	Much opaque matrix	Opaque matrix	Transparent micro-crystalline matrix	Recrystallized matrix	
(ix) Bulk carbon content	~2·8%	0·6–2·8%	0·2–1·0%	<0·2%		
(x) Bulk water content	~20%	4–18%	<2%			

Fig. 1.4. Table used as a guide for sorting chondritic meteorites by petrologic type from Van Schmus & Wood (1967).

The focus of this thesis is on CM and CM-like chondrites, which have all been aqueously altered, and some have been modified by other processes like post-hydration heating and metasomatism (Nakamura 2005; Lee et al. 2019a). They are defined by the mixture of phyllosilicates and tochilinite present within them (Weisberg et al. 2006). The reflectance spectra of CM chondrites resembles those of C-complex asteroids from which they are believed to have originated (Bates et al. 2020; Cloutis et al. 2011). Carbonaceous chondrites and their parent asteroids are volatile-rich and may have delivered water and organic material to the early Earth (Alexander et al. 2012). Understanding the different processes experienced by CM chondrites will enable a better understanding of how their parent asteroids may have contributed to Earth's development in the early Solar system.

1.1 The Condensation of CM Chondrites' Building Blocks

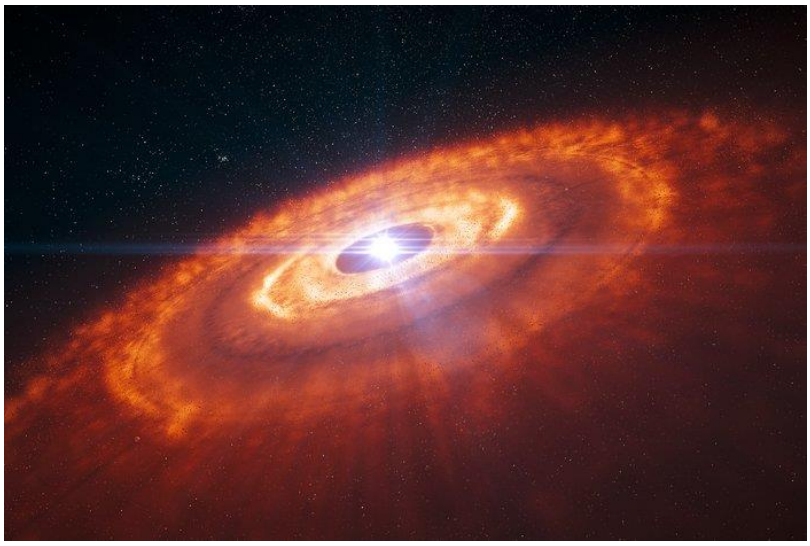

Fig. 1.5. Artist's depiction of a protoplanetary disk (ESO 2014).

The Solar System formed ~4.6 Ga ago when an area of a molecular cloud collapsed in on itself, with much of the matter making the Sun at the centre, and the rest forming a disk of gas and dust (Fig. 1.5). Jets that eject material from near the Sun, perpendicular to the disk developed (Montmerle et al. 2006). These jets are called X-winds (Hu 2010). There are multiple models for how the Solar System formed. Some posit that the early Solar System was quite hot and the components making up the various objects within it condensed as it cooled and are hot disk models (Grossman 2010). Others state that the early Solar System was quite cool and that different components of chondritic meteorites

formed from the melting of nebular dust through shock waves and are cold disk models (Wood 1996). As the formation of chondritic components occurred from hot melt regardless of the conditions of the early Solar System (Grossman 2010; Wood 1996), the following description of chondrite formation will follow the hot disk model, such that the condensation of components follows a simple sequence that can be succinctly summarized. However, these chondritic components would have formed in a similar order according to cold disk models (Wood 1996).
.

According to hot disk models, the first solids of the Solar System condensed out of the cooling high temperature gas. This condensation would likely have started in the inner solar nebula (Grossman 2010).

The first minerals that formed occur within calcium aluminium rich inclusions (CAIs) (Fig. 1.6) and refractory inclusions hosted by chondritic meteorites (Grossman 2010). These CAIs have mineralogies consistent with condensation from a nebular gas (Ebel 2006; Fig. 1.7). Corundum (Al_2O_3) was the first mineral to condense in the protoplanetary disk at 1730 K, however it is rarely found in meteorites (Grossman 2010; Anand & Mezger 2023). This is because much of it reacted with gaseous Ca to form hibonite ($CaAl_{12}O_{19}$). As temperatures cooled to 1650 K, Ca-Al oxides, such as hibonite, grossite ($CaAl_4O_7$), and calcium monoaluminate ($CaAl_2O_4$) condensed. Perovskite ($CaTiO_3$) was the next mineral to appear, having condensed at 1600 K (Grossman 2010; Anand & Mezger 2023). Continual cooling led to the first silicate mineral, melilite ($Ca_2Al_2SiO_7$-$Ca_2MgSi_2O_7$) to condense at 1400 K. In the next stage of

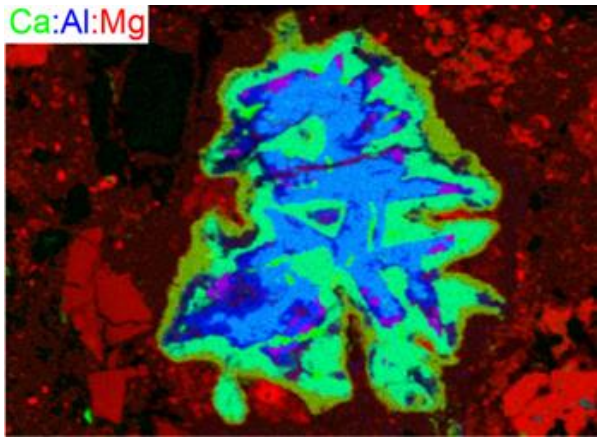

Fig. 1.6. Energy-dispersive X-ray spectroscopy map of a CAI composed of melilite (light green), grossite (blue), perovskite (purple), and diopside (goldenrod) in the CO chondrite Dominion Range 08006. From Zhang et al. (2020).

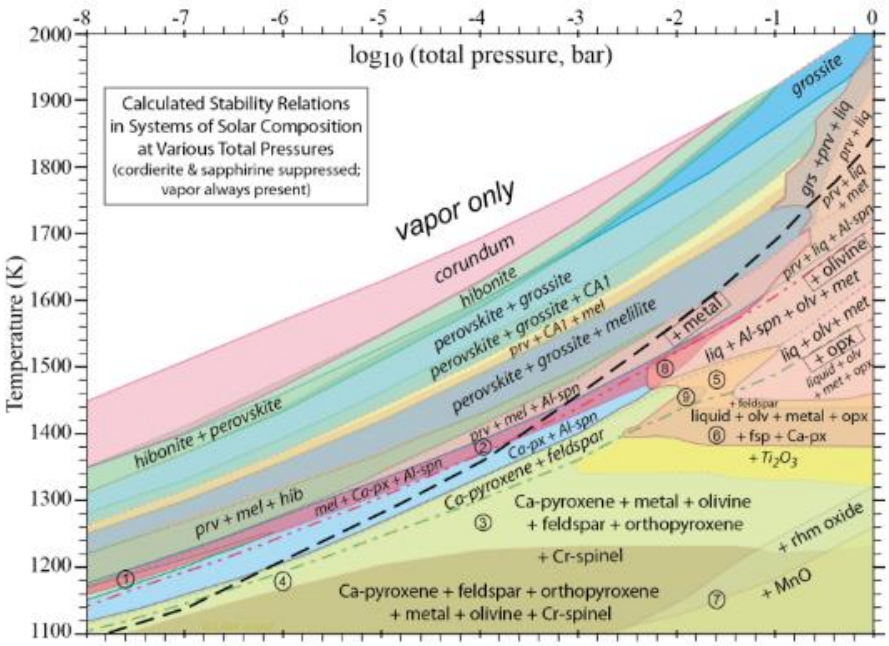

Fig. 1.7. Temperature-pressure stability of the first phases to condense out of the solar nebula. From Ebel (2006).

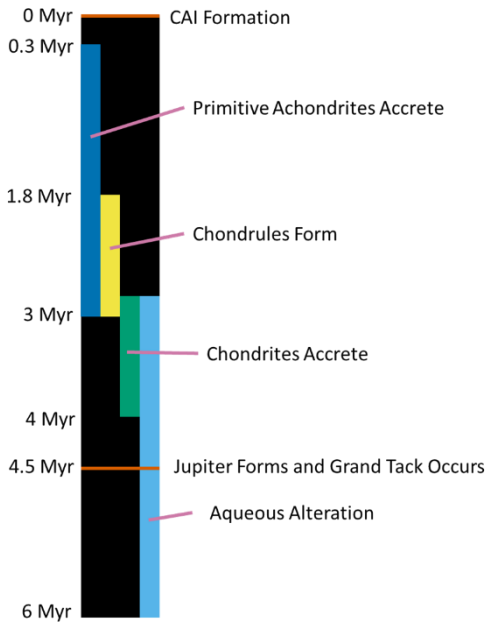

Fig. 1.8. Timeline of major events in the early protoplanetary disk, spanning the first 6 Myr after CAI formation. Years are given in relation to CAI formation, with 0 Myr marking when CAIs formed.

condensation, some of the hibonite reacted with Mg to make spinels, followed by some of the melilite reacting with the nebular gas to form Ti-bearing clinopyroxene, Al-bearing pyroxene, and anorthite (Grossman 2010; Anand & Mezger 2023)(Fig. 1.7). These reactions happened shortly after the collapse of the molecular cloud, at 4.568 Ga (Fig. 1.8), and the production of CAIs spanned 20 kyr (Anand & Mezger 2023). These CAIs and refractory inclusions likely formed close to the early Sun (<0.1 AU) and were transported further out into the

planetary disk prior to their incorporation into chondritic meteorites (Jacquet 2014).

Following the condensation of CAIs and refractory inclusions, was Fe-Ni metal (Grossman 2010). Silicates, like olivine and pyroxene, condensed shortly after the Fe-Ni metal, followed by sulphides and oxides (Ganapathy & Anders 1974). These, alongside CAIs, sulphides, refractory inclusions, dust, and other phases clumped together into the precursors to the chondrules found in many chondrites (Hewins & Zanda 2012; Lofgren & Russell 1986; Krot et al. 2018). Some even posit that fragments of early planetesimals served as chondrule precursors (Krot et al. 2018).

These precursors were later melted and formed the chondrules that make up most chondritic meteorites (Hezel & Palme 2007). How these precursors melted is still debated, however leading models include them being melt droplets from collisions of planetary bodies, precursors being melted by solar flares and then transported by X-winds, and precursors being heated following a shock wave in the protoplanetary disk (Fig. 1.9) (Connolly Jr. & Desch 2004). Chondrules may have undergone multiple heating events, with some showing the remains of previous iterations of the chondrule itself and/or igneous rims (Krot et al. 2018). Overall, chondrules formed ~1.8-3 Ma after CAIs (Fig. 1.8) (Anand & Mezger 2023).

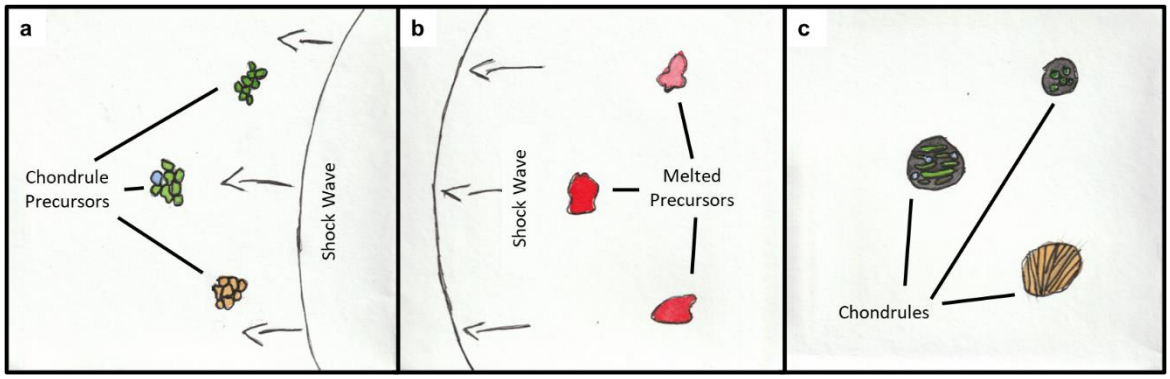

Fig. 1.9. Chondrule formation by nebular shock waves. a) Chondrule precursors encounter a nebular shock wave. b) Precursors melt due to drag heating as the shock wave passes. c) The melt cools and crystallizes into chondrules.

Other components of chondritic meteorites, such as organics and the ices that would later facilitate aqueous alteration likely condensed after chondrules (Jacquet 2014). Graphite (C) formed before organics, which in turn formed before ices (e.g., water ice, CO_2 ice), most of which likely condensed in the

outer Solar System (Wood & Hashimoto 1993). The formation of organics likely involved the reaction of C-bearing gases (e.g., CO_2, CH_4) with other gases within the nebula (e.g., nitrogen, hydrogen) (Cody et al. 2011). The organics that were created would have most likely been insoluble organic matter (IOM), which is composed of complex hydrocarbon polymers that aren't soluble in water, hence their names (Wasson 2008). The condensation of ices would have to occur beyond what is known as the snow line, where temperatures were ≤170K (Jacquet 2014). Where the snow line is within the protoplanetary disk changed over time, getting closer to the Sun as the Solar System cooled (Ciesla & Cuzzi 2006).

Regarding organic matter within carbonaceous chondrite meteorites, it is also important to note that although organic matter may have condensed within the early Solar System (Wood & Hashimoto 1993; Busemann et al. 2006), it could also have been brought in from the interstellar medium (Asaduzzaman et al. 2014; Busemann et al. 2006; Cody et al. 2011). However, the potential interstellar origin of some organic matter within carbonaceous chondrites is still debated (Wasson 2008; Tartese et al. 2018). Additionally, organic matter may have formed after nebular condensation, during parent body alteration at low temperatures (Cody et al. 2011), although this origin is also debated (Tartese et al. 2018).

1.2 Formation of Asteroids

After the creation of CAIs, chondrules, ices and other materials, these materials came together to make the parent asteroids of carbonaceous chondrites in a process called accretion (Weidenschilling 2019). To form their fine-grained rims (FGRs), chondrules collided with fine-grained material (e.g., amorphous silicates, sulphides, anhydrous silicates, organic matter) which stuck to their outer surface. Accretion of these compound objects into what would become the parent bodies of meteorites occurred with chondrules colliding both with each other and with other solid material (e.g., fine-grained material that would become matrix and CAIs) (Zanetta et al. 2021). The asteroids that would serve as the parent bodies of primitive achondrites accreted first (Huss et al. 2001), forming 0.3-3 Ma after CAIs (Fig. 1.8) (Anand & Mezger 2023). This is because in the early Solar System there is an abundance of the radioactive

nuclide ^{26}Al, whose half-life is 730 kyr. Decay of ^{26}Al produced substantial heat, which with its abundance prior to 3 Ma would have lead to melting and recrystallization of the first formed asteroids (Huss et al. 2001).

Chondritic asteroids accreted over a short timescale, 2.8-4 Myr after CAIs (Fig. 1.8) (Huss et al. 2001; Anand & Mezger 2023). The parent bodies of carbonaceous chondrites formed in the outer Solar System, typically beyond the snow line at the time, over 2.8 AU from the Sun (Walsh et al. 2011; Walsh et al. 2012).

Following asteroids, bodies larger than 1 km in diameter, known as planetesimals, began to form. Some planetesimals, such as the originators of many achondritic meteorites, accreted prior to chondritic asteroids (Huss et al. 2001). Jupiter also formed quite early in the Solar System's history, at around 4-5 Myr after CAI formation (Fig. 1.8). Due to Jupiter's large mass, it disrupted the orbits of asteroids and planetary bodies. The most commonly accepted model for how its movements changed asteroid distribution is known as the Grand Tack Hypothesis (Fig. 1.10), which relates to a time shortly after Jupiter's formation (Walsh et al. 2011; Walsh et al. 2012). As planets grow in size, they begin to tidally interact with the star in their star system, exchanging angular momentum (Matsumura et al. 2007; Masset & Snellgrove 2001). Jupiter began to move inwards at first, forcing most asteroids in the inner Solar System (e.g., composed mainly of ordinary chondrite material) closer to the Sun, while expelling a small portion to the outer Solar System. This was followed by Saturn migrating inwards, until the orbits of both Jupiter and Saturn interacted with each other in such a manner that both planets began migrating back out (Walsh et al. 2011). During this outward migration, the orbits of the parent asteroids of carbonaceous chondrites were affected. Along with asteroids of other types, some of the carbonaceous parent bodies were forced into stable orbits where the asteroid belt is now. The parent bodies of carbonaceous chondrites, particularly C-complex asteroids, eventually comprised the bulk of the outer asteroid belt (Walsh et al. 2012).

Today's asteroid belt is composed of a variety of asteroid types and can be sorted into seven zones (Fig. 1.11): Hungaria (1.8-2.1 AU), Inner (2.1-2.5 AU), Middle (2.5-2.9 AU), Outer (2.9-3.3 AU), Cybele (3.3-3.6 AU), Hilda (3.6-4.0 AU),

and Trojan (5.0-5.4 AU) (DeMeo & Carry 2014). The Hungaria zone is mainly composed of highly reflective E-type asteroids (DeMeo & Carry 2014), which are potential parents of enstatite-rich achondrites known as aubrites, although it may represent material that is not present in the meteorite record (Clark et al. 2004). The inner asteroid belt is mainly composed of C-complex asteroids (DeMeo & Carry 2014) but also has an abundance of S-type asteroids (Gradie & Tedesco 1982), from which ordinary chondrites are derived (Nakamura et al. 2011). C-complex asteroids make up the majority of both the inner and outer belt (DeMeo & Carry 2014) and are the originators for carbonaceous chondrites (Bates et al. 2020). Both the Cybele and Hilda regions of the asteroid belt are composed of P-type asteroids (DeMeo & Carry 2014), which have spectra consistent with the presence of organics, which may also link them to carbonaceous chondrites (Brown et al. 2000) or may be material unrepresented in the meteorite record (Hiroi et al. 2001). The Trojan asteroids share their orbit with Jupiter (McNeill et al. 2021) and are mainly composed of D-type asteroids (DeMeo & Carry 2014), which, like P-type bodies also have spectra consistent with an abundance of organics and volatiles. They may also be unrepresented by

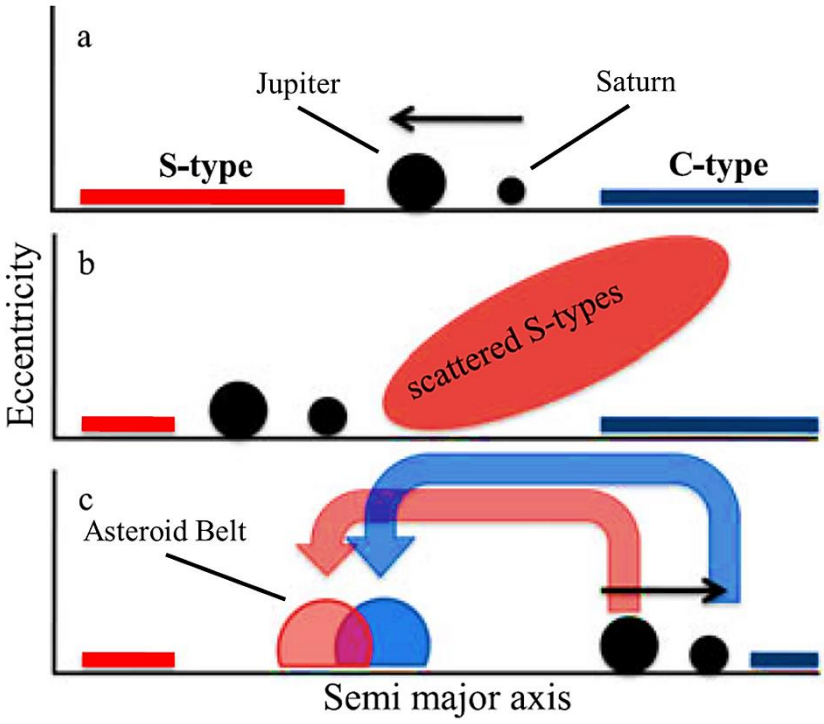

Fig. 1.10. Schematic of the Grand Tack model after Walsh et al. (2012). Volatile poor asteroids are shown in red while volatile rich ones are in blue. Gas planets are black. a) Jupiter and Saturn form. They begin to migrate inwards. b) The migration of Jupiter causes some volatile poor asteroids in the inner solar system (e.g., S-type) to be scattered outwards. c) Saturn gets close enough to Jupiter to cause both to migrate back outwards, pushing a portion of both volatile poor and volatile rich asteroids into their current orbits in the asteroid belt.

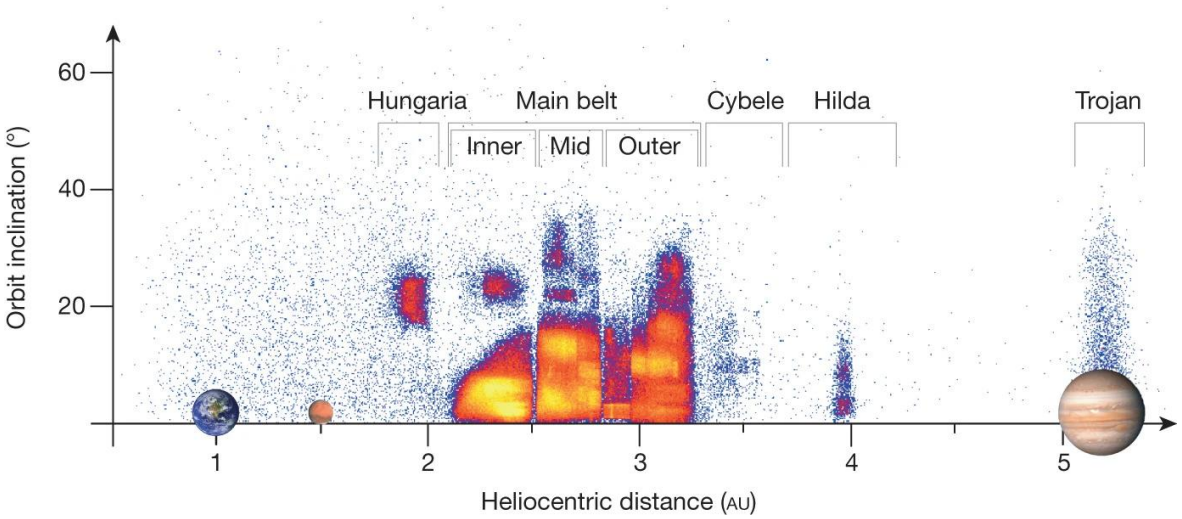

Fig. 1.11 The seven zones of the asteroid belt with the density of asteroids represented by blue (low), red (moderate), and yellow (high). Earth, Mars, and Jupiter are shown for reference. From DeMeo & Carry (2014).

the meteorite record or could be linked to carbonaceous chondrites (Hiroi et al. 2001). As of writing, confirmation of the composition of these asteroids in relation to the meteorite record is only be achievable with sample return missions. However, advances in observations of meteor falls through camera networks may open the possibility of connecting meteorite falls with parent asteroids (Jenniskens 2013). No meteorite has yet to be definitively linked to an asteroid, however.

1.2.1 C-Complex Asteroids

C-complex asteroids are a large grouping that share spectral characteristics, having low albedos and flat spectral slopes beyond wavelengths of 0.4 μm with absorption features that are shallow or non-existent. The C-complex asteroids can be further divided into subclasses based on the presence of an absorption feature related to phyllosilicates at a wavelength of 0.7 μm, with B and C-type asteroids having that absorption feature and G-type asteroids lacking it (Bus & Binzel 2002). B- and C-type asteroids are differentiated by their spectral slopes, with B-type having a negative slope (DeMeo et al. 2009). The C-type asteroids can also be further divided into other subtypes based on various different characteristics of their spectra (Fig. 1.12) (Bus & Binzel 2002; DeMeo et al. 2009). Due to having spectral characteristics consistent with water and phyllosilicates, C-complex asteroids are thought to be the parent bodies of

carbonaceous chondrites. Additionally, their reflectance spectra share certain features with carbonaceous chondrite meteorites (Fig. 1.13), with differences to the meteorites potentially being due to terrestrial and/or space weathering (Otrowski et al. 2011). Samples returned from the C-type asteroid Ryugu are also composed of material analogous to CI chondrites, confirming the role of C-complex asteroids as a source of carbonaceous meteorites (Yokoyama et al. 2022).

CM meteorites, like many carbonaceous chondrites, contain abundant phyllosilicates and share spectral characteristics with C-complex asteroids. Their parent asteroids are likely B-type asteroids (e.g., Bennu, Fig. 1.14) or one of the many subtypes of C-type asteroids (Bates et al. 2020).

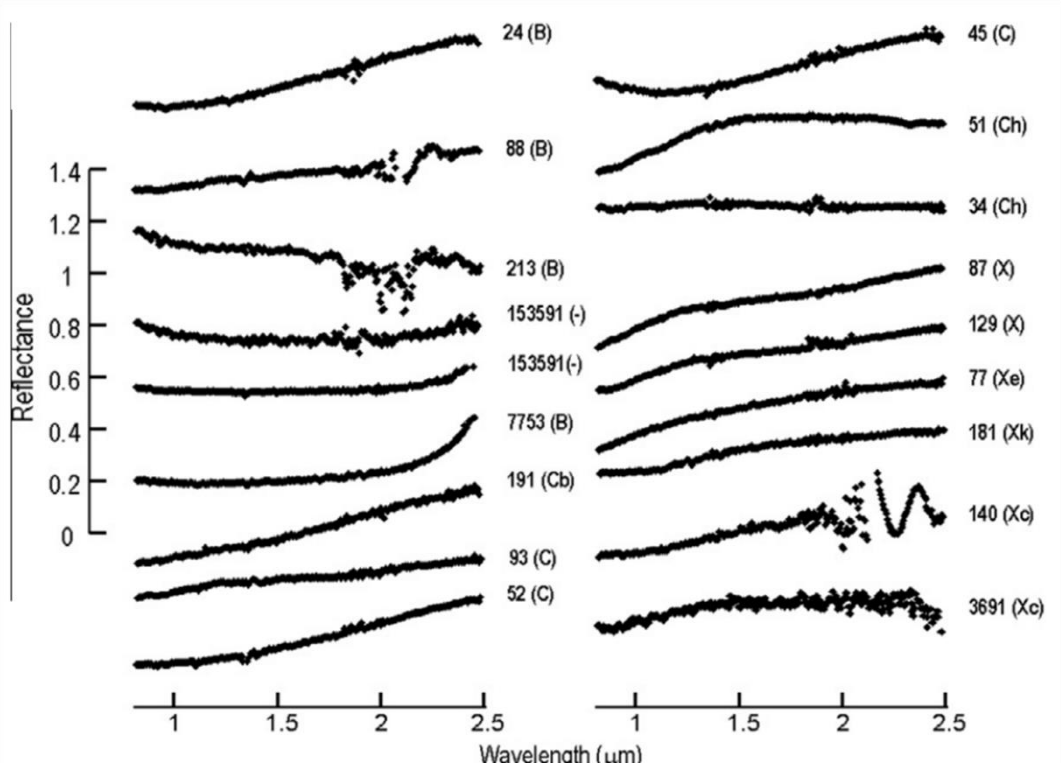

Fig. 1.12. Reflectance spectra of various C-complex and X-complex asteroids. The X-complex includes P-type asteroids. From Otrowski et al. (2011).

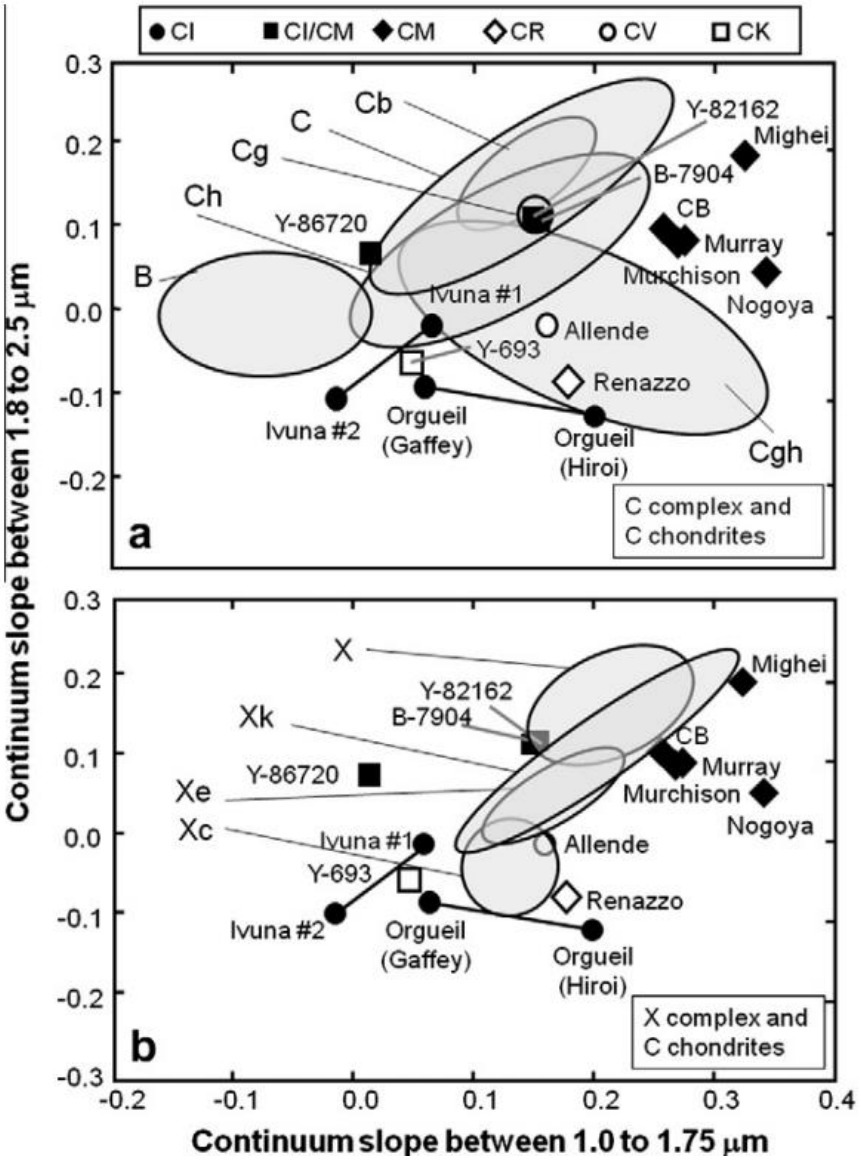

Fig. 1.13. Comparison of the slopes of reflectance spectra between asteroid types and different carbonaceous chondrite meteorites from Otrowski et al. (2011). Asteroidal spectra are marked by large grey circles while meteorite spectra is marked by small circles, squares, and diamonds, either black or white. The continuum slope between 1.8 and 2.5 μm corresponds to absorption features consistent with water, while the continuum slope between 1.0 and 1.75 μm corresponds to a variety of other key absorption features required to differentiate asteroid types. a) Comparison with C-complex asteroids. b) Comparison with X-complex asteroids.

1.3 CM Chondrites and Their Processing

CM chondrites are a highly petrologically variable group of carbonaceous meteorites whose main components are defined by the aqueous alteration that produced them. Even the most primitive CM chondrites have been affected by water and contain minor amounts of phyllosilicates (Kimura et al. 2020). Primary components that are common in CM chondrites are olivine and pyroxene (in chondrules and as individual) silicate fragments, CAIs and refractory inclusions,

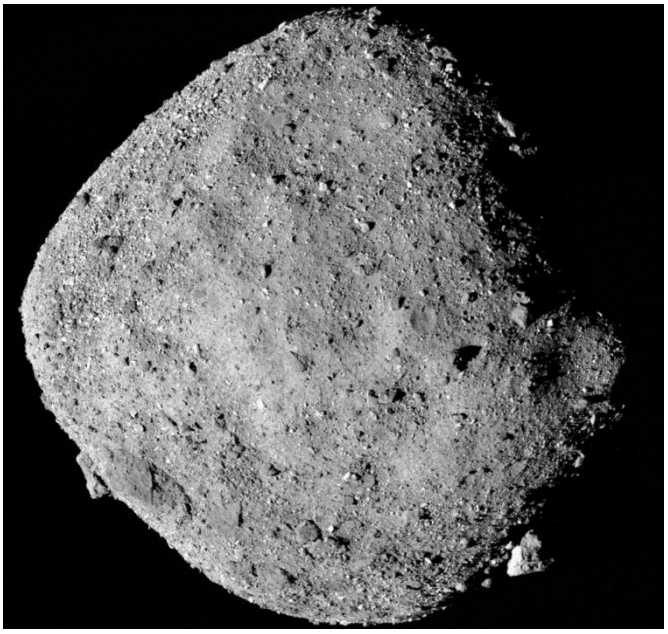

Fig. 1.14. The B-type asteroid Bennu. From Brann (2020).

sulphides, and minor amounts of Fe-Ni metal (Rubin et al. 2007). Other primary components that are usually found in the least altered CM chondrites are chondrule mesostasis glass, plagioclase feldspar, nanosulphides, amorphous silicates, and glass with embedded metal and sulphides (GEMS) (Kimura et al. 2020; Ohtaki et al. 2021). Due to the aqueous alteration CM meteorites have experienced, most CM chondrites are predominately made up of serpentine minerals (lizardite – $Mg_3(Si_2O_5)(OH)_4$, and cronstedtite– $Fe^{2+}_2Fe^{3+}(Si_2O_5)(OH)_4$), as well as the hydrous sulphide tochilinite. These common minerals may occur on their own (e.g., as a serpentine matrix, serpentine FGRs, as globules of tochilinite) or can be intergrown as TCIs. Other alteration phases commonly found in CM chondrites are carbonates, typically calcite, and secondary sulphides (e.g., pyrrhotite - $Fe_{(1-x)}S$, troilite - FeS, pentlandite – $(Fe,Ni)_9S_8$). Phosphates (e.g., apatite – $Ca_{10}(PO_4)_6(OH,F,Cl)_2$), oxides (e.g., magnetite), and clinopyroxenes (Rubin et al. 2007; Palmer & Lauretta 2011; Howard et al. 2015).

The proportion of primary and secondary components in CM chondrites can vary greatly depending on the degree of aqueous alteration that the meteorites have experienced. Typically, a CM chondrite will be made up of mostly lizardite (~22-66 vol%), cronstedtite and tochilinite (~0-50 vol%) (Howard et al. 2015; Rubin et al. 2007), however the least altered CM chondrites might have very little of these phases (Kimura et al. 2020). Chondrules are commonly a significant component (Fig. 1.15a), with up to a third of the volume of CM

chondrites made up of chondrules. Chondrule components like olivine and pyroxene make up ~0-17 vol% and ~0-13 vol% of CM chondrites, respectively (Howard et al. 2015). The most altered CM chondrites will be completely devoid of chondrules and anhydrous silicates, often having chondrule pseudomorphs instead (Fig. 1.15b) (Rubin et al. 2007). What is consistent among the CM chondrites is that over 50 vol% of a CM chondrite will be made up of its matrix, whether it is composed of TCIs, serpentine, or anhydrous phases (Howard et al. 2015; Kimura et al. 2020).

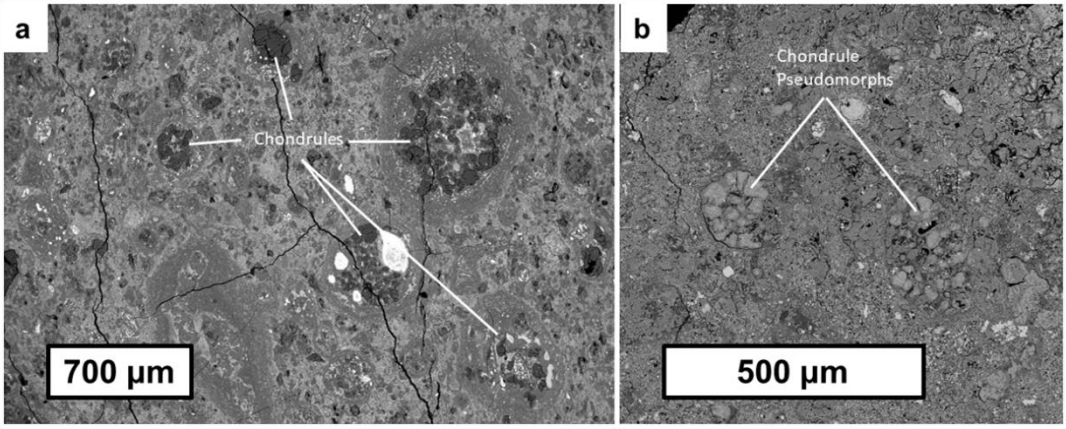

Fig. 1.15. Backscattered electron images of CM chondrites. a) BSE image of the CM2.2 chondrite Shidian showing chondrules with serpentine FGRs set in a matrix composed of both TCIs and serpentine. b) BSE image of a CM1 clast within Winchcombe showing chondrule pseudomorphs set in a matrix of serpentine.

Not only does bulk mineralogy differ between individual meteorites, but a given CM may have a fine-scale variability. Most, if not all, CM chondrites are breccias, containing clasts of varying lithologies (Lentfort et al. 2020; Rubin et al. 2007). They likely originate from the regolith of their parent asteroids, which is supported by the fact that many CM chondrites contain noble gases consistent with being exposed to solar wind (Kriestch et al. 2021).

1.3.1 Aqueous Alteration

Whilst still a part of their parent asteroids, many carbonaceous chondrites underwent alteration, in the form of thermal metamorphism and/or aqueous alteration. Both types of alteration required the parent asteroids to be heated, the most likely means of which was the radioactive decay of ^{26}Al, which was present in most CAIs in chondritic parent bodies (Huss et al. 2001). Both thermal metamorphism and aqueous alteration occurred for at least 2-6 Myr after CAI formation (Fig. 1.8) (Visser et al. 2020), though thermal metamorphism of other

chondrite types (e.g., ordinary chondrites) continued up 17 Myr after CAIs (Anand & Mezger 2023). Aqueous alteration occurred at low temperatures, with estimates ranging from 0°C (Clayton & Mayeda 1999) to 240°C (Busemann et al. 2007). A few CM chondrites have experienced other processes in addition to aqueous alteration. As of writing, there has yet to be a completely unaltered CM chondrite identified.

This thesis looks at many alteration phases within CM chondrites, as there are many questions to be explored through these phases. One aqueous alteration phase that requires discussion is the hydrous sulphide tochilinite, which has many aspects (e.g., decomposition temperature) that are unknown. Historically, before being identified, tochilinite was referred to as a "poorly characterized phase" (PCP), that occurred as intergrowths with other phases, known as type-I and type-II PCPs (Fuchs et al. 1973; Tomeoka & Buseck 1985; Vacher et al. 2019), which later got renamed to type-I and type-II TCIs, despite type-I TCIs containing insignificant amounts of cronstedtite (Vacher et al. 2019). To avoid confusion, in this thesis, type-II TCIs will be referred to as TCIs and type-I TCIs will be referred to as tochilinite globules to better represent their contents. However, both assemblages contain tochilinite and are therefore key-indicators of various alteration processes.

Traditionally, from the alteration experienced, meteorites including CMs are sorted by petrographic type on Van Schmus & Wood's (1967) scale. There have been several other petrologic scales developed to further organise CM chondrites into different types or subtypes based on their degree of aqueous alteration. The main petrographic scales traditionally used are the Rubin scale (Rubin et al., 2007; Rubin 2015), the Alexander scale (Alexander et al. 2013), and the Howard scale (Howard et al. 2015) (Fig. 1.16). Although bulk CM chondrites may be sorted into a singular classification with these scales, it is important to note that most, if not all, CM chondrites are brecciated and may contain clasts spanning a variety of lithologies and alteration levels (Rubin et al. 2007; Lentfort et al. 2020; Bischoff 1998). A singular classification may not represent variation within the CM chondrite itself.

The Rubin scale (Fig. 1.17) was originally created by Rubin et al. (2007), and later updated by Rubin (2015) and Kimura et al. (2020). It was created for a

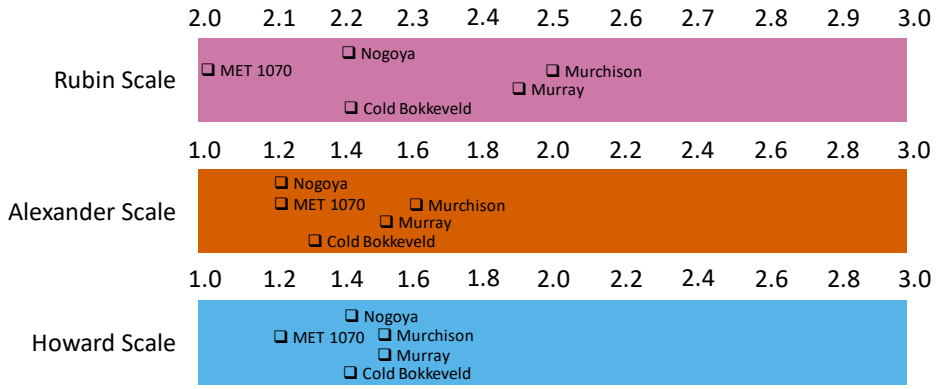

Fig. 1.16. Comparison of the main three petrologic scales used to classify CM chondrites in terms of degree of aqueous alteration experienced. CM chondrites classified by Rubin et al. (2007), Rubin (2015), Alexander et al. (2013), and Howard et al. (2015) are presented.

Petrologic subtype	2.7	2.6	2.5	2.4	2.3	2.2	2.1	2.0
Chondrule mesostases	Phyllosilicate	Phyllosilicate	Phyllosilicate	Phyllosilicate	Phyllosilicate	Phyllosilicate	Phyllosilicate	Phyllosilicate
Matrix phyllosilicates	Abundant	Abundant	Abundant	Abundant	Abundant	Abundant	Abundant	Abundant
Matrix composition: MgO/"feo"	0.35–0.43	0.35–0.43	0.35–0.43	0.35–0.43	0.50–0.70	0.50–0.70	0.50–0.70	0.50–0.70
Matrix composition: S/SiO_2	0.10–0.18	0.10–0.18	0.10–0.16	0.10–0.16	0.07–0.08	0.07–0.08	0.05–0.07	0.05–0.07
Metallic Fe-Ni (vol%)	1–2	~1	0.03–0.30	0.03–0.30	0.03–0.30	0.03–0.30	≤0.02	≤0.02
Mafic silicate phenocrysts in chondrules	Unaltered	Unaltered	Unaltered	Unaltered	2–15% altered	15–85% altered	85–99% altered	Completely altered
Large TCI clumps (vol%)	5–20	15–40	15–40	15–40	15–40	15–40	2–5	2–5
TCI composition: "FeO"/SiO_2	4.0–7.0	2.0–3.3	2.0–3.3	1.5–2.0	1.5–2.0	1.0–1.7	1.0–1.7	1.0–1.7
TCI composition: S/SiO_2	0.40–0.60	0.18–0.35	0.18–0.35	0.14–0.20	0.14–0.20	0.05–0.09	0.05–0.09	0.05–0.09
Sulfide	po + pn	Mainly po + pn	Mainly po + pn	po + pn + int	po + pn + int	Mainly pn + int	Mainly pn + int	Mainly pn + int
Carbonate	Ca carbonate	Ca carbonate	Ca carbonate	Ca carbonate	Ca carbonate	Ca carbonate	Ca carbonate and complex carbonate	Ca carbonate and complex carbonate

"FeO" includes FeO in mafic silicates, oxides, and phyllosilicates, Fe^{3+} in cronstedtite and magnetite, Fe^{2+} in sulfides, and small grains of metallic Fe all recalculated as FeO. Subtype 2.6 is distinguishable from 2.5 on the basis of metallic Fe-Ni abundance; subtype 2.1 is distinguishable from 2.0 on the basis of containing rare but identifiable mafic silicate phenocrysts in chondrules.

Fig. 1.17. Rubin petrologic subtype scale from Rubin (2015). Po refers to pyrrhotite, Pn refers to pentlandite, and int refers to sulphides with compositions between Po and Pn. Complex carbonates are carbonates that have more cations than just Ca making up a significant aspect of their composition (e.g., dolomite).

mixture of CM2 and CM1 meteorites, however best reflects variation among the CM2 group, with CM1 meteorites all getting sorted into 2.0. The Rubin scale accounts for a mixture of petrographic and geochemical characteristics, such as the percentage of altered chondrules, and TCI chemical composition. The updated Rubin (2015) scale ranges from 2.0 to 2.7, where 2.0 is completely altered and 2.7 is least altered. Kimura et al. (2020) has proposed criteria for 2.8-3.0 meteorites as an update for this scale.

According to the Rubin scale, the defining characteristics of a least altered CM chondrite (2.7) is that the mafic silicates are unaltered and that there is a small amount of TCIs, with the TCIs being relatively enriched in S and the serpentine matrix being relatively depleted in MgO (Rubin 2015). As alteration progresses, mafic silicates and any remaining unaltered metal will

alter. TCI abundances will initially increase before the TCIs themselves get replaced by serpentine, with the most altered CM chondrites, CM2.0, having less TCIs than the least altered (Rubin 2015). Additionally, the more altered a CM chondrite is, the less pyrrhotite and the more pentlandite it will have. Geochemical changes according to the Rubin scale consist of the serpentine matrix becoming more MgO rich and the TCIs becoming depleted in S. A less altered CM chondrite will have only calcium carbonate (e.g., calcite, aragonite), however complex carbonates containing significant amounts of other cations (e.g., Mn-bearing carbonates, dolomite – $CaMg(CO_3)_2$) will form as alteration progresses (Rubin 2015).

Kimura et al. (2020) studied some CM chondrites that were even less altered than CM2.7 and expanded the Rubin scale accordingly, proposing that a 3.0 CM chondrite (Asuka 12169) had been found. Their expansion follows the initial Rubin (2015) scale with a decrease in TCIs and an increase in metal abundance as alteration decreases. The 3.0 CM chondrite they propose has an abundance of amorphous silicates, no TCIs and over 2 vol% metal, with rare phyllosilicates and carbonates.

The Alexander scale uses the amount of H in water and OH to quantify the degree of aqueous alteration of bulk meteorite samples and so sort them into petrologic types. These types range from 1.0 to 3.0, with 1.0 representing a meteorite that has 1.44 wt% H, 2.0 representing a meteorite with 0.7 wt% H, and 3.0 representing an anhydrous meteorite (e.g., ~0 wt% H) (Alexander et al. 2013).

The Howard scale takes a mineralogical approach to defining aqueous alteration, using the abundances of phyllosilicates relative to anhydrous silicates. It is distinctly separate from the classification scheme of Van Schmus & Wood (1967) and is intended to be used in addition to it. The scale ranges from petrologic type 1.0 to 3.0, where 1.0 is a CM chondrite whose phyllosilicate fraction is over 95 vol% and 3.0 is a CM chondrite whose phyllosilicate fraction is less than 5 vol% phyllosilicates. A type 1.7 meteorite may be composed of ~50 vol% phyllosilicates, while a type 1.1 will be composed of ~83 vol% phyllosilicates (Howard et al. 2015).

In addition to these three commonly used petrographic scales, there have also been attempts to adapt the scales further, whether it be by adding components to make them more representative of the complex alteration CM chondrites experience, or by attempting to simplify them to only one or two criteria. Lee et al. (2019b) looks at the proportion of unaltered FGRs around chondrules relative to alteration minerals (serpentine, TCIs, carbonates) present in CM chondrites, and compares that to their petrologic subtypes based on the Alexander scale. A formal scale has not been created using Lee et al.'s (2019b) method, however it bears similarity to the Howard scale and accounts for a greater proportion of alteration products beyond phyllosilicate fraction.

Another attempt was conducted by Lentfort et al. (2020), where all petrographic components of the Rubin scale were removed apart for TCI chemical composition. This scale was developed to help classify the clasts, as CM chondrites more often than not are brecciated. Although Lentfort et al. (2020)'s approach simplifies the process, it ignores other aspects of alteration, such as the heterogeneity of fluids responsible for aqueous alteration in CMs (Suttle et al. 2022), so its use is limited.

1.3.2 Metasomatism

Metasomatism is the chemical replacement of minerals facilitated by fluids, but there are no clear temperature-pressure constraints on its operation (Harlov & Austraheim 2013). This definition also fits the process of aqueous alteration experienced by many carbonaceous chondrites, where mineral replacement by serpentine and tochilinite is facilitated by water. Despite similar definitions, aqueous alteration and metasomatism are typically treated as distinct processes. One way to reconcile this overlap was proposed by Brearley and Krot (2013) whereby aqueous alteration is restricted to water-mediated alteration whose primary products are phyllosilicates.

Although CM chondrites usually show evidence for only aqueous alteration, a few do contain metasomatic minerals. The most well-known of these metasomatic mineral bearing CM chondrites is Meteorite Hills 01075, which contains a CAI with sodalite ($Na_8Al_6Si_6O_{24}Cl_2$), indicating metasomatism occurring at temperatures exceeding 100°C (Lee et al. 2019a).

1.3.3 Post-Hydration Heating

Post-hydration heating is the term given to thermal metamorphism that occurs after a carbonaceous chondrite has experienced aqueous alteration (Nakamura 2005). It occurs at temperatures exceeding 150°C and is typically experienced by CM chondrites and CY chondrites (King et al. 2019a). Although other carbonaceous chondrites also have evidence of post hydration heating (Yabuta et al. 2010; Chan et al. 2016; Tonui et al. 2014). Carbonaceous chondrites that have experienced post-hydration heating can be sorted into one of four heat stages defined by Nakamura (2005) based on their mineralogy.

Heat stage I meteorites have experienced heating at temperatures of 150-300°C and tend to lack crystalline tochilinite, which has decomposed to an amorphous phase. If heated for long enough, secondary sulphides and/or magnetite can recrystallize from the amorphous remnants of tochilinite (Fig. 1.18) (Nakamura 2005; Fuchs et al. 1973; Lindgren et al. 2020). The exact decomposition temperature of tochilinite is unknown, however it has been recorded to decompose at 245°C (Fuchs et al. 1973).

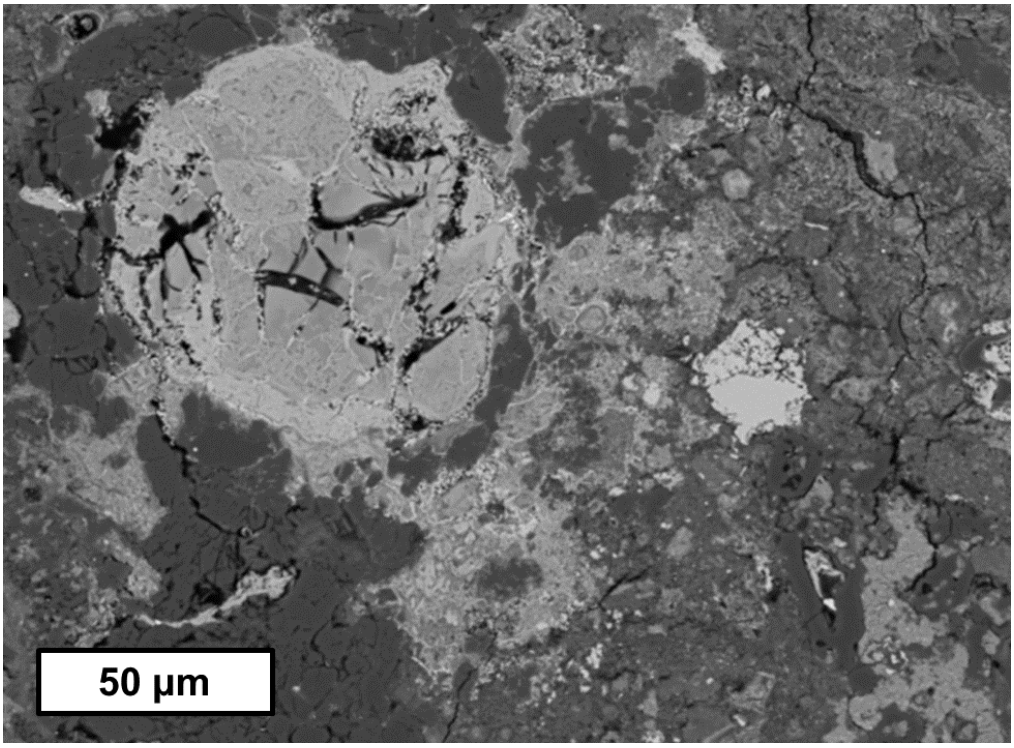

Fig. 1.18. Backscattered electron image of the remnants of a tochilinite globule within the heat stage IV CM chondrite PCA 91008 (upper left), which has experienced post-hydration heating. Large dehydration fractures can be seen, while small grains of sulphides have begun to form in a web-like texture.

Heat stage II meteorites are defined by the temperature range of 300-500°C. Under these conditions serpentine will decompose, becoming amorphous and/or transform into an intermediate transitional phase (Nakamura 2005; Akai 1988).

Heat stage III occurs at temperatures 500-750°C and is defined by the recrystallization of secondary anhydrous silicates, such as olivine and pyroxene (Nakamura 2005; Tonui et al. 2014; Lindgren et al. 2020). Pentlandite may also decompose into a mixture of troilite and taenite (Fe, Ni metal) (Nakato et al. 2008).

Any meteorite that has experienced temperatures exceeding 750°C belongs in heat stage IV. Here calcite decomposes and oldhamite (CaS) and/or clinopyroxene may form from its decomposition (Fig. 1.19) (Lindgren et al. 2020). Magnetite may also decompose into a mixture of taenite and kamacite (Fe, Ni metal) (Nakato et al. 2008). Secondary cristobalite (SiO_2) may also form (Akai 1990).

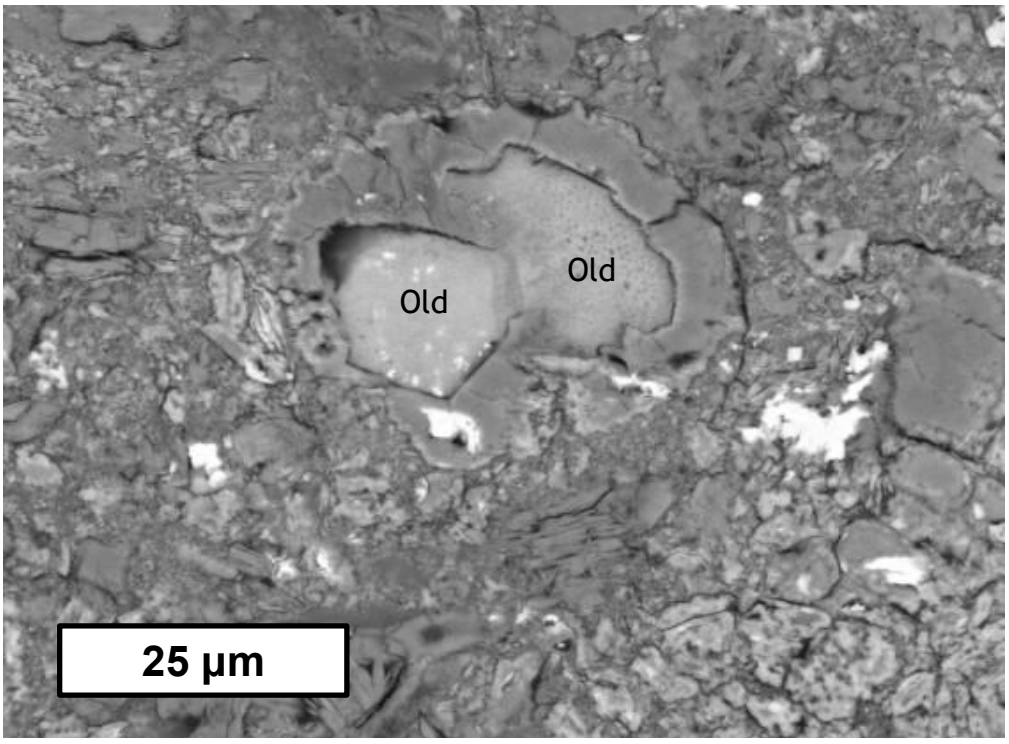

Fig. 1.19. Backscattered electron image of oldhamite (Old) in the CM-like carbonaceous chondrite Sutter's Mill. The oldhamite has pseudomorphically replaced calcium carbonate.

Post-hydration heating requires the meteorites to be thermally altered on their parent asteroids, yet the source of this heat is unknown. However there

have been numerous sources proposed including solar radiation, impact heating, and internal heating from ^{26}Al (Nakato et al. 2008). Despite the unknown cause for post-hydration heating, it has been deduced that the source of heat would have had to be a short-lived (e.g., hours to days), as chondritic olivine within heated CM chondrites shows little diffusion (Nakato et al. 2013) and that experimental reproductions of post-hydration heating required only 10-1000 days to recreate the mineralogy displayed by heated CM chondrites (Nakato et al. 2008). Raman spectra from organics within heated CM chondrites are also consistent with reactions due to heating occurring over short durations (Quirico et al. 2018). Due to the short-lived nature of post-hydration heating, impact and solar heating are the most plausible potential causes.

1.3.4 Shock Metamorphism

Impact events were ubiquitous in the Solar System with all rocky bodies being affected. Impacts lead to rocks experiencing extremely high pressures over short periods of time, changing their mineralogy and texture in distinctive ways. The effects of shock metamorphism on rocks composed of traditionally igneous minerals have been well studied, with numerous systems evaluating the level of shock metamorphism experienced in place (e.g., Stöffler 1971; Stöffler et al. 1991, Stöffler et al. 2018; Stöffler and Hornemann 1972; Uchizono et al. 1999; Izawa et al. 2011; Pickersgill et al. 2015; Rupert et al. 2020).

Traditionally, shock metamorphism is evaluated using a petrographic microscope, where a rock sample is sorted into the relevant shock stage based on the shock effects observed. The most recent commonly used iteration is the Stöffler et al. (1999) shock stage system, which has recently received a comprehensive update in the form of the Stöffler et al. (2018) shock stage system, where shock effects are further differentiated by rock type. However, there have been few studies on the effects of shock metamorphism on carbonaceous chondrites and/or analogue materials. As a consequence, carbonaceous chondrites often have their shock stages evaluated in the same manner of ordinary chondrites (Stöffler et al. 2018). Although this may work in some meteorite groups, because of the high amount of phyllosilicates in many aqueously altered carbonaceous chondrites, their anhydrous silicates (e.g., olivine, pyroxene) experience less strain and higher post-shock temperatures

than ordinary chondrites, as well as experiencing other shock effects like chondrule flattening and alignment (Tomeoka et al. 1999). Thus, the shock stage systems tailored towards ordinary chondrites can be a poor fit for some carbonaceous chondrites. However, as there has yet to be a better formal shock stage system proposed, Stöffler et al.'s (2018) system for chondrites is currently the best classification system in place that is widely used for carbonaceous chondrites.

For CM chondrites, it is recommended that one refer to the experimental work done by Tomeoka et al. (1999) (Fig. 1.20) in addition to applying traditional shock stage classification systems. In CM chondrites, silicates like olivine will start to display undulatory extinction at around ~4 GPa, however straight extinction may persist beyond 21 GPa, with the proportion of olivine displaying undulatory extinction increasing with peak shock pressure. Planar fractures within olivine will become noticeable at ~21 GPa, however are unlikely to continue beyond ~30 GPa due to disruption of silicate grains. The matrix will begin to display significant fracturing at ~10 GPa, with fracture density increasing until cataclasis at ~34 GPa. At ~26 GPa, these fractures may be infilled by porous fine-grained material. Formation of melt veins and pockets

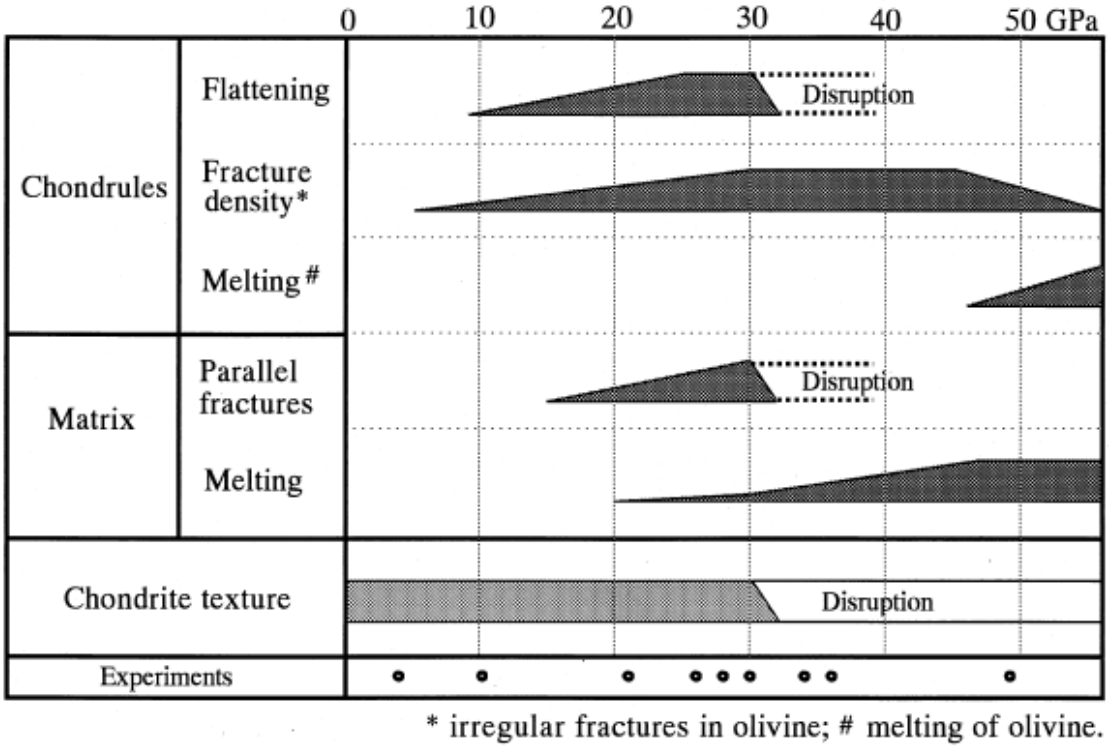

Fig. 1.20. Summary of major shock effects within the experimentally shocked CM chondrite Murchison from Tomeoka et al. (1999).

will begin at ~21 GPa. Chondrules will begin to flatten at ~10 GPa with flattening increasing until they completely disintegrate at ~34 GPa (Tomeoka e t al. 1999). Tomeoka et al. (1999) has proposed a calibration curve to relate chondrule aspect ratio to peak shock pressure, however this calibration curve is likely unsuitable as chondrule flattening can be caused by geologic processes other than impact events (See below and Chapter 7). These flattened chondrules will begin to show a petrofabric at ~21 GPa (Tomeoka et al. 1999). Any CM material that has experienced peak shock pressures beyond 34 GPa is unlikely to survive.

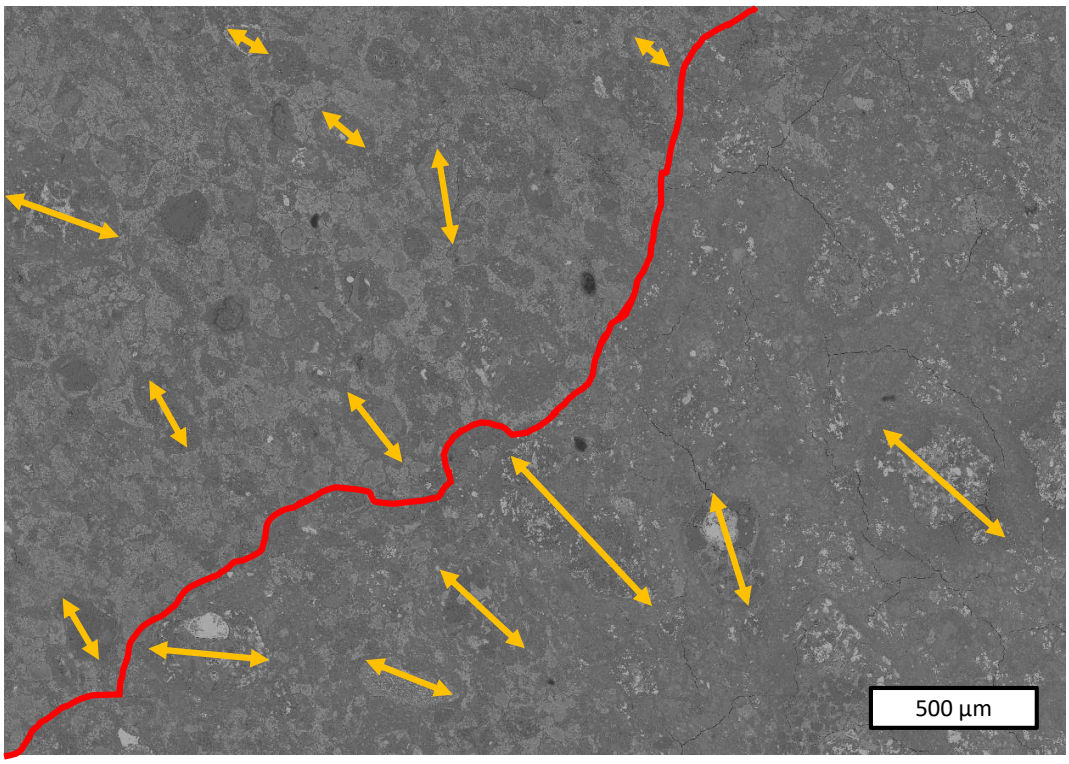

Fig. 1.21. Backscattered electron image of the CM chondrite Kolang showing a petrofabric. Chondrules and their long axes are marked by yellow arrows, while a clast boundary is marked in red.

1.3.5 Petrofabric Formation

Many carbonaceous chondrites have flattened ellipsoidal chondrules whose long axes are aligned into a petrofabric (Fig. 1.21) (Rubin 2012; Lindgren et al. 2015; Zolensky et al. 1997). Both chondrule flattening and alignment are effects shown by carbonaceous meteorites shocked beyond 10 GPa (Tomeoka et al. 1999; Nakamura et al. 1995). However, most carbonaceous chondrites, including those that display prominent petrofabrics, do not display other signs of shock metamorphism, with their olivine and pyroxene often being unstrained (Scott et al. 1992; Rubin 2012; Lindgren et al. 2015; Zolensky et al. 1997). A variety of explanations have been proposed for this incongruency: petrofabrics

being caused by burial compaction (Martin & Mills 1980), being caused by freeze-thaw cycles (Zolenksy et al. 1997), alignment of chondrules that originated as ellipsoids (Miura et al. 2008), petrofabrics forming at lower pressures than that displayed by experimental impacts (Rubin 2012), shock effects being erased by alteration (Rubin 2012), multiple-low intensity impacts being responsible (Lindgren et al. 2015), and brittle deformation accounting for the low degree of shock (Hanna et al. 2015).

1.3.6 Cosmic Ray Exposure Ages

For a meteoroid to reach Earth and become a meteorite, it must first be ejected from its parent body in an impact event. Once ejected, the meteoroid will be exposed to cosmic rays, which alter some of its constituent atoms, removing cations and/or neutrons. This process leads to the creation of various isotopes some of which are radioactive and can be used to measure how long a meteoroid has been exposed to cosmic rays. This is known as a cosmic ray exposure (CRE) age (McSween Jr. 1999). The amount of radioactive isotopes produced by cosmic rays varies with the depth of the exposed material (Wasson 1985). This technique can be used to determine when a meteorite was ejected from its parent body, however some meteorites may be exposed to cosmic rays on the surface of its parent body prior to ejection. The isotope systems used for this technique include ^{56}Fe-^{53}Mn, ^{83}Kr-^{81}Kr, ^{41}K-^{40}K-, ^{26}Al-^{21}Ne, ^{22}Ne-^{21}Ne, ^{38}Ar-^{21}Ne, ^{36}Ar-^{36}Cl, and ^{3}H-^{3}He, (McSween Jr. 1999; Wasson 1985; Herzog 2007). As many of these isotopes are difficult to measure, a mean between multiple isotopic systems is traditionally used to determine a meteorites CRE age (Wasson 1985).

Most CM chondrites typically have CRE ages below 10 Myr, which is considered fairly young when compared to many other meteorite groups. This difference may relate to their potential origin as regolith breccias (Krietsch et al. 2021) or may be due to their serpentine-rich composition preventing them from surviving in space for extended periods of time, leading to a survivorship bias of CM chondrites with young CRE ages (Eugster et al. 2006). A lot of CM chondrites have similar CRE ages and can be grouped together based on them. These similar CRE age groupings are at ~0.2, ~1, ~4.5-6, and ~8 Myr, with each grouping likely representing an impact event on the CM parent body(ies). Not all

CM chondrites have CRE ages that fall into these groupings. The largest of these groupings is the ~0.2 Myr grouping, with most CM chondrites having CRE ages on the order of hundreds of thousands of years (Krietsch et al. 2021).

1.3.7 Terrestrial Weathering

All meteorites experience terrestrial weathering to some degree as Earth's atmosphere is hydrolysing and oxidizing. During its fall, a meteor will form a fusion crust of various high-temperature phases, much of which is amorphous. The fusion crusts of carbonaceous chondrites contain abundant vesicles from phases devolatizing. During fusion crust formation, usually only primary pyroxene and olivine will survive. Various quenched minerals, including magnetite, olivine, and sulphides, will crystallize (Genge & Grady 1999). If a meteor is observed falling and is recovered afterwards, the meteorite is termed a fall and will typically experience minimal terrestrial alteration due to its short exposure time to uncontrolled weather and conditions. If a meteorite's fall is unwitnessed and it is identified later, it is termed a find (McSween Jr. 1999).

Terrestrial alteration is impossible to escape for meteorites, however meteorite finds will tend to be more weathered than meteorite falls. After landing, carbonaceous chondrites will absorb terrestrial water from the atmosphere (Jarosewich 1990; Lee et al. 2021a). Over time, any Fe-Ni metal present in meteorites will oxidize to form Fe-oxides and/or Fe-hydroxides, a process which can be noticeable within a few years of falling (Fuchs et al. 1973; Lee and Bland 2004; Lee et al. 202a1; Rubin et al. 2007).

If a meteorite is exposed to water prior to retrieval, a number of alteration processes can occur. Evaporite minerals can dissolve (Floyd and Lee 2021; Zolensky et al. 2014) as well as precipitate (Fuchs et al. 1973; Lee et al. 2021a). Common terrestrial precipitates found on both CM chondrite falls and finds are sulphates and carbonates (Lee et al. 2021a; Velbel 1988). Additionally, any sample processing undertaken during preparation for data collection or during data collection itself may also further alter CM chondrites.

1.4 Questions Pertaining to Alteration Processes in CM Chondrites

CM chondrites have experienced a series of alteration processes, both on their parent bodies and on Earth. However, there are a lot of unknowns surrounding these processes.

There have been numerous estimates regarding the temperatures CM chondrites have experienced during aqueous alteration and/or metasomatism (e.g., Clayton & Mayeda 1999; Buseman et al. 2007; Alexander et al. 2014), however a definite temperature has yet to be confirmed. By studying metasomatic phases within CM chondrites and the temperatures at which they form, the temperature of alteration may be further constrained. The metasomatic mineral hydroandradite in some CM chondrites has been studied to further constrain this process (Chapter 4).

A portion of CM chondrites are known to have experienced post-hydration heating and although mineral changes and transitions have been described, the exact temperature-timescale of the process has yet to be well constrained. Additionally, some mineral transitions occur at unknown temperatures (e.g., tochilinite decomposition), whereas other transitions have yet to be described (e.g., the formation of a transitional phase during serpentine decomposition). The cause of post-hydration heating is also unknown. By experimentally heating unheated carbonaceous chondrite samples to known temperatures for known durations, these mineral transitions can be studied in detail, giving a clear understanding of the process. This has been done with multiple CM chondrites under a variety of conditions (Chapter 5). Additionally, by comparing the mineralogy and texture of these experimentally heated meteorites to naturally heated ones, estimates of the duration can be further constrained, allowing the cause of post-hydration heating to be inferred. Eight naturally heated meteorites have been compared to two sets of experimentally heated CM chondrites (Chapter 6).

Petrofabrics are known to occur in carbonaceous chondrites and although there are numerous plausible causes, none of them have yet to be confirmed. Additionally, the low amount of shock and strain these carbonaceous chondrites

have often experienced, makes it difficult to reconcile them with the impacts commonly thought to cause them. By studying petrofabric formation in Kolang, where the petrofabric postdates all other alteration processes, the causes of chondrule flattening and alignment can be inferred (Chapter 7).

Terrestrial weathering occurs in all meteorite samples, however rapidly retrieved meteorites are often treated as if they are pristine. This assumption can lead to erroneous interpretations regarding parent body processes. Understanding the timescales of terrestrial weathering will allow for a greater scrutiny of potentially terrestrial phases, leading to more accurate interpretations of parent body processes. Some terrestrial evaporite minerals in the CM chondrite fall Winchcombe, whose retrieval was well documented, have been studied (Chapter 8).

Answering questions regarding the unknowns of varying processes that CM chondrites have experienced, from aqueous alteration and metasomatism to terrestrial weathering, will enable a greater understanding of not only CM chondrite meteorites and their parent C-complex asteroids, but of processes related to other meteorites. Additionally, information regarding terrestrial processes can be gleaned from these samples. It is therefore important to analyse these meteorites from a variety of perspectives.

Chapter 2 – Laboratory Methods

To study alteration processes on C-complex asteroids, a variety of laboratory techniques have been applied to the samples in this study. Each method yields different but complementary datasets from which key aspects of the samples can be discerned. They are summarized in Table 2.1.

2.1 – Scanning Electron Microscopy

Scanning electron microscopy (SEM) uses a focused beam of electrons, negatively charged particles that have an incredibly small mass (~9.11×10^{-31} kg). Electrons typically surround the nuclei of atoms in what are known as probability clouds, which describe the most likely position of electrons around the nucleus. This is because the small mass of the electrons makes it impossible to determine all of their properties (e.g., position, momentum) without altering them in the process (Orchin et al. 2005). It is important to note that although probability clouds are not orbits or shells, they are typically described as such to aid in the visualization of processes affecting atoms (e.g., changes between energy levels).

Due to their small mass, electrons can exhibit properties associated with waves (e.g., light, sound), such as having a wavelength and being able to diffract (Orchin et al. 2005). The wavelength of an electron can be described by Equation (2.1):

$$\lambda = \frac{h}{mv} \tag{2.1}$$

where λ is the wavelength given in m, h is the Planck constant (6.626×10^{-34} kg·m/s^2), m is the mass given in kg, and v is the velocity given in m/s (Egerton 2016).

Because of the wave-like properties of electrons, they can be used to determine properties of materials through their interactions with them (Egerton 2016). Electrons are able to penetrate different materials. The depths the electron penetrates depends on the material and also on their wavelength. The wavelength which can be changed by altering the velocity of electrons in the electron beam. SEM accelerates and focuses a beam of electrons onto a sample,

Table 2.1. Laboratory methods used.

Laboratory Instrument	Laboratory Location	Sample Types	Analytical Technique(s)	Data Obtained
Carl Zeiss Sigma Variable Pressure field emission gun Scanning Electron Microscope (SEM)	University of Glasgow (UoG)	Polished Sections	Backscattered Electron Imaging	Qualitative Chemical Analysis
			Secondary Electron Imaging	Qualitative Textural Analysis
			Energy Dispersive X-ray Spectrometry	Chemical Analysis
			Electron Backscatter Diffraction	Crystallography
FEI Quanta 200F Environmental SEM	UoG	Polished Sections	Cathodoluminescence	Petrography
CAMECA SX100 Electron Probe Microanalysis (EPMA)	University of Edinburgh	Polished Sections	Wavelength Dispersive X-ray Spectrometry (WDS)	High Precision Quantitative Chemical Analysis
CAMECA SX100 EPMA	Natural History Museum (NHM) London	Polished Sections	WDS	High Precision Quantitative Chemical Analysis
FEI T20 Transmission Electron Microscope	UoG	Electron Transparent Lamellae	Transmission Electron Microscopy	Crystallography
Renishaw Invia Raman microscope	UoG	Polished Sections	Raman Spectroscopy	Mineralogy
I11 High Resolution Powder Diffraction	Diamond Lightsource	Bulk Powders	Powdered X-ray Diffraction (pXRD)	Mineralogy
I18 The Microfocus Beamline	Diamond Lightsource	Rock slices	*In situ* micro X-ray Diffraction (μXRD)	Mineralogy
STOE STADI MP X-ray diffractometer	NHM	Bulk Powders	pXRD	Mineralogy
Rigaku Rapid II Micro X-ray diffractometer	NHM	Thin Sections	μXRD	Mineralogy

which can interact with the target in a variety of ways depending on the electron velocity (Fig. 2.1) (Egerton 2016; Reed 2005). The SEM can be utilized to collect a variety of datasets based on these electron specimen interactions and can possess a number of configurations. A traditional SEM setup is shown in Fig. 2.2.

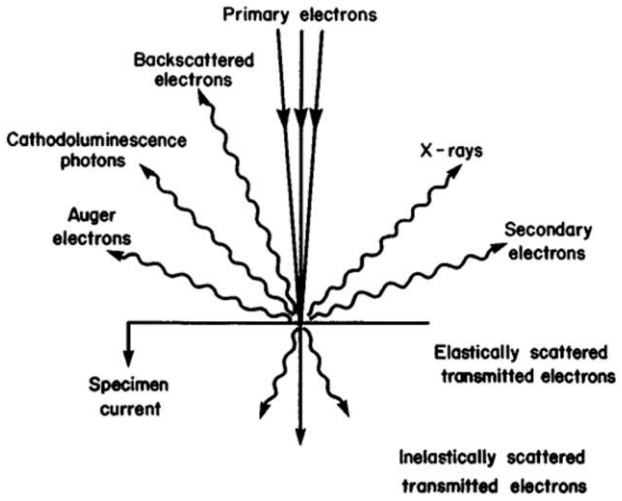

Fig. 2.1. The signals generated by electron-specimen interactions. From Krinsley et al. (1998).

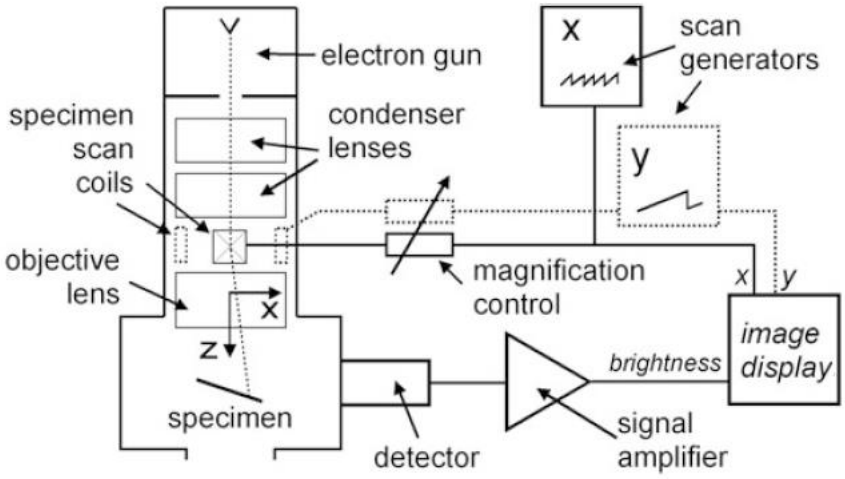

Fig. 2.2. Schematic of an SEM. From Egerton (2016). The electron gun produces the electron beam, the condenser and objective lenses focuses the beam onto the specimen, the scan coils generate a magnetic field to alter the path of the electron beam during scans.

As electrons travel through the targeted sample, they lose energy, with the amount of energy lost increasing with both the density of the target and the distance the electron travels. This phenomenon results in electrons losing energy over a shorter distance when penetrating material made of denser atoms (e.g., Au, Pb) (Reed 2005).

Electrons are further affected by atoms within the sample. Electrons are negatively charged and the positively charged nuclei of the target's atoms will impose an attractive force on them, deflecting the electrons and altering their path (Fig. 2.3). Some of these electrons will be deflected at an angle greater than 90°, allowing them to exit the sample in what is known as backscattering. The probability of backscattering increases with the charge of the nuclei, which is dependent on its number of protons. Atoms containing more protons (and therefore being more massive) backscatter more electrons than atoms with fewer protons (Reed 2005).

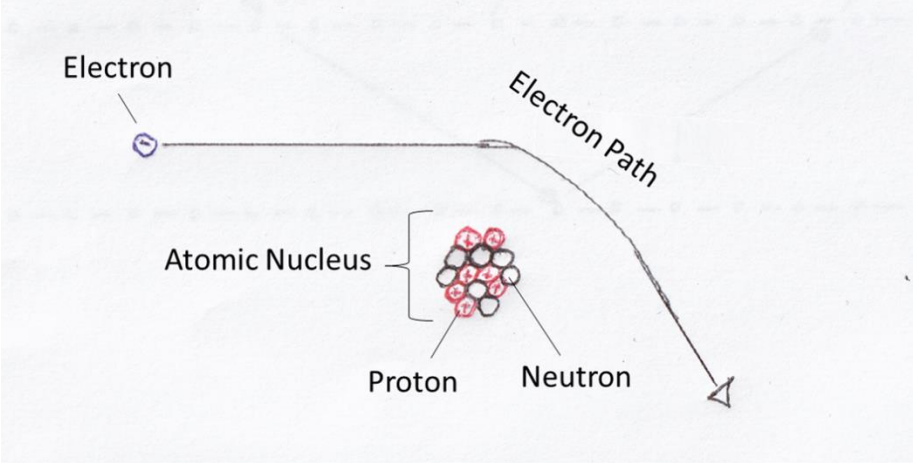

Fig. 2.3. Example of electron scattering, where the path of the negatively charged electron is altered by the positively charged atomic nucleus.

These backscattered electrons are measured with a scintillator, which is a device that produces light when hit with electrons. The light produced is then detected by a photomultiplier which in turn produces an electric signal dependent on the energy involved. The electric signals produced by this process can be used to create various datasets depending on the type of analysis being conducted. With regards to backscattered electrons, the scintillator is customized in a manner such that only electrons of certain energies are measured (Reed 2005). This design results in the production of greyscale backscattered electron (BSE) images, where lighter areas correspond to a greater number of electrons being backscattered than darker areas. Thus, in general brighter areas reflect the mean atomic number of the target (Fig. 2.4).

The primary electron beam can also cause target electrons to absorb energy, resulting in electrons from the sample itself being emitted from the sample (Egerton 2016; Reed 2005). This process is known as secondary electron (SE) emission. These secondary electrons typically originate from the outer few

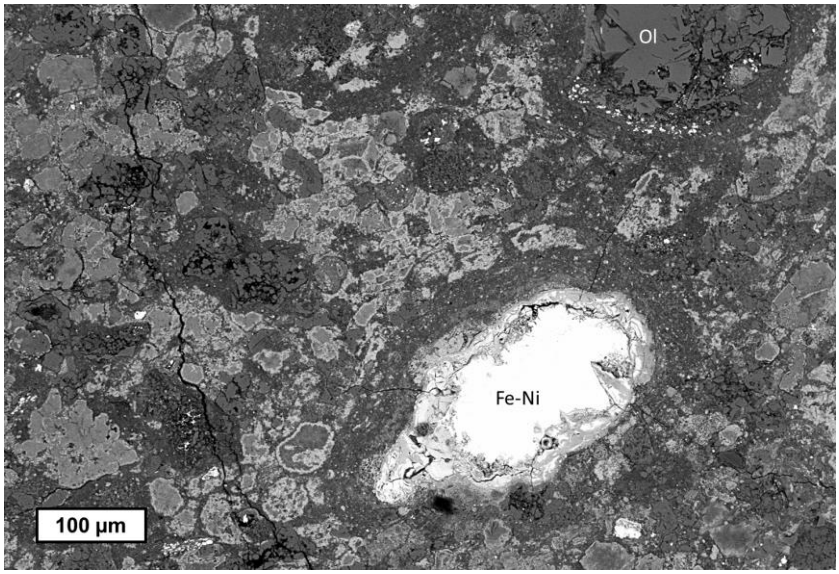

Fig. 2.4. BSE image of an area in the CM chondrite Kolang. A Fe-Ni metal globule is made up of proton-rich elements and shows up bright compared to the forsterite grain (Ol), which is made up of lighter elements with fewer protons (Mg, Si, O). The matrix is mostly made up of TCIs and serpentines and is variable in brightness due to fine-scale spatial differences in Fe-content.

nm of the target's surface and are less energetic than backscattered electrons, allowing them to be measured separately with either a different detector or an alternate setup with the same scintillator detector. The result is an SE image. The production of secondary electrons is less dependent on the charge of the target's atomic nuclei and more dependent on the topography of the sample (Reed 2005).

The interaction of electrons with the target material can also result in the production of X-rays. This process happens when an electron in an orbital that has a low energy level (e.g., is "close" to the nucleus) is emitted or elevated to a higher energy state in an outer orbital (Fig. 2.5). When the atom absorbs an electron to fill in its missing orbital, energy is released in the form of a photon with the wavelength characteristic of X-rays. The intensity and wavelength of the X-rays will be dependent on the element it was produced from, as each element has a different configuration of electron orbitals which will display characteristic energy changes. The orbitals from which the X-ray emitting electron vacancy originates may be referred to as a combination of Latin-script and Greek letters (e.g., Kα, Lß, Mγ), where the Latin-script letter refers to the orbital and the Greek letter refers to the intensity of the X-ray produced by the vacancy in that particular orbital (Reed 2005).

The X-rays produced by SEM can be measured through a detector made out of a semiconductor. At ambient temperatures and unexposed to X-rays,

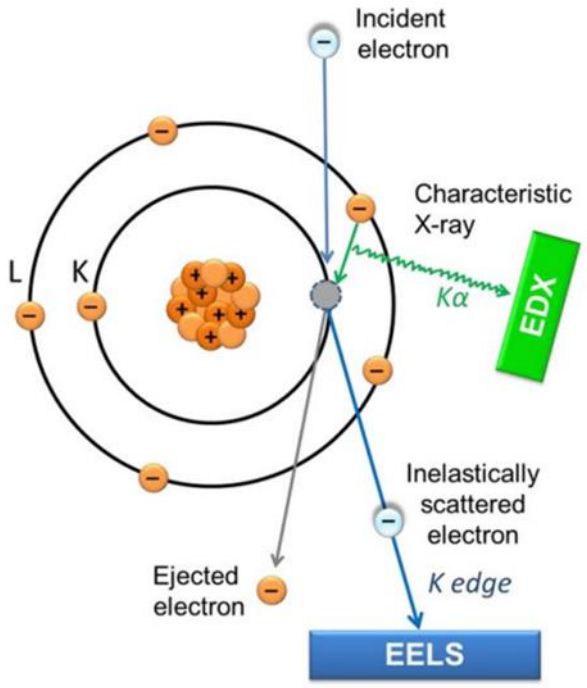

Fig. 2.5. Generation of X-rays for EDS (also referred to as EDX in the literature). From Pirozzi et al. (2018).

these semiconductors are not conductive. However, when they are exposed to X-rays, the electrons within these semiconductors, particularly those involved with molecular bonds, absorb energy and jump to a higher energy level, allowing the semiconductor to become more conductive, leading to a "pulse" of electricity flowing through it. The energy of this pulse is measured in terms of eV. The characteristics of these pulses will be dependent on the original X-rays produced by the targeted material, which in turn is a product of its elemental makeup. These pulses of electricity are presented as X-ray spectra (Reed 2005), known as energy-dispersive X-ray spectrometry (EDS) and can yield information regarding the proportions of different elements making up the targeted area. EDS spectra can be collected as point analyses (Fig. 2.6) or can be collected as maps where the electron beam is rastered across the sample surface.

Sometimes during backscattering the electrons are diffracted by the crystal lattice, which can be used to determine crystallographic information using a technique known as electron backscatter diffraction (EBSD). These diffracted backscattered electrons are measured with a phosphor screen or a complementary metal oxide semiconductor (CMOS) detector, which converts the incoming electrons into visible light which is then recorded by a camera (Reed 2005). The electrons are diffracted as cones (Fig. 2.7a), which when projected onto the flat phosphor screen, creates a pattern of intersecting bands known as a Kikuchi pattern (Fig. 2.7b). The individual bands themselves are referred to as

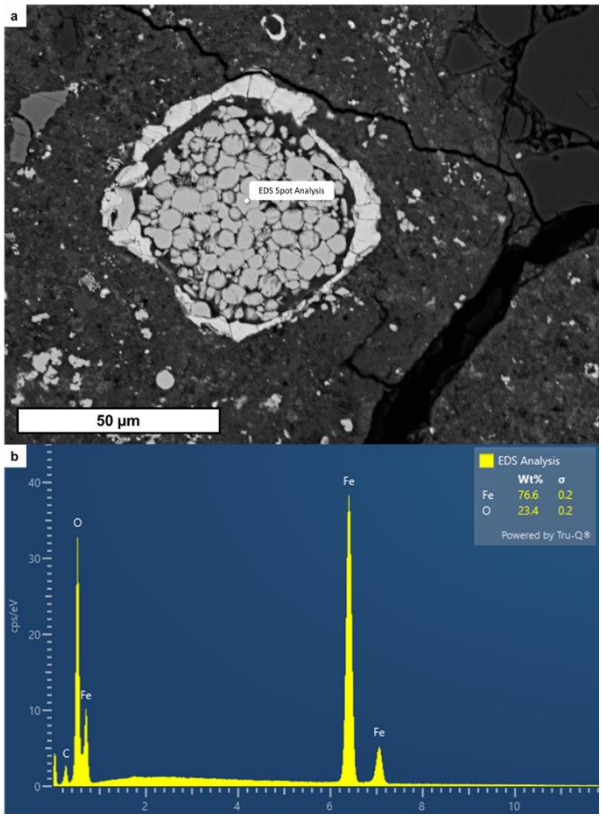

Fig. 2.6. Example of EDS spot analysis. a) BSE image of magnetite-sulphide rosette in Wisconsin Range 91600 showing spot targeted for EDS analysis. b) Resulting EDS spectrum. Corresponds to magnetite.

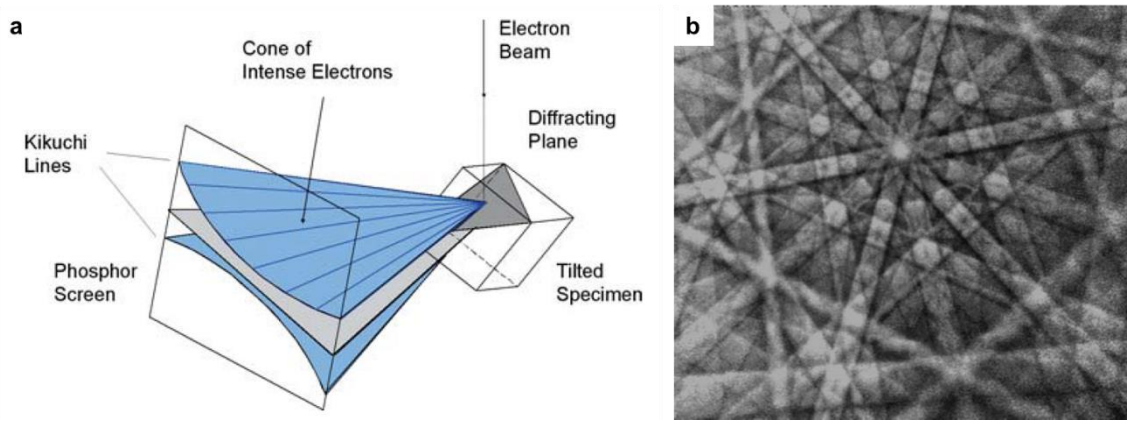

Fig. 2.7. Examples of how EBSD works from Schwarzer et al. (2009). a) Schematic of diffraction cones being backscattered from a tilted sample to a phosphor screen. b) Example of a Kikuchi pattern from cadmium.

Kikuchi bands. The width of the Kikuchi bands can be used to calculate the d-spacing of lattice planes, while the angles between them can be used to figure out the angles between lattice planes, as well as the crystallographic orientation of targeted material (Schwarzer et al. 2009). For EBSD analysis, the sample is tilted at an angle relative to the electron beam and detector to maximise the chances of obtaining a clear Kikuchi pattern (Reed 2005).

When certain materials (e.g., diamond, calcite, diopside) are exposed to an electron beam, the electrons involved with the bonding of atoms will absorb

energy and jump to a higher energy level, allowing the material to become conductive. When an electron returns to its original energy level, a photon is released, with its wavelength ranging from infrared to ultraviolet, typically somewhere within the visible light spectrum. This process of photon emission is known as cathodoluminescence (CL) emission and can be imaged. CL is greatly affected by lattice defects and impurities (e.g., Mn), which can influence whether or not CL emission is produced, and at which wavelengths it occurs (Reed 2005). CL can be used to determine the physical properties of a sample.

An obstacle with SEM analysis is that the electron beam may cause the target area to become charged, leading the electrons to be deflected by the sample. This process degrades the image quality, particularly when using SE where electrons have low energy (Fig. 2.8) (Reed 2005). To mitigate charging, samples are ideally coated with a conductive material (e.g., carbon) to electrically ground the sample to the sample holder, allowing excess charge to be removed.

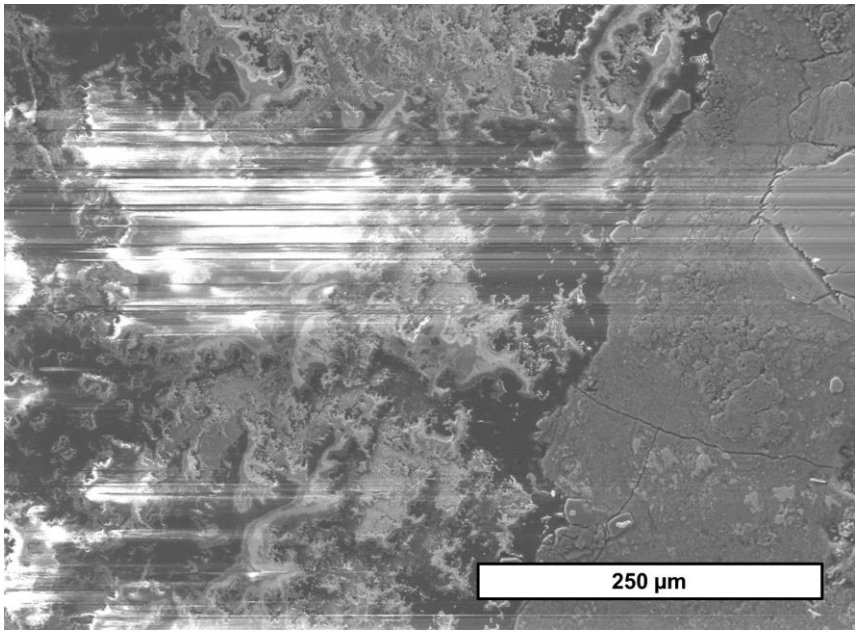

Fig. 2.8. SE image with charging artifacts. The CM chondrite Murray is on the right-hand side of the image.

2.1.1 Data Collection Parameters

Unless stated otherwise, all datasets relating to SEM in this thesis were produced using a Carl Zeiss Sigma Variable Pressure field emission gun SEM operated at 15-20 kV and a beam current of 1-2 nA at the Geoanalytical Electron Microscopy laboratory (GEM) at the University of Glasgow (UoG). Data acquired were processed using the Oxford Instruments AZtec program, version 6.0. Images (BSE/SE)

were collected either as single fields or frames, or as a series of frames and montaged as maps.

There were occasions where a different SEM, a FEI Quanta 200F Environmental SEM, was used at UoG's GEM lab. Where relevant, these occasions will be stated. This SEM was operated at 15 kV and 1-2 nA. The program used to collect and process X-ray data was the EDAX Genesis Microanalysis program, version 6.5.3.

Prior to collection of BSE and SE images, and EDS data, samples were coated with 20 nm of carbon. Prior to collection of EBSD data samples were polished with colloidal silica and coated with 7 nm of carbon. Carbon coating was undertaken using a Quorum Q150T ES turbomolecular pumped coater, where sharpened carbon rods dispersed carbon onto the samples under high vacuum.

2.1.1.1 – Imaging

All SEM-based imaging was undertaken with the Carl Zeiss Sigma SEM. BSE images were acquired and montaged to produce petrographic maps of samples. Additionally higher magnification BSE Images were taken of objects of interest. SE imaging was used to characterise the topography of rock samples. All images were taken with a resolution of 1024 dpi.

2.1.1.2 – Energy Dispersive X-ray Spectrometry

All EDS data were acquired using the Carl Zeiss Sigma SEM that is equipped with an 80 mm^2 silicon-drift detector. EDS maps were made and montaged to supplement petrographic BSE maps to show element distributions. EDS maps were taken for five frames. Process time ranged from 3-4 and the pixel dwell time was 100 µs. Additionally, both point spectra and higher magnification EDS maps were taken of objects of interest.

2.1.1.3 – Electron Backscatter Diffraction

All EBSD data were collected with the Carl Zeiss Sigma SEM using a NordlysMax^2 EBSD detector operated at 20 kV. The sample was tilted 70° for EBSD collection. EBSD maps were initially collected using AZtec but were then processed using the Oxford Instruments AZtec Crystal program version 2.2.

2.1.1.4 – Cathodoluminescence

Cathodoluminescence (CL) data were collected using the FEI Quanta Environmental SEM using a KE Developments panchromatic CL detector. This detector was used only for the Winchcombe P30552 sample.

2.2 – Electron Probe Microanalysis

Collecting electron probe microanalysis (EPMA) data works similarly to EDS in the SEM. An electron beam is used to produce X-rays from the target sample, which can be used to determine its chemical composition. Where EPMA differs is that instead of all the X-rays produced by the sample being measured at the same time, a curved crystal (e.g., LLIF, TAP) is used to diffract and reflect only specific wavelengths of X-rays towards the detector (Fig. 2.9); only a single wavelength is measured by a detector at a given time. This method is known as wavelength-dispersive X-ray spectrometry (WDS) and yields more precise results than EDS, however it does take a longer time to obtain as only one element can be measured by one detector at a time (Reed 1995).

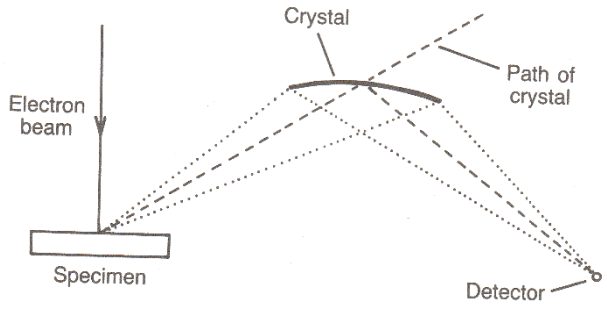

Fig. 2.9. Example EPMA operation. A curved crystal reflects only certain wavelengths of electrons to the detector, allowing for only specific elements to be measured. From Reed (1995).

2.2.1 Data Collection Parameters

EPMA data were collected for hydroandradite in Shidian (5 spots) and Kolang (16 spots) at the University of Edinburgh. This work was done with a SX100 EPMA operated at 15 kV and a beam current of 6 nA (Fe, Si, Ca) and 100 nA (Na, K, Mn, Ni, Cr, Ti, Mg, Al), with a spot size of 2 μm. Kα lines were used to determine elemental abundances. Detection limits and measurement times for each of these elements are given in Table 2.2. Elements were measured using the following analysing crystals: LLIF (Fe, Mn, Ni, Cr); TAP (Si, Al); LPET (Ca, K, Ti); LTAP (Na, Mg); PET (K, Ti). Prior to analysis, the EPMA was calibrated with

the following standards: fayalite (Fe), forsterite (Si), wollastonite (Ca), jadeite (Na), orthoclase (K), Mn metal (Mn), Ni metal (Ni), Cr metal (Cr), rutile (Ti), spinel (Mg, Al).

Table 2.2. Detection limits, and background and peak collection times for various elements measured using the EPMA at the University of Edinburgh.

Element	Detection Limit (ppm)	Peak Collection Time (s)	Background Collection Time (s)
Al	44	60	60
Ca	1043	20	10
Cr	113	60	30
Fe	2569	20	10
K	50	30	15
Mg	270	60	60
Mn	186	80	40
Na	64	30	30
Ni	166	60	30
Si	862	20	10
Ti	48	60	30

EPMA was also conducted at the Natural History Museum, London (NHM), where WDS data were collected for the meteorites Shidian and Kolang, with a focus on tochilinite assemblages (n=10 for Shidian, n=20 for Kolang), the serpentine matrix (n=7 for Shidian, n=20 for Kolang), and the fine-grained rims (FGRs) around chondrules (n=10 for Shidian, n=20 for Kolang). Data were acquired using a Cameca SX100 EPMA operated at 20 keV and a beam current of 20 nA with a spot size of 1 μm. Kα lines were used to determine elemental abundances. Elements were measured using the following crystals: LPET (S, K, Ti, Cr), LLIF (Mn, Fe, Co, Cu, Zn, V), TAP (Na, Mg, Al, Si, P), and PET (Ca). The standards used to calibrate these elements were chalcopyrite (S, Fe, Cu), manganese titanium oxide (Mn), cobalt (Co), nickel (Ni), zinc sulphide (Zn),

Table 2.3. Detection limits, and background and peak collection times for various elements measured using the EPMA at the NHM.

Element	Detection Limit (ppm)	Peak Collection Time (s)	Background Collection Time (s)
Al	311	20	10
Ca	190	30	15
Co	69	30	15
Cu	537	30	15
Cr	252	20	10
Fe	297	20	10
K	284	10	5
Mg	315	20	10
Mn	268	30	15
Na	845	10	5
Ni	325	30	15
P	251	30	15
S	255	30	15
Si	263	20	10
Ti	148	30	15
V	160	60	30
Zn	351	30	15

jadeite (Na), forsterite (Mg), corundum (Al), fayalite (Si), scandium phosphate (P), orthoclase (K), wollastonite (Ca), rutile (Ti), vanadinite (V), and chromium oxide (Cr). Detection limits and measurement times for each of these elements are given in Table 2.3.

2.3 – Transmission Electron Microscopy

Transmission electron microscopy (TEM) utilizes electric and magnetic fields to focus a beam of electrons onto the sample (Egerton 2016). The electrons are accelerated to high velocities (~200 kV), allowing them to be transmitted for many tens of nm through a material, and if the material is crystalline, the electrons will diffract. To enable electrons to be transmitted through the sample (i.e., make it electron transparent) it must be thin (e.g., ~100 nm) (Williams & Carter 2009). As they are transmitted, electrons will be diffracted at a variety of angles depending on both sample crystallography and orientation (Egerton 2016). These are then detected using either a semiconductor detector or a scintillator (see Chapter 2.1) positioned on the other side of the sample to the incident electron beam. An objective aperture is placed between the sample and the detector such that the observed diffraction angles of incoming electrons are controlled, and interpretable data sets are produced (Egerton 2016; Williams & Carter 2009).

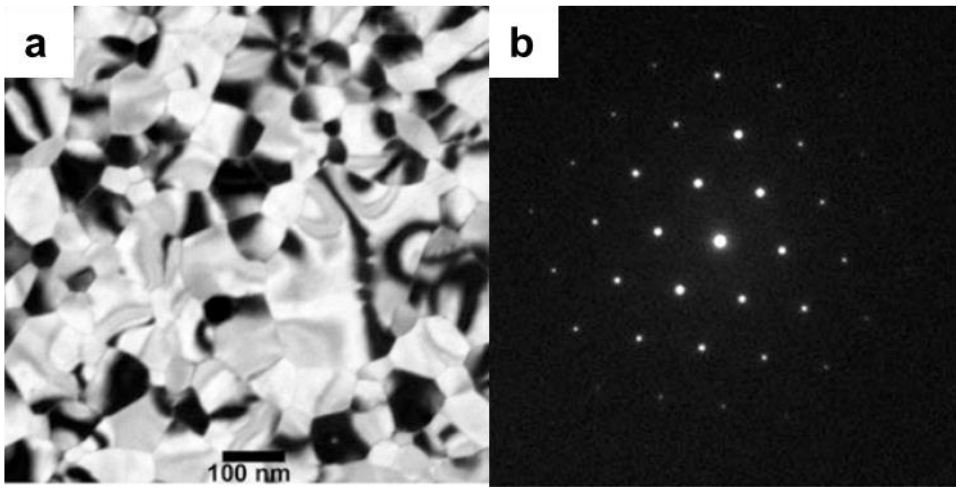

Fig. 2.10. Examples of TEM data from Egerton (2016). a) Brightfield diffraction-contrast image for bismuth. b) SAED image for bismuth.

One type of TEM dataset is a diffraction-contrast image (Fig. 2.10a), which displays the orientation of crystals based on the amount of electrons measured by the detector. These diffraction-contrast images may be brightfield or darkfield depending on the placement of the aperture. In a brightfield image

(Fig. 2.10a), the objective aperture is placed directly in the path of the incident electron beam such that strongly diffracted electrons do not reach the detector; crystals that are oriented such that they are diffracting a high proportion of incident electrons are dark whereas amorphous materials and crystals that diffract poorly appear bright. In a darkfield image, the objective aperture is placed such that only strongly diffracted electrons reach the detector; crystals that diffract appear bright and crystals that do not diffract and amorphous materials are dark (Egerton 2016).

Another type of TEM dataset is a selected-area electron diffraction (SAED) pattern. An SAED pattern is produced by introducing a selected-area aperture between the thin sample and the electron detector. This aperture reduces the area of the sample being analysed to a selected area (as the namesake implies), allowing the SAED pattern to be obtained (Fig. 2.10b). Each spot in the SAED pattern corresponds to electrons that have been diffracted by lattice places of a certain spacing and orientation. An SAED pattern can be used to determine properties of the unit cell of the crystal, such as d-spacing, Miller indices, and axis lengths (Egerton 2016).

2.3.1 Electron Transparent Lamellae Preparation

Prior to collection of TEM data, electron transparent lamellae were prepared using a DualBeam Focused Ion Beam (FIB) microscope equipped with a Ga^+ Sidewinder ion column operated at 30kvV at variable beam currents at the Kelvin Nanocharacterisation Centre (KNC) at UoG. The areas of interest were coated in 1 μm of Pt prior to protect them. The area around the region of interest was milled away using the FIB and the chunk was then extracted from the sample with an *in-situ* micromanipulator and welded to a copper support grid using Pt and a gas injection system. The lamellae was then further milled to a thickness of ~100 nm.

2.3.2 TEM Data Collection

For TEM data collection, the electron transparent lamellae were loaded into a double-tilt holder. TEM data were collected at the KNC using a FEI T20 TEM operated at 200kV. TEM data consists of diffraction-contrast images as well as SAED patterns.

2.4 – Raman Spectroscopy

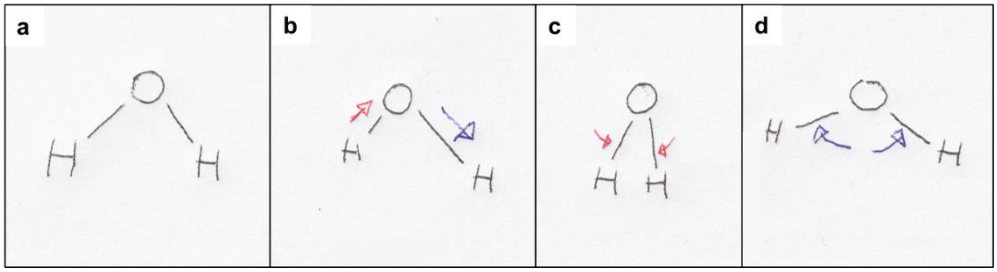

Fig. 2.11. Example of how atoms change position due to molecular vibration within a molecule of water. a) Initial atomic positions. b) Changing position by shortening and lengthening bond lengths. c) Changing position by decreasing the angle between bonds. d) Changing position by increasing the angle between bonds.

Raman spectroscopy utilises the vibration of molecules to gather information about the bonding environments of targeted materials. When molecules vibrate, their atoms change position relative to one another, becoming closer or farther away and/or changing the angle at which their bonds occur (Fig. 2.11) (Larkin 2011). When a photon interacts with a molecule, it interacts with the electrons in the outer shells of its atoms, including the electrons responsible for bonding. These electrons alter the path of the photon, scattering it. During this process the energy level of the molecule will be changed slightly, usually with the molecule absorbing a small amount of energy from the photon, but in some cases giving energy to the photon. The magnitude of this energy transfer and how it occurs will depend on the type of molecular bond involved. Due to a change in energy, the photon coming off the sample will have a different frequency than it started with.

In Raman spectroscopy, a laser generating photons with a known frequency (and thus known energy) is targeted at the sample. The altered frequency of photons coming off the sample is measured with a charged coupled device (CCD) detector, which produces a Raman spectrum (Fig. 2.12), wherein the measured frequency of incoming photons is referred to as Raman shift. The changes to photon frequency can be matched up with specific molecular bonds, allowing for identification of a wide variety of materials with Raman spectra (Smith & Dent 2019).

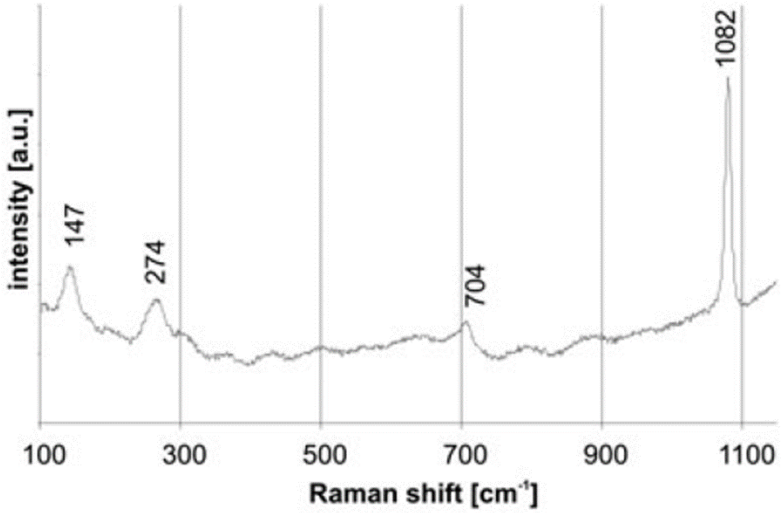

Fig. 2.12. Example of a Raman spectrum for calcium carbonate with the Raman shift (change in frequency) of each peak labelled. From Krzesińska & Fritz (2014).

2.4.1 Raman Spectra Collection

All Raman spectra were collected using Renishaw Invia Raman microscope at UoG's GEM. Spectra were collected with a 514 nm wavelength laser with a power of 45 mW. The laser power was set to 1% with a five second exposure over three accumulations and three acquisitions. The spot size used was 1 μm.

2.5 –X-ray Diffraction and Heating Experiments

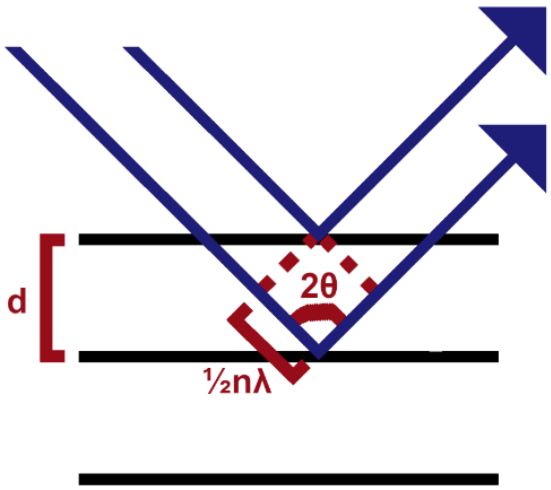

Fig. 2.13. Diagram illustrating Bragg's Law from Jenkins (2019). X-rays are shown in blue, while crystal lattice planes are shown in black. The X-ray that penetrates the crystal travels an extra distance nλ before it is reflected out.

Light is both a particle and a wave, and, like electrons, is subject to diffraction as it moves from one medium to another. Diffraction is used in a wide variety of analytical techniques, from TEM to the optical microscope. One technique that takes advantage of light's ability to diffract is X-ray diffraction (XRD), where photons with wavelengths in the X-ray spectrum are directed at a sample. The X-rays diffract as they interact with the crystal structure of the

sample, then are transmitted through the sample and/or reflected out of it by the lattice planes. The angle at which the X-rays emerge out of the sample is dependent on the spacing between lattice planes (Fig. 2.13) and can be described by Bragg's Law, Equation 2.2 (Bragg & Bragg 1913):

$$n\lambda = 2dsin\theta \quad (2.2)$$

where *n* is the diffraction order and is dependent on instrument's configuration, λ is the wavelength of the X-ray, *d* is the d-spacing of the lattice planes, and θ is the diffraction angle (Bragg & Bragg 2013).

Diffracted X-rays emerge from the sample as a cone (Fig. 2.14) and can be measured via a variety of detectors. The detectors used in some of the earliest experiments were photographic plates where upon these diffraction cones were imprinted as rings (Bragg & Bragg 1913), however modern day XRD detectors are typically CCDs or position sensitive detectors (PSDs). From XRD, the d-spacings of lattice planes can be determined, which yields information regarding crystal structure (Flemming 2007). Most XRD data is collected in reflection, however some configurations allow for XRD data to be collected in transmission.

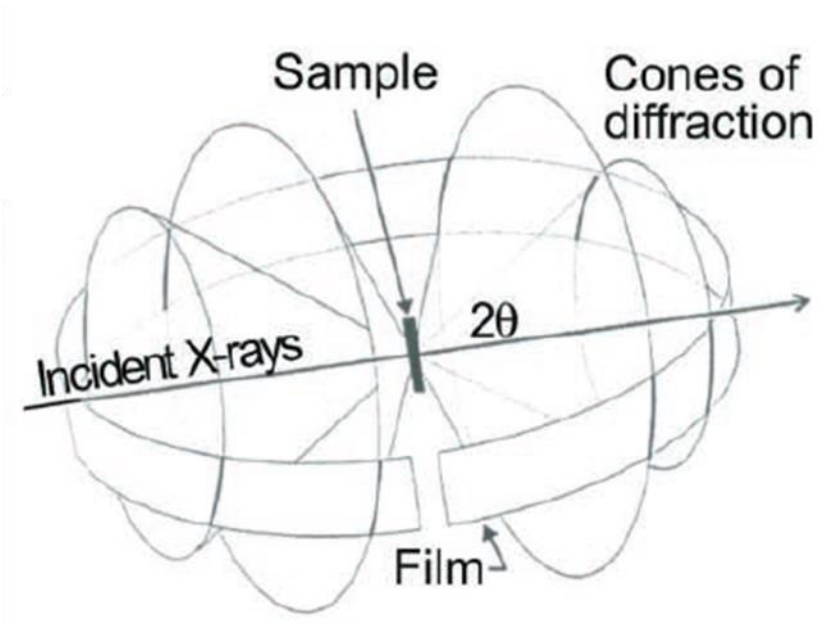

Fig. 2.14. Example of how cones of diffraction work in XRD. From Flemming (2007).

The angle of which X-rays diffract is dependent on lattice planes making up the targeted crystal, however which X-rays get diffracted toward the detector depends on crystal orientation. To maximize the X-rays measured by the XRD detector, it is common practice to powder a sample, such that all

crystal orientations are represented by the resultant diffraction pattern, allowing for easy phase identification. This XRD method is referred to as powdered XRD (pXRD) (Flemming 2007).

Although pXRD is the most common application of XRD, powdering a sample is a destructive process and removes certain pieces of information, such as grain size and subgrain information (Flemming 2007), as well as the context of each phase within the bulk rock. In certain scenarios, it can be advantageous to leave the sample whole and target specific areas in a data collection process known as *in situ* micro XRD (μXRD). Although the number of diffraction peaks are limited in μXRD preventing certain types of analysis (e.g., Rietveld refinement), the targeted phase is observed in context in a non-destructive manner and other sets of information can be determined, such as the misorientation of subgrains (Flemming 2007).

2.5.1 – Diamond Light Source - I11 beamline

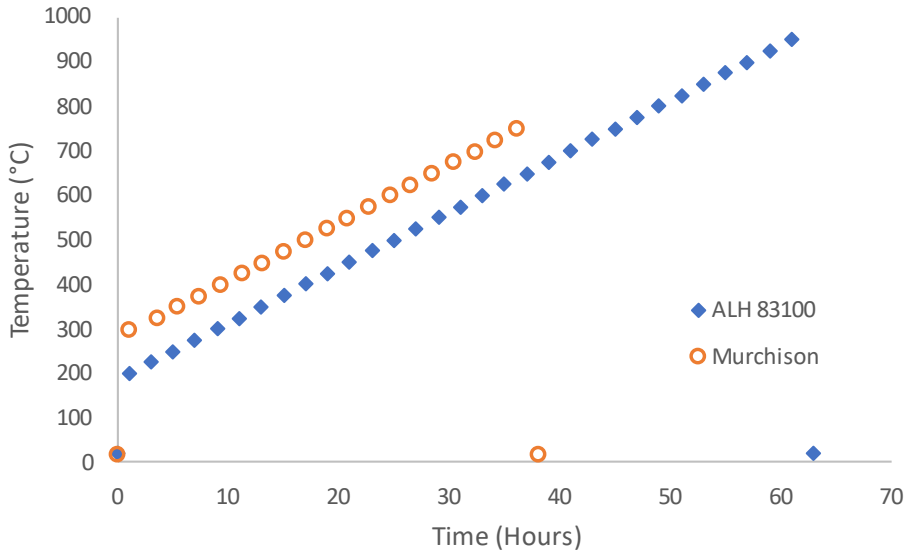

Fig. 2.15. Timing of the collection of each XRD pattern with the MAC devices on the I11 beamline for both ALH 83100 and Murchison.

A sample of ALH 83100 was powdered and mailed to Diamond Light Source (DLS), a synchrotron facility, for an *in situ* heating experiment on the I11 High Resolution Powder Diffraction beamline. There, the powder was sealed in a quartz capillary sample holder with inert nitrogen gas. The sample was heated from 200 to 950°C at 25°C temperature steps, with each temperature step held for an hour prior to collection of high resolution XRD patterns (Fig. 2.15). Collection of XRD patterns was carried out using multiple detectors for varying

durations depending on the detector. After each temperature step, high resolution XRD patterns were collected using five multi-analysing crystal (MAC) devices for 1 hour while at temperature. Additionally, high resolution XRD patterns were collected with the MAC devices for an hour at room temperature before and after heating. While ALH 83100 was held at each temperature step for an hour, lower resolution XRD patterns were collected every five minutes using a PSD for five seconds. All XRD data were collected with a wavelength of 0.826 Å.

To investigate whether the petrography and degree of alteration of a CM chondrite influences mineralogical changes during heating, the I11 experiment was repeated with a ~100 mg powdered sample of Murchison. The inert gas its quartz capillary holder was sealed in was argon. The process of data collection and the conditions of heating were almost identical to that of ALH 83100, except for the range of temperatures it was heated at and the wavelength. The wavelength used to collect XRD patterns for Murchison differed slightly and was 0.824 Å. Instead of being heated from 200 to 950°C, Murchison was heated from 300 to 750°C to cover key temperatures at which reactions occurred. Due to a programming error, the timescales that Murchison was heated at were also slightly different than those for ALH 83100. For all temperature steps, with the exception of the 300°C temperature step, Murchison was held for 55 minutes prior to data collection. At the 300°C temperature step, Murchison was held for 1.5 hours prior to data collection.

All XRD patterns collected at the I11 were processed with Rigaku Smartlab II software.

2.5.2 – Diamond Light Source - I18 beamline

As a follow-up to the work done on the I11 beamline, further *in situ* heating experiments were conducted on the I18 Microfocus Spectroscopy beamline. Instead of powdered samples, this experiment used three demounted, polished thick sections of Murchison, referred to as M-A, M-B, and M-C. Sections M-A and M-B are both ~1.8 mm^2 in area, while M-C is ~3.23×10^{-2} mm^2 in area. All three samples are 100 µm thick. The I18 beamline is able to collect µXRD data in transmission geometry. To heat the samples in a controlled atmosphere external equipment was brought in. This external equipment consisted of a THMS600

Linkam environmental cell equipped with Kapton windows and connected to a TMS 94 temperature controller and an ECP water circulation pump. To hold the samples in place, a vertical sample holder was installed, allowing the sample to be held in place via friction between two pieces of Kapton. Nitrogen gas was pumped through the Linkam cell to create an inert environment. The Murchison samples were heated at 25°C temperature steps for different temperature ranges as it was discovered that the Kapton used to hold the samples in place would eventually melt, halting the experiment. Both M-A and M-B were heated at 400-550°C, while M-C was heated 200-500°C. Each sample was held at each temperature step for 2 hours. During this time XRD data was collected with a 2 μm spot size at a wavelength of 0.826 Å for a defined area (1.2-2.2 mm^2) to produce an XRD map of the sample. XRD pattern collection at each spot took about 5 seconds and begun after the sample had been held at the defined temperature step for an hour. Additionally, XRD maps were collected at room temperature before heating for comparison. XRD patterns of empty Kapton blanks heated at the same conditions as the Murchison samples were also collected to evaluate the melting Kapton's effect on the XRD data. XRD patterns of powdered standards (pyrrhotite, cronstedtite, magnetite, enstatite, antigorite, pentlandite, lizardite, olivine, calcite, augite, and chrysotile) mounted in Kapton tape were collected at room temperature for comparison. XRD patterns were processed using a combination of DAWN 2.27 and Rigaku Smartlab II software.

2.5.3 STOE STADI MP – Powdered X-ray Diffraction

At the NHM, a sample of LEW 85311 was powdered and loaded into a 0.9 mm quartz glass capillary. The capillary was inserted into a STOE HT1 high temperature chamber where it was continuously rotated during heating and XRD data collection.

Prior to heating, an XRD pattern of LEW 85311 was collected. LEW 85311 was then heated from 300°C to 750°C at 25° temperature steps. The atmosphere was not controlled during heating. At each temperature step, LEW 85311 was held for two hours, during which two XRD patterns were collected, each collected for the duration of an hour. After the final heating step, another XRD pattern was collected for LEW 85311.

XRD patterns were collected using a STOE STADI MP powdered X-ray diffractometer equipped with a Mythen 2K double detector. A Mo X-ray source was used. Each XRD pattern took an hour to collect.

2.5.4 Rigaku Rapid II Micro-Diffraction

Six rock chips of Murchison were heated under vacuum using a Degas vacuum oven at the Scottish Universities Environmental Research Centre (SUERC). The samples were heated at the following temperatures and durations: 200°C for 1 day, 200°C for 8 days, 300°C for 1 day, 400°C for 1 day, 500°C for 1 day, and 500°C for 8 days. These samples were later made into thin sections to compare to an unheated sample of Murchison.

These samples were analyzed by SEM and Raman spectroscopy (described in Chapters 2.1 & 2.4) in addition to being studied with μXRD at the NHM. For μXRD data collection, a Rigaku Rapid II Micro-Diffraction diffractometer equipped with a 2D curved imaging plate detector was used. The instrument used a Cu X-ray source and the beam spot size of ~100 μm. Both TCIs and tochilinite clumps on the samples were targeted. XRD patterns were collected for 15 minutes each. During some data collection runs, the samples were rotated to maximize the number of orientations represented in the diffraction patterns. During other data collection runs the samples were kept static to minimize the contribution of adjacent phases (e.g., olivine, serpentine) to the collected XRD patterns.

2.6 Materials

There are two modes of research that can be conducted to understand the alteration processes affecting carbonaceous chondrites originating from C-complex asteroids: the study of meteorites that have already been altered, and experiments to simulate these alteration processes. Both avenues of research were utilized in this study (Table 2.4).

The CM chondrite meteorites Allan Hills (ALH) 83100, Lewis (LEW) Cliff 85311, Murray, and Murchison have experienced varying degrees of aqueous alteration, but little to no post-hydration heating (Howard et al. 2011; Lee et al. 2019b). As a result, they are good meteorites to use in heating experiments so

that phase transitions and effects of post-hydration heating can be better understood. MacAlpine Hills (MAC) 88100; Pescora Escarpment (PCA) 02012, 91008, and 91084, Sutter's Mill, and Wisconsin Range (WIS) 91600 are CM or CM-like meteorites that are reported to have experienced post-hydration heating to varying degrees, making them suitable samples to study the process (Wang & Lipschutz 1998; Quirico et al. 2018; Garenne et al. 2014; Tonui et al. 2014; Lee et al. 2021b; Zolensky et al. 2014; Haberle & Garvie 2017; Hanna et al. 2020). Shidian, Kolang, and Winchcombe are recent CM chondrite falls and thus analysis of them is an opportunity to acquire new insights regarding alteration processes affecting the group. Shidian and Kolang contain evidence for both hydrothermal alteration and post-hydration heating. Winchcombe's retrieval was well documented (King, Daly et al. 2022; Russell et al. 2022), making it an ideal sample to study terrestrial alteration. Additionally, Kolang contains a pervasive petrofabric shared among its clasts (see Chapters 3.2 & 7), making the study of it a unique opportunity to gain new insights into chondrule flattening and alignment. Petrographic descriptions of these samples are presented in Chapter 3.

Table 2.4. Basic characteristics of the meteorites studied.

Meteorite	Source	Size (g)	Find/Fall	Subype[1]	Heat Stage[2]	Shock Stage[2]	Weathering Grade[3]	Cosmic Ray Exposure Age	References
ALH 83100	ANSMET	3019	Find – Antarctica - 1984	CM2.1	Unheated	S1	Be	0.2 Myr	5,6,7,8,9
Kolang	Mendy Ouzillou	2550	Fall - Sumatera Utara, Indonesia – August 1, 2020	CM1/2	Unheated to II[x]	S2[x]	N/A	N/A	10
LEW 85311	ANSMET	199.5	Find – Antarctica - 1985	CM2.7	Unheated	S1	Be	N/A	6,11,12
MAC 88100	ANSMET	177.3	Find – Antarctica - 1988	CM2	III[x]	N/A	Be	N/A	6,13
Murchison	NHM, Mendy Ouzillou	100000	Fall – Murchison, Victoria, Australia – September 28, 1969	CM2.5	Unheated	S1/2	W1-2	1.8 Myr	1,14,15,16
Murray	Mendy Ouzillou	12600	Fall – Murray, Kentucky, United States of America – September 20, 1950	CM2.4/2.5	Unheated	S1	W1-2	3.2 Myr	1,16,17,18
PCA 02012	ANSMET	58.9	Find – Antarctica - 2002	CM2	IV	N/A	B	N/A	19,20
PCA 91008	ANSMET	51.7	Find – Antarctica - 1991	CM2	IV	N/A	B	6.0 Myr	12,20,21,15
PCA 91084	ANSMET	34.4	Find – Antarctica - 1991	CM2	III-IV[x]	N/A	Be	N/A	22
Shidian	Shijie Li	1809	Fall – Yunnan Province, China – November 27, 2017	CM2.2	I[x]	N/A	W0	N/A	23
Sutter's Mill	ASU	993	Fall – California, United States of America – April 22, 2012	C	IV	N/A	W0	0.06 Myr	24,25,26
Winchcombe	NHM	602	Fall – Winchcombe, Gloucestershire, United Kingdon – February 28, 2021	CM2.0-2.6	Unheated	N/A	W0	0.3 Myr	27,28
WIS 91600	ANSMET	184.1	Find – Antarctica -1991	C2-ung	II-III[x]	S1	A/Be	N/A	6,11,20,29

ANSMET stands for The Antarctic Search for Meteorites, NHM stands for Natural History Museum (London), and ASU stands for Arizona State University. [x]According to this study. [1]According to the Rubin et al. (2007)/Rubin (2015) scale. [2]According to Nakamura (2005). [3]According to the Stöffler et al. (1991) shock stage system. [4]According to Grossman (1994) for finds. According to Wlotzka (1993) for falls. [5]Marvin & Mason (1984) [6]Grossman (1994). [7]Zolensky et al. (1997). [8]De Leuw et al. (2010). [9]Nishiizumi & Caffee (2012). [10]Gattacceca et al. (2021). [11]Gooding (1986). [12]Choe et al. (2010). [13]Lindstron (1989). [14]Moore (1970). [15]Soctt et al. (1992). [16]Kriestch et al. (2021). [17]Krinov (1958). [18]Horan (1953). [19]Russell et al. (2004). [20]Quirico et al. (2018). [21]Score & Lindstrom (1992). [22]Score & Lindstrom (1993). [23]Fan et al. (2022). [24]Ruzicka et al. (2014). [25]Haberle & Garvie (2017). [26]Okazaki & Nago (2017) [27]King, Daly et al. (2022). [28]Suttle et al. (2022). [29]Hanna et al. (2020).

Chapter 3 – Petrographic Sample Descriptions

Petrographic sample descriptions are an important aspect of any geologic study. Understanding the various components making up a sample is vital for interpreting the results of analyses and will affect the conclusions drawn. Additionally, CM chondrites are known for being heterogeneous, with most being breccias composed of varying lithologies (Rubin et al. 2007); different samples from the same CM chondrite may show vastly different make-ups. It is therefore important to do petrographic sample descriptions where possible, even if the sample is well-described in the literature.

Herein, I describe each sample using a mixture of literature data as well as my own observations made by scanning electron microscopy (SEM). The samples were described with a mixture of literature sources and the results from this study due to their variable nature. Some samples (e.g., Allan Hills 83100, Lewis Cliff 85311) were studied as powders, making primary petrographic descriptions impossible, while other samples lacked petrographic descriptions of them in the literature (e.g., MacAlpine Hills 88100).

In the following sample descriptions, which are sorted alphabetically, petrologic subtype will be described using the Rubin scale (Rubin et al. 2007; Rubin 2015), as that is the most appropriate scale to apply with the use of SEM data. Mineralogy will be reported either as the referenced results from the literature or will be determined as area percent by SEM point counting. Cronstedtite and tochilinite may be combined for some of the referenced literature results as many literature sources use X-ray diffraction (XRD) to determine the bulk mineralogy, for which there often is not a cronstedtite or tochilinite standard to properly quantify either component (Howard et al. 2011). SEM point counting involves overlaying a grid over various montaged SEM maps (e.g., BSE, EDS) and counting each object that occurs at each intersection of the grid.

3.1 Allan Hills 83100

Allan Hills (ALH) 83100 is a highly altered Mighei-like carbonaceous (CM) chondrite. It is a find from Antarctica. The sample used was acquired from the Antarctic Search for Meteorites (ANSMET). It has a petrologic subtype of 2.1

according to the Rubin scale (De Leuw et al. 2010). ALH 83100 was powdered and thus treated as a bulk rock. Its matrix is mostly composed of lizardite and cronstedtite, with minor amounts of tochilinite. It still has chondrules composed of olivine and enstatite. Other phases found throughout ALH 83100 are pentlandite, pyrrhotite, magnetite, and calcite (Lindgren et al. 2020; De Leuw et al. 2010). The modal mineralogy of ALH 83100 is as follows: 62 vol% lizardite, 24 vol% cronstedtite, 9 vol% olivine, 2 vol% magnetite, 1 vol% pyroxene, 1 vol% calcite, and minor amounts of tochilinite and sulphides (Howard et al. 2011).

3.2 Kolang

Kolang is a brecciated CM chondrite that fell in Indonesia in 2020. It contains a variety of lithologies, both CM2 and CM1 (Lecasble et al. 2022).

Two thin sections, Kolang_01 and Kolang_02, were acquired from Mendy Ouzillou at Skyfall Meteorites. Both are about ~2 cm^2 in area, containing a plethora of clasts and five different CM2 lithologies. Kolang_01 has 12 clasts and Kolang_02 seven (Fig. 3.1). The lithologies found in both thin sections are as follows: Carbonate & Metal-rich (Ca-lith), Heated (H-lith), Sulphide-rich (S-lith), Fe-rich (Fe-lith) and Conventional (Co-lith). All clasts have chondrules that are noticeably flattened and aligned, with the orientations being common across clast boundaries. The abundances of different objects were determined with point-counting (Table 3.1).

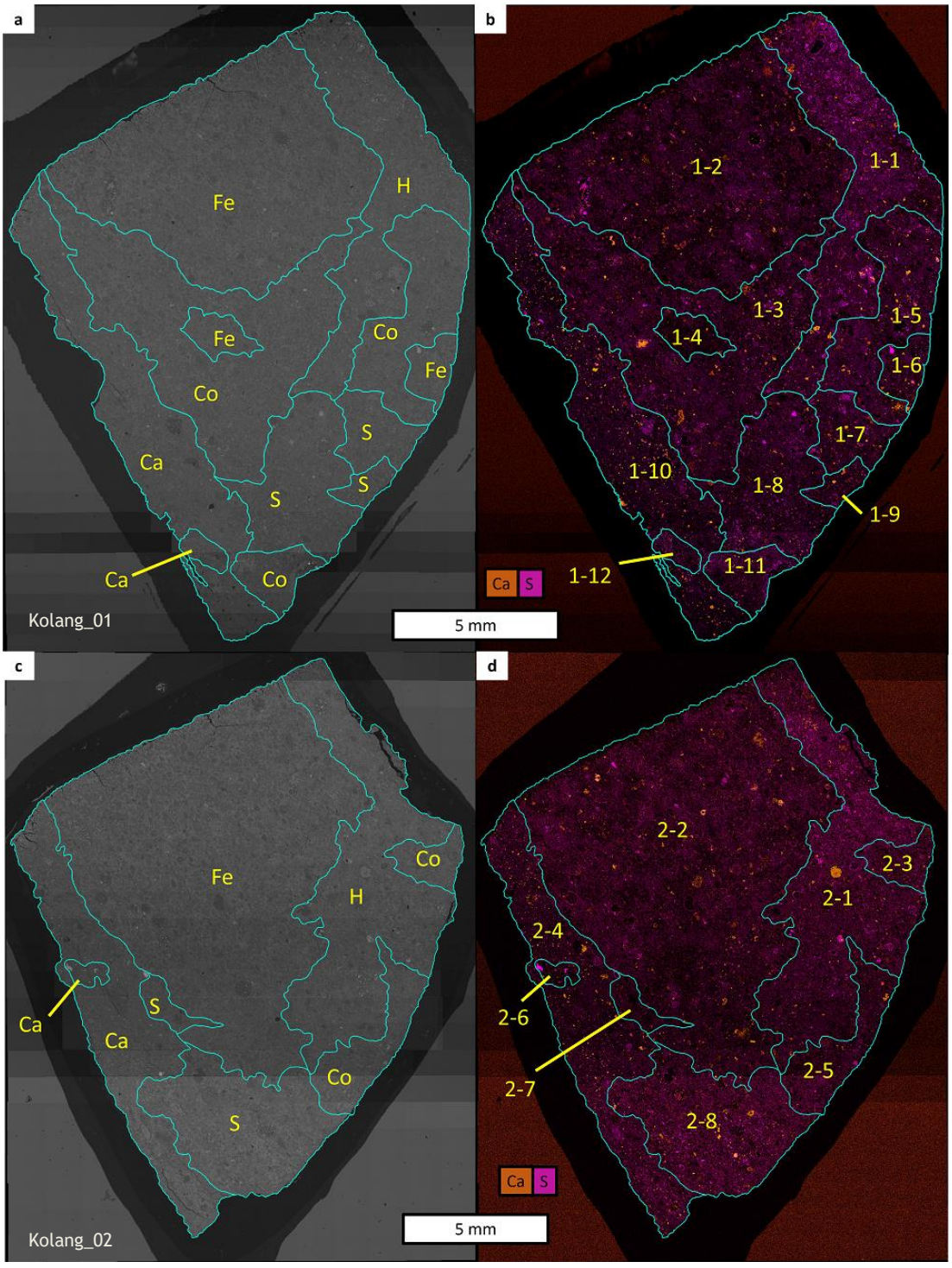

Fig. 3.1. Backscattered electron (BSE) and energy-dispersive X-ray spectroscopy (EDS) Ca-S maps for the studied thin sections of Kolang. Clasts are outlined in cyan. Some changes in contrast are instrument artefacts in images. a) BSE map of Kolang_01 with lithologies labelled. b) EDS map of Kolang_01 with clasts numbered. c) BSE map of Kolang_02 with lithologies labelled. d) EDS map of Kolang_02 with clasts numbered.

Table 3.1. Area percent of each object in each Kolang lithology from scanning electron microscope (SEM) point counting.

Lithology	Number of Points	Chondrule	Carbonate	Serpentine Matrix	Silicate Fragments	FGR	TCIs	CAIs	Sulphides	Oxides	Metal
Co-lith	215	10%	2%	32%	9%	11%	33%	0%	1%	0%	0%
Fe-lith	495	14%	3%	22%	8%	15%	36%	1%	0%	0%	0%
S-lith	151	8%	5%	26%	7%	10%	38%	1%	5%	1%	0%
Ca-lith	188	4%	4%	45%	9%	3%	32%	0%	2%	1%	1%
H-lith	209	9%	3%	34%	4%	11%	31%	0%	7%	0%	0%
Whole Meteorite	1258	10%	3%	30%	8%	11%	34%	1%	2%	0%	0%

3.2.1 Carbonate & Metal-rich Lithology

The Ca-lith is present in four clasts. It is defined by its matrix having lower amounts of Ca and S relative to other lithologies and the proliferation of 10 μm size carbonate grains. Additionally, it has about 1% metal in area, with much of the metal being in the matrix and not in chondrules, despite many of its chondrules being extensively altered. It best fits into a petrologic subtype of CM2.2 according to the Rubin scale.

3.2.2 Heated Lithology

The H-lith is defined by dehydration cracks present throughout its matrix (Fig. 3.2). It is present as two clasts. Much of the tochilinite has dehydrated and recrystallized into anhydrous sulphides. Its matrix is poor in Ca, but rich in S. Sulphides are particularly abundant, and what little unaltered metal is present, is restricted to the interior of chondrules. Many of its chondrules have been aqueously altered. Although it is not possible to apply traditional petrologic classifications due to its heated nature, given the chondrule degradation and minimal presence of metal, prior to heating the H-lith was likely of petrologic subtype CM2.2.

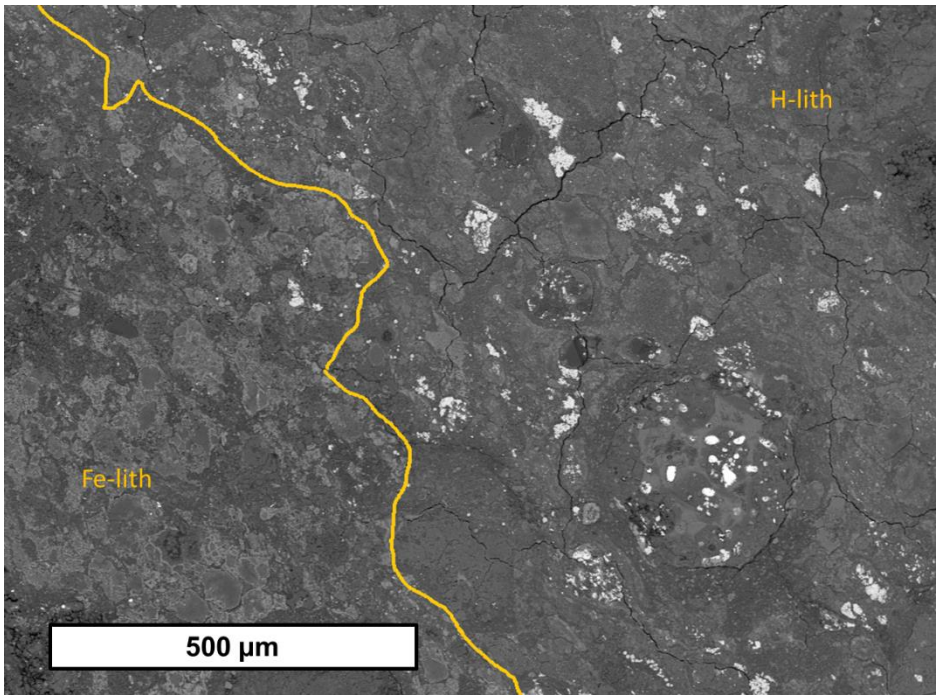

Fig. 3.2. BSE map of Kolang showing boundary between H-lith and Fe-lith. H-lith has an abundance of anhydrous sulphides and dehydration cracks, while the matrix of Fe-lith is rich in Fe. Clast outline is drawn in yellow.

3.2.3 Sulphide-Rich Lithology

The S-lith is defined by an abundance of sulphides. It is present as four clasts in the studied sections. Its tochilinite-cronstedtite intergrowths (TCIs) are rich in Ca, while the matrix is poor in it. The TCIs are poor in S, while the small sulphides are present within the matrix. The chondrules are all fairly altered and there is a low abundance of metal. Like rest of the lithologies, it best fits petrologic subtype CM2.2.

3.2.4 Fe-rich Lithology

The Fe-lith (Fig. 3.2) is defined by the matrix being rich in Fe compared to the other lithologies. It is found as three clasts, and it is the most abundant lithology studied. It is highly aqueously altered with almost no metal and many chondrule pseudomorphs yet has the highest abundance of chondrules out of all the lithologies. Its TCIs are high in S and low in Ca, while its matrix is low in S and high in Ca. It also best fits the petrologic subtype CM2.2 according to the Rubin scale.

3.2.5 Conventional Lithology

The Co-lith is defined by its lack of distinctive characteristics. It is found in five clasts. Many of its chondrules are altered and it has very little metal. Both its matrix and TCIs are low in Ca, and its TCIs are high in S. It fits the standard petrologic subtype of CM2.2.

3.3 Lewis Cliff 85311

Lewis Cliff (LEW) 85311 is a mildly aqueously altered CM chondrite that contains an abundance of refractory phases compared to other CM chondrites (Choe et al. 2010; Lee et al. 2019b). It is an Antarctic find. A thin section from ANSMET was used. Its petrographic subtype is CM2.7 (Choe et al. 2010; Lee et al. 2019b). Unlike many CM chondrites, LEW 85311 is unbrecciated. It is unshocked and has not experienced any post-hydration heating. The modal mineralogy is as follows: 38 vol% cronstedtite & tochilinite, 27 vol% lizardite, 21 vol% olivine, 10 vol% pyroxene, 2 vol% sulphates, 1 vol% magnetite, 0.5 vol% sulphides, and 0.3 vol% metal (Lee et al. 2019b).

3.4 MacAlpine Hills 88100

MacAlpine Hills 88100 (MAC 88100) is a moderately heated CM chondrite that is an Antarctic find (Quirico et al. 2018).

A thin section, 25, from ANSMET was studied. This thin section is composed of two lithologies spanning nine clasts (Fig. 3.3), which show similar degrees of post-hydration heating. Chondrules are present in all clasts. All of MAC 88100's tochilinite has decomposed and recrystallized into sulphides. Dehydration cracks proliferate its matrix. The calcite shows partial decomposition, and one particularly large piece of calcite is rimmed by a sulphate (Fig. 3.4). One of the lithologies has a greater abundance of TCI remnants than the other, so they will be referred to as the TCI-rich and matrix-rich lithologies. The area percent of objects making up each of these lithologies has been determined by point-counting, with 3019 points counted for the TCI-rich lithology and 526 points counted for the matrix-rich lithology. The TCI-rich lithology comprises 45% remnant TCIs, 44% FGRs, 10% matrix, 0.9% chondrules, 0.6% silicate fragments, 0.2% remnant carbonates, 0.1% oxides, 0.07% CAIs, and 0.03% sulphides. The matrix-rich lithology is made up of 53% matrix, 26% remnant TCIs, 9% FGRs, 4%

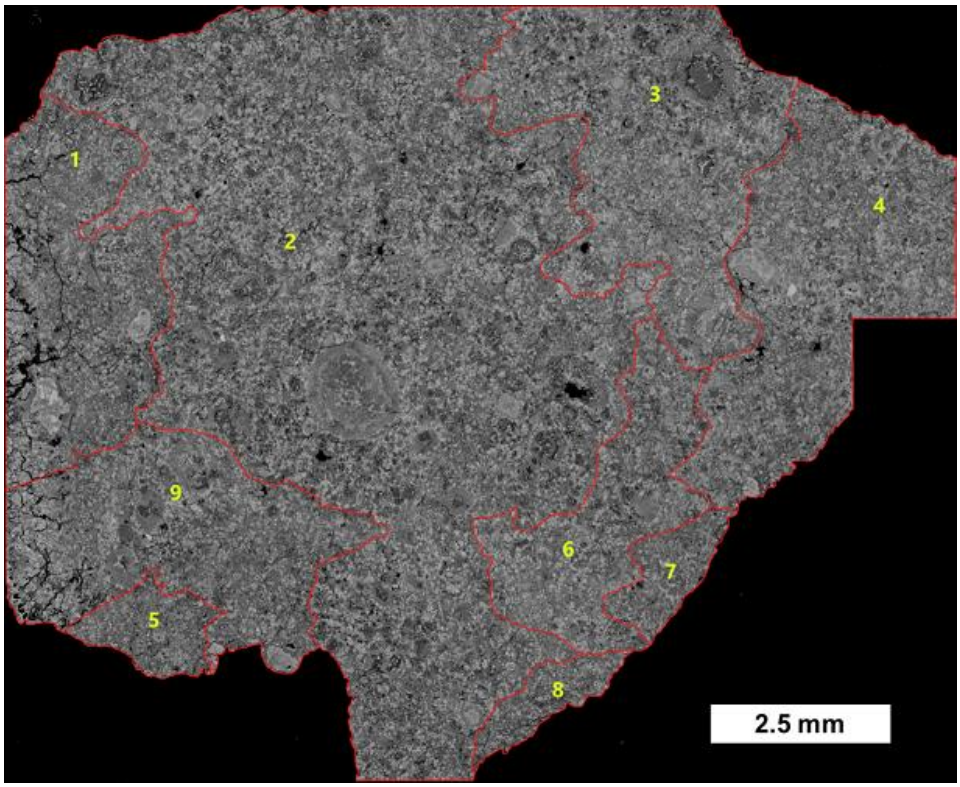

Fig. 3.3. BSE map of MAC 88100 with clasts numbered. Clasts are outlined in red. Clast 2 corresponds to the TCI-rich lithology, while clasts 1 and 3-9 correspond to the matrix-rich lithology.

chondrules, 3% silicate fragments, 3% remnant carbonates, 0.6% oxides, 0.6% sulphides, and 0.2% CAIs.

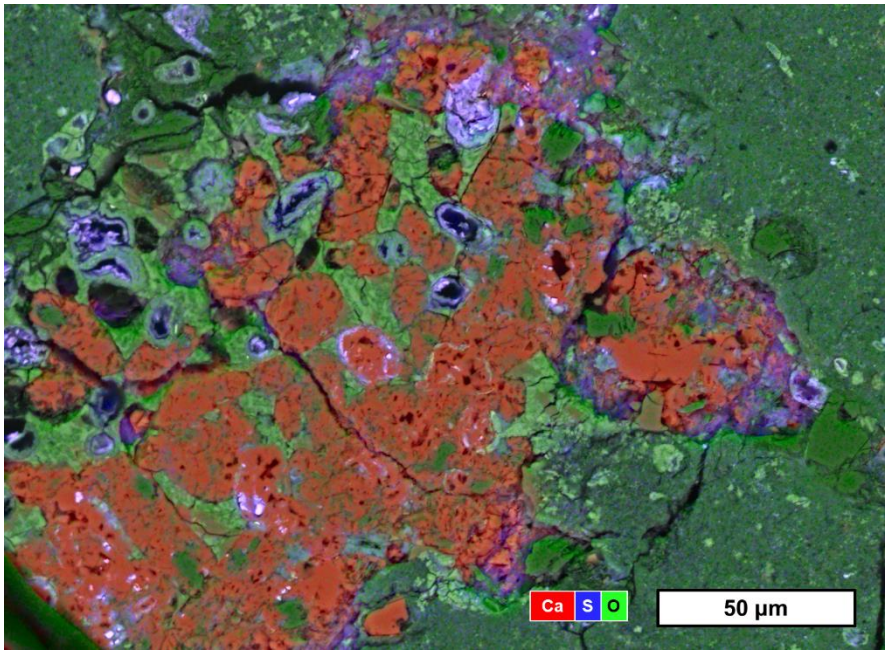

Fig. 3.4. Ca-S-O EDS map overlain on a BSE map of decomposing calcite in MAC 88100. The calcite (red) is porous and rimmed by a sulphate (purple).

3.5 Murchison

Murchison is a CM2.5 chondrite (Rubin et al. 2007) that fell in Australia in 1969 (Moore 1970). Like many CM chondrites, it is brecciated. Chondrules are partially altered; olivine is mostly intact, while the glassy mesostasis has been completely replaced. Much of the matrix is composed of TCIs, however lizardite is still present (Rubin et al. 2007; Lindgren et al. 2015. Murchison also displays a prominent petrofabric, with alignment of chondrules occurring in two perpendicular directions (Rubin et al. 2007; Lindgren et al. 2015). The bulk modal mineralogy of Murchison is as follows: 50 vol% cronstedtite & tochilinite, 22 vol% lizardite, 15 vol% olivine, 8 vol% pyroxene, 1 vol% calcite, 1 vol% magnetite, 1 vol% pyrrhotite, and 0.7 vol% pentlandite (Howard et al. 2009).

Three rock slices of Murchison were provided by the Natural History Museum, London for *in situ* heating experiments on the I18 beamline at Diamond Light Source (DLS), wherein serpentine decomposition was studied. While another set of chips (Table 3.2) from Mendy Ouzillou at Skyfall Meteorites was obtained for experimental heating at the Scottish Universities Environmental Research Centre (SUERC) and the I11 beamline at DLS.

Table 3.2. Masses of Murchison samples heated at SUERC.

Heating Temperature	Heating Duration	Initial Mass	Mass After Heating	Mass Loss
200°C	1 day	81.9 mg	78.4 mg	4%
200°C	8 days	114.1 mg	108.7 mg	5%
300°C	1 day	18.5 mg	17.3 mg	6%
400°C	1 day	20.3 mg	18.8 mg	7%
500°C	1 day	20.8 mg	18.1 mg	13%
500°C	8 days	34.5 mg	31.3 mg	9%

3.6 Murray

Murray is a CM2.4/2.5 breccia (Rubin et al. 2007; Quirico et al. 2018) that fell in Kentucky in the United States of America in 1950 (Horan 1953).

In this work, no observable petrofabric was observed, however many of its chondrules are oblong in shape (Fig. 3.5). Like Murchison, the bulk of its matrix is made up of TCIs with lizardite still present. Six rock samples of Murray were obtained that had been previously experimentally heated within a vacuum oven at SUERC for 24 hours each at the following temperatures: 200°C, 400°C, 600°C, 700°C, 800°C, and 1000°C. These samples were heated for a previous project prior to this work (Lee et al. 2019c). Polished sections of these experimentally heated samples were studied in addition to an unheated thin section, acquired from Mendy Ouzillou at Skyfall Meteorites. This unheated sample shows fractures in the matrix (Fig. 3.6) as well as fractured tochilinite (Fig. 3.7).

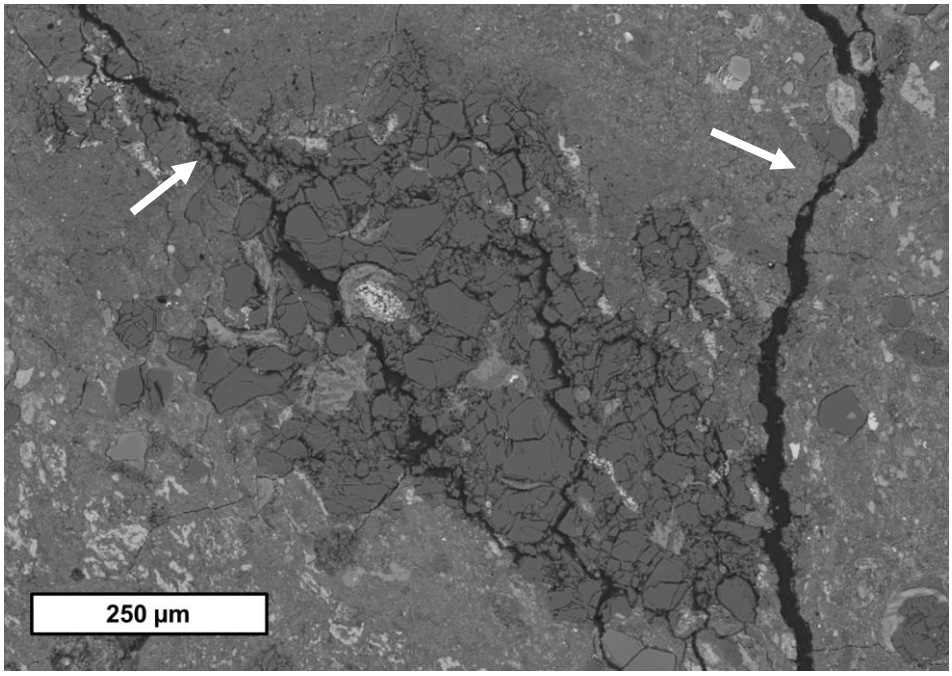

Fig. 3.5. BSE image of a section of Murray that was not experimentally heated. Fractures (marked with white arrows) are observed within the matrix.

The bulk modal mineralogy of Murray is as follows: 49 vol% cronstedtite & tochilinite, 25 vol% lizardite, 17 vol% olivine, 6 vol% pyroxene, and 2 vol% pyrrhotite (Howard et al. 2009).

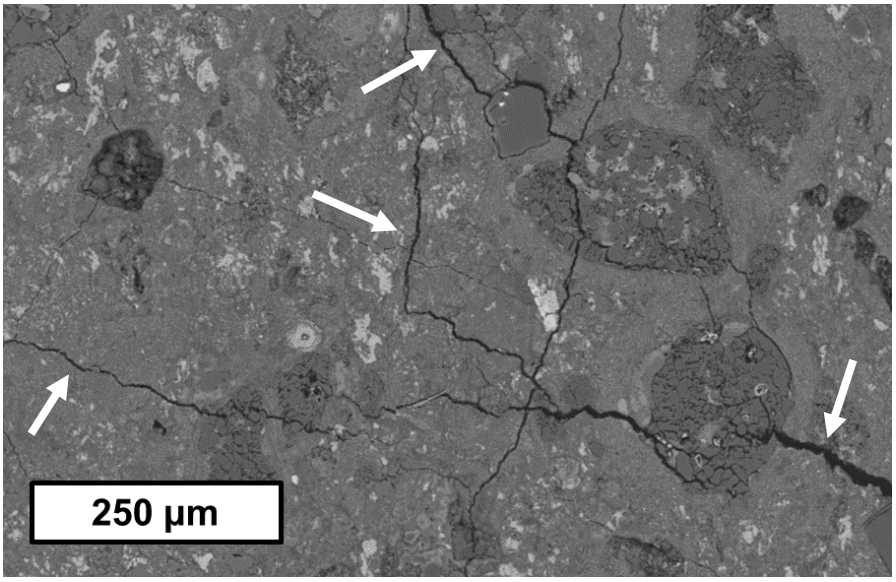

Fig. 3.6. BSE image of a section of Murray that was not experimentally heated. Fractures (marked with white arrows) are observed within the matrix.

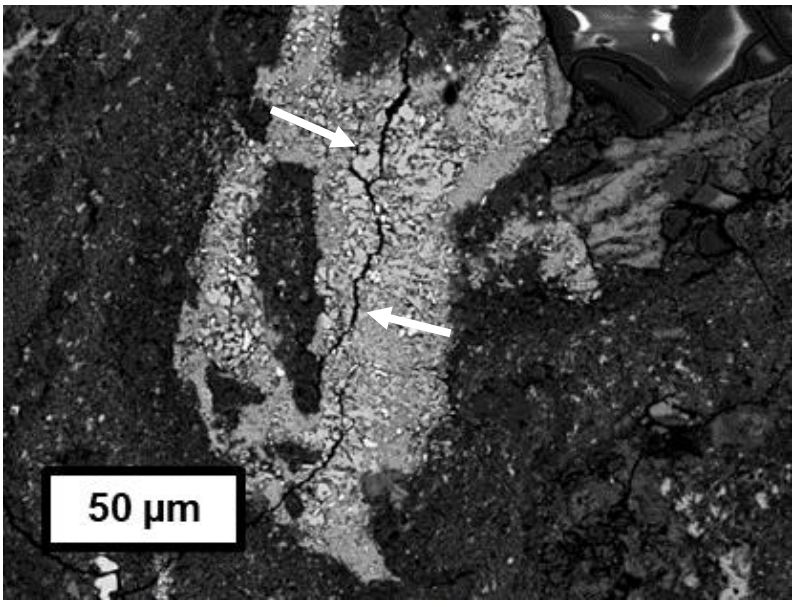

Fig. 3.7. BSE image of tochilinite within Murray showing fractures (marked with white arrows).

3.7 Pecora Escarpment 02012

Pecora Escarpment 02012 (PCA 02012) is a CM chondrite that is mainly anhydrous due to the post-hydration heating it has experienced (Quirico et al. 2018; Garenne et al. 2014).

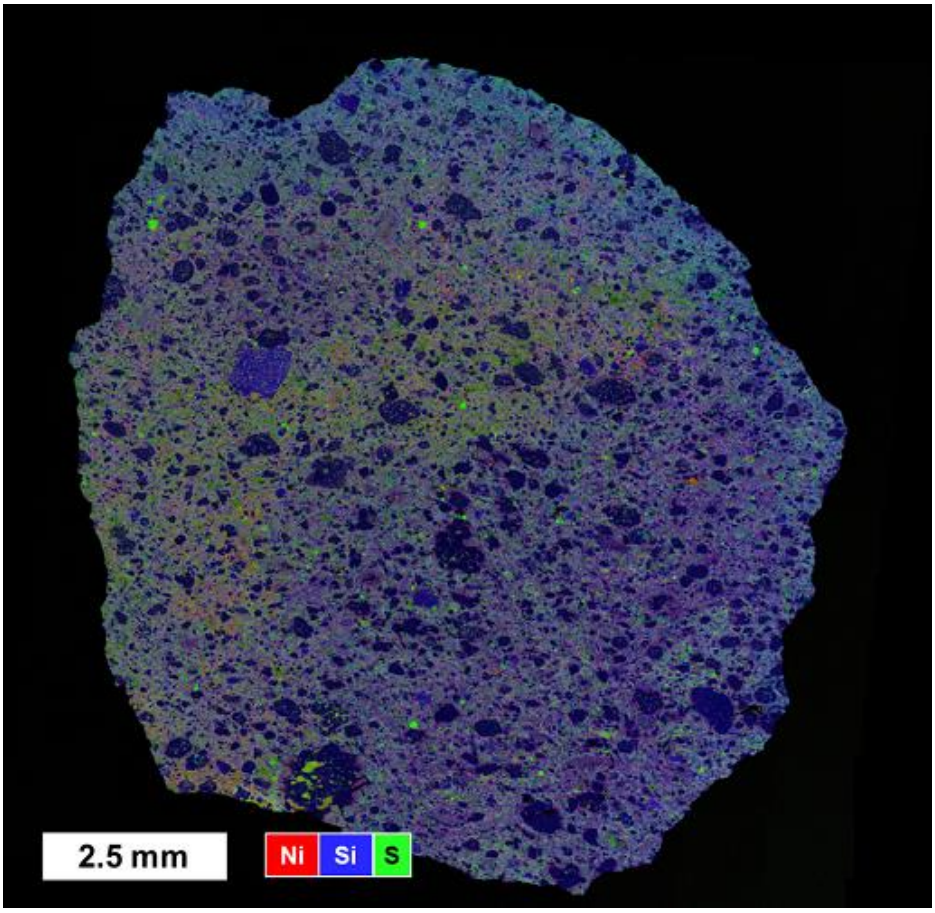

Fig. 3.8. Ni-Si-S EDS map of PCA 02012 showing compositional variation in S and Ni across the sample.

It is an Antarctic find. Thin section PCA 02012, 38, was provided by ANSMET. Although there is distinct compositional variation across PCA 02012, some of which can be observed with the naked eye (one half of the thin section is visibly brighter than the other), no discrete clast boundaries can be drawn; clast boundaries may have melded due to post-hydration heating. The compositional variation is related to a heterogeneous distribution of sulphides (Fig. 3.8). All of the tochilinite within it has decomposed into sulphides and the dehydration cracks are abundant in the matrix. Discrete TCIs are not observable and the FGRs are difficult to distinguish from the matrix. There is no calcite. The chondrules are aligned, showing evidence for a petrofabric (Fig. 3.9). Additionally, compound chondrules (chondrules made up of multiple chondrules) are present (Fig. 3.10). Its modal mineralogy in area% was determined by SEM point counting, with 86 points counted: 52% matrix, 22% FGRs, 14% chondrules, 9% silicate fragments, and 2% sulphides.

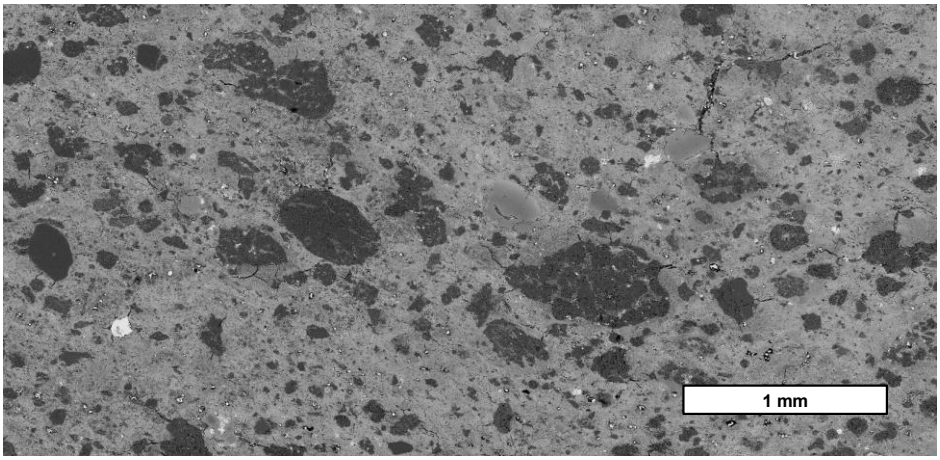

Fig. 3.9. BSE image of flattened and aligned chondrules in PCA 02012. Note how they are roughly aligned.

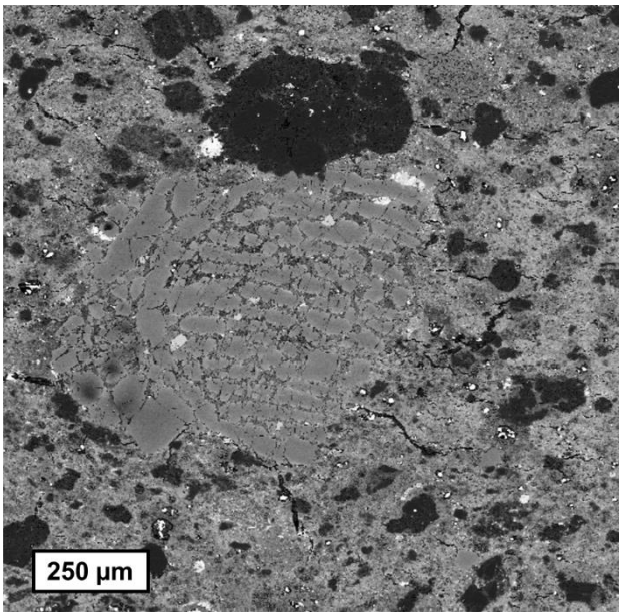

Fig. 3.10. BSE image of a compound chondrule within PCA 02012. A small porphyritic forsterite chondrule has merged with a large, barred fayalite chondrule.

3.8 Pecora Escarpment 91008

Pecora Escarpment 91008 (PCA 91008) is a CM chondrite find from Antarctica that shows evidence for post-hydration heating (Tonui et al. 2014).

Thin section PCA 91008, 52 was acquired from ANSMET. It is composed of two lithologically distinct chondrule-bearing clasts. One is richer in S-rich and has an abundance of silicate fragments (the fragment-rich lithology) while the other is relatively S-poor and has a greater abundance of chondrules (the chondrule-rich lithology) (Fig. 3.11). Dehydration cracks within the matrix are prolific, while tochilinite is observed to be decomposed with secondary sulphides and oxides. There is no calcite, but calcium sulphates are abundant. The proportion of different objects in each lithology was determined by point

counting, with 46 points counted in the fragment-rich lithology and 750 points counted in the chondrule-rich lithology. The area percent of objects making up the fragment-rich lithology is 33% matrix, 30% silicate fragments, 22% remnant TCIs, 11% FGRs, 2% chondrules, and 2% CAIs. The chondrule-rich lithology is composed of 40% matrix, 16% silicate fragments, 15% chondrules, 12% remnant TCIs, 12% FGRs, 3% CAIs, 1% oxides, and 0.4% sulphides.

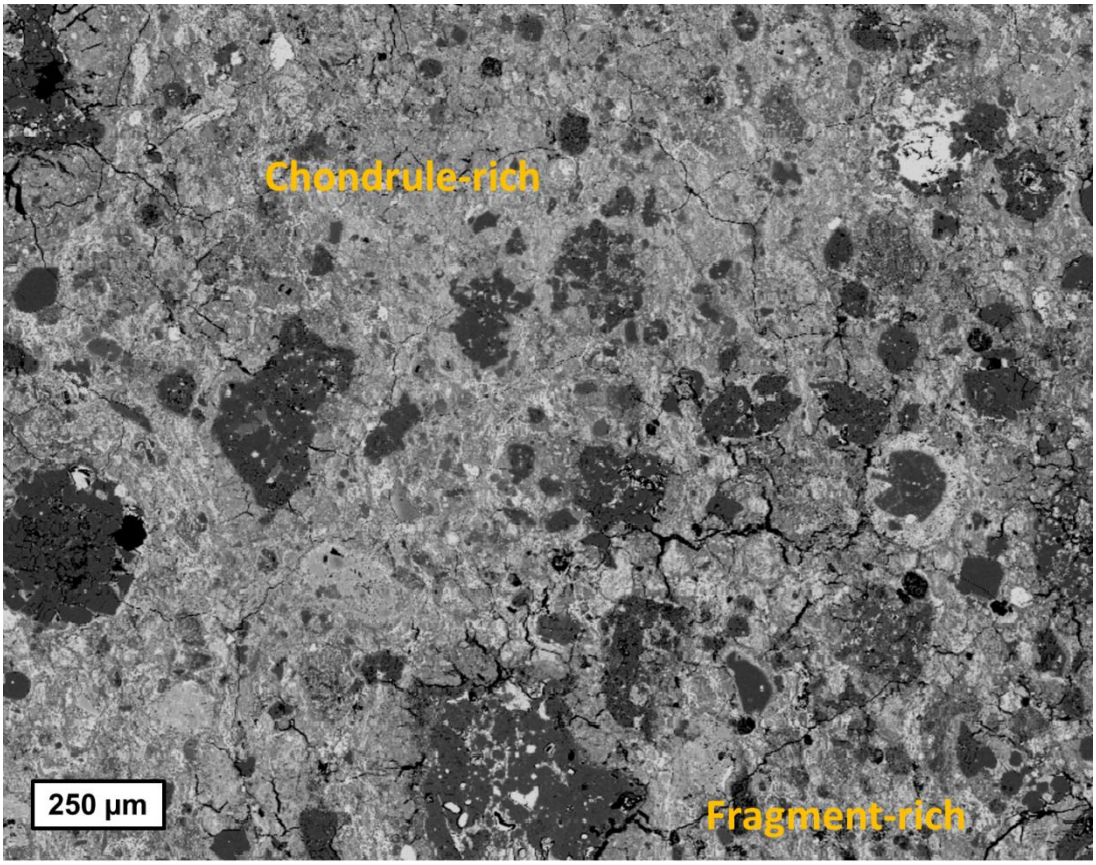

Fig. 3.11. BSE image of PCA 91008. This area shows the boundary between two clasts, with chondrule-rich and fragment-rich lithologies labelled.

3.9 Pecora Escarpment 91084

Pecora Escarpment 91084 (PCA 91084) is a CM chondrite and an Antarctic find. A polished thick section from ANSMET was studied. PCA 91084 has two clasts, each a different lithology, both of which show signs of post-hydration heating. PCA 91084's tochilinite is completely decomposed and its matrix has numerous dehydration cracks. There is no calcite. One of the lithologies has abundant TCI remnants, while the other has none. They will be referred to as the TCI-rich and TCI-absent lithologies, respectively (Fig. 3.12). The area percent of different objects making up each lithology was determined by point-counting, with 253 points counted for the TCI-rich lithology and 84 points counted for the TCI-absent lithology. The TCI-rich lithology is made up of 34%

matrix, 21% chondrules, 16% remnant TCIs, 14% FGRs, 12% silicate fragments, 2% CAIs, and 0.8% sulphides. The TCI-absent lithology is comprised of 56% matrix, 18% chondrules, 11% FGRs, 8% silicate fragments, 5% sulphides, and 2% CAIs.

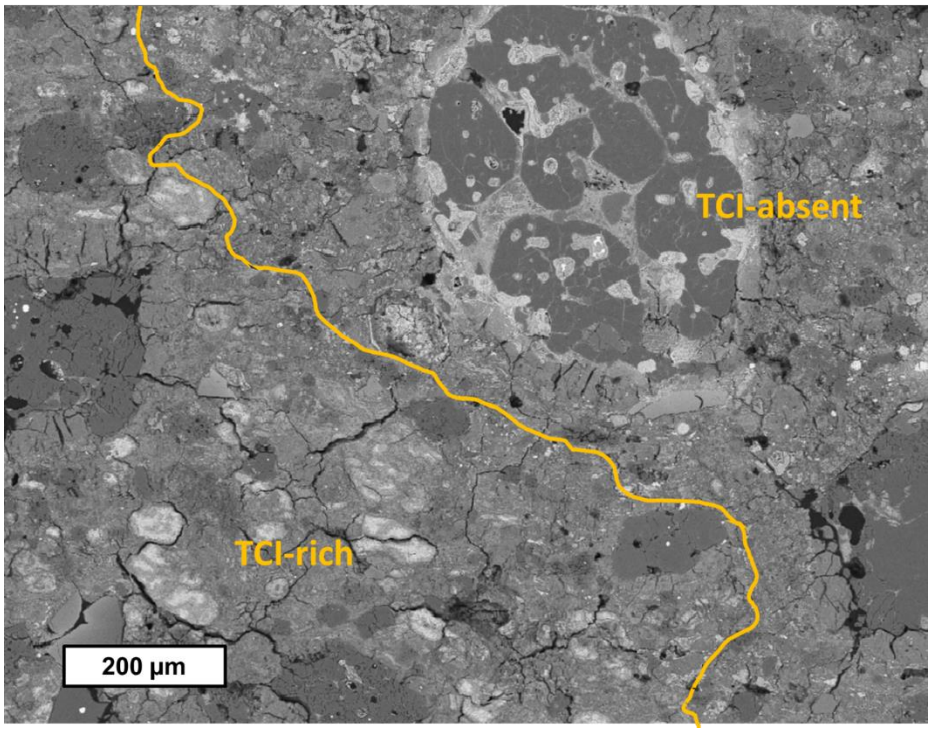

Fig. 3.12. BSE image of PCA 91084 at a clast boundary with TCI-absent and TCI-rich lithologies labelled. Clast boundary is in yellow.

3.10 Shidian

Shidian is a CM meteorite that fell in the Yunnan province, China in 2017 (Fan et al. 2022). It is a brecciated CM chondrite, whose clasts span a wide variety of alteration levels, with subtypes CM2.1-2.6 (Fan et al. 2022).

Polished thick section #1 of Shidian obtained from Shijie Li was studied. The section is composed of a single lithology without clasts. It is heavily aqueously altered, containing no Fe-Ni metal. Its matrix is predominantly composed of TCIs. Its sulphides are a mixture of troilite, pyrrhotite, and pentlandite. Calcium carbonate is present throughout. Chondrules often contain areas of tochilinite, not intergrown with serpentine minerals. These areas of tochilinite have abundant dehydration cracks and secondary sulphides indicating that they've experienced post-hydration heating (Fig. 3.13). The thin section studied best fits a subtype of CM2.2. Point counting of 337 points has revealed that the area percent of objects making up section #1 is 47% TCIs, 24% matrix,

13% chondrules, 10% FGRs, 2% carbonates, 2% sulphides, and 2% silicate fragments.

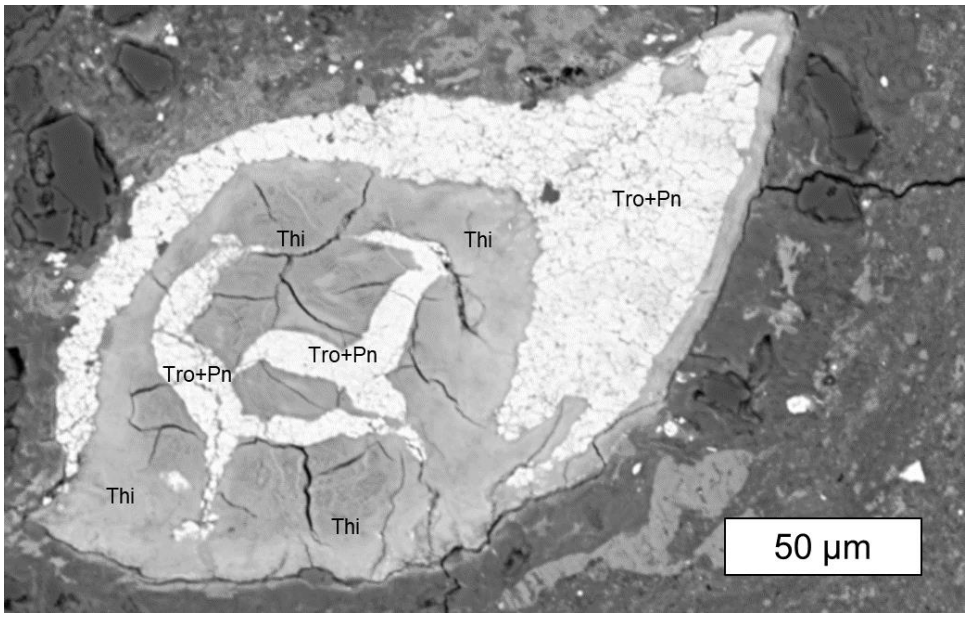

Fig. 3.13. BSE image of decomposed tochilinite in Shidian 1. Secondary sulphides, troilite (Tro) and pentlandite (Pn), from recrystallization of heated tochilinite (Thi) are labelled.

3.11 Sutter's Mill

Sutter's Mill is an ungrouped carbonaceous chondrite that fell in the United States of America in 2012 (Jenniskens et al. 2012; Harbele & Garvie 2017). It contains a great variety of clasts, most of which, but not all, are composed of CM chondrite material (Zolensky et al. 2014). Some clasts within Sutter's Mill are made up of material thermally metamorphosed; they contain oldhamite rimming the decomposed remnants of calcite (Zolensky et al. 2014; Haberle & Garvie 2017). These clasts have been aqueously altered with some of them being devoid of chondrules (Zolensky et al. 2014), and others retain chondrules (Haberle & Garvie 2017). A polished thick section of Sutter's Mill, SM3, the oldhamite-bearing lithology of Sutter's Mill, was acquired from Arizona State University.

3.12 Winchcombe

Winchcombe is a CM meteorite that fell in Winchcombe, Gloucestershire, United Kingdom in 2021 (King, Daly et al. 2022). It is a breccia whose clasts span a wide range of alteration levels, with subtypes CM2.0-2.6 (Suttle et al. 2022; King, Daly et al. 2022). Two polished thick sections of Winchcombe, P30540 and

P30552, were studied. P30540 is composed of three clasts, each a different lithology: F, Mx, and G (Suttle et al. 2022). The F lithology is completely devoid of anhydrous silicates and TCIs; it is of a petrologic subtype CM2.0 (Fig. 3.14a). The Mx lithology is a cataclastic lithology composed of a wide array of mineral and chondrule fragments (Fig. 3.14b). The G lithology is highly altered, yet retains some chondrules and TCIs, and is therefore CM2.1 (Fig. 3.14c) (Suttle et al. 2022). P30552 is made up of two clasts of the same lithology, A (Suttle et al. 2022). The A lithology is comprised of partially altered chondrules and a TCI-serpentine matrix. It has a petrologic subtype of 2.2 (Fig. 3.14d&e). All lithologies discussed contain carbonates (Suttle et al. 2022). SEM point-counting statistics are in Table 3.3.

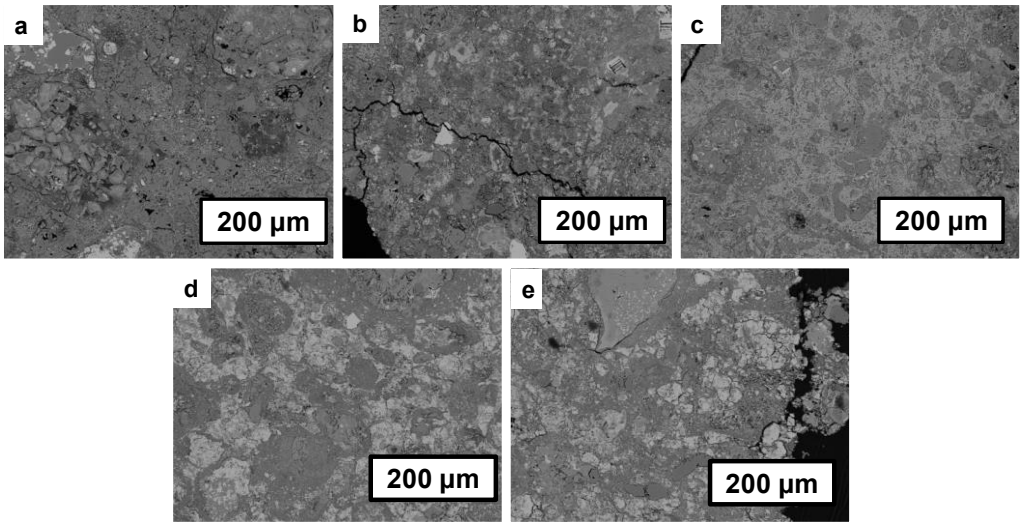

Fig. 3.14. BSE images of select areas in each clast in Winchcombe sections P30540 and P30552. a) BSE image of the F lithology in P30540. b) BSE image of the Mx lithology in P30540. c) BSE image of the G lithology in P30540. d) BSE image of the A lithology in the largest clast in P30552. e) BSE image of the A lithology in the smallest clast in P30552.

In addition to P30540 and P30552, a sample of Winchcombe that had been experimentally heated for another study (King, Daly et al. 2022) was analysed. King, Daly et al. (2022) heated this sample to 1100°C over a time period that was less than a day for hydrogen pyrolysis. It is important to note that although this sample has been heated to 1100°C, it has not spent an entire day at that temperature; it is more representative of gradual heating. The heated sample was made into three thin sections, in which there are 24 clasts from six lithologies.

The lithologies in the experimentally heated samples have been altered from their original makeup, making it difficult to discern what they originally

were. However, the lithologies observed are comparable with the A lithology, the F lithology, and the Mx Lithology (described above), as well as the D lithology, the E lithology, and the H lithology. The D lithology is characterised by being minimally altered (CM2.6), with web-like serpentine and very few TCIs, as well as containing metal within its matrix (Suttle et al. 2022). The E lithology is defined by a distinct petrofabric and elongated chondrules, and is of a petrologic subtype of 2.3 (Suttle et al. 2022). Lithology H is of petrologic subtype 2.3/2.4, having abundant TCIs and pentlandite (Suttle et al. 2022).

Table 3.3. Constituents of each studied Winchcombe lithology in sections P30540 and P30552 from SEM point counting of polished samples. Values in area %.

Lithology	Number of Points	Chondrule	Carbonate	Serpentine Matrix	Silicate Fragments	FGR	TCIs	CAIs	Sulphides	Oxides	Metal
A	73	5%	1%	19%	5%	33%	36%	0%	0%	0%	0%
F	220	0%	7%	85%	0%	2%	0%	0%	7%	0%	0%
G	68	0%	3%	44%	0%	4%	47%	0%	1%	0%	0%
Mx	53	4%	8%	58%	4%	0%	25%	0%	2%	0%	0%

3.13 Wisconsin Range 91600

Wisconsin Range (WIS) 91600 is an anomalous CM-like carbonaceous chondrite that is an Antarctic find (Choe et al. 2010).

A thin section, WIS 91600, 89, was acquired from ANSMET. It was observed to be composed of one lithology and no clasts. The matrix is rich in serpentine, with an abundance of magnetite and sulphides. There is no tochilinite, however there are altered chondrules. It displays dehydration cracks consistent with heating. Carbonates can be observed throughout the matrix. FGRs of chondrules and other objects within WIS91600 vary in composition (Fig. 3.15), with some being Fe and S-rich and others being Fe-poor.

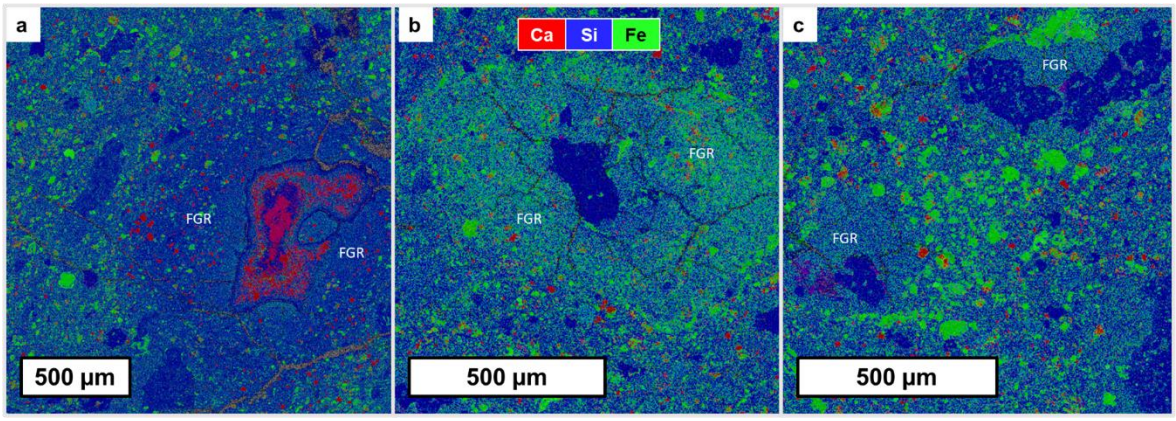

Fig. 3.15. Ca-Si-Fe EDS maps of FGRs within WIS 91600. a) An Fe-poor FGR surrounding a CAI. b) An Fe and S-rich FGR surrounding a chondrule. c) FGRs of moderate composition surrounding chondrules.

WIS 91600 is composed of 74 vol% decomposed lizardite, 10 vol% olivine, 8 vol% magnetite, 4 vol% sulphides, 4 vol% decomposed cronstedtite, 2 vol% pyroxene, and 0.6 vol% calcite (Hanna et al. 2020).

3.14 Representative BSE Images

The following figures are BSE images for each sample they could be collected for. With the exception of Sutter's Mill, these BSE images are produced from montaged BSE maps.

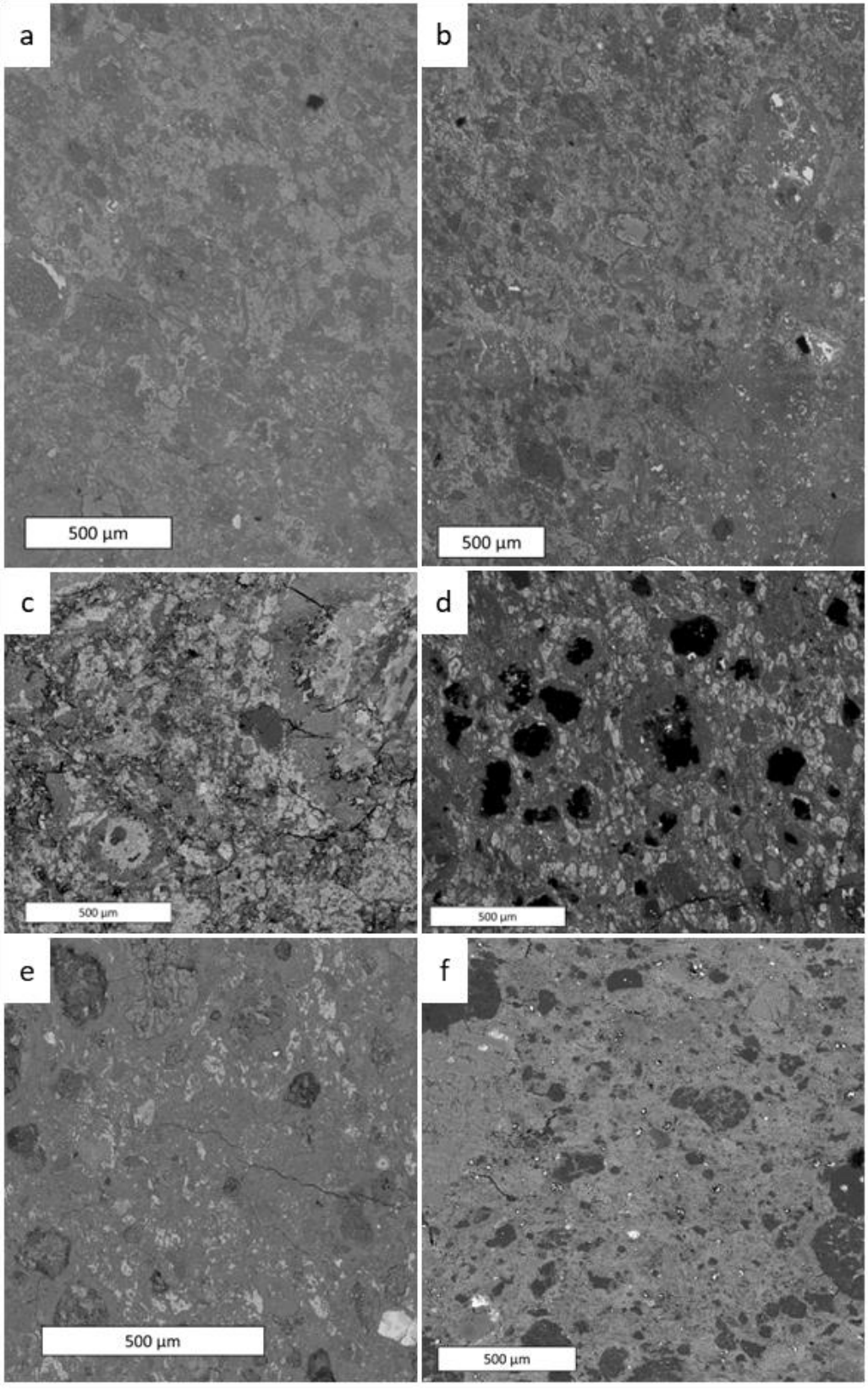

Fig. 3.16. Representative BSE images of studied meteorites. a) Kolang_01. b) Kolang_02. c) MAC 88100. d) Murchison. e) Murray. f) PCA 02012.

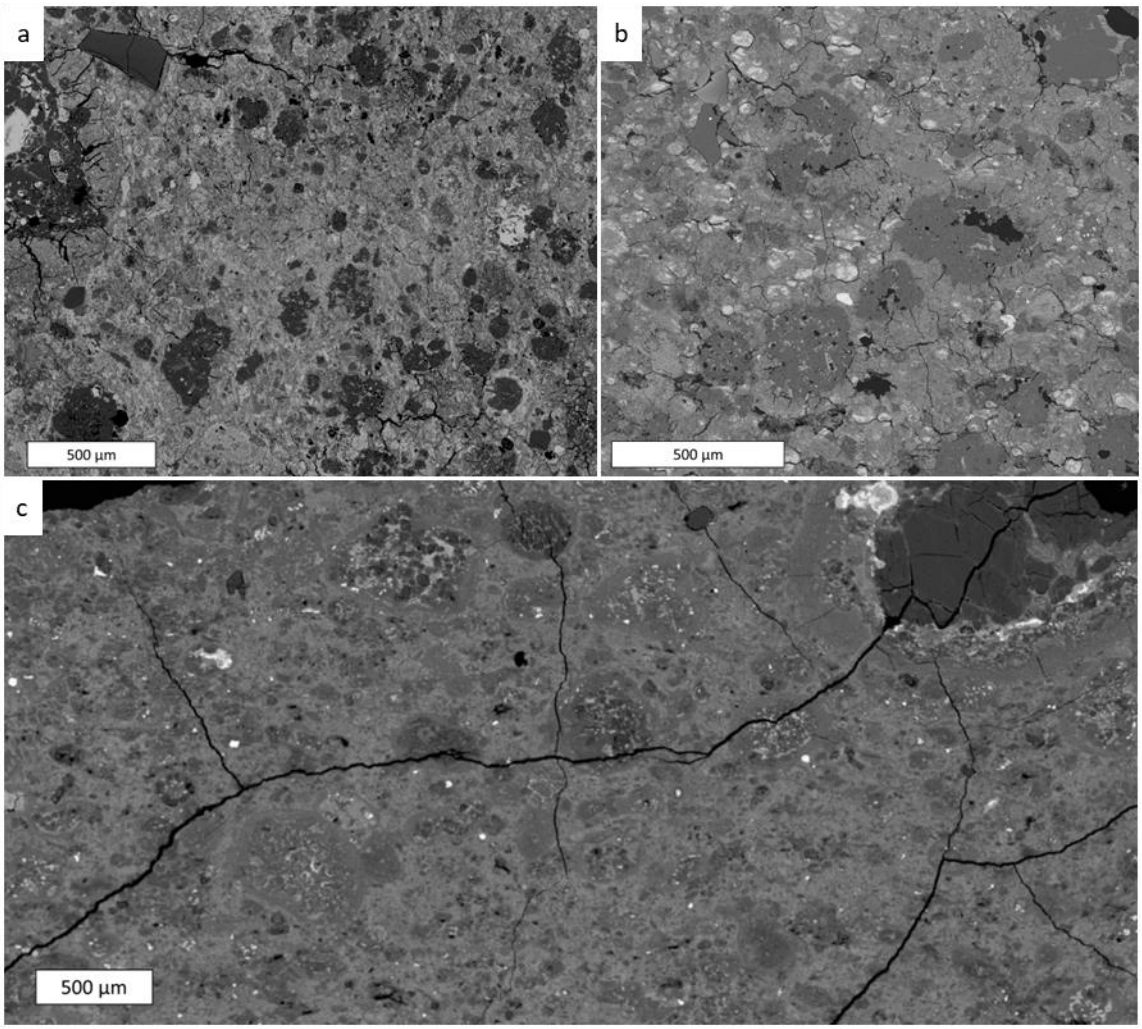

Fig. 3.17. Representative BSE images of studied meteorites. a) PCA 91008. b) PCA 91084. c) Shidian.

Chapter 4 – Hydroandradite – A Metasomatic Mineral Produced During Aqueous Alteration

A Ca-Fe silicate with a high amount of oxygen indicating likely hydration (Fig. 4.1-4.4) was observed in the recent CM chondrite falls Shidian and Kolang. Herein, I characterize this silicate through a combination of EPMA, Raman, and TEM. As established in this chapter, this phase was found to be a hydrogarnet called hydroandradite, $(Ca_3Fe^{+3}_2(SiO_4)_{3-x}(OH)_{4x})$. This is the first report of the occurrence of hydroandradite in CM chondrites; its presence has implications for the geologic processes occurring on Shidian and Kolang's parent body(ies).

Hydroandradite has been previously observed in terrestrial rocks that have experienced calc-silicate metasomatism (Ghosh et al. 2017). Its formation temperature isn't well defined, however its completely hydrated endmember, tricalcium ferrite hexahydrate, can be synthesized at room temperature (Eiger 1937) and its anhydrous endmember, andradite, can form at a maximum temperature of 300°C (Plümper et al. 2014; Ménez et al. 2012). The hydration (amount of OH^- in its crystal structure) of hydroandradite is dependent on temperature, with higher degrees of hydration requiring lower formation temperatures (Huckenholz & Fehr 1982). Additionally, its thermal stability may also vary with temperature; Flint et al. (1941) experimented with extremely hydrous hydroandradites synthesized at 60-100°C and caused them to decompose by heating to 220°C. Little has been established about hydroandradite's thermal stability beyond these experiments.

Hydroandradite forms exclusively by the metasomatic replacement of other minerals and requires a specific fluid composition: high pH, low CO_2, low αSiO_2 with Si in the fluid, and high Ca (Plümper et al. 2014; Ghosh et al. 2017; Beard and Hopkinson 2000). The phases which terrestrial hydroandradite is known to replace include, but are not limited to, perovskite, magnetite, titanite, clinopyroxene, and ilmenite (Ghosh et al. 2017; Ellison et al. 2021; Schmitt et al. 2019).

Hydroandradite is a metasomatic mineral, formed through water-mediated replacement of other phases (Schmitt et al. 2019; Ghosh et al. 2017). Metasomatism is defined as metamorphism that chemically replaces one mineral with another through the use of fluids (Harlov and Austraheim 2013). This definition has no temperature restriction and applies to many of the changes carbonaceous chondrites undergo on their parent asteroids (e.g., replacement of olivine and pyroxene by serpentine). However, more often than not within the planetary science literature, this alteration is referred to as aqueous alteration and is considered separate from metasomatism (Brearley and Krot 2013). CM chondrites contain a number of secondary minerals produced by the aqueous replacement of primary minerals (Table 4.1). This incongruency with terminology is rectified by referring to reactions that produce serpentine minerals as aqueous alteration, and reactions that produce anhydrous minerals without producing serpentine as metasomatism (Brearley and Krot 2013).

Table 4.1 Common alteration minerals that form via replacement of other phases within CM chondrites.

Alteration Minerals	Phases Replaced	References
Apatite	Amorphous materials, Fe-Ni metal	1,2
Calcite	Aragonite, calcium-aluminium rich inclusions (CAIs), dolomite, olivine, pyroxene	3
Cronstedtite serpentine	Amorphous materials, calcite, dolomite, Fe-Ni metal, olivine, pyroxene, sulphides, tochilinite	1,2,3,4,5
Lizardite serpentine	Amorphous materials, calcite, cronstedtite, dolomite, olivine, pyroxene, tochilinite	1,3,4,5
Magnetite	Fe-Ni metal, sulphides	1,2,6
Sulphides	Fe-Ni metal, calcite, dolomite, tochilinite, troilite	1,2,3,5
Tochilinite	Fe-Ni metal, calcite, sulphides	2,3,4

[1]Rubin et al. (2007). [2]Palmer & Lauretta (2011). [3]Lee et al. (2014). [4]Hanowski & Brearley (2001). [5]Grossman et al. (2000). [6]King et al. (2017)

To better understand fluid-facilitated metamorphism (e.g., aqueous alteration, metasomatism), I describe and characterize the occurrence of the hydroandradite within Shidian and Kolang, as well as discuss what conditions it may form and its thermal stability. As the reactions we are discussing do not involve the production of phyllosilicates, I will be referring to hydroandradite as

a metasomatic mineral to be consistent with the literature (Schmitt et al. 2019; Ghosh et al. 2017; Plümper et al. 2014; Beard and Hopkinson 2000), however it is entirely possible for it to have formed alongside phyllosilicates during aqueous alteration. This is the first report of hydroandradite occurring within meteorites. Understanding its occurrence will yield information regarding the fluid compositions within these CM chondrites during aqueous alteration as well as their temperatures. Additionally, further information regarding hydroandradite's stability will aid in understanding its terrestrial occurrences.

4.1 Identification of Hydroandradite in Shidian and Kolang

In BSE and EDS maps for both Kolang and Shidian, an O-rich Ca-Fe silicate was identified (Fig. 4.1-4.4). EDS data showed that the amount of O in the phase was typical for that of a hydrous mineral; hydroandradite was found to be the only mineral to fit the composition displayed by EDS (O-rich, Ca-Fe silicate). This hydroandradite appears to occur in four different morphologies: layered (Fig. 4.1), perovskite-associated (Fig. 4.2), spheroidal (Fig. 4.3), and sulphide-associated (Fig. 4.4).

To confirm the identification of hydroandradite, EPMA data were collected for sulphide-associated hydroandradite in Shidian and perovskite-associated hydroandradite in Kolang. Raman spectra and TEM data were also obtained for perovskite-associated hydroandradite within Kolang.

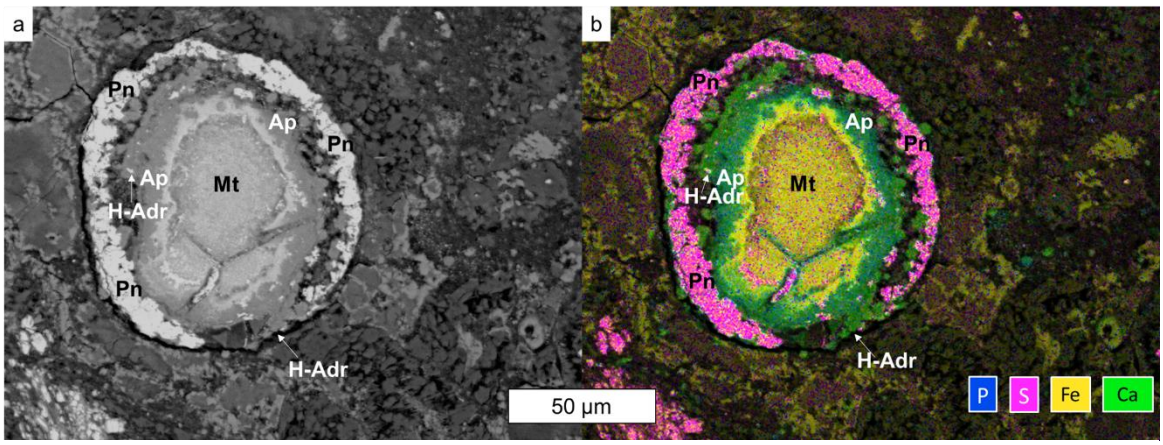

Fig. 4.1. Layered hydroandradite in Kolang. Hydroandradite (H-Adr), pentlandite (Pn), apatite (Ap), and magnetite (Mt) are labelled. a) BSE image. b) Ca-Fe-P-S EDS map. H-Adr is light green, Pn, is pink, Ap, is turquoise, and Mt is yellow.

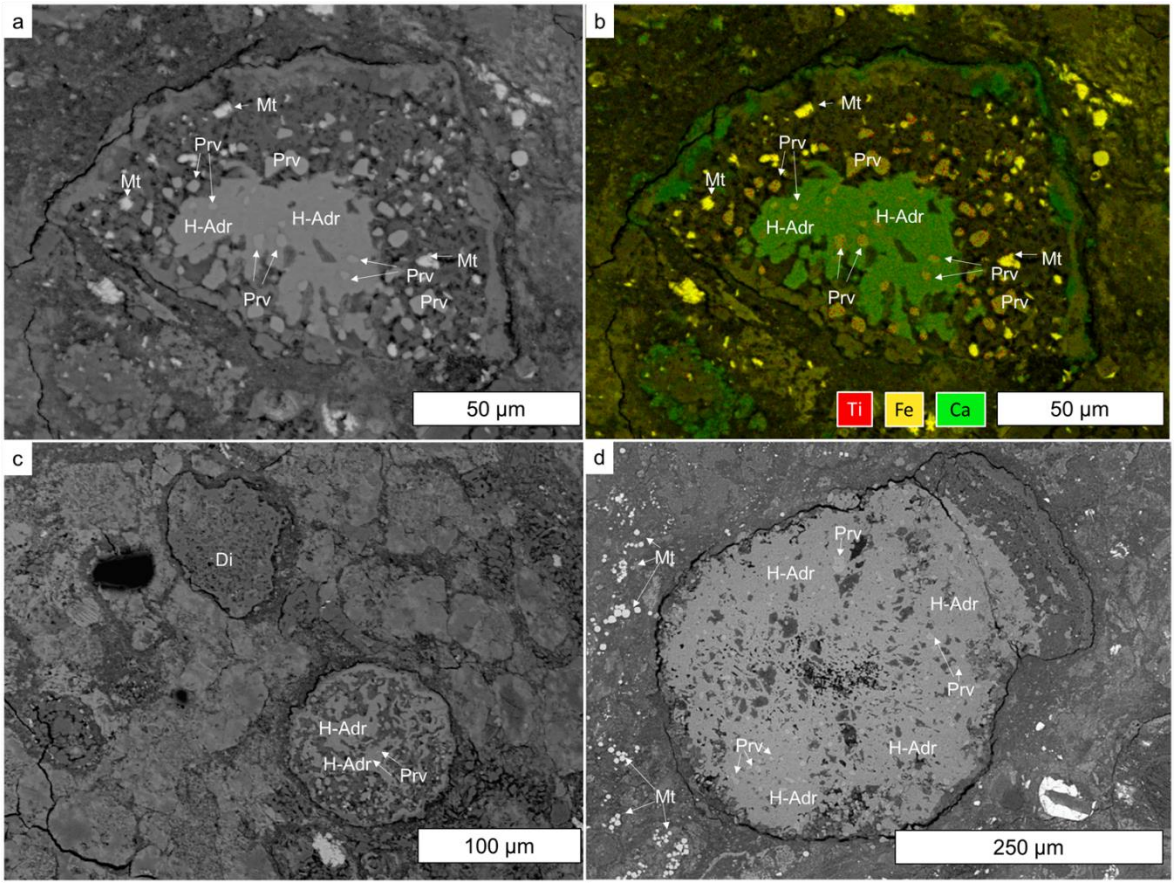

Fig. 4.2. Perovskite associated hydroandradite in Kolang. Hydroandradite (H-Adr), perovskite (Prv), magnetite (Mt), and diopside (Di) are labelled. a) BSE image of aggregate H-Adr. b) Ca-Fe-Ti EDS map of aggregate H-Adr. c) BSE image of web-like H-Adr next to web-like Di. d) BSE image of aggregate H-Adr with a layered rim. Spheroidal Mt can be observed nearby.

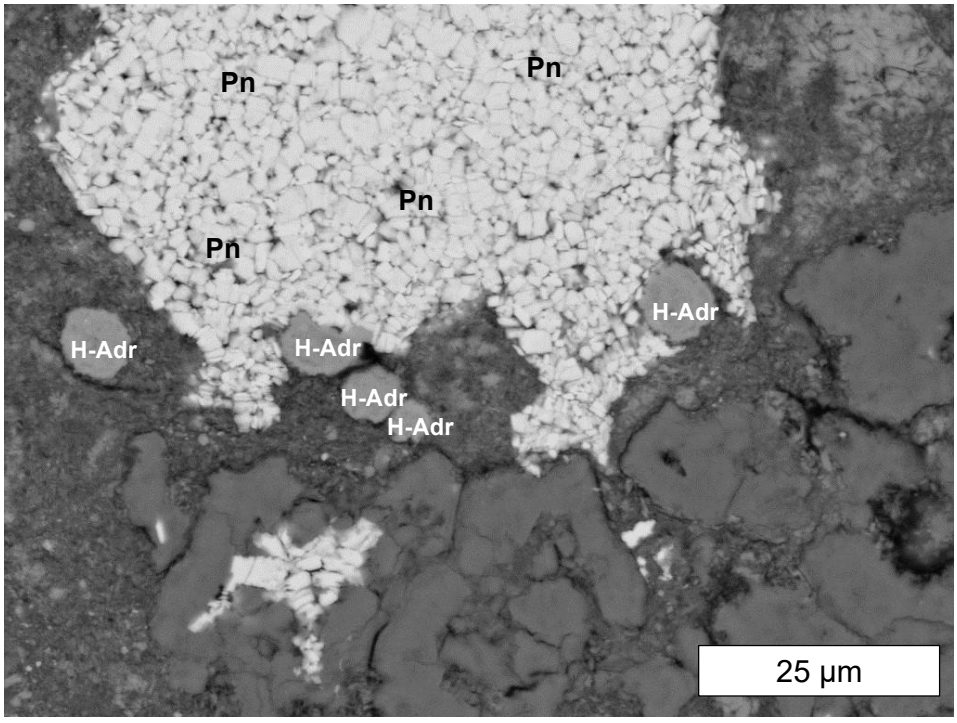

Fig. 4.3. BSE image of spheroidal hydroandradite in Kolang. Hydroandradite (H-Adr) and pentlandite (Pn) are labelled.

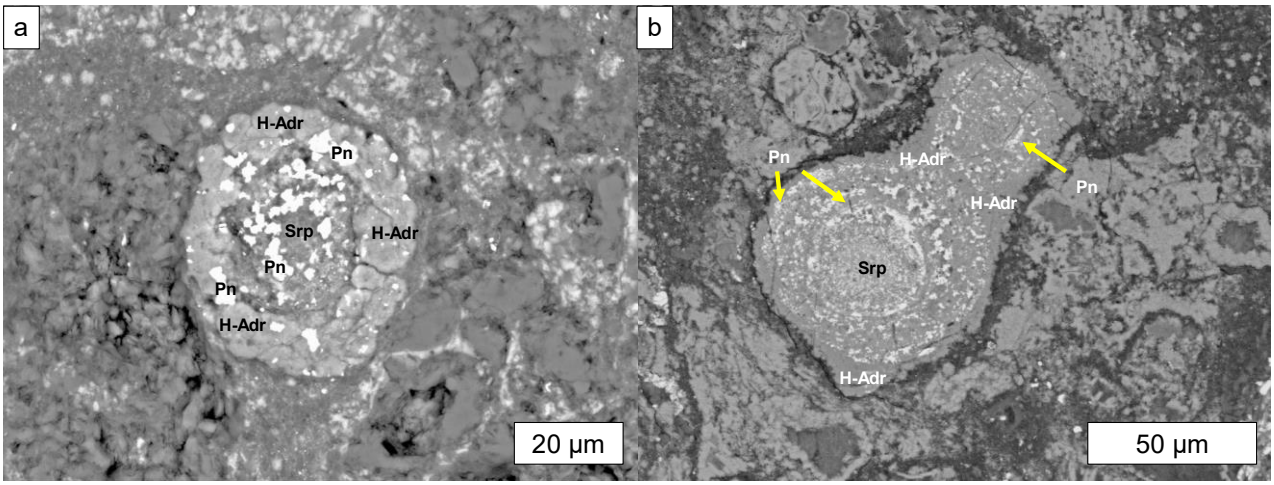

Fig. 4.4. BSE images of sulphide-associated hydroandradites. Hydroandradite (H-Adr), pentlandite (Pn), and serpentine (Srp) are labelled. a) In Shidian. b) In Kolang.

4.1.1 Hydroandradite EPMA

EPMA data collected for the hydroandradites have analytical totals of 84-91 wt. %, indicating an unanalysed component, likely either void space or a volatile (e.g., water, carbonate) component (Table 4.2). The targeted area showed no signs of pores or void space. If this component is assumed to be a volatile, the EPMA determined composition is consistent with that of hydroandradite (Fig. 4.5) (e.g., Ellison et al. 2021; Schmitt et al. 2019; Amthauer and Rossman 1998; Armbuster 1995; Flint et al. 1941). The compositions of the hydroandradite were calculated with the assumption that there are exactly three Ca atoms (Table 4.2). It was found that the perovskite-associated hydroandradite within Kolang is more hydrated than the sulphide-associated hydroandradite in Shidian (Fig. 4.5); the perovskite-associated hydroandradite has ~2.6 OH^- for every SiO_4^{4-}, while Shidian's sulphide-associated hydroandradite has ~1.4 OH^- for every SiO_4^{4-}. Additionally, Kolang's perovskite-associated hydroandradite has minor amounts of Ti, while Shidian's sulphide-associated hydroandradite has minor concentrations of Mg.

Table 4.2. Compositions (wt%) of oxides making up hydroandradites within Kolang and Shidian as determined by EPMA.

Target	Al_2O_3	CaO	Cr_2O_3	Fe_2O_3	K_2O	MgO	MnO	Na_2O	NiO	SiO_2	TiO_2	Total	Final Formula
Shidian -2	1.55	28.19	0.49	25.92	0.02	3.60	0.07	0.56	5.87	23.64	0.58	90.50	$Ca_{3.0}(Fe_{1.9}Mg_{0.5}Al_{0.2})(SiO_4)_{2.3}(OH)_{2.6}$
Shidian -3	1.00	28.74	0.57	27.79	0.01	3.30	0.07	0.21	0.92	23.07	0.61	86.28	$Ca_{3.0}(Fe_{2.0}Mg_{0.5}Al_{0.1})\ (SiO_4)_{2.2}(OH)_{3.0}$
Shidian -4	1.01	31.60	0.19	26.27	0.02	3.33	0.08	0.18	0.54	22.06	0.86	86.16	$Ca_{3.0}(Fe_{1.8}Mg_{0.4}Ti_{0.1}Al_{0.1})\ (SiO_4)_{2.0}(OH)_{4.2}$
Shidian -5	1.39	26.73	0.21	31.17	0.03	3.59	0.11	0.31	0.65	22.93	0.54	87.65	$Ca_{3.0}(Fe_{2.5}Mg_{0.6}Al_{0.2})\ (SiO_4)_{2.4}(OH)_{2.4}$
Kolang -1	0.83	33.16	0.01	23.62	n.d.	0.44	0.09	0.16	0.02	21.43	4.67	84.36	$Ca_{3.0}(Fe_{1.1}Ti_{0.4})\ (SiO_4)_{1.9}(OH)_{4.2}$
Kolang -2	0.73	33.86	0.03	24.06	n.d.	0.31	0.10	0.14	0.03	21.51	3.51	84.22	$Ca_{3.0}(Fe_{1.1}Ti_{0.3})\ (SiO_4)_{1.9}(OH)_{4.4}$
Kolang -6	1.06	34.02	0.02	26.52	n.d.	0.14	0.09	0.13	0.02	20.54	3.69	86.23	$Ca_{3.0}(Fe_{1.6}Ti_{0.2}Al_{0.1})\ (SiO_4)_{1.7}(OH)_{5.2}$
Kolang -7	0.86	34.55	0.03	23.92	n.d.	0.11	0.06	0.13	0.03	20.48	4.33	84.51	$Ca_{3.0}(Fe_{1.5}Ti_{0.3}Al_{0.1})\ (SiO_4)_{1.7}(OH)_{5.4}$
Kolang -8	1.30	34.98	0.03	24.78	0.01	0.12	0.06	0.15	0.03	20.30	4.17	85.92	$Ca_{3.0}(Fe_{1.5}Ti_{0.3}Al_{0.1})\ (SiO_4)_{1.6}(OH)_{5.5}$
Kolang -9	0.50	34.52	0.03	26.57	n.d.	0.07	0.11	0.15	0.04	21.47	3.22	86.68	$Ca_{3.0}(Fe_{1.6}Ti_{0.2})\ (SiO_4)_{1.7}(OH)_{5.0}$
Kolang -10	0.63	34.51	0.01	26.97	n.d.	0.29	0.13	0.14	0.03	22.83	1.24	86.77	$Ca_{3.0}(Fe_{1.6}Ti_{0.1}Al_{0.1})\ (SiO_4)_{1.9}(OH)_{4.6}$
Kolang -11	0.73	34.56	0.01	28.07	n.d.	0.09	0.13	0.16	0.02	22.89	1.21	87.87	$Ca_{3.0}(Fe_{1.7}Ti_{0.1}Al_{0.1})\ (SiO_4)_{1.9}(OH)_{4.6}$
Kolang -12	0.66	33.98	0.01	28.19	n.d.	0.17	0.14	0.14	n.d.	23.81	0.69	87.80	$Ca_{3.0}(Fe_{1.7}Al_{0.1})\ (SiO_4)_{2.0}(OH)_{4.2}$
Kolang -13	1.34	34.34	0.05	25.92	n.d.	0.58	0.14	0.15	0.05	21.84	1.67	86.08	$Ca_{3.0}(Fe_{1.6}Mg_{0.1}Ti_{0.1}Al_{0.1})\ (SiO_4)_{1.8}(OH)_{4.9}$
Kolang -14	2.45	29.28	0.11	26.33	0.01	3.45	0.13	0.13	0.07	24.84	2.48	89.28	$Ca_{3.0}(Fe_{1.9}Mg_{0.5}Ti_{0.2}Al_{0.3})\ (SiO_4)_{2.4}(OH)_{2.5}$

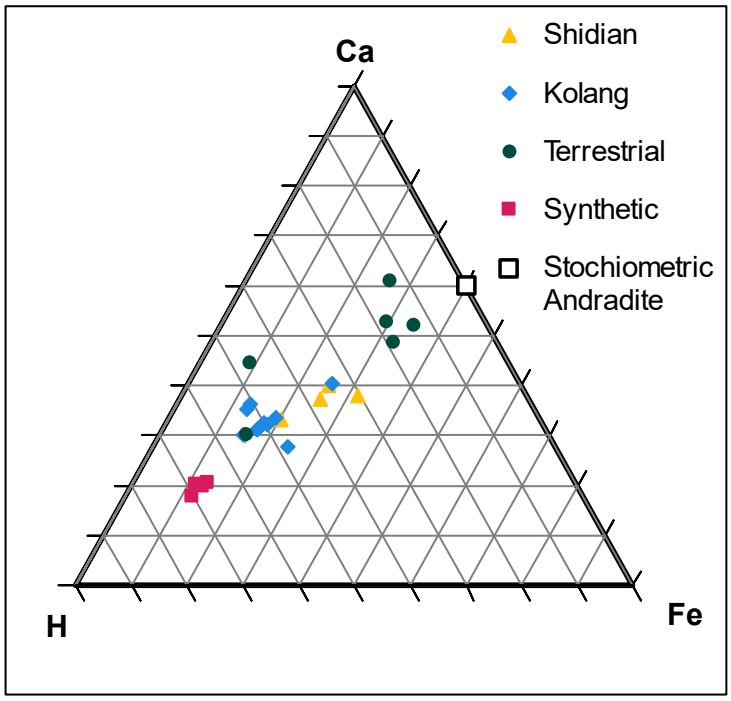

Fig. 4.5. Ca-Fe-H (in at%) ternary diagram of spots measured with EPMA in the PA-HAdr in Kolang and the SA-HAdr in Shidian. Terrestrial (Ellison et al. 2021; Schmitt et al. 2000; Amthauer and Rossman 1998; and Armbuster 1995) and synthetic (Flint et al. 1941) data, as well as stochiometric andradite are presented for comparison. Ternary diagram made using the method developed by Graham and Midgley (2000).

4.1.2 Hydroandradite TEM

Bright-field TEM images from the perovskite-associated hydroandradite show a monomineralic and finely polycrystalline material without any void space (Fig. 4.6a), confirming that the low wt% totals of the EPMA data are volatile-related. The eight SAED images collected correspond to a mineral with cubic symmetry. Miller indices were determined based on the reported unit cell of a=12.25 Å for hydroandradite by Armbruster (1995). The average d-spacings of each reflection set are listed in Table 4.3. The unit cell that best fits the observed d-spacings is a≅12.2 Å (Fig. 4.6b; Table 4.3). As hydroandradite is a cubic mineral with a unit cell whose parameters are 12.0 Å < a < 12.4 Å (Lager et

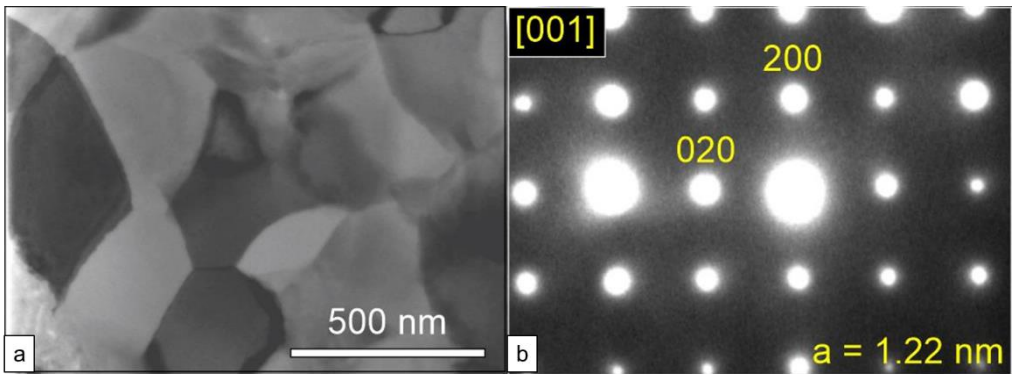

Fig. 4.6. TEM results from PA-HAdr in Kolang. a) Brightfield image. b) SAED image corresponding to an axis length of a≅12.2 Å. (020) and (200) miller indices are annotated.

al 1989; Armbruster 1995; Schmitt et al. 2019), and could potentially have unit cell parameters up to a=12.74 Å (Flint et al. 1941), these TEM results are consistent with this phase being identified as hydroandradite.

Table 4.3. Average d-spacings for electron diffraction spots from the perovskite-associated hydroandradite within Kolang compared to that calculated from literature data. The standard deviation is given for the (1 0 0) d-spacing. Literature data presented in terms of hydration as represented in hydroandradite's chemical formula ($Ca_3Fe^{+3}_2(SiO_4)_{3-x}(OH)_{4x}$), where x=0 corresponds to no hydration and x=3 correspond to complete hydration.

Miller Index (hkl)	This Study (x=0.6-1.4)	d-spacing (Å) x=0[a] a=12.02 Å	x=0.12[b] a=12.06 Å	x=0.16[c] a=12.07 Å	x=0.26[b] a=12.09 Å	x=0.42[b] a=12.11 Å	x=1.35[d] a=12.34 Å	x=3[a] a=12.74 Å
110	8.7±0.1	8.5	8.5	8.5	8.5	8.6	8.7	9.0
200	6.1	6.0	6.0	6.0	6.1	6.1	6.2	6.4
211	5.0	4.9	4.9	4.9	4.9	4.9	5.0	5.2
220	4.3	4.2	4.3	4.3	4.3	4.3	4.4	4.5
222	3.5	3.5	3.5	3.5	3.5	3.5	3.6	3.7
321	3.3	3.2	3.2	3.2	3.2	3.2	3.3	3.4
303	2.8	2.8	2.8	2.8	2.8	2.9	2.9	3.0
420	2.7	2.7	2.7	2.7	2.7	2.7	2.8	2.8
332	2.6	2.6	2.6	2.6	2.6	2.6	2.6	2.7
314	2.4	2.4	2.4	2.4	2.4	2.4	2.4	2.5

[a]Flint et al. (1941), [b]Lager et al. (1989), [c]Schmitt et al. (2019), [d]Armbruster (1995)

4.1.3 Hydroandradite Raman

Raman spectra for the perovskite-associated hydroandradite has major peaks at 249 cm^{-1}, 342 cm^{-1}, 484-508 cm^{-1}, and 799-833 cm^{-1} (Fig. 4.7a), which are consistent with published Raman spectra for andradite (Kolesov & Geiger 1997; Madon et al. 1991) and hydroandradite (Ghosh et al. 2017) (Table 4.4). Additionally, there is a peak at 3589 cm^{-1} (Fig. 4.7b), which is also consistent with published spectra for hydroandradite, commonly attributed to the OH^- band (Schmitt et al. 2019; Ghosh et al. 2017).

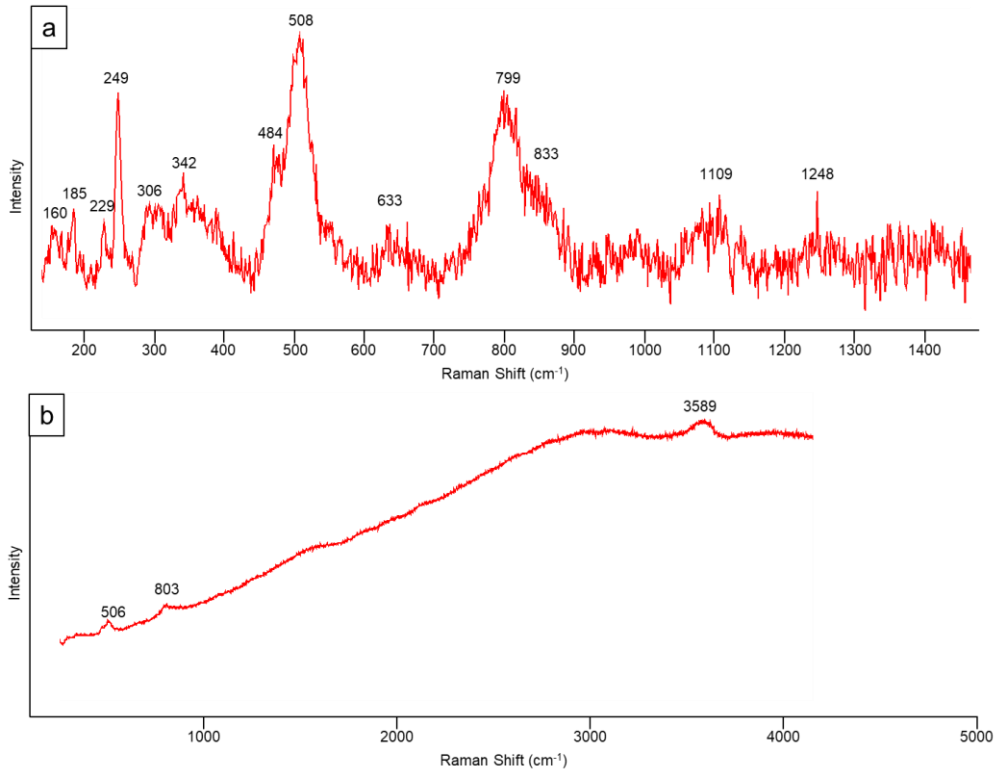

Fig. 4.7. Raman spectra for PA-HAdr in Kolang. a) From 100 to 1450 cm^{-1}. b) From 200 to 5000 cm^{-1}.

Table 4.4. Raman peaks from spectra collected from Kolang's hydroandradite compared to literature andradite and hydroandradite Raman data.

Kolang Hydroandradite	Kolesov & Geiger (1997) Andradite	Madon et al. (1991) Andradite	Ghosh et al. (2017) Hydroandradite	Schmitt et al. (2000) Hydroandradite
	174 cm^{-1}	175 cm^{-1}		
249 cm^{-1}	236 cm^{-1}	238 cm^{-1}		
		267 cm^{-1}		
	325 cm^{-1}	314 cm^{-1}		
342 cm^{-1}	352 cm^{-1}	354 cm^{-1}		
	370 cm^{-1}	372 cm^{-1}	366 cm^{-1}	
		455 cm^{-1}		
484 cm^{-1}	494 cm^{-1}	495 cm^{-1}		
508 cm^{-1}	516 cm^{-1}	518 cm^{-1}	514 cm^{-1}	
		554 cm^{-1}		
		576 cm^{-1}		
799 cm^{-1}	816 cm^{-1}	816 cm^{-1}	815 cm^{-1}	
833 cm^{-1}	842 cm^{-1}	843 cm^{-1}		
	874 cm^{-1}	874 cm^{-1}		
	995 cm^{-1}	995 cm^{-1}		
3589 cm^{-1}			3580 cm^{-1}	3580 cm^{-1}

4.2 Potential Hydroandradite Precursors

The composition of the Ca-Fe silicate as measured with EPMA, as well as its Raman spectra and TEM images, are all consistent with hydroandradite, confirming its identification as such. Hydroandradite forms by the replacement of other minerals through low temperature (≤300°C) calc-silicic metasomatism (Ghosh et al. 2017). Hydroandradite in Shidian and Kolang must have replaced other phases and have precursors. This would be consistent with these meteorites' histories having undergone aqueous alteration. The petrographic contexts which hydroandradite occurs in as well as the minerals that it's known to replace on Earth can be used to narrow down likely precursors.

4.2.1 Layered Hydroandradite

Only one instance of layered hydroandradite was identified, found within Kolang (Fig. 4.1). It occurs in a grain about 90 μm in diameter. This grain has a core of magnetite surrounded by an intergrown layer of hydroandradite and apatite, with a pentlandite rim.

Magnetite, apatite, and pentlandite occur together in other CM chondrites (e.g., Murray) and form from the aqueous alteration of kamacite (Palmer & Lauretta 2011). This alteration occurs with fluids that have limited amounts of dissolved S and Si (Palmer & Lauretta 2011), which are remarkably similar to the fluids required to form hydroandradite (Plümper et al. 2014). The layered hydroandradite probably formed alongside the magnetite, apatite, and pentlandite in the same alteration event, and is therefore most likely to be an alteration product of kamacite. The fluids that produced the layered hydroandradite assemblage were likely high in dissolved Ca, but low in dissolved S and Si (Equation 4.1; equation is unbalanced for illustrative purposes; after Palmer and Lauretta 2011). As kamacite is usually one of the first phases to be affected by aqueous alteration, the layered hydroandradite probably formed early in Kolang's alteration history.

$$Fe_{0.93}Ni_{0.05}P_{0.007} + S_{(aq)} + Si_{(aq)} + Ca_{(aq)} + H_2 + O_{2(aq)}$$
$$\rightarrow Fe_3O_4 + (Fe,Ni)_9S_8 + Ca_{10}(PO_4)_6(OH)_2 + Ca_3Fe_2^{+3}(SiO_4)_{3-x}(OH)_{4x} \quad (4.1)$$

4.2.2 Perovskite-Associated Hydroandradite

The perovskite-associated hydroandradite occurs within multiple clasts in Kolang as clumps that are hundreds of microns in size. The individual hydroandradite grains within these clumps are only ~500 nm in size. Within these clumps, among the hydroandradite, are small grains of perovskite ~2 μm in size. The perovskite-associated hydroandradite clumps often have FGRs and occasionally these clumps occur with web-like textures and/or have minor amounts of oxides or sulphides associated with them (Fig. 4.2). The clumps that have web-like textures bear a morphological similarity to other objects within Kolang that are composed of diopside (Fig. 4.2c).

Perovskite is known to occur within CAIs within carbonaceous chondrites (MacPherson 2007; Simon and Grossman 2011; Krot et al. 2001). It is therefore likely the perovskite-associated hydroandradite clumps are altered CAIs and that the hydroandradite altered either a primary CAI phase or a secondary phase derived from a primary CAI phase.

The texture displayed by hydroandradite is similar to that of other minerals in perovskite-bearing CAIs. These minerals include spinel, hibonite, grossite, diopside, melilite, and an unknown Ca-Al bearing hydrous phase (MacPherson 2007; Simon and Grossman 2011; Krot et al. 2001). Because the perovskite-associated hydroandradite contains up to 3 wt% TiO_2 (Table 4.2) and Ti is typically not fluid-mobile (Ghosh et al. 2017), the perovskite-associated hydroandradite likely formed from the alteration of a Ti-bearing phase. The most common Ti-bearing minerals in CAIs are perovskite, hibonite, and clinopyroxene (MacPherson 2007).

Terrestrially, it is common for hydroandradite to replace perovskite (Schmitt et al. 2019), however perovskite is not known to occur as large masses within carbonaceous chondrites and usually occurs only as small grains (e.g., a few μm in size) (MacPherson 2007; Simon and Grossman 2011; Krot et al. 2001), like those observed in Kolang. Additionally, perovskite within Kolang is not restricted to the interior of these hydroandradite clumps and can occur as isolated grains as well (Fig. 4.2a & 4.2b). The grain boundaries of perovskite are also well defined, showing no sign of alteration. If hydroandradite altered perovskite, it is unlikely that these small perovskite grains would remain.

Perovskite is therefore unlikely to be the precursor to the perovskite-associated hydroandradite.

Ti-bearing hibonite is known to occur in CM2 chondrites (MacPherson 2007; Lee & Greenwood 1994; Ireland et al. 1985) and can contain up to 9 wt% Ti (Brearley & Jones 1998), enough to account for the Ti abundances within the perovskite-associated hydroandradite. No hibonite was observed within Kolang, but it may have been completely replaced during aqueous alteration. It is therefore possible for hydroandradite to have replaced Ti-bearing hibonite.

Ti-clinopyroxene is another common CAI mineral in carbonaceous chondrites and can contain up to 19 wt% Ti (MacPherson 2007; Brearley & Jones 1998). Additionally, terrestrial hydroandradite is known to replace clinopyroxene (Ellison 2021). It is therefore another plausible precursor mineral for hydroandradite. Of note, diopside-bearing objects with similar morphologies to perovskite-associated hydroandradite were observed within Kolang (Fig. 4.2c). Diopside is a primary mineral within CAIs (MacPherson 2007) and diopside-bearing objects are likely CAIs that have survived alteration. Given this morphological similarity, Ti-clinopyroxene is the most probable mineral to be perovskite-associated hydroandradite's precursor. As there is no surviving Ti-clinopyroxene in Kolang, it is likely more susceptible to alteration than diopside. However, hibonite is not ruled out as a precursor for perovskite-associated hydroandradite.

If perovskite-associated hydroandradite formed from the alteration of Ti-clinopyroxene, it would require fluids of differing composition than that which formed the layered hydroandradite. These fluids would need dissolved Fe (Equation 4.2). The timing of the formation of perovskite-associated hydroandradite is unknown, but due to reasons stated below in Chapter 4.4, it likely was not a late alteration event.

$$Ca(Mg,Ti)Si_2O_6 + 2Fe_{(aq)} + 2Ca_{(aq)} + H_2O \rightarrow Ca_3(Fe^{+3},Ti)_2(SiO_4)_{3-x}(OH)_{4x} + Mg_{(aq)} \quad (4.2)$$

4.2.3 Spheroidal Hydroandradite

The spheroidal hydroandradite occurs as ~5 μm spheres in the matrix of some, but not all clasts of Kolang (Fig. 4.3). The spheroidal hydroandradite bears

a nearly identical morphology to that of magnetite spheroids that occur in other clasts within Kolang (Fig. 4.2d), however no clasts containing both magnetite spheroids and spheroidal hydroandradite were found. Because hydroandradite is known to replace magnetite on Earth (Ghosh et al. 2017), it is very likely that spheroidal hydroandradite formed by the alteration of magnetite. To replace magnetite with hydroandradite, the altering fluids would require a mixture of Ca and Si (Equation 4.3; equation is unbalanced for illustrative purposes).

$$Fe_3O_4 + Si_{(aq)} + Ca_{(aq)} + H_2O \rightarrow Ca_3Fe_2^{+3}(SiO_4)_{3-x}(OH)_{4x} \quad (4.3)$$

As magnetite spheroids form during aqueous alteration (Bunch & Chang 1980), the spheroidal hydroandradite reflects differing fluid compositions over time. The perovskite-associated hydroandradite is observed next to magnetite spheroids (Fig. 4.2d). Because perovskite-associated hydroandradite coexists with unaltered magnetite spheroids, it likely formed from an alteration event that preceded the spheroidal hydroandradite. Additionally, only some of Kolang's clasts experienced the metasomatic alteration required to form spheroidal hydroandradite.

4.2.4 Sulphide-Associated Hydroandradite

The sulphide-associated hydroandradite is the only morphology observed in both Kolang and Shidian. It occurs as ~50 μm spheres, where 3 μm sulphides can be seen among the hydroandradite. These sulphides are usually pentlandite. Both the sulphides and hydroandradite occur in shell like structure around a phyllosilicate core (Fig. 4.4). The sulphide-associated hydroandradite was observed in multiple places within Shidian, but only once within Kolang.

There is little to be discerned about the sulphide-associated hydroandradite's precursor. It bears a textural similarity to magnetite-sulphide rosettes in ungrouped CM-like carbonaceous chondrites (Hewins et al. 2021), in that both have circular aggregate structures surrounding a core of matrix material. However, this is a broad assumption as there are very few petrographic clues to narrow down potential precursors for this morphology. Illustrations regarding alteration processes related to this morphology will operate on the assumption that it formed from the replacement of magnetite (see Equation 4.3) in magnetite-sulphide rosettes, however the likelihood of this scenario cannot be

adequately established. It is possible that the precursor for the sulphide-associated hydroandradite is not magnetite.

4.2.5 Overall Timing of Hydroandradite Forming Events

Within Shidian, there is only one morphology of hydroandradite observed, the sulphide-associated hydroandradite, requiring only one hydroandradite formation event. However, in Kolang, there are four morphologies of hydroandradite. These four morphologies would require at least three different fluid compositions to form, not including the alteration events required to form any secondary phases hydroandradite replaced. Kolang experienced an evolving fluid and/or multiple fluid influxes.

To prevent other phases (e.g., calcite) from crystallizing instead, hydroandradite requires specific fluid conditions to form (Plümper et al. 2014; Ghosh et al. 2017; Beard and Hopkinson 2000). The phases hydroandradite replaces are dependent on the composition of the altering fluid. To produce the hydroandradite morphologies observed in Kolang, the fluid compositions are most likely the following (Fig. 4.8):

1) Fluid bearing S, Si, Ca, S, and O. Kamacite is altered, forming the layered hydroandradite alongside pentlandite, apatite, and magnetite. Additionally, secondary pentlandite making up the first stage of magnetite-sulphide rosette formation may form at this stage.

2) Fluid bearing Fe and Ca. A Ti-bearing CAI mineral, likely clinopyroxene, in perovskite-bearing CAIs is altered into hydroandradite to form the perovskite-associated hydroandradite.

3) Fluid bearing Fe and O. Secondary magnetite forms.

4) Fluid bearing Ca. This would only affect a limited amount of clasts within Kolang. Magnetite gets replaced, forming spheroidal hydroandradite.

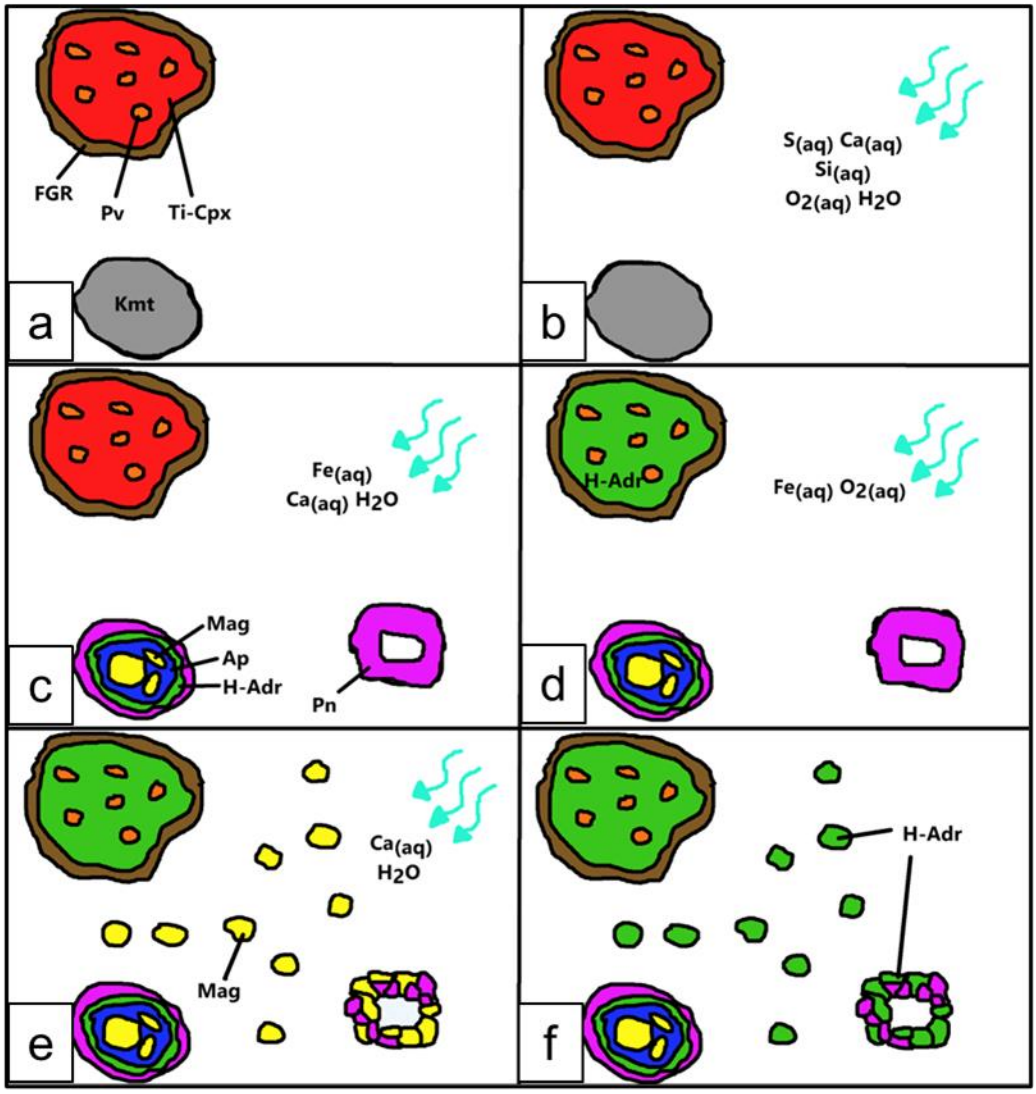

Fig. 4.8. Schematic detailing hydroandradite forming events in Kolang. Note that timing of some events (sulphide forming, PA-HAdr forming) are unconstrained and have been placed in an order that minimizes aqueous alteration events detailed. a) Primary hydroandradite precursors, kamacite (Kmt) and Ti-rich clinopyroxene (Ti-Cpx) with associated phases, perovskite (Pv) and fine-grained rims (FGR). b) Influx of fluid with ions required to form L-HAdr. c) L-HAdr composed of magnetite (Mag), apatite (Ap), hydroandradite (H-Adr), and pentlandite (Pn) has formed. Sulphide rosettes (shown to be composed of Pn here) have also formed. Influx of a second fluid with ions required to form PA-HAdr. d) PA-HAdr has formed. Influx of a third fluid with ions required to form Mag. e) Sulphide rosette has been partially altered to Mag and spheroidal Mag has formed. Influx of a fourth fluid with ions required to form both SA-HAdr and S-HAdr. f) SA-Adr and S-HAdr has formed. All four morphologies can be seen.

It is unknown when sulphide-associated hydroandradite forms or which phase it is most likely to replace. It may have formed alongside the likely fluids presented above. Kolang may have experienced other fluids in addition to these four.

4.3 The Thermal Stability of Hydroandradite

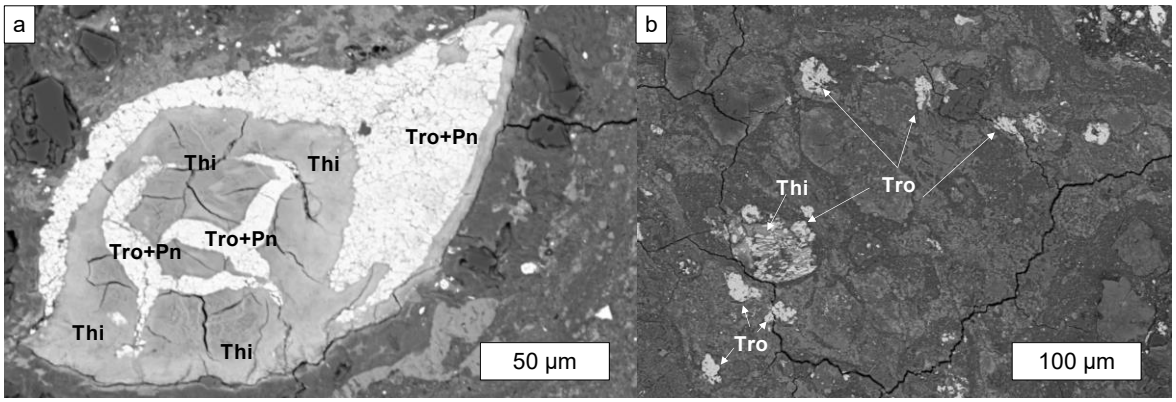

Fig. 4.9. Evidence of post-hydration heating in Shidian and Kolang. a) BSE image of tochilinite in Shidian displaying distinctive decomposition textures, with dehydration fractures and secondary sulphides. Tochilinite (Thi), troilite (Tro), and pentlandite (Pn) are labelled. b) One of the heated clasts within Kolang. There is very little Thi, however there is an abundance of sulphides, primarily Tro. Fractures proliferate its matrix. These fractures are likely from heating.

Hydroandradite is commonly assumed to have the same formation temperature of andradite, which forms at temperatures of up to 300°C (Plümper et al. 2014; Ménez et al. 2012), however its most hydrated form can be synthesized at room temperature (Eiger 1937) and decomposes when heated to 220°C (Flint et al. 1941). There is little established about hydroandradite's formation temperature and thermal stability, beyond its hydration being dependent on the temperature at which it forms (Huckenholz & Fehr 1982). To complicate what is known about its thermal stability further, both Shidian and Kolang contain lithologies that show signs of post-hydration heating. Tochilinite in Shidian has distinct dehydration fractures around which coarse grained sulphides (mostly troilite with minor amounts of pentlandite) have crystallized (Fig. 4.9a). The matrix of some of Kolang's clasts show widespread fracturing as well as a distinct lack of tochilinite, with what little tochilinite that can be observed appearing porous (Fig. 4.9b & 4.10). Because the hydroandradite in these meteorites shows no signs of decomposition, it must be stable at the temperatures to which they have been heated. Understanding the thermal histories of these meteorites yields information regarding hydroandradite's thermal stability.

The thermal histories of these hydroandradite-bearing meteorites can be constrained using the properties of matrix phyllosilicates, particularly their

volatile content. EPMA data of phyllosilicates yields low analytical totals due to the presence of unmeasured elements (i.e., H); for example, serpentine will typically give values of 83-89 wt% (Velbel & Zolensky 2021). As these phases decompose due to heating, they release their volatiles and analytical totals will increase (Velbel & Zolensky 2021). Thus, the totals of volatile bearing phases including serpentine can be utilized as a measure of heating. Velbel & Zolenksy (2021) developed a geothermometer that relies on volatile content of phyllosilicates within CM chondrites, wherein the analytical totals of the serpentine matrix are used to calculate the temperature experienced. This geothermometer is applicable to CM chondrites that have experienced 400-750°C of heating. It is important to note however that porosity may also contribute to low wt% totals (Velbel & Zolensky 2021) and so a low total does not necessarily solely reflect volatile concentrations.

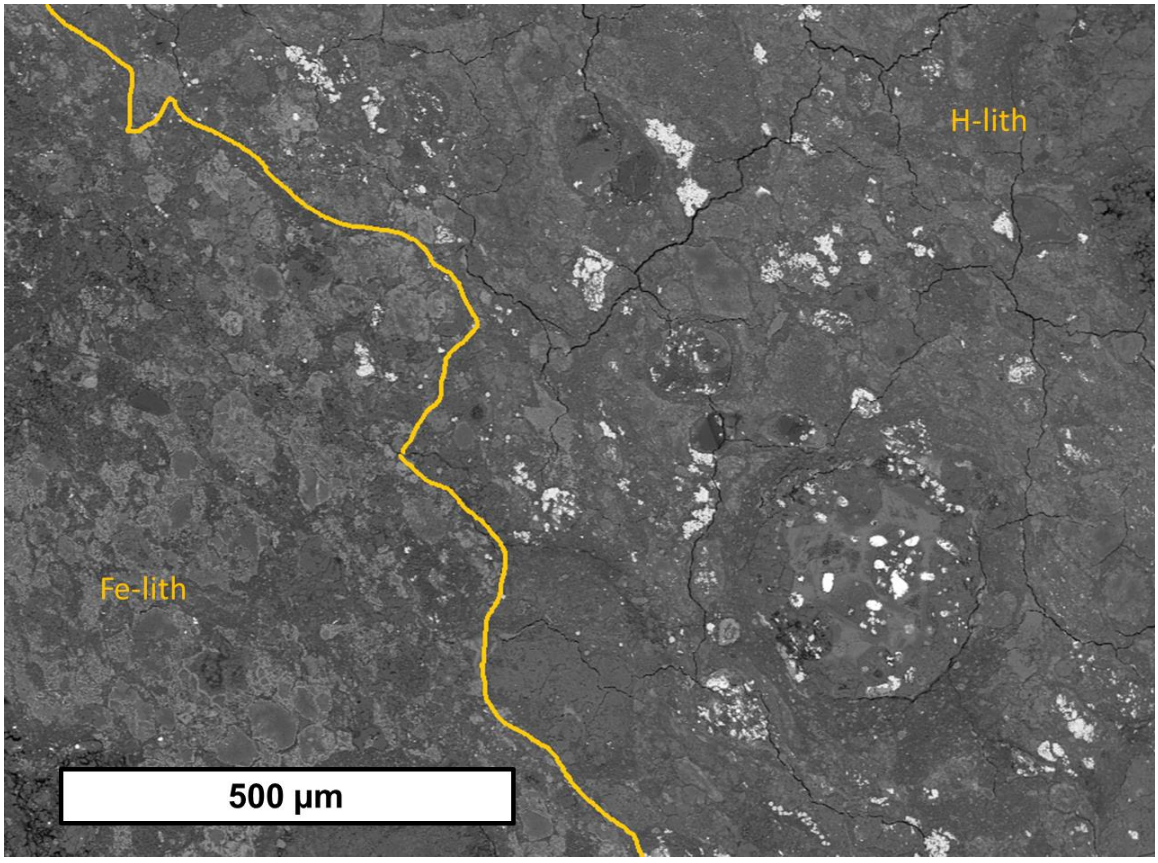

Fig. 4.10. Examples of the lithologies targeted within Kolang. The Fe-rich lithology (Fe-lith) has no signs of dehydration (e.g., fracturing), while the Heated lithology of Kolang (H-lith) has an abundance of dehydration fractures and sulphides, but alack of tochilinite. The studied polish section of Shidian is composed of only one lithology.

To study the degree of heating experienced both by Kolang and Shidian, EPMA data was collected for the matrix, FGRs, and tochilinite that has not completely recrystallized into sulphides of the following: (i) Shidian; (ii) an unheated clast (the Fe-rich lithology) and (iii) a heated clast (the heated

lithology) within Kolang (Fig. 4.10). The matrix wt% totals were applied to a dehydroxylation peak-temperature thermometer proposed by Velbel & Zolensky (2021). Following their method, any total below 83% for a matrix EPMA point was discarded to reduce the effect of porosity on the results.

4.3.1 Tochilinite

For tochilinite, 10 spots in Shidian and 20 spots in Kolang were targeted. Four spots in Kolang had to be discarded due to having chemical compositions that did not match tochilinite.

The measured analytical totals are all within standard deviation from one another (Table 4.5), ranging 81-90 wt%. This is lower than what is reported in the literature for unheated tochilinite, which should have analytical totals of 94-98 wt% (Tomeoka & Buseck 1985). Tochilinite is a volatile bearing mineral that is often intergrown with other phases in CM chondrites (Palmer & Lauretta 2011), however these values are lower than expected even when accounting for those factors through comparison of most literature values from similar assemblages (Palmer & Lauretta 2011; Tomeoka & Buseck 1985; Haack et al. 2012). Additionally, the wt% values of S are particularly low; the measured values are 7-12 wt% on average, while literature reports of tochilinite S compositions are 18-23 wt% (Palmer & Lauretta 2011; Tomeoka & Buseck 1985; Haack et al. 2012; Pignatelli et al. 2016).

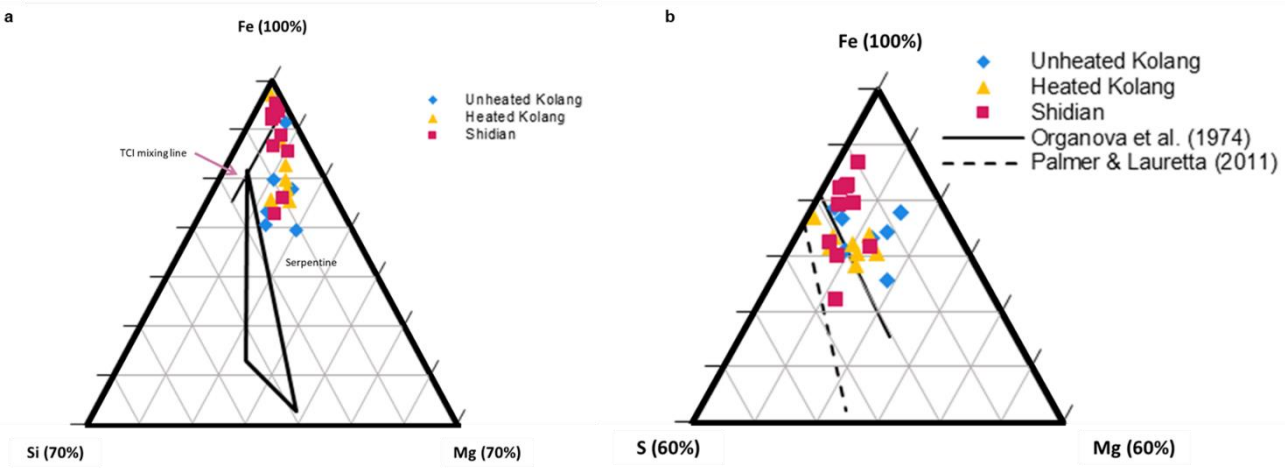

Fig. 4.11. Ternary diagrams comparing the compositions of measured tochilinite. Proportions of different elements are given in wt%. a) Comparison of measured tochilinite to TCIs and serpentine. TCI mixing line and serpentine triangle are after Palmer & Lauretta (2011) and McSween (1987). b) Comparison of measured tochilinite to compositions defined by Palmer & Lauretta (2011) and Organova et al. (1974).

The contributions of Fe, Mg, Si, and S to the tochilinite compositions are plotted on two ternary diagrams to compare their compositions to serpentine and TCIs (Palmer & Lauretta 2011; Mcsween 1987) and to tochilinite compositions reported in the literature (Palmer & Lauretta 2011; Organova et al.1974; Haack et al. 2012). Though some of the tochilinite compositions are comparable to TCIs, none of them have enough Si to have significant contributions from serpentine to account for low S values (Fig. 4.11a). Most compositions plot close to tochilinite in the Fe-Mg-Si plot. When compared to literature compositions of tochilinite, the measured values have less S than that defined by Palmer & Lauretta (2011), though some have similar amounts of S as to what is reported by Organova et al. (1974) (Fig. 4.11b).

4.3.2 Matrix

For the matrix, 20 spots were targeted in Kolang and seven in Shidian. Out of these spots, four in Kolang and four in Shidian were discarded for giving totals less than 83 wt%. In common with tochilinite, all of these totals are within standard deviation of one another (Table 4.6). The maximum total that unheated serpentine should give is 89 wt%. The averages are all below 89 wt%, making it unlikely that Shidian or any clast within the studied thin sections of Kolang experienced more than 400°C of heating. The heated Kolang lithology gives the highest totals, corresponding to a temperature of 297°C.

4.4.3 FGRs

All targeted spots in both samples gave compositions consistent with serpentine, so none were omitted. In common with tochilinite and the matrix, all average totals are within standard deviation with each other (Table 4.7). Unlike the matrix and tochilinite, the lowest average total originates from the unheated lithologies of Kolang (Fig. 4.12).

Table 4.5 Mean composition (wt%) of tochilinite in Shidian and Kolang. Standard deviation is listed alongside wt% values.

Meteorite	Na_2O	MgO	Al_2O_3	SiO_2	CaO	MnO	FeO	K_2O	Cr_2O_3	NiO	CoO	P_2O_5	S	Total
Unheated Kolang (N=8)	0.37±0.15	9.81±4.32	1.07±0.30	8.68±5.54	0.72±0.70	0.26±0.09	48.79±4.99	0.13±0.12	2.88±1.52	4.64±4.09	0.14±0.23	0.65±1.36	8.71±1.84	86.87±5.62
Heated Kolang (N=8)	0.16±0.07	8.53±2.20	0.81±0.39	7.28±3.62	0.37±0.34	0.19±0.12	54.89±8.71	0.04±0.05	2.25±1.90	3.36±2.09	0.16±0.33	0.29±0.52	11.07±2.90	89.42±7.16
Shidian (N=10)	0.18±0.18	5.39±2.90	0.61±0.22	4.81±3.25	0.43±0.47	0.22±0.10	51.32±6.95	0.06±0.02	2.74±1.40	6.07±6.04	0.34±0.42	0.78±0.53	7.86±2.34	81.58±5.51

Table 4.6 Mean composition (wt%) of matrix in Shidian and Kolang. Standard deviation is listed alongside wt% values. Temperature calculated using Velbel & Zolensky's (2021) thermometer also given.

Meteorite	Na_2O	MgO	Al_2O_3	SiO_2	CaO	MnO	FeO	K_2O	NiO	S	Total	Calculated Temperature
Unheated Kolang (N=9)	0.41±0.24	22.77±7.50	2.15±0.71	31.54±6.44	0.12±0.03	0.22±0.02	27.14±10.96	0.06±0.04	0.89±0.78	1.37±1.30	86.84±1.99	233±88°C
Heated Kolang (N=7)	0.92±0.22	23.85±3.00	2.32±0.29	33.95±2.49	0.59±0.82	0.24±0.02	22.48±3.16	0.11±0.03	1.49±1.27	1.89±0.65	88.28±2.76	297±59°C
Shidian (N=4)	0.30±0.09	18.37±4.99	2.29±0.35	28.07±4.49	1.05±1.15	0.22±0.01	28.93±6.94	0.05±0.01	3.05±1.59	1.64±0.57	85.30±2.13	165±31°C

Table 4.7 Mean composition (wt%) of FGRs in Shidian and Kolang. Standard deviation is listed alongside wt% values.

Meteorite	Na_2O	MgO	Al_2O_3	SiO_2	CaO	MnO	FeO	K_2O	Cr_2O_3	NiO	TiO_2	S	Total
Unheated Kolang (N=10)	0.89±0.32	17.18±2.81	1.76±0.28	27.15±2.32	1.24±0.79	0.20±0.03	21.97±2.99	0.09±0.33	0.80±0.33	3.28±1.37	0.12±0.10	2.06±0.67	77.15±4.42
Heated Kolang (N=10)	1.15±0.34	17.91±1.16	2.43±0.20	28.26±3.69	0.68±0.37	0.23±0.01	26.16±4.67	0.13±0.03	0.56±0.18	2.12±1.12	0.04±0.01	2.51±0.95	82.47±2.51
Shidian (N=10)	0.29±0.13	17.96±4.61	2.81±1.21	28.75±4.13	1.03±0.76	0.22±0.02	26.92±3.96	0.04±0.02	0.61±0.14	2.67±0.86	0.06±0.05	1.36±0.25	83.10±4.65

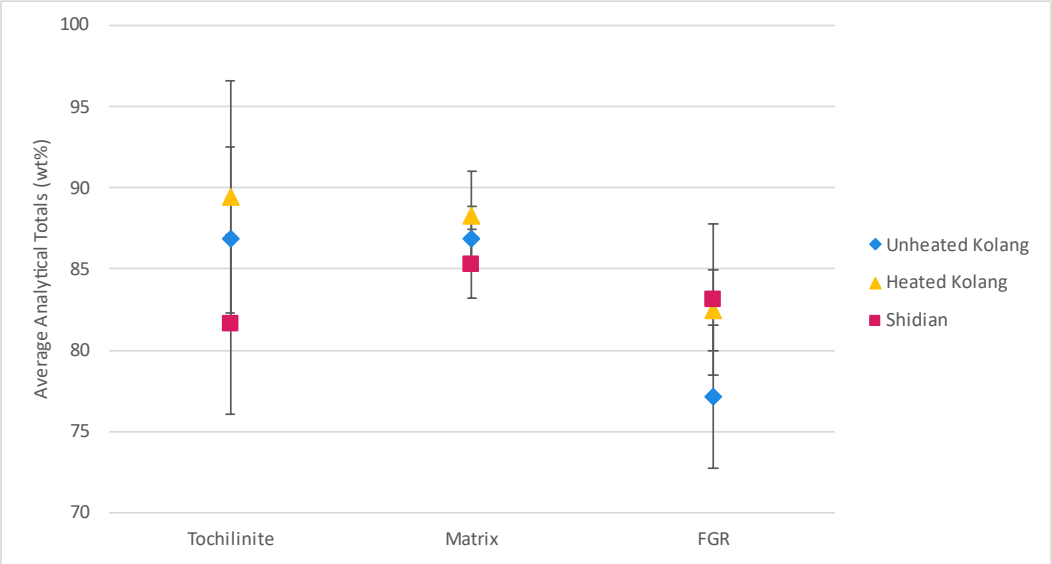

Fig. 4.12. Average analytical totals (wt%) of different components in Kolang and Shidian. Error bars correspond to the standard deviation of these analytical totals.

4.4.4 The Unusual Tochilinite Compositions

Out of the three materials analysed with EPMA, the tochilinite gave the most abnormal values, with wt% totals of all three lithologies in Kolang and Shidian being quite similar with each other (Table 4.5), yet different compared to literature values for meteorite tochilinite (Tomeoka & Buseck 1985; Palmer & Lauretta 2011; Haack et al. 2012). The values measured do bear similarity to that calculated for terrestrial tochilinite by Organova et al. (1974), who studied two varieties of tochilinite with TEM.

Organova et al. (1974) describes these two tochilinite varieties as Phase 1 and Phase 2. Phase 1 is quite similar to the meteorite tochilinite described in the literature (e.g., Palmer & Lauretta 2011), with alternating layers of mackinawite and brucite, having a calculated composition of 2 $Fe_{0.78}S$ ·1.57(Mg,Fe)$(OH)_2$. Phase 2 is similar to Phase 1, in that it has alternating layers, one of which is mackinawite, but differs in its “brucite” layer, which lacks Mg, instead having abundant Fe, as well as having H_2O molecules interspersed throughout its structure. With the Phase 2 tochilinite, the amount of H_2O in some cases was affected by laboratory study, with some of the H_2O being lost when studied with an electron microscope due its interactions with the electron beam. Phase 2 has a calculated formula of $2Fe_{0.78}S{\cdot}0.9Fe(OH)_2 1.5H_2O$ (Organova et al. 1974).

The unusual compositions for tochilinite in Shidian and Kolang could be explained if it were made up of Phase 2 tochilinite instead of the Phase 1 tochilinite commonly reported for other meteorites (Tomeoka & Buseck 1985; Palmer & Lauretta 2011; Haack et al. 2012). However, this is difficult to definitively establish, as many literature sources that study tochilinite composition either exclusively studied TCIs with EPMA (e.g., Rubin et al. 2007; Suttle et al. 2022) or tochilinite globules are grouped with TCIs when the EPMA analyses are presented (e.g., Pignatelli et al. 2016; Fan et al. 2022), making direct comparisons with other meteorites difficult. Of the few comparable datasets available, the tochilinite in Shidian and Kolang do differ, so the following interpretations are based on this fact.

The difference in tochilinite composition does imply that Shidian and Kolang, or at the very least the lithologies of Shidian and Kolang studied, have experienced processes that differed from these other meteorites in some form. This could be differences in aqueous alteration on their parent body(ies), or this could potentially be differences in terrestrial weathering. Shidian and Kolang are both recent falls, having fallen in 2017 and 2020, respectively (Fan et al. 2022; King et al. 2021a). It is possible that all meteorite tochilinite is Phase 2, with much of the H_2O in their crystal structure being lost as they are exposed to Earth's atmosphere, leading to their compositions differing from that of Shidian and Kolang.

Another possibility is that the unusual composition relates to these tochilinite often occurring within meteorites as intergrowths (Vacher et al 2019). The tochilinite that occurs as alteration products of kamacite on the edge of chondrules, like that targeted by EPMA in this study, is often intergrown with minor amounts of cronstedtite or goethite (Vacher et al. 2019). The amount of SiO_2 making up the tochilinite in these meteorites is too low for cronstedtite to play a significant role, however the low amount of S and the low wt% totals would be consistent with goethite being within the assemblage (Table 4.5). However, this explanation again indicates that tochilinite occurs in Kolang and Shidian in a different manner than other CM chondrites, requiring them to experience aqueous alteration under dissimilar conditions.

EPMA data would need to be collected for similar tochilinite assemblages in other recent CM falls to determine whether all meteorite tochilinite is Phase 2 tochilinite or if Shidian and Kolang simply experienced different alteration conditions on their parent body(ies). Additionally, EPMA data would also need to be collected for tochilinite in older CM chondrites to determine a more definitive baseline for tochilinite compositions.

4.4.5 The Temperatures Experienced

For most cases, Shidian gives the lowest average analytical totals of the three areas targeted, with the exception of its FGRs (Fig. 4.12). This is incongruent with petrographic observations, where out of the three areas, it displays the most pronounced heating textures, with secondary sulphides following fractures within decomposed tochilinite (Fig. 4.8a). The tochilinite wt% totals are extremely low, averaging at only 81.58 wt%. This could be indicative of unmeasured volatiles, however given the extensive fracturing throughout it, these low wt% totals are more likely the result of microporosity. Additionally, when collecting the EPMA data, the secondary sulphides were intentionally not targeted, which may have led to a bias towards targets with low analytical totals; targets showing complete recrystallization (and thus high analytical totals) were omitted. It is likely that due to porosity's role in wt% totals, the average analytical total of tochilinite is a poor proxy for temperature experienced. It can be concluded however, from petrographic observations, Shidian experienced temperatures high enough for tochilinite decomposition, likely at least 210°C (For more on tochilinite decomposition, see Chapter 5.5). The analytical totals for Shidian's serpentine matrix are the lowest measured here, however they are quite similar to measurements from other Shidian samples taken by Fan et al. (2022) (e.g., 82-86 wt%). Most of these other Shidian samples show no signs of heating (Fan et al. 2022). The FGRs' analytical totals measured in this study are also consistent with that measured by Fan et al. (2022), who had an average analytical total of 84.75 wt% for FGRs in the other Shidian samples. As Shidian's matrix shows no petrographic sign of decomposition, it is unlikely to have experienced more than 300°C of heating.

The unheated lithologies of Kolang show no petrographic signs of post-hydration heating. The wt% totals collected from them reflect this, with the average wt% total of its FGRs being the lowest of the targeted areas (Table 4.7)

and its average wt% total of its matrix being within the range for unheated serpentine of 83-89 wt% (Table 4.6; Velbel & Zolensky 2021). It is safe to assume that it is unheated.

The heated lithology of Kolang consistently gives the highest totals of the three targeted areas. This finding is consistent with its decomposed tochilinite with abundant sulphides, and the fracturing in its matrix. However, average totals for its matrix are within the range for unheated serpentine (Table 4.6; Velbel & Zolensky 2021) and correspond to a temperature of 297°C when the thermometer of Velbel & Zolensky (2021) is applied to it. It is important to note that this thermometer is tailored towards meteorites that have experienced heating of 400-750°C and its application to mildly heated meteorites is limited. Given the extensive dehydration fracturing in its serpentine matrix, the heated lithology of Kolang likely experienced at least 300°C, the minimum temperature required for serpentine decomposition (Ball & Taylor 1963),but less than 400°C, with its experienced temperature likely being close to 300°C. It can be classified as a low heat stage II meteorite, though it is possible that it is a high heat stage I meteorite.

4.4.6 Hydroandradite's Thermal Stability

The hydroandradite within Kolang and Shidian is more hydrated than that of most terrestrial hydroandradites, with the exception of samples studied by Armbuster (1995) (Table 4.2; Fig. 4.6), which are from the Totalp Serpentine in Davos, Switzerland. The Totalp Serpentine has experienced alteration at low temperatures and pressures (Peters 1965), conditions that are arguably similar to that of C-complex asteroids. The hydroandradite in Kolang and Shidian is less hydrated than that synthesized by Eiger (1937) and Flint et al. (1941). It is therefore probable that hydroandradite in Kolang and Shidian formed at lower temperatures than that experienced by most terrestrial hydroandradites, but at temperatures greater than 100°C, the maximum temperature used to create synthetic hydroandradites (Flint et al. 1941).

Little is known about the thermal stability of hydroandradite. Its extremely hydrated form decomposes at 220°C (Flint et al. 1941), however some hydroandradite-bearing clasts within Kolang have experienced temperatures above that, likely being heated to at least 300°C. Given that hydroandradite was

observed intact with no signs of decomposition in these heated clasts, it can be deduced that it was stable at these elevated temperatures. It is probable that hydroandradite's thermal stability varies with hydration, just as its formation temperature does. Hydroandradite with ~2.6 OH^- for every SiO_4^{4-} is therefore stable at 300°C and may be stable at even higher temperatures.

4.4 Summary of Hydroandradites in CM chondrites

As displayed by Eiger (1937), hydroandradite can form at room temperature; within Shidian and Kolang it likely formed during aqueous alteration alongside other secondary phases. Because hydration of hydroandradite depends on formation temperature and given the hydration of Kolang and Shidian's hydroandradite, this alteration likely occurred above 100°C. Both Shidian and certain clasts in Kolang show evidence of post-hydration heating, however this heating is mild at temperatures below 400°C. Hydroandradite survived these heating events and was stable at these elevated temperatures, its thermal stability likely being related to its hydration.

Although hydroandradite occurs only as a singular morphology in Shidian, it can be only tied to one alteration fluid composition in that context. However, Kolang contains multiple morphologies of hydroandradite, each in a context that indicates multiple precursors. Kolang likely experienced either multiple alteration events or an evolving fluid, accounting for the differences displayed by the hydroandradite it contains.

This is the first report of hydroandradite occurring in CM chondrites and it is a new alteration phase to be aware of in these meteorites. It is a mineral that typically forms under metasomatism terrestrially, however it is likely that it formed during aqueous alteration in Kolang and Shidian, albeit at temperatures higher than 100°C. Within Kolang specifically, multiple morphologies of hydroandradite indicate an evolving fluid. Hydroandradite within Kolang and Shidian show that aqueous alteration was occurring on the CM chondrite parent body(ies) at temperatures about 100°C with fluids that changed composition over time.

Although hydroandradite has yet to be observed in meteorites other than Shidian and Kolang, it is likely present in other CM chondrites and has yet to be

reported due to its low abundance relative to other Ca-rich phases (e.g., calcite). It is also possible that Shidian and Kolang sample a part of the CM parent body with a unique geologic history, accounting for the lack of hydroandradite reported in other CMs. This may also serve as an explanation for their unusual tochilinite compositions.

Chapter 5 – Post-Hydration Heating: Specifics of Mineral Transitions

Many carbonaceous chondrites, including the Mighei-like (CM) group, have experienced aqueous alteration leading to the formation of volatile-bearing phases including tochilinite and serpentine. These carbonaceous chondrites originate from C-complex asteroids that represent important volatile reservoirs within our Solar System and may be the primary sources of water and organics for Earth during its development in the early Solar System (King et al. 2019a; Alexander et al. 2012).

A portion of the CM chondrites, as well as the Yamato-like carbonaceous (CY) chondrites and some of the ungrouped carbonaceous chondrites, have experienced post-hydration heating, affecting their mineralogy and volatile contents (Nakamura 2005; King et al. 2019a; Tonui et al. 2014). Post-hydration heating occurred at a variety of temperatures for unknown timescales (Tonui et al. 2014). Certain phases (e.g., tochilinite, serpentine) may decompose, and from their remnants secondary anhydrous phases may form (Nakamura 2005). The knowledge surrounding these phase transitions (e.g., what temperatures they occur at, how they progress) can be variable.

Tochilinite is one of the first phases to decompose as temperatures increase (Nakamura 2005), yet the exact temperature it does so is unknown. Serpentine starts to decompose at ~300°C before recrystallizing into olivine and enstatite at ~500°C, however there is uncertainty surrounding how it decomposes and the formation of a transitional phase (Akai 1988). Timescale is an important factor when it comes to post-hydration heating, but the exact effect it has on certain phase transitions is also unknown (Nakato et al. 2008). Redox conditions will influence phase transitions and the minerals produced; it is generally assumed that post-hydration heating occurred under reducing or inert conditions (i.e., chemically inactive, lack of redox reactions) (Nakamura 2005), however it is worthwhile to also study heating in oxidizing environments for a comprehensive picture of conditions and effects. Additionally, the initial mineralogy and texture of heated CM chondrites may have also affected the progression of phase transitions; for example, meteorites with a higher proportion of a thermally unstable phase may decompose more slowly than those

with a lower proportion of that phase. Initial mineralogy may also influence the nature of phases produced by heating.

To study how these phase transitions progress, as well as to see how they are affected by starting material and redox conditions, three CM chondrites of different petrologic subtypes were experimentally heated on a timescale of hours. This timescale allows time for mineral reactions to occur, while incorporating the full range of post-hydration heating temperatures during the allotted time for these experiments. Powdered X-ray diffraction (XRD) data were collected during the experiments. The three CM chondrites used were ALHA 83100 (CM2.1), Murchison (CM2.5), and LEW 85311 (CM2.7) (Table 5.1). To avoid confusion with other experiments undertaken for this thesis (Table 5.2), the sample of Murchison involved in this XRD experiment set is referred to as pMurchison. ALHA 83100 was heated from 200-950°C, while pMurchison and LEW 85311 were heated over narrower temperature ranges of 300-750°C to cover key mineral transitions. All three meteorites were heated at 25°C temperature steps. Both ALHA 83100 and pMurchison were heated under inert conditions, while LEW 85311 experienced oxidizing conditions. See Chapter 2.4 for further information regarding experimental setup.

To further study specific phase transitions, particularly those involving tochilinite breakdown and the formation of a transitional phase during serpentine decomposition, additional samples of Murchison were heated under inert conditions from 200 to 500°C at varying timescales (Table 5.2; see chapters 2.5.1 & 6.2.1). These samples are referred to as M_Heat in this chapter. To characterize the transitional phase that forms during serpentine decomposition a third set of Murchison experiments were undertaken. Three rock slices of Murchison (hereby referred to as µMurchison) were heated with a Linkam cell from 200 to 550°C (Table 5.2). During heating *in situ* micro XRD (µXRD) data were collected (for more details regarding set-up, see chapter 2.5.2), such that the transitional phase could be observed in context with minimal peak overlap.

Table 5.1. Modal mineralogy (vol.%) and petrologic subtypes of the three meteorites experimentally heated. From Howard et al. (2011) & Lee et al. (2019b).

Meteorite	Petrologic Subtype	Olivine	Orthopyroxene	Calcite	Magnetite	Sulphides	Cronstedtite & Tochilinite	Lizardite	Sulphates	Fe-Ni Metal
ALH 83100	2.1	8.7	0.7	1.2	1.7	1.7	24.2	62.4	n.d.	n.d.
Murchison	2.5	15.1	8.3	1.2	1.1	1.8	50.3	22.2	n.d.	n.d.
LEW 85311	2.7	21.4	10.1	n.d.	1.2	0.5	37.8	27.0	1.7	0.3

Table 5.2. Summary of Heating Experiments Conducted.

Meteorite	Sample Type	Heating Method	Redox Conditions	Temperature Range	Timescale	Sample Designation
ALH 83100	Powdered	Hot-air blower	Inert	200-950°C	Hours	ALH 83100
	Powdered	Hot-air blower	Inert	300-750°C	Hours	pMurchison
Murchison	Rock Chip	Vacuum Oven	Inert	200-500°C	Days	M_Heat
	Rock Slice	Linkam Cell	Inert	200-550°C	Hours	µMurchison
LEW 85311	Powdered	Temperature Chamber	Oxidizing	300-750°C	Hours	LEW 85311

5.1 – Bulk Mineral Changes from Experimental Heating of ALHA 83100 Under Inert Conditions

A sample of ALHA 83100 was powdered and heated with a hot-air blower from 200 to 950°C at 25°C temperature steps under inert conditions, during which XRD data were collected. ALHA 83100 was held for two hours at each temperature step. XRD patterns of ALHA 83100 were also collected before and after heating was completed. For details of the experimental setup, see Chapter 2.5.1.

5.1.1 Mineral Decomposition and Recrystallization

Relative proportions of minerals can be inferred based off of peak intensity from an XRD pattern. XRD of unheated ALHA 83100 shows that it is composed of a mixture of cronstedtite and lizardite, with minor amounts of olivine, enstatite, calcite, tochilinite, pyrrhotite, and pentlandite (Fig. 5.1). This mineralogy is consistent with other studies on ALHA 83100 (Lindgren et al. 2020; Howard et al. 2011; Zolensky et al. 1997).

Upon heating to 200°C some tochilinite peaks have weakened and some have disappeared. Most peaks disappear by 300°C (Fig. 5.2), however a peak at 7.87° 2θ (6.02 Å) remains until 375°C. Troilite peaks start appearing at 275°C (Fig. 5.3a). Among the sulphides, pentlandite peaks begin to weaken at 675°C (Fig. 5.3b).

Serpentine d-spacings begin to shift at 225°C to lower 2θ angles. Peak weakening does not start until 300°C. Cronstedtite peaks noticeably weaken sooner during heating than those of lizardite. At 525°C, a peak at ~3.56 Å/13.3°2θ overlapping with enstatite has strengthened. This change was initially attributed to enstatite crystallization, however this same peak began to weaken at 750°C (Fig. 5.4 & 5.5), a temperature at which enstatite is stable. This particular peak likely belongs to a transitional phase that was originally described by Akai (1988) and forms by serpentine decomposition. Enstatite peaks started to noticeably strengthen at 575°C and olivine peaks strengthen at 600°C. The last peak associated with serpentine, at 6.52° 2θ (7.28 Å), disappears at 700°C, showing that the mineral has fully decomposed by that temperature (Fig.

5.4). Olivine and enstatite peaks continue to strengthen in intensity for the rest of the heating experiment.

Peaks associated with calcite start weakening slightly at 725°C. Clinopyroxene and oldhamite peaks start appearing at the same time as calcite starts noticeably decomposing, with clinopyroxene peaks being most apparent. Oldhamite peaks are subtle and strengthen slowly over the experiment. Calcite disappears by 800°C (Fig. 5.6). These clinopyroxene and oldhamite peaks continue strengthening for the rest of the experiment, with oldhamite peaks becoming most distinct after 825°C.

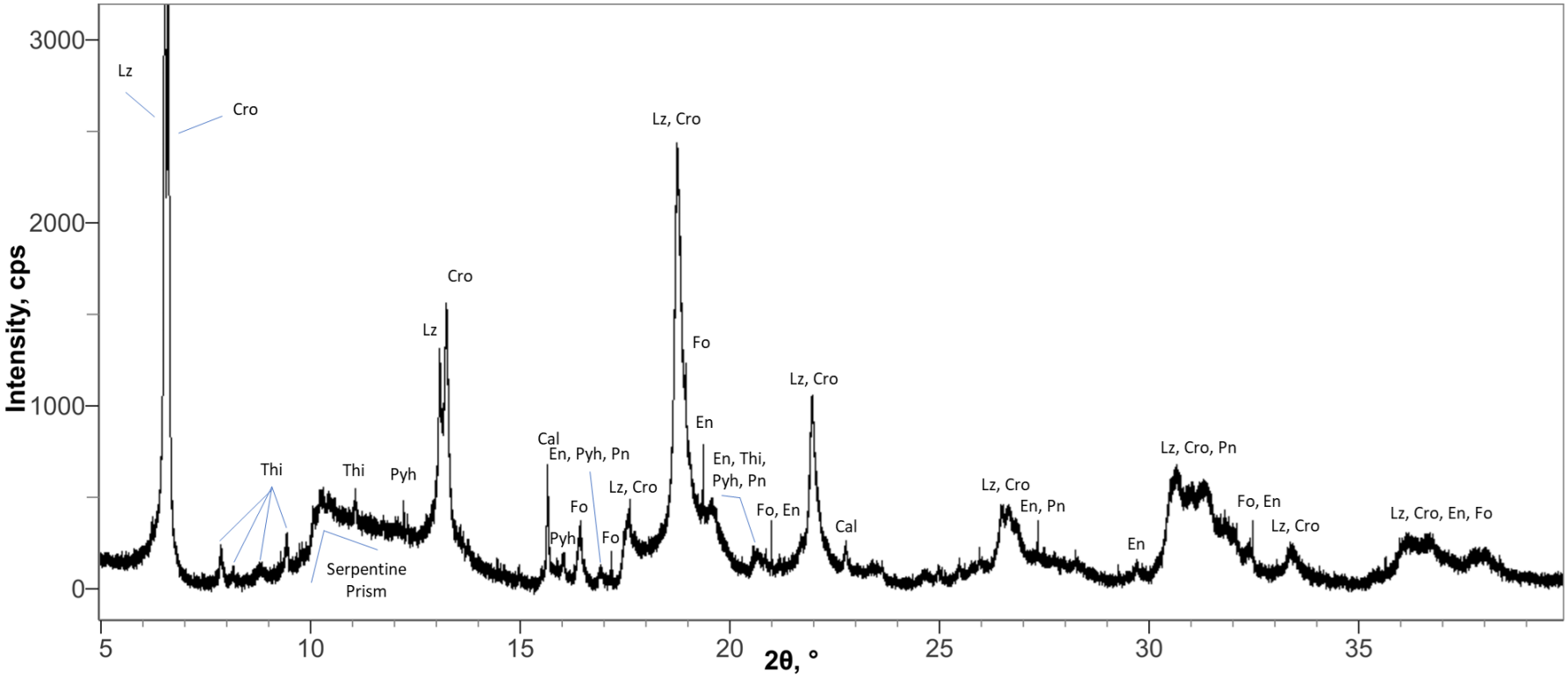

Fig. 5.1. pXRD pattern of ALH 83100 prior to heating. Lizardite (Lz) and cronstedtite (Cro) are the most abundant phases observed. Other phases identified from the pattern include tochilinite (Thi), pentlandite (Pn), pyrrhotite (Pyh), calcite (Cal), forsterite (Fo), and enstatite (En). Pattern collected using synchrotron radiation.

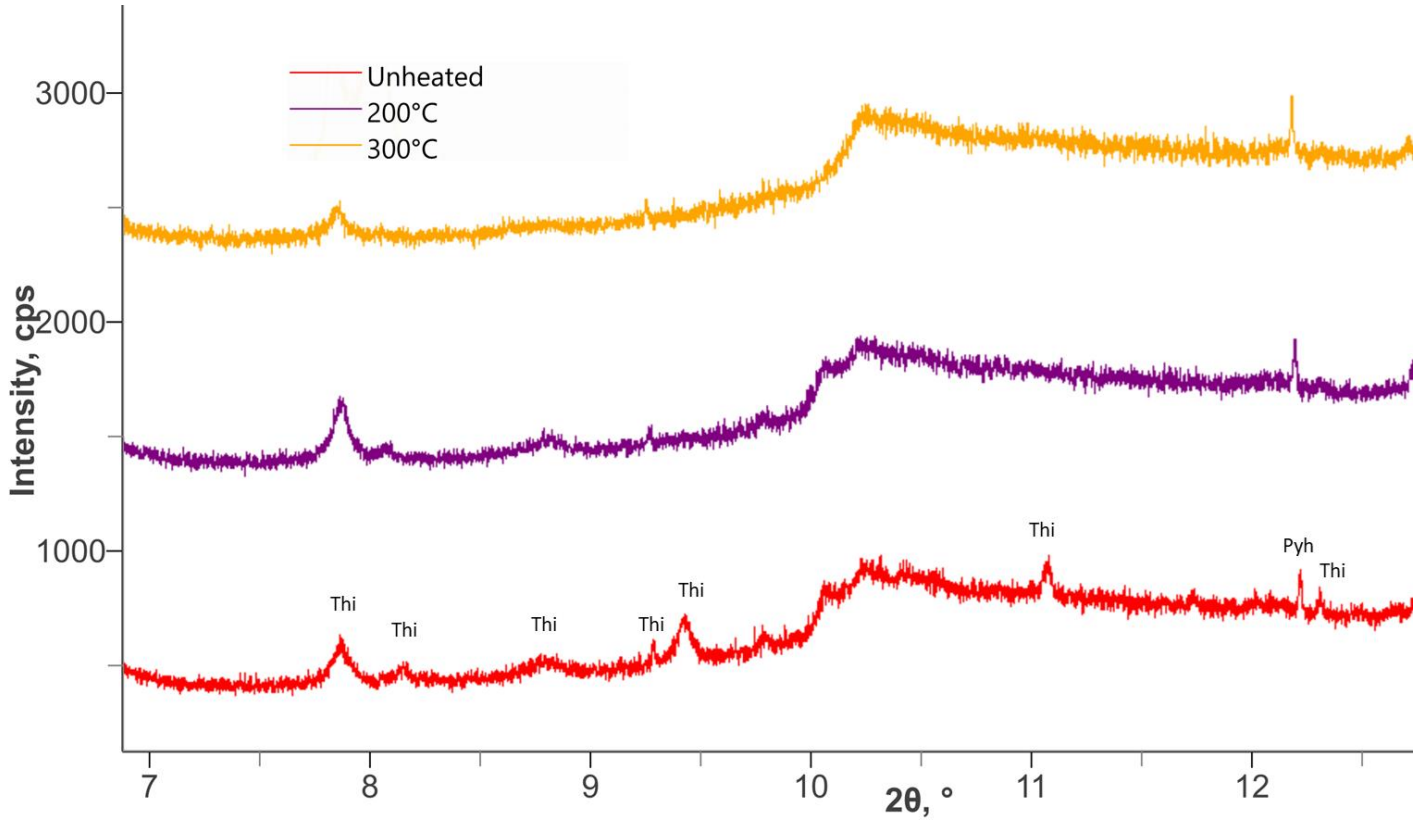

Fig. 5.2. pXRD patterns of ALH 83100 up to 300°C showing tochilinite (Thi) decomposition. Unheated ALH 83100 has Thi among pyrrhotite (Pyh). Thi peaks (e.g., 8.1°, 8.8°, 9.3°, 9.5°, 11.1°, and 12.3° 2Θ) start weakening at 200°C, with most peaks disappearing by 300°C. Patterns collected using synchrotron radiation.

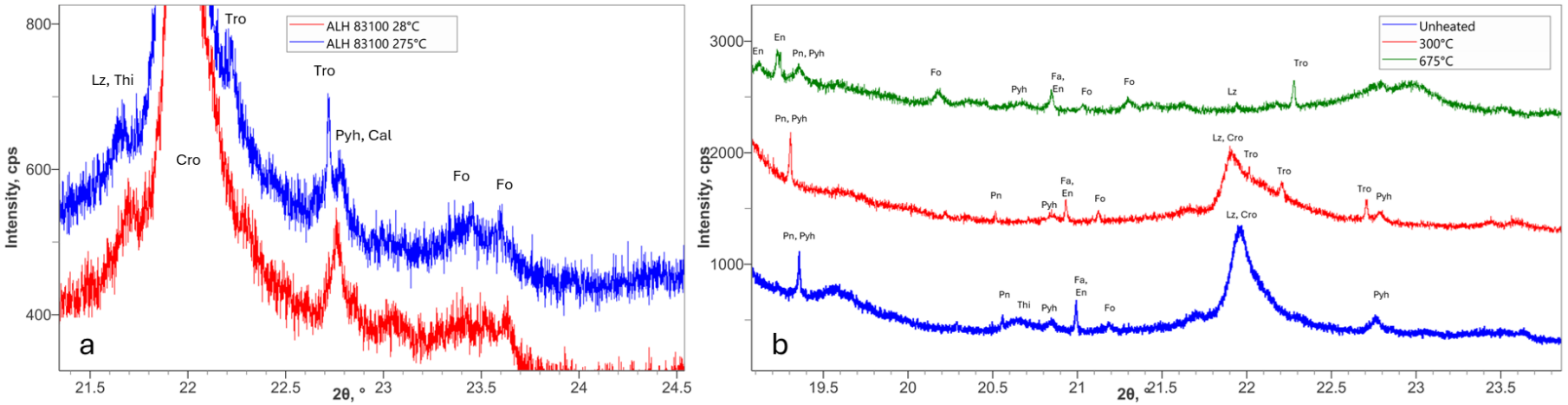

Fig. 5.3. pXRD patterns of ALH 83100 up to 675°C showing changes in anhydrous sulphides. a) Peaks associated with troilite (Tro) (e.g., 22.0°, 22.2°, and 22.7° 2Θ) appear at 275°C. b) Pentlandite (Pn) peaks (e.g., 19.3° and 20.5° 2Θ) start noticeably weakening at 675°C. Other phases labelled in the pXRD patterns are pyrrhotite (Pyh,) tochilinite (Thi), forsterite (Fo), fayalite (Fa), enstatite (En), lizardite (Lz), and cronstedtite (Cro). Patterns collected using synchrotron radiation.

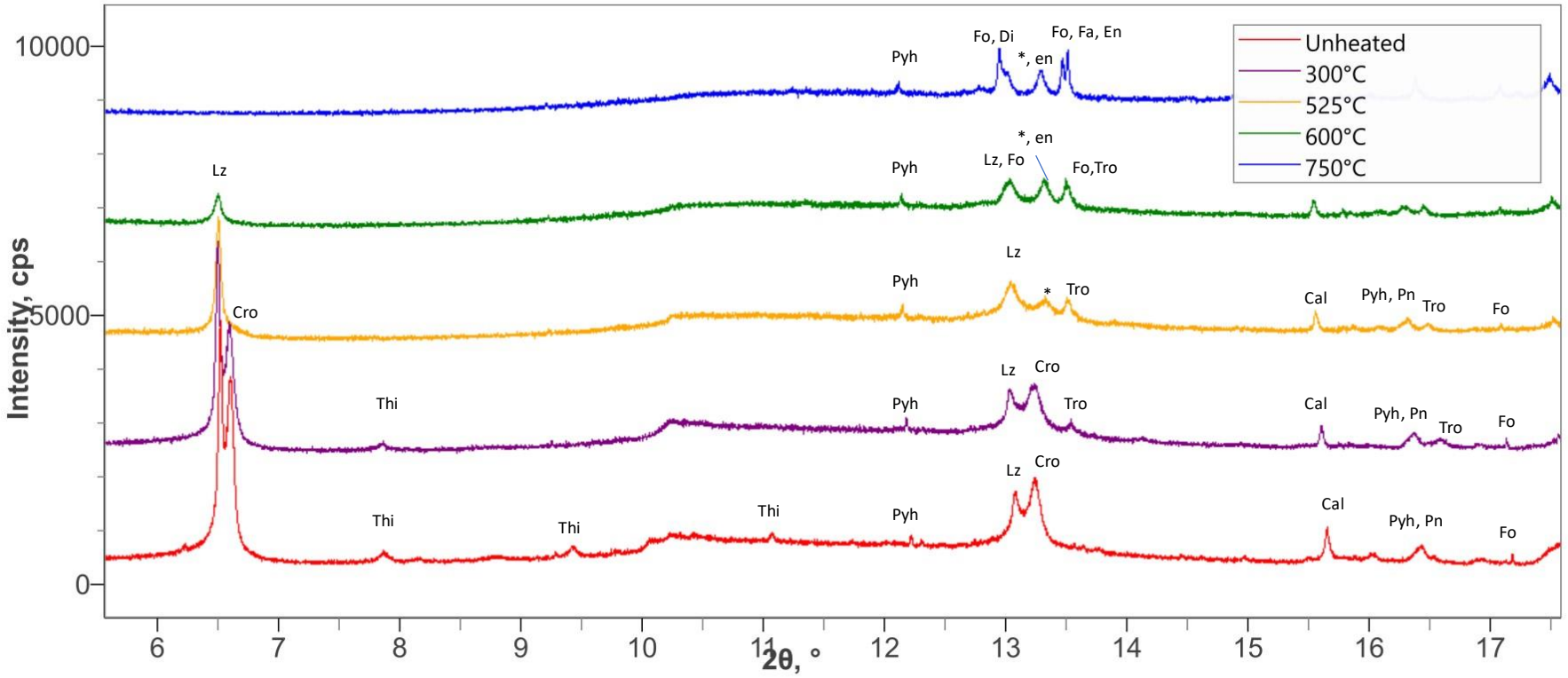

Fig. 5.4. pXRD patterns of ALH 83100 showing key changes during the decomposition of lizardite (Lz) and cronstedtite (Cro). At 300°C, Lz and Cro peaks (e.g., 6.5°, 6.6°, 13.0°, and 13.2° 2Θ) start weakening with Cro weakening faster than Lz. Both Lz and Cro disappear by 700°C. At 525°C, a peak associated with a transitional phase (*) appears at 13.3° 2Θ, which continues strengthening until 750°C, where it starts to weaken. Enstatite (En) peaks (e.g., 13.3° and 13.5° 2Θ) start strengthening at 575°C and forsterite (Fo) peaks (e.g., 13.0°, 13.5°, and 17.1° 2Θ) start strengthening at 600°C, indicating the recrystallization of secondary anhydrous silicates. Fayalite (Fa) also appears at 600°C. Other phases labelled in the pXRD patterns are tochilinite (Thi), pentlandite (Pn), pyrrhotite (Pyh), calcite (Cal), and troilite (Tro). Patterns collected using synchrotron radiation.

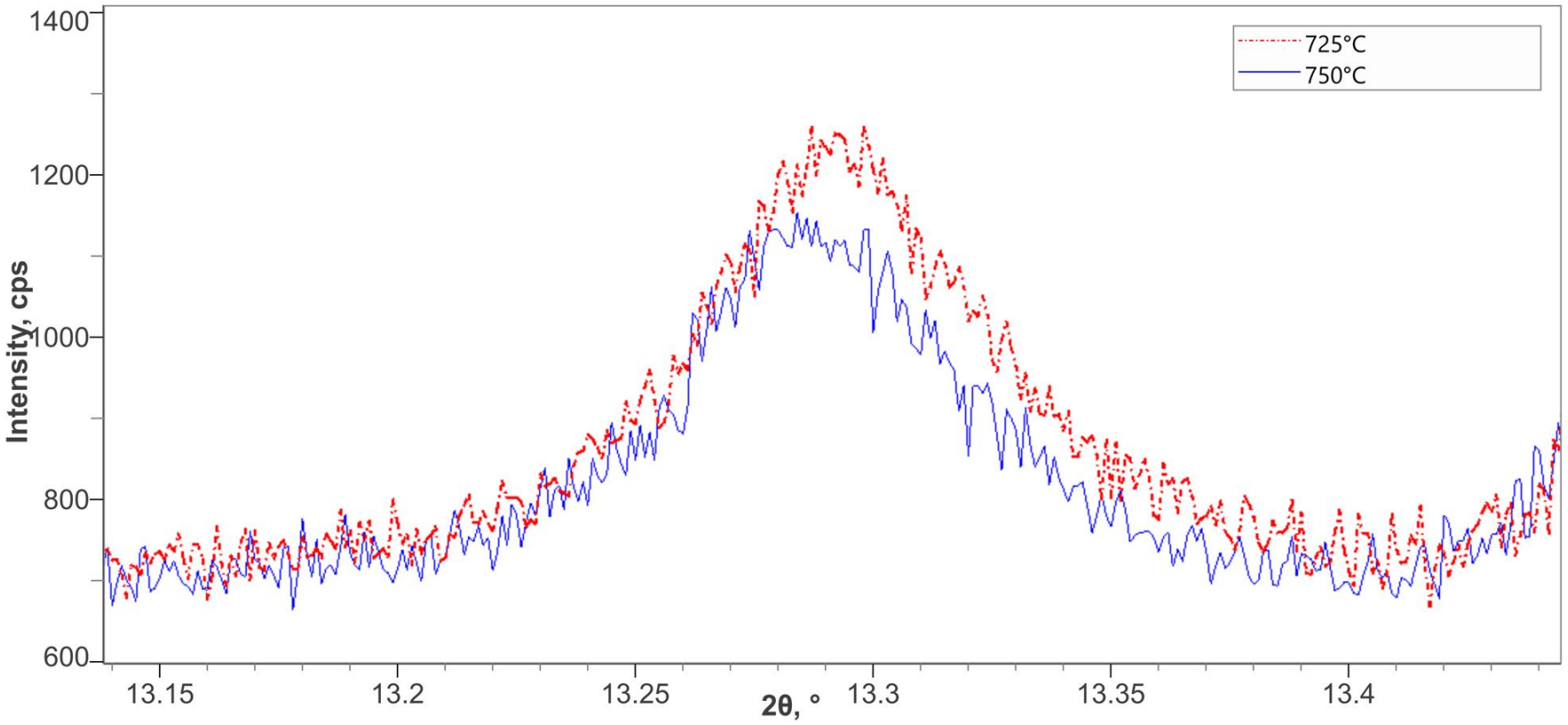

Fig. 5.5. Peak weakening displayed by the transitional phase at 3.56 Å/13.3°2Θ in ALH 83100. Patterns for ALH 83100 heated to 725°C and 750°C are overlain on top of each other to show the weakening in intensity of the transitional phase's peak. Patterns collected using synchrotron radiation.

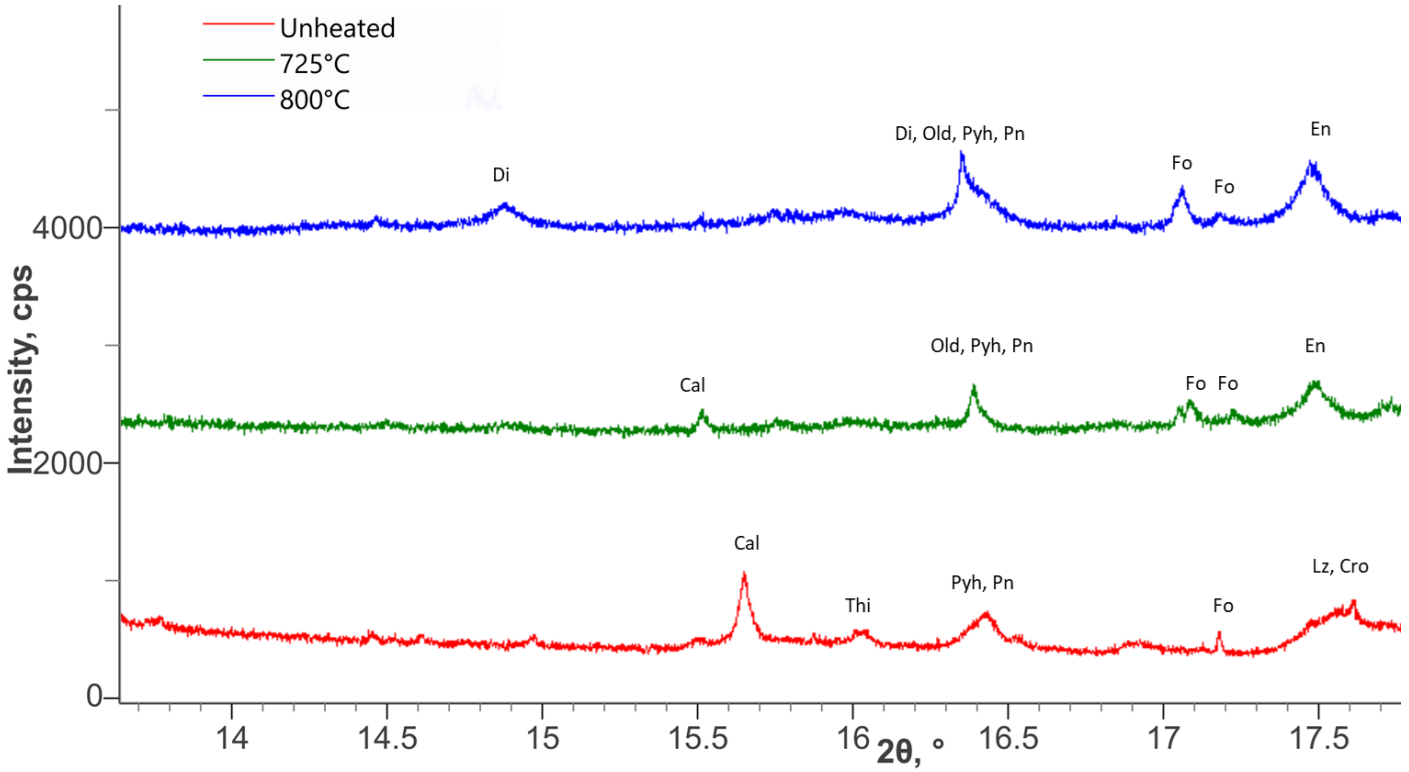

Fig. 5.6. pXRD patterns of ALH 83100 showing key changes during the decomposition of calcite (Cal). At 725°C, calcite peaks (e.g., 15.5° 2Θ) begin noticeably weakening. At the same time, oldhamite (Old) (e.g., 16.4° 2Θ) and diopside (Di) (e.g., 14.9° and 16.4° 2Θ) peaks start to appear. Calcite disappears by 800°C. Other phases labelled are tochilinite (Thi), pentlandite (Pn), pyrrhotite (Pyh), forsterite (Fo), lizardite (Lz), cronstedtite (Cro), and enstatite (En). Patterns collected using synchrotron radiation.

5.1.2 Peak Width Changes During Heating

The width of XRD peaks can be affected by grain size, strain, and crystallinity, wherein peak broadening reflects smaller grain size, lower crystallinity, and/or an increased degree of strain (Williamson & Hall 1953). Because secondary anhydrous phases that form from post-hydration heating start out as fine-grained and poorly crystalline, it should be possible to track recrystallization via the width of their peaks. Additionally, during decomposition of specific phases (e.g., calcite), the crystals will undergo structural changes that might be reflected in peak widths. This idea was tested for the (130) forsterite peak at 2.9 Å/17.2°2Θ and for a calcite peak at 3.0 Å/15.7°2Θ, where the width of each peak at half its intensity was measured as a parameter known as Full-Width Half-Maximum (FWHM) in 2Θ (Fig. 5.7).

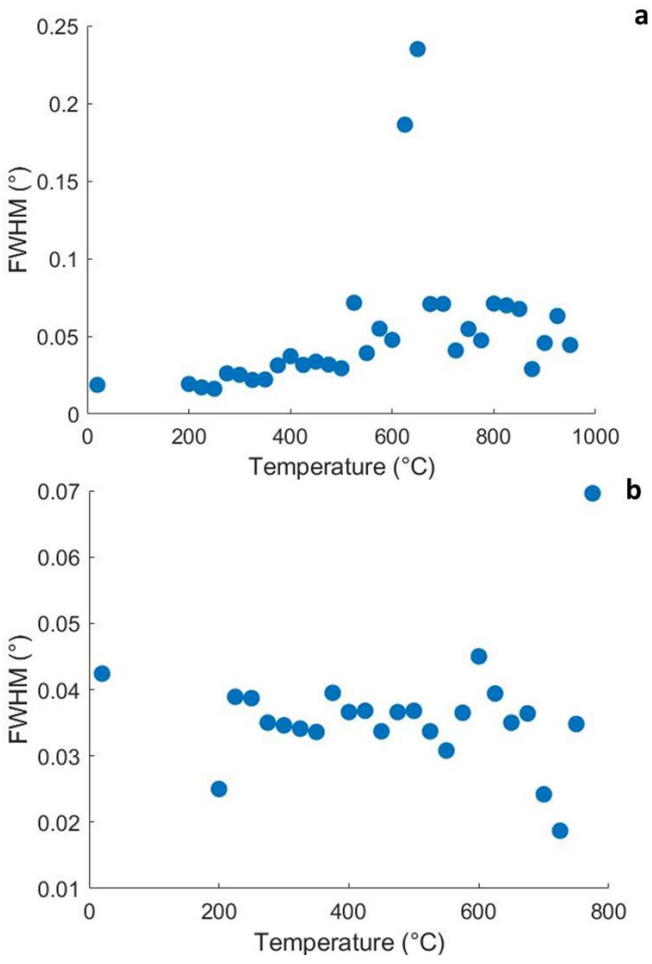

Fig. 5.7. XRD peak width changes of key mineral indices for phases within ALH 83100 during heating. a) Peak widths of (130) forsterite. b) Peak widths of (211) calcite.

Forsterite peak widths started out with narrow FWHMs that gradually increase, but still remain quite narrow until 525°C, where their rate of peak widening increases. This peak widening continues until 650°C, after which peak

widths suddenly narrow, remaining constant until the end of the heating (Fig. 5.7a).

For most of the heating experiment, calcite peak widths remain quite constant until 700°C is reached. At 700°C, calcite peak width decreases, reaching a minimum at 750°C. After 750°C, peak width rapidly increases until calcite's complete decomposition at 800°C (Fig. 5.7b).

5.2 – Bulk Mineral Changes in the Experimental Heating of pMurchison Under Inert Conditions

A sample of pMurchison was powdered and heated from 300 to 750°C at 25°C temperature steps under inert conditions, during which XRD data were collected. The powder spent 115 minutes at each temperature step, except for the 300°C temperature step, where it was held for 50 minutes. A reference XRD pattern was collected before the experiment and at the end after the sample had cooled to room temperature. See Chapter 2.5.1 for more details of the experimental setup.

5.2.1 Mineral Decomposition and Recrystallization

Prior to heating, pMurchison contained significant amounts of lizardite, cronstedtite, forsterite, and enstatite, with minor quantities of tochilinite, magnetite, pyrrhotite, pentlandite, and calcite (Fig. 5.8). This mineralogy is consistent with previous bulk XRD data (Howard et al. 2009).

Following heating to 300°C, all peaks related to tochilinite disappear. Peaks associated with troilite begin to appear at 300°C. Magnetite peaks start strengthening at 350°C (Fig. 5.9). Peaks associated with pentlandite start noticeably weakening at 675°C. This decomposition continues throughout the rest of the experiment and is most noticeable in the XRD pattern collected after heating, when pMurchison had cooled down to room temperature. Additionally, in the room temperature post-experiment XRD pattern troilite peaks show a distinct increase in intensity (Fig. 5.10).

Serpentine peaks begin to weaken at 300°C, with cronstedtite peaks showing a greater degree of weakening than those of lizardite. All lizardite and

cronstedtite peaks disappear by 525°C. A peak likely associated with the transitional phase appears at 525°C and remains until the sample returns to room temperature, where it disappears. Fayalite appears and peaks associated with forsterite start strengthening at 600°C, while enstatite peaks strengthen at 750°C (Fig. 5.11 & 5.12).

Peaks associated with calcite start weakening at 575°C and continue weakening throughout heating, but never completely disappear. Secondary clinopyroxene peaks appear at the same time as calcite starts decomposing and continue strengthening for the rest of heating. At no point during heating was oldhamite observed (Fig. 5.13 & 5.14).

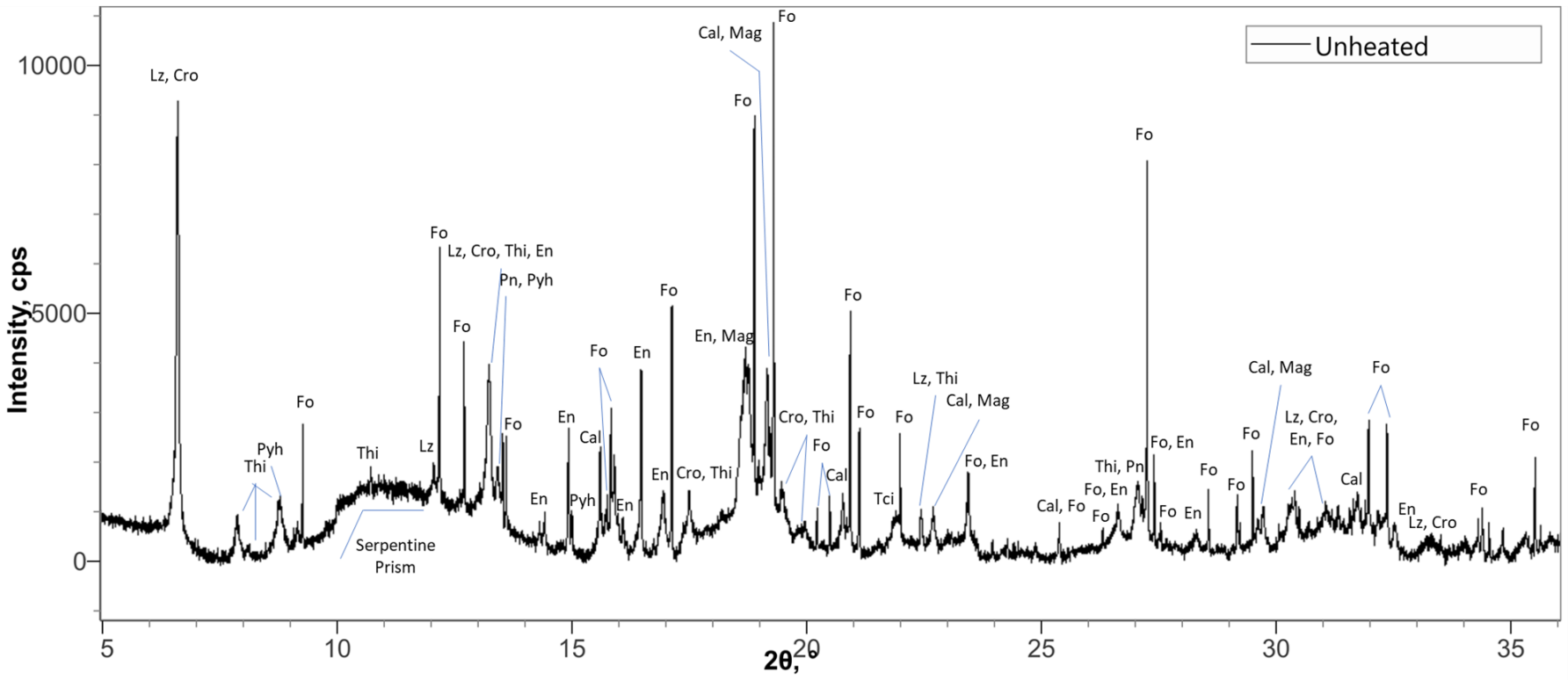

Fig. 5.8. pXRD pattern of pMurchison prior to heating. Lizardite (Lz), cronstedtite (Cro), and tochilinite (Thi) are the most abundant minerals. Other phases observed include magnetite (mag), pentlandite (Pn), pyrrhotite (Pyh), calcite (Cal), forsterite (Fo), and enstatite (En). Pattern collected using synchrotron radiation.

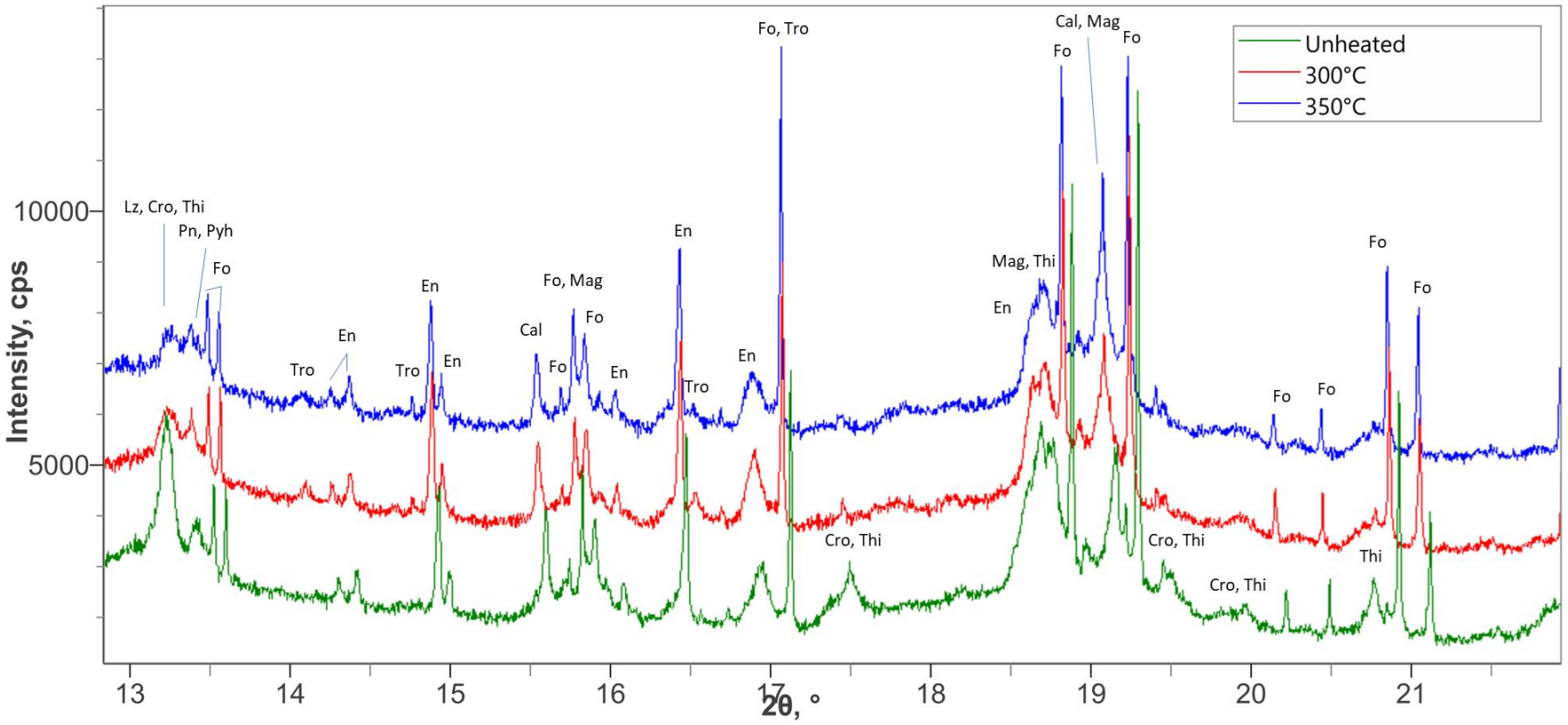

Fig. 5.9. pXRD patterns of pMurchison during heating showing tochilinite (Thi) decomposition. Unheated Murchison has Thi among pyrrhotite (Pyh), pentlandite (Pn), calcite (Cal), enstatite (En), forsterite (Fo), magnetite (Mag), lizardite (Lz), and cronstedtite (Cro). Thi peaks (e.g., 13.2°, 17.5°, 18.7°, 19.5°, 20.0°, and 20.8° 2Θ) disappear at 300°C, which is soon followed by the appearance of troilite (Tro) (e.g., 14.1°, 14.8°, and 16.5° 2Θ) and the strengthening of Mag (e.g., 15.8°, 18.7°, and 19.1° 2Θ) peaks. Patterns collected using synchrotron radiation.

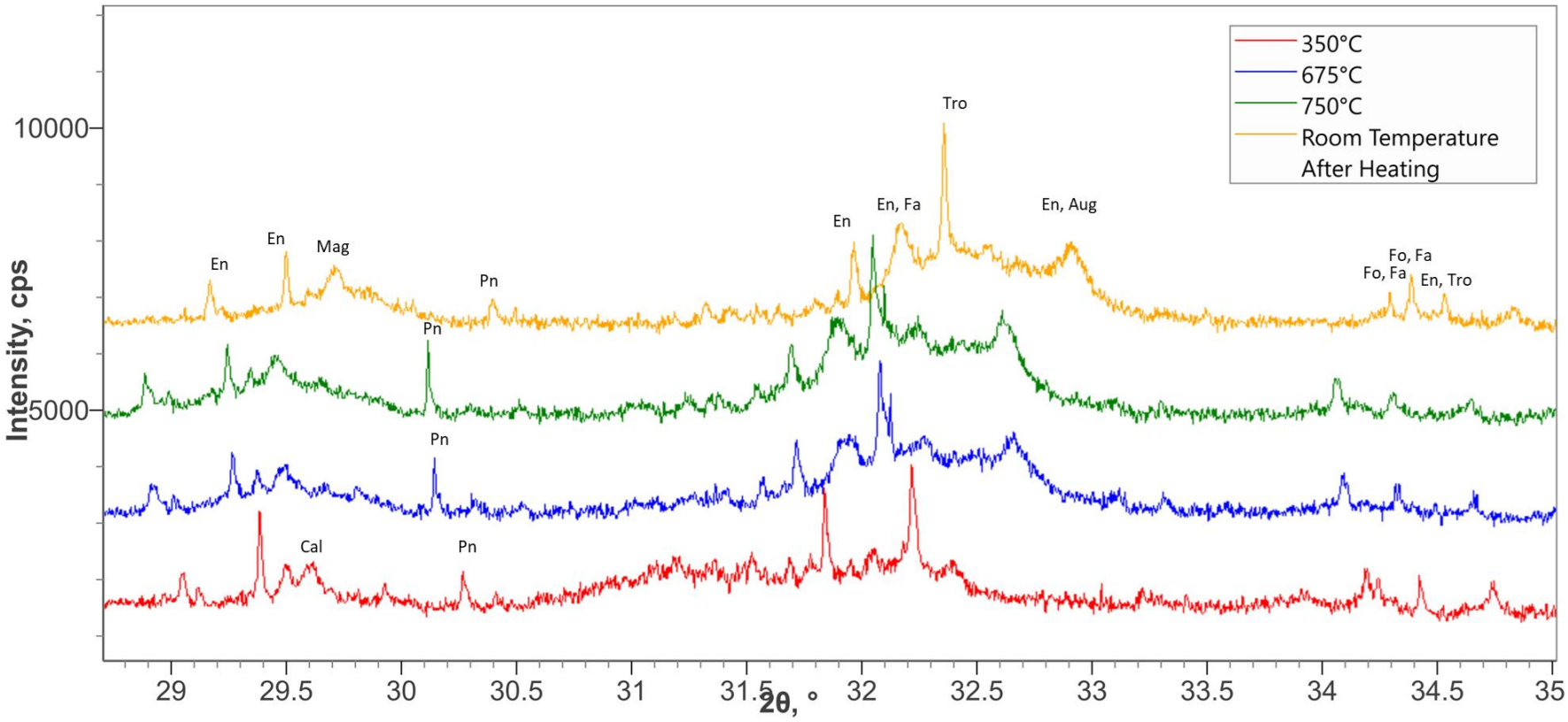

Fig. 5.10. pXRD patterns of pMurchison showing changes in anhydrous sulphides. Peaks associated with pentlandite (Pn) (e.g., 30.3°) start noticeably weakening at 675°C, with the most dramatic weakening occurring during cooling from 750°C. Please note that peak shifting may occur during heating and cooling due to expansion and shrinking of the unit cell. Troilite (tro) peaks (e.g., 32.3° and 34.5° 2Θ) strengthen in response to pyrrhotite and pentlandite decomposition. Other phases labelled in the pXRD patterns are forsterite (Fo), fayalite (Fa), enstatite (En), augite (Aug), calcite (Cal), and magnetite (Mag). Patterns collected using synchrotron radiation.

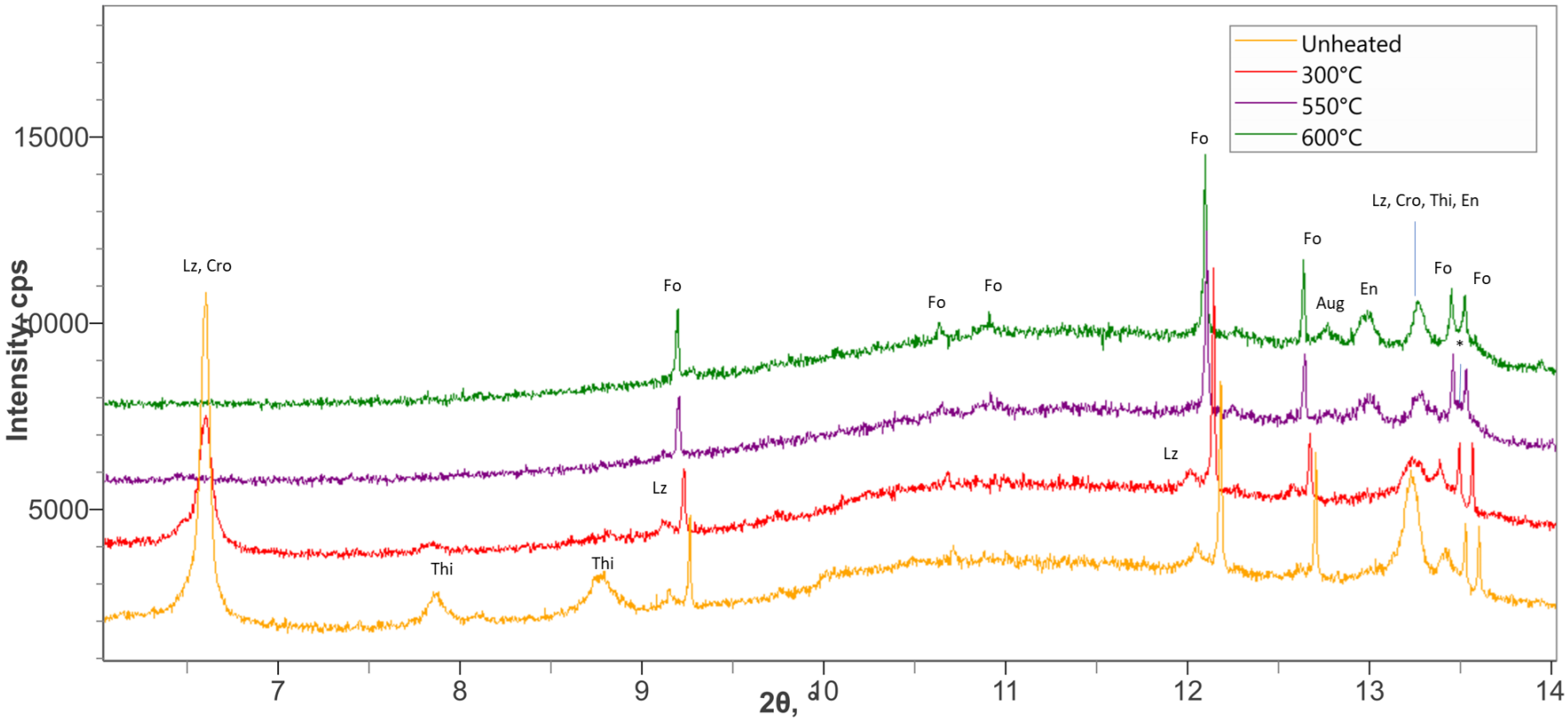

Fig. 5.11. pXRD patterns of pMurchison showing key changes during the decomposition of lizardite (Lz) and cronstedtite (Cro). At 300°C, Lz and Cro peaks (e.g., 6.6°, 9.1°, 12.0°, 13.2°, and 16.9° 2Θ) start weakening with Cro weakening before Lz. Both Lz and Cro disappear by 525°C. At 525°C, a peak at 13.5° 2Θ associated with a transitional phase (*) appears, which continues strengthening until Murchison is brought back down to room temperature. The 550°C pattern is shown here as it displays the weakening of the transitional phase most readily. Fayalite (Fa) peaks (e.g., 12.1°, 13.3°, and 15.7°) appear and forsterite (Fo) peaks (e.g., 9.2°, 12.1°, 12.6°, 13.4°, 15.7°, and 16.4° 2Θ) start strengthening at 600°C and enstatite (En) peaks (e.g., 13.0°, 13.3°, 14.2°, 14.3°, 14.8°, 16.0°, and 17.5° 2Θ) start strengthening at 750°C. Other phases labelled on the pXRD patterns are tochilinite (Thi), pyrrhotite (Pyh), and augite (Aug). Patterns collected using synchrotron radiation.

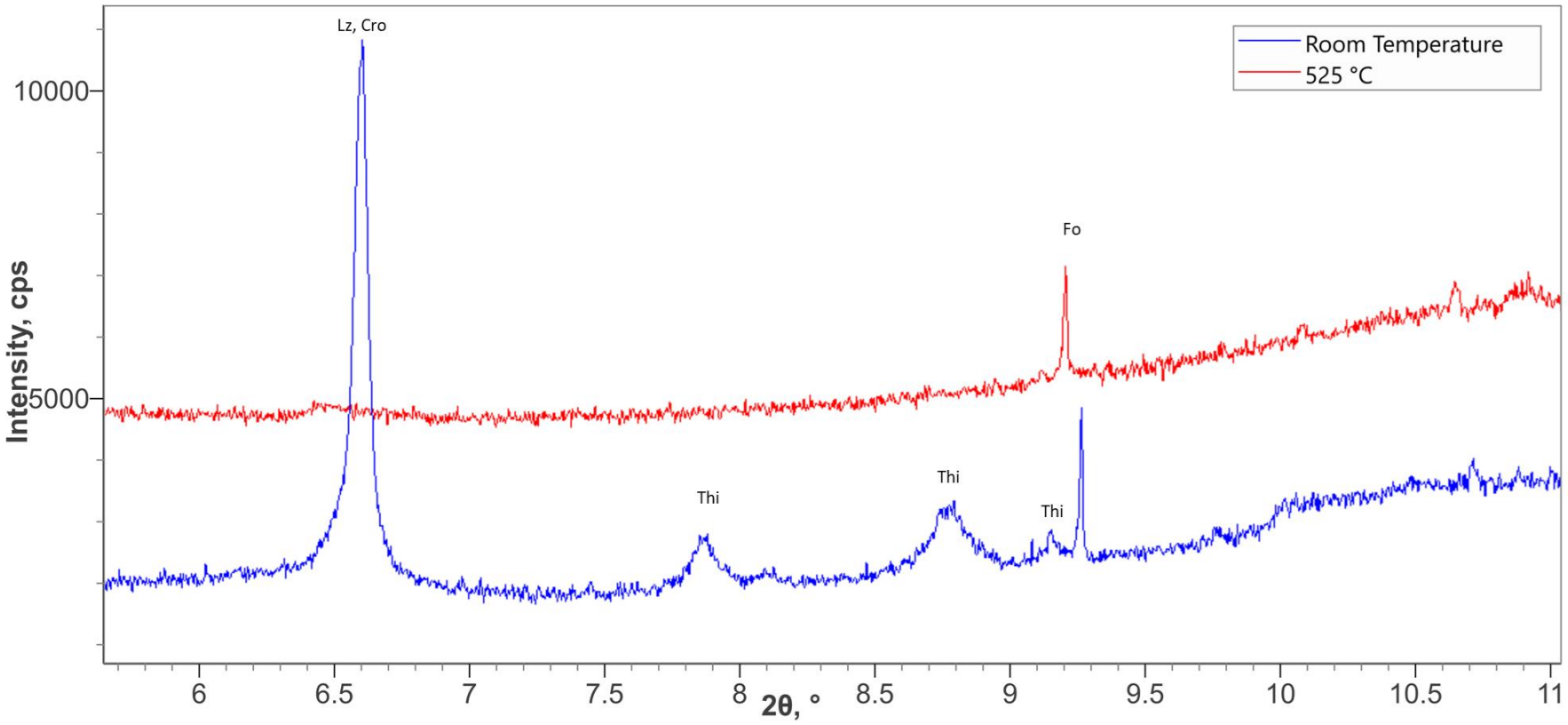

Fig. 5.12. pXRD patterns of pMurchison disappearance of lizardite (Lz) and cronstedtite (Cro) peaks at 525°C. Tochilinite (Thi) and forsterite (Fo) are also labelled. Patterns collected using synchrotron radiation.

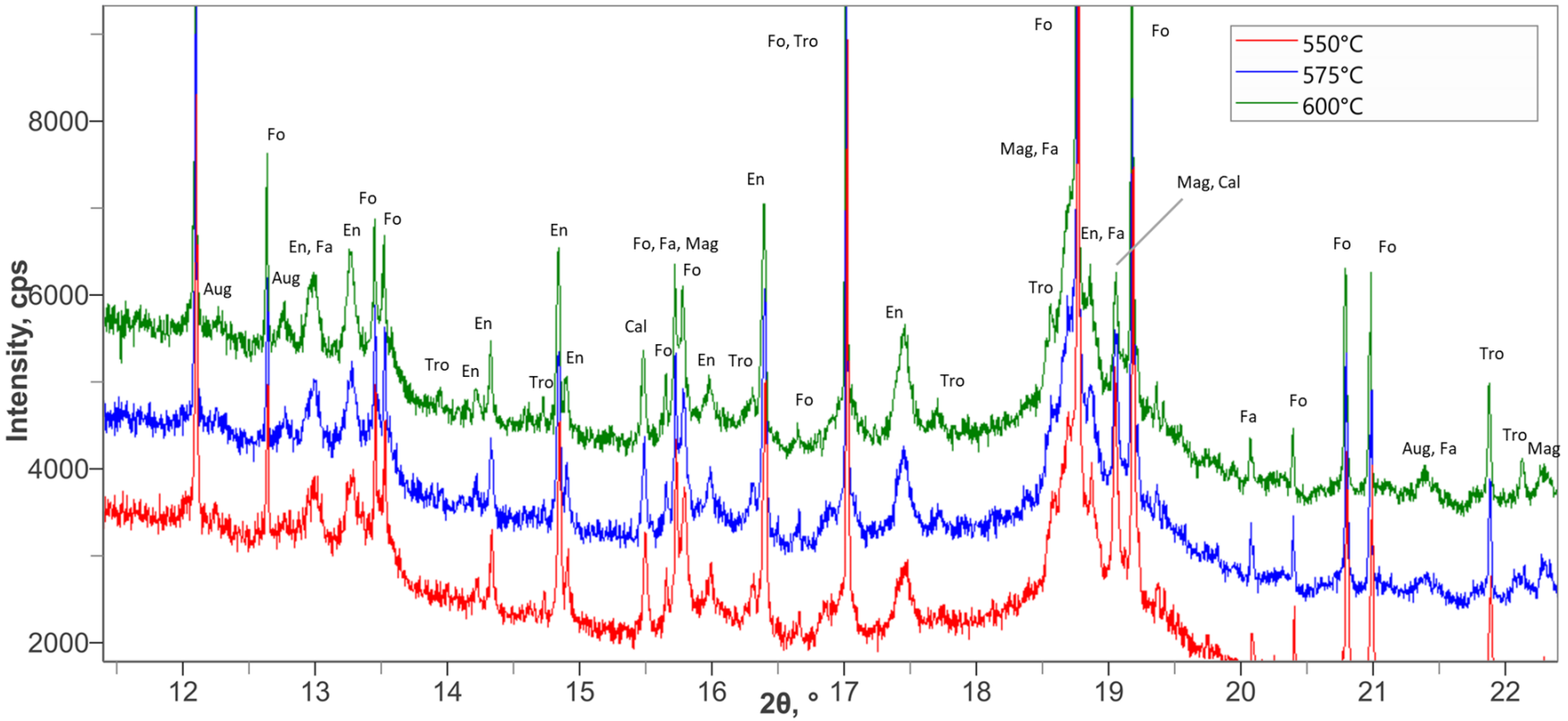

Fig. 5.13. pXRD patterns of pMurchison showing key changes during the decomposition of calcite (Cal). At 575°C, calcite peaks (e.g., 15.5° and 19.0° 2Θ) begin noticeably weakening. At the same time, augite (Aug) peaks (e.g., 12.2°, 12.7°, and 21.4° 2Θ) start appearing. Other phases labelled are forsterite (Fo), fayalite (Fa), enstatite (En), troilite (Tro), and magnetite (Mag). Patterns collected using synchrotron radiation.

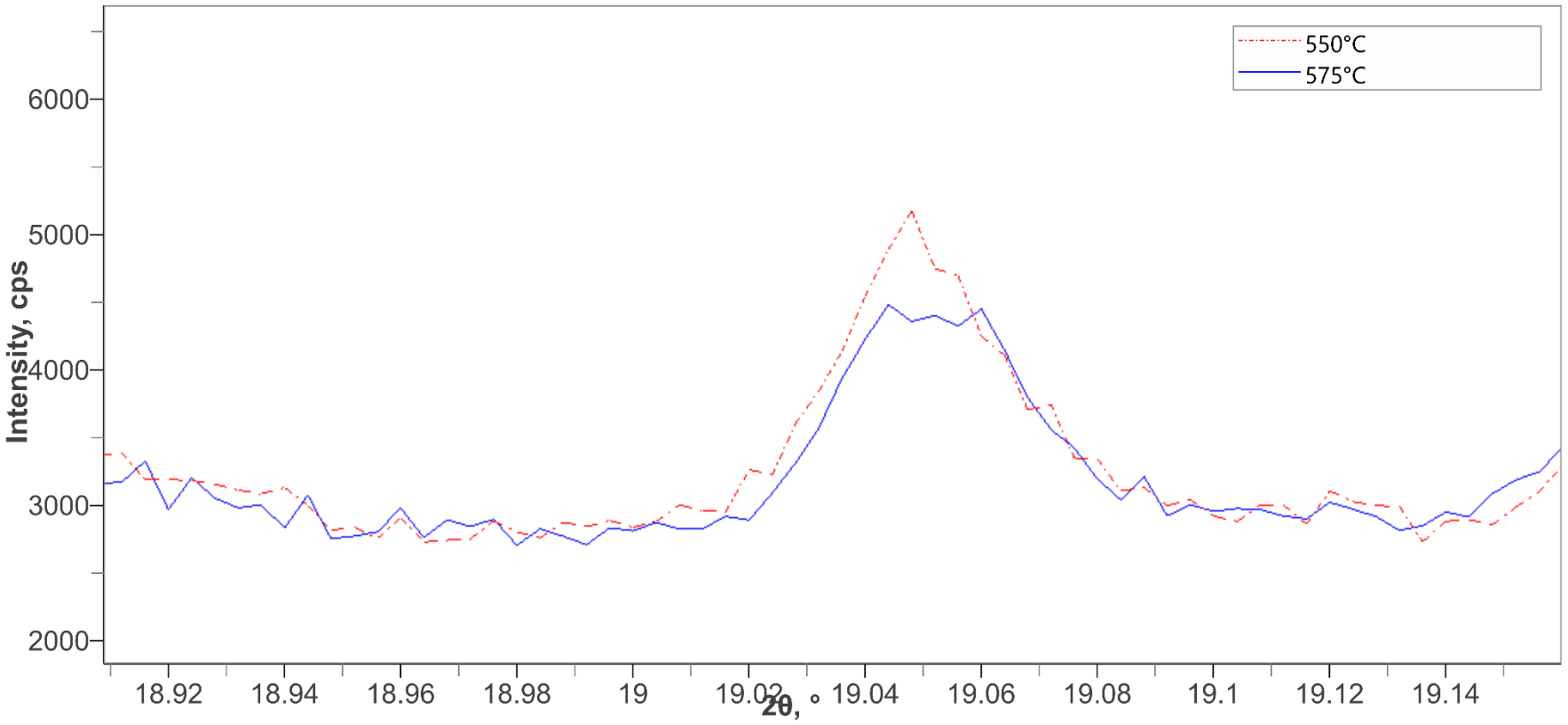

Fig. 5.14. Peak weakening displayed by calcite (19.0° 2Θ) in pMurchison. Patterns for ALH 83100 heated to 550°C and 575°C are overlain on top of each other to show the weakening in intensity of the calcite peak. Patterns collected using synchrotron radiation.

5.2.2 Peak Width Changes During Heating

The width of the (101) forsterite peak at 12.7° 2θ was measured in 2θ as FWHM throughout heating (Fig. 5.15). For most of the experiment, its width remained relatively constant, however there was a brief, but insignificant decrease in peak width at 525°C, before peak widths increase again.

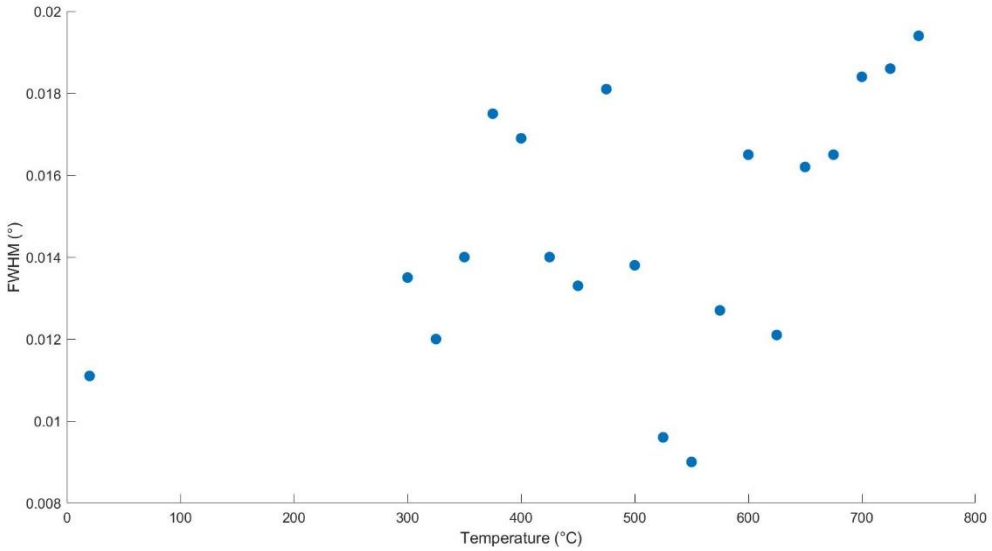

Fig. 5.15. XRD peak width changes for the (101) forsterite peak during heating of pMurchison.

5.3 – Bulk Mineral Changes in the Experimental Heating of LEW 85311 Under Oxidizing Conditions

Before heating, LEW 85311 was composed of a mixture of lizardite, cronstedtite, tochilinite, forsterite, and enstatite, with minor amounts of magnetite, pyrrhotite, calcite, gypsum, and the water-soluble polymorph of anhydrite (Fig. 5.16). Soluble anhydrite is metastable and forms as a precursor to insoluble anhydrite (commonly known as just anhydrite) (Prieto-Taboada et al. 2014). This mineralogy is consistent with data in the literature (Lee et al. 2019b).

A sample of LEW 85311 was heated from 300 to 750°C at 25°C temperature steps under oxidizing conditions (i.e., in air), during which XRD data were collected. LEW 85311 was held for two hours at each temperature step. A reference XRD pattern was collected both before and after heating, when the sample had cooled to room temperature. See Chapter 2.5.3 for more details of the experimental setup.

Tochilinite disappears at 300°C, at the same time magnetite and pyrrhotite peaks increase in intensity, indicating recrystallization. This peak intensity increase becomes most apparent at 325°C (Fig. 5.17). Both magnetite and pyrrhotite peaks continue to strengthen until 600°C, where pyrrhotite begins to weaken in intensity (Fig. 5.18). Pyrrhotite continues to weaken in intensity for the rest of the experiment, however at no point does it disappear.

Like tochilinite, gypsum dehydrates at 300°C, with its peaks disappearing completely. Peaks associated with bassanite appear at the same temperature (Fig. 5.17). The bassanite peaks begin to weaken at 350°C before disappearing altogether at 375°C, wherein the insoluble polymorph of anhydrite takes its place (Fig. 5.19). The soluble anhydrite peaks weaken at 400°C and disappear by 525°C; soluble anhydrite likely recrystallized into insoluble anhydrite (Fig. 5.20).

Serpentine peaks begin to weaken at 375°C and disappear at 425°C (Fig. 5.20 & 5.21). Fayalite appears and forsterite peaks strengthen at 575°C (Fig. 5.22) and continue strengthening for the rest of the experiment. Enstatite peaks remain the same intensity for the entire experiment.

Peaks associated with calcite stay at the same intensity until 600°C, where they quickly disappear, indicating rapid decomposition. At the same temperature clinopyroxene forms, as evident by its high intensity peaks (Fig. 5.23). Clinopyroxene peaks continue strengthening for the rest of the experiment.

Due to peak overlap, no individual peak of any mineral could be tracked throughout the full experiment to study peak width changes.

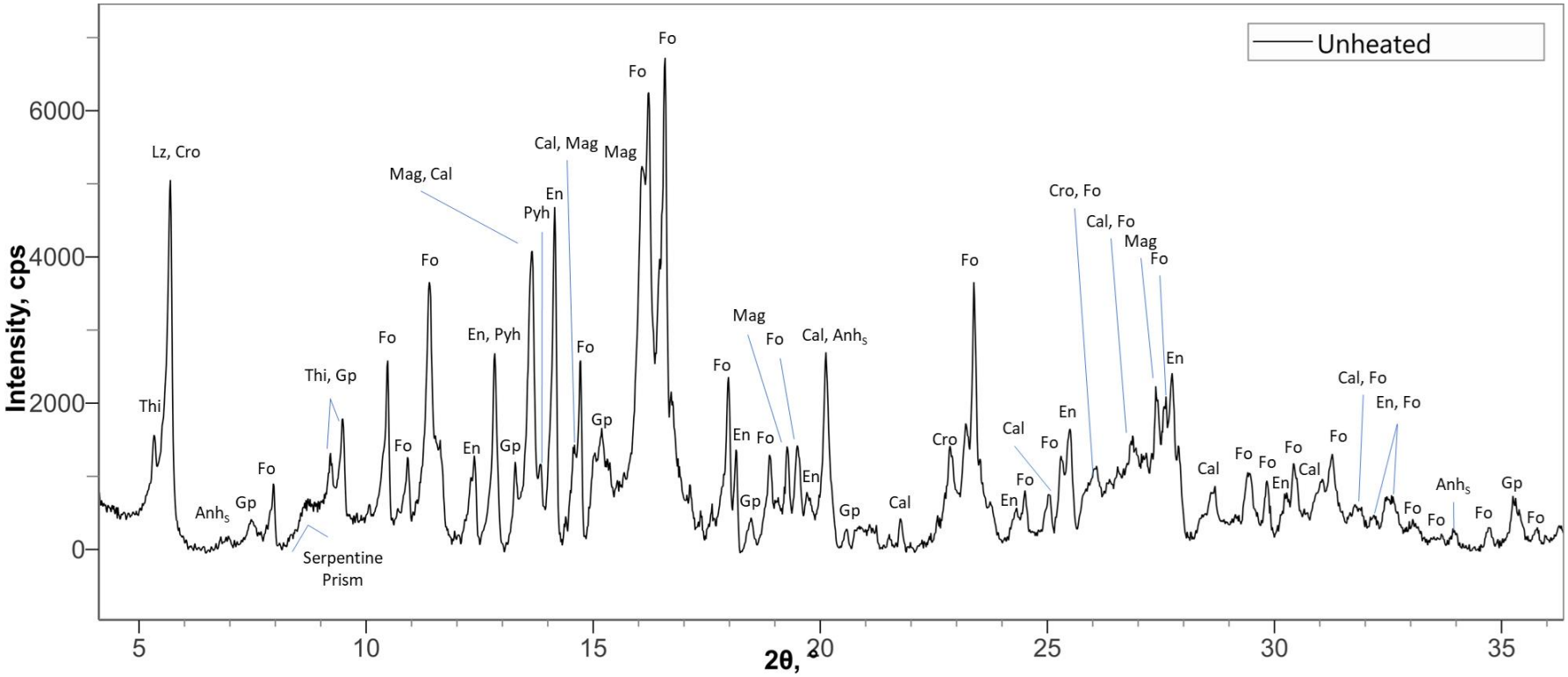

Fig. 5.16. pXRD pattern of LEW 85311 prior to heating. Forsterite (Fo), lizardite (Lz), Cronstedtite (Cro), and tochilinite (Thi) are the most abundant phases. Soluble anhydrite (Anh_s), gypsum (Gp), enstatite (En), pyrrhotite (Pyh), calcite (Cal), and magnetite (Mag) are also present. Pattern collected with a Mo X-ray source.

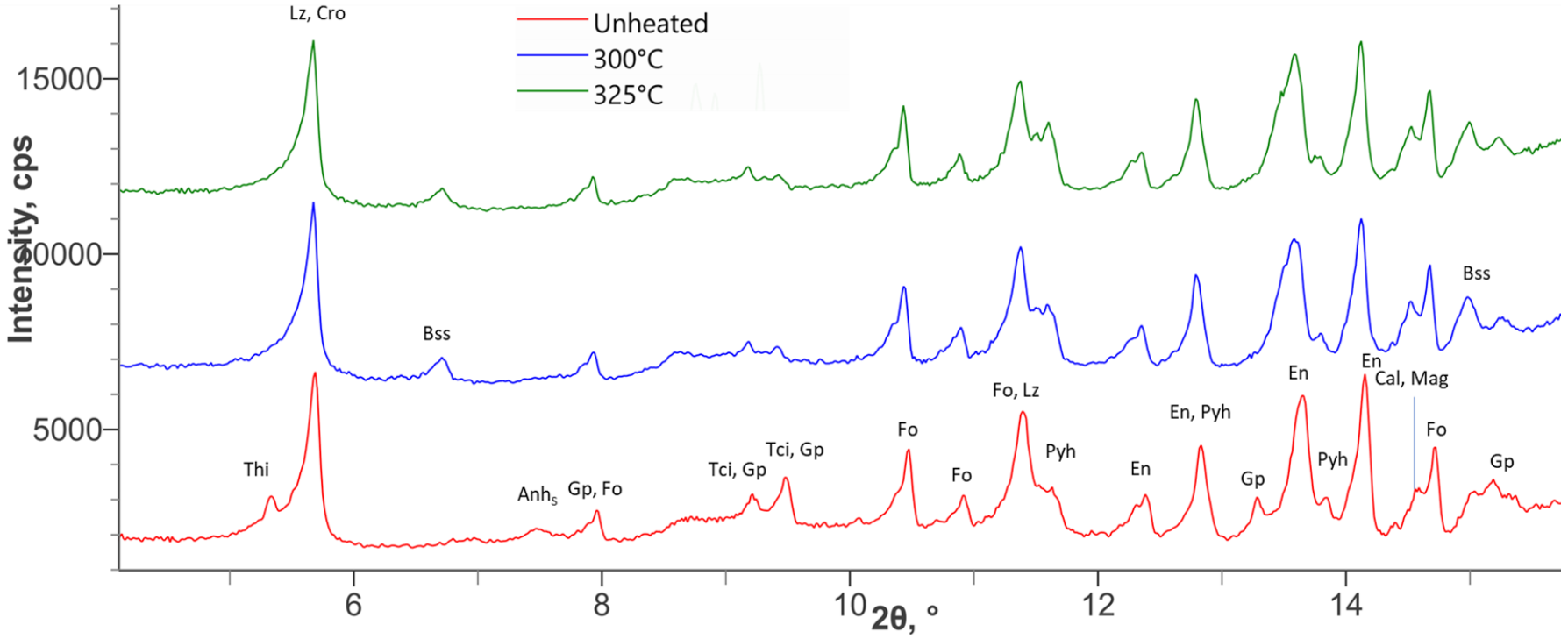

Fig. 5.17. pXRD patterns of LEW 85311 showing tochilinite (Thi) (e.g., 5.3°, 9.2°, and 9.5° 2Θ) and gypsum (Gp) (e.g., 8.0°, 9.2°, 9.5°, 13.3°, and 15.2° 2Θ) decomposition. Both phases are present in the unheated pattern but have gone by 300°C. Bassanite (Bss) peaks (e.g., 6.7° and 15.0° 2Θ) appear at 300°C, while magnetite (Mag) (e.g., 14.5° 2Θ) and pyrrhotite (Pyh) (e.g., 11.6°, 12.8°, and 13.8° 2Θ) peaks begin to strengthen. Other phases labelled are soluble anhydrite (Anh_s), forsterite (Fo), lizardite (Lz), cronstedtite (Cro), and calcite (Cal). Patterns collected with a Mo X-ray source.

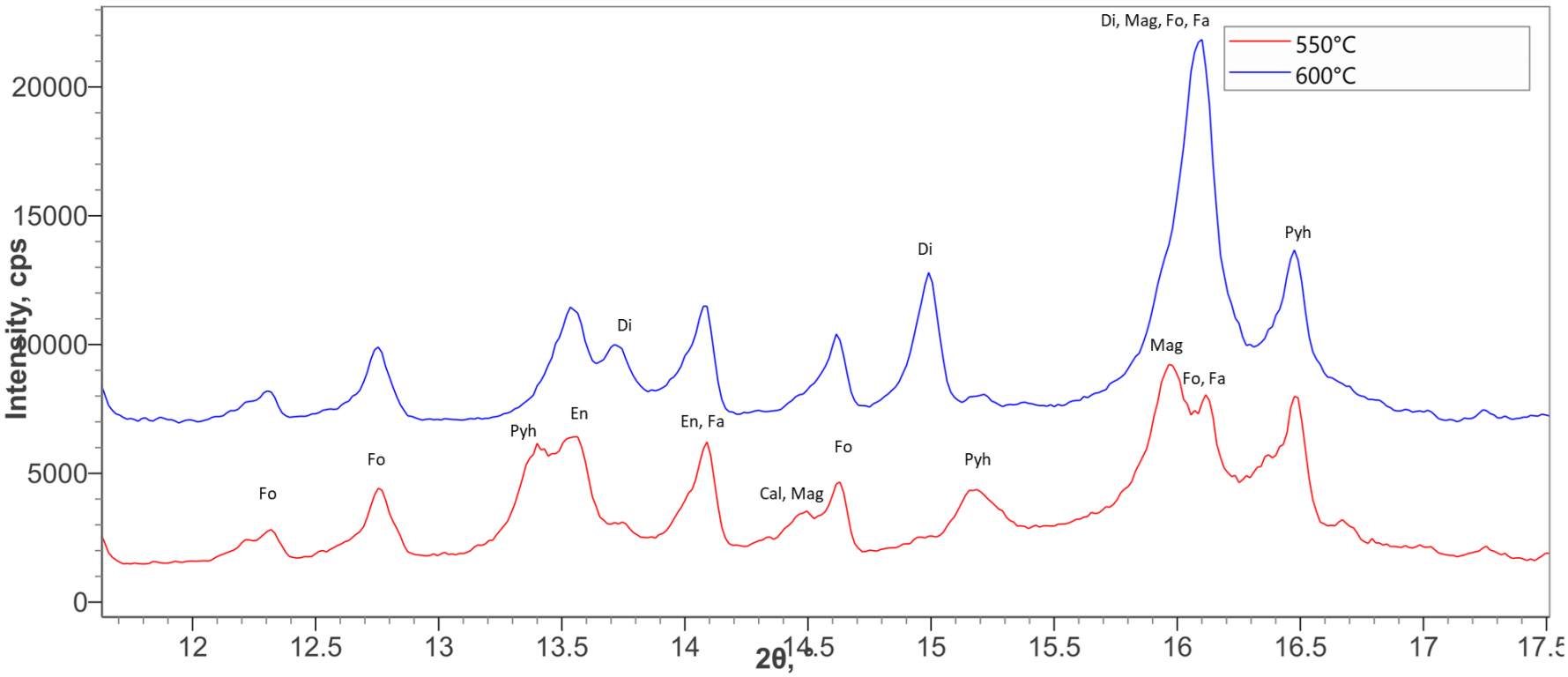

Fig. 5.18. pXRD patterns of LEW 85311 showing pyrrhotite (Pyh) decomposition. At 600°C, Pyh peaks (e.g., 13.4°, 15.2°, and 16.5° 2Θ) begin to weaken. Other phases labelled are forsterite (Fo), fayalite (Fa), enstatite (En), calcite (Cal), magnetite (Mag), and diopside (Di). Patterns collected with a Mo X-ray source.

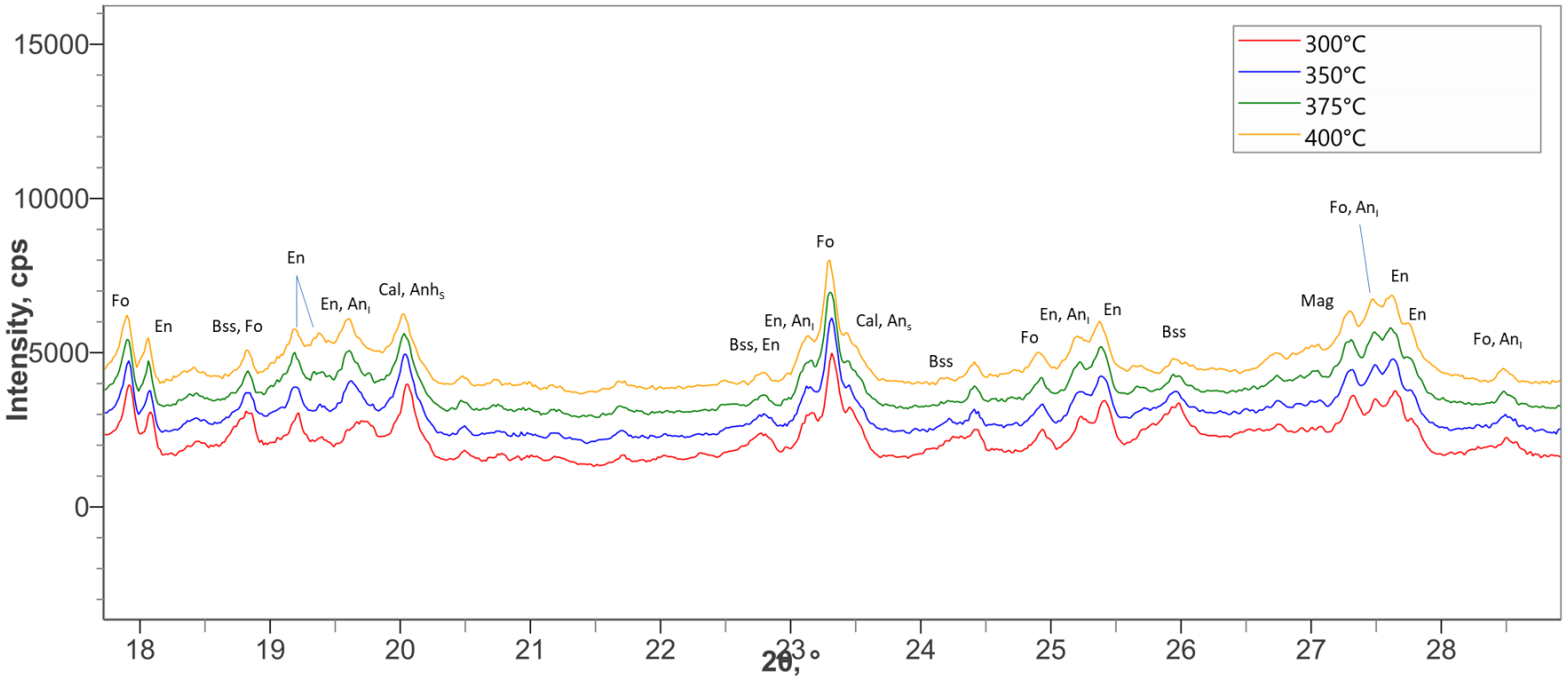

Fig. 5.19. pXRD patterns of LEW 85311 showing changes experienced by bassanite (Bss) during heating. Bss forms from gypsum decomposition and has its peaks (e.g., 18.8°, 22.8°, 24.2°, and 26.0° 2Θ) begin to weaken at 350°C before disappearing at 375°C. After Bss decomposes, peaks associated with insoluble anhydrite (An_I) (e.g., 19.6°, 23.1°, 25.2°, 27.5°, and 28.4° 2Θ) appear at 400°C. Other phases labelled are forsterite (Fo), enstatite (En), calcite (Cal), soluble anhydrite (Anh_S), and magnetite (Mag). Patterns collected with a Mo X-ray source.

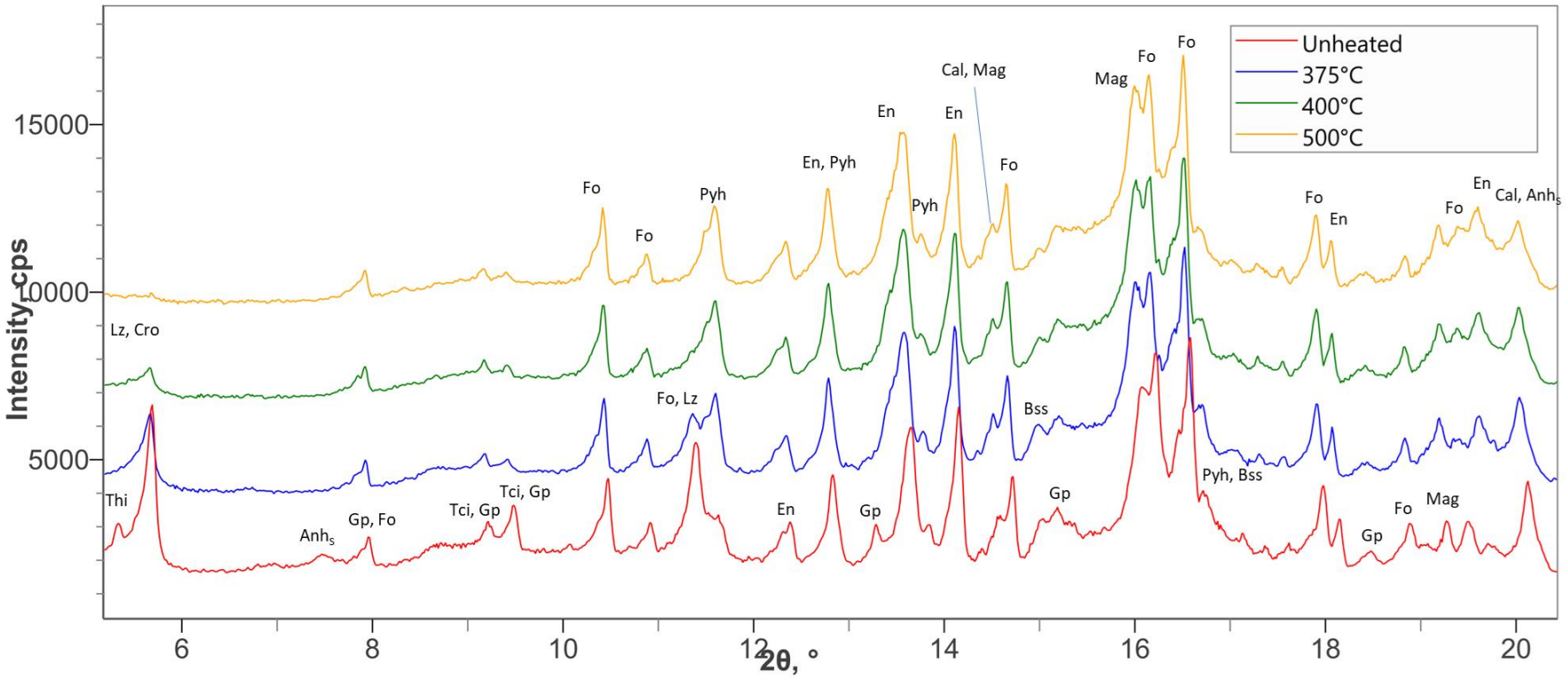

Fig. 5.20. pXRD patterns of LEW 85311 showing changes experienced by soluble anhydrite (Anh_s), lizardite (Lz), and cronstedtite (Cro) during heating. Anh_s has its peaks (e.g., 6.7° and 20.0° 2Θ) begin to weaken at 400°C before disappearing at 525°C, likely recrystallizing into insoluble anhydrite (An_I). Lz and Cro peaks (e.g., 5.7° and 11.4° 2Θ) start weakening at 375°C before disappearing at 475°C. Patterns collected with a Mo X-ray source.

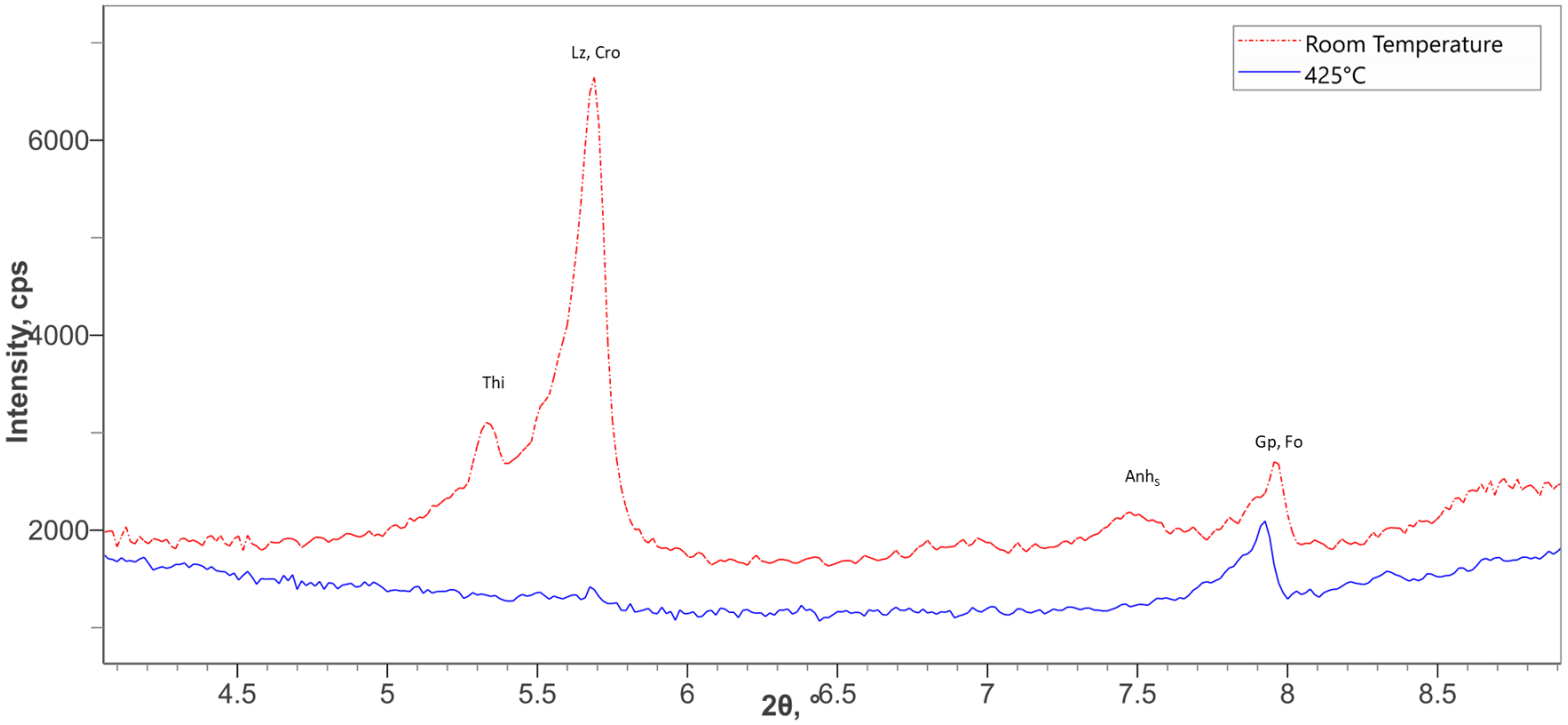

Fig. 5.21. pXRD patterns for LEW 85311 showing disappearance of lizardite (Lz) and cronstedtite (Cro) peaks at 425°C. Tochilinite (Thi), soluble anhydrite (An_s), gypsum (Gp), and forsterite (Fo) are also labelled. Patterns collected with a Mo X-ray source.

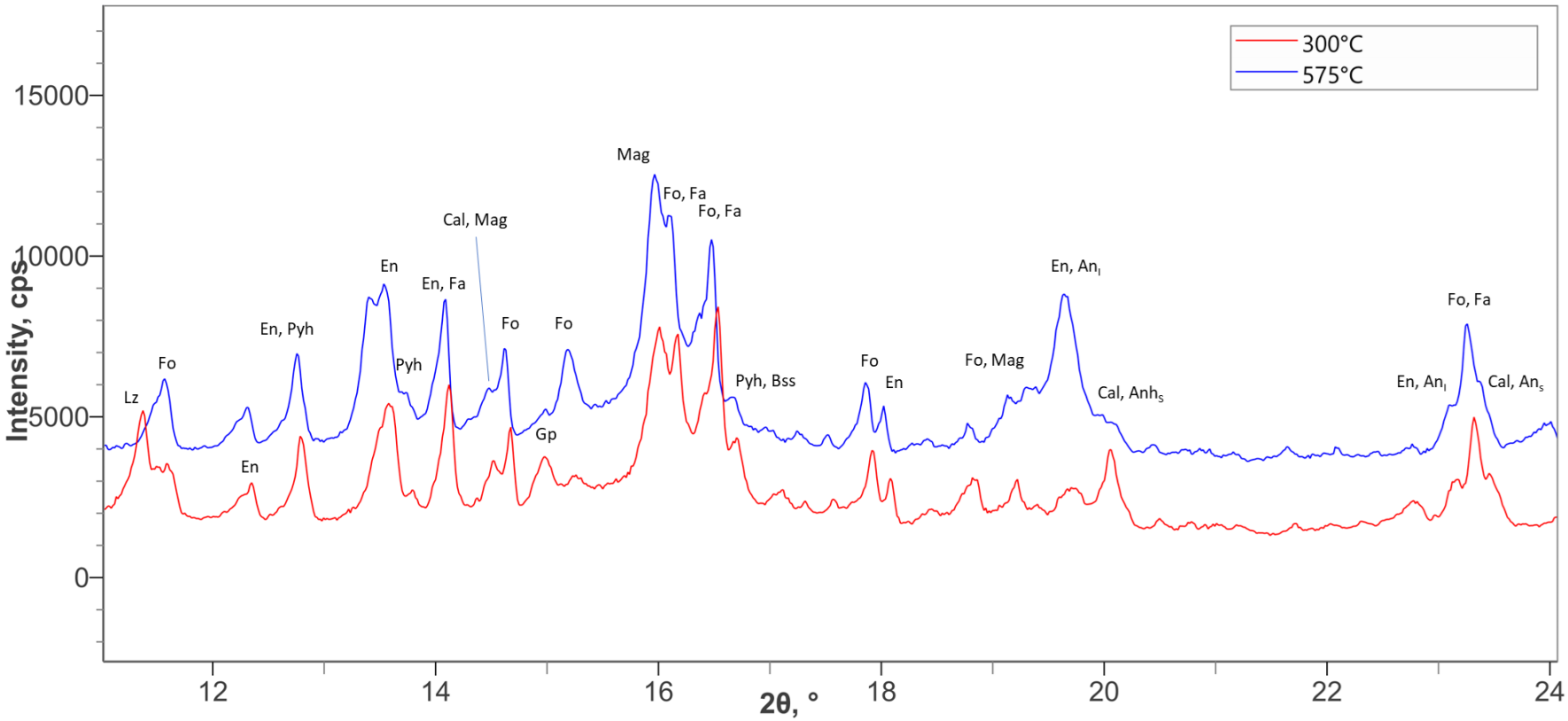

Fig. 5.22. pXRD patterns of LEW 85311 showing changes experienced by olivine. At 575°C, olivine peaks for forsterite (Fo) (e.g., 11.6°, 14.7°, 15.1°, 16.1°, 17.9°, 19.3°, and 23.3° 2Θ) and fayalite (Fa) (e.g., 14.6°, 16.1°, 17.9°, and 23.3° 2Θ) begin noticeably strengthening. Enstatite (En) shows no change. Lizardite (Lz), pyrrhotite (Pyh), calcite (Cal), magnetite (Mag), gypsum (Gp), bassanite (Bss), soluble anhydrite (Anh_s), and insoluble anhydrite (An_l) are also labelled. Patterns collected with a Mo X-ray source.

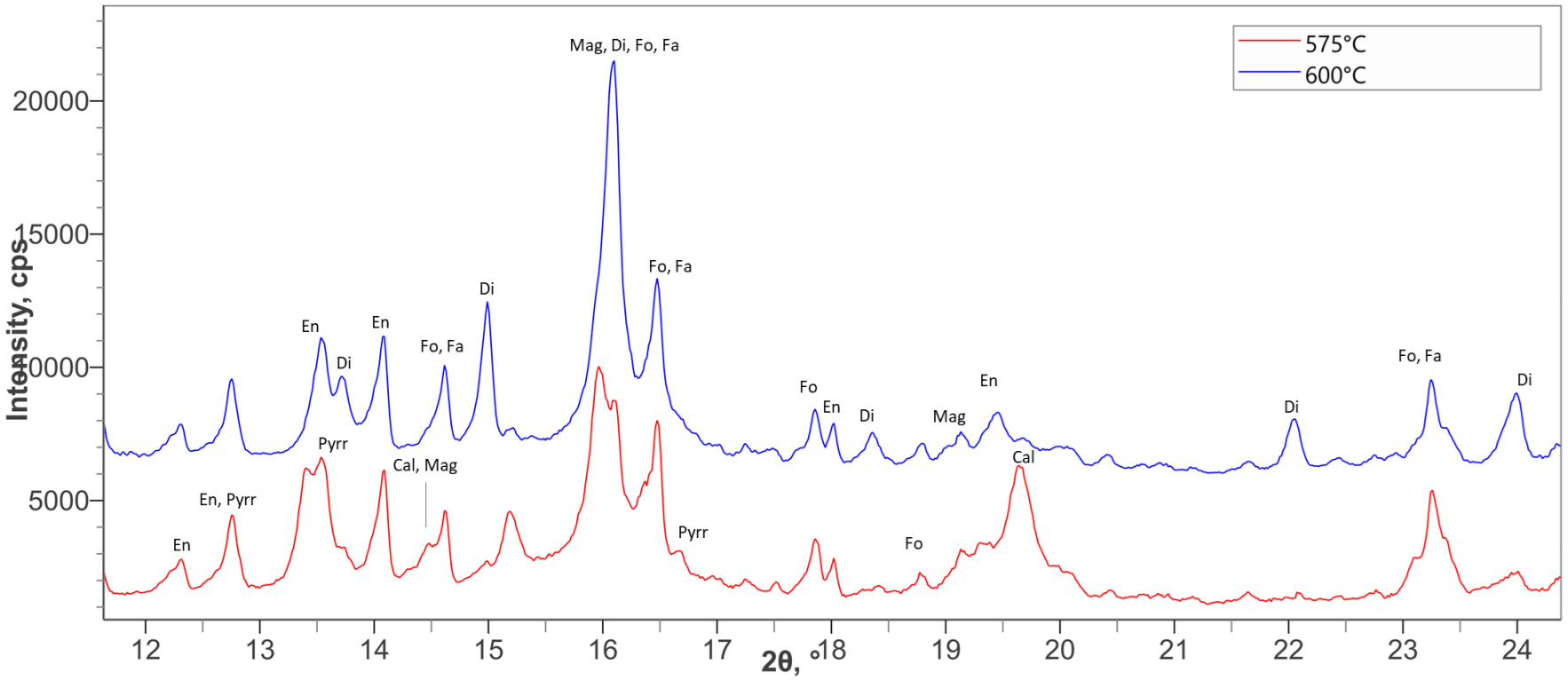

Fig. 5.23. pXRD patterns of LEW 85311 showing calcite (Cal) decomposition. Cal peaks (e.g., 14.5° and 19.5° 2Θ) rapidly disappear at 600°C. At the same time, peaks associated with diopside (Di) (e.g., 13.7°, 15.0°, 16.1°, 18.3°, 22.0°, and 24.0° 2Θ) appear. Other phases labelled are enstatite (En), pyrrhotite (Pyh), forsterite (Fo), fayalite (Fa), and magnetite (Mag). Patterns collected with a Mo X-ray source.

5.4 – How Post-Hydration Heating Effects Vary with Starting Composition

ALH 83100, pMurchison, and LEW 85311 are CM chondrites that have experienced different degrees of aqueous alteration and thus their mineralogy varies. How the initial composition of a CM chondrite affects its response to heating can be discerned from the bulk heating pXRD experiments. Both ALH 83100 and pMurchison were heated in an inert atmosphere, while LEW 85311 was heated in an oxidizing atmosphere. Some phases show similar patterns of decomposition and recrystallization regardless of their starting proportions and oxidation state, while other mineral reactions differ between meteorites (Table 5.3).

Of the three meteorites, ALH 83100 is the most highly aqueously altered and correspondingly serpentine-dominated, whereas LEW 85311 is the least altered with the lowest proportion of serpentine and the highest proportion of anhydrous silicates (Howard et al. 2011; Lee et al. 2019b). Although rough, qualitative estimates can be made based off of its peak intensity relative to other phases, the amount of tochilinite that each meteorite contains is difficult to quantify given the lack of a tochilinite XRD standard (Howard et al. 2011; Lee et al. 2019b). The relative abundances of anhydrous sulphides in each meteorite bears no relation to petrologic subtype; pMurchison has the greatest proportion of sulphides (~1.8 vol%), while ALH 83100 and LEW 85311 have only ~1.0 vol% and 0.5 vol%, respectively (Howard et al. 2011; Lee et al. 2019b). Regarding carbonates, in the literature both ALH 83100 and pMurchison were reported to have ~1.0 vol% calcite (Howard et al. 2011), while LEW 85311's carbonates were undetectable by XRD (Lee et al. 2019b).

For the most part, observations of mineral abundances and transitions in this work are consistent with the literature (Fig. 5.24). In the unheated pXRD patterns of the meteorites studied, LEW 85311 has the most intense peaks associated with tochilinite compared to other mineral phases while ALH 83100 has the least intense peaks compared to other mineral phases (Fig. 5.1, 5.8, & 5.16), indicating that LEW 85311 has a higher abundance of tochilinite. All three meteorites contain minor amounts of calcite (Fig. 5.1, 5.8, & 5.16). The amount of calcite in LEW 85311 differing from that of literature values is likely due to sample heterogeneity.

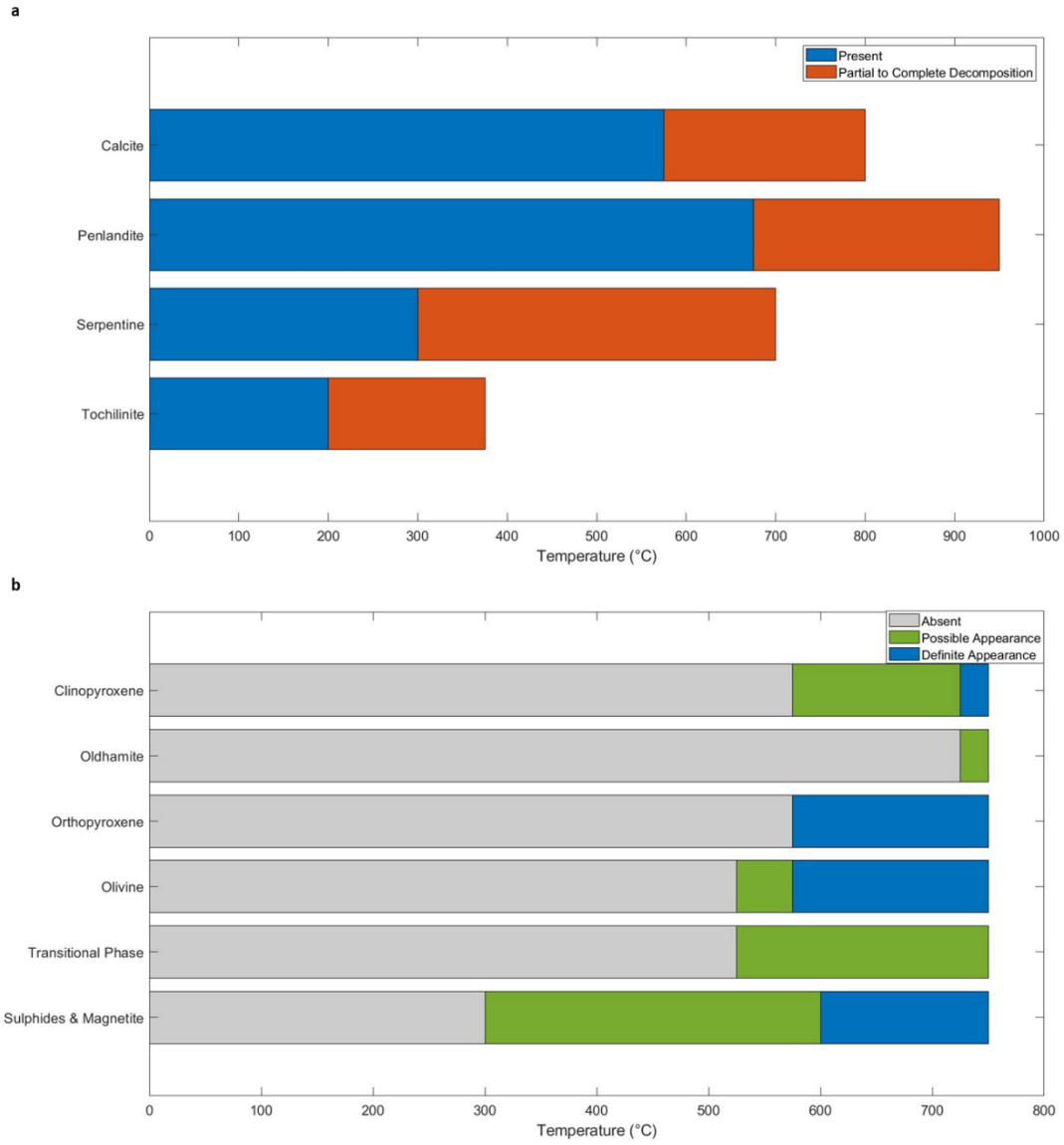

Fig. 5.24. Main phase transitions observed during experimental heating of ALH 83100, Murchison, and LEW 85311. a) Breakdown temperatures of minerals originally present in the sample. b) Temperatures at which secondary anhydrous minerals appear.

Table 5.3. Summary of phase transitions experienced by each heated meteorite.

	ALH 83100	pMurchison	LEW 85311
200°C	Tochilinite peaks weaken.		
300°C	Tochilinite peaks begin to disappear. Troilite peaks strengthen. Serpentine peaks weaken.	Tochilinite peaks disappear. Troilite peaks strengthen. Serpentine peaks weaken.	Tochilinite peaks disappear. Magnetite peaks strengthen. Pyrrhotite peaks strengthen. Gypsum peaks disappear. Bassanite peaks appear.
350°C		Magnetite peaks strengthen.	Bassanite peaks weaken.
375°C	Last tochilinite peak disappears.		Bassanite peaks disappear. Insoluble anhydrite peaks appear. Serpentine peaks weaken.
400°C			Soluble anhydrite peaks weaken.
425°C			Serpentine peaks disappear.
525°C	Transitional phase peaks appear. Olivine peaks widen.	Transitional phase peaks appear. Serpentine peaks disappear.	Soluble anhydrite peaks disappear.
575°C	Enstatite peaks strengthen.	Calcite peaks weaken. Clinopyroxene peaks appear.	Olivine peaks strengthen.
600°C	Olivine peaks strengthen.	Olivine peaks strengthen.	Pyrrhotite peaks weaken. Calcite peaks disappear. Clinopyroxene peaks appear.
650°C	Olivine peaks narrow in width.		
675°C	Pentlandite peaks weaken.	Pentlandite peaks weaken.	
700°C	Serpentine peaks disappear. Calcite peak widths narrow.		
725°C	Calcite peaks weaken. Clinopyroxene peaks appear. Oldhamite peaks appear.		
750°C	Transitional phase peaks weaken. Calcite peaks widen.	Transitional phase peaks weaken. Enstatite peaks strengthen.	
800°C	Calcite peaks disappear.		

5.4.1 Tochilinite Decomposition Under Oxidizing Conditions

Tochilinite decomposition under an inert atmosphere will be discussed in detail in Chapter 5.5, wherein its decomposition rate and temperature are further explored. In this section, the focus for tochilinite is on redox state, however other aspects of its decomposition will also be discussed.

When heated under an inert atmosphere, tochilinite decomposes and recrystallizes to troilite and/or magnetite (Fuchs et al. 1973; Lindgren et al. 2020). Although magnetite is stable under oxidizing conditions, troilite is not, forming only in reducing conditions (Li et al. 2023). When LEW 85311 was experimentally heated under oxidizing conditions, it was expected to form magnetite rather than troilite. Magnetite was indeed observed, but pyrrhotite also formed (Fig. 5.17). Pyrrhotite, like troilite, favours reducing conditions (Hu et al. 2006). A sulphide that is more stable under oxidizing conditions, such as pyrite, may have been expected, but pyrite is not stable at high temperatures. When heated under oxidizing conditions, pyrite will decompose to pyrrhotite, which will eventually oxidize to hematite and/or magnetite (Prasad et al. 1985). In the LEW 85311 experiment, pyrrhotite decomposed at 600°C. The pyrrhotite produced from tochilinite decomposition was likely unstable under oxidizing conditions and decomposed into magnetite as heating progressed. If a heated CM chondrite has abundant magnetite and potentially pyrrhotite but no troilite, it may be an indicator that it was heated under oxidizing conditions.

5.4.2 Pentlandite Decomposition

In both ALH 83100 and pMurchison, XRD peaks associated with pentlandite start weakening at 675°C. In contrast, LEW 85311's pentlandite peaks weaken alongside pyrrhotite at 600°C. Because LEW 85311 was heated in an oxidizing atmosphere, this early decomposition of pentlandite is likely related to redox conditions, not its initial mineralogy or temperature-timescale.

In the literature, pentlandite is reported to form in a stable manner only at temperatures below 610°C (Durazzo & Taylor 1982) and is thought to have a decomposition temperature as low as that (Nakato et al. 2008), 65°C cooler than what was observed in ALH 83100 and pMurchison. This observation differing from literature conjecture may be because pentlandite’s decomposition temperature

is 675°C and not 610°C. Alternatively, this difference could be related to timescale; ALH 83100 and pMurchison were heated on timescales of hours and may not have spent enough time at each temperature step for pentlandite to noticeably decompose before 675°C. It may be possible that if they were held at 610°C for long enough pentlandite would start to decompose.

5.4.3 Serpentine Decomposition

In both ALH 83100 and pMurchison, peaks associated with both lizardite and cronstedtite start to weaken at 300°C (Fig. 5.4 & 5.11), while in LEW 85311 these peaks begin to weaken at 375°C (5.20). It is possible that serpentine is more stable when heated under oxidizing conditions, however further experimentation with serpentine decomposition and redox conditions is required to confirm this.

The temperature at which serpentine peaks disappears differs between meteorites: LEW 85311 is 425°C (Fig. 5.20); pMurchison is 525°C (Fig. 5.11); ALH 83100 is 700°C (Fig. 5.4). Although starting composition does not appear to affect decomposition temperature, the starting amount present within the sample does, with ALH 83100 having the most serpentine and LEW 85311 having the least. It is possible that the release of volatiles by serpentine affects the redox conditions, potentially making it more oxidizing, leading to varying rates of decomposition.

In both ALH 83100 and pMurchison, a peak associated with a transitional phase appears at 525°C, with this peak being most intense in the patterns for ALH 83100's, likely due to it having more serpentine (Fig. 5.4 & 5.11). This transitional phase was absent from LEW 85311, however its serpentine likely decomposed too quickly for it to be observable. It is also possible that serpentine in LEW 85311 fully decomposed before temperatures were high enough to make the transitional phase. In ALH 83100, this transitional phase's peak started weakening at 750°C. pMurchison was not heated beyond 750°C, although the transitional phase's peak disappeared in the room temperature pattern collected after heating. The level of aqueous alteration experienced by a CM chondrite has little effect on the temperatures at which this transitional phase appears and disappears. This transitional phase is further discussed in Chapter 5.6.

Olivine and enstatite form from serpentine decomposition, typically at temperatures above 500°C (Nakamura 2005; Ball & Taylor 1963). In LEW 85311, the peaks associated with olivine started strengthening at 575°C (Fig. 5.22), while enstatite peaks showed no change. In pMurchison, olivine and enstatite peaks started strengthening at 600°C and 750°C, respectively (Fig. 5.11). In ALH 83100, enstatite peaks started strengthening at 575°C and olivine at 600°C (Fig. 5.4). In most previous studies, olivine is reported to appear at lower temperatures than enstatite, if the latter occurs at all (Nakamura 2005; Nakato et al. 2008; Lindgren et al. 2020; Ball & Taylor 1963).

In all three meteorites, olivine peaks increase in intensity at ~575-600°C, indicating that this is a threshold temperature for secondary silicate formation. In pMurchison, peak widths of forsterite were mostly consistent throughout heating (Fig. 5.15); the relatively high abundance of primary forsterite within pMurchison may have had a significant effect on peak widths. It is also possible that more fayalite recrystallized than forsterite. In ALH 83100, forsterite peaks started widening at the same temperature as the transitional phase (525°C). The forsterite peaks started to narrow at the same temperature as peak intensities started to increase (600°C) (Fig. 5.6). It is likely that the recrystallization of secondary silicates begins at ~525°C, accounting for the peak widening (and thus smaller grain sizes and poorer crystallinity) but accelerates at ~600°C at which annealing may occur, leading to the increase in peak intensities.

Crystallization of secondary enstatite within the three meteorites is not as consistent as with olivine: LEW 85311 had no secondary enstatite; in pMurchison it forms at 750°C (Fig. 5.11); and in ALH 83100 it forms at 575°C. With the appearance of secondary olivine being consistent among the samples, it is unexpected that enstatite would differ as both minerals result from the same decomposition process. However, enstatite itself is a minor product of serpentine decomposition, with olivine being the primary one (Ball & Taylor 1963). Among the three meteorites, ALH 83100 has the lowest amount of primary pyroxene, only about ~ 1 vol%, and the highest proportion of serpentine (Howard et al. 2011) from which secondary enstatite may form. It is possible that secondary enstatite forms at the same temperature as secondary olivine but in small quantities such that for it to be detectable, a high proportion of serpentine or a longer duration of heating is needed.

5.4.4 Calcite Decomposition

The decomposition temperature commonly reported for calcite is ~700-800°C (Karunadasa et al. 2019) although it has also been reported to break down at ~600°C (Lee et al. 2019c; Rodriguez-Navarro et al. 2009). Under inert heating conditions, oldhamite is the commonly reported product of calcite decomposition although clinopyroxene and/or portlandite may also occur (Haberle & Garvie 2017; Lee et al. 2019c; Lindgren et al. 2020; Haberle & Garvie 2017).

The decomposition temperature of calcite differs between the three heated meteorites. pMurchison saw the lowest decomposition temperature, with calcite peaks weakening at 575°C (Fig. 5.13). In LEW 85311, calcite decomposition is quite rapid, with peaks showing no weakening until 600°C, where they completely disappear (Fig. 5.23). Although ALH 83100's calcite peaks didn't begin to weaken until 725°C (Fig. 5.6), peak widths started changing at 700°C (Fig. 5.7). However, this variable decomposition temperature for calcite is not unusual and can be determined by factors including crystal size, impurities, and defects, and other factors (Galan et al. 2012). Although all three meteorites have similar proportions of calcite (~1 vol%; Howard et al. 2011; Lee et al. 2019b), LEW 85311 and ALH 83100 are both finds, possibly having a portion of their calcite originating from terrestrial weathering and not parent body aqueous alteration, while pMurchison is a fall. Additionally, CM carbonates form in multiple stages and with different morphologies as aqueous alteration progresses (Lee et al. 2014). pMurchison and ALH 83100 have different populations of calcite by morphology (Lee et al. 2014). pMurchison has an abundance of type 1a and 2a calcites; type 1a calcites are equant crystals with phyllosilicate rims while type 2a calcites are polycrystalline assemblages intergrown with sulphides. In contrast, ALH 83100's calcites are mostly equant grains rimmed by sulphides, known as type 1b calcites (Lee et al. 2014). Additionally, ALH 83100 contains other carbonates, such as dolomite, that partially to completely replace calcite, a feature that is typically only observed in CM chondrites with high degrees of alteration (Lee et al. 2014). The difference in calcite decomposition temperature between the three meteorites can be explained by differing parent body alteration histories forming calcite of different morphologies and/or composition (e.g., Mg impurities), although terrestrial weathering may also play a role. Calcite can start to decompose

anywhere within the range of 575-700°C, with the mildly altered CM chondrites more likely to show calcite decomposition at lower temperatures.

The only common product of calcite decomposition in all three meteorites is clinopyroxene, with oldhamite only being detectable by XRD in ALH 83100. The lack of oldhamite in LEW 85311 was expected as it was heated under oxidizing conditions, however its absence in pMurchison was unexpected especially given the meteorite's greater abundance of sulphides compared to ALH 83100 to supply S (Howard et al. 2011). The temperature of calcite decomposition is probably a factor in oldhamite formation as calcite in ALH 83100 and pMurchison decomposed at different temperatures, 700°C and 575°C, respectively. Oldhamite may require a minimum temperature (e.g., 700°C) to form, or the S for oldhamite may be derived from pentlandite, which wasn't observed decomposing until 675°C. More studies on calcite decomposition in CM chondrites are required to test these hypotheses. However, it is clear that calcite decomposition may not necessarily lead to oldhamite formation.

5.4.5 Sulphates in LEW 85311

Sulphates in most CM chondrites are likely to be terrestrial alteration products (Lee et al. 2021a; also see Chapter 8), with very few meteorites showing any indication for it to be forming due to parent body processes (Lee 1993). Due to the rarity of CM chondrites with sulphates from parent body alteration, a sulphate-bearing CM or CM chondrite experiencing post-hydration heating would be an unusual occurrence, especially if it were to experience this heating under oxidizing conditions. The experimental heating experienced by LEW 85311's sulphates would not be representative of any naturally heated meteorite. However, it is still worthwhile to study heating experienced by sulphates to cover a broad range of mineralogies, albeit under conditions that are more akin to terrestrial metamorphism.

LEW 85311 contains a mixture of gypsum and soluble anhydrite. Gypsum within LEW 85311 decomposes to bassanite at 300°C, which then decomposes to insoluble anhydrite at 375°C. This reaction is consistent with the reported decomposition temperatures of gypsum and bassanite, which are 45°C and 116°C, respectively (Seufert et al 2009; Ballirano & Melis 2009). It is likely that bassanite only persisted in some of the XRD patterns due to incomplete

decomposition; if LEW 85311 was heated for long enough, the bassanite would have likely decomposed at 300°C. The soluble anhydrite begins disappearing after bassanite at 400°C, reforming into its polymorph, insoluble anhydrite. These reactions are consistent with what is known about the stability of soluble anhydrite, which is reported to transform into insoluble anhydrite at 200-490°C (Christensen et al. 2008).

The presence of insoluble anhydrite in a CM chondrite would be indicative of the meteorite having experienced sulphate-forming aqueous alteration processes prior to heating. Fujiya et al. (2022) observed anhydrite in the CM chondrite Jbilet Winselwan and attributed its presence to parent body processes, however they did not specify which polymorph of anhydrite it is (soluble or insoluble). An XRD pattern of the sulphates within Jbilet Winselwan would be able to ascertain the polymorph and possibly confirm Fujiya et al.'s (2022) findings. However, King et al. (2019b), who also observed anhydrite in Jbilet Winselwan, found it alongside gypsum, making it more likely to be a result of terrestrial weathering than of post-hydration heating.

5.5 – Temperature-Timescale Effects on Tochilinite Decomposition

Tochilinite is a hydrous sulphide and little is known about its thermal stability. It is composed of intergrown layers of mackinawite, brucite, and/or amakinite (Palmer & Lauretta 2011). Tochilinite requires reducing conditions to form, crystallizing from aqueous solutions at a pH of 7.8-14 (Vacher et al. 2019), with laboratory experiments synthesizing tochilinite at temperatures up to 180°C (Gubaidulina et al. 2007). It was first reported on Earth in the Nizhnii Mamon copper deposit (Organova et al. 1971). In meteorites, it was first discovered by Fuchs et al. (1973) in Murchison, however, was not recognized as tochilinite, and was instead referred to as a "Poorly Characterized Phase (PCP)." Mackinnon & Zolensky (1984) later showed that PCP has a crystal structure and chemistry that matches tochilinite. It is now recognized as one of the most common phases within CM chondrites, though not all CM chondrites contain tochilinite (e.g., Rubin et al. 2007).

During post-hydration heating tochilinite is the first phase to dehydrate, with its decomposition being the only way to differentiate Heat Stage I and

unheated meteorites (Nakamura 2005). Its decomposed remnants commonly recrystallize into sulphides (e.g., troilite), but may also decompose to magnetite (Nakamura 2005; Lindgren et al. 2020). The lowest temperature at which tochilinite has been observed to decompose experimentally is 245°C after 7.7 days of heating (Fuchs et al. 1973); however other estimates of its decomposition temperature are as low as 120°C (Zolensky et al. 1997). To better understand the thermal stability of tochilinite and its decomposition temperature, tochilinite bearing meteorites were experimentally heated at varying temperatures and timescales.

5.5.1 Bulk Heating with ALH 83100

ALH 83100 has been extensively aqueously altered on its parent asteroid and has minor amounts of tochilinite (Lindgren et al. 2020; Zolensky et al. 1997). When a powdered sample of ALH 83100 was experimentally heated under inert conditions, tochilinite peaks weakened at 200°C (Fig. 5.2), with the weakening of one peak at 9.42° 2θ (5.04 Å) becoming apparent after only 10 minutes of heating (Fig. 5.25). However, most tochilinite peaks remained stable at 200°C. Significant peak weakening does not occur until 275°C and tochilinite does not completely disappear until 375°C (Fig. 5.2). It is possible that tochilinite is unstable at 200°C, however its decomposition is not observable on a timescale of hours until 275°C. The temperature range of 200-300°C is where tochilinite decomposes, which is consistent with the literature (e.g., Fuchs et al. 1973).

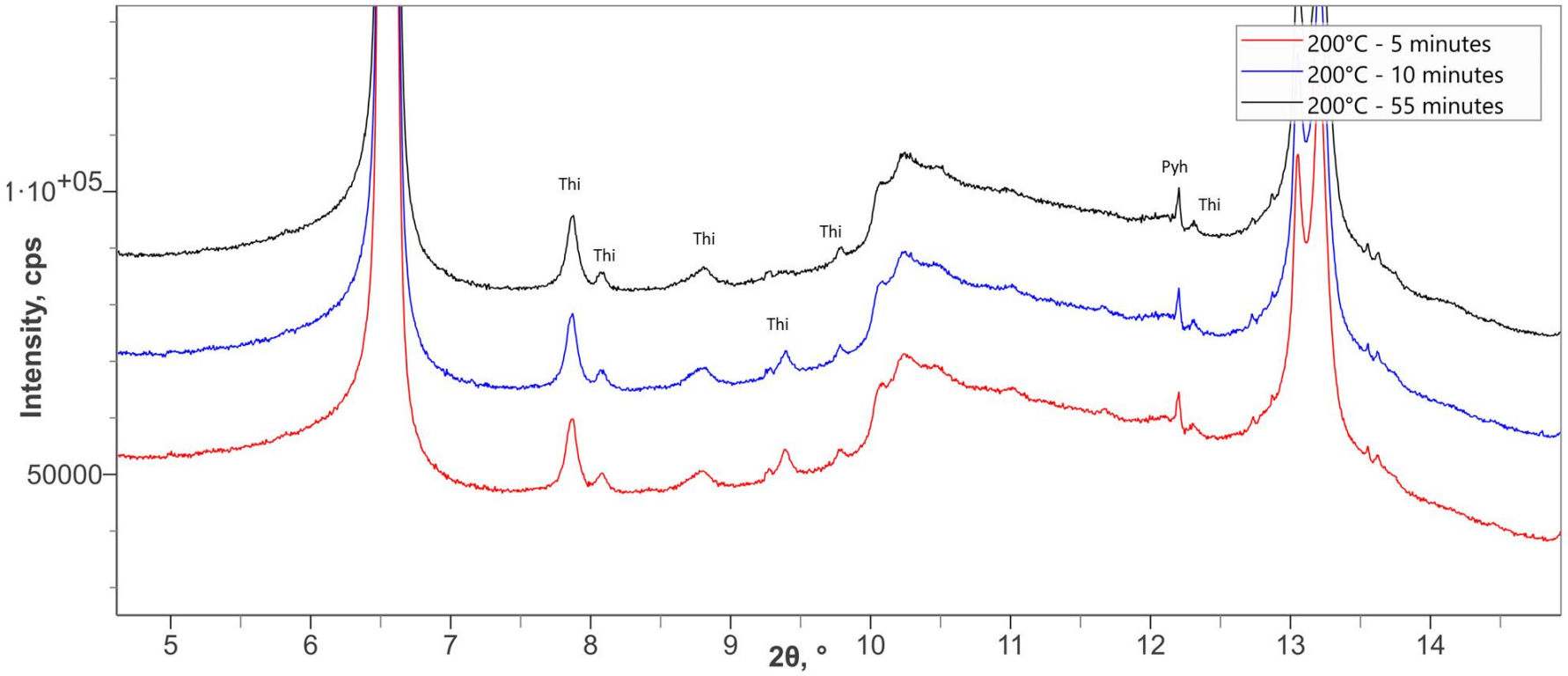

Fig. 5.25. pXRD patterns of ALH 83100 showing tochilinite (Thi) peak changes over time at 200°C. Most Thi peaks show little change, however some peaks begin weakening, with one peak at 9.42° 2θ (5.04 Å) disappearing after 55 minutes. Pyrrhotite (Pyh) is also labelled. Patterns collected with synchrotron radiation.

5.5.2 Heating of Murchison – Rock Chips

To better understand tochilinite decomposition and how it varies with temperature-timescale, six samples of M_Heat were heated under vacuum at the following temperatures and timescales: 200°C/1 day (M_200_1), 200°C/8 days (M_200_8), 300°C/1 day (M_300_1), 400°C/1 day (M_400_1), 500°C/1 day (M_500_1), and 500°C/8 days (M_500_8). These samples were made into polished thin sections to be compared to an unheated control sample of M_Heat (M_Blank). For more details regarding the experimental setup, please see Chapter 2.5.4.

The 200°C and 300°C samples cover the range of temperatures at which tochilinite may possibly decompose, whereas the 400°C and 500°C samples will potentially display the crystallization of secondary sulphides. These samples were studied with a combination of SEM, reflected light microscopy, Raman spectroscopy, and *in situ* micro XRD (μXRD). This chapter describes the Raman and μXRD analyses, while the results of the SEM and reflected light microscopy analyses are discussed in Chapter 6.

In M_Heat, tochilinite occurs as large globules from the alteration of kamacite and in the matrix as an intergrowth with cronstedtite, traditionally referred to as type-I tochilinite-cronstedtite intergrowths (TCIs) and type-II TCIs, respectively (Vacher et al. 2019). To avoid confusion between the two types of TCIs and to use more representative terminology, type-I TCIs shall hereby be referred to as tochilinite globules and type-II TCIs shall simply be referred to as TCIs.

5.5.2.1 Raman Characterization of Tochilinite Globules and TCIs

Tochilinite and TCIs have rarely been studied by Raman spectroscopy and as a result there are only two sets of Raman spectra in the literature for comparison: (i) from terrestrial tochilinite (RRUFFa n.d.); (ii) from shocked xenolithic TCIs in the ordinary chondrite Pałtusk (Krzesińska & Fritz 2014). The peaks from these spectra are compared to spectra collected from the M_Heat samples as well as to that of troilite from Martian meteorites from Weber et al. (2017) (Tables 5.4 & 5.5).

For tochilinite globules, the Raman spectrum collected for M_blank has considerably more peaks than that found in the literature, however some of these peaks are similar to troilite and may be due to P-bearing sulphides present in M_Heat's tochilinite globules (Table 5.4 & Fig 5.26a). The key tochilinite peaks are present at 237 cm^{-1} and 300 cm^{-1}. These peaks change as M_Heat is heated, with none of the heated samples' tochilinite Raman spectra bearing similarity to M_Blank's, with the exception of a broad peak at ~670 cm^{-1} that is likely related to the P-bearing sulphides (Table 5.4 & Fig. 5.26). These spectra do match troilite for the most part, with the exception of a peak at ~460 cm^{-1} that is attributed to neither tochilinite nor troilite. It has not been matched to a phase.

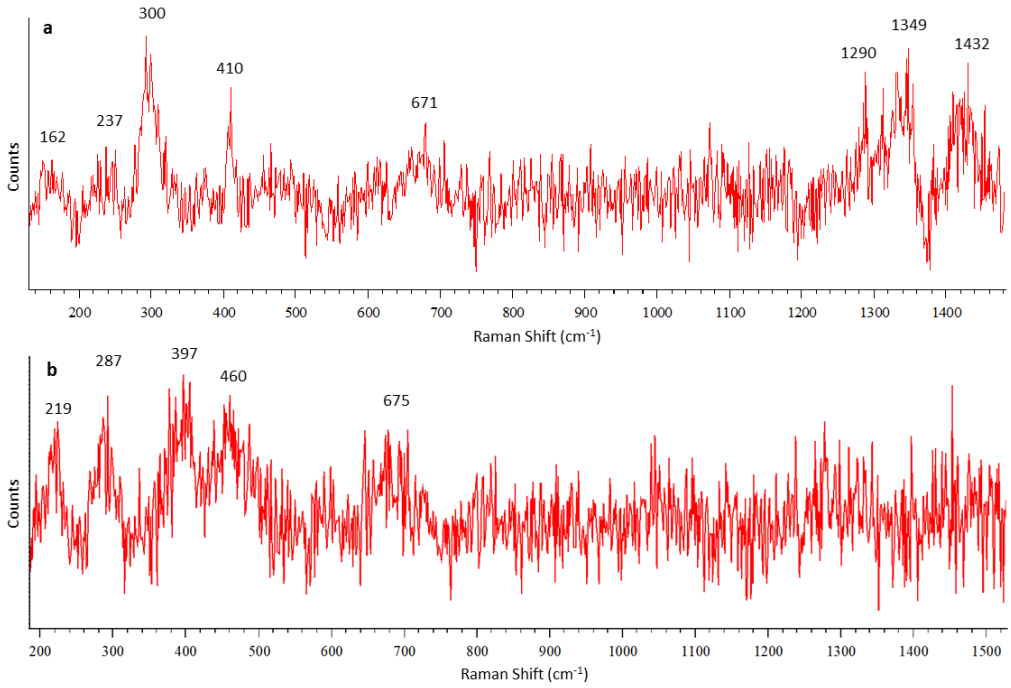

Fig. 5.26. Representative Raman spectra from tochilinite globules in M_Heat. a) From M_blank, matching a mixture of tochilinite (237 and 300 cm^{-1}) and sulphides (410 and 671 cm^{-1}). b) From M_200_8, corresponding to Thi-C in Table 5.4. Tentatively matched to sulphides.

For the TCIs, M_blank's Raman spectrum bears little similarity to that of the Pałtusk TCIs. However, Krzesińska & Fritz (2014) indicate that their TCIs may have been mildly heated and shocked as their water contents are lower than those in unheated CMs. This suggestion is supported by M_200_1 which, unlike M_Blank, has similar peaks to the TCIs in Pałtusk (Table 5.4). M_Blank and M_200_1 were the only samples for which Raman spectra containing peaks could be collected from TCIs; other samples only produced featureless spectra (Fig. 5.27). M_Blank's TCI Raman spectra are consistent with a mixture of cronstedtite and tochilinite (Table 5.4; Fig 5.27a). For M_200_1, only one Raman

spectrum could be successfully collected for TCIs (Fig. 5.27b). None of its peaks matched tochilinite or troilite, however it is consistent with the Pałtusk TCIs, whose peaks are attributed to a mixture of cronstedtite, brucite, and mackinawite (Krzesińska & Fritz 2014). It is important to note that M_200_1's TCI Raman spectrum displays far fewer peaks than that of the Pałtusk TCIs and is far noisier. Its three noisy peaks can be tentatively matched to mackinawite and cronstedtite (Krzesińska & Fritz 2014; RRUFFb n.d.; Bourdoiseau et al. 2008).

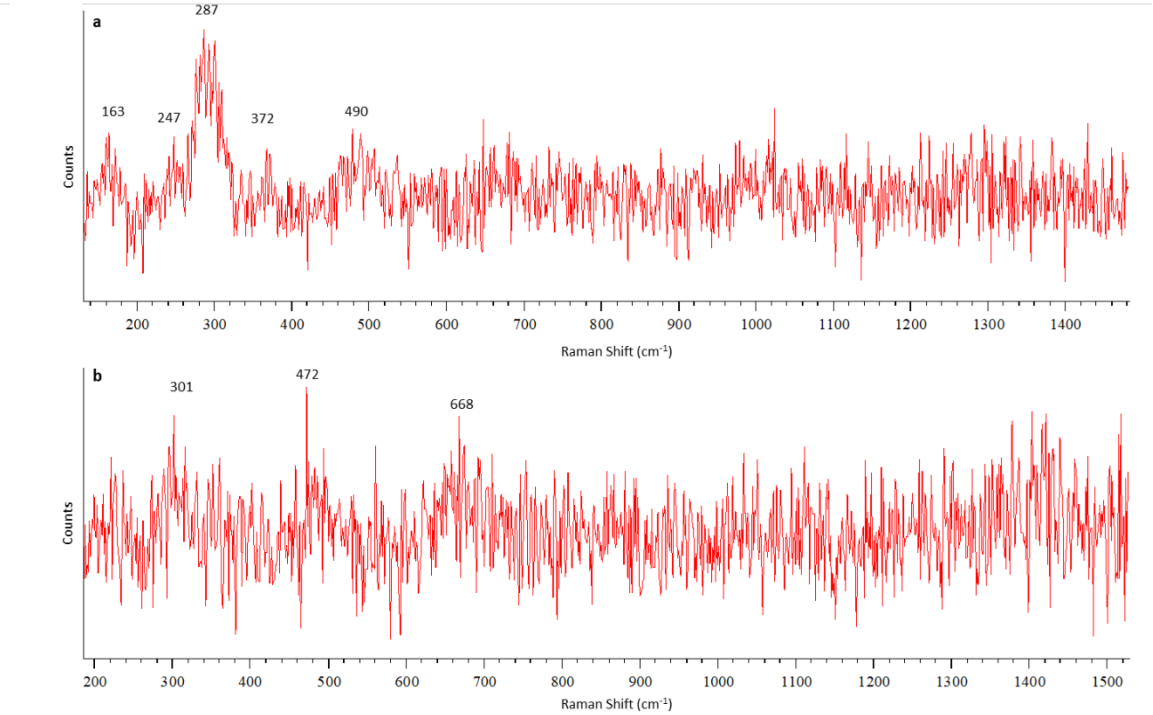

Fig. 5.27. Representative Raman spectra from TCIs in M_Heat. a) From M_blank, corresponding to TCI-A in Table 5.5, matching a mixture of cronstedtite (247 and 490cm^{-1}) and tochilinite (287 cm^{-1}). b) From M_200_1. Tentatively matched to a mixture of mackinawite (301 and 472 cm^{-1}) and cronstedtite (668 cm^{-1}).

Table 5.4. Raman peaks from spectra taken from tochilinite globules in the M_Heat samples compared to those from terrestrial tochilinite, martian troilite, and terrestrial mackinawite.

Terrestrial Thi (RRUFFa n.d.)	Troilite (Weber et al. 2017)		Mackinawite (RRUFFc n.d.)	M_ Blank Thi	M_200_1 Thi - A	M_200_8 Thi - A	M_200_8 Thi - B	M_200_8 Thi - C	M_300_1 Thi - A	M_300_1 Thi - B
				162 cm^{-1}						
	240 cm^{-1}	220 cm^{-1}	218 cm^{-1}		217 cm^{-1}		219 cm^{-1}	219 cm^{-1}	218 cm^{-1}	
237 cm^{-1}			236 cm^{-1}	237 cm^{-1}						
	290 cm^{-1}	288 cm^{-1}	285 cm^{-1}		289 cm^{-1}		284 cm^{-1}	287 cm^{-1}	287 cm^{-1}	
303 cm^{-1}				300 cm^{-1}						
360 cm^{-1}										
			398 cm^{-1}				388 cm^{-1}		398 cm^{-1}	
	407 cm^{-1}	405 cm^{-1}		410 cm^{-1}						
					442 cm^{-1}					
								460 cm^{-1}		
			490 cm^{-1}			486 cm^{-1}				
	608 cm^{-1}	610 cm^{-1}	607 cm^{-1}							
			656 cm^{-1}							
	668 cm^{-1}	670 cm^{-1}		671 cm^{-1}		669 cm^{-1}		675 cm^{-1}		678 cm^{-1}
					819 cm^{-1}					
				1290 cm^{-1}						
	1305 cm^{-1}	1310 cm^{-1}								
				1349 cm^{-1}						
				1432 cm^{-1}						

Table 5.5. Raman peaks from spectra taken from TCIs in the M_Heat samples compared to those of xenolithic TCIs in the Pałtusk ordinary chondrite, and terrestrial cronstedtite and mackinawite.

Pałtusk TCIs (Krzesińska & Fritz 2014)		Cronstedtite (RRUFFc n.d.)	M_Blank TCI - A	M_Blank TCI - B	M_Blank TCI - C	M_200_1 TCI - B
			163 cm^{-1}			
199 cm^{-1}	213 cm^{-1}	192 cm^{-1}				
		246 cm^{-1}	247 cm^{-1}	242 cm^{-1}	243 cm^{-1}	
	278 cm^{-1}		287 cm^{-1}			
306 cm^{-1}	312 cm^{-1}			301 cm^{-1}	309 cm^{-1}	301 cm^{-1}
	370 cm^{-1}		372 cm^{-1}	367 cm^{-1}		
458 cm^{-1}	465 cm^{-1}					472 cm^{-1}
		503 cm^{-1}	490 cm^{-1}	500 cm^{-1}		
		574 cm^{-1}				
685 cm^{-1}	692 cm^{-1}	672 cm^{-1}				668 cm^{-1}
		832 cm^{-1}				
		913 cm^{-1}				
1330 cm^{-1}	1320 cm^{-1}					
1580 cm^{-1}	1584 cm^{-1}					

5.5.2.3 µXRD Characterisation of Tochilinite Globules and TCIs

µXRD patterns were collected for tochilinite globules and TCIs in M_Blank, M_200_1, M_200_8, and M_300_1. This µXRD data were acquired using a Rigaku Rapid II Micro-Diffraction diffractometer. Some analyses were conducted with the sample rotating to maximize the number of peaks measured, while other patterns were collected in a static set-up to ensure the correct region-of-interest was targeted by the primary X-ray beam. See Chapter 2.5.4 for more information about the experimental setup.

For M_Blank, tochilinite globules produced patterns consisting of a mixture of tochilinite, cronstedtite, and troilite (Fig. 5.28). Patterns collected for tochilinite globules in M_200_1 did not yield any tochilinite peaks even with rotation (Fig. 5.29), whereas M_200_8 did (Fig. 5.30). M_200_8 tochilinite globules contain pentlandite and pyrrhotite but it is unknown if the sulphides predated heating. Globules in M_300_1 are completely devoid of tochilinite and have abundant troilite (Fig. 5.31).

The XRD patterns for TCIs were congruent with those for the tochilinite globules. M_Blank TCIs have abundant cronstedtite and significant amounts of tochilinite (Fig. 5.32). Some, but not all, TCIs in M_200_1 and M_200_8 have tochilinite. TCIs in both M_200_1 and M_200_8 often have minor amounts of pyrrhotite (Fig. 5.33). TCIs in M_300_1 were all devoid of tochilinite and all had peaks associated with troilite (Fig. 5.34).

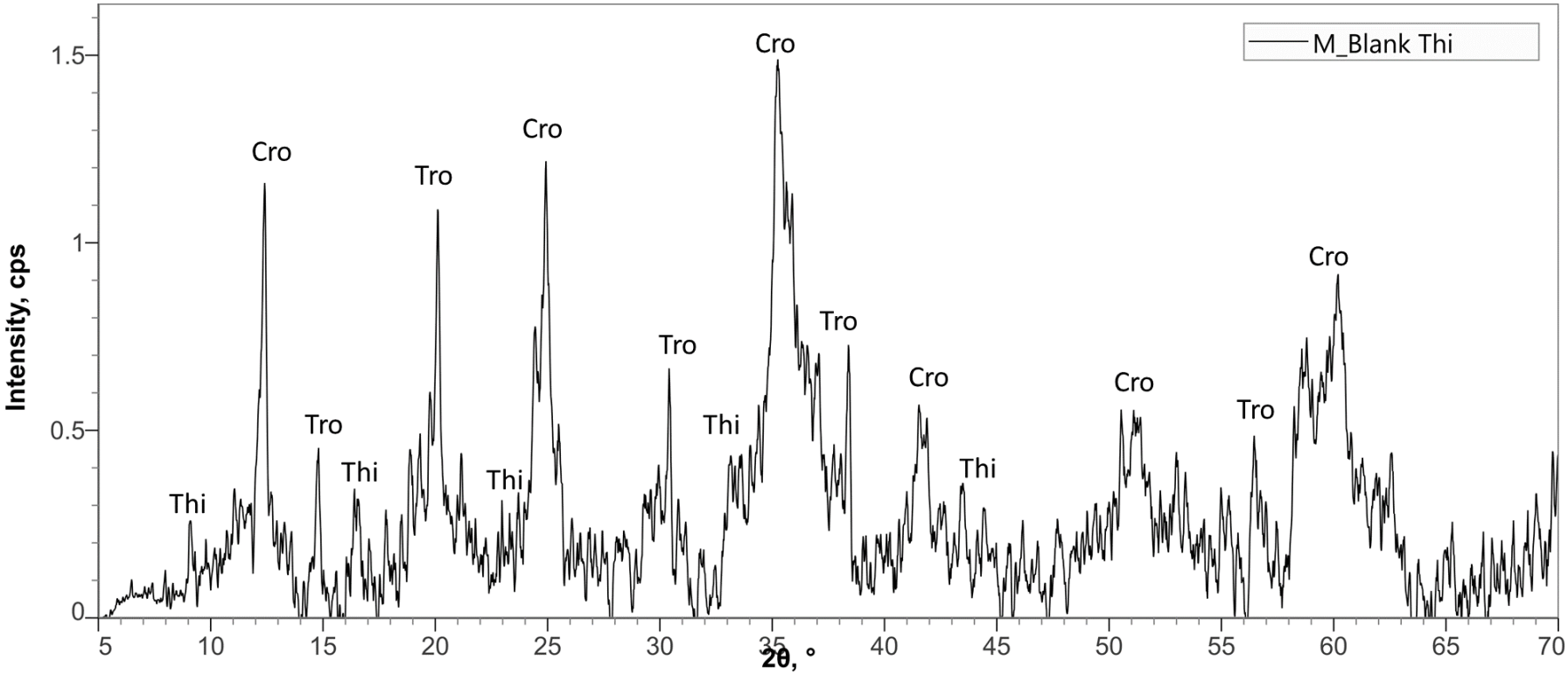

Fig. 5.28. μXRD pattern from a tochilinite (Thi) globule in M_blank. Peaks match Thi, cronstedtite (Cro), and troilite (Tro). Pattern collected with a Cu X-ray source.

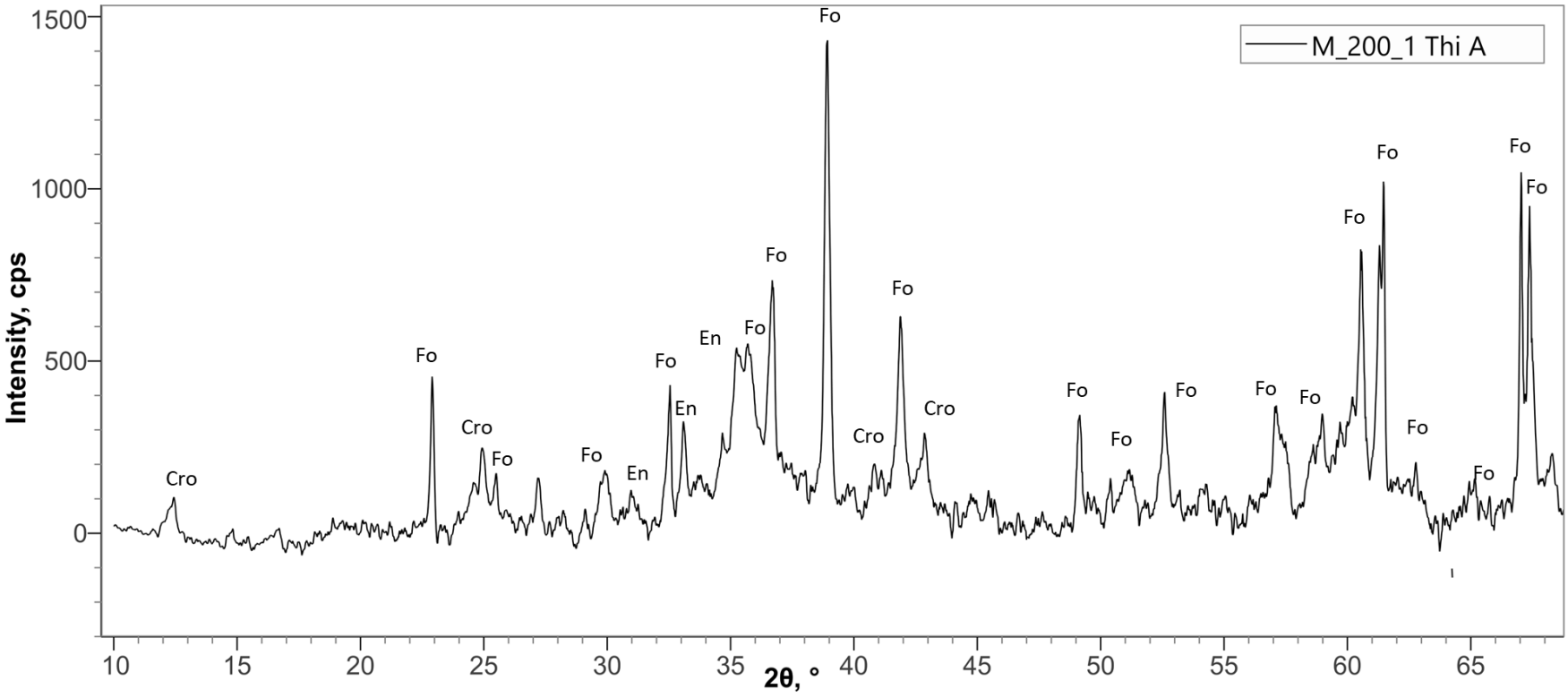

Fig. 5.29. μXRD pattern from a tochilinite globule in M_200_1. Peaks match cronstedtite (Cro), forsterite (Fo), and enstatite (En). No tochilinite is observed. Pattern collected with a Cu X-ray source.

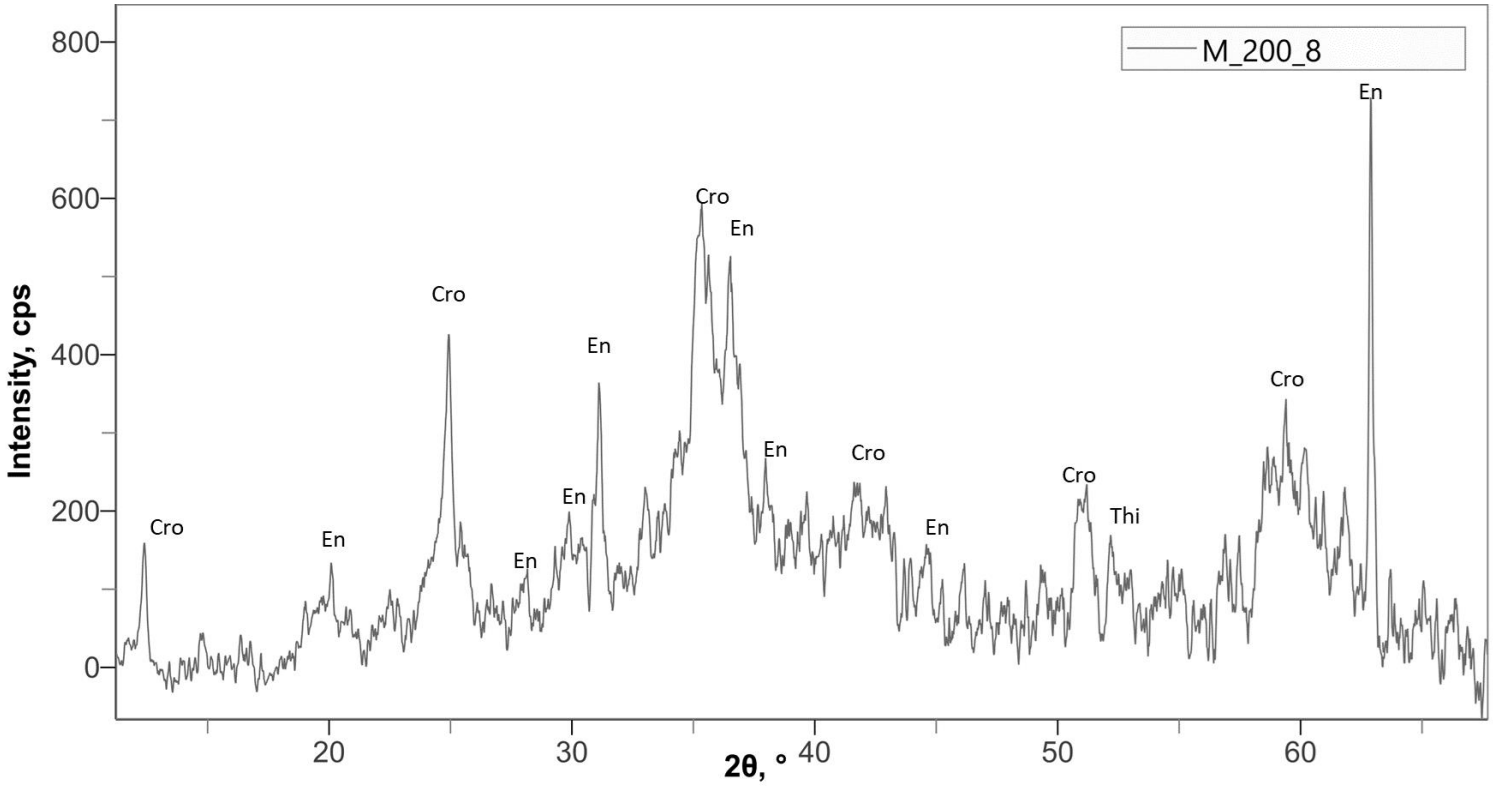

Fig. 5.30. μXRD pattern from a tochilinite (Thi) globule in M_200_8. Peaks match Thi, cronstedtite (Cro), and enstatite (En). Pattern collected with a Cu X-ray source.

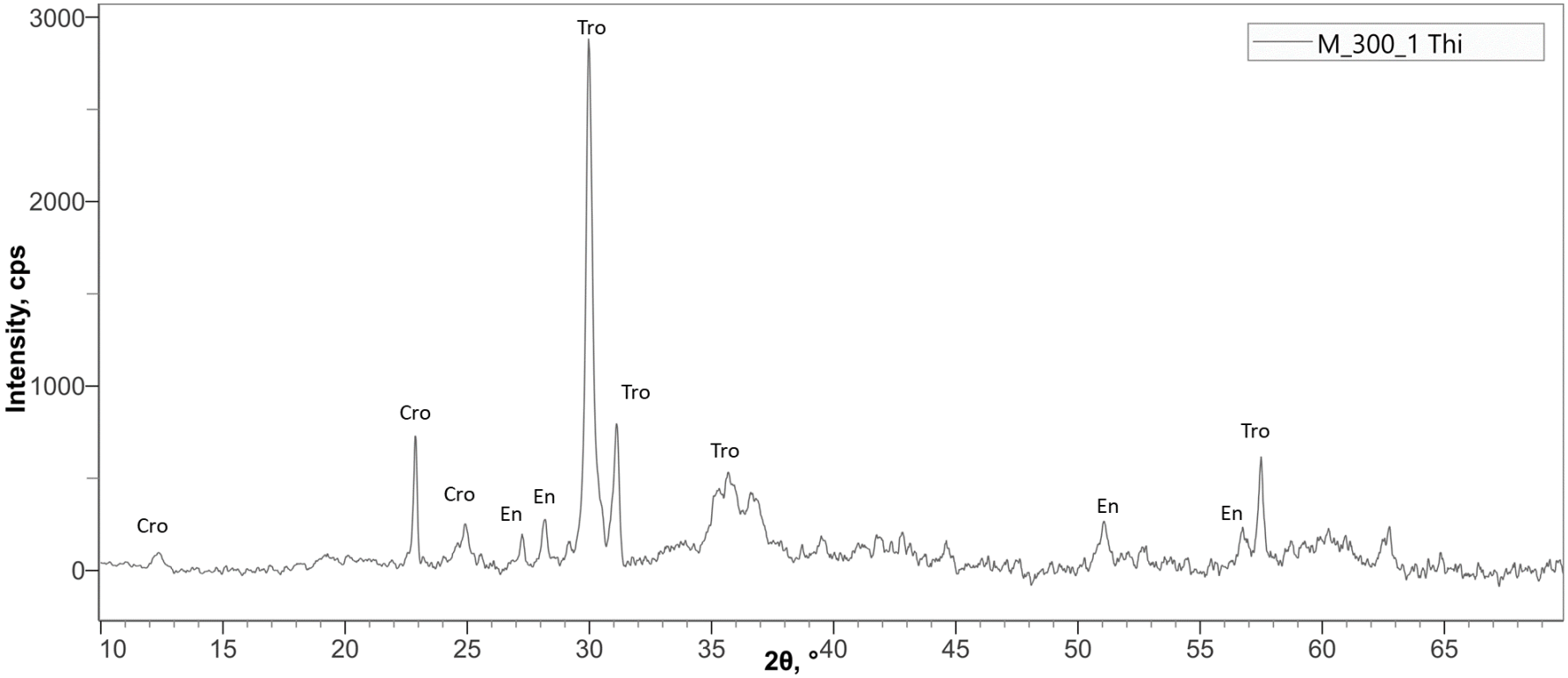

Fig. 5.31. μXRD pattern from a tochilinite globule in M_300_1. Peaks match cronstedtite (Cro), troilite (Tro), and enstatite (En). No tochilinite is observed. Pattern collected with a Cu X-ray source.

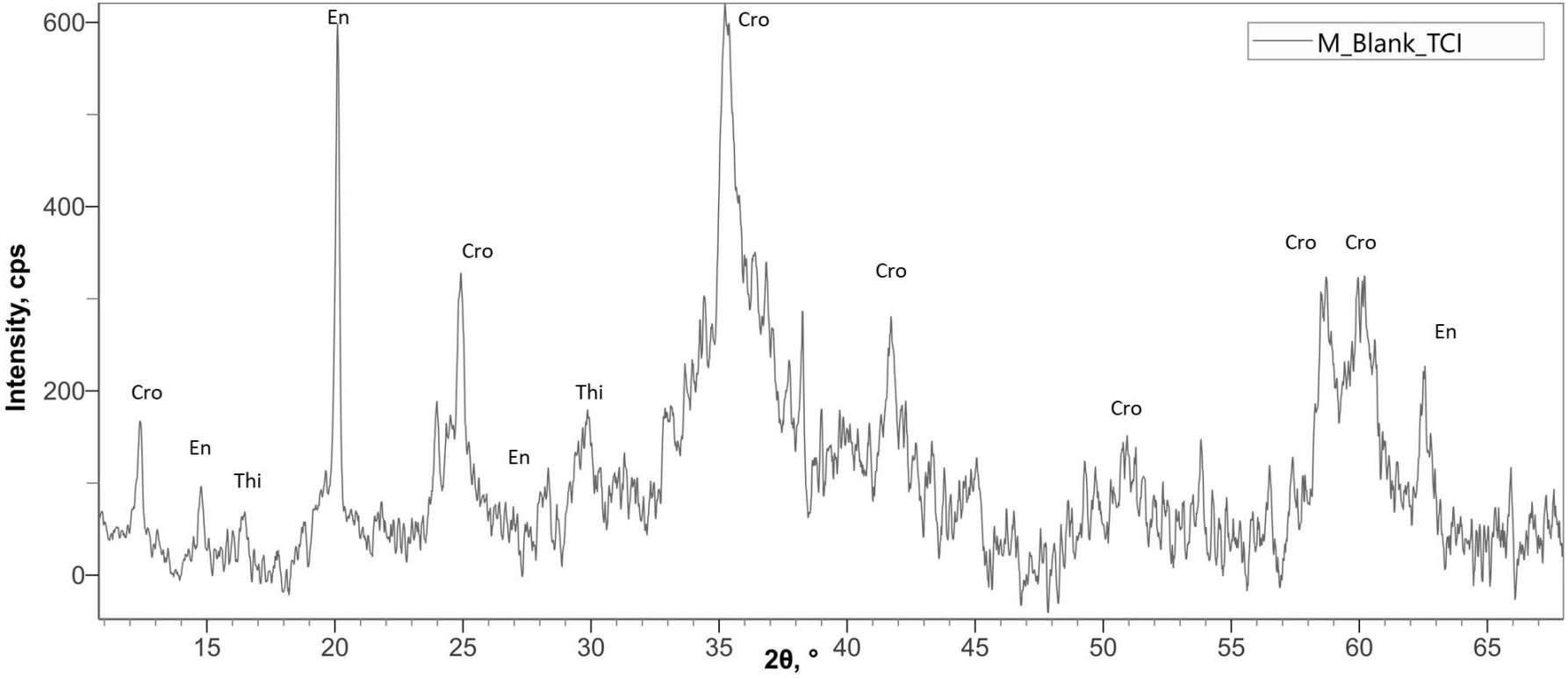

Fig. 5.32. μXRD pattern from a TCI in the unheated M_Blank. Peaks match cronstedtite (Cro), tochilinite (Thi), and enstatite (En). Pattern collected with a Cu X-ray source.

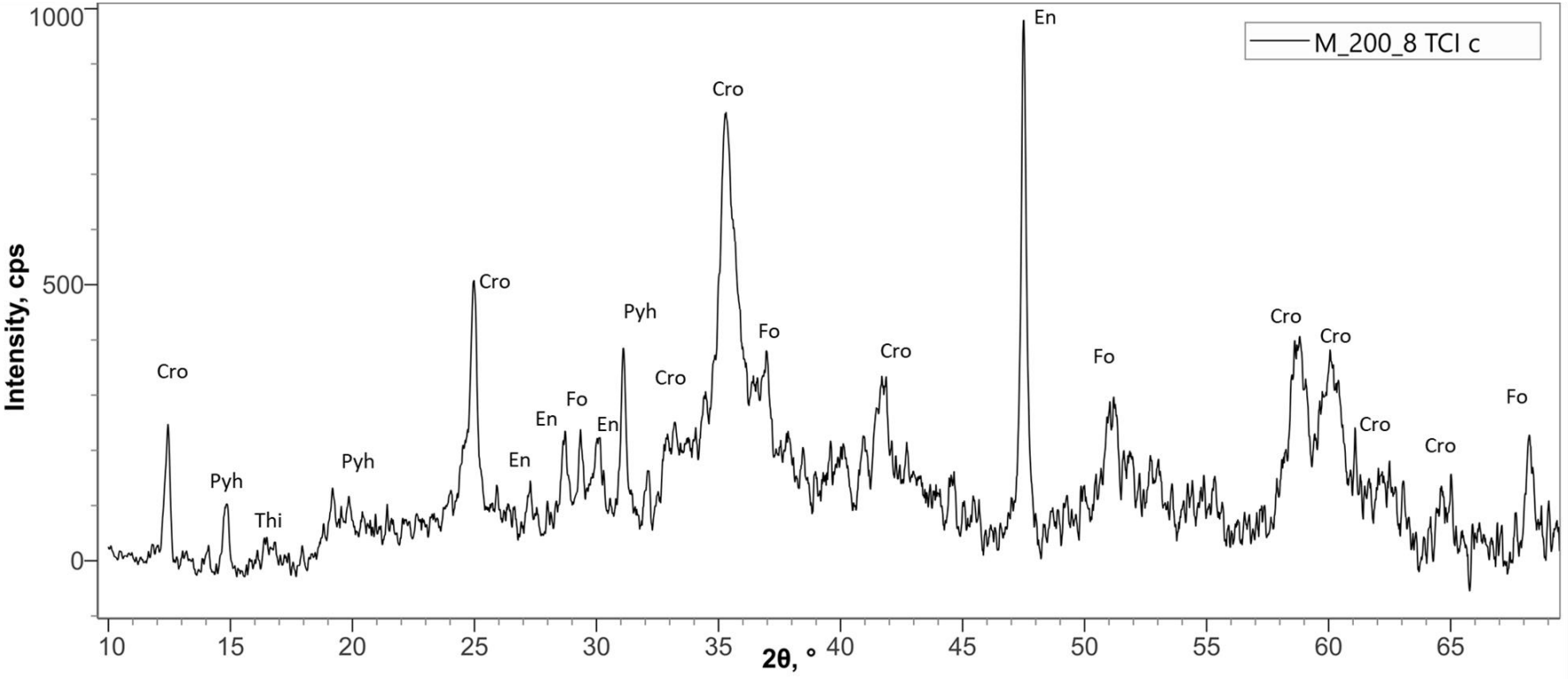

Fig. 5.33. µXRD pattern from a TCI in M_200_8. Peaks match cronstedtite (Cro), tochilinite (Thi), pyrrhotite (Pyh), forsterite (Fo), and enstatite (En). Pattern collected with a Cu X-ray source.

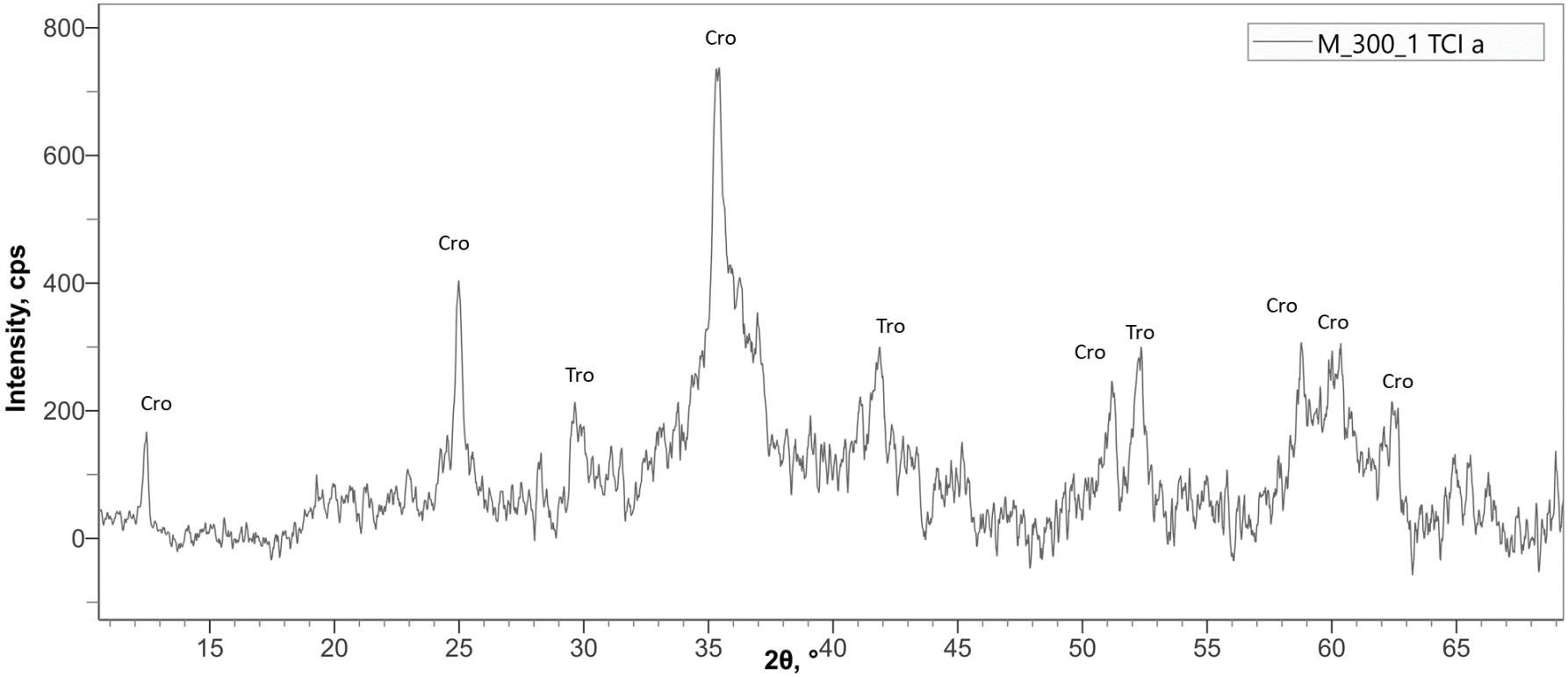

Fig. 5.34. μXRD pattern from a TCI in M_300_1. Peaks match a mixture of cronstedtite (Cro) and troilite (Tro) are observed. No tochilinite was observed. Pattern collected with a Cu X-ray source.

5.5.3 Thermal Stability of Tochilinite

Prior to this work, the lowest temperature at which tochilinite was observed to decompose at was 245°C. The reaction was from heating Murchison for 7.7 days and produced troilite (Fuchs et al. 1973). In this work, tochilinite is observed changing at 200°C (Table 5.6), however consistent with previous studies, its complete decomposition and the recrystallization of secondary phases did not occur until 300°C.

Table 5.6. Summary of changes tochilinite underwent during heating experiments.

Sample	Temperature	Change
ALH 83100	200°C	Some tochilinite XRD peaks weaken.
Murchison	200°C	Tochilinite Raman peaks disappear. Sulphide Raman peaks appear.
ALH 83100	275°C	Most tochilinite XRD peaks weaken.
Murchison	300°C	All tochilinite μXRD peaks disappear.
ALH 83100	375°C	All tochilinite XRD peaks disappear.

5.5.3.1 ALH 83100

With the bulk heating of ALH 83100 powder, during XRD data collection, a portion of tochilinite peaks weakened when 200°C was reached, indicating that the mineral may be unstable at that temperature. ALH 83100 was only heated for a timescale of hours, spending only two hours at each temperature step; given that the original observation of tochilinite decomposition took days to occur (Fuchs et al. 1973), it is possible that the original ALH 83100 experiment was too short of a duration to allow for tochilinite decomposition at 200°C.

5.5.3.2 Murchison

Heating experiments using the M_Heat chips ran over longer periods, with one of the samples being heated at 200°C for 8 days (M_200_8). Both samples heated to 200°C, M_200_1 and M_200_8, showed changes in the Raman spectra collected from their TCIs and tochilinite, indicating decomposition of tochilinite into sulphides starting to occur at 200°C.

TCI Raman spectra display a similar story to that of the tochilinite globules. M_Blank's TCIs have peaks consistent with both tochilinite and cronstedtite (Table 5.5), while most TCIs in the heated samples are completely devoid of peaks (Fig. 5.27), with the exception of M_200_1, which has a single TCI whose Raman

spectrum is closest to the heated Pałtusk TCIs (Krzesińska & Fritz 2014). This appears to indicate tochilinite decomposition at 200°C, however it is important to note that TCIs contain cronstedtite, which does not begin decomposition until 300°C (Nakamura 2005). Even with tochilinite decomposing, Raman peaks associated with cronstedtite should still be observed. However, the intensity of Raman peaks in the original M_Blank spectra were low (Fig. 5.27), and a substance becoming amorphous does not stop molecular vibration and Raman shift; instead, Raman shift becomes more variable, resulting in broader lower intensity peaks that are similar to noise (Lin et al. 1993). It is therefore probable that the cronstedtite Raman peaks have been obscured by broad peaks related to decomposed tochilinite in these spectra.

Despite the Raman spectra collected for the M_Heat samples showing evidence of possible tochilinite decomposition at 200°C, the μXRD patterns shows the opposite. For both tochilinite globules and TCIs, diffraction peaks associated with tochilinite persist in M_200_8, and troilite from recrystallization of decomposed tochilinite does not appear until 300°C (Fig. 5.30-5.34). Not all μXRD patterns from M_200_1 and M_200_8 contain tochilinite peaks, however this may be a result of orientation biases. The μXRD patterns indicate that the tochilinite is crystalline at 200°C.

5.5.3.3 Differing Results Between Raman Spectra and XRD Patterns

At first glance, the μXRD patterns seem to contradict the Raman spectra. One dataset indicates that tochilinite is crystalline at 200°C, while the other indicates that it has decomposed. However, this contradiction can be rectified by looking at the tochilinite crystal structure itself. Tochilinite is composed of mackinawite with layers of brucite and/or amakinite (Palmer & Lauretta 2011). Brucite can decompose at temperatures as low as ~200°C (Wang et al. 1998), while mackinawite transforms into pyrrhotite at a minimum temperature of 210°C, with the transition temperature being heavily dependent on composition (Sarkar 1971). The layers of tochilinite likely respond differently to heating, with the brucite/amakinite layers beginning decomposition at 200°C while the mackinawite layers remain intact. This would explain why at 200°C some tochilinite XRD peaks weakened and/or disappeared, while others showed little to no change. Raman spectra are consistent with this as the tochilinite globules in M_200_1 and M_200_8 display peaks most consistent with sulphides, like

mackinawite (Table 5.5). Decomposition of the brucite/amakinite layers would add noise to Raman spectra, accounting for the lack of sulphide peaks in the TCIs of M_200_1 and M_200_8.

I propose that tochilinite decomposition is a two-stage process. The first stage is partial decomposition at ~200°C, affecting only its brucite/amakinite layers. The mackinawite layers remain intact leading to tochilinite remaining as a partially crystalline phase at 200°C. Significant dehydration should occur at this temperature. If heated to at least 210°C, the mackinawite layers begin recrystallizing into a more stable sulphide phase, like troilite. It's important to note that 210°C is the minimum temperature required for this transformation; certain compositions of tochilinite may require higher temperatures. At no point is tochilinite required to be completely amorphous during this process.

5.6 – *In situ* Characterization of Serpentine Decomposition and the Formation of a Transitional Phase

Serpentine undergoes decomposition at 300-500°C, and at temperatures above 500°C, secondary silicates begin to recrystallize from its decomposed remnants. During this process, a transitional phase is formed. It was first described by Akai (1988) and observed in three different forms by transmission electron microscopy (TEM). In selected area electron diffraction data Akai (1988) found that the transitional phase had reflections at 9-13 Å. They also found this phase in Murchison samples heated to 500°C and 600°C. However, beyond the original observations by Akai (1988), there is little known about this phase.

In the present study, when ALH 83100 and pMurchison were experimentally heated, an XRD peak at ~3.5-3.6 Å resulting from the decomposition of serpentine was observed. It appeared at 525°C and persisted until 750°C, where it began to lose intensity (Fig. 5.4 & 5.11). This XRD peak can be attributed to the transitional phase, as it appears in the same temperature range as recorded by Akai (1988), and it disappears as secondary silicates start to crystallize. No other peaks associated with the transitional phase were observed, which may be attributed to peak overlap as there are many minerals within CM chondrites.

To further investigate this transitional phase and characterize its crystal structure, three rock slices of µMurchison (hereby referred to as M_A, M_B, and M_C) were experimentally heated and *in situ* micro XRD (µXRD) data were collected in transmission at the I18 beamline at Diamond Light Source. µXRD was used to minimize the peak overlap that occurred with the pXRD heating experiments, such that additional diffraction peaks associated with the transitional phase could potentially be identified. To heat the samples, a THMS600 Linkam cell was used. The samples were held in place within the Linkam cell with Kapton. The original experimental design was to heat all three samples from 400°C to 600°C at 25°C temperature steps. However, the Kapton disintegrated at 550°C. Instead, M_A and M_B were heated from 400°C to 550°C, while M_C was heated from 200°C to 500°C. A set of empty Kapton "blanks" were also heated from 200°C to disintegration at 550°C to monitor the background during heating. XRD patterns were collected in a grid at each temperature step from the same area on a sample. The initial intent was to track specific spots within the sample during heating, however due to the sample shifting during the experiment, this proved to not be viable. The µXRD patterns collected for µMurchison were compared to a series of patterns collected for several different standards listed in Chapter 2.5.2. The most relevant standards discussed here are enstatite and antigorite. See Chapter 2.5.2 for more information on the experimental setup.

5.6.1 Isolating the Transitional Phase

The µXRD patterns were all evaluated for the presence of a peak at ~3.5-3.6 Å, the indicator of the transitional phase in the original experiment with ALH 83100. In M_A, four spots at 525°C were observed with this peak, however these spots were often associated with enstatite. In M_B, two spots at 525°C were observed with this peak, one of which had no other phases associated with it (Fig. 5.35). The transitional phase was not observed in M_C.

The transitional phase has four major peaks at 2.31 Å, 2.49 Å, 3.04 Å, and 3.51 Å, as well as four minor peaks at 2.28 Å, 2.35 Å, 2.46 Å, and 2.54 Å. There is also an increase in intensity towards the end of the pattern beyond 7 Å (Fig. 5.35). This increase in intensity is likely another major peak that had been cut off by the detection limits, however this cannot be confirmed.

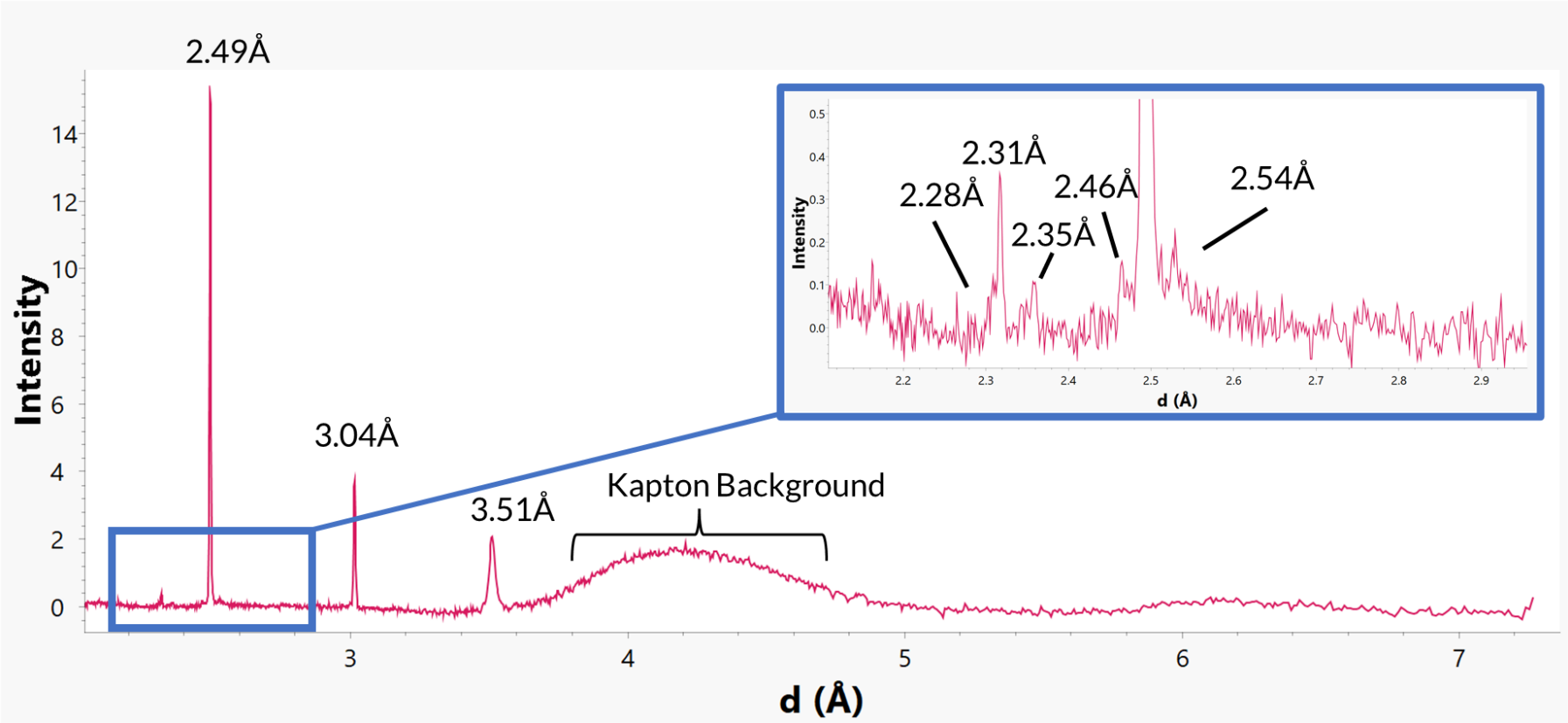

Fig. 5.35. µXRD pattern from M_B collected at 525°C. The µXRD pattern does not match any known mineral and is attributed to the transitional phase. The µXRD pattern shows a slight increase in intensity at the end of its d-spacing range beyond 7 Å that might be another peak.

5.6.2 Identifying the Transitional Phase

When compared to the XRD patterns collected from the standards, the transitional phase did not match any of them, including enstatite, but its peak shape was similar to antigorite (Fig. 5.36). As the peak positions do not match, the transitional phase cannot be antigorite.

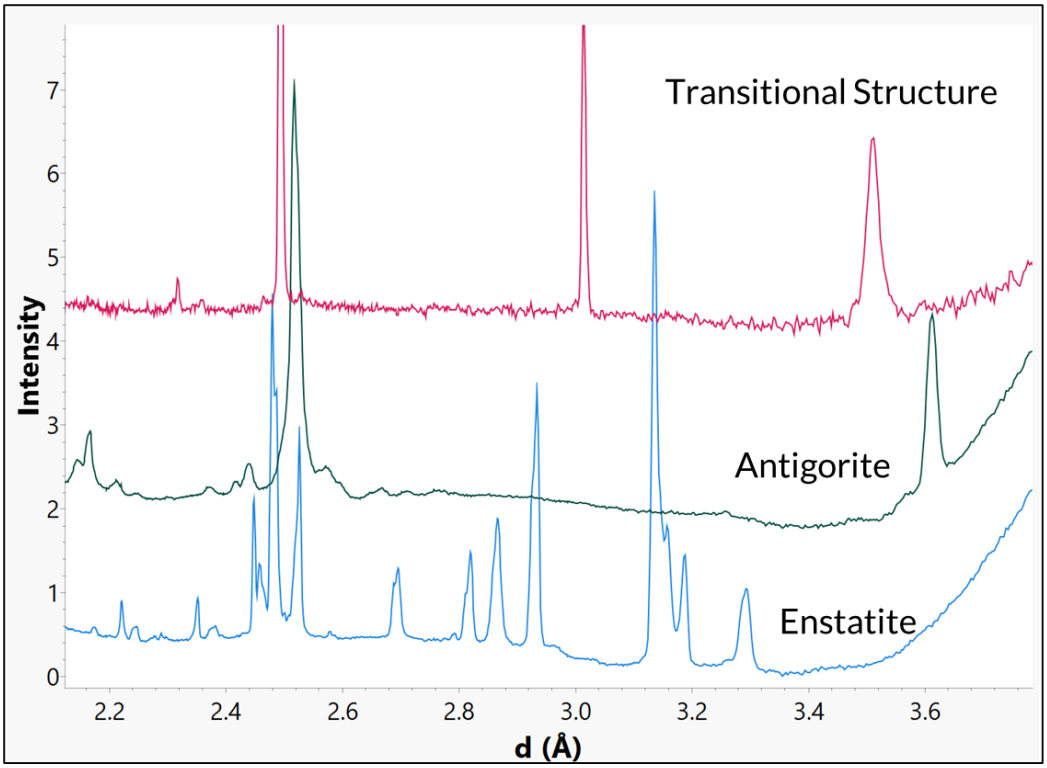

Fig. 5.36. Comparison of the μXRD pattern for the transitional structure collected from M_B at 525°C to the enstatite and antigorite standards. Neither standard matches, however antigorite bears some similarities in peak morphology to the transitional phase.

The peak positions of the transitional phase were compared to several minerals within the literature. The only mineral whose diffraction pattern matches all the peaks displayed by the transitional phase was carlosturanite ($(Mg, Fe)_{21}Si_{12}O_{28}(OH)_{34}\cdot H_2O$) (Compagnoni et al. 1985). However, despite the XRD pattern matching carlosturanite, that mineral is unlikely to be present as it decomposes at 400°C (Compagnoni et al. 1985).

It is more likely that the transitional phase shares structural similarities to carlosturanite, accounting for similarities in XRD peak positions. Carlosturanite has an octahedral sheet (cations Mg, Fe), and a tetrahedral sheet (cations Si) broken up into triple chains. Water molecules occur in the gaps between these triple chains, while the hydroxyl anions connect the two sheets (Mellini et al.1985). The transitional phase's structure likely consists of an octahedral sheet

and a broken tetrahedral sheet, while lacking the water and hydroxyl anions normally present in carlosturanite.

When Akai (1988) originally observed the transitional phase, they speculated that the Ball & Taylor (1963) model for serpentine decomposition may have been occurring. In this model, serpentine is divided into donor and acceptor regions. The donor regions give the acceptor regions (Mg, $Fe)^{2+}$ and Si^{4+} and in turn receive H^{+}. The donor regions become H_2O, which gets outgassed, while the accepter regions form a partially disordered structure. To balance their equation, Ball & Taylor (1963) propose that the structure has a composition of ~$(Mg,Fe)_{27}Si_{18}O_{63}$, but note that this is unlikely to be exact in nature. This transitional phase then gets divided into Mg-rich and Si-rich regions, which recrystallize into olivine and pyroxene, respectively.

The process for serpentine decomposition proposed by Ball & Taylor (1963) is consistent with observations made here. The transitional structure appears before complete serpentine decomposition, but at the start of the recrystallization of secondary anhydrous silicates, like olivine. Because this transitional structure appears to have a similar crystal structure to carlosturanite, it is likely that during serpentine's decomposition its tetrahedral sheet begins breaking into triple chains, similar to that displayed in carlosturanite. It is important to note that serpentine is never required to become amorphous during this process.

The transitional phase displayed by moderately heated CM chondrites has a structure similar to carlosturanite. It is an intermediary product that occurs in a rather narrow temperature window of 500-600°C (Akai 1988), with 525°C being the key temperature. Both this work and the original experiments by Akai (1988) were only on the timescale of hours; it is possible that if heated for long enough, this transitional structure would recrystallize into olivine and pyroxene. Regardless, its presence is indicative of the meteorite having experienced 500-600°C of heating and it can be used to understand the thermal history of both it and its parent asteroid. This phase should be present in more moderately heated CM chondrites but would likely only be readily observable with μXRD or TEM.

5.7 Summary of Mineral Transitions

Through a combination of XRD and Raman spectroscopy on experimentally heated samples, a number of phase transitions caused by heating were observed. The temperatures at which these reactions occur under inert conditions are summarized in Table 5.7. It is important to note that these experiments were conducted at timescales ranging from hours to eight days; it is possible that the reactions studied may occur at lower temperatures if heated over a longer duration.

Table 5.7. Summary of temperatures at which mineral transitions were observed during experimental recreations of post-hydration heating of CM chondrites.

Mineral Transition	Observed Temperature	Miscellaneous Notes
Tochilinite Decomposition	200-300°C	Likely a two-stage decomposition process, with complete decomposition happening above 210°C.
Troilite & Magnetite Recrystallization from Tochilinite Decomposition	300°C	Observed occurring at 245°C by Fuchs et al. (1973)
Serpentine Decomposition	300°C	
Formation of Transitional Phase from Serpentine Decomposition	525°C	Observed in samples experimentally heated to 500°C by Akai (1988)
Olivine Recrystallization from Serpentine Decomposition	525-600°C	Reported to start occurring at 500°C (Ball & Taylor 1973)
Enstatite Recrystallization from Serpentine Decomposition	575°C≤	May not always occur.
Calcite Decomposition	575-700°C	
Clinopyroxene Recrystallization from Calcite Decomposition	575-700°C	
Pentlandite Decomposition	675°C	
Oldhamite Recrystallization from Calcite Decomposition	700°C	May not always occur.
Decomposition of the Transitional Phase	750°C	

Chapter 6 – Post-Hydration Heating II – Timescales and Causes

As explored in Chapter 5, there are a number of phase transitions that occur due to post-hydration heating. Tochilinite decomposes into sulphides and oxides at temperatures above 210°C; serpentine begins decomposing at 300°C, eventually recrystallizing into a combination of olivine and/or enstatite; and calcite decomposes at 575-700°C, recrystallizing into clinopyroxene and/or oldhamite (CaS). All these phase changes are observable by X-ray diffraction (XRD), however can yield different sets of information when studied through other methods, such as scanning electron microscopy (SEM). Additionally, petrographic features, like fractures and grain size, may give clues as to the timescale and cause of post-hydration heating.

There is little known about the timescale of post-hydration heating. Most estimates indicate that it is likely of short duration (hours to days). Any secondary phases that formed during post-hydration heating are typically fine-grained, indicating that they did not have a long enough time to grow (Nakamura 2005). Additionally, during heating, olivine grains in chondrules will exchange Fe-Mg with the matrix through diffusion, resulting in Fe-Mg zoning, with a greater degree of mineral zoning indicating longer timescales. As this region of zoning in heated carbonaceous chondrites is often narrow, the heating they have experienced must be on the order of several hours to days (Nakato et al. 2008; Ikeda 1992). Studies on organic matter within heated carbonaceous chondrites also show that they have experienced post-hydration heating over timescales of short duration (Quirico et al. 2018). The short duration of post-hydration makes the decay of ^{26}Al, which would take millions of years, an unlikely contender for post-hydration heating's cause (Nakato et al. 2008).

One difficulty with estimating the timescale of post-hydration heating is that its phase transitions are dependent on both duration and temperature (Nakato et al. 2008; Nakamura 2005). A meteorite heated at a lower temperature for a longer duration may show similar post-hydration heating indicators as a meteorite heated at a higher temperature for a shorter timescale. For example, a meteorite heated at 245°C may take 7.7 days for its

tochilinite to recrystallize into troilite, whereas if it was heated to 300°C, the same reaction would only take 20 minutes (See Chapter 5).

Longer timescales enable a greater degree of recrystallization to occur, and thus produce larger grain sizes for secondary anhydrous phases (Nakato et al. 2008). Relative timescales of naturally heated meteorites can be determined by comparing the grain sizes of secondary phases with each other, as well as with meteorites experimentally heated at known temperature-timescales.

In this chapter, eight naturally heated meteorites (six CM chondrites and two CM-like ungrouped carbonaceous chondrites) are compared to three sets of experimentally heated samples through SEM and reflected light petrography. Based on the heating effects these meteorites display, as well as the relative size of heating products (e.g., grain size of secondary anhydrous minerals, fracture width), the temperature-timescales these meteorites have experienced can be estimated. These estimates are based on qualitative observations and are not meant to be precise, but rather a means to gauge a general understanding of the metamorphism experienced by heated CM and CM-like chondrites.

The petrographic features focused upon in this chapter are 1) fracturing, 2) tochilinite-cronstedtite intergrowths (TCIs), 3) tochilinite globules, 4) pentlandite decomposition, 5) olivine diffusion, and 6) calcite decomposition.

Fracturing due to post-hydration heating occurs due to the dehydration and dehydroxylation of hydrous phases, like serpentine and tochilinite. Fracturing of the serpentine-rich matrix and fine-grained rims (FGRs) of meteorites should become apparent when serpentine starts to decompose, at 300°C. Fractures have been known to grow and proliferate with increased heating duration (Patzek et al. 2023).

Tochilinite is one of the first phases to decompose upon post-hydration heating, with its potential decomposition temperature being as low as 210°C (see Chapter 5). To avoid confusion and to use terminology more reflective of their constituents (see Chapter 1), the terms tochilinite globules and TCIs shall be used here for the equivalents to the literature terminology type-I and type-II TCIs, respectively (e.g., Fuchs et al. 1973; Tomeoka & Buseck 1985; Vacher et al. 2019). Both assemblages contain tochilinite and are therefore key-indicators

of post-hydration heating. Grain sizes of sulphides and oxides produced from their decomposition may give an indication of timescale.

Because pentlandite only forms stably at temperatures below 610°C (Durazzo & Taylor 1982), it is thought to begin decomposition at temperatures exceeding 610°C (Nakato et al. 2008). However, in this study, it was observed decomposing at 675°C (see Chapter 5). In either case, its decomposition is an indicator of high temperatures.

Previous studies have shown olivine diffusion to relate to both temperature and timescale, with greater amounts of diffusion corresponding to higher temperatures and/or longer timescales (Nakato et al. 2008; Ikeda 1992).

In Chapter 5, calcite was observed decomposing at temperatures as low as 575°C, recrystallizing into clinopyroxene and in some cases oldhamite. Like pentlandite, its decomposition is indicative of high temperatures. The grain sizes of clinopyroxene and oldhamite can be used as an indicator of timescale.

Understanding the timescale experienced by CM and CM-like chondrites will not only enable better characterization of extraterrestrial materials but will give clues as to the currently unknown cause of post-hydration heating. The potential cause of post-hydration heating is also explored in this chapter.

Impact heating and solar heating occur over short durations and are not constrained to a particular timeframe (Nakamura 2005), making them the most likely causes for post-hydration heating. Meteorites that experienced solar heating should display depletions in certain noble gases, like ^{3}He, due to proximity to the Sun (Nakamura 2005), while it is reasonable to assume that meteorites that have experienced heating due to impact events should show corresponding shock effects, as a minimum shock pressure of 21 GPa is required to dehydrate serpentine (Sekine et al. 2015; King et al. 2021b).

It is assumed that meteorites heated by solar radiation were more likely to be heated on more variable timescales, up to days to weeks as the orbits of asteroids around the Sun can also be variable. Meteorites heated by impacts are assumed to be heated on timescales that are quite short, as known post-shock heating durations for igneous material are only elevated for durations shorter

than a few seconds (Schmitt 2000). Porous sedimentary material, like terrestrial sandstone, will also experience elevated temperatures for extremely short durations, such as micro- and milli-seconds (Kieffer 1971). Given this, it is unlikely that impact heating could significantly heat material for even the short durations (hours to days) of post-hydration heating. However, there have been few studies on post-shock temperatures experienced by carbonaceous material, and it could be possible that it retains heat for longer than other well-studied materials. The temperatures displayed by impact experiments in carbonaceous chondrites are also likely lower than that experienced by naturally impacted meteorites due to the limited scale in both size and duration of experimental impacts (Quirico et al. 2018). Yet, modelling of impacts on carbonaceous parent bodies have shown that like, extraterrestrial igneous and terrestrial sedimentary impactites, the heating experienced by hydrous carbonaceous material is likely of extremely short duration, lasting only seconds (Bland et al. 2014), or does not occur at all, with no elevated post-shock temperatures (e.g., ≥300°C) experienced (Wakita & Genda 2009). If impacts were responsible for post-hydration heating, it is expected that the duration of heating would more likely be on the order of hours rather than days.

The timescales of heating estimated for the studied samples may be an indicator of which contender for the cause of post-hydration heating is the most likely, with variable timescales favouring solar radiation and shorter timescales favouring impacts. In addition to timescale estimates, where possible, the naturally heated meteorites studied are evaluated for shock metamorphism, as if impact heated, these samples should show corresponding shock effects. Unfortunately, as of writing, there is no ready way to test whether or not solar heating is responsible for post-hydration heating.

6.1 Experimentally Heated Meteorites

Three unheated CM chondrites, Murchison, Murray, and Winchcombe were experimentally heated at different temperatures and durations, either to study post-hydration heating specifically, or as part of a parallel study. These samples are described in Chapters 3.5, 3.6, and 3.12, and the methods by which they were heated are described in Chapter 2.5. The relevant analysis methods for samples in this chapter are SEM and optical petrography.

6.1.1 Murchison

Murchison is a brecciated CM2.5 chondrite (Rubin et al. 2007) that displays a prominent petrofabric and evidence of being impacted (Lindgren et al. 2014), however as of writing, there is no record of any clasts that have experienced post-hydration heating. To study recrystallization of various secondary anhydrous phases and how they vary with temperature conditions, six rock chips of Murchison were experimentally heated in a vacuum oven at the Scottish Universities Environmental Research Centre (SUERC) using the following temperature-timescales: 200°C for 1 day (M_200_1), 200°C for 8 days (M_200_8), 300°C for 1 day (M_300_1), 400°C for 1 day (M_400_1), 500°C for 1 day (M_500_1), and 500°C for 8 days (M_500_8). These temperature-timescales were chosen to cover the range of temperatures at which tochilinite and serpentine may decompose at. Each of these rock chips, along with an unheated sample of Murchison (M_Blank) were made into polished rock sections for study.

6.1.1.1 Fracturing of the Matrix and Fine-Grained Rims

Backscattered electron (BSE) images of M_Blank show significant fracturing close to the fusion crust, but the degree of fracturing decreases with distance from the fusion crust until becoming absent (Fig. 6.1a). M_200_1 shows a lower degree of fracturing than M_Blank (Fig. 6.1b), however this is likely due to the absence of a fusion crust. If the lack of a fusion crust is accounted for, M_200_1 shows a similar degree of fracturing as M_Blank. Both M_200_8 and M_300_1 also show a similar degree of fracturing as M_200_1 (Fig. 6.1c & d). If the fusion crust fracturing is accounted for, all three samples have fractures up to ~2 μm in width.

The degree of fracturing shows significant changes at 400°C. M_400_1 shows large fractures in both the fine-grained rims (FGRs) surrounding its chondrules and serpentine-rich areas within its matrix (Fig. 6.1e). The fractures in FGRs are up to ~7 μm wide. Although this section contains fusion crust like M_Blank, the fracturing persists in areas far from the fusion crust, indicating that it is the result of laboratory heating.

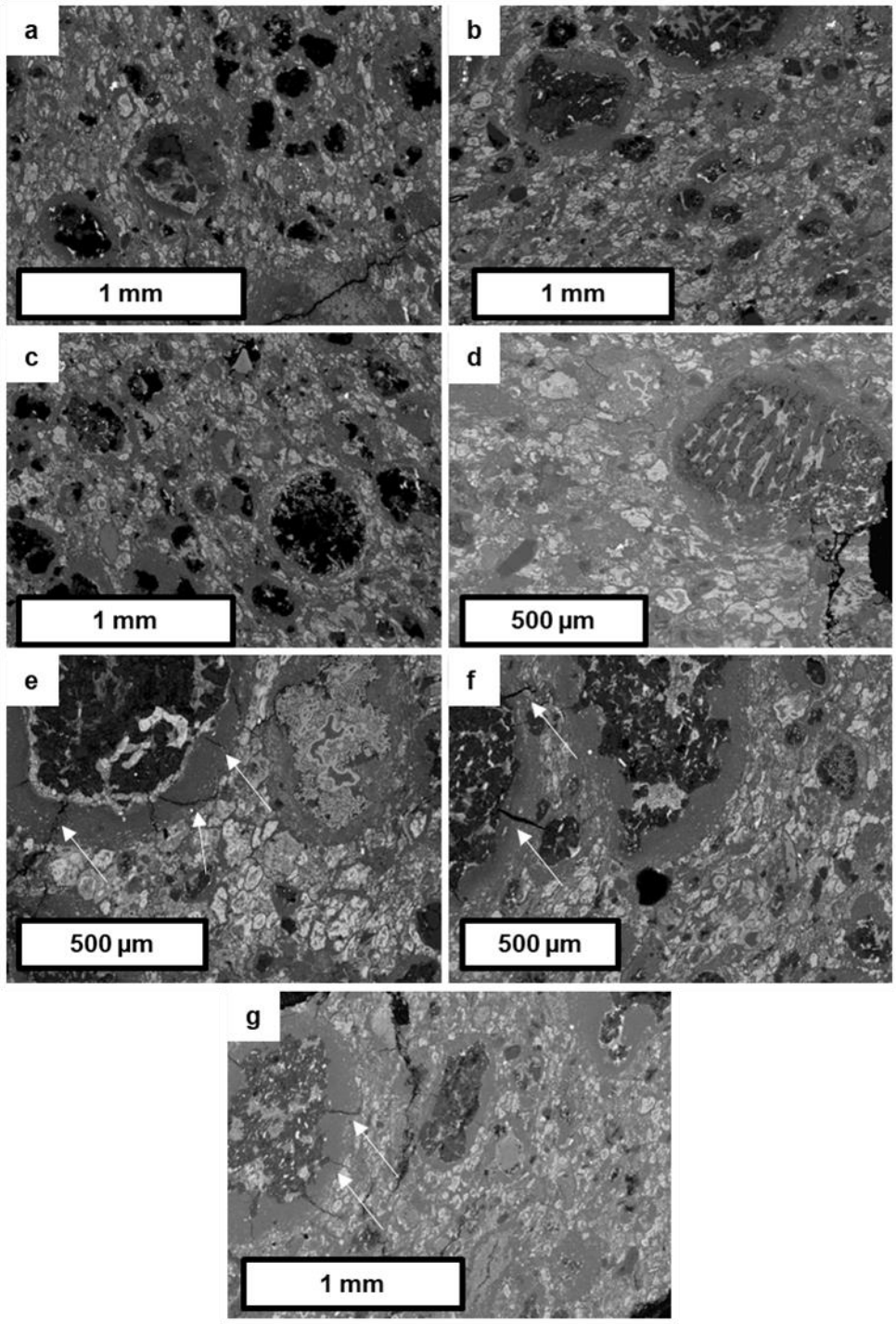

Fig. 6.1. BSE images of fracturing or lack thereof in unheated and experimentally heated Murchison samples. Some fractures in FGRs are marked with white arrows. a) Lack of fractures in M_Blank. b) Lack of fractures in M_200_1. c) Lack of fractures in M_200_8. d) Lack of fractures in M_300_1. e) Fracturing in M_400_1. f) Fracturing in M_500_1. g) Fracturing in M_500_8.

M_500_1 has the same apparent abundance of fractures as M_400_1, with fracturing in both FGRs and serpentine rich areas in the matrix (Fig. 6.1f). The fractures in M_500_1 appear larger than in M_400_1, up to ~14 µm wide in FGRs.

M_500_8 has significantly more fracturing than M_500_1, with fractures more prevalent in both the matrix and FGRs (Fig. 6.1f). Fractures in M_500_8 FGRs are similar in size to M_500_1, with fractures up to ~10 μm thick.

6.1.1.2 TCIs

When studied with SEM, TCIs in Murchison tend to look quite similar until 300°C is reached. Both M_200_1 and M_200_8's TCIs look like M_Blank's TCIs, with needle-like intergrowths (Fig. 6.2a-c). M_300_C shows more differentiation of the components, with areas in BSE images brighter and more separated, likely indicating the formation of sulphides and/or magnetite. These textures persist throughout the other experimentally heated Murchison samples (Fig. 6.2d-g). Aside from changes in brightness in BSE images, there is little change within the TCIs observable by SEM. This lack of change is likely due to secondary anhydrous phases, like sulphides, pseudomorphically replacing the original components.

When viewed with reflected light, TCIs show distinct changes as temperature increases. Both M_Blank and M_200_1's TCIs are a grey with a reflectivity slightly higher than that of silicates (Fig. 6.3a&b). However, M_200_8's TCIs show a slight patchiness in their reflectivity, with some areas brighter than others (Fig. 6.3c). When 300°C is reached, this patchiness is more dramatic, with the patches being significantly brighter (Fig. 6.3d). At 400°C, this patchiness disappears and instead the entirety of the TCIs have brighter reflectivity than those in M_Blank (Fig. 6.3e). This brightness steadily increases with temperature, with M_500_8 having the most reflected TCIs. Additionally, in both 500°C samples, TCIs begin to show a more golden hue in reflected light (Fig. 6.3f-g). It is also worth noting that TCIs near the edges and fractures in M_200_1, M_200_8, and M_300_1 are brighter than those within the interior of the samples, indicating that these samples may have not been evenly heated.

6.1.1.3 Tochilinite Globules

Within Murchison, tochilinite globules are not common but where they do occur, they are typically associated with chondrules. M_Blank had the lowest abundance of tochilinite globules and within them, P-bearing sulphides were observed. There was also little to no fracturing noted in these globules (Fig. 6.4a).

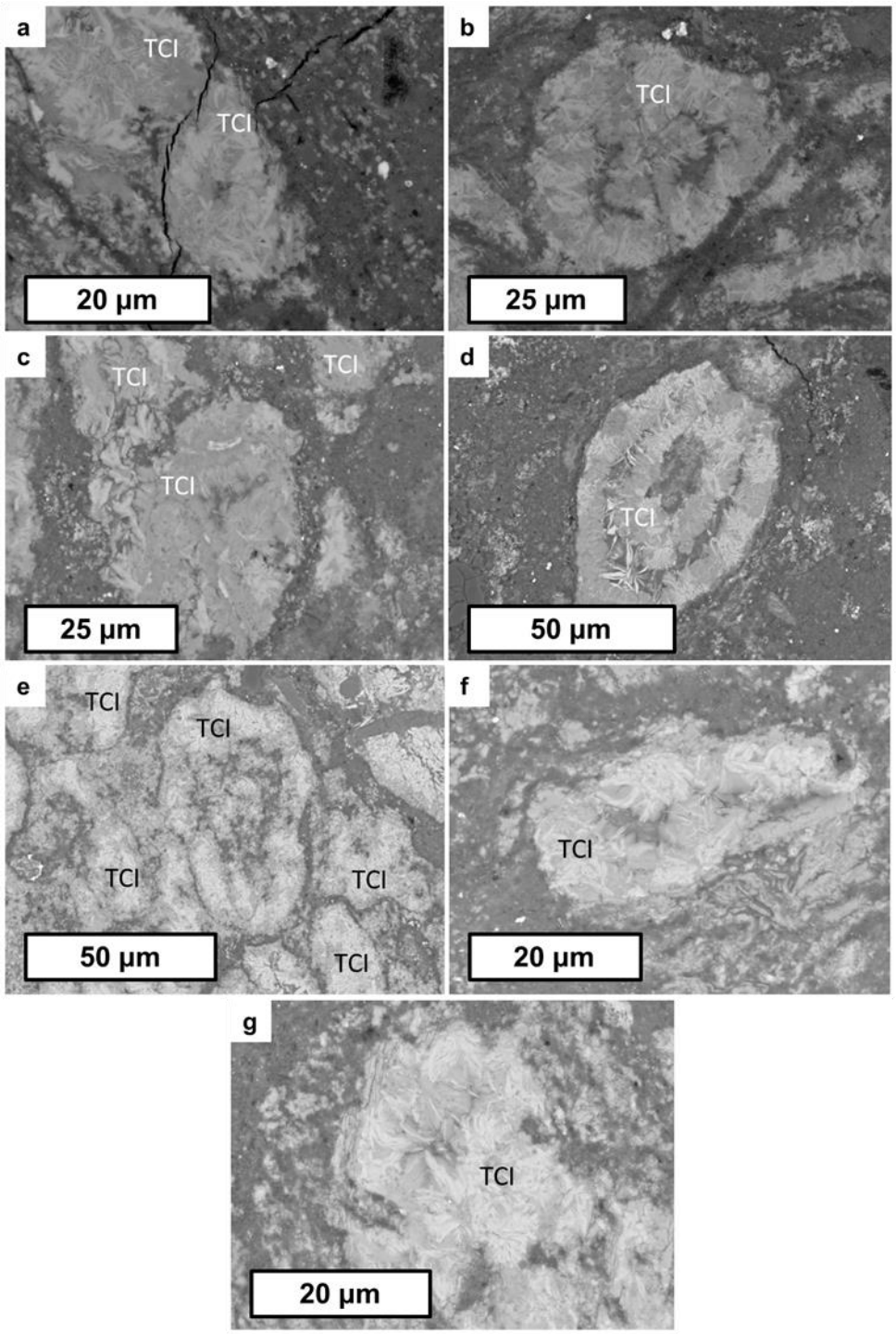

Fig. 6.2. BSE images of TCIs in unheated and experimentally heated Murchison samples showcasing TCI evolution with heating. a) TCI in M_Blank. b) TCI in M_200_1. c) TCI in M_200_8. d) TCI in M_300_1. e) TCI in M_400_1. f) TCI in M_500_1. g) TCI in M_500_8.

In some cases, tochilinite globules in M_200_1 look similar in appearance to tochilinite in the unheated sample, with the presence of P-bearing sulphides and little to no fracturing, however in other cases they were quite different in appearance, with distinct compositional zoning and apparent fracturing (Fig. 6.4b). This pattern continues for M_200_8, where some tochilinite globules show little to no fracturing, whereas other globules show distinct compositional zoning

(Fig. 6.4c). No sulphides associated with heating were observed in either M_200_1 or M_200_8.

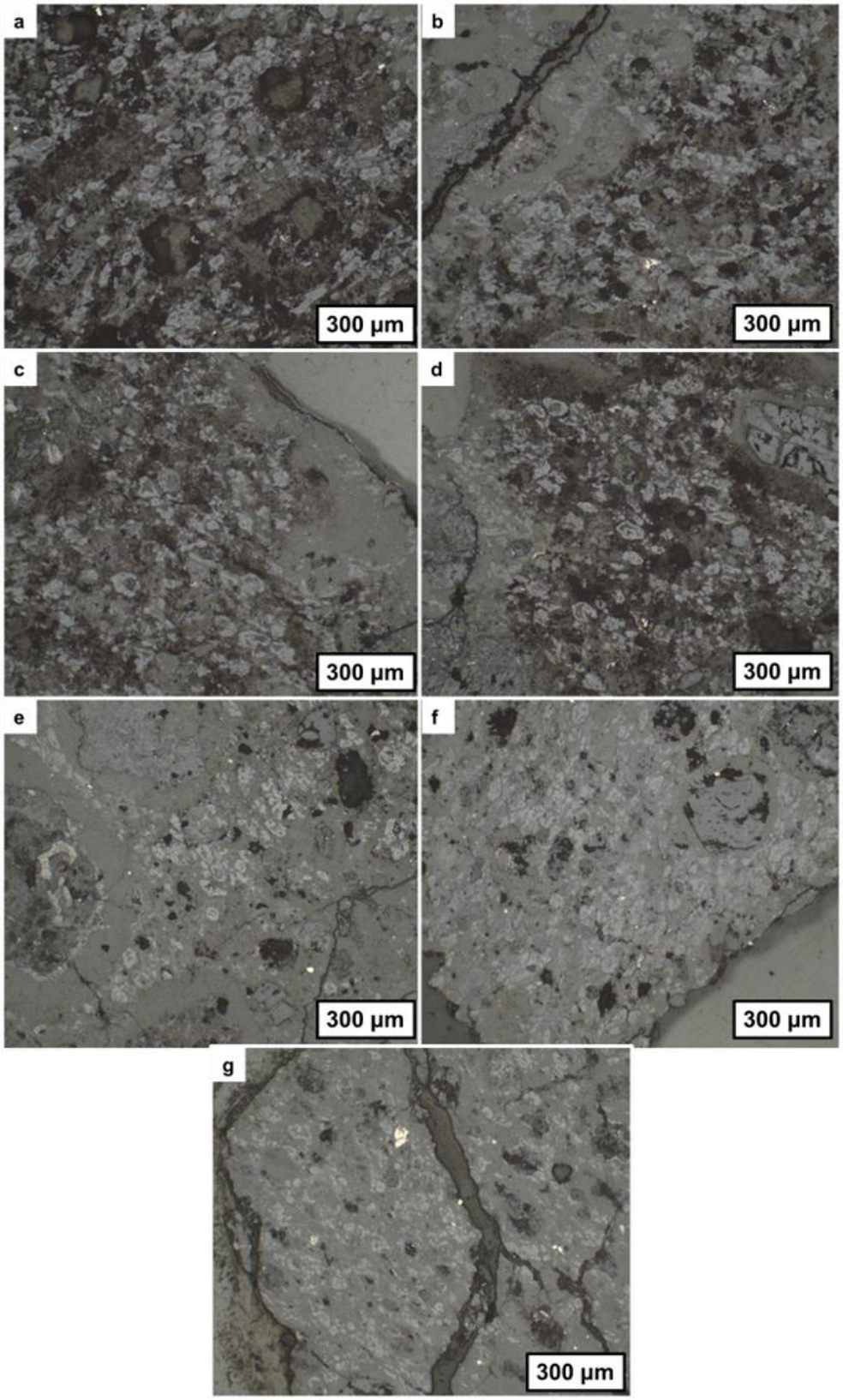

Fig. 6.3. Reflected light images of TCI dense matrix areas in unheated and experimentally heated Murchison samples showcasing TCI evolution with heating. TCIs look similar until 300°C is reached. At 300°C, TCIs in the matrix start to show brightening which continues with heating. a) M_Blank. b) M_200_1. c) M_200_8. d) M_300_1. e) M_400_1. f) M_500_1. g) M_500_8.

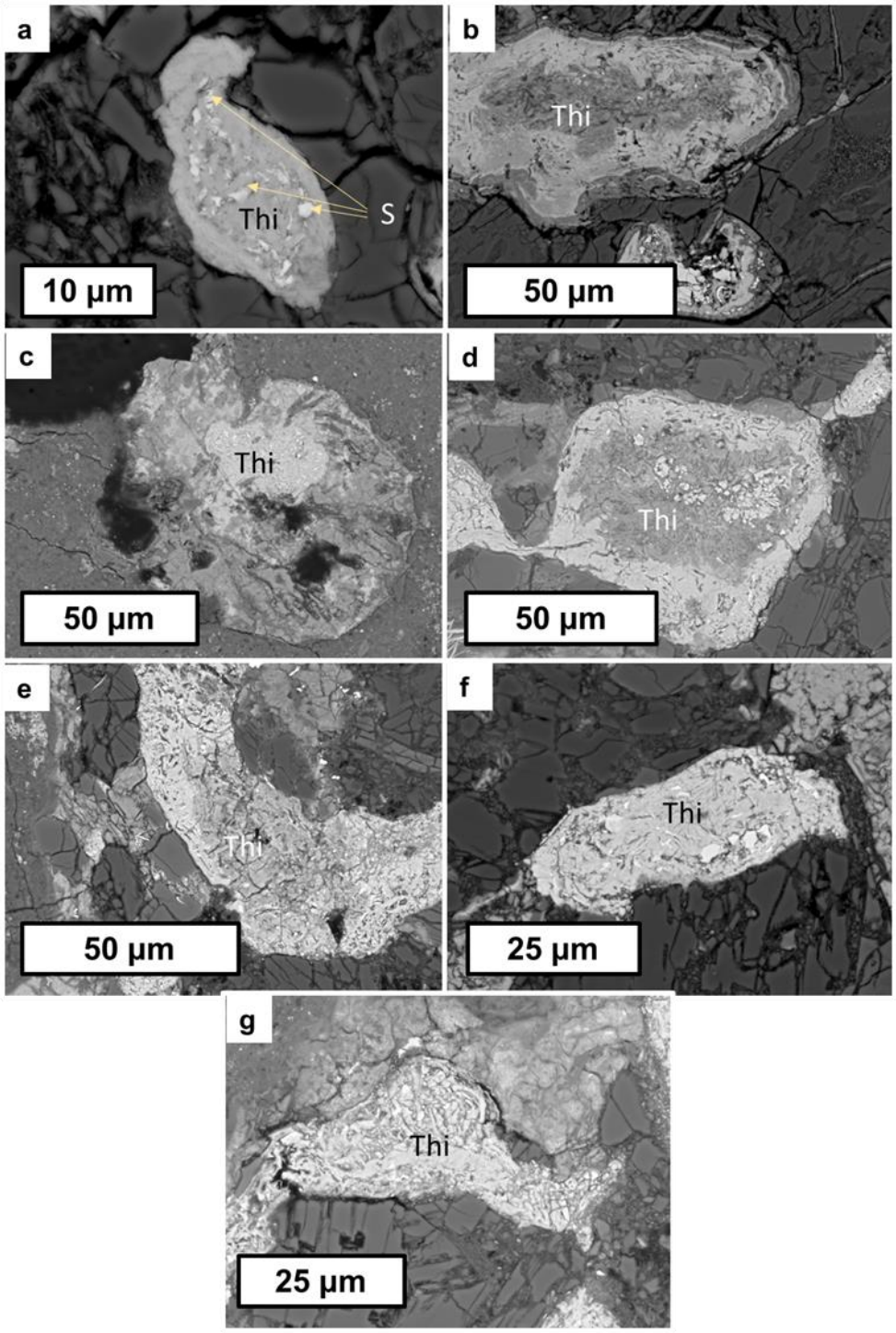

Fig. 6.4. BSE images of tochilinite (Thi) globules in Murchison samples showing their changes with heating. a) M_Blank. There is little to no fracturing, and P-bearing sulphides (S) are present. b) M_200_1. Fracturing and zoning is observed. c) Tochilinite in M_200_8. Fracturing and zoning observed. d) M_300_1. A higher degree of fracturing and zoning observed. e) M_400_1. A greater degree of fracturing and zoning observed. f) M_500_1. A lower degree of fracturing is observed with little to no zoning. g) M_500_8. Degree of fracturing is similar to that in M_500_1.

Tochilinite globules in M_300_1 show distinct differentiation between components and fracturing (Fig. 6.4d) and although they contain sulphides, these sulphides are P-bearing and unlikely the result of heating. Dehydration

fractures within tochilinite globules become more apparent at 400°C, with the globules in M_400_1 being even more porous (Fig. 6.4e).

In contrast, in the 500°C samples, M_500_1 and M_500_8, tochilinite globules no longer show distinct zoning, appearing uniformly bright in BSE images. Additionally, although they appear fractured, their fractures tend to be smaller than those displayed by M_400_1 (Fig. 6.4f&g). These bright sulphides may be due to the recrystallization of sulphides, however no distinct grains were observed beyond P-bearing sulphides. These sulphides may be too fine-grained to be resolvable in BSE images.

6.1.1.4 Olivine Diffusion

When CM chondrites are heated, olivine will undergo Fe-Mg exchange with the matrix through diffusion (Nakato et al. 2008; Ikeda 1992). This should be observable as zoning within forsteritic olivine, with the rims being Fe-rich in heated samples compared to unheated. However, EDS maps of olivine within Murchison shows that zoning of olivine is largely similar between all samples (Fig. 6.5). Given calculated rates for olivine diffusion in the literature which are on the order of nm (e.g., Nakato et al. 2008), the diffusion that would be experienced by the olivine at the temperature timescales experienced would be, at most, on the order of nanometers which is unobservable at the scale at which I was able to collect EDS data.

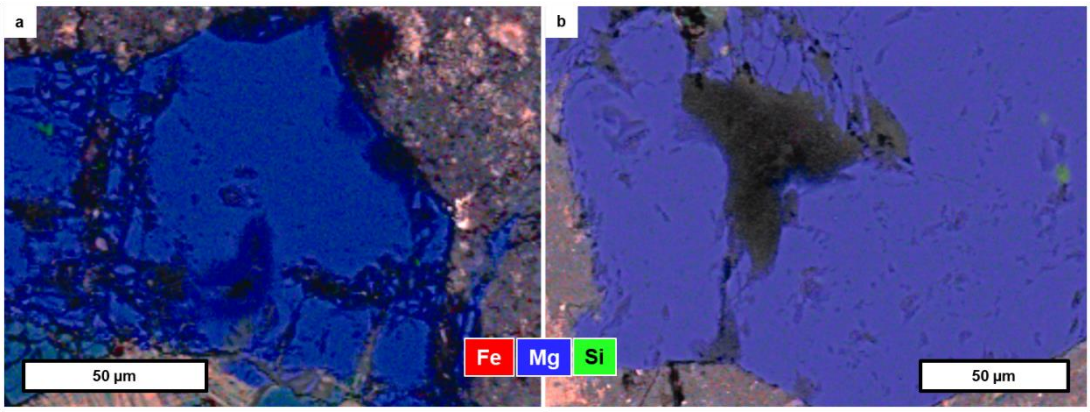

Fig. 6.5. Fe-Mg-Si EDS maps of olivine in Murchison. Olivine is blue. No Fe-Mg zoning was observed. a) M_Blank. b) M_500_8.

6.1.2 Murray

Murray is a CM2.4/2.5 chondrite breccia (Rubin et al. 2007; Quirico et al. 2018). For the most part, Murray is not thought to be heated, however unusual results from organic matter studied by Quirico et al. (2018) may indicate that Murray could have some heated clasts, however this has yet to be confirmed. From a previous study before this thesis was started, a series of Murray samples were heated for 24 hours at each of the following temperatures: 200°C (Murr_200), 400°C (Murr_400), 600°C (Murr_600), 700°C (Murr_700), 800°C (Murr_800), and 1000°C (Murr_1000). This heating was done in a vacuum oven at

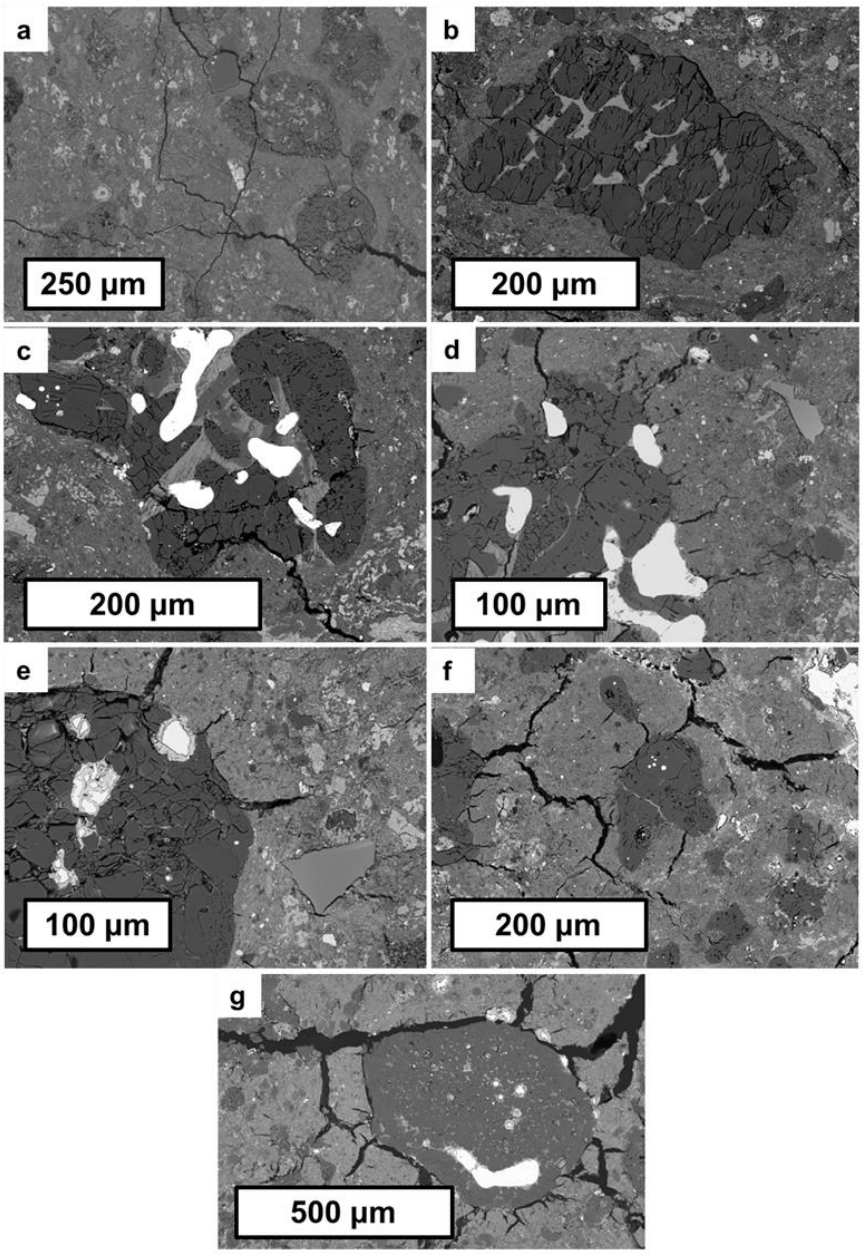

Fig. 6.6. BSE images of FGRs in Murray samples showing fracturing. a) Murr_Blank (unheated). b) Murr_200 (heated to 200°C) c) Murr_400 (heated to 400°C) d) Murr_600 (heated to 600°C) e) Murr_700 (heated to 700°C) f) Murr_800 (heated to 800°C) g) Murr_1000 (heated to 1000°C)

SUERC in a similar manner as the Murchison samples (Lee et al. 2019c). The heated Murray samples are used to study how textures change at different temperatures during post-hydration heating. They were compared to a sample of Murray that had not experienced any experimental heating, Murr_Blank.

6.1.2.1 Fracturing of the Matrix and Fine-Grained Rims

Thin fractures, up to ~2 μm thick, are prevalent throughout the matrix and FGRs in Murr_Blank (Fig. 6.6a). These fractures may be due to post-hydration heating on Murray's parent body as it is a breccia and it is possible for some of its clasts to have experienced post-hydration heating (Quirico et al. 2018). Additionally, as described below, Murr_Blank has features within its TCIs and tochilinite that are also consistent with heating. However, it is also entirely possible that these fractures are unrelated to heating and are a result of other processes, such as impacts or sample preparation.

Murr_200 is less fractured than Murr_Blank, with fractures rare and thin (Fig. 6.6b). The level of fracturing seems to be similar to that of the unheated Murchison sample studied with fractures up to ~1 μm in width.

In common with the Murchison samples, significant amounts of fracturing appear at 400°C, with large fractures becoming prevalent in the matrix and FGRs in Murr_400 (Fig. 6.6c). Fractures in FGRs are up to ~ 5 μm thick. The pattern of widening and more prevalent fracturing continues as temperature increases, with FGR fracture thickness being up to ~10 μm in Murr_600, ~20 μm in Murr_700, ~25 μm in Murr_800, and ~40 μm in Murr_1000 (Fig. 6.6d-g).

6.1.2.2 TCIs

Murray is more aqueously altered than Murchison and has a greater proportion of lizardite, and a smaller proportion of TCIs as a result (Howard et al. 2009). TCIs are still plentiful, however. TCIs in Murr_Blank are distinctly different than those observed in the Murchison samples, both heated and unheated. Murr_Blank displays distinct separation of phases more akin to that observed in tochilinite globules in the heated Murchison samples. Additionally, Murr_Blank's TCIs show small fractures not observed in M_Blank's TCIs (Fig. 6.7a). It is likely that this may be due to heating on its parent body. In contrast, Murr_200's TCIs are quite similar to Murchison's TCIs. They are relatively

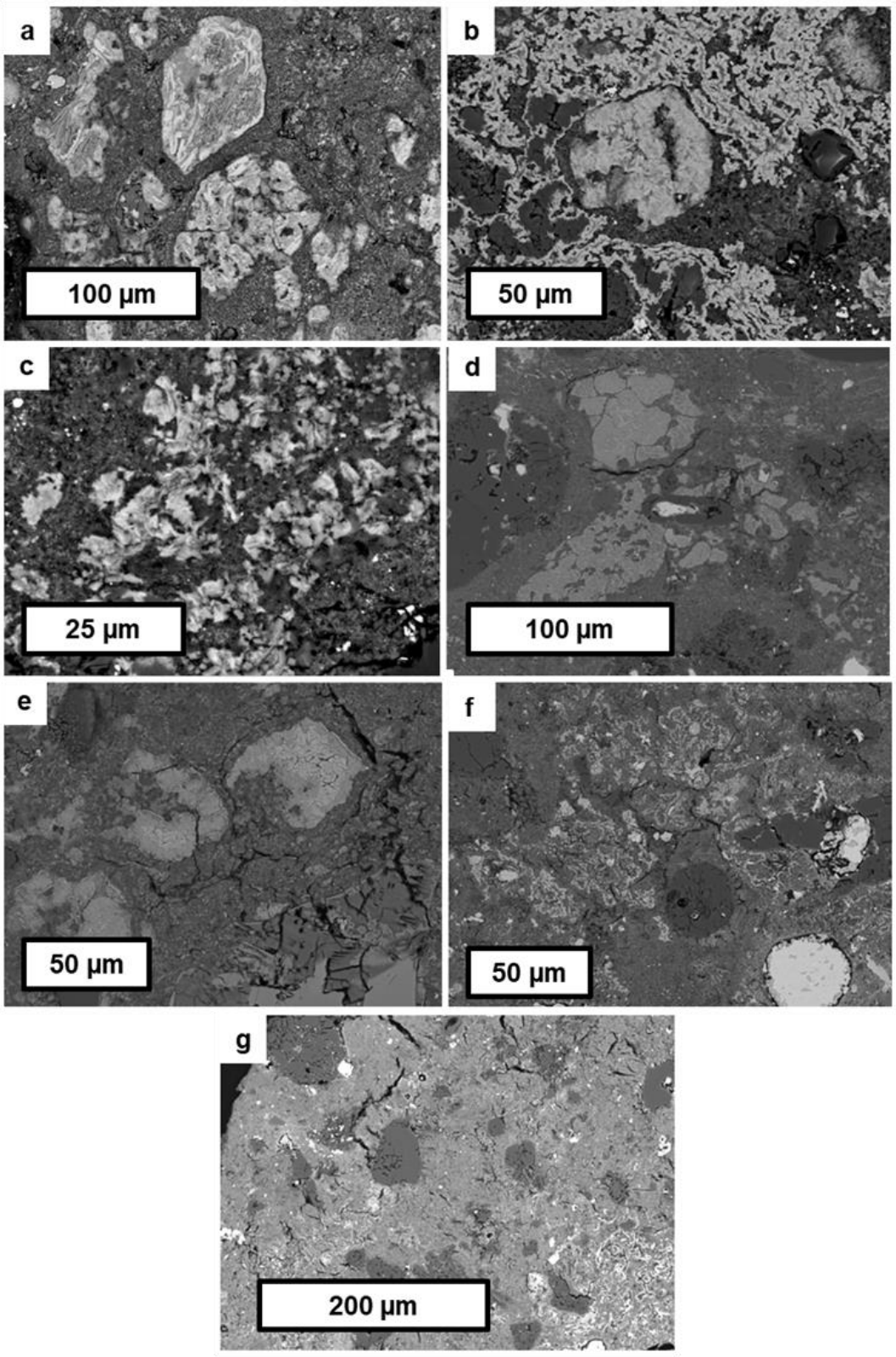

Fig. 6.7. BSE images of either TCIs or where TCIs were expected to be in Muray samples showcasing TCI evolution with heating. a) TCIs in Murr_Blank. b) TCIs in Murr_200. c) TCIs in Murr_400. d) TCIs in Murr_600. e) TCIs in Murr_700. f) TCIs in Murr_800. g) Matrix of Murr_1000 that lacks TCIs.

homogeneous in appearance, a clear intergrowth with needle-like fibres (Fig. 6.7b). Murr_Blank and Murr_200 likely originated from different lithologies accounting for the difference in the texture of their TCIs.

Like with the Murchison samples, TCIs in Murray samples heated beyond 300°C show distinct bright patches. Murr_400, Murr_600, Murr_700, and Murr_800 all show these textures, with the bright patches becoming more distinct and separate from the dark patches with increasing temperature (Fig. 6.7c-f). In Murr_1000, the TCIs are indistinguishable from the recrystallized remnants of the serpentine matrix, with small individual grains scattered throughout the matrix (Fig. 6.7g).

6.1.2.3 Tochilinite Globules and Sulphides

Like with its TCIs, Murr_Blank's tochilinite globules show textural similarities with experimentally heated Murchison. There is distinct fracturing as well as zoning within the tochilinite (Fig. 6.8a). There are sulphides within these tochilinite globules, however they are P-bearing and therefore are likely unrelated to post-hydration heating.

Murr_200's tochilinite is distinctly different from both Murr_Blank and any of the heated Murchison samples. The tochilinite is homogeneous in composition yet has large distinctive dehydration fractures. The edges of the tochilinite have small amounts of oxides that occurs in a morphology atypical for CM chondrites (Fig. 6.8b), which could be a result of terrestrial weathering. Although Murray is a fall, it fell in 1950 (Horan 1953) and Earth's atmosphere is oxidizing; reducing phases, like tochilinite, will oxidize over time.

Murr_400's tochilinite starts to show the distinct zoning displayed by the Murchison samples. However, unlike the heated Murchison samples, the fractures within the tochilinite are much larger and prevalent (Fig. 6.8c).

Murr_600 doesn't show distinct tochilinite globules, however along the edges of chondrules, there are distinct patches of fine-grained sulphides that may have resulted from tochilinite decomposition (Fig. 6.8d). Murr_700 shows sulphides that are also quite fine-grained but occur in a different texture, and are porous where they are rich in Ni, indicating the decomposition of pentlandite (Fig. 6.8e). Like with Murr_600 and Murr_700, where tochilinite may have been is difficult to identify in Murr_800. However, kamacite is often

rimmed by troilite (Fig. 6.8f), likely the result of tochilinite recrystallizing into troilite. This pattern persists in Murr_1000 (Fig. 6.8g).

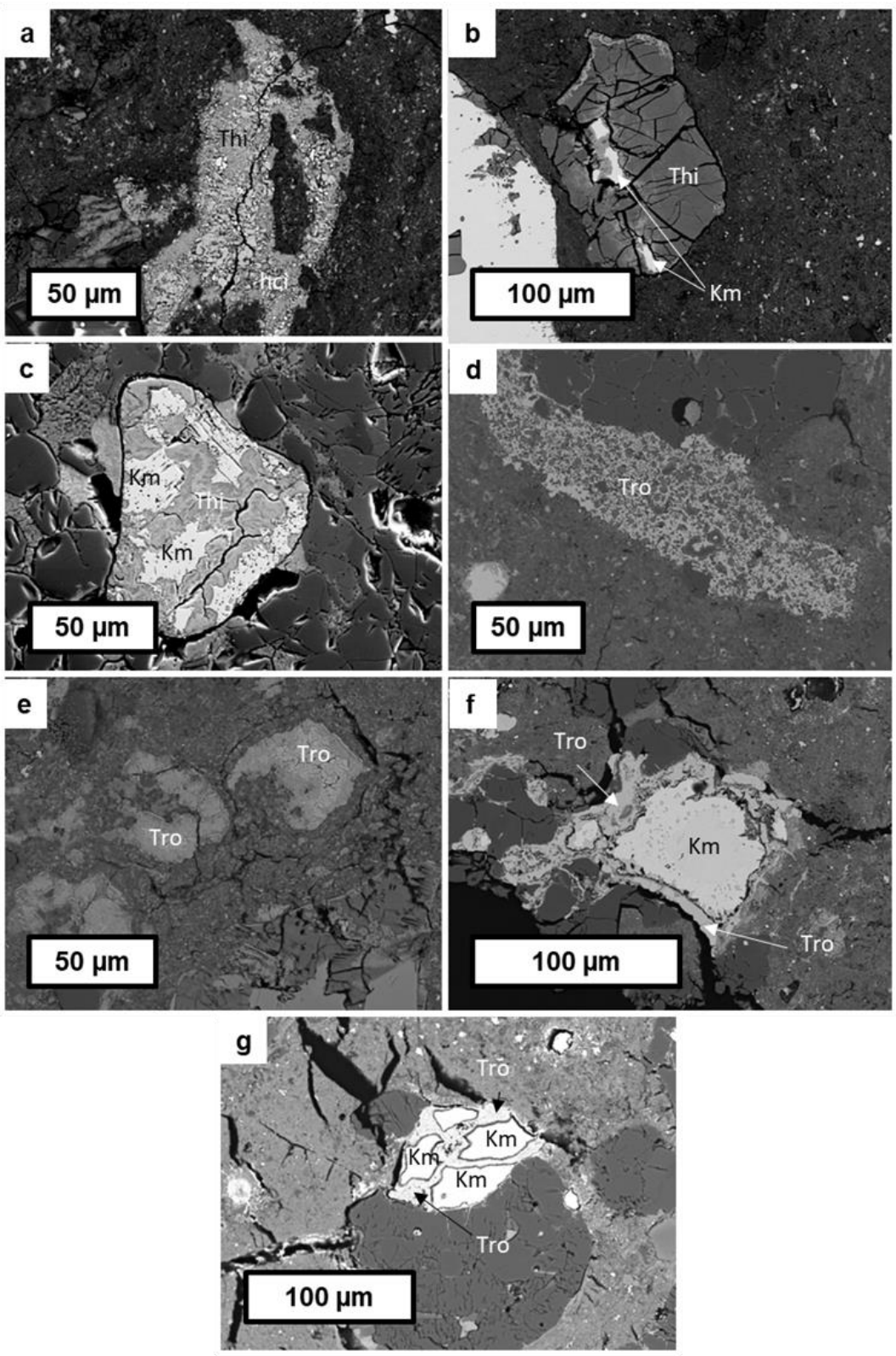

Fig. 6.8. Images of tochilinite (Thi) globules in unheated and experimentally heated Murray samples showcasing changes. Thi is an alteration product of kamacite (Km). Thi decomposes and recrystallizes into troilite (Tro). a) BSE image of Murr_Blank. b) BSE image of Murr_200. c) SE image of Murr_400. d) BSE image of Murr_600. e) BSE image of Murr_700. f) BSE image of n Murr_800. g) BSE image of Murr_1000.

6.1.2.4 Olivine Diffusion

Like with the heated Murchison samples, olivine within the heated Murray samples does not show any diffusion at the scale at which EDS data was collected. It is again likely that if olivine diffusion occurred, it was at a scale too small to be observed.

6.1.2.5 Calcite

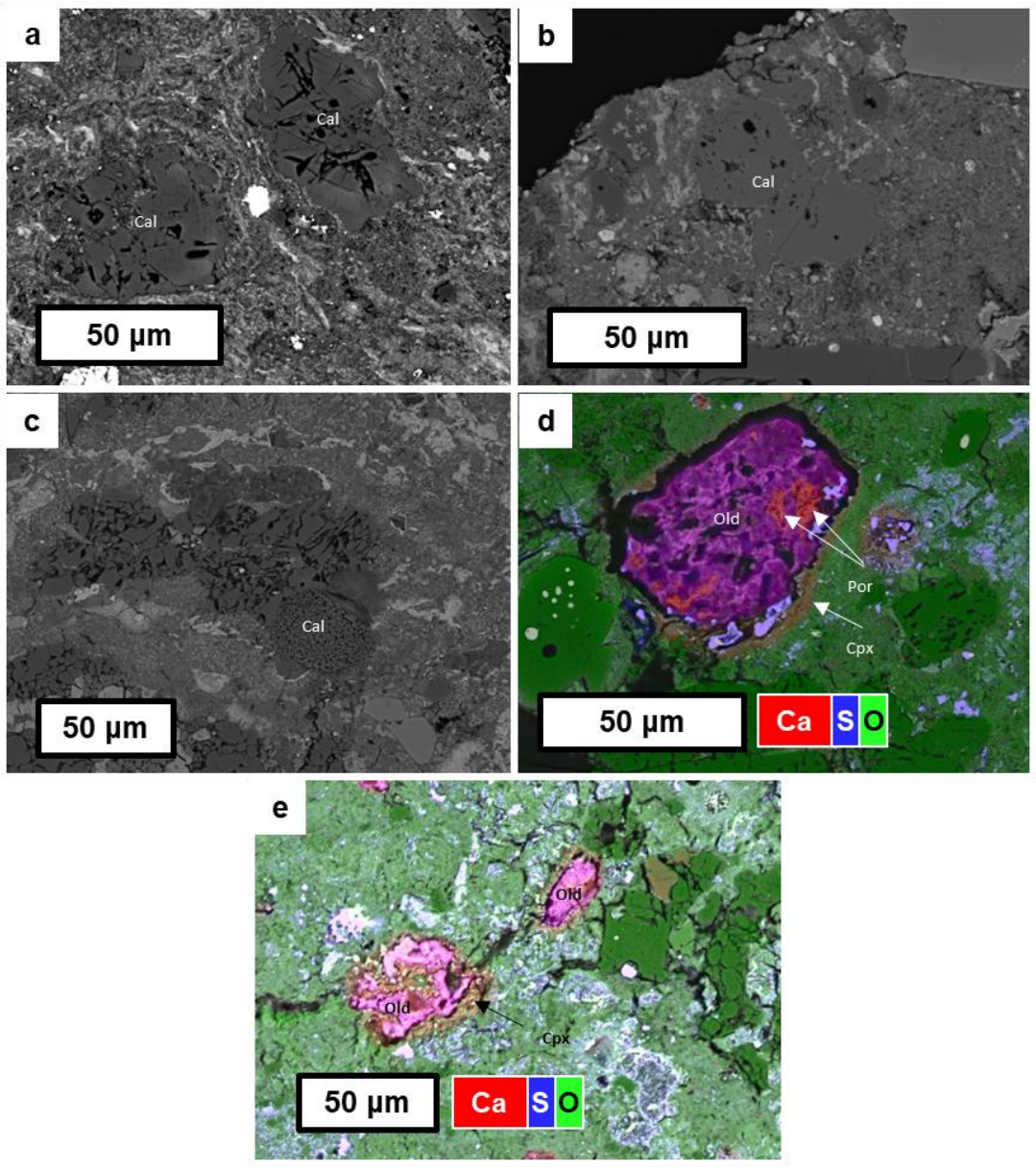

Fig. 6.9. Images showcasing calcite (Cal) decomposition in experimentally heated Murray samples. a) BSE image of Cal in Murr_400. b) BSE image of Cal in Murr_600. c) BSE image of Cal in Murr_700. d) Ca-S-O EDS map of decomposed Cal, portlandite (Por), oldhamite (Old), and clinopyroxene (Cpx) in Murr_800. e) Ca-S-O EDS map of Old and Cpx in Murr_1000.

The calcite in Murr_Blank, Murr_200, and Murr_400 are all large grains, usually ~50 µm in size, showing fracturing which may be due to terrestrial weathering (Fig. 6.9a). Their texture is subhedral to anhedral.

Calcite starts to show signs of decomposition at 600°C, where in Murr_600 it becomes more porous independent of fracturing (Fig. 6.9b). This decomposition progresses with increasing temperature and in Murr_700, calcite begins to show a wormy texture (Fig. 6.9c).

By 800°C, calcite has mostly decomposed into a mixture of portlandite ($Ca(OH)_2$), oldhamite, and clinopyroxene (Fig. 6.9d). In Murr_1000 calcite has completely decomposed and much of it has been replaced by oldhamite. The oldhamite grains are often rimmed by clinopyroxene (Fig. 6.9e).

6.1.3 Winchcombe

Winchcombe is a brecciated CM chondrite whose clasts vary considerably in alteration level, with petrologic types ranging from 2.0-2.6 (Suttle et al. 2022). A sample of Winchcombe was heated at up to 1100°C over a time period that was at least 3.5 hours long for a separate study (King, Daly et al. 2022). It spent at least 30 minutes at each of the following temperature steps: 100°C, 200°C, 300°C, 400°C, 700°C, and 1100°C (King, Daly et al. 2022). This sample is composed of six lithologies.

6.1.3.1 Winchcombe heated up to 1100°C

In the experimentally heated Winchcombe samples, there is extensive fracturing, with some clasts showing higher degrees of fracturing than others (Fig. 6.10). The clasts that show a higher degree of fracturing tend to have more chondrules, and therefore more FGRs, wherein many of the fractures are concentrated. The FGRs themselves are difficult to identify, often blending in with the matrix.

In BSE images, TCIs in the heated Winchcombe samples are still distinguishable from the serpentine matrix, however textural features within their interiors are unobservable. They are identified as uniform S-rich masses (Fig. 6.11a). In reflected light, TCIs are bright with a golden sheen, almost comparable to sulphides (Fig. 6.11b).

Fig. 6.10. BSE map of thin section 3 of the heated Winchcombe samples. Clast boundaries are marked in yellow. A small portion of the numerous fractures are labelled with white arrows. Some clasts show a higher degree of fracturing than others.

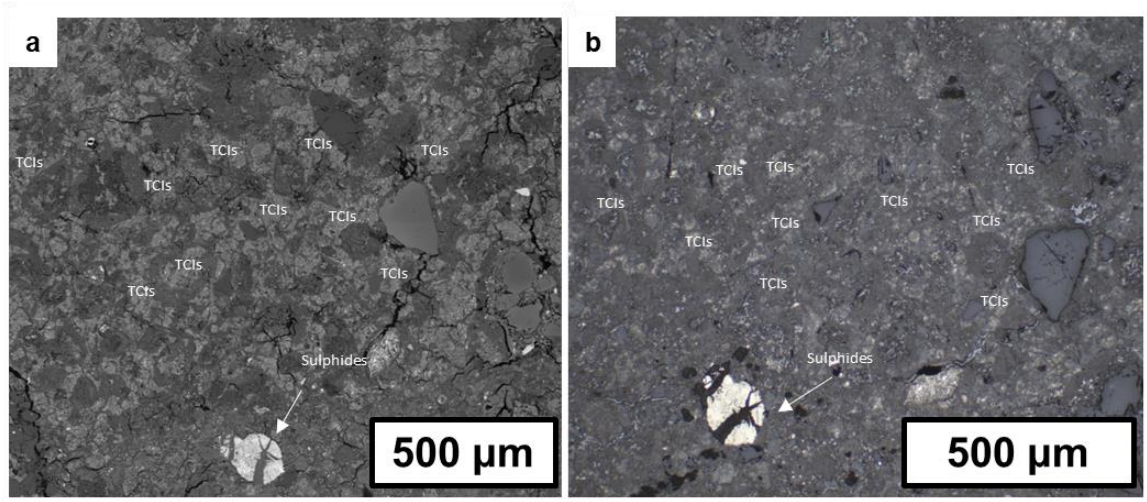

Fig. 6.11. TCIs in same area in thin section 1 of the heated Winchcombe samples. a) BSE map of TCIs. They are discernible from the matrix, however they lack clear textural features. b) Reflected light image of TCIs. They are bright with a golden sheen, however they still have a lower reflectivity than that of sulphides formed through aqueous alteration and metal.

Olivine shows no sign of diffusion on a micron scale.

The calcite within all samples has decomposed to portlandite, which was identified based by its lack of C and porous texture. The portlandite has rims ~5 µm thick of oldhamite (Fig. 6.12). Sulphides, when present, also show signs of decomposition with pentlandite often showing a porous, vein like texture (Fig. 6.13).

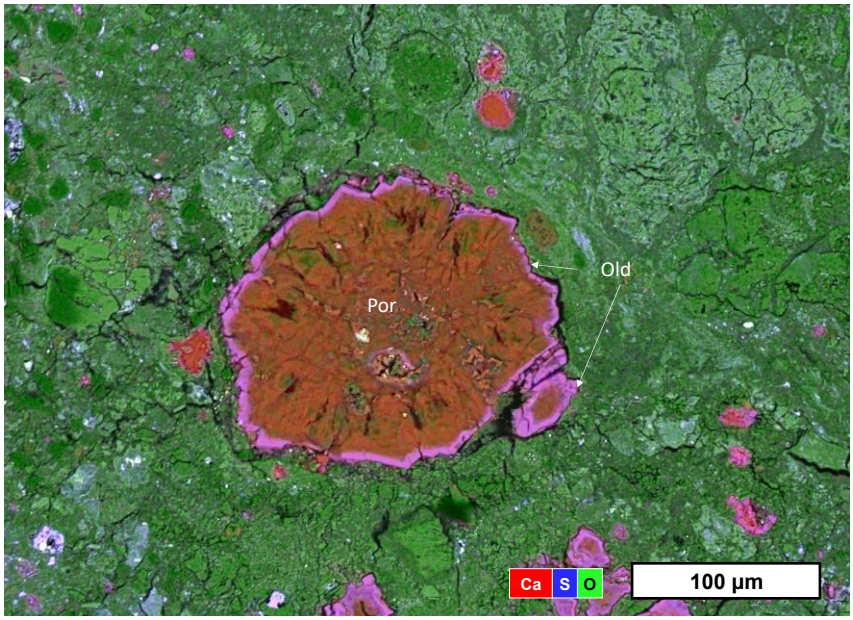

Fig. 6.12. Ca-S-O EDS map of portlandite (Por) with rims of oldhamite (Old) from thin section 1 of the heated Winchcombe samples.

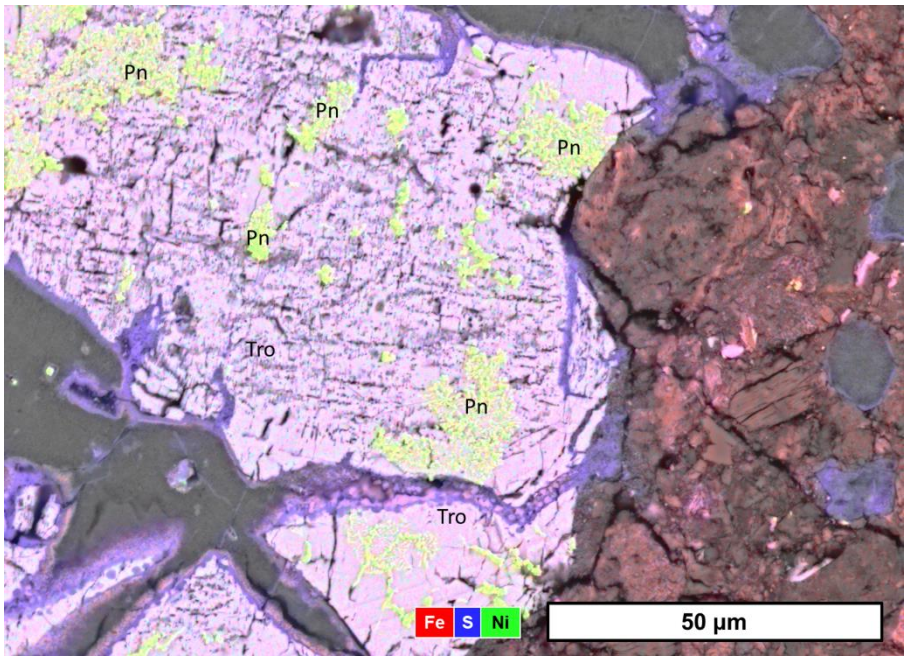

Fig. 6.13. Fe-S-Ni EDS map of sulphides in thin section 1 of the heated Winchcombe samples. Pentlandite (Pn) shows vein like texture and appears to be in the process of decomposing within the fractured troilite (Tro).

6.2 Key Features of Different Temperature-Timescales

Although these experimentally heated samples cover a broad range of temperatures (200-1100°C), they cover short timescales (hours to days). This is important to note as although certain features may appear at higher temperatures (e.g., secondary anhydrous phases), it is entirely possible for them to occur at lower temperatures at longer timescales (Nakato et al. 2008). However, when considered, there are patterns observed, especially when timescale is varied. For example, fractures may widen with increasing temperature, however their proliferation seems to be dependent on a combination of timescale and starting lithology. A summary of key petrographic features observed at each temperature are given in Table 6.1.

6.3 Naturally Heated Meteorites

The experimentally heated samples (heating effects summarized in Table 6.1) were compared to eight naturally heated meteorites to estimate both the temperatures and timescales these meteorites have experienced. These estimates are based on qualitative observations and are not precise, but rather a general means of understanding the degree of post-hydration heating experienced by these samples.

6.3.1 Kolang's Heated Clasts

Kolang is a CM2.2 chondrite (King et al. 2021a) made up of numerous clasts, two of which shows signs of post-hydration heating. Their matrix has prevalent fracturing, with fractures in FGRs up to 4 μm in width. The clasts have little tochilinite, yet many sulphides compared to other clasts. The tochilinite available is fractured and/or porous (Fig. 6.14). In BSE images, TCIs show distinct zoning with bright laths of sulphides, while under reflected light they are bright with distinct golden grains of sulphides among them (Fig. 6.15). The calcite within these heated clasts appears to be intact. Coarse-grained sulphides are observed throughout the clast.

Kolang shows extensive fracturing, however these fractures are not as wide as those displayed by samples heated to 400°C. Kolang is unlikely to have

Table 6.1. Post-hydration heating effects and their variation with temperature. Based on this study's observations with experimentally heated samples.

Temperature	Feature	Variation with Timescale	Variation with Temperature
200°C	TCIs brighten under reflected light.	TCIs will brighten more significantly as heating duration increases.	TCIs will brighten as temperature increases.
200°C	Tochilinite globules show dehydration cracks and zoning.		Dehydration cracks widen and zoning becomes more distinctive until 500°C.
300°C	TCIs will begin to show zoning in BSE images.		
400°C	Fractures greater than 2 μm in width occur.	Fracture density will increase as heating duration increases.	Fracture width will increase as temperature increases
500°C	Fractures in tochilinite globules start to close. Tochilinite globules become more uniform in colour.		
600°C	Calcite becomes more porous as it starts decomposing into portlandite.		Calcite porosity will increase with temperature.
700°C	Pentlandite begins decomposing.		
800°C	Oldhamite and clinopyroxene form from decomposed calcite.	Oldhamite thickness will increase with heating duration.	Oldhamite thickness will increase with temperature.
1000°C	TCIs and FGRs begin blending in with serpentine matrix.	TCIs and FGRs become less distinguishable with increased heating duration.	

been heated to 400°C, which is congruent with the conclusions of Chapter 4, wherein it was found that Kolang had EPMA data from serpentine consistent with being heated at temperatures below 400°C. However, the fracturing present does seem to indicate that these clasts have experienced heating to some level. The low abundance of tochilinite and the high abundance of coarse-grained sulphides may be an indicator of tochilinite decomposition, especially given the

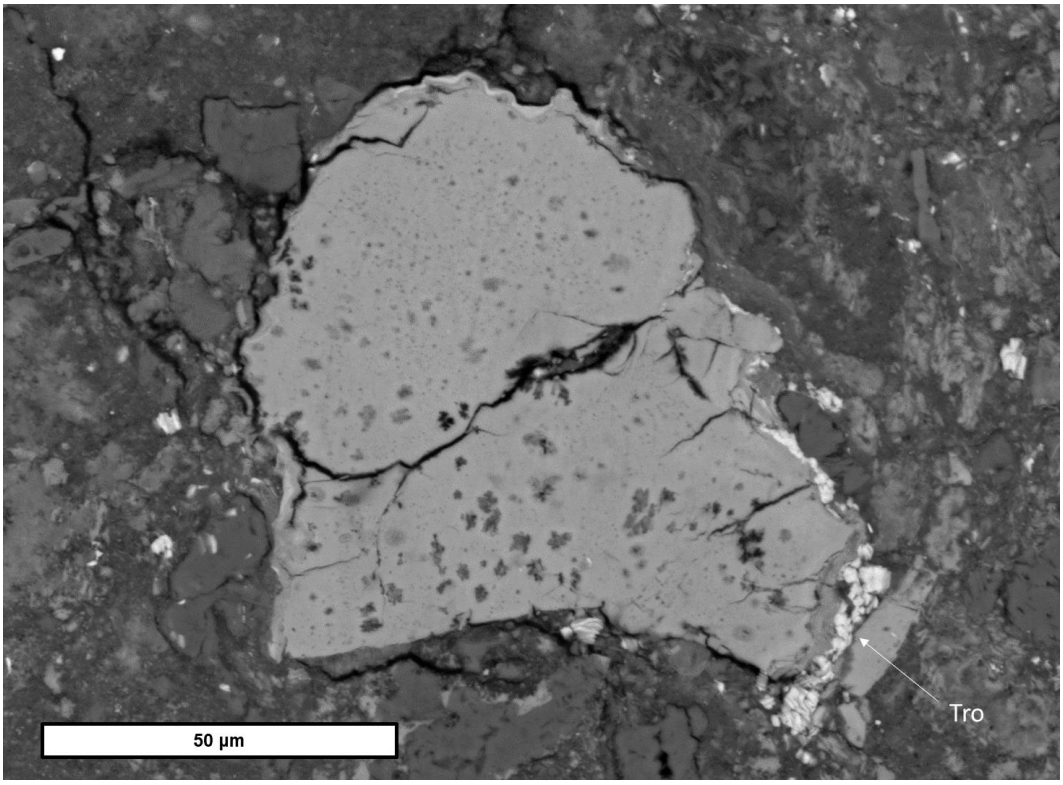

Fig. 6.14. BSE image of porous tochilinite in Kolang. Some fine-grained troilite (Tro) lines its rim.

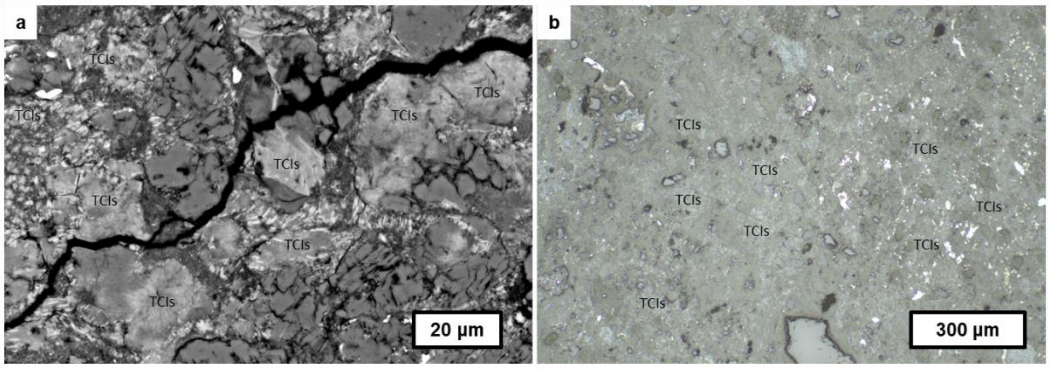

Fig. 6.15. TCIs in the heated lithology of Kolang. a) BSE image of TCIs showing bright lathes of sulphides. b) Reflected light image of TCIs, showing them bright with small grains that appear golden under reflected light.

porous nature of what tochilinite is present (Fig. 6.14). Kolang must have experienced heating at temperatures of at least 210°C (See Chapter 5) of heating to achieve this. It is estimated that Kolang experienced heating of 210-400°C, though the timescale is unknown. The heated clasts of Kolang are either of a high heat stage I or a low heat stage II. If the abundant sulphides are the result of post-hydration heating, then the timescale is likely greater than 8 days, as no coarse-grained secondary sulphides were observed in M_500_8.

6.3.2 MacAlpine Hills 88100

MacAlpine Hills 88100 (MAC 88100) is a CM chondrite reported to have experienced moderate post-hydration heating (e.g., heat stage II; Quirico et al. 2018). The thin section studied is composed of nine clasts spanning two lithologies, the TCI-rich lithology and the matrix-rich lithology; the TCI-rich lithology was less aqueously altered than the matrix-rich lithology. Both clasts appear to have experienced similar degrees of heating. Fractures within FGRs are about 10 μm wide. There are no remnant tochilinite globules, however large aggregates of coarse-grained sulphides (~10 μm in size) are present (Fig. 6.16). Pentlandite is intact. In BSE images, TCIs show distinct zoning (Fig. 6.17a). In reflected light, TCIs are bright, a golden-grey in colour (Fig. 6.17b). There is calcite within MAC 88100, however it is porous, indicating that it is partially decomposed. No oldhamite was observed.

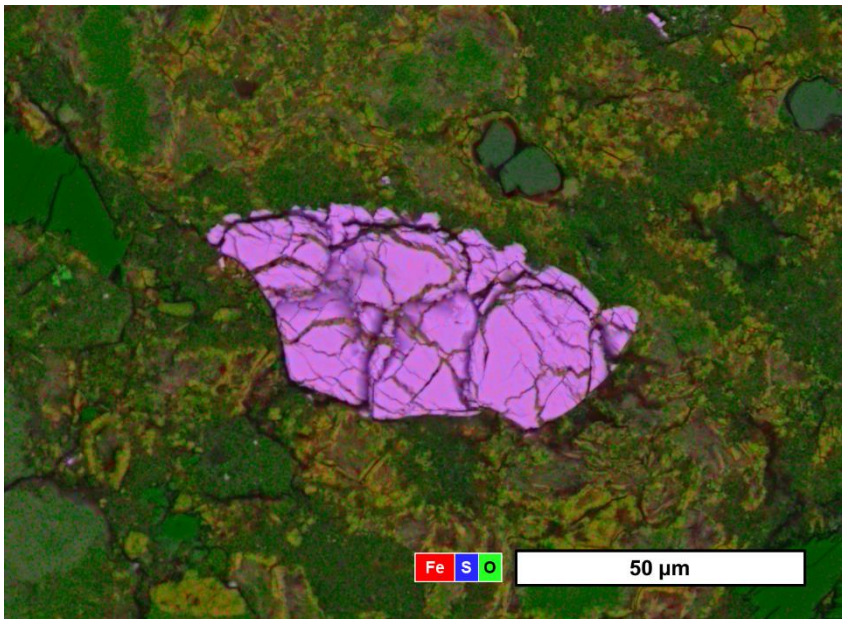

Fig. 6.16. Fe-S-O EDS map of sulphides in MAC 88100. They are typically coarse grained (~10 μm). No tochilinite is observed. It is unknown if these sulphides resulted from aqueous alteration or post-hydration heating.

The partially decomposed calcite and intact pentlandite indicates that MAC 88100 likely experienced ~600°C of heating, putting it into heat stage III (Nakamura 2005). As there is a lack of tochilinite globules, but an abundance of sulphide aggregates, it is possible that these sulphide aggregates originated from these tochilinite globules. If so, the heating MAC 88100 experienced would have taken place on a scale longer than that of a day, likely on the order of a few days.

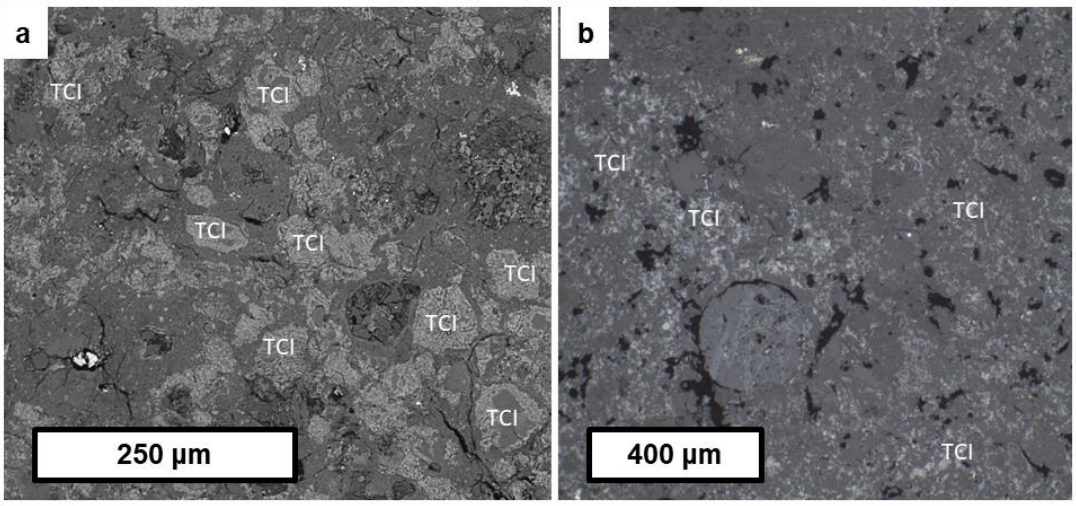

Fig. 6.17. TCIs in the matrix of MAC 88100. a) BSE image of TCIs showing separation between silicates and sulphides. b) Reflected light image with TCIs that have components with varying reflectivity, fluctuating between grey and gold.

6.3.3 Pecora Escarpment 02012

Pecora Escarpment 02012 (PCA 02012) is a completely anhydrous CM chondrite that shows evidence for post-hydration heating (Quirico et al. 2018; Garenne et al. 2014). TCIs are absent and the matrix lacks identifiable phyllosilicate textures. Small nm sized sulphides are sprinkled throughout matrix (Fig. 6.18). PCA 02012 also shows compositional variation, with one part of the section being more Ni and S rich than the other, likely due to the past presence of clasts, however no clast boundaries are observable. FGRs are difficult to

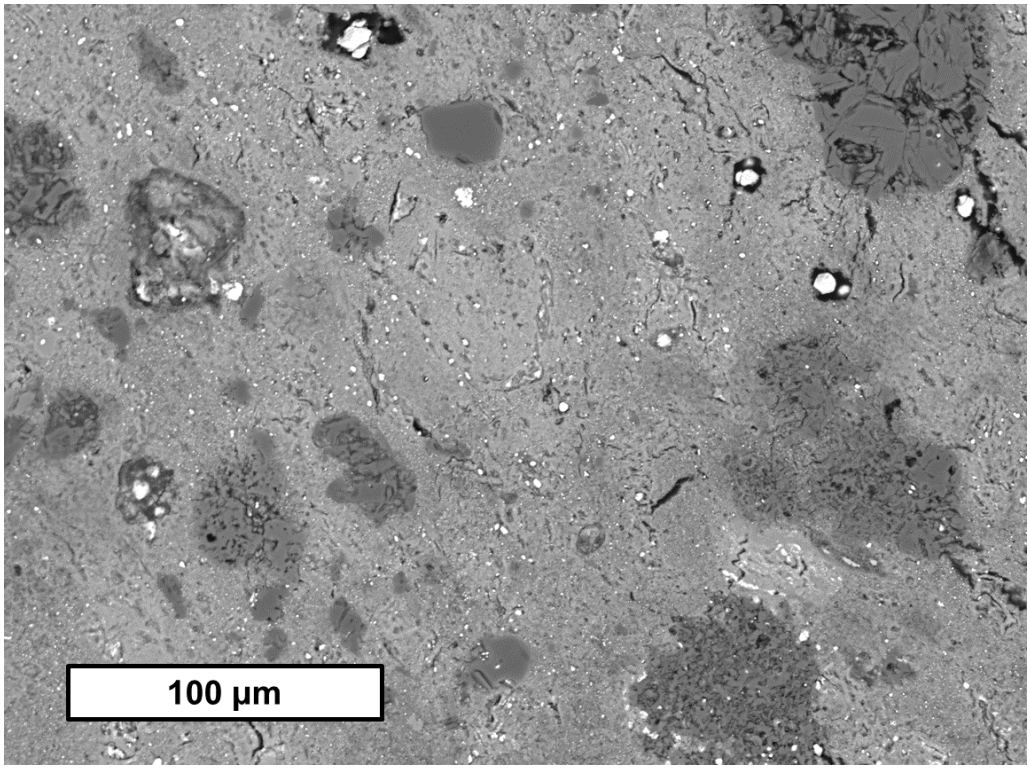

Fig. 6.18. BSE image of the matrix of PCA 02012. Distinctive TCIs are absent.

identify, with their boundaries blending in with the matrix. Fractures within FGRs are up to 40 μm wide. Remnants of tochilinite globules are identifiable within chondrules. They have dehydration cracks as well as secondary sulphides and oxides with nm to μm grain sizes (Fig. 6.19). Despite one part of PCA 02012 being more Ni rich than the other very few pentlandite grans were observed and those that were present were porous, showing signs of decomposition. No calcite was observed.

Samples heated up to 800°C typically still show evidence for the remnants of TCIs and still have easily distinguishable FGRs. Though there are no samples heated to 900°C to compare to, the complete erasure of TCIs and the blending of FGRs with the matrix is typical of samples heated to 1000°C. The complete absence of carbonates is supportive of this high temperature as calcite would have completely decomposed at those temperatures. Fracture widths within observable FGRs are similar to those observed within Murr_1000, so PCA 02012 likely experienced similar degrees of heating. The temperatures it could have been heated at are 800-1000°C, with ~900-1000°C being most likely. PCA 02012 is of heat stage IV (Nakamura 2005). Despite the absence of TCIs, remnants of tochilinite are still observable with small grain sizes for secondary sulphides. The heating PCA 02012 experienced is therefore likely shorter than that of the experimentally heated Murray and Murchison samples, probably on the order of hours. PCA 02012 having experienced ~900-1000°C of heating on a timescale of hours is consistent with Nakato et al.'s (2013) observations, where through

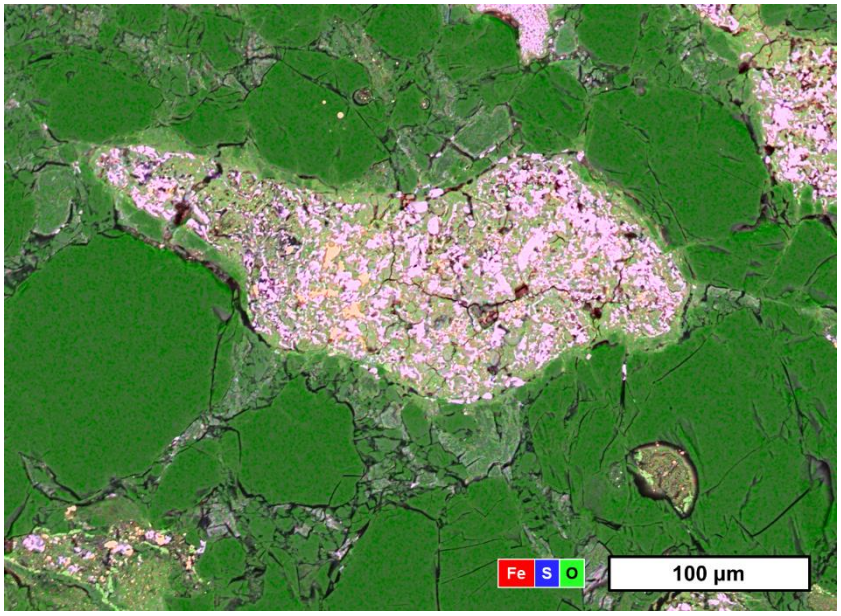

Fig. 6.19. Fe-S-O EDS map of the remnant of a tochilinite globule within PCA 02012 filled with small sulphides (pink) and oxides (orange). Recrystallization of sulphides has not completed.

studying olivine diffusion, they found that PCA 02012 likely experienced 900-950°C of heating with duration estimates ranging from 4-400 hours.

6.3.4 Pecora Escarpment 91008

Pecora Escarpment 91008 (PCA 91008) is a heated CM chondrite. It is composed of two clasts, which shows fractures up to 30 μm wide within their FGRs. The fractures are particularly prevalent in tochilinite globules which do show signs of recrystallization, albeit with crystals of extremely small size on the order of nm (Fig. 6.20). Its matrix is reported to have been completely recrystallized (Tonui et al. 2014) and its former TCIs appear to be uniformly divided into silicates and oxides, having the same brightness as coarse-grained sulphides under reflected light (Fig. 6.21). Pentlandite is not present in significant amounts. The meteorite is completely devoid of calcite.

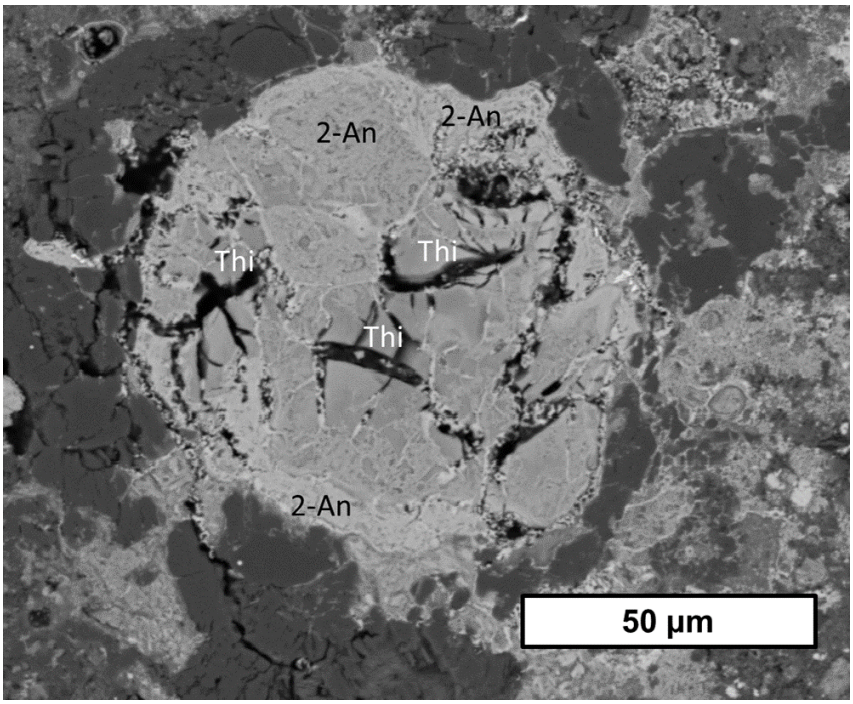

Fig. 6.20. BSE image of the decomposed remnant of a tochilinite (Thi) globule in PCA 91008. Dehydration fractures are prominent, while nm sized secondary sulphides and oxides (2-An) occur in a web-like structure.

Given the fine-grained nature of its recrystallization products, PCA 91008 likely experienced heating over brief durations (e.g., hours) at high temperatures, likely exceeding 700°C to account for the lack of calcite and pentlandite. To completely remove calcite over such a short duration, this heating was likely at least 800°C as Murr_700 still has remnants of its calcite. PCA 91008 is of Heat Stage IV, which is consistent with King et al. (2021b). Some literature sources have classified it as Heat Stage III due to poor crystallinity of

secondary olivine (Nakamura 2005; Tonui et al. 2014), however this poor crystallinity is likely due to a short duration of heating and not high temperatures.

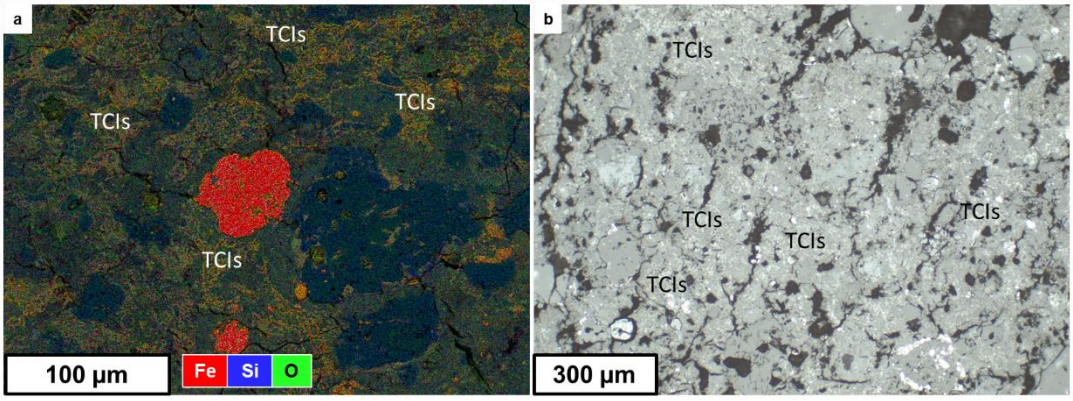

Fig. 6.21. TCIs in PCA 91008. a) Fe-Si-O EDS map of TCIs around some coarse-grained sulphides. They show distinct separation between silicates and oxides. b) Reflected light image of TCIs. They are extremely bright with a similar brightness as sulphides.

6.3.5 Pecora Escarpment 91084

Pecora Escarpment 91084 (PCA 91084) is a CM chondrite composed of two clasts, both of which have experienced post-hydration heating. There is extensive fracturing, with fractures within the FGRs up to 15 µm wide. No tochilinite globules were observed. Areas around kamacite are rimmed with oxides, like magnetite and akageneite, which are common weathering products

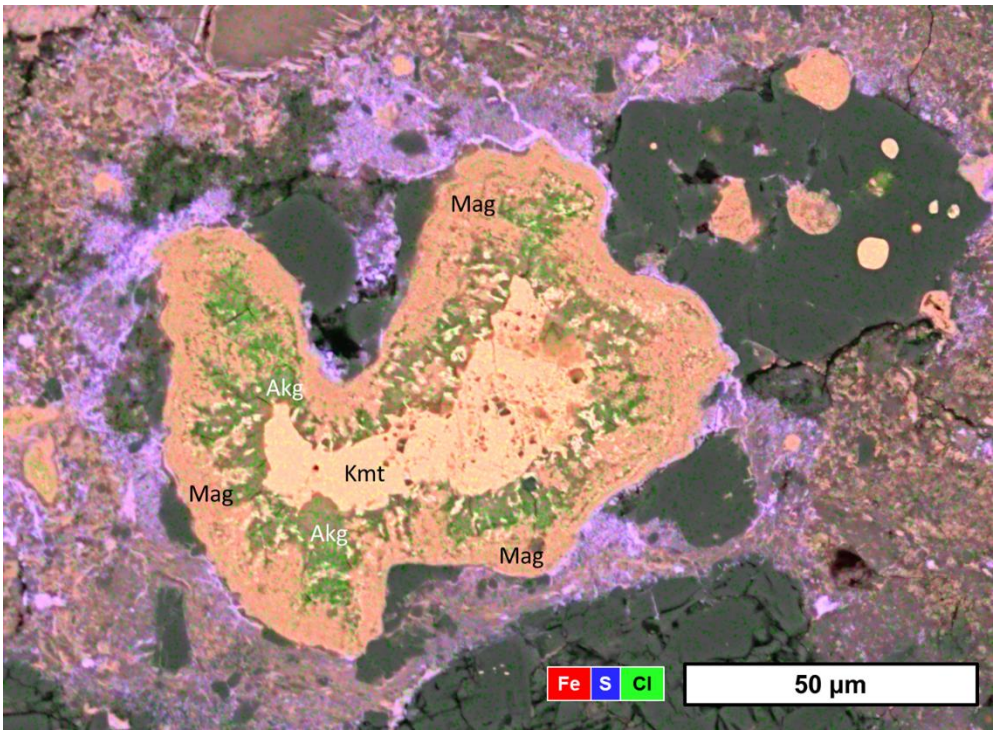

Fig. 6.22. Fe-S-Cl EDS map of magnetite (mag) and akageneite (Akg) rimming kamacite (Kmt) in PCA 91084. The Akg contains minor amounts of Cl. No tochilinite was observed.

of Antarctic meteorites (Lee & Bland 2004). Magnetite and akageneite are surrounded by sulphides (Fig. 6.22) and may be weathering products of an S-rich phase, however this has yet to be confirmed. Sulphides in PCA 91084 tend to be fine-grained (Fig. 6.23). In BSE images, TCIs show distinct compositional separation between silicates and sulphides. There is no calcite. There is very little pentlandite, with small remnants appearing to be partially decomposed (Fig. 6.23).

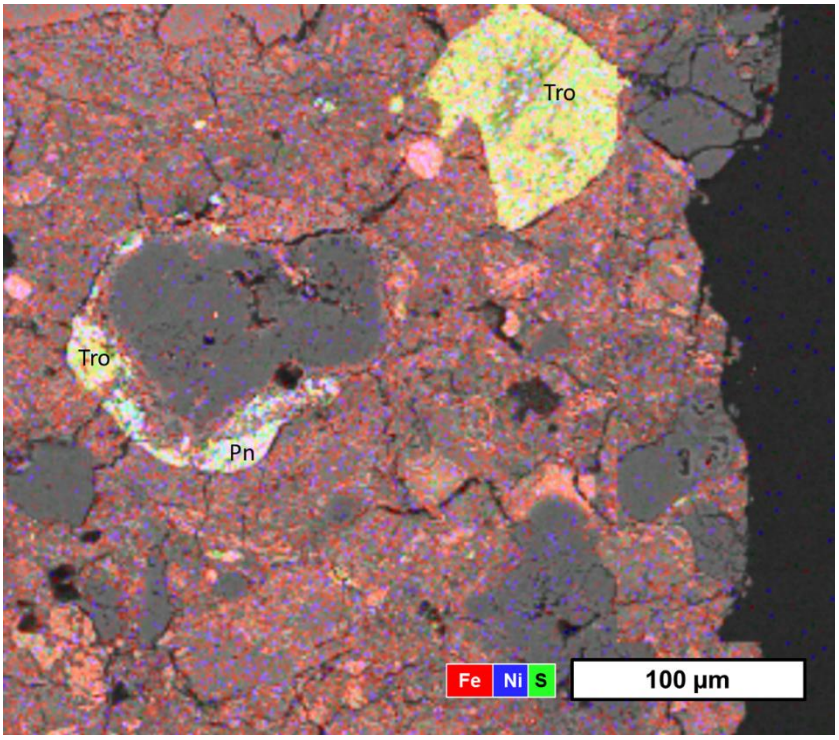

Fig. 6.23. Fe-Ni-S EDS map of a rare pentlandite (Pn) grain in PCA 91084. Troilite (Tro) is far more abundant in PCA 91084 and what little Pn there is appears to be associated with it.

The complete absence of calcite and relative lack of pentlandite indicates a minimum temperature of 610°C for PCA 91084's heating, putting it in a minimum Heat Stage of III, with a possibility of PCA 91084 being heat stage IV. Most of the sulphides observed were fine-grained with very few coarse euhedral grains. If any of these sulphides originated from the decomposition of tochilinite, then heating would have had to have been on the order of hours or days. The fractures within PCA 91084 are thinner than those in Murr_700. This may be due to differences in lithology. If PCA 91084 experienced heating on the order of hours, then it likely was heated to temperatures of at least 800°C to fully breakdown calcite. However, it is possible for PCA 91084 to experience heating at temperatures lower than 800°C for a duration on the order of days.

6.3.6 Shidian

Shidian is a CM2 chondrite (Fan et al. 2022). The polished section studied is composed of CM2.2 material from a single lithology. There is fracturing in the matrix and FGRs, however this fracturing is typical of unheated meteorites. Many of the tochilinite globules show prevalent dehydration fractures and often contain coarse grained sulphides, a mixture of pentlandite and troilite, that follow these dehydration fractures. The sulphides are ~3 µm in crystal size (Fig. 6.24). Shidian TCIs differ in morphology to Murray and Murchison, in that they are blockier and less fibrous, so a comparison to experimentally heated samples is difficult. However, they have a blocky texture with phases neatly separated (Fig. 6.25). Both calcite and pentlandite are abundant throughout Shidian and are intact.

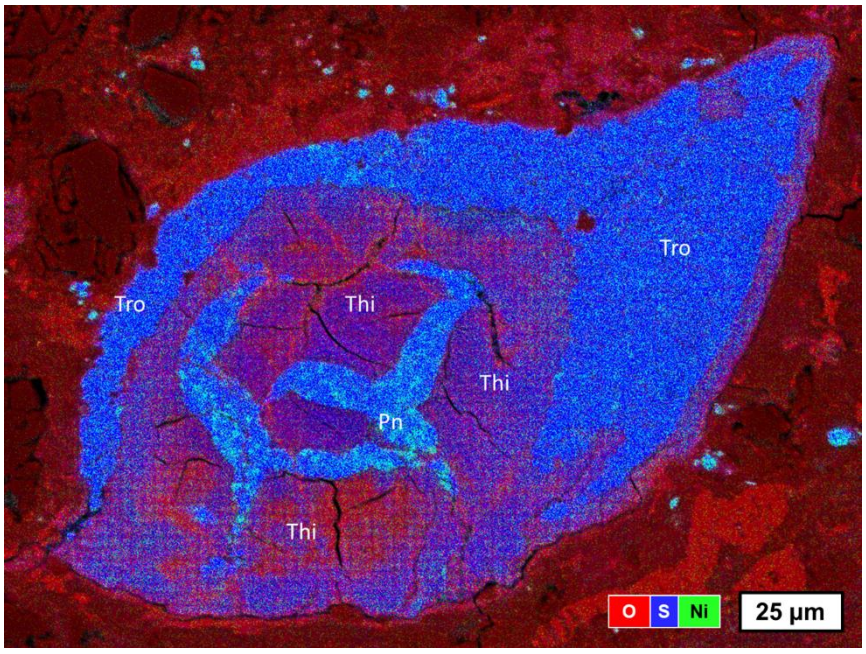

Fig. 6.24. O-S-Ni EDS map of a tochilinite (Thi) globule in Shidian. Dehydration fractures are prevalent and along these fractures are coarse-grained sulphides. Most of these sulphides are troilite (Tro), but a few are pentlandite (Pn).

Shidian's tochilinite shows signs of decomposition and recrystallization into sulphides, while its serpentine is likely intact, with a lack of fractures or any other petrographic indicators of heating. This indicates that it experienced at least 200°C of heating, likely greater than 210°C, as a minimum temperature of 210°C is required for the mackinawite layers in tochilinite to recrystallize (Sarkar 1971; See Chapter 5.5.4). However, because Shidian's serpentine shows no signs of decomposition, it likely has not experienced more than 300°C of heating. This puts it into Heat Stage I, with the temperature experienced being 210-300°C. In regard to heating duration, Shidian's sulphides from tochilinite

decomposition are distinctive and coarse grained, indicating that it must have been heated for a long time – more than eight days as not even M_500_8 shows secondary sulphides this coarse. Shidian likely experienced 210-300°C of heating over a duration of several days, possibly for weeks.

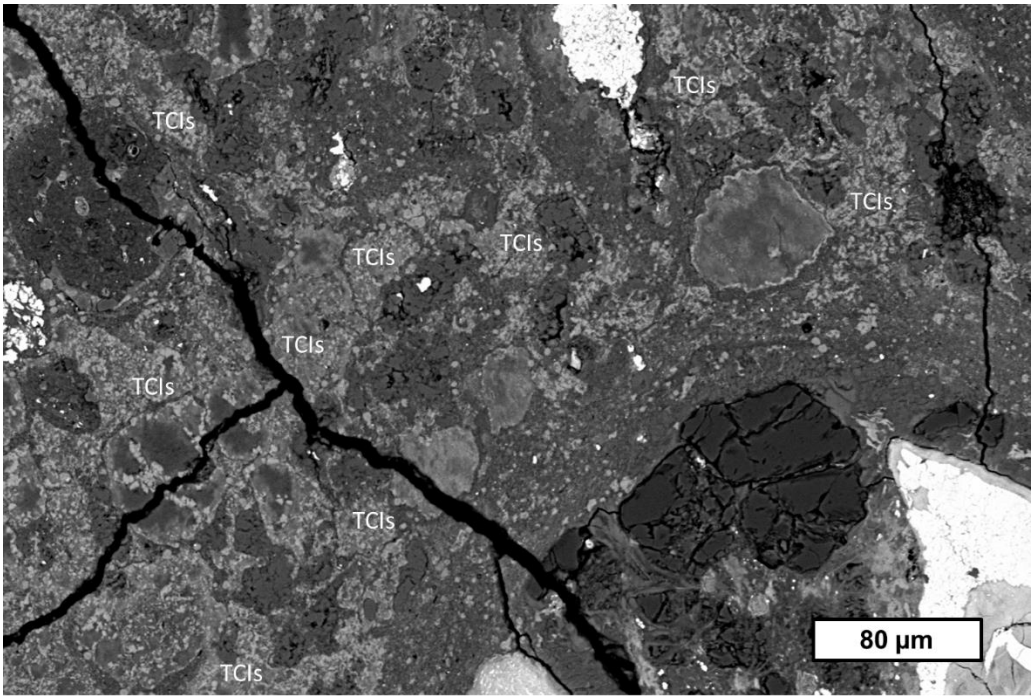

Fig. 6.25. BSE image of TCIs within Shidian. They have a blocky texture that differs from the fibrous texture displayed by the other meteorites studied (e.g., Fig. 6.2, Fig. 6.7).

6.3.7 Sutter's Mill

Sutter's Mill is an ungrouped carbonaceous chondrite composed of a variety of clasts, most of which are CM chondrite material. One of its clasts bears oldhamite rimming portlandite, a sign of post-hydration heating (Zolensky et al. 2014; Haberle & Garvie 2017). A polished section of Sutter's Mill (SM3) was studied. Carbonaceous chondrite material and its decomposed remnants were observed throughout the polished section. These included chondrule pseudomorphs composed of secondary anhydrous silicates and sulphides, porous magnetite in the midst of decomposition (Fig. 6.26), and numerous decomposed carbonates. The decomposed carbonate remnants include grains of pure oldhamite up to 50 µm in size, portlandite with oldhamite rims up to 5 µm thick, and a Mg-Ca-S-O phase (Fig. 6.27a). The portlandite within Sutter's Mill is often porous and occasionally contains enrichments in Cl (Fig. 6.28b). In some cases, the portlandite and oldhamite are zoned (Fig. 6.27b).

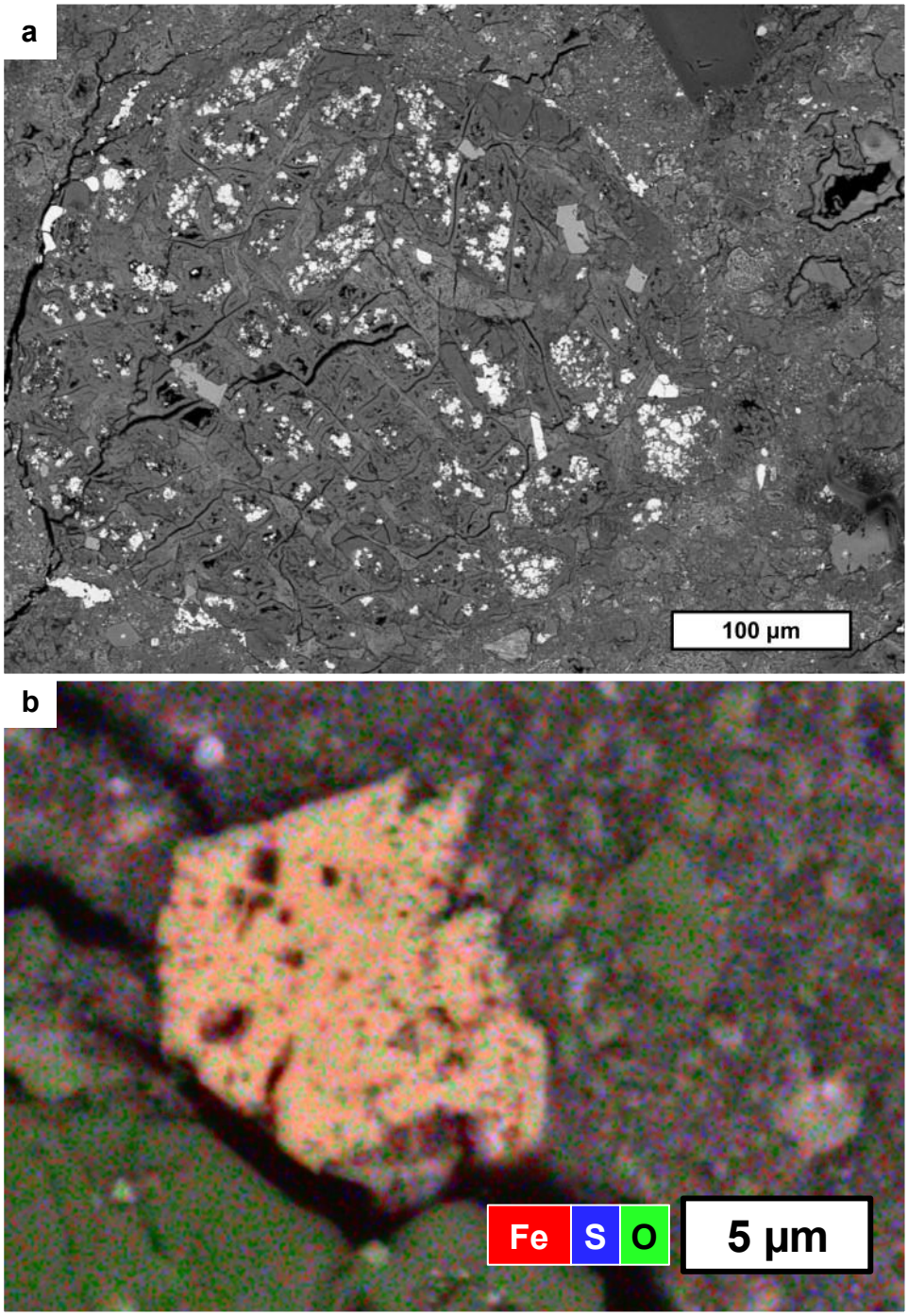

Fig. 6.26. General petrography of Sutter's Mill. a) BSE image of a chondrule pseudomorph in Sutter's Mill. It is composed of secondary silicates and sulphides. b) Fe-S-O EDS map of a pentagon of porous magnetite in the midst of decomposition due to heating.

The decomposed carbonates and their products in Sutter's Mill come in a variety of morphologies, indicating a complex alteration history prior to heating. Many of the decomposed carbonates were originally calcium carbonates, as that is evidenced by the abundant portlandite, which requires calcium carbonate as a precursor (Haberle & Garvie 2017). However, the Mg-Ca-S-O material observed is likely the remnants of dolomite. Some grains of oldhamite and portlandite are anhedral, while others are sub to euhedral, forming distinct hexagons. Some of

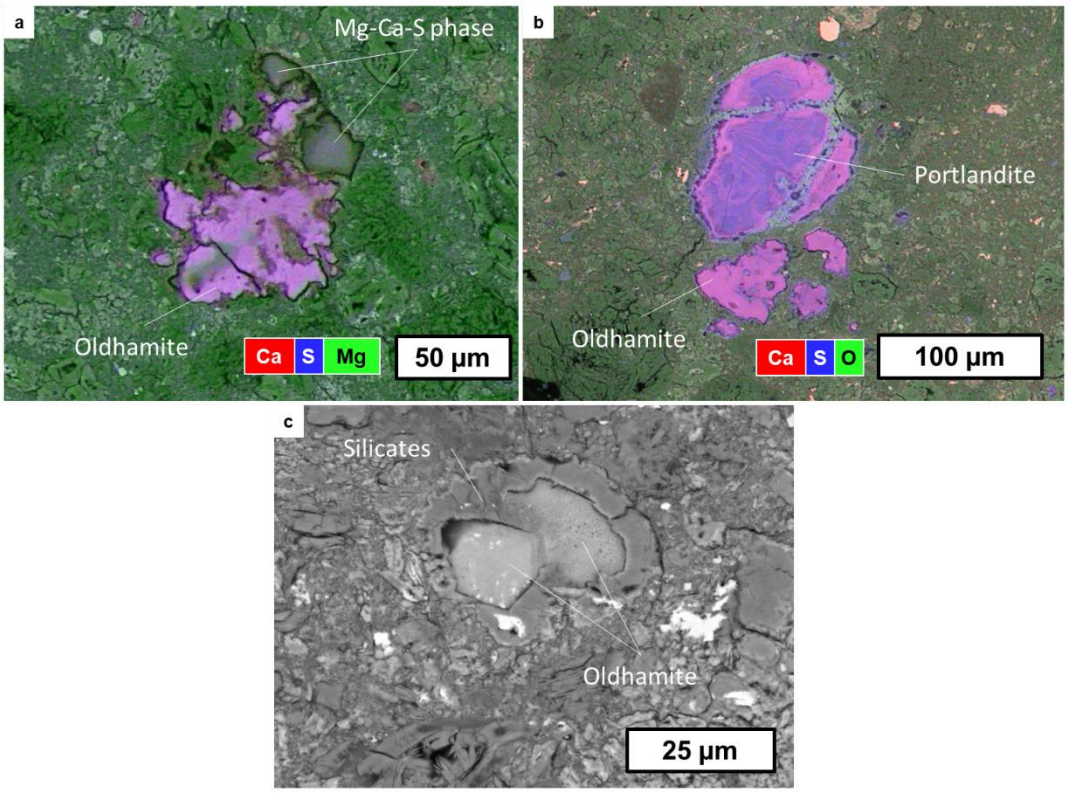

Fig. 6.27. Examples of oldhamite in Sutter's Mill. a) Ca-S-Mg EDS map of oldhamite and an Mg-Ca-S phase. b) Ca-S-O EDS map of a zoned assemblage of oldhamite and portlandite. c) BSE image of hexagonal oldhamite rimmed by silicates. These silicates were likely serpentine prior to post-hydration heating.

these decomposed carbonates are rimmed by silicates, likely the remnants of serpentine (Fig. 6.27c). Occasionally, these carbonates are associated with sulphides other than oldhamite. There is one notable instance, originally described by Haberle & Garvie (2017), of a large 500 µm assemblage of mainly portlandite, oldhamite, and pentlandite (Fig. 6.28). The portlandite is quite porous and has a ~5 µm rim of oldhamite. Like much of the portlandite throughout Sutter's Mill, it has minor amounts of Cl, with the highest concentration close to the oldhamite (Fig. 6.28b). Other grains of portlandite within Sutter's Mill also have this Cl enrichment, though it is not as pronounced as it is in this large assemblage. The pentlandite, although not occurring in veins, has a vein-like texture with dendrites intruding into the oldhamite-portlandite core of the assemblage. There is an enrichment of oxygen on the rims of the pentlandite intruding into the oldhamite-portlandite core, potentially magnetite (Fig. 6.28c).

Sutter's Mill is a complex carbonaceous breccia, with much of its material being that of CM material. The thermally metamorphosed material of polished section SM3 bears similarity to CM chondrites: it has chondrule pseudomorphs, chondrules, as well as the remnants of what was likely once tochilinite.

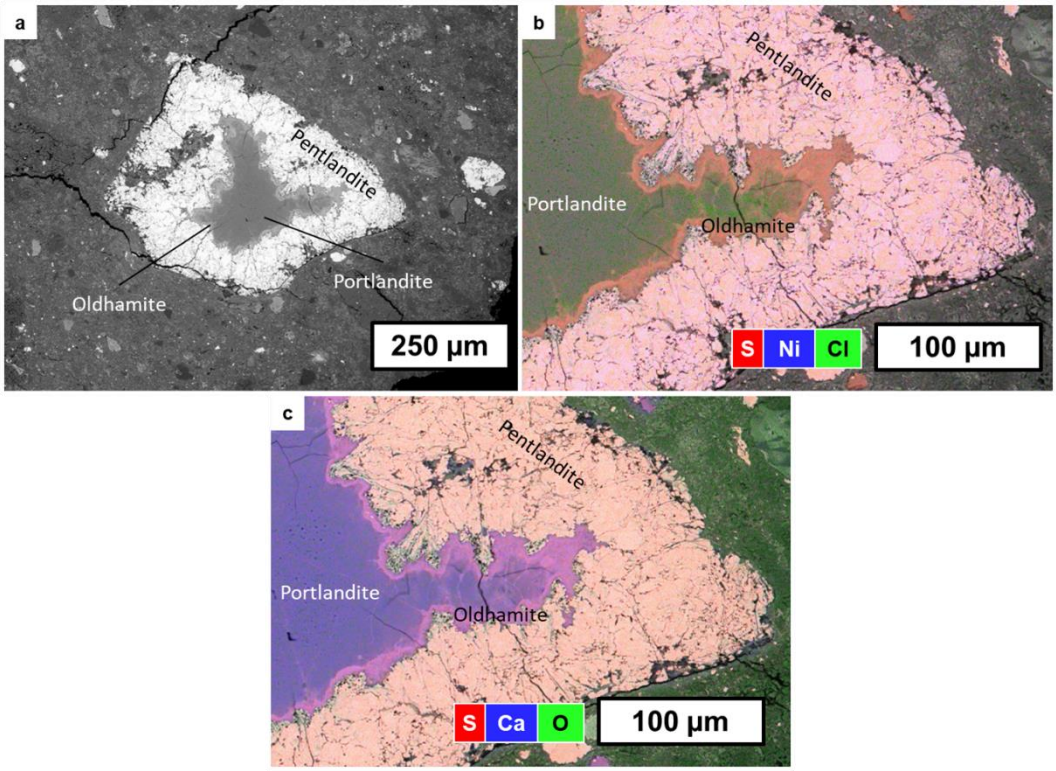

Fig. 6.28. Large portlandite, oldhamite, and pentlandite assemblage in Sutter's Mill. a) BSE image of the whole assemblage. b) S-Ni-Cl EDS map showing Cl enrichment in the portlandite, particularly close to the oldhamite. c) S-Ca-O EDS map showing oxides on the rims of the pentlandite dendrites intruding into the portlandite and oldhamite.

However, it also has aspects that are more similar to Ivuna-like carbonaceous (CI) chondrites: the remnants of dolomite being abundant as well as the presence of decomposing euhedral magnetite. It is likely that the starting material was neither a CM chondrite nor a CI chondrite, but rather an ungrouped carbonaceous chondrite that has affinities to both.

The 500 µm assemblage of portlandite, oldhamite, and pentlandite is the most distinctive assemblage within the sample, having an enrichment of Cl as well as thick rim of pentlandite intruding into the portlandite and oldhamite. The boundary between the pentlandite and oldhamite is rimmed with oxides. The precursor of the portlandite and oldhamite is most likely calcite, though aragonite is also possible. The pentlandite could have formed during aqueous alteration or by heating tochilinite.

The dendritic pentlandite intruding into the portlandite indicates that it or its precursor must have formed after the calcite. This sequence of events agrees with Haberle & Garvie's (2017) conclusion regarding the assemblage, who also deduced that the sulphides are a replacement rim. Although tochilinite may decompose and recrystallize into pentlandite (see Chapter 6.2.7), there is no

evidence that it does so in significant amounts, its primary decomposition products being troilite and/or magnetite (Fuchs et al. 1973; Lindgren et al. 2020). The pentlandite rimming this assemblage therefore is unlikely have formed by heating and thus is the product of aqueous alteration. Highly altered CM chondrites often have their carbonates replaced by sulphides, particularly Fe-Ni sulphides like pentlandite (Lee et al. 2014). This pentlandite in Sutter's Mill likely formed through a similar mechanism. The O-rich boundary between the pentlandite and the oldhamite is likely due to the decomposition of the calcite: S from the pentlandite is reacting with the Ca in the calcite to form oldhamite, while the remaining O is reacting with the Fe-Ni in the pentlandite.

The presence of Cl within portlandite is unusual, especially given that it has not been recorded in any of the experimentally heated samples, and is not typical of most of the other heat stage IV meteorites; PCA 91084 is the only other meteorite with notable distributions of Cl. The Cl in PCA 91084 has been attributed to a phase called akageneite (see Chapter 6.3.5). Sutter's Mill however, unlike PCA 91084, has its Cl enrichment within the remnants of calcite. It is more concentrated near the oldhamite, which likely indicates that it is incompatible with the oldhamite, but compatible with the calcite and portlandite. It is likely that during heating the Cl was expelled from areas of oldhamite formation, concentrating itself in the nearby portlandite. The Cl was likely present in the calcite prior to heating. Outside of bulk meteorite measurements, there are few studies on Cl in CM chondrites, however CI chondrites known to have a high Cl abundance relative to other carbonaceous chondrites, though the phases in which it occurs are unknown (Brearley & Jones 2018). The heated lithology of Sutter's Mill is not a CI chondrite but is similar to one. It is possible that, like CI chondrites, it has an inherent abundance of Cl with calcite bearing the Cl as an impurity. The decomposition of calcite into oldhamite has likely concentrated the Cl into its remnants, the portlandite, making the presence of Cl more apparent. However, more studies on Cl distribution in both CI and CM chondrites are needed to evaluate the validity of this hypothesis.

Magnetite was not present in the experimentally heated samples studied here, however other studies have observed it decomposing at temperatures greater than 900°C (Nakato et al. 2008). As the magnetite in Sutter's Mill shows

signs of the beginning stages of decomposition, it likely experienced ~900°C of heating, though the exact temperature is unknown. This thermal history is supported by the decomposed remnants of volatile rich phases, with calcite decomposing into oldhamite and phyllosilicates decomposing into anhydrous silicates. The abundance of sulphides in chondrule pseudomorphs may be from the decomposition of tochilinite. This heating temperature places Sutter's Mill into heat stage IV. Former grains of calcite up to 50 μm in size have completely transformed into oldhamite, while larger grains only show partial recrystallization with portlandite remaining. These mineral textures are somewhat similar to the experimentally heated Winchcombe samples which experienced gradual heating up to 1100°C over the period of a few hours, though the oldhamite rims in Sutter's Mill appear to be thicker than those in the heated Winchcombe samples. Sutter's Mill therefore likely experienced heating for longer durations than the heated Winchcombe samples, likely for around a day or a couple days.

6.3.8 Wisconsin Range 91600

Wisconsin Range (WIS) 91600 is an ungrouped carbonaceous chondrite. It bears similarity to CM chondrites in that it contains chondrules and has abundant alteration products, like serpentine, sulphides (pentlandite and troilite), and calcite. However, WIS 91600 lacks tochilinite and TCIs, but contains abundant magnetite, with magnetite-sulphide rosettes as well as framboids and plaquettes. The thin section studied is composed of a single lithology. WIS 91600 is fairly fractured, however this fracturing is most prevalent in the FGRs surrounding its chondrules and calcium-aluminium rich inclusions (CAIs). These fractures are up to 10 μm wide (Fig. 6.29). The calcite, magnetite, and pentlandite within WIS 91600 are all intact and show no signs of decomposition. Other studies of WIS 91600 have found that its matrix is decomposed, with a lack of volatiles and with transmission electron microscopy (TEM) images showing lattice spacings congruent with the transitional phase that forms during serpentine decomposition (Tonui et al. 2014; For more information on this transitional phase, see Chapter 5.6).

The width of fractures within WIS 91600 is most consistent with samples that have been heated to 400-600°C. The intact calcite indicates that WIS 91600 must have experienced less than 600°C. The transitional phase making up WIS

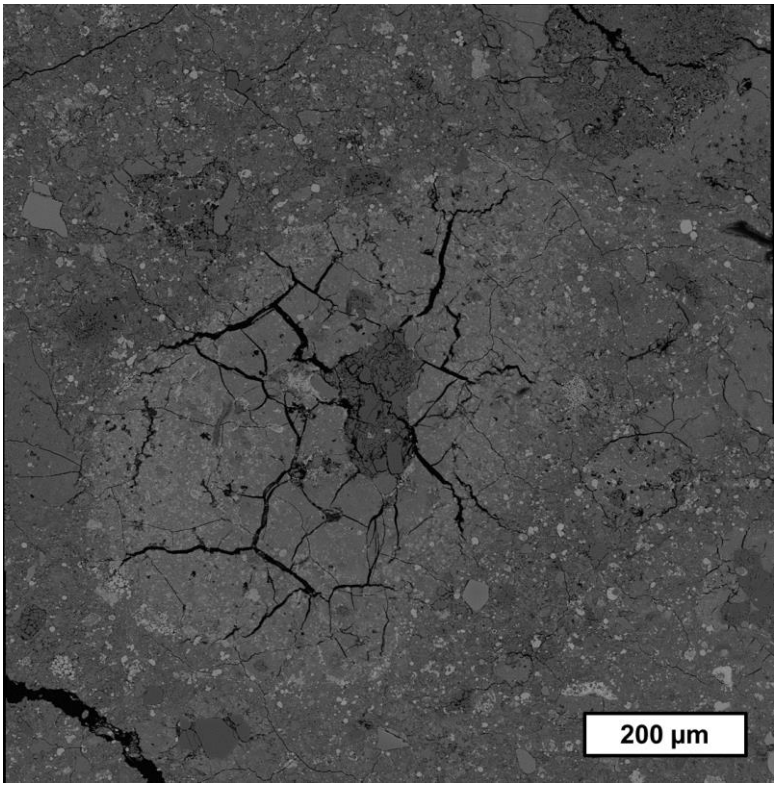

Fig. 6.29. BSE image of a chondrule within WIS 91600 showing extensive fracturing in its FGR. The matrix of WIS 91600 is also fractured, however its fracturing is not as prevalent.

91600's matrix (Tonui et al. 2014; King et al. 2021b) requires at least 500°C to form (Akai 1988), with the temperature it most readily forms at being ~525°C (see Chapter 5.6). Other studies have placed it into Heat Stage II due the lack of olivine in its decomposed matrix (King et al. 2021b), however the presence of this transitional phase requires a minimum temperature of 500°C (Akai 1988; Ball & Taylor 1963). To account for its mineralogy, WIS 91600 must be Heat Stage III, however it is likely a low Heat Stage III. The fracturing within WIS 91600 is prevalent in its FGRs, but are not extensive in the matrix, indicating that this heating was of short duration, likely on the order of hours.

6.3.9 Naturally Heated Sample Summary

Table 6.2. Summary of temperature-timescale estimates experienced by naturally heated samples.

Sample	Heating Temperature	Heating Duration
Kolang	210-400°C	Weeks
MAC 88100	~600°C	Days
PCA 02012	900-1000°C	Hours
PCA 91008	800°C≤	Hours
PCA 91084	610°C≤	Hours to Days
Shidian	210-300°C	Weeks
Sutter's Mill	~900°C	Days
WIS 91600	500-600°C	Hours

6.4 The Shock Metamorphism of Heated Meteorites

One of the proposed causes of post-hydration heating is impacts (Nakamura 2005). It is therefore reasonable to assume that if impacts are responsible, then heated meteorites should show signs of shock metamorphism. However, post-shock heating of carbonaceous material is not well understood. Laboratory experiments are limited in physical size and duration; they cannot accurately recreate post-shock temperatures (Kurosawa et al. 2021; Fritz et al. 2019). Whether or not carbonaceous material can be heated to high enough temperatures required for post-hydration heating while still remaining intact is unknown; there are modelling studies into the prospect, however, most have shown that post-shock heat dissipates within seconds or does not reach the required temperatures (e.g., Bland et al. 2014; Wakita & Genda 2019). Additionally, the few moderately shocked CM chondrites in the literature do show signs of localized elevations in temperature and pressure from pore collapse, such as melt veins, but do not show overall signs of post-hydration heating (Zolensky et al. 2022). However, there are still many unknowns (e.g., attenuation of force by pore collapse, how rubble pile asteroids affect heat dissipation) regarding how heat from an impact is transmitted through a carbonaceous chondrite parent body on a large scale. The absence of shock in heated meteorites by itself cannot disprove impacts as a mechanism for post-hydration heating. Nevertheless, based on proximity to the impacts that are possibly responsible for post-hydration heating, shocked meteorites should still be more likely to be heated than unshocked meteorites.

Traditional methods of evaluating shock metamorphism in meteorites involve searching for optical shock effects, such as undulatory and mosaic extinction (Stöffler et al. 2018). However, CM chondrites share a shock classification table with ordinary chondrites, despite them experiencing shock metamorphism differently. Due to their porosity, CM chondrites show changes in optical extinction displayed by olivine and pyroxene at slightly higher pressures than those of ordinary chondrites (Tomeoka et al. 1999). Despite this, the differences between CM chondrites and ordinary chondrites are small enough such that evaluation of optical extinction can still be applied to the evaluation of the peak shock pressures experienced. Additionally, CM chondrites may experience chondrule flattening and alignment in response to an impact, with

higher peak shock pressures causing more pronounced chondrule flattening and alignment (Tomeoka et al. 1999). If mineral shock effects are erased during post-hydration heating, chondrule flattening and alignment should still be observable as a shock effect.

To evaluate impacts as a potential cause for post-hydration heating, the heat stage of available samples was compared to their shock stages as determined optically, when thin sections are available, as well as to the degree of chondrule flattening and alignment in randomly cut polished meteorite thin and thick sections. If impacts are responsible for post-hydration heating, then more heated meteorites should either have higher shock stages and/or a greater degree of chondrule flattening than less heated meteorites.

6.4.1 Optical Shock Stages

Of the eight heated carbonaceous chondrites studied, five (Kolang, MAC 88100, PCA 02012, PCA 91008, and WIS 91600) are available as thin sections within which shock metamorphism can be evaluated optically. As clasts cannot be distinguished in transmitted light, they are treated as whole rocks, however it is important to note that clasts may display different degrees of shock. To evaluate the shock stages of these meteorites, the Stöffler et al. (2018) system is used, wherein the 50% most shocked grains are used to categorize a meteorite. The chondritic shock stage table was used for this.

The key shock effect focused on is the optical extinction of olivine and pyroxene. An unstrained mineral will display straight optical extinction, however when strained (e.g., by shock), it will begin to show undulatory extinction. If this level of strain increases (e.g., by higher shock pressure), then misorientation of subgrains may occur leading to mosaic extinction (Stöffler et al. 2018; Flemming 2007). The proportion of olivine and pyroxene grains displaying each shock effect or lack thereof for the studied meteorites, as well as their corresponding shock stages, are in Table 6.3. None of the samples studied displayed melt veins.

Many of these heated meteorites have an abundance of undulatory with some mosaic extinction (Table 6.3) compared to other CM chondrites (Scott et al. 1992), indicating that they have experienced a higher degree of shock. Out of

the studied meteorites, Kolang is the least shocked, having experienced no more than 10 GPa of peak shock pressure. As discussed in detail in the next chapter, Kolang likely experienced ~5 GPa of peak shock pressure (see Chapter 7), however for the purposes of this chapter, it is simply classified as a shock stage C-S2 (5-10 GPa) meteorite. PCA 91008 displays a similar degree of shock as Kolang, having a few grains that show mosaic extinction, but with the majority of its grains still displaying straight extinction. It is more shocked than Kolang, but not significantly so. WIS 91600 and MAC 88100 are the next most shocked, with the majority of grains displaying undulatory to mosaic extinction, while more than a third of their grains still show straight extinction. They've likely experienced marginally more than 10 GPa of peak shock pressure. PCA 02012 is the most shocked meteorite studied, with only a third of its grains still displaying straight extinction; most of its grains display undulatory extinction and a significant portion show mosaic extinction. PCA 02012 experienced more than 10 GPa of shock, with its peak shock pressure likely being at least 15 GPa to account for lack of straight extinction. Because it does not have any melt veins, PCA 02012 cannot have experienced more than 20 GPa of peak shock pressure.

Table 6.3. Shock effects displayed by olivine and pyroxene in each meteorite and matching shock stage. For peak shock pressure ranges experienced, C-S2 equates to 5-10 GPa, while C-S3 equates to 5-20 GPa.

Meteorite & Heat Stage	Mineral	Number of Grains	Proportion Displaying Straight Extinction	Proportion Displaying Undulatory Extinction	Proportion Displaying Mosaic Extinction	Shock Stage
Kolang	Olivine	18	56%	44%	0%	C-S2
0-II	Pyroxene	7	43%	57%	0%	
MAC 88100	Olivine	38	42%	50%	8%	C-S3
III	Pyroxene	40	45%	38%	17%	
PCA 02012	Olivine	69	39%	46%	15%	C-S3
IV	Pyroxene	17	29%	53%	18%	
PCA 91008	Olivine	80	50%	45%	5%	C-S2
IV	Pyroxene	13	69%	31%	0%	
WIS 91600	Olivine	37	46%	41%	13%	C-S3
III	Pyroxene	11	64%	27%	9%	

6.4.2 Chondrule Flattening and Alignment

In addition to traditional shock effects (e.g., changes in optical extinction), carbonaceous chondrite meteorites also display chondrule flattening and alignment as petrofabrics (Tomeoka et al. 1999; Nakamura et al. 1995). These petrofabrics start to develop at peak shock pressures greater than 10 GPa, with chondrules becoming more flattened with increasing pressure (Tomeoka et al. 1999). Although chondrule flattening and alignment can be a shock effect, it is important to note that many carbonaceous chondrite samples that have flattened and/or aligned chondrules are unshocked or mildly shocked (Scott et al. 1992; Rubin 2012; Lindgren et al. 2015; Zolensky et al. 1997). It is possible that chondrule flattening and/or alignment can be caused by mechanisms other than impacts (Martin & Mills 1980; Zolenksy et al. 1997; Miura et al. 2008). This is further discussed in Chapter 7, however it is important to note that although the flattening and alignment of chondrules can be caused by impacts, they are not necessarily indicative of shock. However, a carbonaceous chondrite lacking flattened and aligned chondrules means that it has not experienced more than 10 GPa of peak shock pressure.

To further evaluate shock metamorphism, the aspect ratios (ARs) and alignment of chondrules in each heated meteorite were measured. To do this, the method described by Floyd et al. (submitted) was used, wherein montaged BSE maps of each sample were imported into the GNU Image Manipulation Program (GIMP). Chondrules were identified and segmented, then recoloured into black and white images. This procedure was undertaken both including and excluding their FGRs. These black and white images were then uploaded into ImageJ, where the analyse particles function was used to fit ellipses around each chondrule. Comparison of ellipses produced by ImageJ and chondrules found that ImageJ's ellipse fitting is reliable and that AR and AA measurements were similar to any taken by hand. ImageJ then measured both the AR and the azimuthal angle (AA) relative to the right-hand side of the image of each chondrule. The median and average AR of chondrules within each meteorite, as well as the percentage of chondrules whose AA deviates less than 10° from the median AA is reported in Table 6.4.

The chondrules studied have ARs comparable to those of unheated CMs studied by Lindgren et al. (2015). The CM chondrites that Lindgren et al. (2015)

studied are mostly unshocked, with the exception of Murchison, which falls into a maximum shock stage of S2 (up to 10 GPa of peak shock pressure). Although all of the heated meteorites that were studied optically have been shocked to at least 5 GPa, most have average ARs, which if caused by a single impact event, are more consistent with having experienced more than 20 GPa of peak shock pressure (Table. 6.3). None of these meteorites show any signs of having melt veins or relicts, which is incongruent with their optical shock stages. Either the flattened chondrules of these meteorites are not caused by a single impact event or the impact event responsible for chondrule flattening occurred prior to aqueous alteration, erasing any melt veins or other shock effects. This incongruency is explored further in a Kolang-focused study in Chapter 7. At this point in time, chondrule flattening can not be properly compared to shock stage and thus cannot be used to evaluate shock metamorphism. It is also therefore unlikely to be related to post-hydration heating.

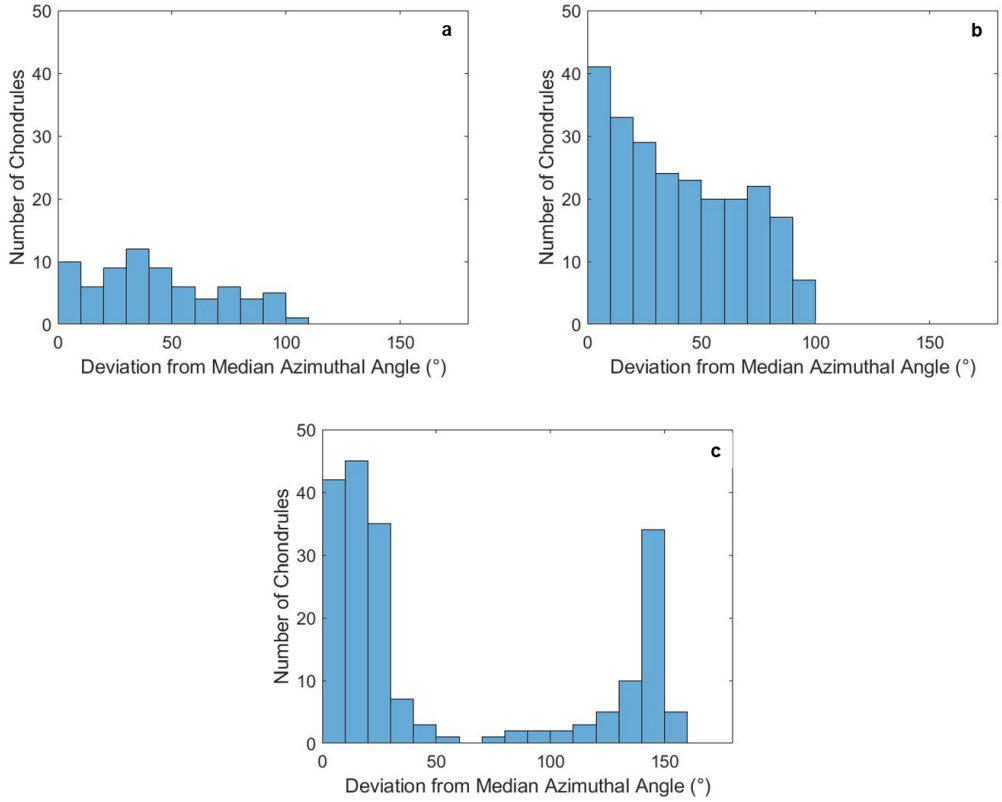

Fig. 6.30. Example histograms showing the alignment of chondrules including their FGRs within the meteorites studied. a) MAC 88100 which has 14% of its chondrules within 10° of the median and shows no petrofabric. b) PCA 91008 which has 17% of its chondrules within 10° of the median and shows a possible petrofabric. c) PCA 02012 which has 21% of its chondrules within 10° of the median and displays a petrofabric.

Chondrule alignment is another effect of shock metamorphism in carbonaceous chondrites (Tomeoka et al. 1999). The polished and thin sections

studied were randomly cut, so the chondrule alignment observed may not be indicative of the maximum alignment displayed by the samples.

Only about half the samples studied show some form of petrofabric (e.g., at least 15-20% of chondrules within 10° of the median azimuthal angle; Fig. 6.30), with the most extreme petrofabrics being displayed by mildly heated meteorites like Shidian and Kolang (Table 6.4). As the samples were randomly cut, this does not mean that half of them are necessarily devoid of petrofabrics, however it is improbable that half the samples would not show petrofabrics. Additionally, petrofabrics reported for unheated CM chondrites in the literature (Rubin 2012; Lindgren et al. 2015), tend to be more pronounced than the heated meteorites studied. Again, the samples being randomly cut may play a factor in reducing the degree of chondrule alignment observed, however other studies (Rubin 2012; Lindgren et al. 2015) also looked at randomly cut meteorites. It is unlikely that the samples being randomly cut would have a major role in the comparative petrofabrics.

An absence of petrofabrics does not mean a sample has not experienced shock metamorphism, just that it cannot have experienced more than 10 GPa of peak shock pressure from a single event, as that is when petrofabrics are observed in experimental impact studies (Tomeoka et al. 1999). The lack of chondrule alignment is not incongruent with the optical shock stages (Table 6.3), however it is important to note that in the case of Kolang, it has a low optical shock stage yet displays the most prominent petrofabric. Kolang's petrofabric is explored further in Chapter 7.

Table 6.4. Degree of chondrule flattening and alignment of each heated meteorite. Errors are given in standard deviation. Peak shock pressures calculated from Tomeoka et al.'s (1999) calibration curve using average AR.

Meteorite & Heat Stage	Median AR		Average AR		Percentage of Chondrules that Deviate ≤10° From Median AA		Calculated Peak Shock Pressure (GPa)	
	With FGR	Without FGR	With FGR	Without FGR	With FGR	Without FGR	With FGR	Without FGR
Kolang – 0-II	1.36±0.34	1.47±0.44	1.46±0.34	1.55±0.44	32	23	21	27
MAC 88100 – III	1.27±0.25	1.46±0.42	1.33±0.25	1.56±0.42	14	15	13	27
Murray – 0	1.43±0.31	1.61±0.53	1.47±0.31	1.66±0.53	6	3	22	33
PCA 02012 – IV	1.57±0.38	1.54±0.45	1.63±0.38	1.64±0.45	21	15	32	32
PCA 91008 – IV	1.33±0.26	1.41±0.37	1.37±0.26	1.49±0.37	17	14	16	23
PCA 91084 – III-IV	1.30±0.25	1.38±0.32	1.36±0.25	1.45±0.32	3	9	15	20
Shidian – I	1.45±0.30	1.57±0.43	1.48±0.30	1.62±0.43	28	24	22	31
WIS 91600 - III	1.45±0.34	1.53±0.50	1.51±0.34	1.64±0.50	9	9	24	32

6.4.3 Shock Metamorphism vs Thermal Metamorphism

The heated meteorites studied all show some sign of shock metamorphism and optically, none of the studied meteorites could be deemed unshocked. However, the degree of shock metamorphism experienced by these heated meteorites has no correlation with heat stage (Fig. 6.31); a heat stage IV meteorite like PCA 91008 shows the same degree of shock as Kolang, whose primary constituents are unheated.

It is possible that heating may have erased the mineral shock effects used to determine shock stage through annealing. If this were the case however, other shock effects should be observable. These shock effects include melt veins and petrofabrics (Tomeoka et al. 1999). However, no melt veins were observed in any of the samples, with the samples that showed the most prominent petrofabrics being the least heated (Fig. 6.31). With the samples studied, no relation between shock metamorphism and post-hydration heating can be established.

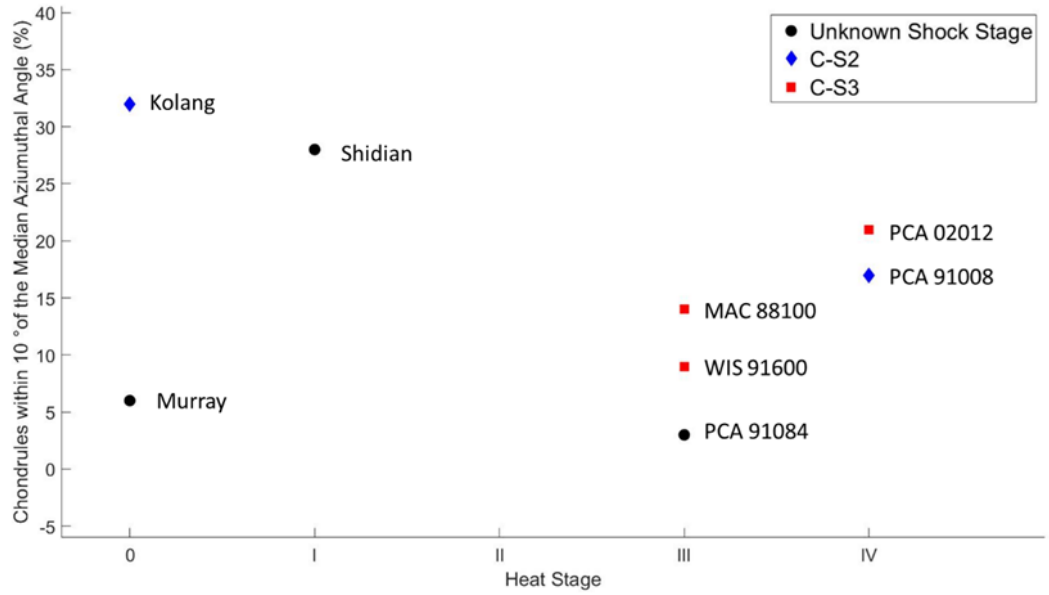

Fig. 6.31. Comparison between experienced level of shock metamorphism and experienced level of post-hydration heating. X-axis corresponds to degree of heating, while the y-axis corresponds to the alignment of chondrules. If a sample has clasts in multiple heat stages or a heating temperatures estimate that spanned multiple heat stages, the lowest heat stage was used. Shock stages are differentiated by marker shape and colour. Samples studied are labelled.

6.5 The Cause of Post-Hydration Heating

The main two proposed causes of post-hydration heating are impact heating and solar heating (Nakamura 2005). Both are short duration, though for how long each would heat carbonaceous material on the CM parent body(ies) is unknown. It is assumed that impact heating would heat samples on the order of hours, while solar heating would be able to heat samples for more variable durations.

Multiple sets of unheated CM chondrites were heated at known temperatures for known durations such that they could be compared to naturally heated meteorites. The temperature-timescales experienced by these naturally heated meteorites (Table 6.2) were estimated based on qualitative observations. The estimated temperatures experienced by these naturally heated meteorites were generally consistent with those reported in the literature. Estimated timescales were also consistent with those reported in the literature, however these estimated timescales varied (Table 6.2). Some meteorites (e.g., PCA 02012, PCA 91008), showed incomplete recrystallization textures with fine-grained secondary anhydrous minerals, indicating that they likely were heated on the order of hours. Other meteorites (e.g., MAC 88100, Shidian) showed heating on the order of days to weeks, with secondary anhydrous minerals being quite coarse-grained compared to experimentally heated samples. The timescales of post-hydration heating, although short, are incredibly variable. If there is a singular cause for post-hydration heating it must account for this variability.

As of writing, there are no ready ways to disprove or prove solar heating as a cause for post-hydration heating. Impact heating however should shock the meteorites they have heated. If impact heating is responsible, heated meteorites should all be shocked, with the most heated meteorites showing the highest degree of shock.

All the samples evaluated optically did show mineral effects for shock metamorphism and all were sorted into either the C-S2 and C-S3 shock stages. It is estimated that these samples experienced 5-20 GPa of peak shock pressure. However, there is no relation between peak shock pressures experienced and heat stage, with many of the heated meteorites lacking the petrofabrics

presented by the more shocked carbonaceous chondrites (Fig. 6.31). Additionally, none of the studied meteorites have experienced the 21 GPa of peak shock pressure required to induce serpentine dehydration (Sekine et al. 2015; King et al. 2021b). It is possible that all these samples originated from the surfaces of their parent asteroid(s), leading to them being more likely to be shocked.

Impact heating has not been disproven as a possible cause for post-hydration heating. However, the samples studied show variability of timescales with a small range of peak shock pressures experienced. It is unlikely that impact events would be able to generate this variability without varying the experienced peak shock pressures. Additionally, when heat stage is compared to shock stage and chondrule alignment, no correlation can be observed, indicating that the heated meteorites can only be mildly shocked. If impact heating is the cause for post-hydration heating, there must be other factors that have yet to be established involved. Given the incongruency between the level of post-hydration heating experienced and shock stage, as well as the variability in the timescales of post-hydration heating displayed by the studied meteorites, impact heating is unlikely to be the cause of post-hydration heating.

Solar heating as a cause of post-hydration heating cannot be readily evaluated at this point in time. The timescales of heating experienced by these samples are variable, however if there are multiple CM parent bodies, it is possible to vary their orbits around the Sun, leading them to experience variable timescales of post-hydration heating. This would require heated CM chondrites to originate from asteroids whose orbits bring them close to the Sun. The variability in the timescales experienced by heated CM and CM-like chondrites can easily occur if they were heated through solar heating. An example of this would be the C-complex asteroid 3200 Phaethon, whose orbit takes it to a perihelion distance of 0.14 AU away from the Sun, leading it to experience surface temperatures up to ~827°C for weeks at time (Ohtsuka et al. 2009). Given the existence of C-complex asteroids whose orbits take them close enough to the Sun to reach the required temperatures for post-hydration heating, solar heating is its most likely cause. However, more research would need to be conducted to confirm this.

A cause for post-hydration heating has not been definitively proven or disproven, however solar heating has been shown to be more likely than impact heating. Heated CM and CM-like chondrites may originate from asteroids whose orbits take them close to the Sun and may have been heated that way. It may still be possible that they have been heated indirectly by impacts, with their parent body(ies) being impacted but with the heated CM chondrites themselves escaping shock, however there has yet to be any evidence for this. It may also be possible that both impact and solar heating are responsible.

Chapter 7 – Petrofabrics in Kolang

Like aqueous alteration and thermal metamorphism, physical deformation (e.g., shock metamorphism) is an important alteration process many meteorites have experienced. Understanding the causes of physical deformation is important for the analysis of geological processes experienced by meteorite parent bodies. Many carbonaceous chondrites have chondrules that are non-spherical (e.g., ellipsoidal, lobate) and aligned into what are known as petrofabrics as a result of deformation. Petrofabrics have been shown to result from impact events (Tomeoka et al. 2011) and can be indicators of shock metamorphism. However, most carbonaceous chondrites are either unshocked or mildly shocked according to olivine microstructures (Scott et al. 1992), displaying mineral shock effects corresponding to shock pressures too low to allow for petrofabric formation (Rubin 2012). Knowing which process(es) flattened and aligned chondrules within carbonaceous chondrites and/or erased shock effects will enable a better understanding of the deformation processes they have experienced on their parent asteroids.

There are several explanations proposed to explain this incongruency between mineral shock effects and petrofabrics in carbonaceous chondrites; some posit that impact events are the sole cause, with explanations surrounding the lack of measurable shock, while others seek alternative mechanisms to chondrule flattening and alignment. Some of these explanations have been later disproven, while others are still plausible.

Explanations for petrofabrics in carbonaceous chondrites that can be disproven include that the experiments conducted to put pressure limits on shock effects experienced by carbonaceous chondrites are not adequate in recreating the effects of impact events (Rubin 2012) and flattening and alignment of spherical chondrules by burial compaction (Martin and Mills 1980; Stacey et al. 1961).

Although impact experiments cannot perfectly recreate natural impacts due to their limited size, occurring over shorter durations with lower post-shock temperatures (Kurosawa et al. 2021; Fritz et al. 2019), any differences would be negligible pertaining to the level of mineral strain displayed by carbonaceous chondrites. Impact duration has little to no effect on the mineral strain

displayed (Fritz et al. 2019), while the matrices of these carbonaceous chondrites are composed of crystalline, hydrated tochilinite and serpentine (Rubin 2012; Lindgren et al. 2015), indicating that post-shock temperatures must be low as these minerals would decompose in response to any significant heating (See Chapter 5).

Regarding burial compaction, to deform olivine without dehydrating the serpentine-tochilinite matrix, a minimum pressure of 1 GPa is needed (Cain et al. 1986), which would require a parent body whose minimum diameter is 750 km (Yang et al. 2022). Most parent body diameter estimates for carbonaceous chondrites are only in the realm of a few tens of kilometers (Trigo-Rodríguez et al. 2019), making this explanation unviable for spherical chondrules.

Possible explanations for the incongruency between petrofabrics and lack of shock within carbonaceous chondrites include freeze-thaw cycles on the parent asteroid weathering and rotating chondrules into alignment during aqueous alteration (Zolensky et al. 1997), traditional mineral strain shock effects being erased by alteration (Rubin 2012), multiple-low intensity impacts (Lindgren et al. 2015), brittle deformation of olivine (Hanna et al. 2015), and chondrules not being spheres to begin with, removing the requirement for flattening and potentially making them easier to align (Miura et al. 2008).

Kolang is a brecciated CM chondrite whose clasts all vary in geologic history. Most fall into the petrologic subtype of CM2.2, however each lithology has a distinctly separate set of alteration products and defining features, with at least one set of clasts showing signs of post-hydration heating (See chapters 3.2, 4, and 6.3.1). BSE images show that despite the clasts varying in alteration history, their chondrules are flattened and appear to be aligned within the same direction (Fig. 7.1). This indicates that this petrofabric postdates the juxtaposition of the clasts and must therefore postdate any other alteration Kolang experienced on its parent body, making it an ideal sample to study petrofabric formation.

Because Kolang's petrofabric postdates aqueous alteration, freeze-thaw cycles cannot be its cause. Additionally, if impacts were responsible for the

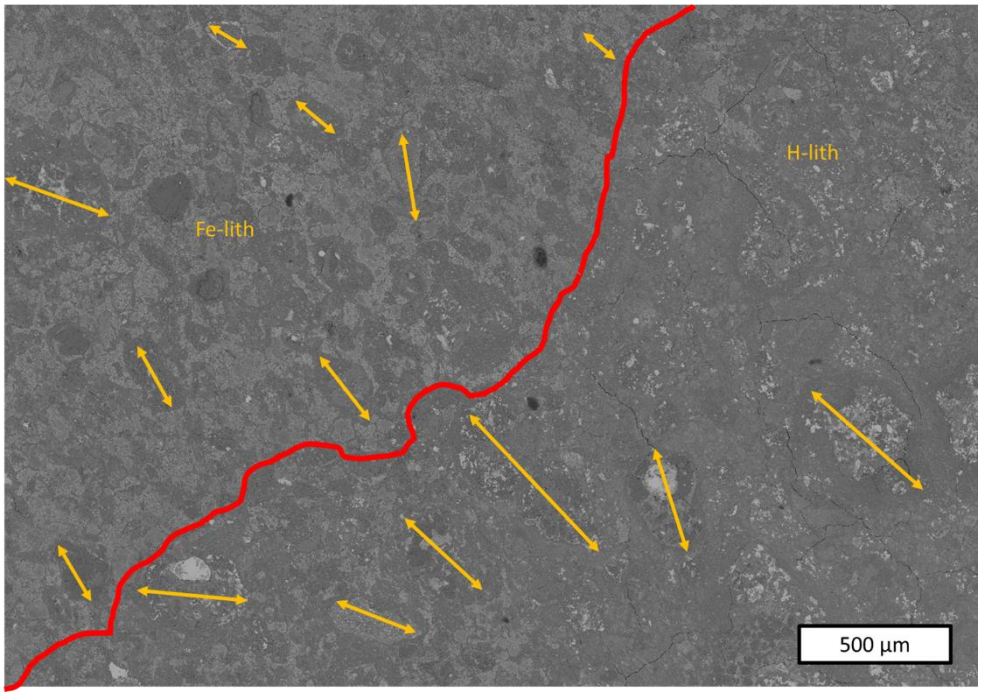

Fig. 7.1. Backscattered electron image (BSE) of an area in Kolang_01 showing its petrofabric. The boundary between two clasts comprised of the heated lithology (H-lith) and Fe-rich lithology (Fe-lith) is outlined in red. The orientations of chondrules and other objects are marked out by yellow arrows.

petrofabrics, the mineral strain they would cause wouldn't be erased. Any evidence for the cause of petrofabric formation within Kolang should still be present.

Kolang's shock stage was determined with a combination of optical and electron backscattered diffraction (EBSD) methods (see Chapter 2). The degree of chondrule flattening and alignment was measured with ImageJ and compared to Tomeoka et al.'s (1999) impact experiments with the CM Murchison, where the aspect ratios (ARs) of chondrules were related to the peak shock pressures experienced. If impacts were responsible for the flattening and alignment of Kolang's chondrules, then its shock stage as determined by optical and EBSD methods should be comparable to that determined by the AR of its chondrules, with its optical shock stage being consistent with having experienced more than 10 GPa of peak shock pressure, as more than 10 GPa of peak shock pressure required to flatten and align chondrules (Tomeoka et al. 1999). If Kolang has a shock stage consistent with experiencing 10 GPa or less of peak shock pressure, then other indicators of shock (e.g., melt veins, brittle deformation features) should either be observable, or another mechanism other than impacts was responsible for its petrofabric.

7.1 – Measuring Degree of Chondrule Flattening and Alignment

7.1.1 Using ImageJ

The method described by Floyd et al. (submitted) was used to measure chondrule flattening and alignment. Montaged BSE maps of both Kolang_01 and Kolang_02 were imported into the GNU Image Manipulation Program (GIMP). Chondrules were identified and segmented, before being recoloured into black and white images (Fig. 7.2). These measurements were performed both with and without the chondrule's fine-grained rims (FGRs). These black and white images were then uploaded into ImageJ, wherein the analyse particle function was used to measure both the AR and azimuthal angle (AA) of the ellipse ImageJ fits around each chondrule. ImageJ measures AA relative to the right-hand side of the image. Comparison of ellipses produced by ImageJ and chondrules found that ImageJ's ellipse fitting is reliable and that AR and AA measurements were similar to any taken by hand.

To determine the degree of chondrule flattening, the mean and median ARs of the chondrules, both with and without their FGRs, were measured. The chondrule ARs were compared to Tomeoka et al.'s (1999) results, both with and without their FGRs, as Tomeoka et al. (1999) does not specify whether or not FGRs were included in their measurements.

To study chondrule alignment, the median AA of each thin section was calculated and the deviation of each chondrule from the median was determined. The percentage of chondrules that deviate less than 10° from the median AA was then calculated, with higher proportions of chondrules deviating less than 10° equating to a more pronounced petrofabric. Like with AR, this procedure was undertaken both with and without the chondrules' FGRs.

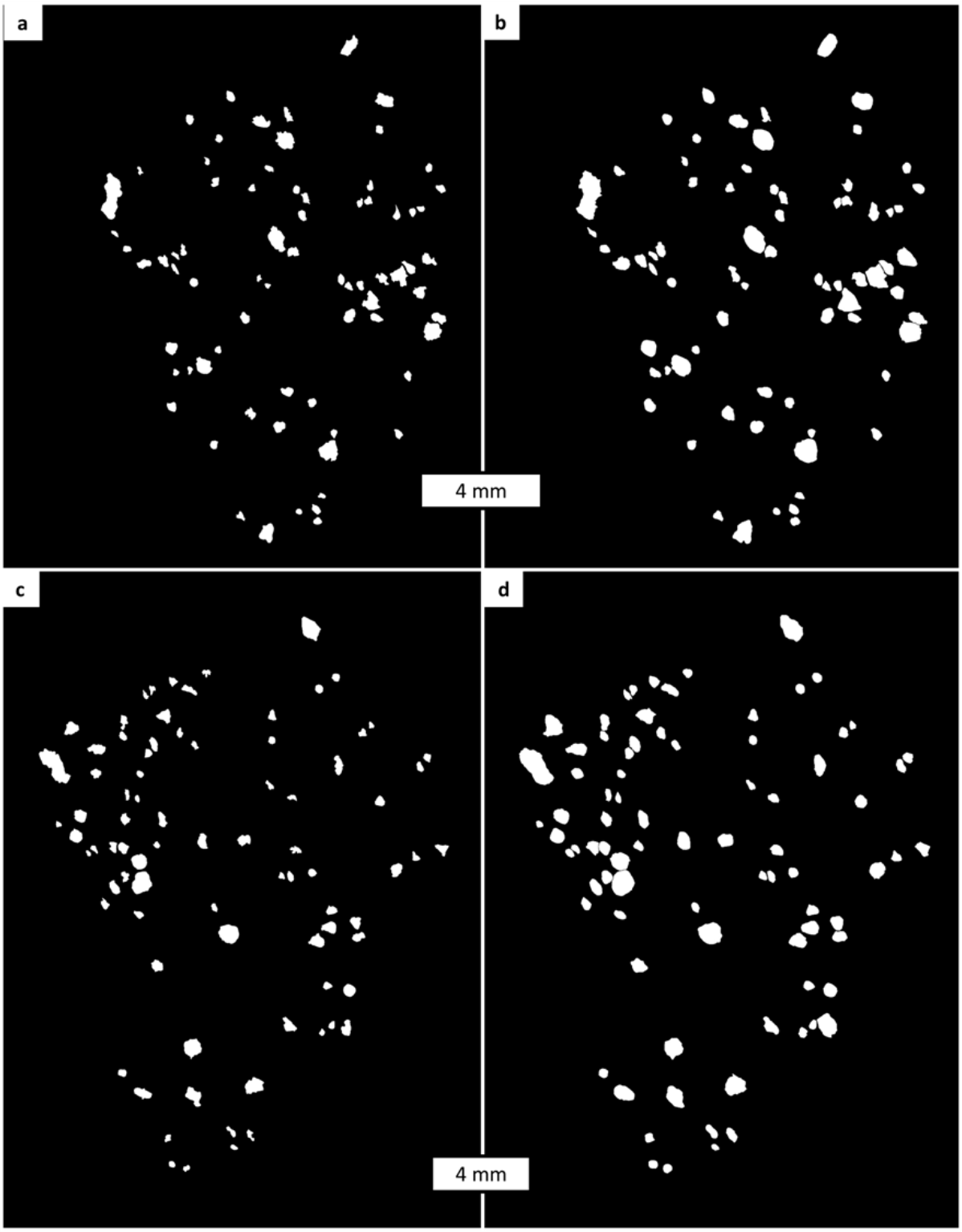

Fig. 7.2. Black and white images defining chondrules in Kolang. a) Chondrules in Kolang_01 without FGRs, b) Chondrules in Kolang_01 with FGRs, c) Chondrules in Kolang_02 without FGRs, d) Chondrules in Kolang_02 with FGRs.

7.1.2 Results

7.1.2.1 Aspect Ratio

If FGRs are not included in the AR measurements, the median and mean AR of chondrules in all clasts are comparable. If FGRs are included, then their mean and median ARs are still comparable for most lithologies (see Chapter 3.2), with the exception of the Ca-lith, whose chondrule ARs are smaller than that of other lithologies (Table 7.1). Although the mean and median ARs of chondrules, both with and without their FGRs, are all within error of each other, chondrule ARs are consistently lower when FGRs are included (Table 7.1).

Tomeoka et al. (1999) developed a calibration curve that can be used to determine peak shock pressure experienced by a CM chondrite based on the mean AR of its chondrules. It is not specified whether or not this mean includes FGRs. When the mean ARs of Kolang's chondrules are applied to this calibration curve, it is found that the degree of chondrule flattening is consistent with 21 and 26 GPa of peak shock pressure, with and without FGRs, respectively.

Table 7.1 Median AR of chondrules, both with and without their FGRs, within each clast in the two thin sections of Kolang. The clasts are labelled by where they occur in the thin sections (e.g., 1-4 corresponds to clast 4 in Kolang_01). For a complete clast map, see Chapter 3.2.

		With FGR		Without FGR	
Clast	Number of Chondrules	Median AR	Standard Deviation	Median AR	Standard Deviation
1-1	17	1.41	0.37	1.51	0.29
1-2	24	1.50	0.33	1.57	0.49
1-3	14	1.38	0.47	1.39	0.55
1-4	1	1.16	N/A	1.14	N/A
1-5	5	1.40	0.50	1.44	0.33
1-7	1	1.51	N/A	1.52	N/A
1-8	9	1.19	0.16	1.19	0.21
1-10	1	1.31	N/A	1.39	N/A
2-1	18	1.24	0.26	1.33	0.36
2-2	46	1.39	0.32	1.49	0.47
2-4	6	1.10	0.26	1.47	0.33
2-5	4	1.32	0.41	1.35	0.29
2-7	1	1.31	N/A	1.19	N/A
2-8	7	1.48	0.42	1.72	0.60
H-lith	35	1.32	0.33	1.40	0.33
Fe-lith	71	1.39	0.32	1.55	0.48
Co-lith	24	1.38	0.33	1.39	0.46
S-lith	17	1.33	0.32	1.38	0.47
Ca-lith	7	1.14	0.23	1.47	0.31
Whole Meteorite	155	1.36	0.34	1.47	0.44

7.1.2.1 Azimuthal Angle

The median AA of Kolang_01 is 121±35° and 108±40° with and without FGRs, respectively. The median AA of Kolang_02 is 123±36° and 119±39° with and without FGRs, respectively. Fig. 7.3 shows rose diagrams depicting the AAs of chondrules in both thin sections. The median AA of each clast varies little from the median AA of the whole thin section, with most variance from those clasts with less than 10 chondrules (Fig. 7.4). If FGRs are included, then 32% of Kolang's chondrules have AAs within 10° of the median AA. If FGRs are excluded, then only 23% of Kolang's chondrules have AAs within 10° of the median AA. When compared to Tomeoka et al.'s (1999) experiments, the chondrule alignment is most comparable to Murchison shocked to 26 GPa.

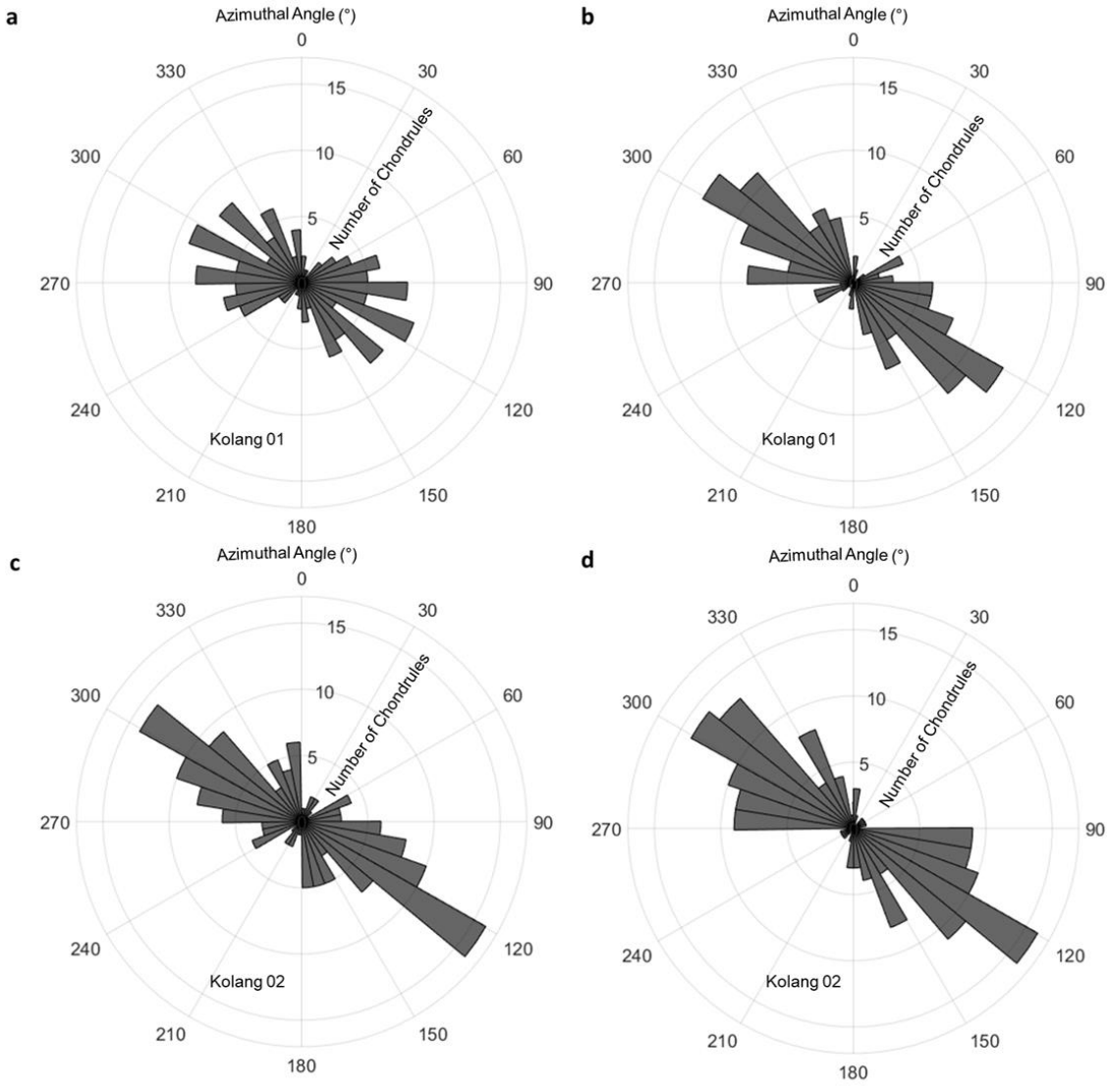

Fig. 7.3. Rose diagrams showing the alignment of chondrules in Kolang. a) Chondrules in Kolang 01 without their FGRs. b) Chondrules in Kolang 01 with their FGRs. c) Chondrules in Kolang 02 without their FGRs. d) Chondrules in Kolang 02 with their FGRs.

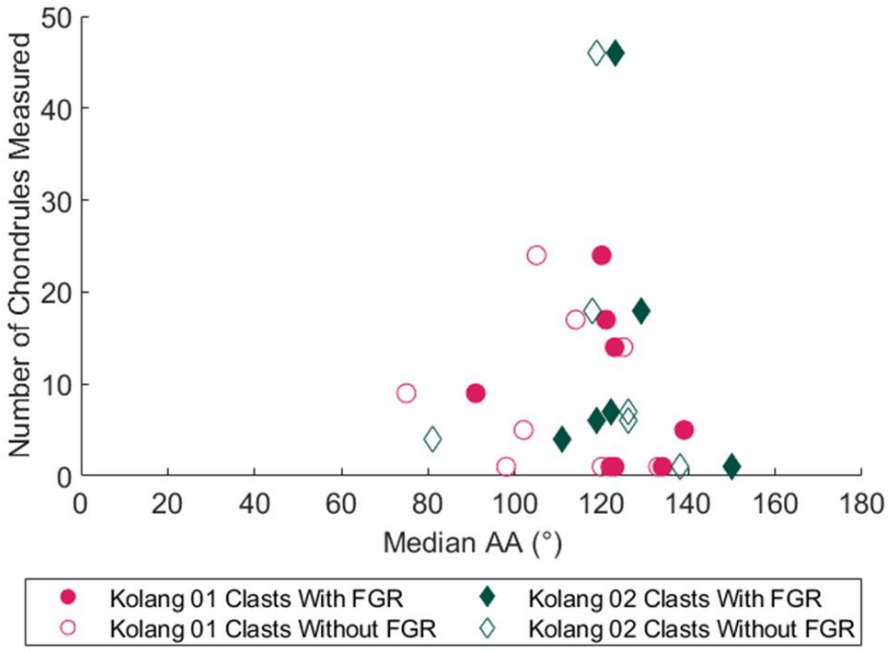

Fig. 7.4. Comparison of the median AA of each clast in each thin section of Kolang. Most clasts have AAs within 20° of 120°, with the exception of clasts with fewer than 10 chondrules.

7.2 – Shock Stage

7.2.1 Optical Shock Stage

Neither of the Kolang thin sections display any melt veins. In BSE images, most clasts did not show any significant fracturing in the matrix, with the exception of the heated lithology and the carbonate-rich lithology (Fig. 7.5). The carbon coat was removed from Kolang_02 and it was studied optically with a transmitted light petrographic microscope for mineral shock effects. 18 olivine and seven pyroxene grains were investigated. The olivine did not display any planar fractures, and of the 18 grains studied, only eight showed undulatory extinction, with the rest displaying straight extinction. Four pyroxene grains showed undulatory extinction and three showed straight extinction. These optical properties are consistent with a shock stage of C-S2, corresponding to 4-10 GPa of peak shock pressure. Additionally, if compared to Tomeoka et al.'s (1999) experiments, the shock effects displayed are most comparable to Murchison shocked to 4 GPa.

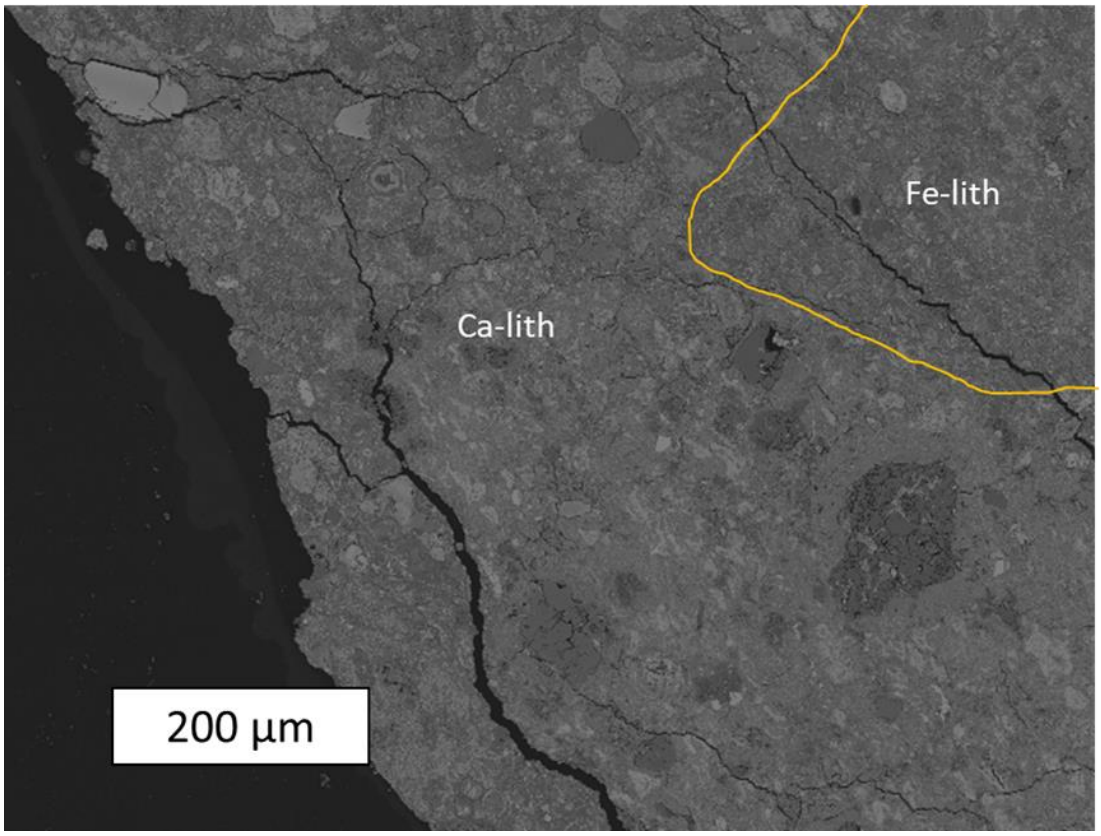

Fig. 7.5. BSE image of carbonate-rich lithology (Ca-lith) in Kolang showing mild fracturing. Fe-rich lithology (Fe-lith) is also present.

7.2.2 EBSD Shock Evaluation

Kolang_01 was polished for EBSD analysis. EBSD data were collected from eight chondrules and compared to the EBSD results of Ruzicka & Hugo (2018), who used the technique to study olivine in shocked ordinary chondrites. Seven out of the eight chondrules contained olivine.

Table 7.2. Average MeGOS, MaGOS, and KAM of each olivine bearing chondrule studied with EBSD in Kolang_01. Errors are given as standard deviation.

Chondrule	Average MeGOS (˚)	Average MaGOS (˚)	Average KAM (˚)
1	0.8±0.5	4.0±3.0	0.62±0.35
2	1.1±1.0	3.9±3.1	0.66±0.36
3	0.9±0.6	3.0±1.9	0.65±0.36
4	0.8±0.4	3.6±2.4	0.65±0.36
6	0.9±0.6	3.3±2.7	0.63±0.33
7	0.9±0.5	3.4±2.0	0.61±0.31
8	1.0±0.7	3.6±3.4	0.70±0.35

The grain reference orientation deviation (GROD) maps for olivine consistently show mild strain, concentrated either along grain edges or within small grains (Fig. 7.6). The average mean grain orientation spread (MeGOS) and average Kernal Average Misorientation (KAM) of olivine within Kolang's chondrules (Table 7.2) is similar to that of unshocked ordinary chondrites (Ruzicka & Hugo 2018). The average maximum grain orientation spread (MaGOS) of olivine within Kolang's chondrules (Table 7.2) is higher than that of unshocked ordinary chondrites, but lower than that of S4 ordinary chondrites (Ruzicka & Hugo 2018). There are no comparable datasets from S2 or S3 chondrites. The EBSD data from olivine within Kolang is consistent with a C-S2 classification, likely on the lower end of the C-S2 shock stage.

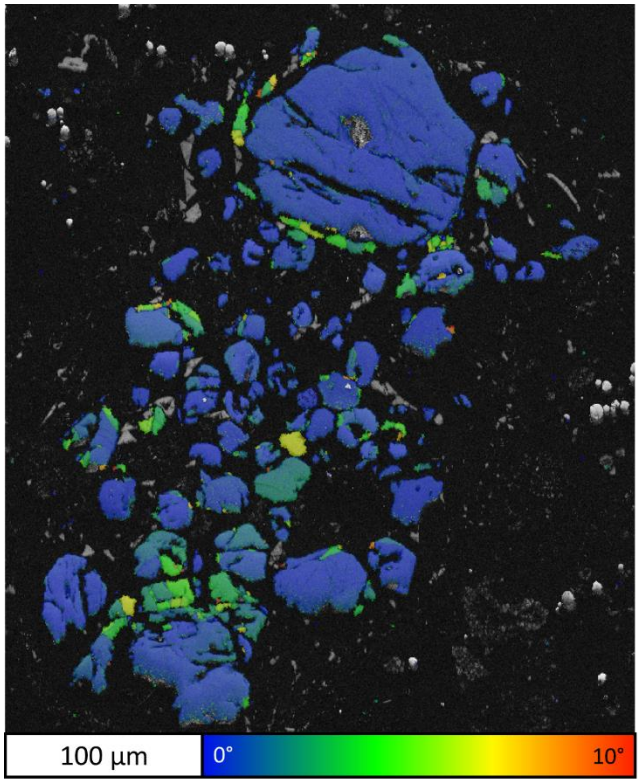

Fig. 7.6. GROD map for olivine in chondrule 2 in Kolang_01. Colour bar refers to misorientation from the average grain orientation for olivine, wherein higher misorientation corresponds to a greater degree of strain. Grey areas are minerals measured by EBSD that are not olivine. Black areas correspond to the matrix, for which EBSD data could not be collected for.

Crystal rotation axis (CRA) plots for olivine can show which slip systems are dominant. This information can help infer the conditions of deformation, as the dominant olivine slip system is temperature dependent (Ruzicka & Hugo 2018). CRA plots were made for all chondrules, but none were sufficiently highly strained to have a dominant slip system (Fig. 7.7). Only the [010] a+c screw

system seems to show any slight indication of dominance and that slip system is not associated with temperature (Ruzicka & Hugo 2018).

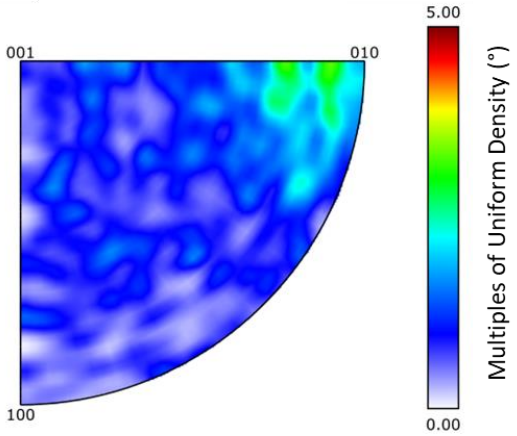

Fig. 7.7. CRA plot for olivine in chondrule 7, which displayed the most prominent slip system ([010] a+c screw slip) out of all seven chondrules.

7.3 – The Incongruency Between Petrofabric and Shock Stage

According to both its optical shock stage and the results from the EBSD data of its olivine, Kolang is mildly shocked with a shock stage of C-S2. It cannot have experienced more than 10 GPa of peak shock pressure and it most likely experienced closer to 5 GPa of peak shock pressure. However, its chondrules are elliptical in shape and aligned into a prominent petrofabric. If this petrofabric and chondrule alignment were caused by a single impact affecting spherical chondrules plastically, then at least 20 GPa of peak shock pressure would be required. Kolang cannot have had spherical chondrules flattened and aligned in a single impact.

Multiple low intensity impacts are a proposed cause of petrofabrics within CM chondrites that accounts for the low degree of shock they have experienced (Lindgren et al. 2015). Multiple low intensity impacts can flatten chondrules to the same degree as a single high intensity impact, however the mineral shock effects increase to reflect this, with minerals showing more fracturing and undulatory and mosaic extinction. This is because although the shock pressures are low, the minerals are still deforming plastically and thus show the related effects of plastic deformation (Nakamura et al. 2000). If plastic deformation from multiple low intensity impacts were the cause, Kolang should still show

considerable mineral strain to reflect solid spherical chondrules deforming into ellipsoids. However, Kolang's olivine and pyroxene are only mildly strained. Additionally, for multiple low-intensity impacts to be responsible for the flattening and alignment of chondrules observed, the shock waves would have to come from the same direction. This would require Kolang to be buried (Lindgren et al. 2015) or for these impacts to be happening from the same location on the parent asteroid. Given the random nature of impacts, the probability of the latter is low, while how much burial is required for the former and if it is possible on carbonaceous parent asteroids have yet to be established. Additionally, CM chondrites are likely regolith breccias (Kriestch et al. 2021), making significant burial unlikely to occur. Multiple low-intensity impacts are not likely to be responsible for chondrule flattening and alignment within Kolang and other CM chondrites. However, multiple low-intensity impacts may be responsible for alignment of features in multiple directions (e.g., sets of parallel fractures running in differing directions), which may be observed in other meteorites, like Murchison (Hanna et al. 2015).

Brittle deformation is another argument for impact-induced chondrule flattening and alignment. This mechanism relies on the softer meteorite matrix and chondrule mesostasis preferentially deforming, reducing the strain experienced by anhydrous silicates and leading to comminution of the matrix, and anhydrous silicates rearranging in the soft mesostasis of their chondrules (Hanna et al. 2015). Part of the brittle deformation explanation involves the collapse of pores within the meteorite matrix; as they are collapsed, the chondrules are "squeezed" into them, leading to their flattened shape (Hanna et al. 2015; Nakamura et al. 1995; Scott et al. 1992). However, this pore collapse explanation for brittle deformation originates from observations from Kieffer (1971), wherein the shocked Coconino sandstone from Meteorite Crater was observed to have elongated and aligned quartz grains being "squeezed" into collapsing pore spaces. Kieffer (1971) observes that pore collapse magnified both shock pressures and temperatures within their vicinity, and that the "squeezing" of quartz is a plastic process, not a brittle one. As serpentine-rich carbonaceous chondrites and sandstone are different materials, the plastic deformation of quartz in Coconino sandstone disproves neither brittle deformation as a cause for chondrule flattening in carbonaceous chondrites, nor the role of pore

collapse regarding it. However, it does highlight the need for more study regarding shock metamorphism in hydrous carbonaceous chondrites as there is yet to be evidence relating brittle deformation to pore collapse.

If brittle deformation was responsible for the elliptical shape of Kolang's chondrules, then softer silicates, such as serpentine, should show evidence of comminution, with shear stress indicators. Additionally, if chondrule flattening and alignment is impact induced in any manner, it should be more pronounced when FGRs are accounted (e.g., higher ARs) for as the serpentine making up the FGRs is more susceptible to deformation (Fig. 7.8).

Kolang only shows mild strain in its olivine, and no significant fracturing in its meteorite matrix, ruling out multiple low intensity impacts as causes for the deformation of its chondrules. No shear stress indicators were observed, with many elongated chondrules showing no sign of olivine displacement; olivine grains still encircle kamacite, appearing to be in their original location within the chondrule (Fig. 7.9). There are also a few chondrules that are unaligned but distinctly nonspherical with high ARs (Fig. 7.10). Additionally, with the exception of the heated and carbonate-rich lithologies, the serpentine meteorite matrix is lacking in fractures. Most clasts show little to no signs of shock in their matrices. Brittle deformation is unlikely to be the cause of chondrule flattening and alignment. When including the FGRs in chondrule measurements, alignment is stronger (Fig. 7.3), however AR is reduced (Table 7.1). This pattern would make sense if Kolang's chondrules were flattened before they acquired their FGRs but were aligned after being incorporated into Kolang's parent body and after brecciation. This suggestion leaves Kolang's chondrules forming not as spheroids, but as ellipsoids or perhaps another irregular shape, and then being aligned after the juxtaposition of its clasts by either lithostatic compaction or impact events. It is assumed that ellipsoidal objects are easier to align, however, further research (e.g., modelling, experimental impacts performed on CM chondrites with ellipsoidal unaligned chondrules) is required to confirm this.

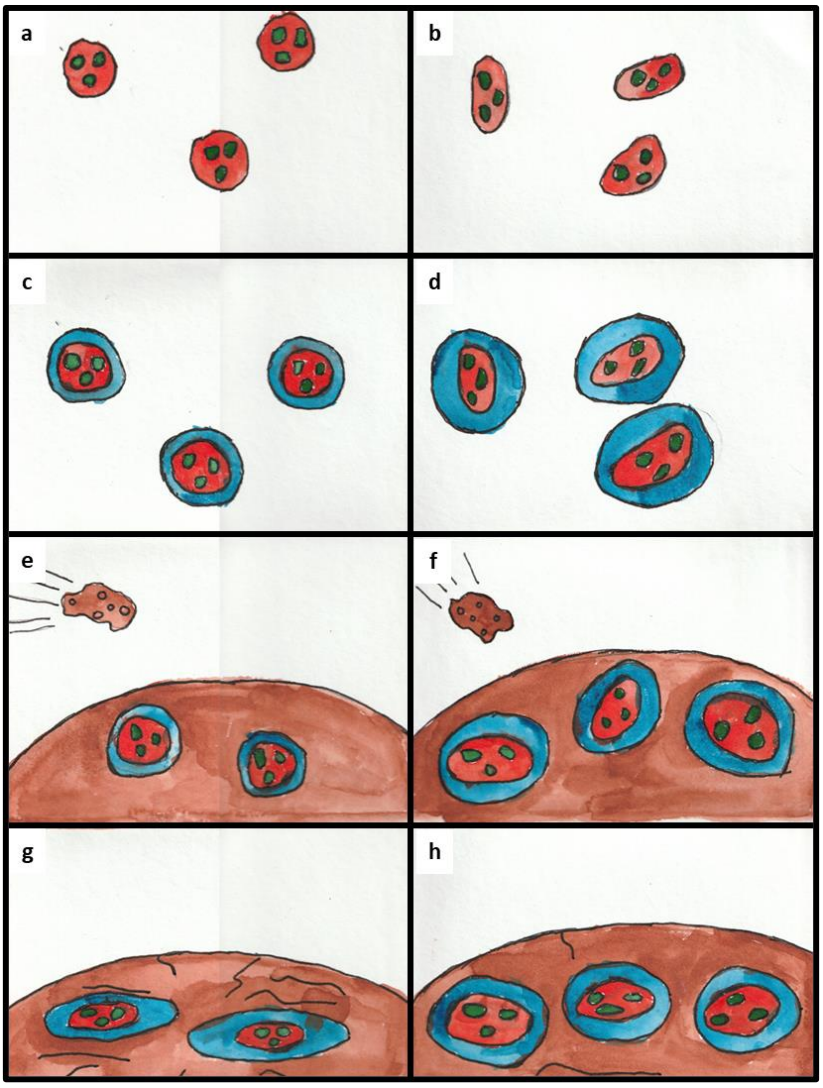

Fig. 7.8. Illustrated scenario of chondrule alignment by impact event comparing impact deformation of spherical chondrules with alignment of ellipsoidal chondrules. a) Formation of spherical chondrules. b) Formation of ellipsoidal chondrules. c) Spherical chondrules acquire FGRs, which collect around them evenly. d) Ellipsoidal chondrules acquire FGRs, where material preferentially collects in a manner that reduces their ARs, making them more spherical in shape. e) Spherical chondrules have accreted onto a parent body and been aqueously altered. They are about to experience an impact event which will both flatten and align the chondrules. f) Ellipsoidal chondrules have accreted onto a parent body and been aqueously altered. They are about to experience an impact event which will only align the chondrules. g) Spherical chondrules have been flattened and aligned, with softer material being preferentially shocked. FGRs deform more readily and increase the AR of the chondrules, while the soft matrix has more shock effects. h) Ellipsoidal chondrules are aligned. Minimal deformation has occurred and FGRs are largely unchanged beyond alignment. Matrix displays minimal shock effects.

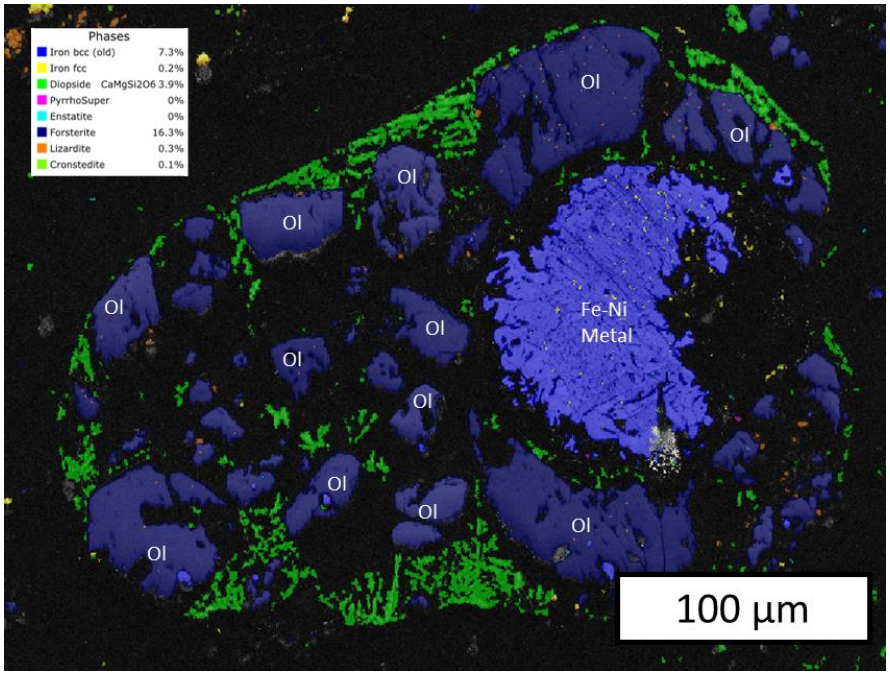

Fig. 7.9. EBSD phase map of chondrule 1 in Kolang showing an altered spheroid of Fe-Ni metal (labelled Iron bcc and Iron Fcc in legend) surrounded by primary olivine (Ol) grains. The primary olivine grains show no sign of displacement from their original orientation within the chondrule. Black areas correspond to the matrix for which EBSD data could not be measured for.

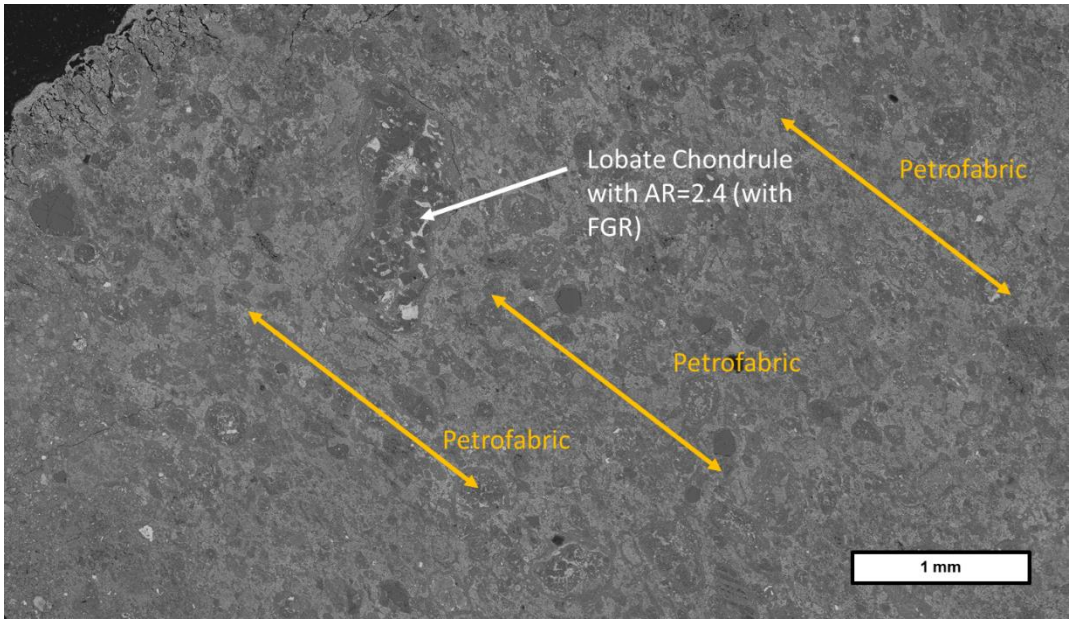

Fig. 7.10. BSE map of Kolang_01 showing a high-AR lobate chondrule. Although most chondrules are aligned in a petrofabric, this particular lobate chondrule's AA deviates from the median by 86° (including FGR).

7.3.1 Non-Spherical Chondrule Formation Mechanisms

Chondrules formed through the melting of precursors in the early solar nebula (Hezel & Palme 2007; Connolly Jr. & Desch 2004), with chondrules traditionally thought to have formed as molten spheres (Hood & Horanyi 1991; Hood & Horanyi 1993; Sekiya et al. 2003; Miura et al. 2008). Chondrules forming

as spheres may still be the case for many chondrites, however they cannot have formed spherically for Kolang. This is not the first meteorite whose chondrules display evidence for a non-spherical origin. The Vigarano-like carbonaceous (CV) chondrite Allende has two populations of chondrules, one that is spherical and another that is ellipsoidal (Miura et al. 2008), which cannot easily be explained by compaction. Many Ornans-like carbonaceous (CO) chondrites are also reported to contain irregularly shaped lobate chondrules (Jacquet 2021; Rubin & Wasson 2005), which due to their irregular shapes, also cannot be explained by compaction. The CM chondrite Murchison shows FGRs infilling surface irregularities in the chondrules, indicating that they were not spherical when they acquired their FGRs (Hanna & Ketcham 2018). A study by Floyd et al. (submitted) on the sizes and shapes of chondrules within 10 CM chondrites has found that none of the samples studied had spherical chondrules. Another study looking at chondrule shapes in multiple meteorite types (ordinary, enstatite, and carbonaceous chondrites) found that most chondrules were ellipsoidal in a manner that required deformation prior to accretion (Kadlag et al. 2023). It is evident that there is a population of chondrules that did not form as spheres, and it is likely that many carbonaceous chondrites have sampled this population.

There are multiple explanations as to how chondrules may form as non-spherical objects (Miura et al. 2008; Jacquet 2021; Rubin & Wasson 2021). It is also possible that some chondrules formed as irregular shapes which only acquired a semblance of being spherical during the acquisition of their FGRs (Hanna & Ketcham 2018).

One explanation for ellipsoidal chondrule formation is that when molten, chondrules may rotate, leading to the axis parallel to the rotation axis elongating (Miura et al. 2008). This rotation may occur prior to solidification, with chondrule precursors rotating due to shock waves in the early nebula. This rotation may continue through the melting of these precursors and lead to them recrystallizing into elongated chondrules, with the pressure of the gas flow defining their final shapes (Miura et al. 2008). Alternatively, this rotation may be caused by the shock waves themselves, with most chondrules crystallizing after they have stopped rotating (and thus forming spherically), while a subset may crystallize while still being exposed to the shock wave – and thus still rotating (Miura et al. 2008). This premature crystallization may be caused by the molten

chondrule being impacted, such as by a dust particle. Another possibility may be that an impact would cause the molten chondrule to rotate, leading to its ellipsoidal shape (Miura et al. 2008).

Impacts are involved with another set of explanations regarding the ellipsoidal shape of chondrules. While still partially molten, chondrules may have collided and merged, forming a compound chondrule, which may either have an ellipsoidal, lobate, or “dumbbell” shape (Jacquet 2021; Rubin & Wasson 2005). It is also possible for the partially molten chondrules to be deformed into non-spherical shapes by impact events. It is proposed that these deformed chondrules would become more rounded and ellipsoidal with multiple melting events (Rubin & Wasson 2005).

7.4 Implications of Kolang’s Petrofabric

Although it is entirely possible for Kolang’s chondrules to be aligned during an impact event, it is unlikely that they have been flattened by impacts. Kolang only shows evidence, both optically and by EBSD, for mild shock, with experiencing a maximum shock pressure of 10 GPa, a shock pressure too low for chondrule flattening (Tomoeka et al. 1999). There is yet to be any evidence for brittle deformation observed, with many of olivine grains within chondrules appearing to be in their original positions within the chondrule mesostasis and unaligned chondrules still having high ARs. Chondrule flattening through brittle deformation is an unlikely scenario. The fact that carbonaceous chondrites in general do not have spherical chondrules (Floyd et al. submitted; Kedlag et al. 2023) is also an indicator that chondrules may not necessarily form as spheres. Kolang’s chondrules therefore would have had to been flattened prior to accretion and petrofabric formation. Kolang’s mildly strained and elliptical chondrules are evidence that not all chondrules formed as spheres and that there is a population of chondrules that are ellipsoidal in shape. Many carbonaceous chondrites likely sampled this population explaining the abundance of non-spherical chondrules among them.

These ellipsoidal chondrules may require lower peak shock pressures to become aligned by an impact event than that required to flatten spherical chondrules, however further studies are required to confirm this. Impact events

may still be responsible for petrofabrics, albeit ones of lower intensity than previously thought. Impact experiments into CM chondrites with ellipsoidal, but unaligned chondrules would need to be conducted to confirm this.

Chapter 8 – Winchcombe: An Example of Rapid Terrestrial Alteration of a CM Chondrite

The contents of this chapter have previously been published in an article in *Meteoritics & Planetary Sciences* with the coauthors Martin R. Lee, Ashley J. King, Cameron J. Floyd, Pierre-Etienne Martin, Natasha V. Almeida, and Matthew J. Genge. The formatting of this article has been altered for the purposes of this thesis and its references are included with the other chapter references. The contents of this chapter are identical to the article. The full reference for the article is as follows:

Jenkins, L.E., Lee, M.R., Daly, L., King, A.J., Floyd, C.J., Martin, P.-E., Almeida, N.V. and Genge, M.J. (2024) 'Winchcombe: An example of rapid terrestrial alteration of a CM chondrite.' *Meteoritics & Planetary Sciences*, https://doi.org/10.1111/maps.13949

8.1 Abstract

Winchcombe is a CM chondrite that fell in England on February 28, 2021. Its rapid retrieval was well characterized. Within two polished sections of Winchcombe, terrestrial phases were observed. Calcite and calcium sulfates were found in a sample recovered from a field on March 6, 2021, and halite was observed on a sample months after its recovery from a driveway on March 2, 2021. These terrestrial phases were characterized by scanning electron microscopy, Raman spectroscopy, and transmission electron microscopy. Calcite veins crosscut the fusion crust and therefore postdate it. The calcite likely precipitated in the damp environment (sheep field) where the meteorite lay for six days prior to its retrieval. The sulfates occur on the edges of the sample and were identified as three minerals: gypsum, bassanite, and anhydrite. Given that the sulfates occur only on the sample's edges, including on top of the fusion crust, they formed after Winchcombe fell. Sulfate precipitation is attributed to the damp fall environment, likely resulted from sulfide-derived H2S reacting with calcite within the meteorite. Halite occurs as euhedral crystals only on the surface of a polished section and exclusively in areas relatively enriched in sodium. It was likely produced by the interaction of the polished rock slice with the humid laboratory air over a period of months. The sulfates, fusion-crust

calcite, and halite all post-date Winchcombe's entry into Earth's atmosphere and showcase how rapidly meteorite falls can be terrestrially altered.

8.2 Introduction

Meteorite falls are typically treated as near pristine with minimal terrestrial alteration, save for the fusion crust. However, there are various processes that they experience after landing that can alter their mineralogical, chemical, and isotopic compositions (Bland et al. 2006; Lee et al. 2021a). Unless these processes are considered when studying falls, terrestrial phases can be misidentified as extraterrestrial, leading to incorrect interpretations of the history of their parent body(ies). Knowing what changes meteorite samples have undergone due to terrestrial alteration will allow the mineralogy of meteorites to be better compared to asteroid samples. Additionally, understanding terrestrial alteration can lead to improved curatorial practices. It is also important to note that sample return missions are key in investigating other planetary bodies as they are the most pristine samples that can be obtained; any terrestrial contamination they will have undergone will be restricted to curatorial practices and sample analysis. Samples returned by the Japan Aerospace Exploration Agency's (JAXA) Hayabusa and Hayabusa2 missions to Itokawa and Ryugu, respectively and the National Aeronautics and Space Agency's (NASA) OSIRIS-REx missions to Bennu, respectively, will be the some of the few samples from another planetary body that have not been terrestrially compromised (Ito et al. 2022; Lauretta et al. 2017; Lee et al. 2021a; Nagao et al. 2011; Watanabe et al. 2017).

All meteorites experience terrestrial alteration to some degree, starting from the moment a meteoroid enters Earth's oxidizing and hydrolyzing atmosphere. During a meteor's initial descent, its exterior surface will experience temperatures of up to 12 000 K over a time period of no more than 40 seconds (Hezel et al. 2015). Much of its original mass is lost and the meteorite that reaches the Earth's surface is only a fraction of the original meteoroid (Hezel et al. 2015). A distinctive fusion crust will form on the meteorite's outer surface and is host to a variety of high temperature phases. They can include amorphous phases, anhydrous minerals with textures

associated with quenching, and the remnants of phases not destroyed by the rapid temperature increase (Genge & Grady 1999).

After making it through the Earth's atmosphere, the surviving meteorite may land in any environment, such as a frozen lake (Grossman 2000), a desert, or even in someone's home (Gattacceca et al. 2021). In the time between a meteorite's fall and when it is recovered it will be exposed to the terrestrial environment and may undergo a number of changes. The extent to which a meteorite is modified depends on its composition, the environment within which it has landed, and the time it has spent on the Earth's surface before being recovered. Meteorite falls are typically recovered quickly. Finds are often subaerially exposed for thousands of years (Jull et al. 1993), up to 2 Myr in some cases (Drouard et al. 2019), before they are collected; they will experience terrestrial alteration. The effects of terrestrial alteration may include the production of oxides, sulfates, carbonates, sulfides, arsenides, phosphates, hydrous silicates, and/or hydroxides (Bland et al. 2006; Ivanov et al. 2019; Jenniskens et al. 2012; King et al. 2020; Lee et al. 2021a; Tyra et al. 2007; Zurfluh et al. 2013); the dissolution of extraterrestrial minerals (Bland et al. 2006; Jenniskens et al. 2012; Lee et al. 2021); and contamination by terrestrial organics and atmospheric hydrocarbons (Cronin & Pizzarello 1990).

Terrestrial alteration is often treated as if it stops after the meteorite is recovered. This, however, is not the case. Simply being present in Earth's oxidizing and water-rich atmosphere can be enough to cause metals to alter and terrestrial water to be incorporated into the meteorite (Bland et al. 2006; Lee et al. 2021a). For example, pieces of the fall Ivuna (CI1) were stored in different conditions after being received by the Natural History Museum (NHM) in 2008; some fragments were stored in a controlled inert N2 atmosphere while others were wrapped in fluoropolymer film and kept in an uncontrolled atmosphere. Terrestrial sulfates formed within the fragments that were in an uncontrolled atmosphere within a few years whereas the fragments kept in a controlled atmosphere did not have these terrestrial phases (King et al. 2020). Gypsum is sometimes found in carbonaceous chondrites and although it can be attributed to parent body processes, it is also a common terrestrial weathering product, making interpreting its formation difficult (Losiak & Velbel 2011).

The growth of terrestrial phases in meteorite falls are not restricted to Ivuna. Orgueil (CI1) is well known to have large veins of terrestrial sulfates, some of which are associated with grains of magnetite, which can also be found throughout the meteorite (Gounelle & Zolensky 2001; Gounelle & Zolensky 2014). The magnetite originates from the alteration of pyrrhotite, believed to have occurred on Orgueil's parent body (Gounelle & Zolensky 2014). Terrestrial sulfates have also been reported in Tonk (CI1), Alais (CI1), and Revelstoke (CI1) (Gounelle & Zolensky 2001; Gounelle & Zolensky 2014). Additionally, terrestrial carbonates are reported in Vigarano (CV3) (Abreu & Brearley 2005); and Fe-Ni metal has been observed altering to oxides in New Concord (L6), Murchison (CM2), and Murray (CM2) (Lee & Bland 2004; Rubin et al. 2007).

Several procedures undertaken during sample storage, preparation, and data collection can also alter a meteorite. As exemplified by the Ivuna samples, meteorites can be contaminated by both the sample preparation processes (e.g., epoxy, coating) and data collection (e.g., electron beam damage) (King et al. 2020). The use of water during sample preparation may also cause evaporite minerals to grow and/or dissolve (Floyd & Lee 2021).

The Winchcombe meteorite is a Mighei-like (CM) carbonaceous chondrite that fell in Gloucestershire, United Kingdom, on the evening of February 28, 2021. Although some fragments were recovered on March 1, 2021, within 12 hours of the fall, others took weeks to find, with the last documented fragment being collected on April 1, 2021 (Russell et al. 2022). Most of the Winchcombe samples were recovered within the first week of its fall. After retrieval, samples were placed into sealed plastic bags. Despite this rapid collection, Genge et al. (2023) observed electron beam-sensitive calcium oxalates growing within the fusion crust of some samples from the piece of Winchcombe recovered after it spent six days in a sheep paddock after the fall. Additionally, on the same stone, Russell et al. (2022) also observed a white-yellow substance growing on its exterior.

As the fall, recovery, and curation of Winchcombe is very well documented (King, Daly et al. 2022; Russell et al. 2022), it is an ideal sample with which to study the effects of terrestrial alteration on CM falls. We describe carbonate, sulfate, and halide phases in Winchcombe that may be interpreted as

having a parent body or a terrestrial origin. We argue that these phases formed after Winchcombe's fall during its brief time exposed to Earth's environment. This work has important implications for understanding how terrestrially compromised even the newest meteorite falls can be, as well as how curation and analysis may affect both meteorites and returned samples, including those from the C-complex asteroids Ryugu and Bennu.

8.3 Materials

Winchcombe is a CM chondrite breccia composed of numerous lithologies. These lithologies have different geologic histories on Winchcombe's parent body and are distinct in their degree of aqueous alteration (Suttle et al. 2022). Here we focus on two polished rock sections (BM.2022,M2-42 P30540 and BM.2022,M9-14 P30552), each from a different fragment of Winchcombe, each recovered from a different location at a different time after the fall. The fragment from which P30540 was made was collected from a domestic garden lawn on the morning of March 2, 2021. The weather remained dry between the time when Winchcombe fell and when the fragments were recovered by the Wilcock family (King, Daly et al. 2022). It was placed into a plastic pot from a supermarket that was, prior to recovery, rinsed with warm water and then cleaned with a dishwasher and dishwashing powder. The fragment from which P30552 was made was collected on March 6, 2021, six days after its fall, from a sheep grazing field using nitrile gloves and was placed into a plastic bag with other pieces that were coated in soil from the site. Prior to recovery, P30552 was exposed to a damp and humid environment, which although was free from rainfall, often had dew and potentially frost, experiencing temperatures ranging from -3°C to 13°C and humidity ranging from 44% to 95% (Met Office Weather Observations Website: Observation Site Bishops Cleeve). About 2 months after recovery, on May 10, 2021, an amorphous white-yellow phase was observed on its fusion crust (Russell et al. 2022). This material was not recorded during recovery.

On March 5, 2021, and March 8, 2021, respectively, the containers were received by the NHM, London and opened. With tweezers and nitrile gloves, the pieces of meteorite were transferred into glass vials with polyethylene caps, which were in turn stored in labelled polyethylene bags and kept within a desiccator until pieces were selected for the preparation of polished sections.

The two polished rock sections used in this study (P30540 and P30552) were prepared at the NHM during the first week of May 2021. They were set in epoxy resin and then polished with ethanediol and alumina. The samples were transferred to the University of Glasgow (UoG), where they were kept in plastic boxes in a laboratory environment under ambient conditions.

8.4 Methods

8.4.1 Sample Preparation

An overview of the general sample processing of each sample prior to analysis is shown in Fig. 8.1. Before data collection using scanning electron microscopy (SEM) and transmission electron microscopy (TEM), the polished sections were coated with 20 nm of carbon. The carbon coat was removed and reapplied every few months. Removal used 0.3 µm alumina glycol or 0.3 µm alumina paraffin on 0.3 µm alumina disks, before being cleaned with ethanol or acetone and patted dry with a Kimwipe. In the Results section it is stated whether data sets have been collected before or after any reapplication of the carbon coat.

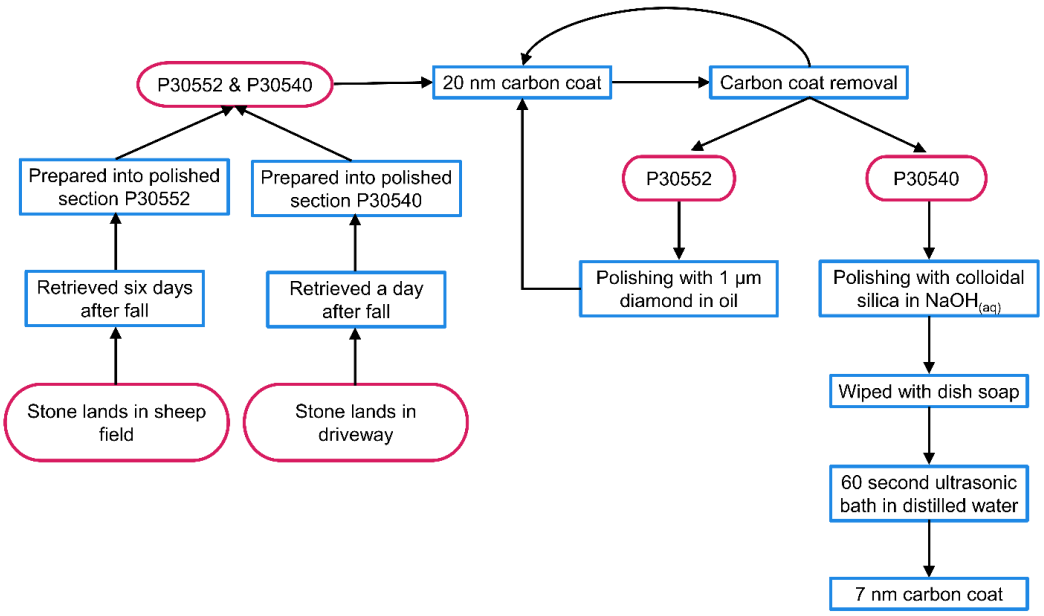

Fig. 8.1. Overview of the sample processing both polished sections P30552 and P30540 experienced prior to data collection.

P30540 was also prepared for electron backscatter diffraction (EBSD) analysis as part of a parallel study. For this, the carbon coats were removed using 0.3 µm alumina glycol on 0.3 µm alumina disks, before P30540 was rinsed with distilled water and patted dry with a Kimwipe. P30540 was then polished

for 30 minutes using a vibromat with a 0.1 μm diamond polishing plate, 100 nm colloidal silica in a $NaOH_{(aq)}$ solution. After being polished with colloidal silica, P30540 was wiped with dish soap to remove the colloidal silica and spent 60 seconds in distilled water in an ultrasonic bath, before being patted dry with a Kimwipe. P30540 was then coated with 7 nm of carbon. The data from P30540 described here was collected prior to preparation for EBSD.

Raman data were collected for P30552 after it had been carbon coated for SEM analysis. To obtain the Raman data, the carbon coat was removed. P30552 was also polished prior to focused ion beam (FIB) work by applying 1 μm diamond suspended in an oil composed of petroleum distillates, quaternium-18 bentonite, and trace amounts of quartz (Buehler MetaDi oil-based monocrystalline diamond suspension) on a 1 μm diamond mat. The sample was cleaned afterwards using ethanol and Kimwipes. This polishing took place on May 9, 2022. Note that other electron transparent lamellae were also extracted using the FIB from select areas in both samples prior to collection of any of the data described here. These particular FIB lamellae were not investigated as part of this work, but their extraction process will be discussed where relevant, and results from TEM and atom probe tomography analysis of these lamellae are presented in Daly et al. (submitted).

8.4.2 Microanalysis

Backscattered electron (BSE) and secondary electron (SE) images, and EDS maps and spectra were acquired using a Carl Zeiss Sigma Variable Pressure field emission gun SEM operated at 20 kV and 1-2 nA at the Geoanalytical Electron Microscopy lab (GEM), UoG. For the EDS maps and spectra, X-rays were collected using an 80 mm2 silicon-drift detector. BSE images and EDS maps were montaged and analyzed using version 5.1 of the Oxford Instruments AZtec program. Sample P30552 was also studied by cathodoluminescence (CL) using a FEI Quanta 200F Environmental SEM equipped with a KE Developments panchromatic CL detector using the method described by Lee et al. (2014).

Raman data were collected using a Renishaw Invia Raman microscope at GEMusing a 514 nm wavelength laser source with a laser power of 45 mW and a spot size of 1 μm. During Raman data collection for P30552, reflected light

microscopy was used to navigate around P30552 to find analysis areas. As some of the areas in the carbonates displayed anomalous optical properties, reflected light microscopy was used further to study them.

Electron transparent lamellae were extracted from carbonates in the fusion crust, as well as the sulfates around the edges, of P30552 at the Kelvin Nanocharacterization Centre (KNC), UoG, using a DualBeam FIB microscope. Diffraction-contrast images and selected area electron diffraction (SAED) patterns were collected from the lamellae using a FEI T20 TEM operated at 200 kV in the KNC.

8.5 Results

8.5.1 Sample Descriptions

CM chondrites are composed of the primary materials from nebular condensation, including chondrules and calcium-aluminum rich inclusions (CAIs) along with finer grained materials that form an enclosing matrix as well as rims around chondrules and CAIs. These materials have been aqueously altered to produce a wide range of secondary minerals that may include but are not limited to serpentines (lizardite and cronstedtite), tochilinite, carbonates, and sulfides (Bunch & Chang 1980). Many CM chondrites are breccias and can be classified in their degree of aqueous alteration based on the relative abundance of primary anhydrous components and their secondary alteration products (Howard et al. 2015). These classifications often range CM1 to CM3, where CM1 is most altered and CM3 is least altered (Van Schmus & Wood 1967). For CM2 chondrites, one of the classification systems for degree of alteration further sorts them into subtypes ranging from CM2.0 to CM2.7 (Rubin et al. 2007; Rubin et al. 2015).

Sample P30540 (Fig. 8.2) is a polished rock slice in an epoxy puck and is ~6.0 mm^2 in area. It is composed of three clasts, each lithologically distinct: the F lithology, the Mx lithology, and the G lithology (Suttle et al. this issue). The F lithology is characterized by its altered chondrule pseudomorphs and its lack of tochilinite-cronstedtite intergrowths (TCIs), having been extensively aqueously altered. The F lithology is of the petrologic type CM1. The Mx lithology is characterized by its cataclastic nature and is made up of a variety of

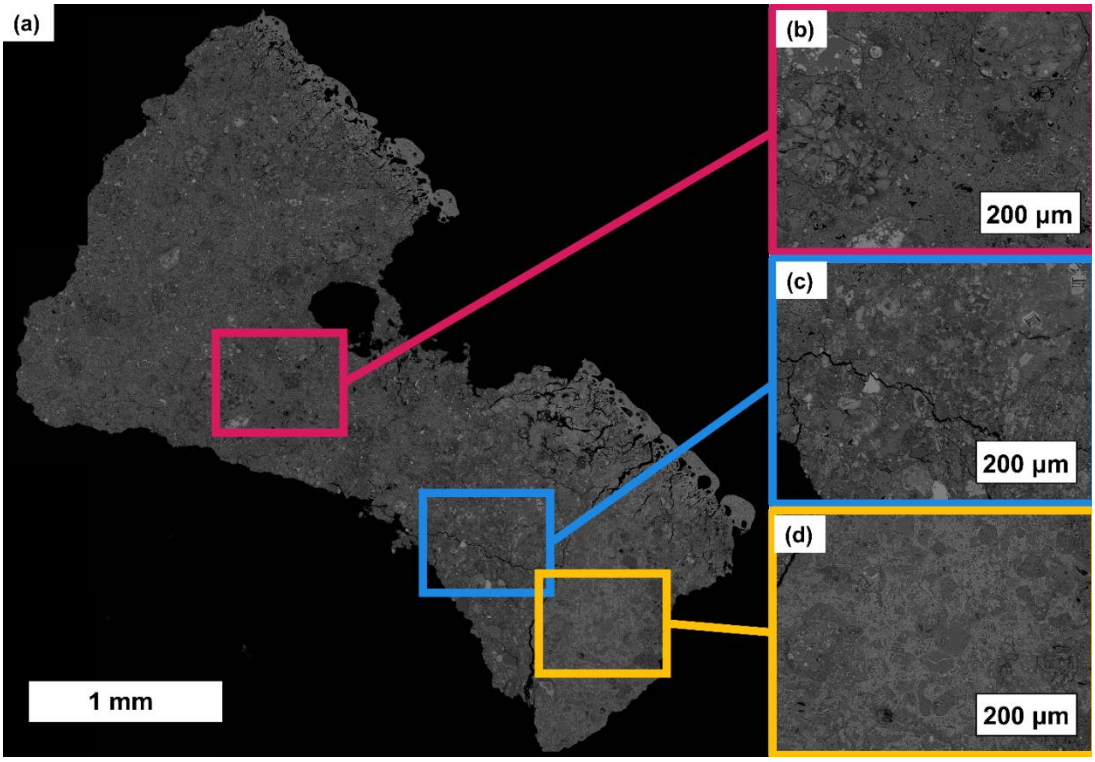

Fig. 8.2. BSE images of the P30540 polished section of Winchcombe. a) The whole rock sample. b) The F lithology. c) The Mx lithology. d) The G lithology.

components, including primary silicate mineral fragments, chondrules, TCIs, fine-grained serpentine-rich matrix, and CAIs. The G lithology is mainly composed of a mixture of fine-grained serpentine-rich matrix and TCIs, with some chondrules (Suttle et al. 2022). As it retains some chondrules, the G lithology is less altered than the F lithology and has a petrologic subtype of CM2.1. The F and G lithologies are in contact with the fusion crust, and all lithologies contain carbonate mineral grains.

Sample P30552 (Fig. 8.3) is a rock slice ~9.8 mm^2 in area in an epoxy puck. Also within the epoxy puck is 100 μm^2 of soil from the landing site (Fig. 8.3b). P30552 is composed of two clasts that are both of the A lithology (Fig. 8.3b and 8.3d) and are composed of partially altered chondrules among a matrix rich in TCIs and serpentine (Suttle et al. 2022). Lithology A has less altered components than the G lithology and has a petrologic subtype of CM2.2. Lithology A also contains carbonates (Suttle et al. 2022). Both clasts are in contact with the fusion crust.

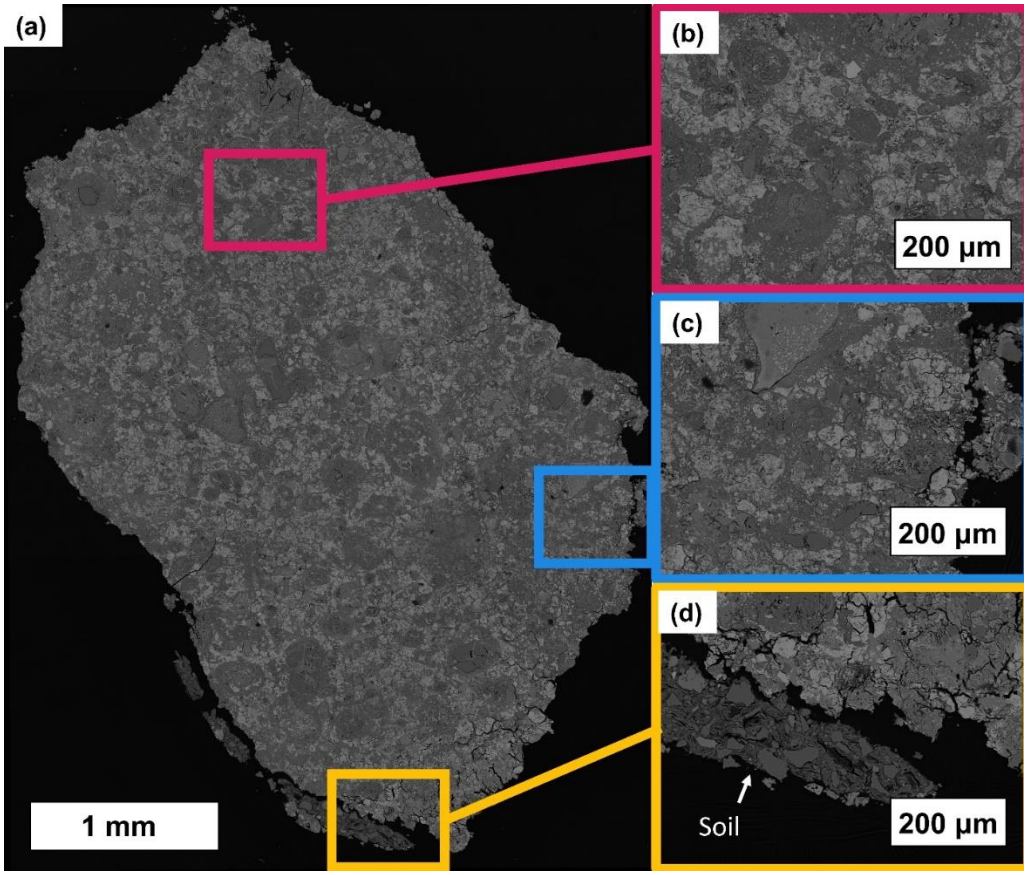

Fig. 8.3. BSE images of the P30552 polished section of Winchcombe. a) The whole rock sample. b) The larger main clast. c) The smaller clast. d) The soil on the edge of the sample.

8.5.2 Calcite

The fusion crusts of both samples are fractured. Some of the fractures in P30552 are filled by a phase with an elemental composition of C, O, and Ca as determined by qualitative EDS (Fig. 8.4) and best matches $CaCO_3$. These carbonate veins are about 10 to 20 µm in width and are uniform in both chemical composition and texture, showing no signs of vesiculation. The carbonate veins are non-luminescent when observed by SEM-CL, thus suggesting that they are Mn-poor (<10 ppm) (Habermann et al. 1996).

Under reflected light, the calcium carbonate has two different appearances. Most of the carbonate is light grey-blue in color, whereas that at the edges of the veins is dark grey (Fig. 8.5). Although the dark grey appearance of the carbonate at the veins' edges is typical for calcite, the appearance of the light grey-blue phase is not.

Raman spectra collected for the dark grey carbonate (Fig. 8.6a) have peaks at 127 cm^{-1}, 154 cm^{-1}, 281 cm^{-1}, 710 cm^{-1}, and 1085 cm^{-1}, which best

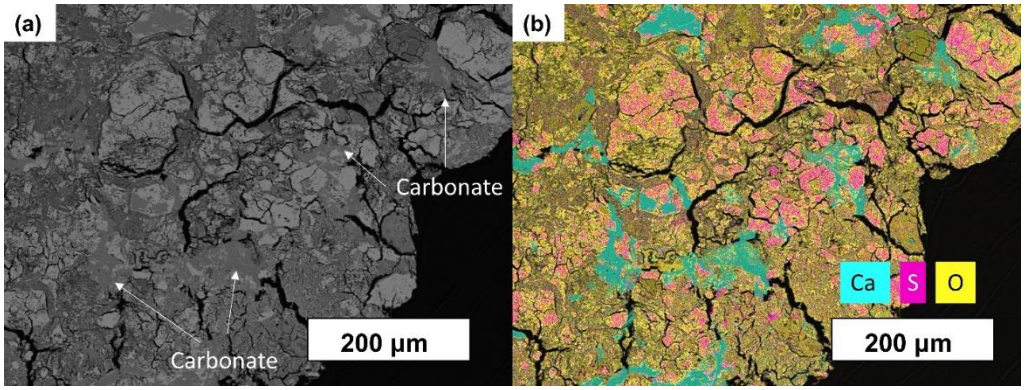

Fig. 8.4. The fusion crust of P30552 with veins of calcium carbonate. a) BSE image. b) Ca-S-O false color EDS map showing veins of calcium carbonate in turquoise.

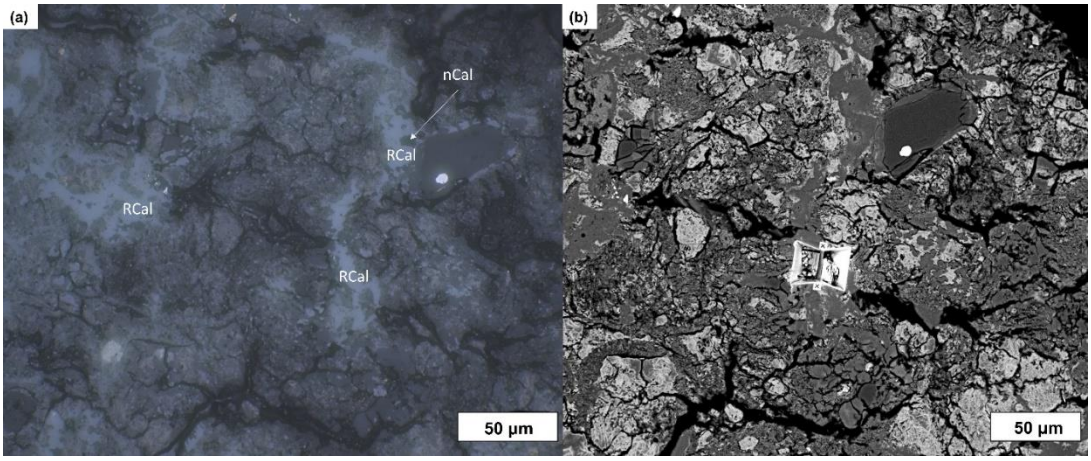

Fig. 8.5. Images of calcite in P30552. a) Reflected light image. The dark grey phase is nCal, while the light blue-grey phase is RCal. b) BSE image of the same area in (a) taken on May 17, 2022, after an electron transparent lamella was extracted using FIB.

matches calcite (e.g., Kim et al. 2021). Spectra from the light grey-blue phase (Fig. 8.6b) had very few peaks, which could be due to the sample being strained, poorly crystalline, or amorphous. Those peaks that were identified are at 284 cm^{-1}, 1085 cm^{-1}, and 1261 cm^{-1}, and are again consistent with calcite. Hereafter, the carbonate that has optical properties under reflective light typical for calcite is referred to as “nCal” (normal calcite) and the carbonate that is anomalously reflective is referred to as “RCal” (reflective calcite).

TEM images of the electron transparent lamella produced by FIB for the RCal show a crystalline phase composed of multiple parallel subgrains (Fig. 8.7). The boundaries between the subgrains display dislocations. Most of the subgrains are in similar crystallographic orientations, save for one subgrain on the very edge, which likely belongs to the nCal. The SAED patterns acquired for all subgrains indexed calcite.

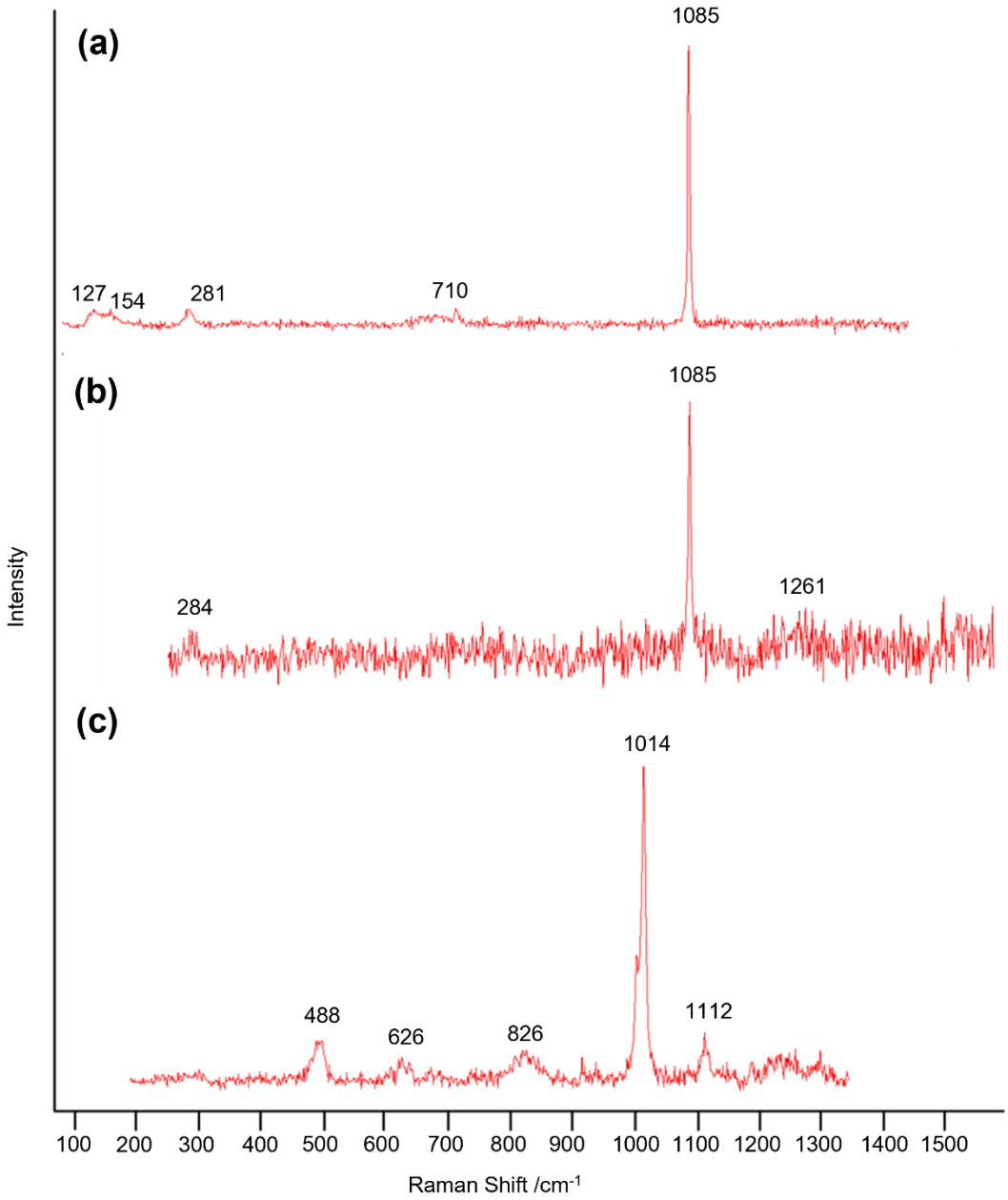

Fig. 8.6. Raman spectra from P30552. a) For the dark grey phase matching calcite, referred to as nCal. b) For the light grey-blue phase whose few peaks match calcite, referred to as RCal. c) For sulfates which best match bassanite.

8.5.3 Calcium Sulfates

The BSE images, and EDS and Raman data relating to the sulfates in P30552 were collected on different dates (September 14, 2021; November 1, 2021; January 13, 2022) between which the carbon coat had been removed and reapplied. EDS maps show that a Ca, S, and O-rich phase (likely calcium sulfate) occurs exclusively on the edges of the sample in patches that range in size from 10 to 130 μm (Fig. 8.8a) and is not present anywhere else within the meteorite. One of these areas is on top of the fusion crust (Fig. 8.8b). There are also small patches of calcium sulfate on the outer edge of the adhering soil, but not within

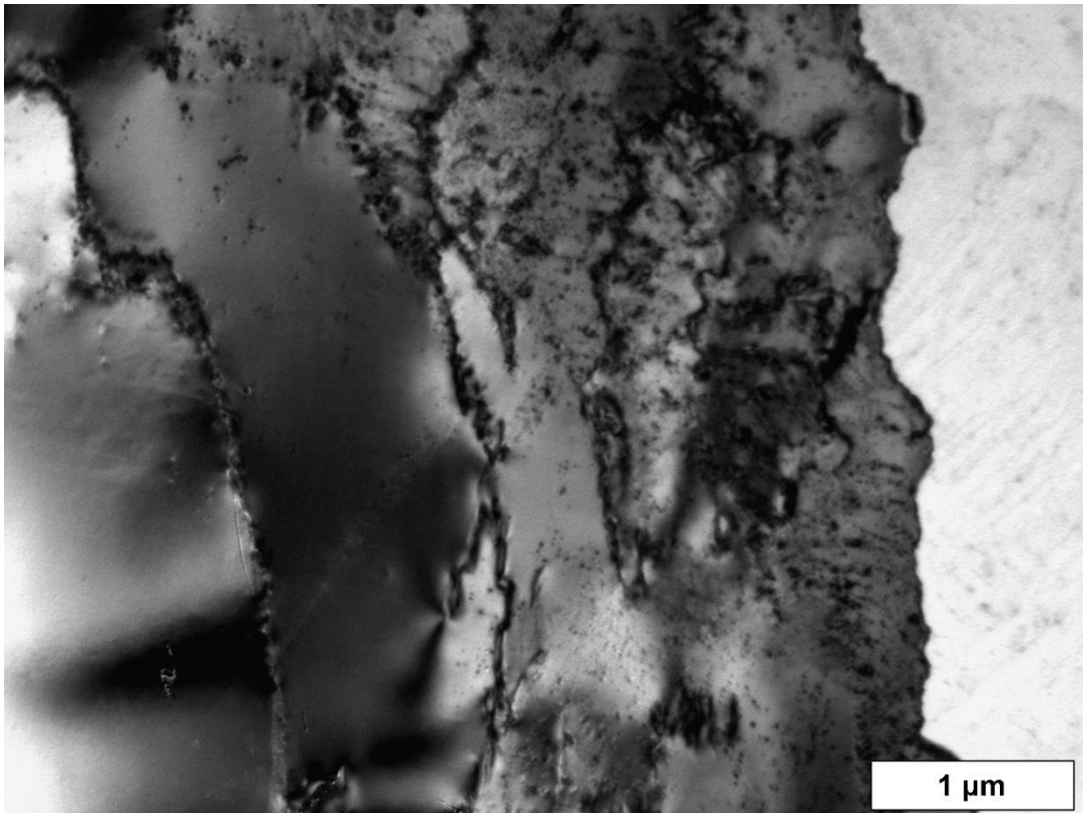

Fig. 8.7. Brightfield TEM image of a FIB section of carbonates taken from the RCal in P30552. Most of the subgrains (dark grey) are in a similar crystallographic orientation except for the subgrain (white) on the rightmost edge.

the soil itself. BSE images show that the calcium sulfate is embedded within the epoxy (Fig. 8.8c), and there are multiple instances of the calcium sulfates being in contact with calcite. The phase must be soft and friable because images of the same areas before and after removal and reapplication of the carbon coat show that it has degraded (Fig. 8.9a & 8.9b). Raman spectra of the calcium sulfates have several peaks whose closest match are bassanite, although some peaks match gypsum and/or anhydrite better (Fig. 8.6c, Table 8.1). It is thus likely that the calcium sulfate is primarily bassanite intergrown with minor amounts of gypsum and anhydrite. Two of the spectra show peaks centered ~820 cm^{-1} that likely originated from a nearby phase, although there is insufficient data to identify it.

TEM images were collected on June 15, 2022, for a FIB lamella extracted from an area of calcium sulfate. The TEM images show that the FIB section contains a high density of pores, many of them elongate and sinuous, up to ~1 µm in length (Fig. 8.10a). Within the calcium sulfate are patches of finely crystalline phyllosilicate up to a couple of micrometers in size (Fig. 8.10a). Individual calcium sulfate crystals are sub-micrometer in size. SAED patterns

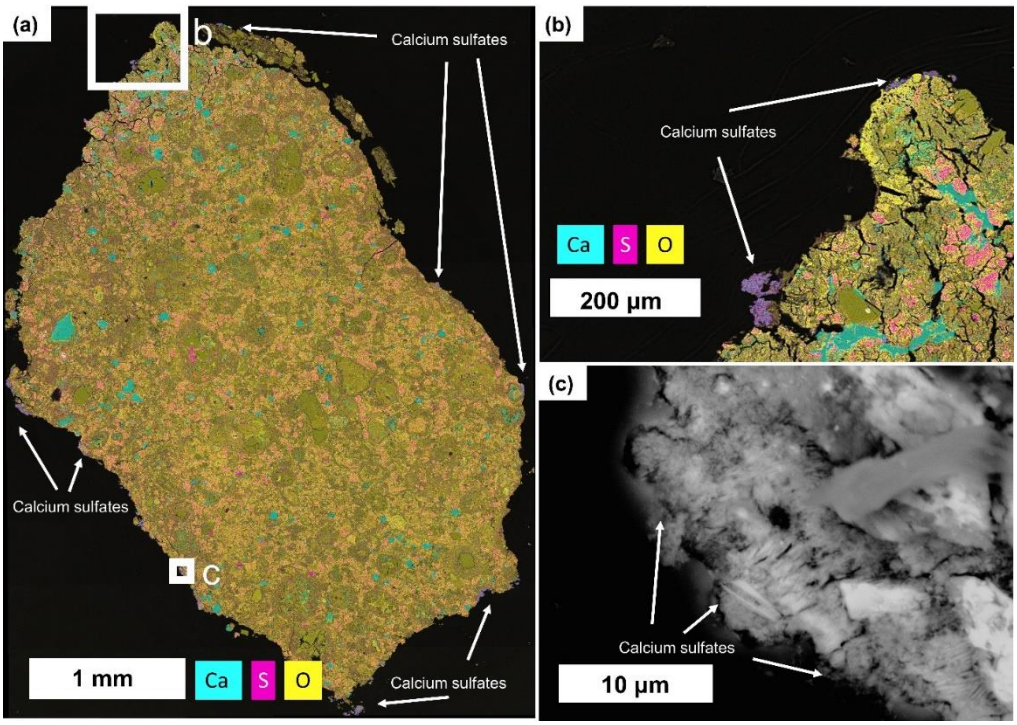

Fig. 8.8. Calcium sulfates in P30552. a) Ca-S-O EDS map of whole sample. Calcium sulfate can be seen along the sample's edges in purple. b) Ca-S-O EDS map of the fusion crust. Clumps of calcium sulfate occur on the exterior of the fusion crust. c) BSE image of calcium sulfate showing it embedded within the epoxy.

Table 8.1. Raman peak positions for gypsum, bassanite, anhydrite (from Liu et al. 2009), and for the spectra collected from the calcium sulphate phase.

Gypsum	Bassanite	Anhydrite	Spectra 1	Spectra 2	Spectra 3
415		416			
	427				
439					
	489	499	492	484	493
		612			
620	628	629	626	625	638
670	668	676			
				820	826
1008				1002	
	1015	1017	1014	1014	1014
		1110	1111	1113	1112
1135	1128	1128			
		1159			

acquired with a large 4 µm diameter aperture yielded broken rings. The strongest reflections have d-spacings of 0.600 nm, 0.344 nm, 0.300 nm, and 0.275 nm, which are indicative of bassanite lattice spaces with miller indices (100), (310), (200), and ($\bar{1}$14), respectively (Fig. 10b). These reflections are consistent with previous SAED work on bassanite in carbonaceous chondrites (Lee 1993) and synthetic materials (Anduix-Canto et al. 2021). If gypsum or anhydrite were present, reflections would be expected with d-spacings of 0.458 nm for the

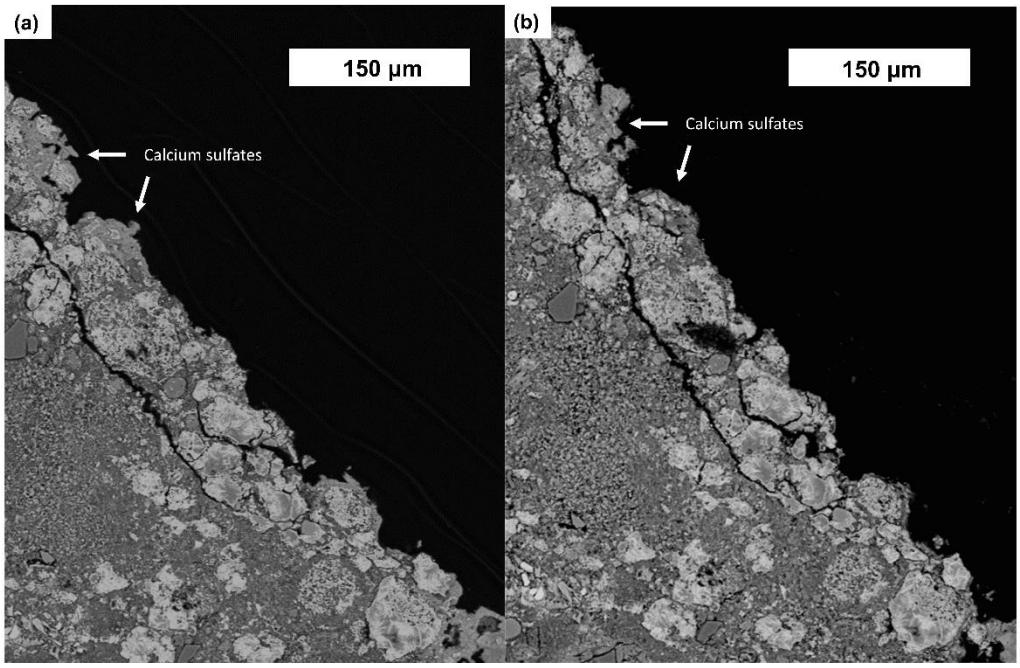

Fig. 8.9. Degradation of calcium sulfates in P30552. a) BSE image of an area with calcium sulfates taken on September 14, 2021. Calcium sulfates, among other phases, can be seen on the meteorite's edge. b) BSE image of the same area as (a) taken on November 1, 2021. Although some of the calcium sulfates remain, others are missing.

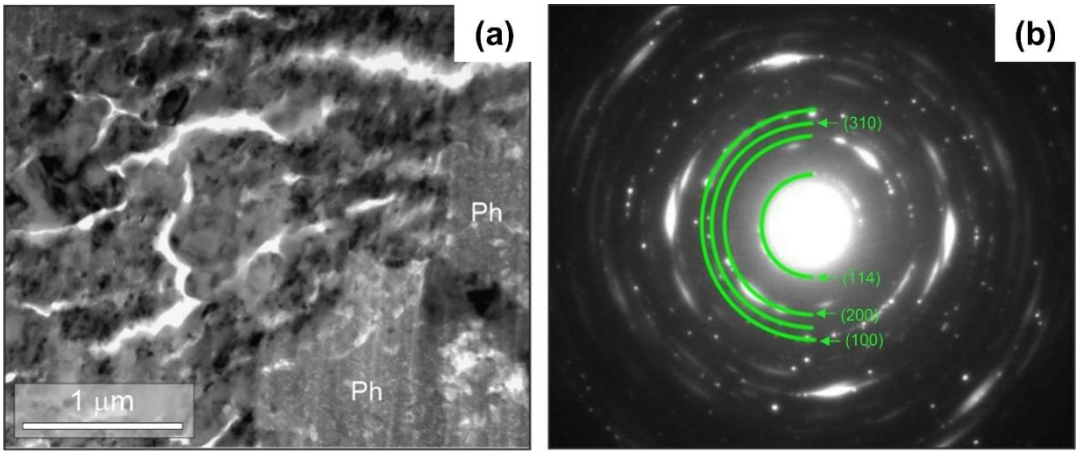

Fig. 8.10. a) Bright-field TEM image of an area of calcium sulfate, which is finely polycrystalline and contains patches of phyllosilicate (Ph). The sinuous white features are pores. b) SAED pattern of the calcium sulfate. The innermost four rings have been highlighted in green and are attributable to the (100), (310), (200), and ($\bar{1}$14) miller indices of bassanite.

miller index (021) for gypsum (Saha et al. 2012), and 0.350 nm for the miller index (200) for anhydrite (Lee 1993). None of the gypsum or anhydrite reflections were observed. Bassanite is the main calcium sulfate present within Winchcombe and is the only sulfate composing the FIB lamella, however the gypsum and anhydrite observed with Raman likely exist in small quantities within Winchcombe.

8.5.4 Halite

All of the data relating to halite in P30540 were collected on September 11, 2021, prior to any carbon coat removals and prior to the sample being polished for EBSD. EDS maps show that Na is concentrated in small patches in serpentine-rich areas of the Mx and G lithologies (Fig. 8.11a). The Na-rich area in the Mx lithology has been previously targeted by FIB sample preparation techniques (Fig. 8.11b). Higher resolution BSE images and EDS maps show that this concentration of Na is related to a phase composed of both Na and Cl (Fig. 8.11b and 8.11c). SE images collected for the NaCl phase show that it occurs as euhedral cubes sitting on top of the sample's polished surface (Fig. 8.11d). Due to both the chemical composition and cubic crystal shape of the NaCl phase, it is identified as halite. Nearby the halite are areas within the fine-grained matrix that are enriched in Na, but not Cl.

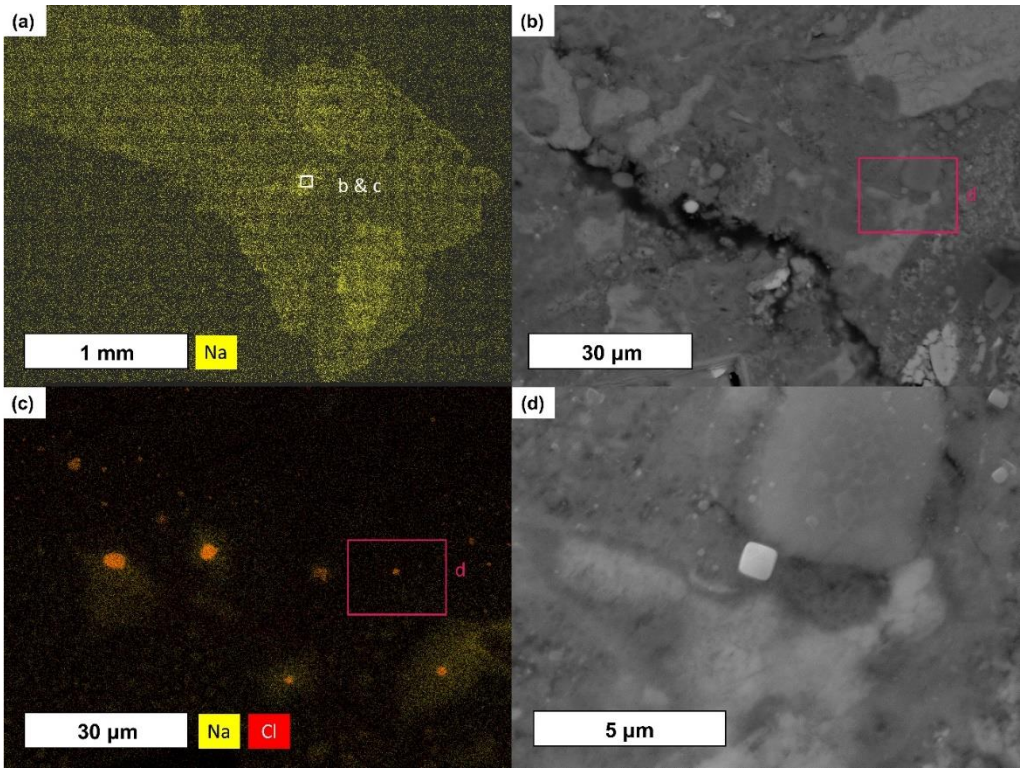

Fig. 8.11. Na-rich areas in P30540. a) Na EDS map of Mx and G lithologies. The white box indicates the area depicted in Fig. 8.11a and 8.11b. b) BSE image of an Na-rich area within the Mx lithology. The edge of a FIB pit can be seen on the bottom left-hand side of the image. The pink box indicates the area depicted in Fig. 8.11d. c) Na and Cl EDS map of an Na-rich area within the Mx lithology showing NaCl in orange. The pink box indicates the area depicted in Fig. 8.11d. d) SE image of NaCl phase in the Na-rich area. The NaCl cube in the center of the image is bright indicating that it is sitting on top of the sample's surface.

8.6 Discussion

There are three potentially terrestrial alteration phases observed within Winchcombe samples P30540 and P30552: calcite, calcium sulfates (bassanite, gypsum, and anhydrite), and halite. Due to the petrographic contexts these three alteration phases occur in, we argue that these phases are terrestrial in origin. In some other CM chondrite falls (e.g., Murchison, Cold Bokkeveld), sulfates and halite have been observed in similar contexts, however they are usually attributed to parent body processes (Barber 1981; Lee 1993; Lee et al. 2021a). Regarding sulfates, when a terrestrial origin is posited for them in CM chondrites, the timescale given for their growth is reported to be a few years (Fuchs et al. 1973; Lee et al. 2021a).

8.6.1 Calcite

Some of the calcite in P30552 infills fractures in the fusion crust that formed as the meteoroid entered Earth's atmosphere. If the calcite deposition was synchronous with fracture formation, then it is likely to have originated as a high temperature carbonate melt. If its deposition occurred after fracturing, then the calcite is a terrestrial alteration phase that precipitated after the meteorite's landing.

Carbonate melts occur on Earth at pressures exceeding 4 MPa or when fluorine is incorporated into the melt (Gozzi et al. 2014). When a meteor enters Earth's atmosphere, it experiences temperatures in the range of 2000-12 000 K and 2-5 MPa of pressure (Hezel et al. 2015). Thus, it is possible for carbonate melts to form under these conditions, however analogue experiments on fusion crust formation have yet to produce carbonate melts; carbonates usually decompose into CO_2 gas and oxides instead (Branstätter et al. 2008). It is also important to note that the calcite veins in Winchcombe do not show any quench textures or vesiculation (Fig. 8.5) that would support formation as a carbonate melt. Finally, modelling of the peak pressures experienced by the Winchcombe meteoroid during atmospheric entry show that it reached only 0.6 MPa (King, Daly et al. 2022; McMullan et al. 2023), and therefore a carbonate melt would not have been stable during Winchcombe's atmospheric entry and is unlikely to have formed the calcite veins.

It is therefore most probable that these calcite veins formed after the fusion crust, likely from a precipitate, either during the six days that the stone P30552 was made from spent in a field, or during the two months prior to the polished section P30552 being prepared. Terrestrial carbonates typically form in meteorites when atmospheric CO_2 reacts with Ca and other ions dissolved in liquid water in contact with the meteorite (Bland et al. 2006). Precipitation of P30552 calcite veins under low temperature and oxidizing conditions is consistent with its non-luminescence, which reflects low concentrations of Mn (<10 ppm) and is typical of carbonates that have formed at Earth's surface in other contexts, such as speleothems (Richter et al. 2018). The scenario of calcite veins within the fusion crust being the result of terrestrial weathering post-fall is thus plausible and is supported by the presence of Ca-oxalate that formed by post-fall terrestrial alteration of another sample of Winchcombe that was also made from the same stone (Genge et al. 2023).

There are two distinct phases of calcite defined by their optical properties in reflective light. There is nCal which has typical optical properties for calcite, and RCal which has an anomalously high reflectivity. The RCal constitutes the majority of the fusion crust's carbonate, while the nCal is restricted to isolated patches and the veins' edges (Fig. 8.5). The differences in reflectivity between RCal and nCal is unusual as they are chemically identical and the RCal's Raman spectra do not match any other known polymorph of calcium carbonate. One possibility is that the differences in optical properties are due to crystallographic orientation. Minerals that display bireflectance, like calcite, will reflect light differently depending on their orientation (Ebert et al. 2009). However, there are very few studies on non-ore minerals under reflected light at visible light wavelengths and as a result there is little documentation on how calcite's optical properties vary in reflected light microscopy. All the grains of the RCal typically grow in a similar crystallographic orientation (Fig. 8.7), and it is possible that the rapid crystallization of the calcite allowed it to preferentially grow in a set of similar orientations. It is likely that the high reflectance of the calcite is due to this orientation and P30552 happened to be cut in a way that made it highly reflective. The rapid growth may have also led to the RCal being strained, resulting in a Raman spectrum with few peaks. The nCal typically occurs on the vein's edges, in contact with other phases like

phyllosilicates and TCIs. It is likely that edges of the fractures offered a solid surface for the nCal to nucleate on at a different orientation to the rest of the RCal, forming the thin layer of nCal observed.

Winchcombe is also not the first meteorite fall with terrestrial carbonates. Vigarano (CV3) is also reported to have veins of carbonate. The carbonate veins in Vigarano are the result of terrestrial alteration of a piece of the meteorite that spent a month outdoors during the winter in the Ferrara province of Italy after it landed on January 22, 1910 (Abreu & Brearley 2005). The carbonates within Vigarano are more abundant than they are in Winchcombe because Vigarano spent a longer time subaerially exposed. Thus, there is a historical precedent for the calcite veins within the fusion crust of Winchcombe to be products of terrestrial alteration.

8.6.2 Calcium Sulfates

Calcium sulfates are common terrestrial alteration products for carbonaceous chondrites that are Antarctic finds (Losiak & Velbel 2011). However these minerals have also been reported in carbonaceous chondrite falls, including Cold Bokkeveld, Orgueil, and Ivuna (Gounelle & Zolensky 2001; King et al. 2020; Lee 1993). Regarding Ivuna, euhedral crystals of gypsum have been previously observed on top of the polished section, consistent with a terrestrial origin (King et al. 2020). However, Cold Bokkeveld contains calcium sulfates occurring in several generations and habits, indicating multiple precipitation events under varying conditions, such as what would be expected to occur during parent body aqueous alteration (Lee 1993).

Calcium sulfates in Winchcombe P30552 are embedded in epoxy, and therefore they must have grown before the sample was prepared on May 3, 2021. A terrestrial origin for these sulfates requires rapid growth occurring over a period no longer than two months. However there is petrographic evidence for its post-fall formation. The sulfates occur only on the outer edges of P30552, which are also likely the outer edges of the meteorite, and on top of the fusion crust. Bassanite, the main sulfate observed, breaks down into anhydrite (CaSO4) at about 390 K (Balliarno & Melis 2009) and anhydrite decomposes into CaO and SO_3 gas at about 1670 K (Newman 1941); neither mineral could have survived the

high temperatures of fusion crust formation. Furthermore, if the sulfates formed on Winchcombe's parent body, they should be found throughout the meteorite, not just on its edges. Therefore, the calcium sulfates in P30552 are terrestrial in origin, and show that these minerals can form rapidly within months of the fall.

Ivuna-like carbonaceous (CI) chondrites also commonly have terrestrial sulfates that are reported to form over timescales on the order of years (Gounelle & Zolensky 2001; King et al. 2020). CI chondrites also contain sulfates that are reported to be extraterrestrial due to being observed only weeks after their retrieval (Gounelle & Zolensky 2001). However, these sulfates might be terrestrial as well; sulfate growth within Ivuna has been induced in a laboratory setting using ethanol over a time period of only 3 days (Gounelle & Zolensky 2001), and CI-like samples returned from the asteroid Ryugu by Hayabusa2 are devoid of sulfates (Yokoyama et al. 2022). Given that the sulfates within Winchcombe formed quickly, the growth of terrestrial sulfates in CI chondrites could have been just as rapid.

The sulfates are likely to have formed as a by-product of the alteration of various minerals within Winchcombe. Like other CM chondrites, Winchcombe contains abundant sulfides (e.g., pentlandite, pyrrhotite) and carbonates (e.g., calcite and dolomite) (Suttle et al. 2022). Bassanite is metastable and can be formed by the dehydration of gypsum at temperatures of at least 368 K (Strydom et al. 1995), by the rapid quenching of calcium sulfate solutions, or as a precursor phase to gypsum (Tritschler et al. 2015). Terrestrially, sulfates can form during the evaporation of brines (Hardie & Eugster, 1970) or from a series of reactions, whereby sulfides (e.g., pyrrhotite) dissolve in water to form H_2S that is then oxidized to SO_4^{2-}, which in turn reacts with calcium carbonate in a hydrous environment to form calcium sulfates (Galdenzi & Maruoka 2003; Hose & Rosales-Lagarde 2017; Pirlet et al. 2010). This reaction is exemplified by equations 8.1-8.3, derived from Pirlet et al. (2010), which assume that pyrrhotite is the sulfide being altered and that the oxidization product is magnetite; oxidation of pyrrhotite to magnetite can result from the alteration of carbonaceous chondrites by water (Trigo-Rodríguez et al. 2019). Both gypsum and bassanite can also be produced synthetically, for example by flue gas desulfurization in coal power plants, where SO_x gas reacts with Ca-bearing

minerals, like calcite and portlandite, to produce calcium sulfates (Ambedkar et al. 2011; Caillahua & Moura 2018; Hajar et al. 2016).

$$2FeS_{(s)} + 3H_2O_{(l)} \rightarrow Fe_2O_{3(s)} + H_2S_{(aq)} + H^+_{(aq)} \quad (8.1)$$

$$H_2S_{(aq)} + 2O_{2(aq)} \rightarrow SO^{2-}_{4(aq)} + H_{2(aq)} \quad (8.2)$$

$$CaCO_{3(s)} + SO^{2-}_{4(aq)} + O.5H_2O_{(l)} \rightarrow CaSO_4 \cdot 0.5H_2O_{(s)} + CO^{2-}_{3(aq)} \quad (8.3)$$

SAED patterns and TEM brightfield images only identify bassanite (Fig. 8.10), however Raman spectra shows peaks that can be attributed to gypsum and anhydrite in addition to the bassanite peaks (Table 8.1). It is likely all three sulfates are present with bassanite being the most abundant. It is possible that bassanite and anhydrite formed alongside gypsum, as its precursor phases, or as dehydration products. Given the damp, humid, and cool conditions of the Winchcombe sheep field, gypsum dehydration is unlikely to be the source of bassanite and anhydrite. P30552 spent six days in a damp and oxidizing environment, and the calcium sulfates on the edges of P30552 are often in contact with calcite, making the reaction between dissolved sulfides and carbonates within the meteorite the most likely scenario for the sulfates' formation. This mechanism is also the likely source of sulfates in other falls, such as CI chondrites.

8.6.3 Halite

Halite occurs as euhedral cubes that sit on top of the polished rock slice of P30540 (Fig. 8.11d). This mode of occurrence indicates that the halite formed after the sample had been prepared into a rock slice and embedded into an epoxy puck. The P30540 sample had not been exposed to any fluids at the time of SEM data acquisition. The halite therefore formed in the months between the polished sample being produced on May 3, 2021, and the SEM imaging on September 11, 2021. It occurs only in specific areas within the P30540 sample and is not pervasive throughout the meteorite.

This is not the first report of halides within a CM chondrite. Barber (1981) has reported halite and sylvite in Murchison (CM2). These crystals were euhedral, similar in morphology to the halite in Winchcombe. The halides Barber

(1981) observed were found on a relatively recently prepared thin section that had not been in any contact with water. As a result, Barber (1981) interpreted them to be pre-terrestrial. However, as the terrestrial halite-bearing section of Winchcombe P30540 had also not been in any contact with liquid water, it is possible that the halides observed by Barber (1981) were also terrestrial.

The order in which evaporite minerals crystallize is dependent on the proportions of ions within a system, with halite crystallizing when there is a significant proportion of Na^+ and Cl^- (Hardie & Eugster 1970). Carbonaceous chondrites typically do not have a significant source of Na+ for halite and tend to precipitate Mg-rich phases when terrestrially weathered (Izawa et al. 2010), which makes the occurrence of halite in Winchcombe unexpected. Additionally, given the relatively high S abundance in carbonaceous chondrites, sulfates are more likely to precipitate than halides (Fanale et al. 2001; Hardie & Eugster 1970; Izawa et al. 2010). Carbonaceous chondrites that have areas with significant amounts of Na^+ may have contributions from cometary material (Nittler et al. 2019), however no evidence of cometary material has been identified in Winchcombe so far.

Regarding the source of Na for the halite within the meteorite, Na-rich minerals that may occur in carbonaceous chondrites are montmorillonite, panetheite, blödite, saponite, Na-phlogopite, nepheline, sodalite, melilite, and plagioclase (Barber 1981; Brearley 2006; Lee et al. 2019a; Nakamuta et al. 2006; Rubin 1997; Schrader et al. 2015). Carbonates in CM chondrites tend to have higher amounts of Na than is usual for terrestrial calcites (Riciputi et al.1993). Additionally, there are a number of Na-bearing phosphate minerals known to occur in iron meteorites (Rubin 1997). One of these Na-bearing phosphate minerals, buchwaldite, was observed within the P30540 section of Winchcombe, although it occurs in the F lithology and not where the halite was observed. Any one of the minerals listed could be a potential source of Na to facilitate the precipitation of terrestrial halite in carbonaceous chondrites. Daly et al. (submitted) also found Na concentrated in the boundaries between cronstedtite and lizardite in TCIs in section P30552 using FIB-based time of flight secondary ion mass spectrometry and atom probe tomography. This serpentine boundary concentrated Na may also be a source of Na for the halite, especially as the mobility of elements is elevated along grain boundaries (Lee 1995; Reddy et al.

2020) and water may trap positive ions like Na on the edges of minerals (Trigo-Rodríguez et al. 2019).

Within Winchcombe itself, the non-halite Na does not appear to be associated with P, ruling out any Na-phosphates as the source of Na. There is also not a significant amount of Al or Ca associated with the Na, discounting any aluminosilicates and Ca-bearing minerals as Na sources. This leaves the following three possibilities for the Na source: a Na-bearing phyllosilicate like Na-montmorillonite, an Na-sulfate like blödite, or Na concentrated in the boundaries between minerals. The latter is the most likely source as it has been observed by Daly et al. (submitted) in TCIs that have replaced carbonates within P30552, however none of the possible sources for the Na have been positively identified in the fine-grained matrix. Future studies with atom probe tomography may be able to confirm the source of Na.

8.6.4 Comparison to Other CM Falls

At the time of writing, the Winchcombe meteorite is one of 21 known CM chondrite falls. A year before Winchcombe fell, on August 1, 2020, Kolang (CM1/2) landed in Kolang, Indonesia. The main mass fell in a coffin-maker's home, while the rest of the meteorite fell in a rice-paddy. The majority of the meteorite was recovered within seconds to hours of it falling (Gattacceca et al. 2021). Kolang is a CM1/2 chondrite that is, like Winchcombe, a rapidly recovered breccia. However, to date, there are no reports of sulfates or fusion crust carbonates within Kolang. It is important to note that the method of retrieval for Kolang (e.g., with or without gloves), was not recorded.

Three years before Kolang, on November 27, 2017, Shidian (CM2) fell in the Yunan Province of China, landing in the areas around two villages (Fan et al. 2020). Within hours of the fall, many of the pieces were recovered (Shijie Li, personal correspondence). Shidian is similar to Kolang and Winchcombe in its overall degree of aqueous alteration (Fan et al. 2020; King et al. 2021a; Suttle et al. 2022), however its degree of terrestrial alteration is more similar to Kolang than Winchcombe as there are no reports of sulfate growth within Shidian at the time of writing. The retrieval process for Shidian was also not recorded.

In September 1969, the well-known CM2 chondrite, Murchison, fell in Australia. Some fragments were retrieved hours after the fall (Botta & Bada 2002), but others were not recovered until months later in February and March of 1970 (Kvenvolden et al. 1970). Although the majority of Murchison exhibits less parent body aqueous alteration than Winchcombe (Rubin et al. 2007; Suttle et al. 2022), it contains similar alteration phases to Winchcombe that may have a terrestrial origin, including halite and sulfates (Barber 1981; Fuchs et al. 1973). Some sulfates are observed within the meteorite itself, typically associated with calcite (Armstrong et al. 1982) and within the meteorite's fractures (Fuchs et al. 1973). Whether the sulfates in Murchison are terrestrial or extraterrestrial has yet to be conclusively confirmed. If terrestrial, it is assumed that the extended time some of the Murchison samples spent subaerially exposed before retrieval, the environment it was curated in, and/or its overall age led to the proliferation of terrestrial sulfates throughout the meteorite.

Cold Bokkeveld is the oldest CM2 chondrite fall, having landed in South Africa in 1838 (Lee 1993). The Cold Bokkeveld meteorite fragmented and landed in a variety of environments ranging from fields to swamps, however many of the fragments were recovered almost immediately after the fall (Maclear 1840). Cold Bokkeveld is known to have abundant sulfate phases occurring in a variety of morphologies that crosscut each other, indicating multiple generations of alteration. Whether these sulfate generations are terrestrial or extraterrestrial is currently unknown (Lee et al. 2021a). The fibrous morphology of some of the calcium sulfate within Cold Bokkeveld indicates that, like Winchcombe, its calcium sulfates grew quickly. Unlike Winchcombe, the sulfates within Cold Bokkeveld are not restricted to the outside edges of the meteorite and occur along fractures and patches within the meteorite itself, in a similar manner to the sulfates observed in Murchison (Lee 1993).

Older CM falls like Murchison and Cold Bokkeveld typically contain more sulfates than younger CM falls, although whether these sulfates are extraterrestrial or terrestrial is often unknown. In the short term, the amount of terrestrial phases observed is primarily affected by the time exposed to outdoor conditions before retrieval. This can be seen in not onlythe stark difference in degree of terrestrial alteration between Winchcombe samples, but also between Winchcombe and other recent CM falls like Shidian and Kolang. The Winchcombe

sample P30540, which was recovered within hours of falling, only shows halite precipitating on the surface of certain areas of the meteorite as a result of it being stored in a non-inert atmosphere and having areas with an unusual enrichment in Na, whereas the Winchcombe sample P30552, recovered from a damp sheep field a week after falling, has terrestrial carbonates in its fusion crust and terrestrial sulfates growing along its edges. Neither Kolang nor Shidian show any immediate signs of terrestrial alteration (beyond the formation of their fusion crusts) despite being older than Winchcombe. It is likely that their near immediate retrieval is the reason for the minimal levels of terrestrial alteration observed so far. All three meteorite falls will probably become more terrestrially altered with time and will likely show signs of oxidation unless they are stored in an inert atmosphere. To understand the terrestrial alteration of carbonaceous chondrites in the long term, it is imperative that these more recent falls are periodically assessed for the presence and abundance of sulfates and other alteration phases. Additionally, by studying how terrestrial alteration may occur in falls, better protocols for sample storage and curation can be developed for both meteorite falls and samples returned by missions (e.g., Herd et al. 2016).

8.7 Conclusions

Winchcombe is a relatively fresh meteorite fall, but within it are a variety of terrestrial phases that formed over different timescales. Carbonates precipitated within the fusion crust in a damp environment, while those same damp conditions produced calcium sulfates, primarily bassanite, from the reaction of calcite with dissolved sulfides. It took no more than two months for both the carbonates and sulfates to form from the six days the sample spent in the damp field. In addition, laboratory storage of P30540 in a non-inert atmosphere allowed halite to precipitate on areas of the meteorite that are enriched in Na. The precipitation of halite took place in two months. The formation of these phases showcases how rapid terrestrial alteration can be.

Terrestrial alteration begins to occur the moment a meteorite enters Earth’s atmosphere, and thus meteorite falls cannot be completely pristine. Assuming that a meteorite has escaped terrestrial alteration can lead to incorrect interpretations regarding certain phases, like evaporites. The extent of terrestrial alteration developed from the fall site can be limited by rapid

recovery and appropriate curation of the sample. Thus, when studying meteorites, it is important to keep in mind how long the sample has spent on Earth's surface and in what environment, as well as the procedures that were used in sample storage, preparation, and data collection. It is also important to consider the petrographic contexts of various minerals as this is not only good practice for understanding the processes the meteorite has experienced but will yield clues as to whether a given phase is terrestrial or extraterrestrial in origin.

Rapid retrieval of a meteorite can mitigate terrestrial alteration, however even then alteration (e.g., halite precipitation) may still occur, as Earth's atmosphere is hydrolyzing and oxidizing. To mitigate this, rapidly recovered falls need to be stored in an inert atmosphere. The most pristine samples of asteroids that can be acquired are from missions like Hayabusa2 and OSIRIS-REx. This is one of the many reasons why sample return is critical to expanding our knowledge of the Solar System. Understanding weathering of meteorite falls will help improve curation protocols for these asteroidal samples and aid in relating them to terrestrially altered meteorites.

8.8 Acknowledgements

This publication is part of the Winchcombe science team consortium, organized by the UK Fireball Alliance and conducted by the UK Cosmochemistry Network. The authors of this paper would like to thank the UK Fireball Alliance, its constituent networks (UK Fireball Network, SCAMP, UKMON, AllSky7, NEMATODE, GMN), international collaborators (FRIPON, Global Fireball Observatory, Desert Fireball Network, University of Western Ontario and University of Helsinki) and the meteor observation camera owners who participate in the UK Fireball Alliance network for their aid in observing the fireball and helping to predict its fall position. We would also like to thank the scientists and volunteers that participated in the UK Fireball Alliance led search and recovery of the Winchcombe meteorite, and the local community, who generously reported and donated meteorite finds and enabled the team to search the strewn field. Science and Technology Facilities Council (STFC) are acknowledged for supporting the "Curation and Preliminary Examination of the Winchcombe Carbonaceous Chondrite Fall" project (ST/V000799/1), and Natural History Museum staff for curatorial support. We would like to thank Sara Russell

and Helena Bates for details regarding the curation of the Winchcombe meteorite and Callum Hatch for preparing the polished sections. We thank Connor Brolly for assistance with sample polishing. We would also like to thank Liene Spruziniece for maintaining the SEM and Joshua Einsle for assistance with using the reflected microscope. We thank Rory Porteous and Fengke Cao for their advice regarding the operation of the Raman microscope and interpretation of the Raman data. We thank William Smith for extracting the FIB sections from P30552 and Colin How for aid in the operation of the TEM. We also thank Sammy Griffin for advice and assistance regarding polishing procedures. We would like to thank Shijie Li and Mendy Ouillizou for answering questions about the Shidian and Kolang meteorite samples, respectively. We thank the Scottish Alliance for Geoscience, Environment and Society (SAGES) Small Grants Scheme award for support regarding FIB extractions and TEM work. Luke Daly thanks the University of Glasgow COVID-19 Research Support Scheme grant. Luke Daly and Martin R. Lee thank the STFC (ST/T002328/1 and ST/W001128/1) for support. Ashley J. King is funded by the UK Research and Innovation (UKRI) grant number MR/T020261/1.

9 – Conclusions

Mighei-like carbonaceous (CM) chondrites are defined by the series of alteration processes they have experienced. All known CM chondrites are aqueously altered to some degree, and some have even experienced metasomatism (Lee et al. 2019a), though the difference between metasomatism and aqueous alteration are purely related to the reaction products (Brearley & Krot 2013). A portion of CM and CM-like chondrites have experienced thermal metamorphism after this water-mediated alteration in a process known as post-hydration heating. The cause of post-hydration heating remains unknown. Many CM chondrites display non-spherical chondrules and/or chondrule alignment (Rubin 2012), which can be attributed to shock (Tomeoka et al. 1999), however many of these meteorites lack mineral shock effects (Rubin 2012), indicating that there is some aspect regarding these impacts that have left them unshocked or that an alternative process may also cause these petrofabrics. After landing on Earth, all CM chondrites will undergo terrestrial alteration to some degree. These alteration processes are summarized in Fig. 9.1.

Herein, I answered several questions pertaining to these many alteration processes affecting CM chondrites. What metasomatic minerals can be found within CM chondrites and how might they form? During post-hydration heating, at which temperatures do specific phase transitions occur at and how do they progress? How does duration of heating affect these phase transitions? What are the temperature-timescales experienced by naturally heated CM chondrites? Is chondrule flattening and alignment within the CM chondrites always caused by impacts? Can evaporite minerals within recent CM chondrite falls be terrestrial?

9.1 Metasomatism

The metasomatic mineral hydroandradite was discovered in the CM chondrites Shidian and Kolang. This is the first report of hydroandradite in meteorites, however it may be found in more CM chondrites. It formed by the replacement of other phases (e.g., magnetite, clinopyroxene, kamacite) with a fluid of an evolving chemical composition at temperatures exceeding 100°C. Hydroandradite may have formed at the same time as serpentine minerals. Hydroandradite's hydration is dependent on its formation temperature

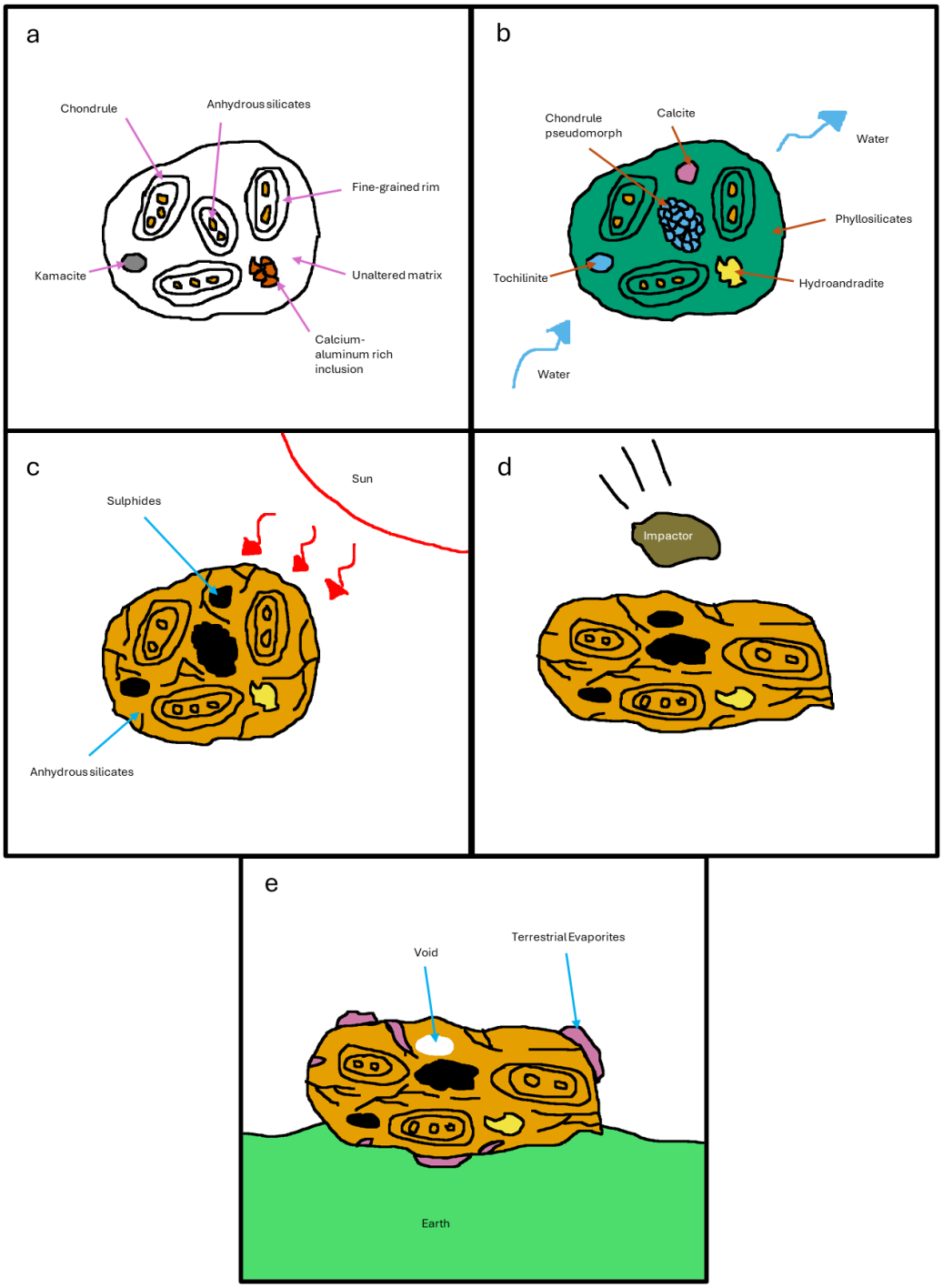

Fig. 9.1. Summary of alteration processes experienced by CM and CM-like meteorites studied. a) Unaltered CM meteorite composed of anhydrous materials, like calcium aluminum-rich inclusions, silicate chondrules, and kamacite. b) Depiction of aqueous alteration and hydrothermal metamorphism. Fluids alter primary material into phyllosilicates, tochilinite, carbonates, and other secondary phases (e.g., hydroandradite). c) Depiction of post-hydration heating. Volatile bearing phases (e.g., tochilinite, phyllosilicates, carbonates) decompose into anhydrous phases (e.g., sulphides, silicates). d) Depiction of the effects of a mild impact. Objects are aligned. e) Depiction of terrestrial weathering. Some primary minerals (e.g., sulphides like oldhamite) are dissolved, while terrestrial evaporite minerals (e.g., calcite, sulphates) precipitate, concentrating themselves in fractures and the meteorite exterior.

(Huckenholz & Fehr 1982), and its persistence in mildly heated (heated to 210-400 C) lithologies in Kolang and Shidian indicate that its thermal stability is also related to its hydration. The presence of hydroandradite in meteorites can yield

information regarding the conditions (e.g., fluid composition, temperature) of alteration.

9.2 Post-Hydration Heating

9.2.1 Phase Transitions

There are a number of phase transitions that occur during post-hydration heating of CM chondrites. The first is decomposition of tochilinite, which is a two-stage process, starting with the breakdown of its brucite/amakinite layers at ~200°C, followed by its mackinawite layers recrystallizing into sulphides at a higher temperature. Complete decomposition of tochilinite may occur at temperatures as low as 210°C, however the exact temperature is dependent on its composition.

The next observable phase transition is the decomposition of serpentine minerals at 300°C, with cronstedtite breaking down before lizardite. These serpentine minerals may decompose into a transitional phase at 500-600°C with a crystal structure similar to that of carlosturanite, before recrystallizing into olivine and enstatite.

Calcite's decomposition temperature is highly variable and potentially dependent on the degree of alteration experienced by its host meteorite. It can decompose anywhere from 575-700°C, with lower temperatures possibly being favored by less aqueously altered lithologies. Clinopyroxene is always produced from calcite decomposition, whereas oldhamite is only sometimes formed.

9.2.2 Timescales

The effects of post-hydration heating can be observed with petrographic methods like optical and scanning electron microscopy (SEM). They include fracturing, changes in tochilinite-cronstedtite intergrowths (TCIs) (e.g., separation of components, brightening under reflected light), decomposition of volatile-bearing phases (e.g., tochilinite, calcite), growth of secondary anhydrous phases (e.g., sulphides), as well as textural features (e.g., fracturing) relating to fine-grained rims (FGRs) around chondrules.

Fracturing of the serpentine-rich matrix becomes evident at 400°C, with fractures widening as temperature increases and becoming more abundant as heating duration lengthens.

Changes to TCIs and tochilinite correspond well with the decomposition of tochilinite, with changes to TCIs' appearance under reflected light and SEM starting at 200°C. However, the development of coarse-grained sulphides requires either heating of several days or temperatures of at least 600°C.

Calcite also undergoes thermal alteration in line with its decomposition temperature, with signs of decomposition first appearing at 600°C. Complete breakdown of calcite either requires heating of several days or rapid heating at temperatures of at least 800°C. Secondary phases produced from calcite decomposition become more abundant at greater temperatures and heating durations.

FGRs will begin to merge with the matrix at temperatures exceeding 800°C, with an increased heating duration making them harder to identify.

Each of these indicators of heating were used to estimate the temperature-timescales experienced by naturally heated CM and CM-like chondrites. It was found that the temperature-timescales experienced were highly variable, ranging from the order of hours to weeks. The cause of post-hydration heating therefore needs to account for this variability.

9.2.3 Cause

The leading two explanations for post-hydration heating are solar heating and impact heating. To evaluate whether impact heating is the cause, the shock metamorphism experienced by naturally heated meteorites was evaluated. It was found that although naturally heated meteorites have all experienced shock metamorphism of some kind, it is mild and bears no relation to the level of heating experienced. It is unlikely that impacts are the cause of post-hydration heating, however due to limited study on post-shock temperatures experienced by CM chondrites, this is yet to be definitively confirmed. CM parent bodies having differing orbits around the Sun can account for the variability in

temperature-timescale of heating experienced by CM chondrites. Solar heating is more likely to be the cause of post-hydration heating. It is also possible that both impacts and solar heating are responsible for post-hydration heating.

9.3 Chondrule Flattening and Alignment

Petrofabrics, displayed by chondrules that are flattened and aligned, are a common feature in CM chondrites that can be caused by impacts, yet many of the meteorites they occur within are unshocked. These shock effects may have been erased by alteration processes (e.g., aqueous alteration, thermal metamorphism), however it is also possible that another mechanism is responsible for petrofabrics. Understanding the cause of petrofabrics within CM chondrites will give information regarding their impact histories or lack thereof.

Kolang is a CM chondrite that displays a prominent petrofabric that is shared among its clasts, and thus must postdate their alteration and juxtaposition. Kolang was evaluated for indicators of impacts to see if they were responsible for chondrule flattening and alignment. Kolang only experienced ~5 GPa of peak shock pressure and is not shocked enough to deform chondrules plastically. Additionally, no signs of brittle deformation were observed in Kolang. The most likely explanation for Kolang's non-spherical chondrules and petrofabric is that the chondrules were not spherical to begin with and formed as ellipsoids and/or irregular shapes. The formation of the petrofabric would have had to occur in a separate event as chondrule flattening, and may still be caused by impacts, albeit milder than the ones required to deform chondrules.

9.4 Terrestrial Weathering

Winchcombe is a recent CM chondrite fall whose recovery is well documented. Despite its rapid recovery, terrestrial alteration phases (e.g., calcite, calcium sulphates, halite) were observed on polished sections. The calcite and calcium sulphates were the result of one of the Winchcombe stones spending six days in a damp sheep paddock prior to retrieval, while the formation of halite on a polished section was due to the sample being stored in non-inert laboratory conditions. These terrestrial weathering phases formed within months of the fall. Terrestrial weathering can be an extremely rapid

process and a meteorite being a fall does not mean it is pristine. It is therefore important to establish the origin of minerals that can occur as terrestrial weathering products in meteorites, regardless of how they were recovered, when analyzing the processes they have experienced.

9.5 Future Work

This work includes the first report of hydroandradite occurring within meteorites, however it may be found in more. Searching for hydroandradite in other meteorites and seeing how they compare to Shidian and Kolang will give a better understanding of metasomatic alteration processes occurring within CM chondrites. Additionally, the O isotopic composition of hydroandradite may elucidate information regarding the fluids responsible for aqueous alteration as well as its other products.

Through experimental heating of meteorites, many reactions were better understood. However, there are other aspects regarding them that could be explored. The decomposition of tochilinite was found to be a two-stage process that starts at 200°C but requires at least 210°C to complete. Conducting further in-situ heating experiments on tochilinite at 200-300°C while collecting selected area electron diffraction (SAED) images through transmission electron microscopy (TEM) may give more detail on how this reaction progresses. The temperature at which calcite decomposes was found to vary, with differences potentially related to the initial petrologic subtype of the CM chondrite. Additional heating experiments at similar conditions with different meteorites may either confirm or disprove this potential relationship between petrologic subtype and calcite decomposition. Broad timescale estimates for the post-hydration heating experienced by naturally heated meteorites were made based on the grain sizes of secondary anhydrous phases in experimentally heated meteorites. By experimentally heating meteorites for longer durations (e.g., weeks), it may be possible to more accurately recreate the post-hydration heating effects displayed by naturally heated meteorites.

The cause of chondrule flattening and alignment within Kolang was found to be most likely two separate mechanisms. Chondrules initially formed in non-spherical shapes before being aligned on Kolang's parent body, likely by

impacts. However, there have yet to be experimental studies on the alignment of ellipsoidal objects in a serpentine matrix. To further explore petrofabrics, impact experiments should be conducted either on a CM chondrite with unaligned chondrules, or on analog material.

Terrestrial weathering was shown to be an incredibly rapid process, with some products developing purely through exposure to ambient air. Periodic evaluation of CM chondrite falls for fresh evaporite phases over time will give a better idea of how they change with time and can inform sample curation and storage procedures.

Appendix A – Electron Microprobe Analysis (EPMA) Data

Table A1. EPMA data collected for the matrix in unheated clasts in Kolang given in wt%.

Na2O	MgO	Al2O3	SiO2	CaO	MnO	FeO	K2O	Cr2O3	TiO2	NiO	CoO	V2O5	P2O5	S	Total
0.09	28.54	1.45	38.3	0.06	0.25	18.63	0.02	-0.01	0.02	0.05	n.d.	0.01	n.d.	0.05	87.41
0.54	11.74	2.66	22.47	0.13	0.2	40.11	0.03	0.21	0.03	0.69	0.05	n.d.	n.d.	0.89	79.74
0.12	29.44	1.88	39.86	0.13	0.24	18.19	0.01	0.01	0.02	0.10	n.d.	0.02	0.07	0.13	90.22
0.61	25.55	1.84	31.94	0.12	0.21	23.3	0.10	0.13	0.02	1.15	0.02	0.01	n.d.	1.53	86.53
0.48	11.23	3.40	22.73	0.07	0.18	45.03	0.04	0.19	0.04	0.59	0.03	0.01	0.13	0.93	85.05
0.42	8.82	3.36	22.45	0.16	0.19	46.43	0.04	0.11	0.05	0.48	n.d.	n.d.	0.04	0.73	83.29
0.12	27.63	1.79	38.12	0.09	0.24	18.1	0.01	0.04	0.03	0.21	n.d.	0.02	n.d.	0.10	86.52
0.62	25.81	1.91	32.32	0.13	0.24	23.12	0.10	0.19	0.01	1.54	0.01	0.01	n.d.	2.44	88.43
0.61	24.46	1.85	29.6	0.14	0.22	25.6	0.10	0.21	0.02	1.94	0.03	0.01	n.d.	3.12	87.87
0.64	23.41	1.85	28.57	0.14	0.22	25.83	0.12	0.14	0.02	1.98	n.d.	0.01	n.d.	3.32	86.23

Table A2. EPMA data collected for the fine-grained rims of chondrules in unheated clasts in Kolang given in wt%.

Na2O	MgO	Al2O3	SiO2	CaO	MnO	FeO	K2O	Cr2O3	TiO2	NiO	CoO	V2O5	P2O5	S	Total
0.94	14.76	1.55	23.51	1.32	0.17	19.59	0.09	0.78	0.02	4.74	0.36	0.02	0.86	2.46	71.17
1.05	20.24	1.94	30.12	1.16	0.27	21.68	0.12	1.47	0.17	2.38	0.12	0.01	0.06	2.04	82.83
0.98	15.82	1.55	24.40	2.37	0.19	18.77	0.10	0.72	0.29	2.60	0.17	0.02	0.13	1.48	69.59
0.77	14.08	2.12	26.35	1.86	0.18	29.12	0.08	0.45	0.22	2.5	0.15	0.01	0.17	1.53	79.60
0.11	23.10	1.33	30.98	0.09	0.22	19.30	0.01	0.55	0.04	0.90	0.06	0.02	n.d.	0.94	77.64
0.81	18.69	1.59	27.82	0.47	0.21	21.09	0.08	0.48	0.03	1.92	0.09	0.01	0.15	1.50	74.94
1.04	16.73	1.55	26.40	0.90	0.19	21.66	0.08	0.53	0.05	4.24	0.26	0.01	0.09	2.36	76.08
1.34	16.41	2.08	27.11	0.98	0.20	23.75	0.15	1.04	0.09	4.73	0.43	0.01	0.13	2.90	81.34
0.84	14.67	1.81	26.30	2.48	0.18	21.43	0.10	1.15	0.21	4.32	0.35	0.01	0.15	2.64	76.63
1.03	17.25	2.04	28.47	0.73	0.21	23.34	0.10	0.82	0.04	4.42	0.32	n.d.	0.13	2.79	81.68

Table A3. EPMA data collected for tochilinite in unheated clasts in Kolang given in wt%.

Na2O	MgO	Al2O3	SiO2	CaO	MnO	FeO	K2O	Cr2O3	TiO2	NiO	CoO	V2O5	P2O5	S	Total
0.39	16.74	1.23	11.46	0.07	0.12	45.38	0.03	0.84	n.d.	0.26	0.04	0.01	n.d.	8.37	84.93
0.67	16.15	3.37	26.18	0.16	0.21	39.22	0.08	0.26	0.04	0.44	0.03	n.d.	0.03	3.75	90.59
0.09	5.48	0.76	1.56	1.42	0.36	56.54	0.02	4.37	n.d.	3.91	n.d.	n.d.	n.d.	10.02	84.53
0.24	3.25	0.50	0.71	1.94	0.38	53.95	0.06	4.83	0.01	4.08	0.01	0.01	0.04	9.41	79.42
0.38	11.08	1.40	16.71	0.33	0.25	44.76	0.24	0.84	0.02	4.28	0.05	n.d.	0.42	5.36	86.12
0.62	9.30	1.25	13.87	0.18	0.23	42.63	0.23	4.01	0.01	4.95	0.10	0.02	0.44	6.51	84.35
0.43	7.63	0.98	9.15	1.18	0.16	45.25	0.33	2.16	0.14	16.80	0.70	0.03	3.98	9.77	98.69
0.13	2.42	1.26	21.23	28.04	0.14	27.93	n.d.	0.38	3.06	0.67	0.01	0.04	0.20	2.28	87.79
0.39	12.62	1.24	8.16	0.33	0.27	51.33	0.08	2.81	0.01	1.98	0.16	0.03	0.22	10.35	89.98
0.39	12.36	1.21	7.84	0.30	0.28	50.44	0.04	3.16	0.01	0.87	0.07	0.03	0.08	9.89	86.97

Table A4. EPMA data collected for the matrix in a heated clast in Kolang given in wt%.

Na2O	MgO	Al2O3	SiO2	CaO	MnO	FeO	K2O	Cr2O3	TiO2	NiO	CoO	V2O5	P2O5	S	Total
0.80	27.94	2.08	38.98	0.10	0.26	16.79	0.14	n.d.	0.03	0.34	0.01	0.03	n.d.	0.81	88.27
0.73	26.70	1.92	33.51	0.17	0.24	21.18	0.08	0.03	0.01	0.74	0.02	n.d.	0.04	2.08	87.43
1.10	21.20	2.42	31.46	0.69	0.26	24.19	0.10	0.49	0.04	3.73	0.24	0.01	0.18	2.74	88.85
0.87	21.99	2.34	31.93	0.31	0.23	24.63	0.12	0.25	0.03	1.36	0.08	n.d.	0.05	1.52	85.72
0.88	22.34	2.46	32.92	0.22	0.23	26.68	0.09	0.17	0.02	0.46	n.d.	n.d.	0.02	2.53	89.01
1.32	20.56	2.82	34.40	2.40	0.22	21.95	0.17	0.37	0.04	2.73	0.21	0.01	0.63	1.81	89.61
0.62	15.90	1.99	27.17	0.78	0.17	20.30	0.10	0.84	0.04	4.19	0.28	n.d.	0.11	2.42	74.94
0.73	26.20	2.23	34.46	0.21	0.21	21.93	0.10	0.16	0.02	1.09	0.01	0.01	0.01	1.74	89.10
0.33	13.29	2.49	23.66	0.21	0.23	38.97	0.04	0.18	0.02	1.25	0.03	0.01	0.04	1.47	82.23
0.50	14.08	2.43	23.51	0.39	0.23	35.80	0.06	0.19	0.27	0.79	0.01	0.02	0.03	2.32	80.64

Table A5. EPMA data collected for the fine-grained rims of chondrules in a heated clast in Kolang given in wt%.

Na2O	MgO	Al2O3	SiO2	CaO	MnO	FeO	K2O	Cr2O3	TiO2	NiO	CoO	V2O5	P2O5	S	Total
0.98	19.34	2.71	30.81	0.59	0.23	26.47	0.14	0.53	0.04	1.46	0.12	0.01	0.08	1.80	85.31
1.14	18.99	2.40	31.13	0.98	0.23	22.30	0.13	0.36	0.04	1.86	0.12	0.01	0.19	1.90	81.76
1.43	19.11	2.24	29.51	0.48	0.22	21.08	0.12	0.35	0.04	2.78	0.23	0.01	0.03	2.31	79.97
0.94	17.06	2.49	28.06	0.40	0.24	25.63	0.11	0.64	0.04	1.22	0.13	0.02	n.d.	2.03	79.02
0.60	17.02	2.11	20.29	0.26	0.23	35.42	0.07	0.49	0.02	0.62	0.03	0.01	n.d.	4.58	81.75
1.45	17.08	2.55	29.61	1.34	0.24	24.66	0.17	0.85	0.06	3.50	0.27	0.01	0.25	2.45	84.50
1.52	16.80	2.51	28.41	0.71	0.22	27.53	0.16	0.71	0.05	3.41	0.29	n.d.	0.13	2.53	84.98
1.14	16.60	2.41	28.38	0.55	0.24	26.05	0.19	0.73	0.04	2.62	0.23	0.01	0.06	2.37	81.63
0.98	15.94	2.11	24.74	0.71	0.19	21.82	0.12	4.64	0.04	4.70	0.54	0.02	0.09	2.69	79.35

Table A6. EPMA data collected for tochilinite in a heated clast in Kolang given in wt%.

Na2O	MgO	Al2O3	SiO2	CaO	MnO	FeO	K2O	Cr2O3	TiO2	NiO	CoO	V2O5	P2O5	S	Total
0.23	12.75	1.01	9.23	0.07	0.15	47.40	0.02	2.03	0.02	1.64	0.05	0.03	n.d.	7.78	82.41
0.16	1.25	0.05	1.71	0.28	0.02	72.52	0.02	n.d.	0.02	5.79	0.02	0.01	0.19	15.98	98.01
0.14	7.49	0.52	5.38	0.02	0.04	65.35	0.01	0.03	n.d.	6.34	n.d.	0.01	n.d.	15.63	100.95
0.11	8.92	0.72	6.19	0.73	0.34	50.81	0.06	4.39	0.01	1.81	0.39	0.03	0.49	9.79	84.79
0.27	11.32	1.45	14.67	0.05	0.11	55.09	0.02	0.05	0.01	4.36	0.04	n.d.	n.d.	8.34	95.76
0.41	26.52	1.58	30.31	0.18	0.18	30.33	0.08	0.26	0.02	1.70	0.04	0.02	0.01	4.21	95.85
0.23	5.40	1.04	5.05	0.85	0.27	51.20	0.13	2.96	0.03	4.73	0.77	0.02	1.26	11.09	85.03
0.04	10.92	0.83	8.15	0.57	0.29	47.09	n.d.	4.51	0.04	0.86	0.03	0.02	0.18	9.79	83.32
0.13	10.20	0.88	7.88	0.36	0.26	49.62	0.03	4.03	0.02	1.34	n.d.	0.01	0.19	10.12	85.07
0.46	5.35	1.59	19.87	0.27	0.21	59.06	0.01	0.16	0.01	0.12	n.d.	n.d.	0.07	0.67	87.81

Table A7. EPMA data collected for the matrix in Shidian given in wt%.

Na2O	MgO	Al2O3	SiO2	CaO	MnO	FeO	K2O	Cr2O3	TiO2	NiO	CoO	V2O5	P2O5	S	Total
0.28	25.78	1.99	34.65	0.24	0.22	19.52	0.05	0.33	0.01	1.35	0.08	0.01	0.02	1.01	85.52
0.19	16.86	2.20	26.57	0.63	0.21	31.06	0.03	0.63	0.04	3.79	0.29	0.01	0.08	2.28	84.85
0.31	15.20	2.57	27.82	2.82	0.21	27.28	0.05	0.45	0.11	2.66	0.20	0.02	0.39	1.17	81.26
0.37	15.37	1.98	26.74	2.57	0.19	28.34	0.04	0.43	0.17	3.82	0.30	0.02	0.43	1.69	82.46
0.19	14.88	1.59	23.87	0.70	0.20	27.30	0.03	0.39	0.04	4.00	0.26	0.01	0.09	1.28	74.84
0.38	15.52	2.79	26.49	0.57	0.22	36.10	0.05	0.32	0.04	2.17	0.14	0.01	0.07	1.34	86.20
0.36	15.30	2.16	24.56	2.75	0.24	29.03	0.06	0.63	0.04	4.89	0.36	0.00	2.31	1.93	84.63

Table A8. EPMA data collected for the fine-grained rims of chondrules Shidian given in wt%.

Na2O	MgO	Al2O3	SiO2	CaO	MnO	FeO	K2O	Cr2O3	TiO2	NiO	CoO	V2O5	P2O5	S	Total
0.61	14.91	2.44	26.43	0.75	0.22	29.47	0.07	0.84	0.06	3.04	0.26	n.d.	0.12	1.45	80.67
0.29	15.29	2.37	26.20	0.96	0.19	29.13	0.02	0.87	0.04	3.68	0.34	0.01	0.13	1.51	81.03
0.31	16.58	4.33	29.01	0.70	0.20	30.68	0.05	0.56	0.05	1.77	0.15	n.d.	0.21	1.07	85.65
0.23	16.46	2.68	29.10	0.80	0.25	31.05	0.04	0.48	0.04	2.93	0.22	0.01	0.71	1.46	86.48
0.23	16.85	2.03	27.73	0.67	0.24	25.74	0.02	0.54	0.02	3.78	0.32	n.d.	0.06	1.74	79.96
0.25	25.27	2.01	36.74	2.64	0.25	16.92	0.05	0.57	0.09	1.57	0.01	0.01	0.16	0.91	87.48
0.27	14.10	1.96	24.58	2.04	0.22	28.26	0.03	0.66	0.20	3.25	0.24	0.01	0.12	1.13	77.08
0.16	27.72	5.63	35.40	0.13	0.19	19.33	0.03	0.50	0.02	1.40	0.05	0.02	0.01	1.54	92.14
0.35	16.37	2.10	26.99	1.17	0.23	26.25	0.05	0.54	0.05	3.03	0.22	0.01	0.06	1.51	78.94
0.17	16.08	2.59	25.31	0.42	0.23	32.38	0.03	0.53	0.04	2.27	0.16	n.d.	0.03	1.31	81.55

Table A9. EPMA data collected for tochilinite in Shidian given in wt%.

Na2O	MgO	Al2O3	SiO2	CaO	MnO	FeO	K2O	Cr2O3	TiO2	NiO	CoO	V2O5	P2O5	S	Total
0.44	3.10	0.52	3.56	0.40	0.12	52.44	0.07	3.89	0.01	2.74	0.14	0.02	1.34	6.59	75.38
0.54	3.22	0.68	3.13	0.38	0.16	54.62	0.05	5.16	n.d.	1.95	0.12	0.02	0.42	7.09	77.54
0.12	5.14	0.75	6.07	0.47	0.19	49.90	0.04	1.75	0.02	5.22	0.12	n.d.	1.10	6.96	77.85
0.24	3.07	0.57	3.59	n.d.	0.13	60.37	0.06	2.22	0.02	4.23	0.25	n.d.	0.80	5.32	81.07
0.06	2.61	0.21	1.48	0.27	0.33	57.71	0.03	2.75	n.d.	5.06	0.27	n.d.	0.65	8.07	79.50
0.15	5.33	0.39	3.60	0.14	0.25	49.21	0.07	3.54	0.01	4.45	0.26	0.02	0.50	11.38	79.30
0.11	10.88	0.90	9.94	0.35	0.29	45.80	0.08	1.53	0.01	5.95	0.18	n.d.	0.58	7.65	84.25
n.d.	3.76	0.49	1.77	0.43	0.36	58.19	0.05	3.51	n.d.	3.12	0.07	n.d.	0.50	9.57	81.81
0.03	9.34	0.92	11.05	n.d.	0.08	37.04	0.07	0.17	0.01	22.90	1.49	0.01	0.01	11.95	95.04
0.09	7.48	0.64	3.95	1.68	0.29	47.93	0.09	2.92	n.d.	5.07	0.52	0.04	1.85	11.54	84.09

Appendix B Raman Spectra

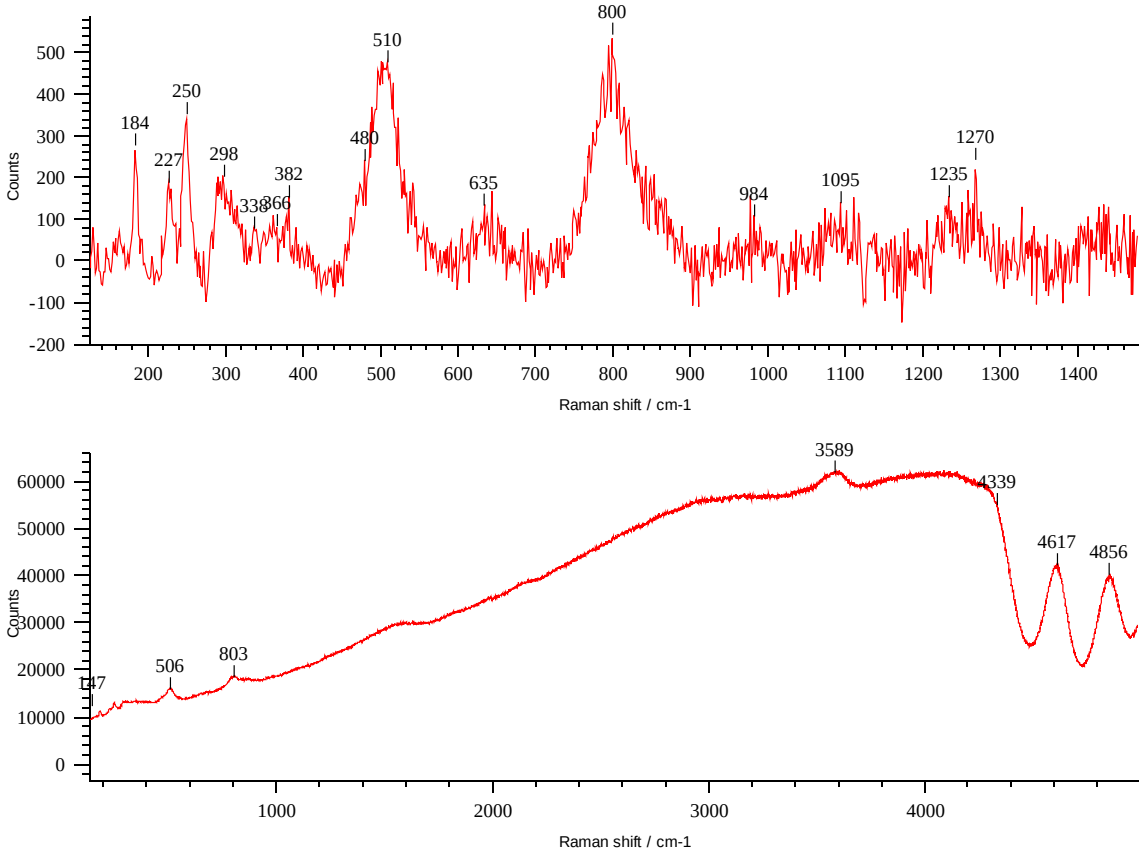

Fig. B1. Additional Raman spectra for perovskite-associated hydroandradite in Kolang – Target 1.

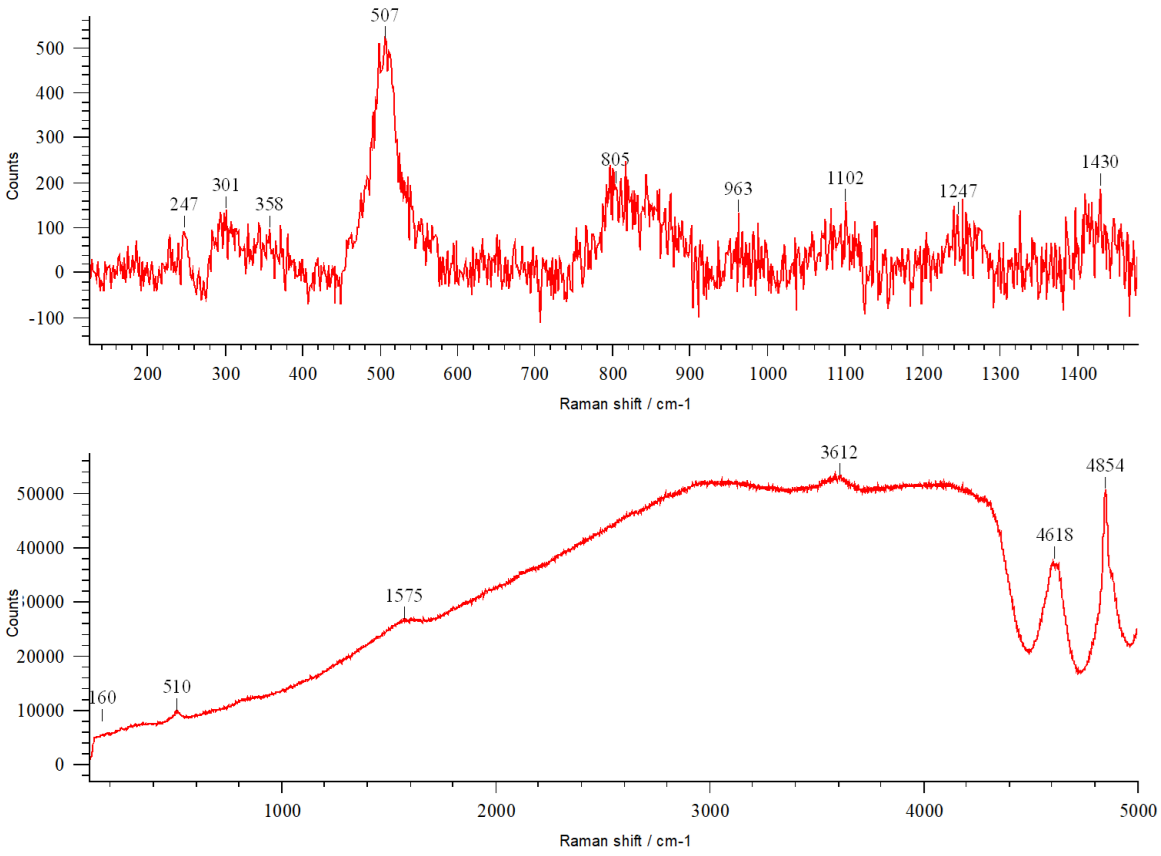

Fig. B2. Additional Raman spectra for perovskite-associated hydroandradite in Kolang – Target 2.

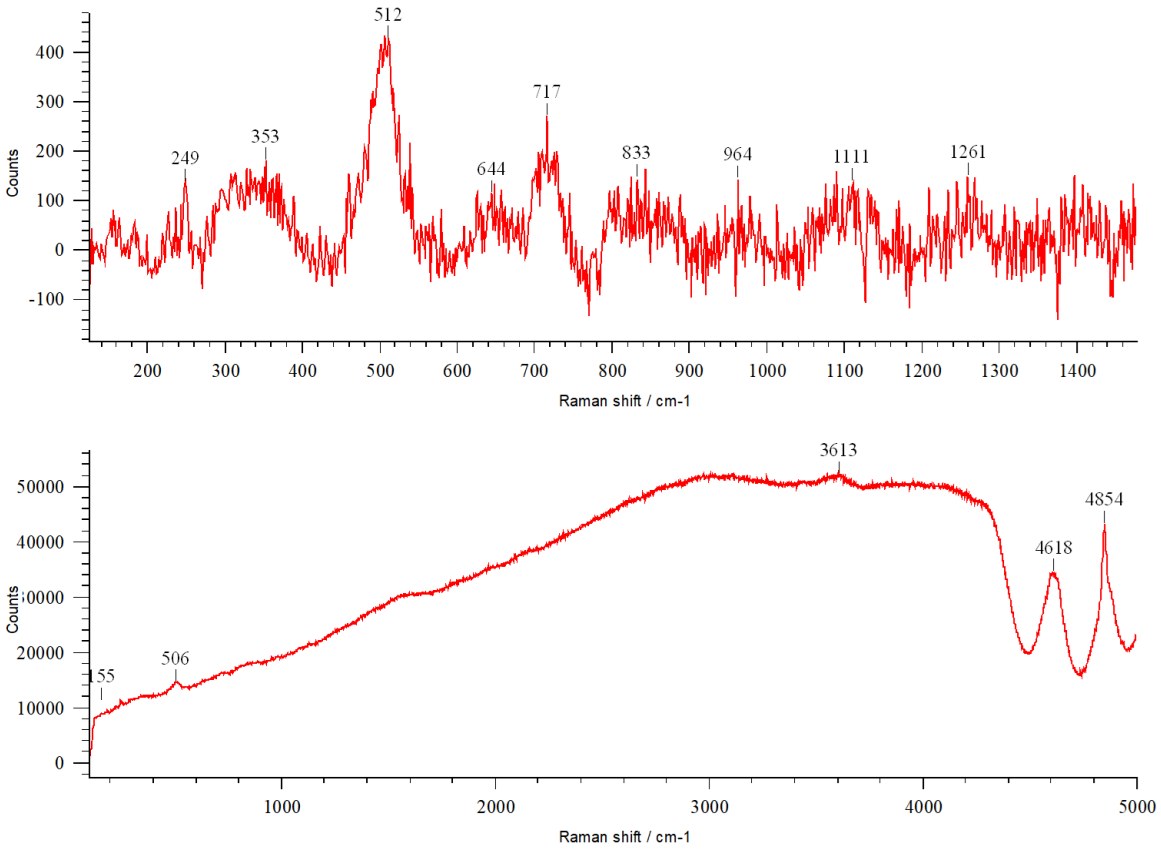

Fig. B3. Additional Raman spectra for perovskite-associated hydroandradite in Kolang – Target 3.

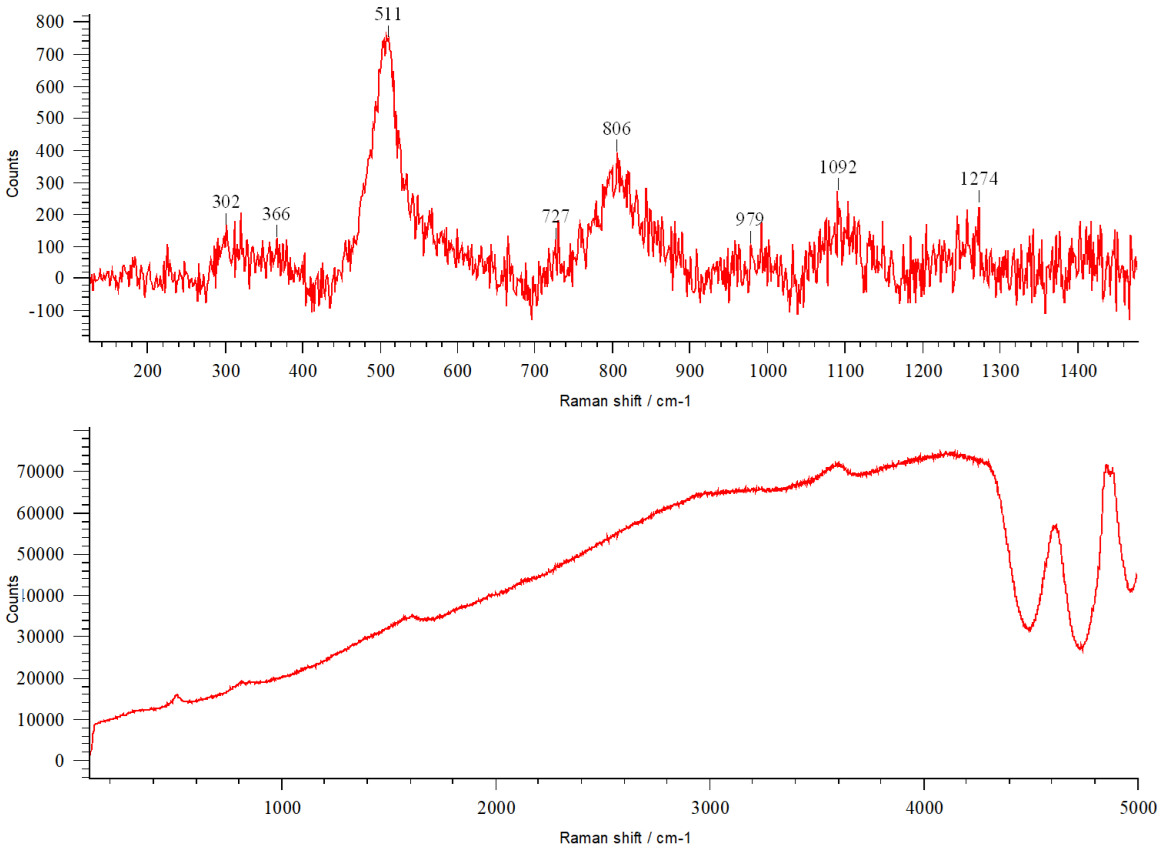

Fig. B4. Additional Raman spectra for perovskite-associated hydroandradite in Kolang – Target 4.

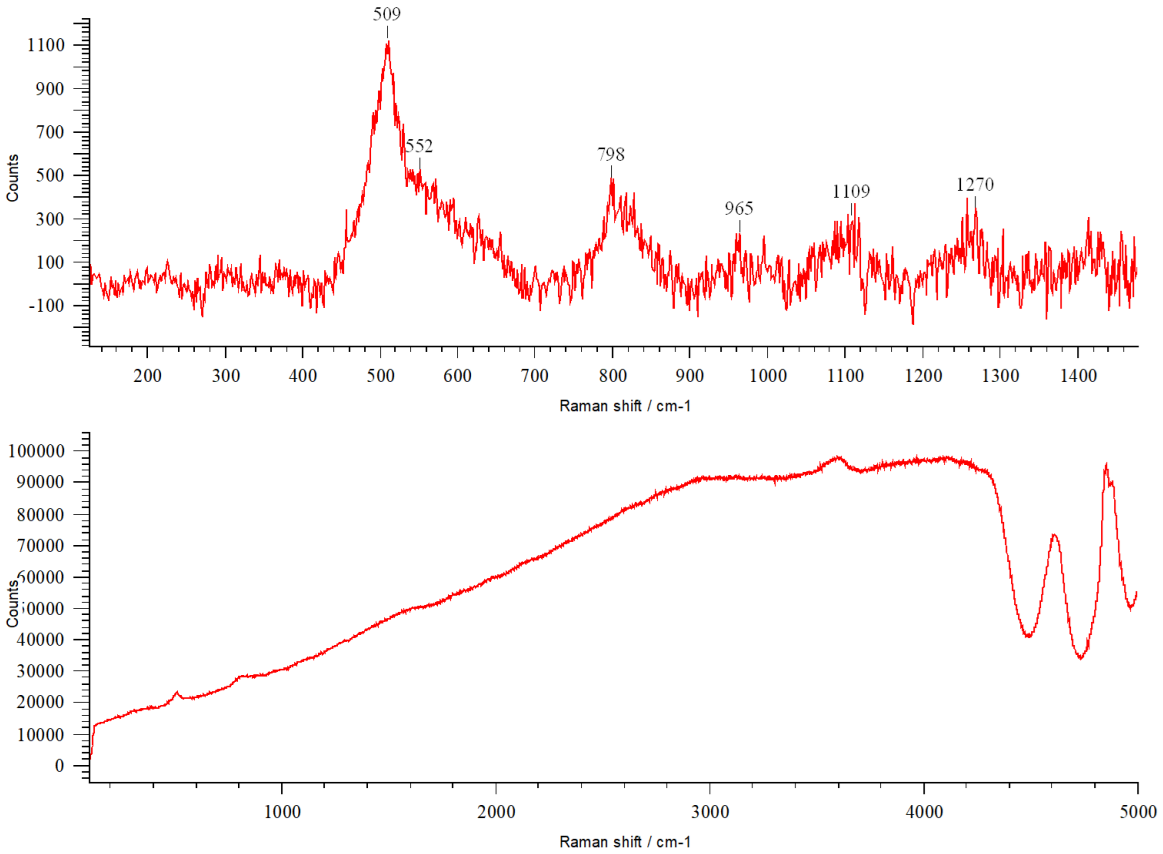

Fig. B5. Additional Raman spectra for perovskite-associated hydroandradite in Kolang – Target 5.

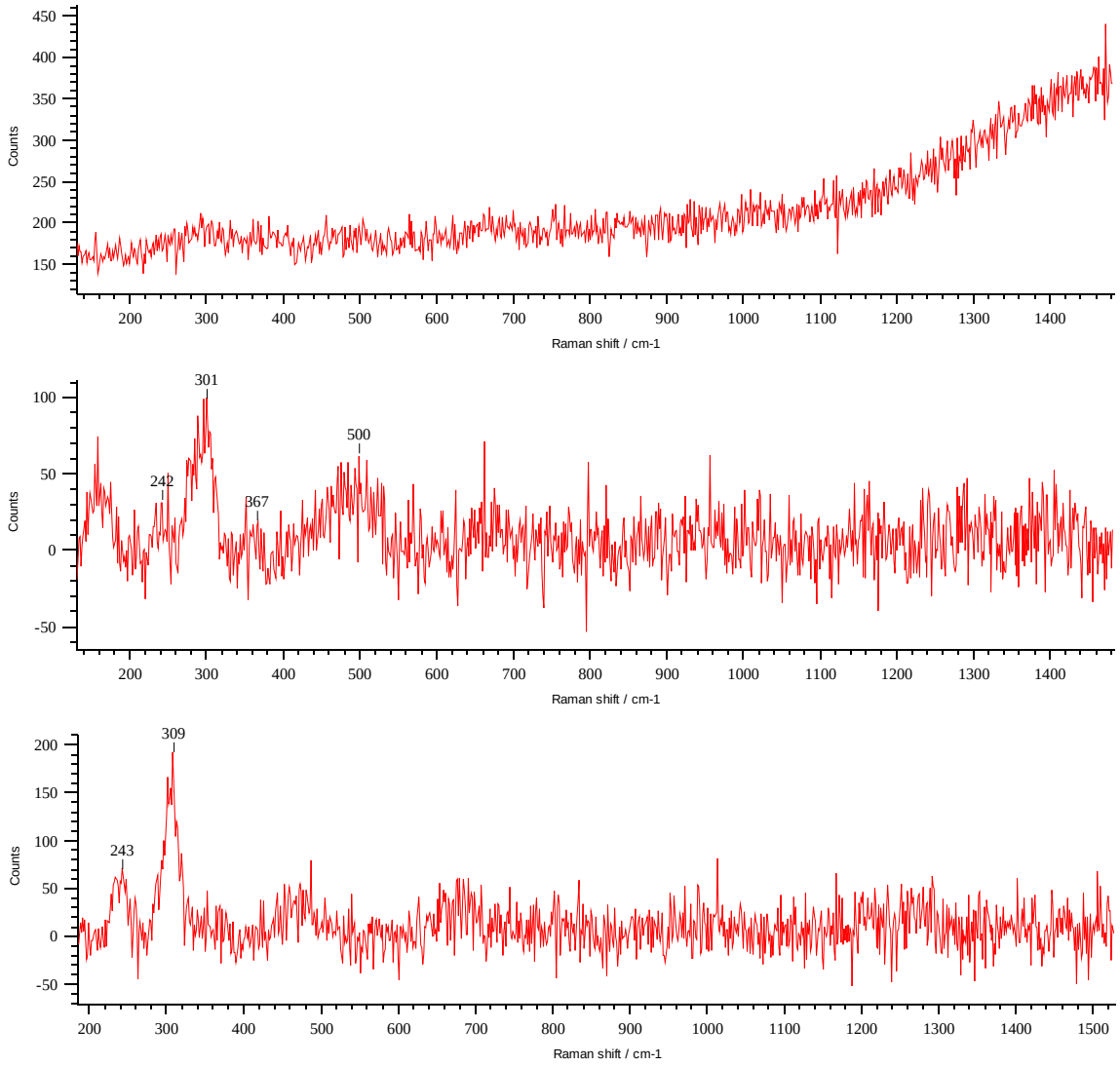

Fig. B6. Additional Raman spectra for tochilinite-cronstedtite intergrowths in an unheated Murchison sample (M_Blank).

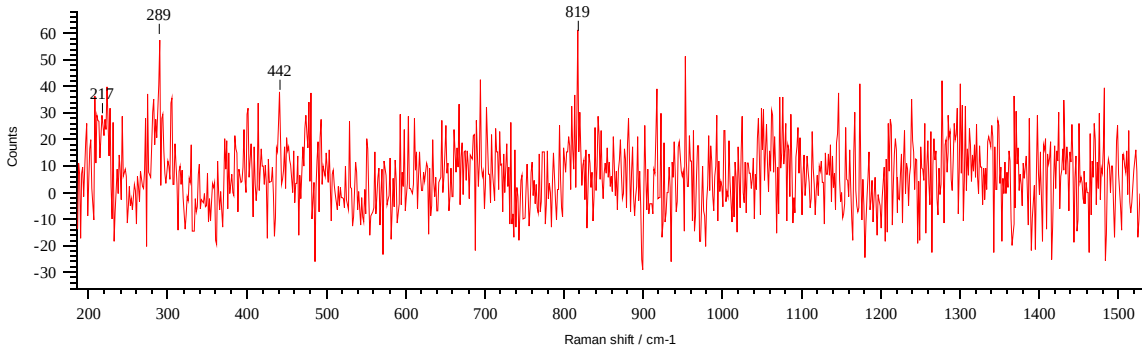

Fig. B7. Raman spectra for a tochilinite globule in a sample of Murchison heated to 200°C for 1 day (M_200_1).

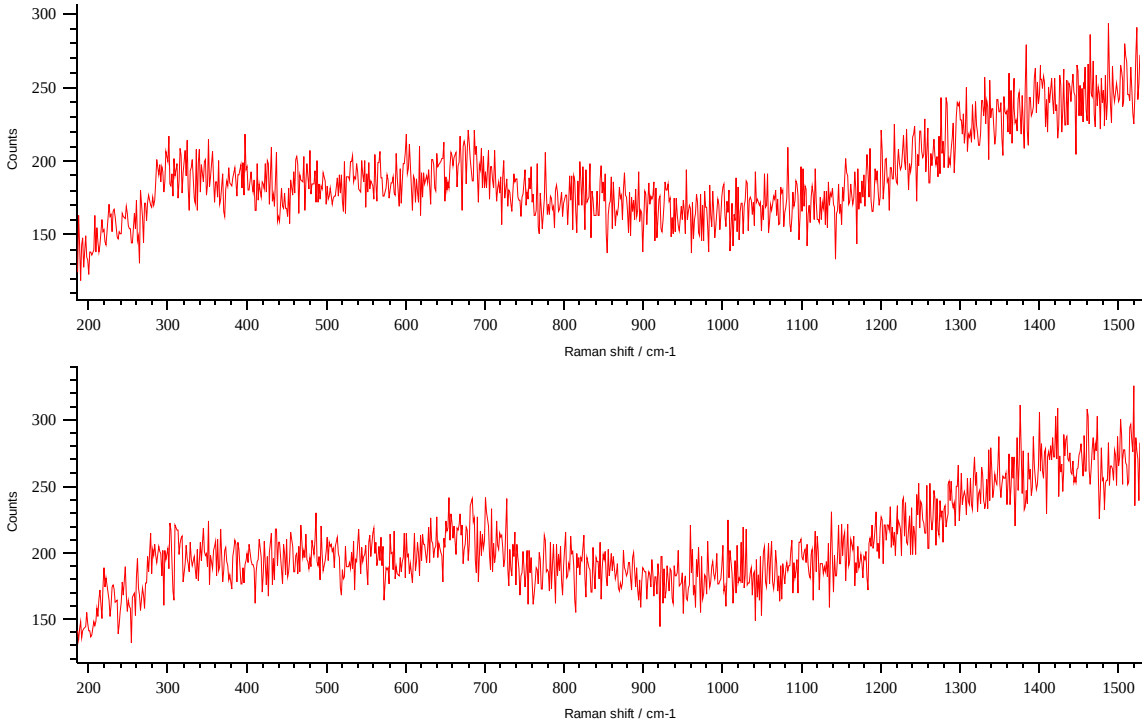

Fig. B8. Additional Raman spectra for tochilinite-cronstedtite intergrowths in a sample of Murchison heated to 200°C for 1 day (M_200_1).

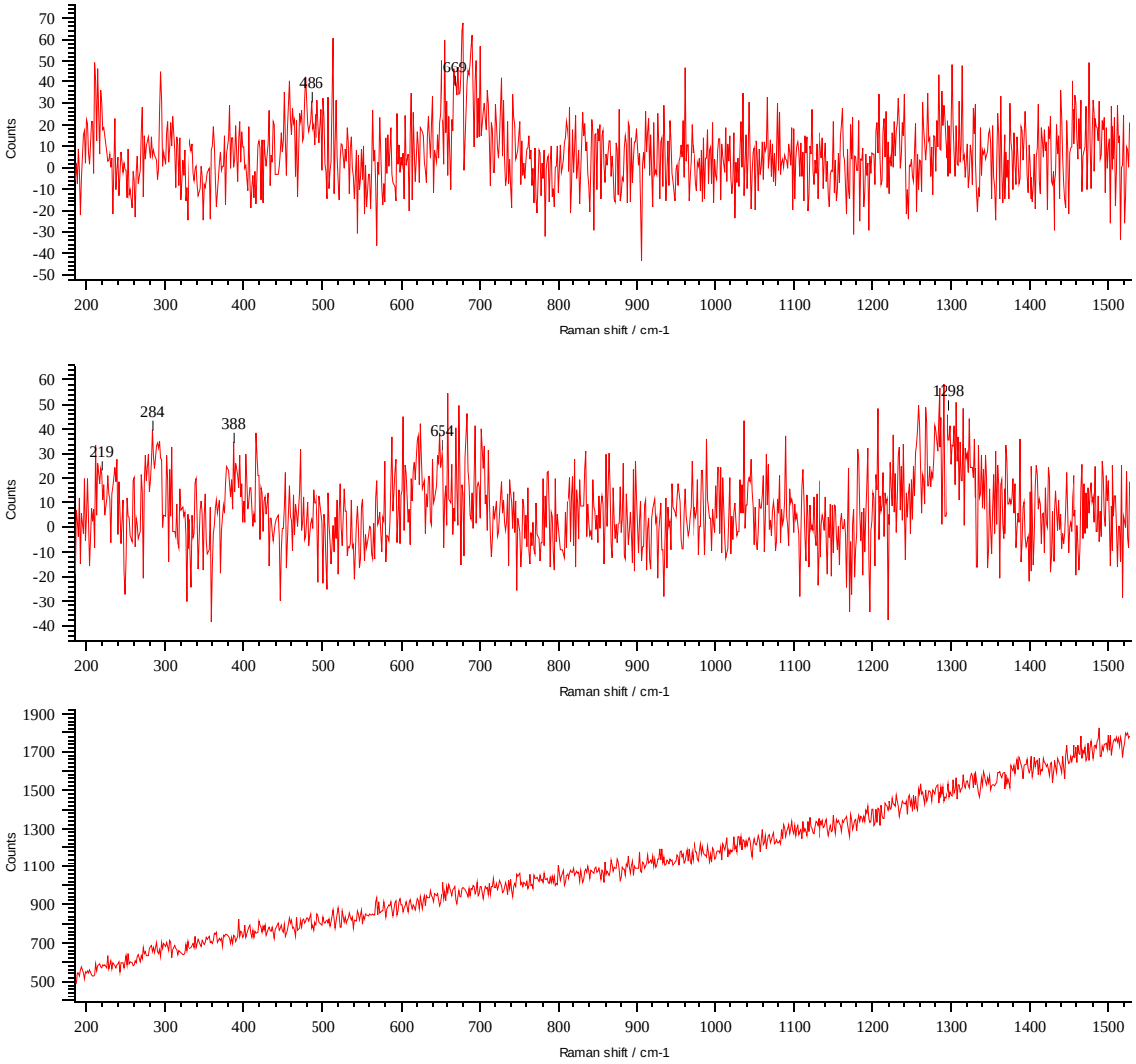

Fig. B9. Additional Raman spectra for tochilinite globules in a sample of Murchison heated to 200°C for 8 days (M_200_8).

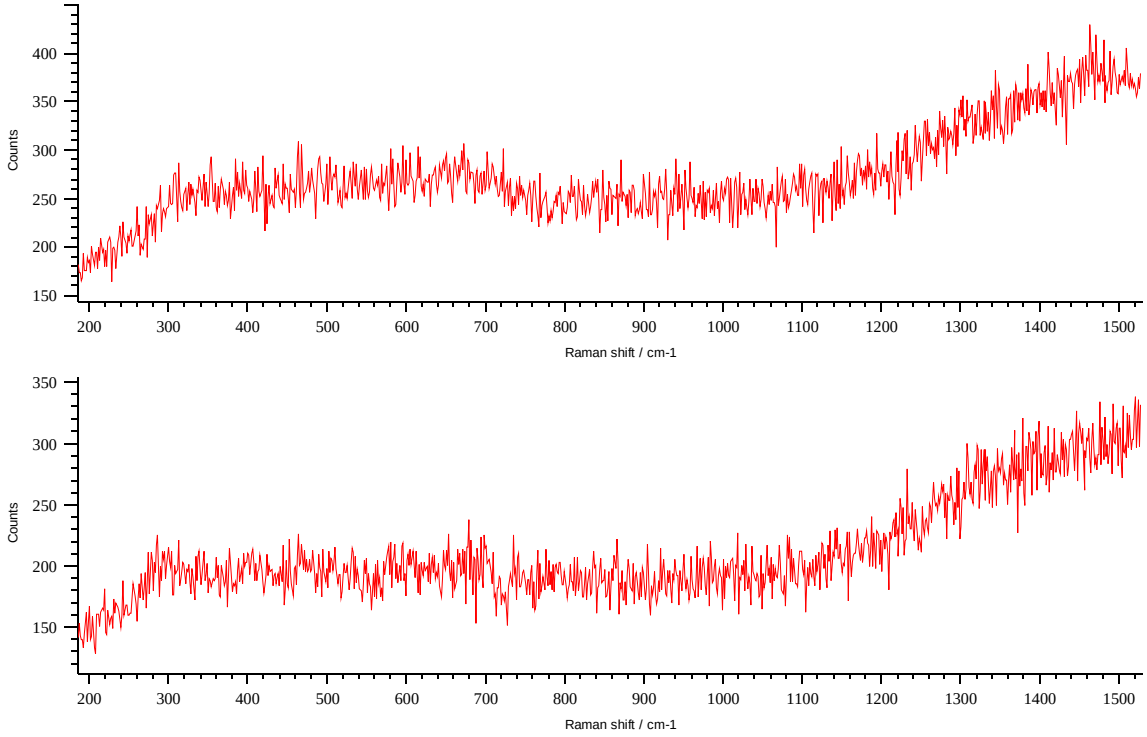

Fig. B10. Raman spectra for tochilinite-cronstedtite intergrowths in a sample of Murchison heated to 200°C for 8 days (M_200_8).

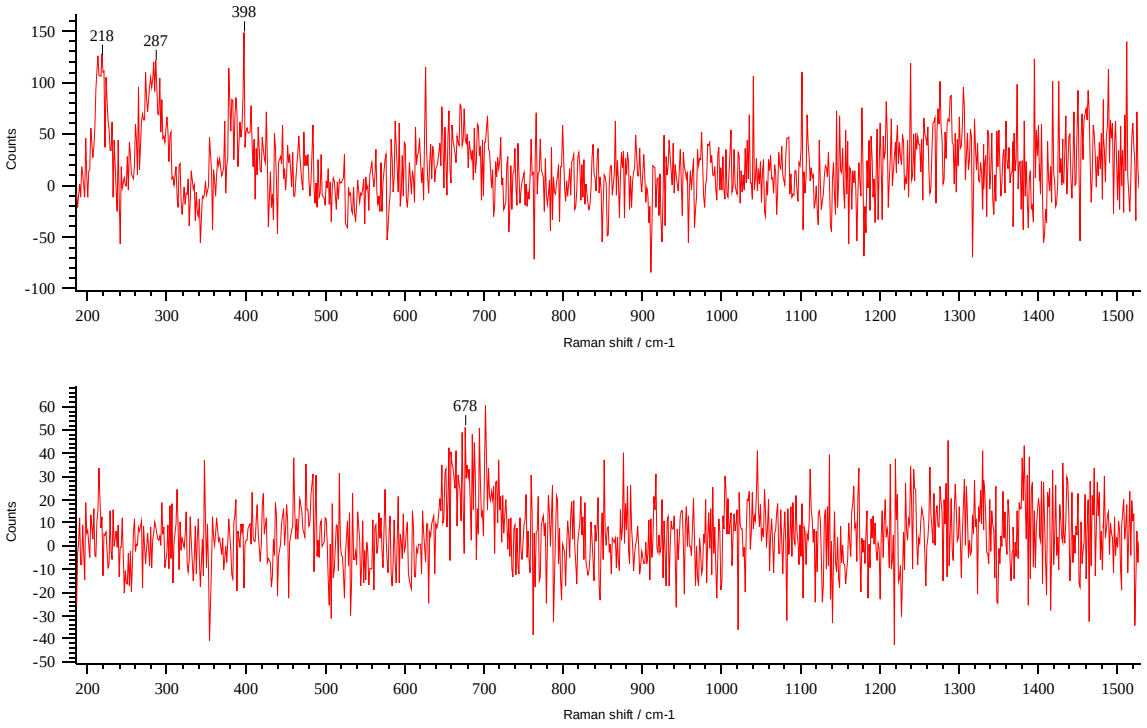

Fig. B11. Raman spectra for tochilinite globules in a sample of Murchison heated to 300°C for 1 day (M_300_1).

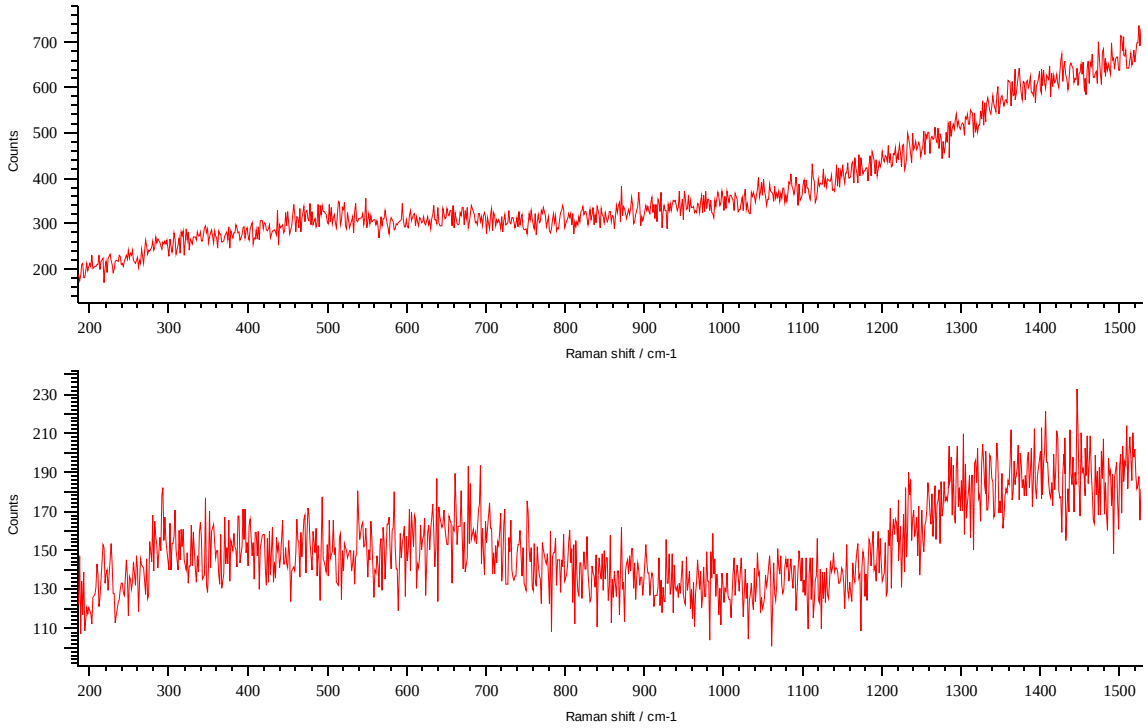

Fig. B12. Raman spectra for tochilinite-cronstedtite intergrowths in a sample of Murchison heated to 300°C for 1 day (M_300_1).

References

Abreu, N.M., & Brearley, A.J. (2005) 'Carbonates in Vigarano: Terrestrial, preterrestrial, or both?' *Meteoritics & Planetary Science*, 40, pp. 609-625.

Akai, J. (1988) 'Incompletely transformed serpentine-type phyllosilicates in the matrix of Antarctic CM chondrites.' *Geochimica et Cosmochimica Acta,* 52, pp. 1593-1599.

Akai, J. (1990) 'Mineralogical evidence of heating events in Antarctic carbonaceous chondrites, Y-86720 and Y-82162.' *Proceedings of the NIPR Symposium on Antarctic Meteorites,* 3, pp. 55-68.

Alexander, C.M.O'D., Bowden, R., Fogel, M.L., Howard, K.T., Herd, C.D.K., and Nittler, L.R. (2012) 'The Provenances of Asteroids, and Their Contributions to the Volatile Inventories of the Terrestrial Planets.' *Science,* 337, pp. 721-723.

Alexander, C.M.O'D., Howard, K.T., Bowden, R., & Fogel, M.L. (2013) 'The classification of CM and CR chondrite using H, C and N abundances and isotopic compositions.' *Geochimica et Cosmochimica Acta*, 123, pp. 244-260.

Alexander, C.M.O'D., Bowden, R., Fogel, M.L., & Howard, K.T. (2015) 'Carbonate abundances and isotopic compositions in chondrites.' *Meteoritics & Planetary Science,* 50, pp. 810-833.

Ambedkar, B., Nagarajan, R., & Jayanti, S. (2011) 'Ultrasonic coal-wash for de-sulfurization.' *Ultrasonics Sonochemistry,* 3, pp. 718-726.

Anand, A. & Mezger, K. (2023) "Early solar system chronology from short lived chronometers." *Geochemistry.*

Anduix-Canto, C., Levenstein, M. A., Kim, Y.-Y., Godinho, J. R. A., Kulak, A. N., Niño, C. G., Withers, P. J., Wright, J. P. et al. (2021) 'Exploiting

confinement to study the crystallization pathway of calcium sulfate.' *Advanced Functional Materials,* 31, 2107312.

Armbruster, T. (1995) 'Structure refinement of hydrous andradite $Ca_3Fe_{1.54}Mn_{0.20}Al_{0.26}(SiO_4)_{1.65}(O_4H_4)_{1.35}$, from the Wessels mine, Kalahari manganese field, South Africa.' *European Journal of Mineralogy*, 7, pp. 1221-1225.

Armstrong, J.T., Meeker, G.P., Huneke, J.C., & Wasserburg, G.J. (1982) 'The Blue Angel: I. The mineralogy and petrogenesis of a hibonite inclusion from the Murchison meteorite.' *Geochimica et Cosmochimica Acta,* 46, pp. 575-595.

Armthauer, G. and Rossman, G.R. (1998) 'The hydrous component in andradite garnet.' *American Mineralogist*, 83, pp. 835-840.

Asaduzzaman, A.M., Zega, T.J., Laref, S., Runge, K., Deymier, P.A., & Muralidharan, K. (2014) 'A computational investigation of adsorption of organics on mineral surfaces: Implications for organics delivery in the early solar system.' *Earth and Planetary Science Letters,* 408, pp. 355-361.

Ball, M.C., & Taylor, H.F.W. (1963) 'The dehydration of chyrsotile in air and under hydrothermal conditions.' *Mineralogical Magazine,* 33, pp. 467–482.

Ballirano, P. & Melis, E. (2009) 'Thermal behaviour and kinetics of dehydration in air of bassanite, calcium sulphate hemihydrate ($CaSO_4 \cdot 0.5H_2O$), from X-ray powder diffraction.' *European Journal of Mineralogy,* 21, pp. 985-993.

Barber, D.J. (1981) 'Matrix phyllosilicates and associated minerals in C2M carbonaceous chondrites.' *Geochimica et Cosmochimica Acta,* 45, pp. 945-970.

Bates, H.C., King, A.J., Donaldson Hanna, K.L., Bowles, N.E., and Russell, S.S. (2020) 'Linking mineralogy and spectroscopy of highly aqueously altered

CM and CI carbonaceous chondrites in preparation for primitive asteroid sample return.' *Meteoritics & Planetary Science,* 55, pp. 77-101.

Beard, J.S. & Hopkinson, L. (2000) 'A fossil, serpentinization-related hydrothermal vent, Ocean Drilling Program Leg 173, Site 1068 (Iberia Abyssal Plain): Some aspects of mineral and fluid chemistry.' *Journal of Geophysical Research,* 105, pp. 16527-16539.

Bischoff, A. (1998) 'Aqueous alteration of carbonaceous chondrites: Evidence for preaccretionary alteration – A review.' *Meteoritics & Planetary Sciences,* 33, pp. 1113-1122.

Bland, P.A., Zolensky, M.E., Benedix, M.E., & Sephton, M.A. (2006) 'Weathering of Chondritic Meteorites.' In Ed. Lauretta, D.S. & McSween Jr., H.Y. (Eds.) *Meteorites and the Early Solar System II.* Tuscon, Arizona, USA: The University of Arizona Press. pp. 853-867.

Bland, P.A., Collins, G.S., Davison, T.M., Abreu, N.M., Ciesla, F.J., Muxworthy, A.R., & Moore, J. (2014) 'Pressure-temperature evolution of primordial solar system solids during impact-induced compaction.' *Nature Communications*, 5, pp. 5451.

Botta, O. & Bada, J.L. (2002) 'Extraterrestrial organic compounds in meteorites.' *Surveys in Geophysics,* 23, pp. 411-467.

Bourdoiseau, J.-A., Jeannin, M., Sabot, R., Rémazeilles, C., & Refait, Ph. (2008) 'Characterisation of mackinawite by Raman spectroscopy: Effects of crystallization, drying and oxidation.' *Corrosion Science,* 50, pp. 3247-3255.

Bragg, W.H. & Bragg, W.L. (1913) 'The Reflection of X-rays by Crystals.' *Proceedings of the Royal Society of London,* 88, pp. 428-438.

Brandstätter, F., Brack, A., Baglioni, P., Cockell, C. S., Demets, R., Edwards, H. G. M., Kurat, G., Osinski, G. R. et al. (2008) 'Mineralogical alteration of

artificial meteorites during atmospheric entry. The STONE-5 experiment.' *Planetary and Space Science*, 56, pp. 976–984.

Brann, T. (2020) *Ten Things to Know About Bennu.* Available at: https://www.nasa.gov/feature/goddard/2020/bennu-top-ten

Brearley, A.J. (2006) 'The Action of Water.' In Ed. Lauretta, D.S. & McSween Jr., H.Y. (Eds.) *Meteorites and the Early Solar System II*. Tuscon, Arizona, USA: The University of Arizona Press. pp. 587-624.

Brearley, A.J. & Jones, R.H. (1998) 'Chondritic Meteorites.' In Papike, J.J. (ed.) *Review in Mineralogy: Planetary Materials*. 36. pp. 3-01-3-398.

Brearley, A.J. & Krot, A.N. (2013) 'Metasomatism in the Early Solar System: The Record from Chondritic Meteorites.' In Harlov, D.E. & Austrheim, H. (eds.) *Metasomatism and the Chemical Transformation of Rock: The Role of Fluids in Terrestrial and Extraterrestrial Processes*. pp. 659-791.

Brearley, A.J. & Jones, R.H. (2018) 'Halogens in Chondritic Meteorites.' In Harlov, D.E. & Aranovich, L. (eds.) *The Role of Halogens in Terrestrial and Extraterrestrial Processes*. pp. 871-958.

Brown, P.G., Hildebrand, A.R., Zolensky, M.E., Grady, M., Clayton, R.N., Mayeda, T.K., Tagliaferri, E., Spalding, R. et al. (2000) 'The Fall, Recovery, Orbit, and Composition of the Tagish Lake Meteorite: A New Type of Carbonaceous Chondrite.' *Science*, 290, pp. 320-325.

Bunch, T.E. & Chang, S. (1980) 'Carbonaceous chondrites – II. Carbonaceous chondrite phyllosilicates and light element geochemistry as indicators of parent body processes and surface conditions.' *Geochimica et Cosmochimica Acta*, 44, pp. 1543-1577.

Bus, S.J. & Binzel, R.P. (2002) 'Phase II of the Small Main-Belt Asteroid Spectroscopic Survey: A Feature-Based Taxonomy.' *Icarus*, 158, pp. 146-177.

Busemann, H., Young, A.F., Alexander, C.M. O'D., Hoppe, P., Mukhopadhyay, S., & Nittler, L.R. (2006) 'Interstellar Chemistry Recorded in Organic Matter from Primitive Meteorites.' *Science,* 312, pp. 727-729.

Busemann, H., Alexander, C.M.O'D., and Nittler, L.R. (2007) 'Characterization of insoluble organic matter in primitive meteorites by microRaman spectroscopy.' *Meteoritics & Planetary Science*, 42, pp. 1387-1416.

Caillahua, M.C. & Moura, F.J. (2018) 'Technical feasibility for use of FGD gypsum as an additive setting time retarder for Portland cement.' *Journal of Materials Research and Technology,* 7, pp. 190-197.

Cain, P.M., McSween Jr., H.Y., & Woodward, N.B. (1986) 'Structural deformation of the Leoville chondrite.' *Earth and Planetary Science Letters,* 77, pp. 165-175.

Chan, Q.H.S., Chikaraishi, Y., Takano, Y., Ogawa, N.O., & Ohkouchi, N. (2016) 'Amino acid compositions in heated carbonaceous chondrites and their compound-specific nitrogen isotopic ratios.' *Earth, Planets and Space,* 68, pp. 7

Choe, W.H., Huber, H., Rubin, A.E., Kallemeyn, G.W., & Wasson, J.T. (2010) 'Compositions and taxonomy of 15 unusual carbonaceous chondrites.' *Meteoritics & Planetary Science,* 45, pp. 531-554.

Christensen, A.N., Oleson, M., Cerenius, Y., & Jensen, T.R. (2008) 'Formation and Transformation of Five Different Phases in the $CaSO_4$-H_2O System: Crystal Structure of the Subhydrate β-$CaSO_4 \cdot 0.5H_2O$ and Soluble Anhydrate $CaSO_4$.' *Chemistry of Materials,* 20, pp. 2124-2132.

Ciesla, F.J. & Cuzzi, J.N. (2006) 'The evolution of the water distribution in a viscous protoplanetary disk.' *Icarus,* 181, pp. 178-204.

Clark, B.E., Bus, S.J., Rivkin, A.S., McConnochie, T., Sanders, J., Shah, S., Hiroi, T., & Shepard, M. (2004) 'E-type asteroid spectroscopy and compositional modelling.' *Journal of Geophysical Research,* 109, E02001.

Clayton, R.N. & Mayeda, T.K. (1999) 'Oxygen isotope studies of carbonaceous chondrites.' *Geochimica et Cosmochimica Acta*, 63, pp. 2089-2104.

Cloutis, E.A., Hudon, P., Hiroi, T., Gaffey, M.J., & Mann, P. (2011) 'Spectral reflectance properties of carbonaceous chondrites: 2. CM chondrites.' *Icarus,* 216, pp. 309-346.

Cody, G.D., Heying, Alexander, C.M.O., Nittler, L.R., Kilcoyne, D.A.L., Sandford, S.A., & Stroud, R.M. (2011) 'Establishing a molecular relationship between chondritic and cometary organic solids.' *Proceedings of the National Academy of Sciences of the United States of America,* 108, pp. 19171-19176.

Connolly Jr., H.C. & Desch, S.J. (2004) 'On the origin of the "kleine Kügelchen" called Chondrules.' *Chemie der Erde,* 64, pp. 95-125.

Compagnoni, R., Ferraris, G., & Mellini, M. (1985) 'Carlosturanite, a new asbestiform rock-forming silicate from Val Varaita, Italy.' *American Mineralogist,* 70, pp. 767-772.

Cronin, J.R., & Pizzarello, S. (1990) 'Aliphatic hydrocarbons of the Murchison meteorite.' *Geochimica et Cosmochimica Acta,* 54, pp. 2859-2868.

Daly, L., Suttle, M.D., Lee, M.R., Bridges, J., Hicks, L., Martin, P-E., Floyd, C.J., et al. (submitted) 'Nano-Scale Heterogeneity in the Extent of Aqueous Alteration within the Lithologies of the Winchcombe CM Carbonaceous Chondrite.' *Meteoritics & Planetary Science*

De Leuw, S., Rubin, A.E., & Wasson, J.T. (2010) 'Carbonates in CM chondrites: Complex formational histories and comparison to carbonates in CI chondrites.' *Meteoritics & Planetary Sciences,* 45, pp. 513-530.

DeMeo, F.E. & Carry, B. (2014) 'Solar System evolution from compositional mapping of the asteroid belt.' *Nature,* 505, pp. 629-634.

DeMeo, F.E., Binzel, R.P., Slivan, S.M., & Buse, S.J. (2009) 'An extension of the Bus asteroid taxonomy into the near-infrared.' *Icarus,* 202, pp. 160-180.

Drouard, A., Gattacceca, J., Hutzler, A., Rochette, P., Baucher, R., Bourlès, D., ASTER Team, Gounelle, M. et al. (2019) 'The meteorite flux of the past 2 m.y. recorded in the Atacama Desert.' *Geology,* 47, pp. 673-676.

Durazzo, A & Taylor, L.A. (1982) 'Exsolution in the Mss-Pentlandite System: Textural and Genetic Implications for the Ni-Sulfide Ores.' *Mineralium Deposita,* 17, pp. 313-332.

Ebel, D.S. (2006) 'Condensation of Rocky Material in Astrophysical Environments.' In Ed. Lauretta, D.S. & McSween Jr., H.Y. (Eds.) *Meteorites and the Early Solar System II*. Tuscon, Arizona, USA: The University of Arizona Press. pp. 253-277.

Ebert, A., Rieke-Zapp, D., Herwegh, M., Ramseyer, K., Gnos, E., & Decrouez, D. (2009) 'Microstructures of coarse-grained marbles, analyzed using a new technique based on the bireflectance of calcite.' *Tectonophysics,* 463, pp. 175-184.

Egerton, R.F. (2016) *Physical Principles of Electron Microscopy: An Introduction to TEM, SEM, and AEM*, 2.

Eiger, A. (1937) 'Un nouveau ferrite de chaux hydrate.' *Les Revue des Matériaux de Construction et de Travaux Publics*. 33, pp. 141-142.

Ellison, E.T., Templeton, A.S., Zeigler, S.D., Mayhew, L.E., Kelemen, P.B., Matter, J.M., & the Oman Drilling Project Science Party. (2021) 'Low-Temperature Hydrogen Formation During Aqueous Alteration of Serpentinized Peridotite in the Samail Ophiolite.' *Journal of Geophysical Research: Solid Earth,* 126, e2021JB021981.

Eugster, O., Herzog, G.F., Marti, K., & Caffee, M.W. (2006) 'Irradiation Records, Cosmic-Ray Exposure Ages, and Transfer Times of Meteorites.' In Ed. Lauretta, D.S. & McSween Jr., H.Y. (Eds.) *Meteorites and the Early Solar*

System II. Tuscon, Arizona, USA: The University of Arizona Press. pp. 829-851.

European Southern Observatory (2014) *Artist's impression of a young star surrounded by a protoplanetary disc.* Available at: https://www.eso.org/public/images/eso1436f/

Fan, Y., Li, S., Liu, S., Yin, Q., Song, G., Xu, R., Zhang, J., Liu, C. et al. (2022) 'Shidian meteorite, a new fall analog of near-Earth asteroid (101955) Bennu.' *Meteoritics & Planetary Science,* 57, pp. 2192-2215.

Fanale, F.P., Li, Y-H., De Carlo, E., Farley, C., Sharma, S.K., Horton, K., & Granahan, J.C. (2001) 'An experimental estimate of Europa's Ocean composition independent of Galileo orbital remote sensing.' *Journal of Geophysical Research,* 106, pp. 14595-146000.

Flemming, R.L. (2007) 'Micro X-ray diffraction (μXRD): a versatile technique for characterization of Earth and planetary materials.' *Canadian Journal of Earth Sciences,* 44, pp. 1333-1346.

Flint, E.P., McMurdie, H.F., & Wells, L.S. (1941) 'Hydrothermal and X-ray studies of the garnet-hydrogarnet series and the relationship of the series to hydration products of Portland cement.' *Journal of Research of the National Bureau of Standards*, 26, pp. 13-33.

Floyd, C.J. & Lee, M.R. (2021) 'Rapid calcite dissolution in the CM carbonaceous chondrites and its implications.' *52nd Lunar and Planetary Science Conference,* Abstract#1335.

Floyd, C., Martin, P-E., Jenkins, L.E, & Lee, M. (submitted) 'An Updated Analysis into the Chondrule Sizes of the Carbonaceous CM Chondrites and the methodologies used.' *Meteoritics & Planetary Science*

Fritz, J., Assis Fernandes, V., Greshake, A., Holzwarth, A., & Böttger, U. (2019) 'On the formation of diaplectic glass: Shock and thermal experiments with

different chemical compositions.' *Meteoritics & Planetary Science,* 54, pp. 1533-1547.

Fuchs, L.H., Olsen, E., & Jensen, K.J. (1973) 'Mineralogy, Mineral-Chemistry, and Composition of the Murchison (C2) Meteorite.' *Smithsonian Contributions to the Earth Sciences,* 10.

Fujiya, W., Higashi, H., Hibiya, Y., Sugawara, S., Yamaguchi, A., Kimura, M., & Hashizume, K. (2022) 'Hydrothermal Activities on C-Complex Asteroids Induced by Radioactivity.' *The Astrophysical Journal Letters,* 924, L16

Galan, I., Glasser, F.P., & Andrade, C. (2013) 'Calcite carbonate decomposition.' *Journal of Thermal Analysis and Calorimetry,* 111, pp. 1197-1202.

Galdenzi, S. & Maruoka, T. (2003) 'Gypsum deposits in the Frasassi Caves, Central Italy.' *Journal of Cave and Karst Studies,* 65, pp. 111-125.

Ganapathy, R. & Anders, E. (1974) 'Bulk compositions of the moon and earth, estimated from meteorites.' *Proceedings of the Fifth Lunar Conference,* 2, pp. 1181-1206.

Garenne, A., Beck, P., Montes-Hernandez, G., Chiriac, R., Toche, F., Quirico, E., Bonal, L., & Schmitt, B. (2014) 'The abundance and stability of "water" in type 1 and 2 carbonaceous chondrites (CI, CM and CR).' *Geochimica et Cosmochimica Acta,* 137, pp. 93-112.

Gattacceca, J., McCubbin, F.M., Grossman, J., Bouvier, A., Bullock, E., Chennaoui Aoudjehane, H., Debaille, V., D'Orazio, M. et al. (2021) 'The Meteoritical Bulletin, No. 109.' *Meteoritics & Planetary Sciences,* 56, pp. 1626-1630.

Genge, M.J. & Grady, M.M. (1999). 'The fusion crusts of stony meteorites: Implications for the atmospheric reprocessing of extraterrestrial materials.' *Meteoritics & Planetary Science,* 34, pp. 341-356.

Genge, M.J., Alesbrook, L., Almeida, N.V., et al. (2023) 'The fusion crust of the Winchcombe meteorite: a preserved record of atmospheric entry processes.' *Meteoritics & Planetary Sciences*

Ghosh, B., Morishita, T., Ray, J., Tamura, A., Mizukami, T., Soda, Y., & Ovung, T.N. (2017) 'A new occurrence of titanian (hydro)andradite from the Nagaland ophiolite, India: Implications for element mobility in hydrothermal environments.' *Chemical Geology*, 457, pp. 47-60.

Gooding, J.L. (1986) *Antarctic Meteorite NEWSLETTER*, 9.

Gounelle, M. & Zolensky, M.E. (2001) 'A terrestrial origin for sulfate veins in CI1 chondrites.' *Meteoritics & Planetary Science,* 36, pp. 1321-1329.

Gounelle, M. & Zolensky, M.E. (2014) 'The Orgueil meteorite: 150 years of history.' *Meteoritics & Planetary Science*, 49, pp. 1769-1794.

Gozzi, F., Gaeta, M., Freda, C., Mollo, S., Di Rocco, T., Marra, F., Dallai, L., & Pack, A. (2014) 'Primary magmatic calcite reveals origin from crustal carbonate.' *Lithos,* 190-191, pp. 191-203.

Gradle, J. & Tedesco, E. (1982) 'Compositional Structure of the Asteroid Belt.' *Science,* 216, pp. 1405-1407.

Graham, D.J. & Midgley, N.G. (2000) 'Graphical representation of particle shape using triangular diagrams: an excel spreadsheet method.' *Earth Surface Processes and Landforms*, 25, pp. 1473-1477.

Grossman, J.N. (2000) 'A meteorite falls on ice.' *Science*. 290, pp. 283.

Grossman, J.N. (1994) 'The Meteoritical Bulletin, No. 76, 1994 January: The U.S. Antarctic Meteorite Collection.' *Meteoritics,* 29, pp. 100-143.

Grossman, J.N., Alexander, C. M.O'D., Wang, J., & Brearley, A.J. (2000) 'Bleached chondrules: Evidence for widespread aqueous processes on the parent asteroids of ordinary chondrites.' *Meteoritics & Planetary Science,* 35, pp. 467-486.

Grossman, L. (2010) ‘Vapor-condensed phase processes in the early solar system.’ *Meteoritics & Planetary Science*, 45, pp. 7-20.

Gubaidulina, T.V., Christyakova, N.I., & Rusakov, V.S. (2007) ‘Mössbauer Study of Layered Iron Hydroxysulfides: Tochilinite and Valleriite.’ *Bulletin of the Russian Academy of Sciences: Physics,* 71, pp. 1269-1272.

Haack, H., Grau, T., Bischoff, A., Horstmann, M., Wasson, J., Sørensen, A., Laubenstein, M., Ott, U. et al. (2012) ‘Maribo – A new CM fall from Denmark.’ *Meteoritics & Planetary Science*, 47, pp. 30-50.

Haberle, C.W. & Garvie, L.A.J. (2017) ‘Extraterrestrial formation of oldhamite and portlandite through thermal metamorphism of calcite in the Sutter’s Mill carbonaceous chondrite.’ *American Mineralogist*, 102, pp. 2415-2421.

Habermann, D., Neuser, R.D., & Richter, D.K. (1996) ‘REE-activated cathodoluminescence of calcite and dolomite: high-resolution spectrometric analysis of CL emission (HRS-CL).’ *Sedimentary Geology,* 101, pp. 1-7.

Hajar, Y., McAuley, K., & Zeman, F. (2016) ‘Sulfur as a Fuel Source in a Combined Power Cycle Equipped with a Dry Flue Gas Desulfurization System.’ *Energy & Fuels* 30, pp. 8511-8519.

Hanna, R.D. & Ketchan, R.A. (2018) ‘Evidence for accretion of fine-grained rims in a turbulent nebula for CM Murchison.’ *Earth and Planetary Science Letters,* 481, pp. 201-211.

Hanna, R.D., Ketcham, R.A., Zolensky, M., & Behr, W.M. (2015) ‘Impact-induced brittle deformation, porosity loss, and aqueous alteration in the Murchison CM chondrite.’ *Geochimica et Cosmochimica Acta*, 171, pp. 256-282.

Hanna, R.D., Hamilton, V.E., Haberle, C.W., King, A.J., Abreu, N.M., & Friedrich, J.M. (2020) ‘Distinguishing relative aqueous alteration and heating among CM chondrites with IR spectroscopy.’ *Icarus,* 346, pp. 113760.

Hanowski, N.P. & Brearley, A.J. (2001) ‘Aqueous alteration of chondrules in the CM carbonaceous chondrite, Allan Hills 81002: Implications for parent body alteration.’ *Geochimica et Cosmochimica Acta,* 65, pp. 485-518.

Hardie, L.A. & Eugster, H.P. (1970) ‘The Evolution of Closed-Basin Brines.’ *Mineralogical Society of America Special Papers,* 3, pp. 273-290.

Harlov, D.E. & Austrheim, H. (2013). ‘Metasomatism and the Chemical Transformation of Rock: Rock-Mineral-Fluid Interaction in Terrestrial and Extraterrestrial Environments.’ In Harlov, D.E. & Austrheim, H. (eds.) *Metasomatism and the Chemical Transformation of Rock: The Role of Fluids in Terrestrial and Extraterrestrial Processes*. pp. 1-16.

Herd, C.D.K., Hilts, R.W., Skelhorn, A.W., & Simkus, D.N. (2016) ‘Cold curation of pristine astromaterials: Insights from the Tagish Lake meteorite.’ *Meteoritics & Planetary Science,* 51, pp. 499-519.

Herzog, G.F. (2007) ‘Cosmic-Ray Exposure Ages of Meteorites.’ In Holland, H.D. & Turekian, K.K. (eds.) *Treatise on Geochemistry*. pp. 1-36.

Hewins, R.H. & Zanda, B. (2012) ‘Chondrules” Precursors and interactions with the nebular gas.’ *Meteoritics & Planetary Science,* 47, pp. 1120-1138.

Hewins, R.H., Zanetta, P.-M., Zanda, B., Le Guillou, C., Gattacceca, J., Sognzoni, C., Pont, S., Piani, L. et al. (2021) ‘NORTHWEST AFRICA (NWA) 12563 and ungrouped C2 chondrites: Alteration styles and relationships to asteroids.’ *Geochimica et Cosmochimica Acta,* 311, pp. 238-273.

Hezel, D.C. & Palme, H. (2007) ‘The conditions of chondrule formation, Part I: Closed system.’ *Geochimica et Cosmochimica Acta,* 71, pp. 4092-4107.

Hezel, D.C., Poole, G.M., Hoyes, J., Coles, B.J., Unsworth, C., Albrecht, N., Smith, C., Rehkämper, M. et al. (2015) ‘Fe and O isotope composition of meteorite fusion crusts: Possible natural analogues to chondrule formation?’ *Meteoritics & Planetary Science,* 50, pp. 229-242.

Hiroi, T., Zolensky, M.E., & Pieters, C.M. (2001) 'The Tagish Lake Meteorite: A Possible Sample from a D-Type Asteroid.' *Science,* 293, pp. 2234-2236.

Hood, L.L. & Horanyi, M. (1991) 'Gas Dynamic Heating of Chondrule Precursor Grains in the Solar Nebula.' *Icarus,* 93, pp. 259-269.

Hood, L.L. & Horanyi, M. (1993) 'The Nebular Shock Wave Model for Chondrule Formation: One-Dimensional Calculations.' *Icarus,* 106, pp. 179-189.

Horan, J.R. (1953) 'The Murray, Calloway County, Kentucky Aerolite (CN -+ 0881,366).' *Meteoritics,* 1, pp. 114-121.

Hose, L.D. & Rosales-Lagarde, L. (2017) 'Sulfur-Rich Caves of Southern Tabasco, Mexico.' In Klimchouk, A.N., Palmer, A., De Waele, J.S., Auler, A., & Audra, P. (eds.) *Hypogene Karst Regions and Caves of the World. Cave and Karst Systems of the World*. Springer, Cham.

Howard, K.T., Benedix, G.K., Bland, P.A., & Cressey, G. (2009) 'Modal mineralogy of CM2 chondrites by X-ray diffraction (PSD-XRD). Part 1: Total phyllosilicate abundance and the degree of aqueous alteration.' *Geochimica et Cosmochimica Acta,* 73, pp. 4576-4589.

Howard, K.T., Benedix, G.L., P.A. Bland, & Cressey, G. (2011) 'Modal mineralogy of CM chondrites by X-ray diffraction (PSD-XRD): Part 2. Degree, nature and settings of aqueous alteration.' *Geochimica et Comsmochimica Acta,* 75, pp. 2735-2751.

Howard, K.T., Alexander, C.M.O'D., Schrader, D.L., & Dyl, K.A. (2015) 'Classification of hydrous meteorites (CR, CM and C2 ungrouped) by phyllosilicate fraction: PSD-XRD modal mineralogy and planetesimal environments.' *Geochimica et Cosmochimica Acta,* 149, pp. 206-222.

Hu, R. (2010) 'Transport of the first rocks of the solar system by X-winds.' *The Astrophysical Journal,* 725, pp. 1421-1428.

Hu, G., Dam-Johansen, K., Wedel, S., & Hansen, J.P. (2006) 'Decomposition and oxidation of pyrite.' *Progress in Energy and Combustion Science,* 32, pp. 295-314.

Huckenholz, H.G. & Fehr, K.T. (1982) 'Stability relationships of grossular + quartz + wollastonite + anorthite II. The effect of grandite-hydrograndite solid solution.' *Neues Jahrbuch für Mineralogie: Abhandlungen*, 145, pp. 1-33.

Huss, G.R., MacPherson, G.J., Wasserburg, G.J., Russell, S.S., & Srinivasan, G. (2001) 'Aluminum-26 in calcium-aluminum-rich inclusions and chondrules from unequilibrated ordinary chondrites.' *Meteoritics & Planetary Science,* 36, pp. 975-997.

Ikeda, Y. (1992) 'An overview of the research consortium "Antarctic carbonaceous chondrites with CI affinities, Yamato-86720, Yamato-82162, and Belgica-7904.' *Proceedings of the NIPR Symposium on Antarctic Meteorites,* 5, pp. 49-73.

Ireland, T.R., Compston, W., & Heydegger, H.R. (1985) 'Titanium isotopic anomalies in hibonites from the Murchison carbonaceous chondrite.' *Geochimica et Cosmochimica Acta,* 49, pp. 1989-1993.

Ireland, T.R., Avila, J., Greenwood, R.C., Hicks, L.J., & Bridges, J.C. (2020) 'Oxygen Isotopes and Sampling of the Solar System.' *Space Science Reviews*, 216, pp. 25.

Ito, M., Tomioka, N., Uesugi, M., Yamaguchi, A., Shirai, N., Ohigashi, T., Liu, M-C., Greenwood, R.C. et al. (2022) 'A pristine record of outer Solar System materials from asteroid Ryugu's returned sample.' *Nature Astronomy*

Ivanov, A.V., Yaroshevskiy, A.A., & Ivanova, M.A. (2019) 'Meteorite Minerals.' *Geochemistry International,* 57, pp. 931-939.

Izawa, M.R.M., Nesbitt, H.W., MacRae, N.D., & Hoffman, E.L. (2010) 'Composition and evolution of the early oceans: Evidence from the Tagish Lake meteorite.' *Earth and Planetary Science Letters,* 298, pp. 443-449.

Izawa, M.R.M., Flemming, R.L., Banerjee, N.R., & McCausland, P.J.A. (2011) 'Micro-X-ray diffraction assessment of shock stage in enstatite chondrites.' *Meteoritics & Planetary Science,* 36, pp. 638-651.

Jacquet, E. (2014) 'Transport of solids in protoplanetary disks: Comparing meteorites and astrophysical models.' *Comptes Rendus Geoscience,* 346, pp. 3-12.

Jacquet, E. (2021) 'Collisions and compositional variability in chondrule-forming events.' *Geochimica et Cosmochimica Acta,* 296, pp. 18-37.

Jarosewich, E. (1990). 'Chemical analyses of meteorites: A compilation of stony and iron meteorite analyses.' *Meteoritics,* 25, pp. 323-337.

Jenniskens, P. (2013) 'Recent documented meteorite falls, a review of meteorite-asteroid links.' *Meteoroids 2013, Proceedings of the Astronomical Conference,* pp. 57-78.

Jenniskens, P., Fries, M.D., Yin, Q-Z., Zolensky, M., Krot, A.N., Sandford, S.A., Sears, D., Beauford, R. et al. (2012) 'Radar-enabled recovery of the Sutter's Mill meteorite, a carbonaceous chondrite regolith breccia.' *Science,* 338, pp. 1583-1587.

Jenkins, L.E. (2019) *Creating Calibration Curves using In Situ X-ray Diffraction to Determine the Shock Pressure Experienced by Clinopyroxene,* M.Sc. thesis, the University of Western Ontario.

Jull, A.J.T., Donahue, D.J., Cielazy,k E., & Wlotzka, F. (1993) 'Carbon-14 terrestrial ages and weathering of 27 meteorites from the southern high plains and adjacent areas (USA).' *Meteoritics,* 28, pp. 188-195.

Kadlag, Y., Haberthür, D., Leya, I., Hlushchuk, R., & Mezger, K. (2023) 'Physical properties and average atomic numbers of chondrules using computed tomography.' *Planetary and Space Science,* 238, pp. 105799

Karunadasa, K.S.P., Manoratne, C.H., Pitawala, H.M.T.G.A., & Rajapakse, R.M.G. (2019) 'Thermal decomposition of calcium carbonate (calcite polymorph) as examined by in-situ high-temperature X-ray powder diffraction.' *Journal of Physics and Chemistry of Solids,* 134, pp. 21-28.

Kieffer, S.W. (1971) 'Shock Metamorphism of the Coconino Sandstone at Meteor Crater, Arizona.' *Journal of Geophysical Research,* 76, pp. 5449-5473.

Kim, Y., Caumon, M-C., Barres, O., Sall, A., & Cauzid, J. (2021) 'Identification and composition of carbonate minerals of the calcite structure by Raman and infrared spectroscopies using portable devices.' *Spetrochimica Acta Part A: Molecular and Biomolecular Spectroscopy,* 261, pp. 119980.

Kimura, M., Imae, N., Komatsu, M., Barrat, J.A., Greenwood, R.C., Yamaguchi, A., & Noguchi, T. (2020) 'The most primitive CM chondrites, Asuka 12085, 12169, and 12236, of subtypes 3.0-2.8: Their characteristic features and classification.' *Polar Science,* 26, pp. 100565.

Kolesov, B.A., & Geiger, C.A. (1997) 'Raman Scattering in Silicate Garnets: An Investigation of their Resonance Intensities.' *Journal of Raman Spectroscopy*, 28, pp. 659-662.

King, A.J., Schofield, P.F., & Russell, S.S. (2017) 'Type 1 aqueous alteration in CM carbonaceous chondrites: Implications for the evolution of water-rich asteroids.' *Meteoritics & Planetary Science,* 52, pp. 1197-1215.

King, A.J., Bates, H.C., Krietsch, D., Busemann, H., Clay, P.L., Schofield, P.F., & Russell, S.S. (2019a). 'The Yamato-type (CY) carbonaceous chondrite group: Analogues for the surface of the asteroid Ryugu?' *Geochemistry,* 79, pp. 125531.

King, A.J., Russell, S.S., Schofield, P.F., Humphreys-Williams, E.R., Strekopytov, S., Abernethy, F.A.J., Verchovsky, A.B., & Grady, M.M. (2019b) 'The alteration history of the Jbilet Winselwan CM carbonaceous chondrite: An analog for C-type asteroid sample return.' *Meteoritics & Planetary Science,* 54, pp. 521-543.

King, A.J., Phillips, K.J.H., Strekopytov, S.S., Vita-Frinzi, C., & Russell S.S. (2020) 'Terrestrial modification of the Ivuna meteorite and a reassessment of the chemical composition of the CI type specimen.' *Geochimica et Cosmochimica Acta,* 268, pp. 73-89.

King, A.J., Bates, H.C., Schofield, P.F., & Russell, S.S. (2021a). 'The bulk mineralogy and water contents of the carbonaceous chondrite falls Kolang and Tarda.' *52nd Lunar and Planetary Science Conference,* Abstract #1909.

King, A.J., Schofield, P.F., & Russell, S.S. (2021b) 'Thermal alteration of CM carbonaceous chondrites: Mineralogical changes and metamorphic temperatures.' *Geochimica et Cosmochimica Acta,* 289, pp. 167-190.

King, A.J., Daly, L., Rowe, J., et al. (2022) 'The Winchcombe meteorite, a unique and pristine witness from the outer solar system.' *Science Advances,* 8, eabq3925.

Krietsch, D., Busemann, H., Riebe, M.E.I., King, A.J., Alexander, C.M.O'D., & Maden, C. (2021) 'Noble gases in CM carbonaceous chondrites: Effect of parent body aqueous and thermal alteration and cosmic ray exposure ages.' *Geochimica et Cosmochimica Acta,* 310, pp. 240-280.

Krinov, E.L. (1958) 'The Meteoritical Bulletin.' *The Permanent Commission on Meteorites of the International Geological Congress,* 8

Krinsley, D.H., Pye, K., Boggs Jr., S., & Tovey, N.K. (1998) *Backscattered Scanning Electron Microscopy and Image Analysis of Sediments and Sedimentary Rocks,* Cambridge University Press: Cambridge.

Krot, A.N., Ulyanov, A.A., Meibom, A., & Keil, K. (2001) 'Forsterite-rich accretionary rims around calcium-aluminum-rich inclusions from the reduced CV3 chondrite Efremovka.' *Meteoritics & Planetary Science*, 36, pp. 611-628.

Krot, A.N., Nagashima, K., Libourel, G., & Miller, K.E. (2018) 'Multiple Mechanisms of Transient Heating Events in the Protoplanetary Disk: Evidence from Precursors of Chondrules and Igneous Ca, Al-rich Inclusions.' In Russell, S.S., Connolly Jr., H.C., & Krot, A.B. (eds.) *Chondrules: Records of Protoplanetary Disk Processes*. pp. 11-56.

Krzesińska, A. & Fritz, J. (2014) 'Weakly shocked and deformed CM mircoxenoliths in the Pułtusk H chondrite.' *Meteoritics & Planetary Sciences,* 49, pp. 595-610.

Kurosawa, K., Genda, H., Azuma, S., & Okazaki, K. (2021) 'The Role of Post-Shock Heating by Plastic Deformation During Impact Devolatilization of Calcite (CaCO3).' *Geophysical Research Letters*, 48, pp. e2020GL091130.

Kvenvolden, K., Lawless, J., Pering, K., Peterson, E., Flores, J., Ponnamperuma, C., Kaplan, I.R., & Moore, C. (1970) 'Evidence for Extraterrestrial Amino-acids and Hydrocarbons in the Murchison Meteorite.' *Nature,* 228, pp. 923-926.

Lager, G.A., Armbruster, T., Rotella, F.J., & Rossman, G.R. (1989) 'OH substitution in garnets: X-ray and neutron diffraction, infrared, and geometric-modeling studies.' *American Mineralogist*, 74, pp. 840-851.

Larkin, P. (2011) *Infrared and Raman Spectroscopy: Principles and Spectral Interpretation,* London: Elsevier.

Lauretta, D.S., Balram-Knutson, S.S., Beshore, E., Boynton, W.V., Drouet d'Aubigny, C., DellaGiustina, D.N., Enos, H.L., Golish, D.R. et al. (2017) 'OSIRIS-REx: Sample Return from Asteroid (101955) Bennu.' *Space Science Reviews*, 212, pp. 925-984.

Lecasble, M., Remusat, L., Viennet, J-C., Laurent, B., & Bernard, S. (2022) 'Polycyclic aromatic hydrocarbons in carbonaceous chondrites can be used as tracers of both pre-accretion and secondary processes.' *Geochimica et Cosmochimica Acta,* 335, pp. 243-255.

Lee, J. K. W. (1995) 'Multipath Diffusion in Geochronology.' *Contributions to Mineralogy and Petrology,* 120, pp. 60–82.

Lee, M.R. (1993) 'The petrography, mineralogy and origins of calcium sulphate within the Cold Bokkeveld CM carbonaceous chondrite.' *Meteoritics,* 28, pp. 53-62.

Lee, M.R. & Bland, P.A. (2004) 'Mechanisms of weathering of meteorites recovered from hot and cold deserts and the formation of phyllosilicates.' *Geochimica et Cosmochimica Acta,* 68, pp. 893-916.

Lee, M.R. & Greenwood, R.C. (1994) 'Alteration of calcium- and aluminium-rich inclusions in the Murray (CM2) carbonaceous chondrite.' *Meteoritics,* 29, pp. 780-790.

Lee, M.R., Lindgren, P., & Sofe, M.R. (2014) 'Aragonite, breunnerite, calcite and dolomite in the CM carbonaceous chondrites: High fidelity recorders of progressive parent body aqueous alteration.' *Geochimica et Cosmochimica Acta,* 144, pp. 126-156.

Lee, M.R., Cohen, B.E., & King, A.J. (2019a) 'Alkali-halogen metasomatism of the CM carbonaceous chondrites.' *Meteoritics & Planetary Science,* 54, pp. 3052-3063.

Lee, M.R., Cohen, B.E., King, A.J., & Greenwood, R.C. (2019b) 'The diversity of CM carbonaceous chondrite parent bodies explored using Lewis Cliff 85311.' *Geochimica et Comsmochimica Acta,* 264, pp. 224-244.

Lee, M.R., Cohen, B.E., & Boyce, A. (2019c) 'Quantifying the intensity of post-hydration heating of CM carbonaceous chondrites using carbonates.' *50th Lunar and Planetary Science Conference,* Abstract #1540.

Lee, M.R., Daly, L., Floyd, C., & Martin, P-E. (2021a) 'CM carbonaceous chondrite falls and their terrestrial alteration.' *Meteoritics & Planetary Science,* 56, pp. 34-48.

Lee, M.R., Cohen, B.E., Boyce, A.J., Hallis, L.J., & Daly, L. (2021b) 'The pre-atmospheric hydrogen inventory of CM carbonaceous chondrites.' *Geochimica et Cosmochimica Acta,* 309, pp. 31-44.

Li, X., Chen, Y., Tang, X., Gu, L., Yuan, J., Su, W., Tian, H., Luo, H. et al. (2023) 'Thermally induced phase transition of troilite during micro-raman spectroscopy analysis.' *Icarus,* 390, pp. 115299

Lin, Y., Lan, G., & Wang, H. (1993) 'Pressure-induced amorphization of crystalline $Pb_5Ge_3O_{11}$.' *Solid State Communications,* 86, pp. 99-101.

Lindgren, P., Hanna, R.D., Dobson, K.J., Tomkinson, T., & Lee, M.R. (2015) 'The paradox between low shock-stage and evidence for compaction in CM carbonaceous chondrites explained by multiple low-intensity impacts.' *Geochimica et Cosmochimica Acta,* 148, pp. 159-178.

Lindgren, P., Lee, M.R., Sparkes, R., Greenwood, R.C., Hanna, R.D., Franchi, I.A., King, A.J., Floyd, C. et al. (2020) 'Signatures of the post-hydration heating of highly aqueously altered CM carbonaceous chondrites and implications for interpreting asteroid sample returns.' *Geochimica et Cosmochimica Acta,* 289, pp. 69-92.

Lindstrom, M.M. (1989) *Antarctic Meteorite Newsletter,* 12(3).

Liu, Y., Wang, A., & Freeman, J.J. (2009) 'Raman, MIR, and NIR spectroscopic study of calcium sulfates: gypsum, bassanite, and anhydrite.' *40th Lunar and Planetary Science Conference,* Abstract #2128.

Lofgren, G. & Russell, H.J. (1986) 'Dynamic crystallization of chondrule melts of porphyritic and radial pyroxene composition.' *Geochimica et Cosmochimica Acta,* 50, pp. 1715-1726.

Losiak, A. & Velbel, M.A. (2011) 'Evaporite formation during weathering of Antarctic meteorites – A weathering census analysis based on the ANSMET database.' *Meteoritics & Planetary Science,* 46, pp. 443-458.

Mackinnon, I.D.R. & Zolensky, M.E. (1984) 'Proposed structures for poorly characterized phases in C2M carbonaceous chondrite meteorites.' *Nature,* 309, pp. 240-242.

Maclear, T. (1840) 'VIII. Further particulars of the fall of the cold Bokkeveld meteorolite. By Thomas Maclear, Esq. F.R.S. &c., in a letter to Sir John F. W. Herschel, Bart. K. H. V. P. R. S. &c. &c. Communicated by Sir John F. W. Herschel.' *Philosophical Transactions of the Royal Society,* 130, pp. 177-182.

MacPherson, G.J. (2007) '1.08 – Calcium-Aluminum-Rich Inclusions in Chondritic Meteorites.' In Holland, H.D. & Turekian, K.K. (eds.) *Treatise on Geochemistry*. Pergamon.

Madon, M., Ibarguchi, J.I.G., Via, J., & Girardeau, J. (1991) 'Characterization and thermodynamic properties of andradite, $Ca_3Fe_2Si_3O_{12}$.' *American Mineralogist*, 76, pp. 1249-1260.

Martin, P.H. & Mills, A.A. (1980) 'Preferred chondrule orientations in meteorites.' *Earth and Planetary Science Letters*, 51, pp. 18-25.

Marvin, U.B. & Mason, B. (1984) 'Field and Laboratory Investigations of Meteorites from Victoria Land, Antarctica.' *Smithsonian Contributions to the Earth Sciences,* 26.

Masset, F. & Snellgrove, M. (2001) 'Reversing type II migration: resonance trapping of a lighter giant protoplanet.' *Monthly Notices of the Royal Astronomical Society,* 320, pp. L55-L59.

Matsumura, S., Pudritz, R.E., & Thommes, E.W. (2007) 'Saving planetary systems: dead zones and planetary migration.' *The Astrophysical Journal,* 660, pp. 1609-1623.

McCubbin, F.M., Boyce, J.W., Novác-Szabó, T., Santos, A.R., Tartès, R., Muttik, N., Domokos, G., Vazquez, J. et al. (2016) 'Geologic history of Martian regolith breccia Northwest Africa 7034: Evidence for hydrothermal activity and lithologic diversity in the Martian crust.' *Journal of Geophysical Research: Planets*, 121, pp. 2120-2149.

McMullan, S., Vida, D., Devillepoix, H.A.R., et al. (2023) 'The Winchcombe fireball – That lucky survivor.' *Meteoritics & Planetary Sciences,*

McNeill, A., Erasmus, N., Trilling, D.E., Emery, J.P., Tonry, J.L., Denneau, L., Flewelling, H., Heinze, A. et al. (2021) 'Comparison of the Physical Properties of the L4 and L5 Trojan Asteroids from ATLAS Data.' *The Planetary Science Journal,* 2, pp. 6.

McSween Jr., H.Y. (1987) 'Aqueous alteration in carbonaceous chondrites: Mass balance constraints on matrix mineralogy.' *Geochimica et Cosmochimica Acta,* 51, pp. 2469-2477.

McSween Jr., H.Y. (1999) *Meteorites and Their Parent Planets,* 2: Cambridge Academic Press, New York.

Mellini, M., Ferraris, G., & Compagnoni, R. (1985) 'Carlosturanite: HRTEM evidence of a polysomatic series including serpentine.' *American Mineralogist,* 70, pp. 773-781.

Ménez, B., Pasini, V., & Brunelli, D. (2012) 'Life in the hydrated suboceanic mantle.' *Nature: Geoscience*, 5, pp. 133-137.

Met Office Weather Observations Website. Observation Site Bishops Cleeve. Last modified May 16, 2022. https://wow.metoffice.gov.uk/observations/details/20210301o3j4kbd4sae6zd8pyyb96scn9y

Miura, H., Nakamota, T., & Doi, M. (2008) 'Origin of three-dimensional shapes of chondrules I. Hydrodynamics simulations of rotating droplet exposed to high-velocity rarefied gas flow.' *Icarus*, 197, pp. 269-281.

Montmerle, T., Augereau, J-C., Chaussidon, M., Gounelle, M., Marty, B., & Morbidelli, A. (2006) 'Solar System Formation and Early Evolution: The First 100 Million Years.' *Earth, Moon, and Planets,* 98, pp. 39-95.

Moore, C.B. (1970) 'New falls and discoveries.' *Meteoritics,* 5, pp. 173-176.

Nagao, K., Okazaki, R., Nakamura, T., Miura, Y.N., Osawa, T., Bajo, K-I., Matsuda, S., Ebihara, M. et al. (2011) 'Irradiation History of Itokawa Regolith Material Deduced from Noble Gases in the Hayabusa Samples.' *Science*, 333, pp. 1128-1131.

Nakamura, T. (2005) 'Post-hydration thermal metamorphism of carbonaceous chondrites.' *Journal of Mineralogical and Petrological Sciences,* 100, pp. 260-272.

Nakamura, T., Tomeoka, K., Sekine, T., & Takeda, H. (1995) 'Impact-induced chondrule flattening in the Allende CV3 carbonaceous chondrite: Shock experiments.' *Meteoritics*, 30, pp. 344-347.

Nakamura, T., Tomeoka, K., Takaoka, N., Sekine, T., & Takeda, H. (2000) 'Impact-induced textural changes of CV carbonaceous chondrites: experimental reproduction.' *Icarus*, 146, pp. 289-300.

Nakamura, T., Noguchi, T., Tanaka, M., Zolensky, M.E., Kimura, M., Tchuchiyama, A., Nakato, A., Ogami, T. et al. (2011) 'Itokawa Dust Particles: A direct Link Between S-Type Asteroids and Ordinary Chondrites.' *Science,* 333, pp. 1113-1116.

Nakamuta, Y., Nakamura, T., & Nakamura, N. (2006) 'Structural state of plagioclase from the Kobe CK chondrite: Implications for the thermal history of the CK parent body.' *Journal of Mineralogical and Petrological Science,* 101, pp. 308-318.

Nakato, A., Nakamura, T., Kitajima, F., & Noguchi, T. (2008) 'Evaluation of dehydration mechanism during heating of hydrous asteroids based on

mineralogical and chemical analysis of naturally and experimentally heated CM chondrites.' *Earth Planets Space,* 60, pp. 855-864.

Nakato, A., Brearly, A.J., Nakamura, T., Noguchi, T., Ahn, I., Lee, J.I., Matsuoka, M., & Sasaki, S. (2013) 'Diversity of thermal evolution processes in the hydrous asteroids identified in thermally metamorphosed carbonaceous chondrite PCA 02012.' *76th Annual Meteoritical Society Meeting*. Abstract#5282

Newman, E.S. (1941) 'Behavior of calcium sulfate at high temperatures.' *Journal of Research of the National Bureau of Standards,* 27, pp. 191-196.

Nittler, L.R., Stroud, R.M. Trigo-Rodríguez, J.M., De Gregorio, B.T., Alexander, C.M.O'D., Davidson, J., Moyano-Cambero, C.E., & Tanbakouei, S. (2019) 'A cometary building block in a primitive asteroidal meteorite.' *Nature Astronomy,* 3, pp. 659-666.

Nishiizumi, K. & Caffee, M.W. (2012) 'EXPOSURE HISTORIES OF CI1 AND CM1 CARBONACEOUS CHONDRITES.' *43rd Lunar and Planetary Science Conference,* Abstract#2758.

Ohtaki, K.K., Ishii, H.A., Bradley, J.P., Villalon, K.L., Davis, A.M., Stephan, T., Bustillo, K.C., & Ciston, J. (2021) 'Search for meteoritic GEMS I: Comparison of amorphous silicates in Paris and Acfer 094 chondrite matrices and in anhydrous chondritic interplanetary dust particles.' *Geochimica et Cosmochimica Acta,* 310, pp. 320-345.

Ohtsuka, K., Nakato, A., Nakamura, T., Kinoshita, D., & Ito, T. (2009) 'Solar-Radiation Heating Effects on 3200 Phaethon.' *Publications of the Astronomical Society of Japan,* 61(6), pp. 1375-1387.

Okazaki, R. & Nagao, K. (2017) 'Primordial and cosmogenic noble gases in the Sutter's Mill CM chondrite.' *Meteoritics & Planetary Science,* 52, pp. 669-689.

Orchin, M., Macomber, R.S., Pinhas, A., & Wilson, R.M. (2005) *The Vocabulary and Concepts of Organic Chemistry*, 2.

Organova, N.I., Genkin, A.D., Drits, V.A., Molotkov, S.P., Kuz'mina, O.V., & Dmitrik, A.L. (1971) 'Tochilinite, a new sulfide-hydroxide of iron and magnesium.' *Zapiski Vsesoyuznogo Mineralogicheskogo Obschestva,* 100, pp. 477-487.

Organova, N.I., Drits, V.A., & Dmitrik, A.L. (1974) 'Selected Area Electron Diffraction Study of a Type II "Valeriite-Like" Mineral.' *American Mineralogist,* 59, pp. 190-200.

Otrowski, D.R., Lacy, C.H.S., Gietzen, K.M., & Sears, D.W.G. (2011) 'IRTF spectra for 17 asteroids from the C and X complexes: A discussion of continuum slopes and their relationships to C chondrites and phyllosilicates.' *Icarus,* 212, pp. 682-696.

Palmer, E.E. & Lauretta, D.S. (2011) 'Aqueous alteration of kamacite in CM chondrites.' *Meteoritics & Planetary Science*, 46, pp. 1587-1607.

Patzek, M., Rüsch, O., & Molaro, J.L. (2023) 'On the Response of Chondrites to Diurnal Temperature Change – Experimental Simulation of Asteroidal Surface Conditions.' *Journal of Geophysical Research: Planets,* 129, e2023JE007944.

Pickersgill, A.E., Flemming, R.L., & Osinski, G.R. (2015) 'Toward quantification of strain-related mosaicity in shocked lunar and terrestrial plagioclase by in situ micro-X-ray diffraction.' *Meteoritics & Planetary Science*, 50, pp. 1851-1862.

Pignatelli, I., Marrocchi, Y., Vacher, L.G., Delon, R., & Gounelle, M. (2016) 'Multiple precursors of secondary mineralogical assemblages in CM chondrites.' *Meteoritics & Planetary Science,* 51, pp. 785-805.

Pirlet, H., Wehrmann, L.M., Brunner, B., Frank, N., Dewanckele, J., Van Rooij, D., Foubert, A., Swennen, R. et al. (2010) 'Diagenetic formation of

gypsum and dolomite in a cold-water coral mound in the Porcupine Seabight, off Ireland.' *Sedimentology* 57, pp. 786-805.

Pirozzi, N.M., Hoogenboom, J.P, & Giepmans, B.N.G. (2018) 'ColorEM: analytical electron microscopy for element-guided identification of the building blocks of life.' *Histochemistry and Cell Biology,* 150, pp. 509-520.

Plümper, O., Beinlich, A., Bach, W., Janots, E., & Austrheim, H. (2014) 'Garnets within geode-like serpentinite veins: Implications for element transport, hydrogen production and life-supporting environment formation.' *Geochimica et Cosmochimica Acta*, 141, pp. 454-471.

Prasad, A., Singru, R.M., & Biswas, A.K. (1985) 'Study of the Roasting of Pyrite Minerals by Mössbauer Spectroscopy.' *Physica Status Solidi,* 87, pp. 267-271.

Prieto-Taboada, N., Gómez-Laserna, O., Martínez-Arkarazo, I., Ángeles Olazabal, M., & Manuel Madariaga, J. (2014) 'Raman Spectra of the Different Phases in the $CaSO_4$-H_2O System.' *Analytical Chemistry,* 86, pp. 10131-10137.

Quirico, E., Bonal, L., Beck, P., Alexander, C.M.O'D., Yabuta, H., Nakamura, T., Nakato, A., Flandinet, L. et al. (2018) 'Prevalence and nature of heating processes in CM and C2-ungrouped chondrites as revealed by insoluble organic matter.' *Geochimica et Cosmochimica Acta,* 241, pp. 17-37.

Ramsay, J.G., & Huber, M.I. (1983) *Techniques of Modern Structural Geology: Strain Analysis,* 1. London: Academic Press.

Reddy, S.M., Saxey, D.W., Rickard, W.D.A., Fougerouse, D., Montalvo, S.D., Verberne, R., & van Riessen, A. (2020) 'Atom Probe Tomography: Development and Application to the Geosciences.' *Geostandards and Geoanalytical Research,* 44, pp. 5-50.

Reed, S.J.B. (1995) 'Electron Probe Microanalysis.' In Potts, P.J., Bowles, J.F.W., Reed, S.J.B., & Cave, M.R. (eds.) *Microprobe Techniques in the Earth Sciences*. Glasgow: Chapham & Hall.

Reed, S.J.B. (2005) *Electron Microprobe Analysis and Scanning Electron Microscopy in Geology,* Cambridge: Cambridge University Press.

Richter, D.K., Neuser, R.D., Harder, M., Schabdach, H., & Scholz, D. (2018) 'Unusual internal structure of cm-sized coldwater calcite: Weichselian spars in former pools of the Zinnbergschacht Cave (Franconian Alb/SE Germany).' *International Journal of Speleology* 47, pp. 145-154.

Riciputi, L.R., McSween Jr., H.Y., Johnson, C.A., & Prinz, M. (1994) 'Minor and race element concentrations in carbonates of carbonaceous chondrites, and implications for the compositions of co-existing fluids.' *Geochimica et Cosmochimica Acta,* 58, pp. 1343-1351

Rodriguez-Navarro, C., Ruiz-Agudo, E., Luque, A., Rodriguez-Navarro, A.B., & Ortega-Huertas, M. (2009) 'Thermal decomposition of calcite: Mechanisms of formation and textural evolution of CaO nanocrystals.' *American Mineralogist,* 94, pp. 578-593.

RRUFFa (n.d.) *Tochilinite R060887*. accessed September 11, 2023, https://rruff.info/tochilinite/display=default/

RRUFFb (n.d.) *Mackinawite R060388*. accessed September 18, 2023, https://rruff.info/Mackinawite/R060388

RRUFFc (n.d.) *Cronstedtite R061026*. accessed September 11, 2023, https://rruff.info/tochilinite/display=default/

Rubin, A.E. (2015) 'An American on Paris: Extent of aqueous alteration of a CM chondrite and the petrography of its refractory and amoeboid olivine inclusions.' *Meteoritics & Planetary Science*, 50, pp. 1595-1612.

Rubin, A.E. (2012) 'Collisional facilitation of aqueous alteration of CM and CV carbonaceous chondrites.' *Geochimica et Cosmochimica Acta*, 90, pp. 181-194.

Rubin, A.E. (1997) ‘Mineralogy of meteorite groups.’ *Meteoritics & Planetary Science,* 32, pp. 231-247.

Rubin, A.E. & Wasson, J.T. (2005) ‘Non-spherical lobate chondrules in CO3.0 Y-81020: General implications for the formation of low-FeO porphyritic chondrules in CO chondrules.’ *Geochimica et Cosmochimica Acta,* 90, pp. 211-220.

Rubin, A.E., Trigo-Rodríguez, J.M., Huber, H., & Wasson, J.T. (2007) ‘Progressive aqueous alteration of CM carbonaceous chondrites.’ *Geochimica et Cosmochimica Acta,* 71, pp. 2361-2382.

Rupert, A.N., McCausland, P.J.A., & Flemming, R.L. (2020) ‘Ordinary chondrite shock stage quantification using in situ 2-D X-ray diffraction of olivine.’ *Meteoritics & Planetary Science,* 55, pp. 2224-2240.

Russell, S.S., Folco, L., Grady, M.M., Zolensky, M.E., Jones, R., Righter, K., Zipfel, J., & Grossman, J.L. (2004) ‘The Meteoritical Bulletin, No. 88, 2004 July.’ *Meteoritics & Planetary Science,* 39, pp. A215-A272.

Russell, S. S., Salge, T., King, A., Daly, L., Joy, K., Bates, H., Almeida, N. V., Suttle, M., & Schofield, P. (2022) ‘The Winchcombe CM2 Meteorite Fall: Curation and Preliminary Analysis.’ *Microscopy and Microanalysis*, 28, pp. 2732–2733.

Ruzicka, A., Grossman, J.N., & Garvie, L. (2014) *The Meteoritical Bulletin, No. 100, 2014 June*.

Saha, A., Lee, J., Pancera, S. M., Bräeu, M. F., Kempter, A., Tripathi, A. and Bose, A. (2012) ‘New insights into the transformation of calcium sulfate hemihydrate to gypsum using time-resolved cryogenic transmission electron microscopy.’ *Langmuir,* 28, pp. 11182–11187

Sarkar, S.C. (1971) ‘Mackinawite from the sulfide ores of the Singhbhum copper belt, India.’ *The American Mineralogist,* 56, pp. 1312-1318.

Schmitt, A.C., Tokuda, M., Yoshiasa, A., and Nishiyama, T. (2019) 'Titanian andradite in the Nomo rodingite: Chemistry, crystallography, and reaction relations.' *Journal of Mineralogical and Petrological Sciences,* 114, pp. 111-121.

Schmitt, R.T. (2000) 'Shock experiments with he H6 chondrite Kernouvé: Pressure calibration of microscopic shock effects.' *Meteoritics & Planetary Science,* 35, pp. 545-560.

Schrader, D.L., Connolly Jr., H. C., Lauretta, D.S., Zega, T.J., Davidson, J., & Domanik, K.J. (2015) 'The formation and alteration of the Renazzo-like carbonaceous chondrites III: Toward understanding the genesis of ferromagnesian chondrules.' *Meteoritics & Planetary Sciences,* 50, pp. 15-50.

Schwarzer, R.A., Field, D.P., Adams, B.L., Kumar, M., & Schwartz, A.J. (2009) 'Present State of Electron Backscatter Diffraction.' In Schwartz, A.J., Kumar, M., Adams., B.L., & Field, D.P. (eds.)n *Electron Backscatter Diffraction in Materials Science*. pp. 1-20.

Score, R. & Lindstrom, M. (1992) *Antarctic Meteorite Newsletter,* 15(2).

Score, R. & Lindstrom, M. (1993) *Antarctic Meteorite Newsletter,* 16(1).

Scott, E.R.D., Keil, K., and Stöffler, D. (1992) 'Shock metamorphism of carbonaceous chondrites.' *Geochimica et Cosmochimica Acta*, 56, pp. 4281-4293.

Sekiya, M., Uesugi, M., & Nakamoto, T. (2003) 'Flow in a Liquid Sphere Moving with a Hypersonic Velocity in a Rarefied Gas.' *Progress of Theoretical Physics,* 109, pp. 717-728.

Sephton, M.A. (2005) 'Organic matter in carbonaceous meteorites: past, present and future research.' *Philosophical Transactions of the Royal Society,* 363, pp. 2729-2742.

Seufert, S., Hesse, C., Goetz-Neunhoeffer, F., & Neubauer, J. (2009) 'Discrimination of bassanite and anhydrite III dehydrated from gypsum at different temperatures.' *Zeitschrift fur Kristallographie, Supplement,* 30, pp. 447-452.

Simon, S.B. & Grossman, L. (2011) 'Refractory inclusions in the unique carbonaceous chondrite Acfer 094.' *Meteoritics & Planetary Science*, 46, pp. 1197-1216.

Smith, E. & Dent, G. (2019) *Modern Spectroscopy: A Practical Approach.* 2. West Sussex: Wiley.

Stacey, F.D., Lovering, J.F., & Parry, L.G. (1961) 'Thermomagnetic Properties, Natural Magnetic Moments, and Magnetic Anisotropies of Some Chondritic Meteorites.' *Journal of Geophysical Research,* 66, pp. 1523-1534

Stöffler, D. (1971) 'Progressive metamorphism and classification of shocked and brecciated crystalline rocks at impact craters.' *Journal of Geophysical Research,* 76v 5541-5551.

Stöffler, D. & Hornemann, U. (1972) 'Quartz and feldspar glasses produce by natural and experimental shock.' *Meteoritics & Planetary Science,* 7, pp. 371-394.

Stöffler, D., Hamann, C., & Metzler, K. (2018) 'Shock metamorphism of planetary silicate rocks and sediments: Proposal for an updated classification system.' *Meteoritics & Planetary Science*, 53, pp. 5-39.

Stöffler, D., Keil, K., & Scott, E.R.D. (1991) 'Shock metamorphism of ordinary chondrites.' *Geochimica et Cosmochimica Acta*, 55, pp. 3845-3867.

Strydom, C.A., Hudson-Lamb, D. L., Potgieter, J. H., & Dagg, E. (1995) 'The thermal dehydration of synthetic gypsum.' *Thermochimica Acta,* 269/279, pp. 631-638.

Suttle, M.D., King, A.J., Harrison, C.S., Chan, Q.H.S., Greshake, A., Bartoschewitz, R., Tomkins, A.G., Salge, T. et al. (2023) 'The mineralogy and alteration history of the Yamato-type (CY) carbonaceous chondrites.' *Geochimica et Cosmochimica Acta,* 361, pp. 245-264.

Suttle, M.D., Daly, L., Jones, R.H., Jenkins, L., Van Ginneken, M., Mitchell, J.T., Bridges, J.C., Hicks, L.J. et al. (2022) 'The Winchcombe meteorite – A regolith breccia from a rubble pile CM chondrite asteroid.' *Meteoritics & Planetary Science*

Tartèse, R., Chaussidon, M., Gurenko, A., Frédéric, D., & François, R. (2018) 'Insights into the origin of carbonaceous chondrite organics from their triple oxygen isotope composition.' *Proceedings of the National Academy of Sciences of the United States of America,* 115, pp. 8535-8540.

Telus, M., Alexander, C.M.O'D., Hauri, E.H., & Wang, J. (2019) 'Calcite and dolomite formation in the CM parent body: Insight from *in situ* C and O isotope analyses.' *Geochimica et Cosmochimica Acta,* 260, pp. 275-291.

Tomeoka, K., Yamahana, Y., & Sekine, T. (1999) 'Experimental shock metamorphism of the Murchison CM carbonaceous chondrite.' *Geochimica et Cosmochimica Acta,* 63, pp. 3683-3703.

Tomeoka, K. & Buseck, P.R. (1985) 'Indicators of aqueous alteration in CM carbonaceous chondrites: Microtextures of a layered mineral containing Fe, S, O an Ni.' *Geochimica et Cosmochimica Acta,* 49, pp. 2149-2163.

Tonui, E., Zolensky, M., Hiroi, T., Nakamura, T., Lipshutz, M.E., Wang, M-S., & Okudaira, K. (2014) 'Petrographic, chemical and spectroscopic evidence for thermal metamorphism in carbonaceous chondrites I: CI and CM chondrites.' *Geochimica et Cosmochimica Acta,* 126, pp. 284-306.

Trigo-Rodríguez, J.M., Romola, A., Tanbakouei, S., Soto, V.C., & Lee, M. (2019) 'Accretion of Water in Carbonaceous Chondrites: Current Evidence and Implications for the Delivery of Water to Early Earth.' *Space Science Reviews*, 215, pp. 18.

Tritschler, U., Van Driessche, A. E. S., Kempter, A., Kellermeier, M., & Cölfen, H. (2015) 'Controlling the Selective Formation of Calcium Sulfate Polymorphs at Room Temperature.' *Angewandte Chemie International Edition*, 54, pp. 4083–4086.

Tyra, M.A., Farquhar, J., Wing, B.A., Benedix, G.K., Jull, A.J.T., Jackson, T., & Thiemens, M.H. (2007) 'Terrestrial alteration of carbonate in a suite of Antarctic CM chondrites: Evidence from oxygen and carbon isotopes.' *Geochimica et Cosmochimica Acta,* 71, pp. 782-795.

Uchizono, A., Shinno, I., Nakamuta, Y., Nakamura, T., & Sekine, T. (1999) 'Characterization of Artificially Shocked forsterites: (1) Diffraction Profile Analysis by Gandolfi Camera.' *Mineralogical Journal*, 21, pp. 15-23.

Vacher, L.G., Truche, L., Faure, F., Tissandier, L., Mosser-Ruck, R., & Marrocchi, Y. (2019) 'Deciphering the conditions of tochilinite and cronstedtite formation in CM chondrites from low temperature hydrothermal experiments.' *Meteoritics & Planetary Science,* 54, pp. 1870-1889.

Van Schmus, W.R. & Wood, J.A. (1967) 'A chemical-petrologic classification for the chondritic meteorites.' *Geochimica et Cosmochimica Acta,* 81, pp. 747-765.

Velbel, M.A. (1988) 'The Distribution and Significance of Evaporitic Weathering Products on Antarctic Meteorites.' *Meteoritics,* 23, pp. 151-159.

Velbel, M.A. & Zolensky, M.E. (2021) 'Thermal metamorphism of CM chondrites: A dehydroxylation-based peak-temperature thermometer and implications for sample return from asteroids Ryugu and Bennu.' *Meteoritics & Planetary Science,* 56, pp. 546-585.

Visser, R., John, T., Whitehouse, M.J., Patzek, M., & Bischoff, A. (2020) 'A short-lived ^{26}Al induced hydrothermal alteration event in the outer solar system: Constraints from Mn/Cr ages of carbonates.' *Earth and Planetary Science Letters,* 547, pp. 116440.

Wakita, S. & Genda, H. (2019) ‘Fates of hydrous materials during planetesimal collisions.’ *Icarus,* 328, pp. 58-68.

Walsh, K.J., Morbidelli, A., Raymond, S.N., O’Brien, D.P., & Mandell, A.M. (2011) ‘A low mass for Mars from Jupiter’s early gas-driven migration.’ *Nature Research: Letters,* 475, pp. 206-209.

Walsh, K.J., Morbidelli, A., Raymond, S.N., O’Brien, D.P. & Mandell, A.M. (2012) ‘Populating the asteroid belt from two parent source regions due to the migration of giant planets – “The Grand Tack.”’ *Meteoritics & Planetary Science,* 47, pp. 1941-1947.

Wang, M-S. & Lipschutz, M.E. (1998) ‘Thermally metamorphosed carbonaceous chondrites from data for thermally mobile trace elements.’ *Meteoritics & Planetary Sciences,* 33, pp. 1297-1302.

Wang, J.A., Novaro, O., Bokhimi, X., López, T., Gómez, R., Navarrete, J., Llanos, M.E., & López-Salinas, E. (1998) ‘Characterizations of the thermal decomposition of brucite prepared by sol-gel technique for synthesis of nanocrystalline MgO.’ *Materials Letters,* 35, pp. 317-323.

Wasson, J.T. (2015) *Meteorites: Their Record of Early Solar-System History*. New York: W.H. Freeman and Company.

Wasson, J.Y. (2008) ‘Evaporation of nebular fines during chondrule formation.’ *Icarus,* 195, pp. 895-907.

Watanabe, S-I., Tsuda, Y., Yoshikawa, M., Tanaka, S., Saiki, T., & Nakazawa, S. (2017) ‘Hayabusa2 Mission Overview.’ *Space Science Reviews,* 208, pp. 3-16.

Weber, I., Böttger, U., Pavlov, S.G., Hübers, H-W., Hiesinger, H., & Jessberger, E.K. (2017) ‘Laser alteration on iron sulfides under various environmental conditions.’ *Journal of Raman Spectroscopy,* 48, pp. 1509-1517.

Weidenschilling, S.J. (2019) ‘Accretion of the asteroids: Implications for their thermal evolution.’ *Meteoritics & Planetary Science,* 54, pp. 1115-11132.

Weisberg, M.K., McCoy, T.J., & Krot, A.N. (2007) ‘Systematics and Evaluation of Meteorite Classification.’ In Ed. Lauretta, D.S. & McSween Jr., H.Y. (Eds.) *Meteorites and the Early Solar System II*. Tuscon, Arizona, USA: The University of Arizona Press. pp. 19-52.

Williams, D.B. & Carter, C.B. (2009) *Transmission Electron Microscopy Part 1: Basics*. 2. New York: Springer.

Williamson, G.K. & Hall, W.H. (1953) ‘X-ray line broadening from filed aluminium and wolfram.’ *Acta Mettalurgica,* 1, pp. 22-31.

Wlotzka, F. (1993) ‘A weathering scale for the ordinary chondrites.’ *Meteoritics,* 28, pp. 460.

Wood, J.A. (1996) ‘Processing of chondritic and planetary material in spiral density waves in the nebula.’ *Meteoritics & Planetary Science,* 31, pp. 641-645.

Wood, J.A. & Hashimoto, A. (1993) ‘Mineral equilibrium in fractionated nebular systems.’ *Geochimica et Cosmochimica Acta,* 57, pp. 2377-2388.

Yabuta, H., Alexander, C.M.O’D., Fogel, M.L., Kilcoyn, A.L.D., and Cody, G.D. (2010) ‘A molecular and isotopic study of the macromolecular organic matter of the ungrouped C2 WIS 91600 and its relationship to Tagish Lake and PCA 91008.’ *Meteoritics & Planetary Science,* 45, pp. 1446-1460.

Yang, X., Hanna, R.D., Davis, A.M., Neander, A.I., and Heck, P.R. (2022) ‘A record of post-accretion asteroid surface mixing preserved in the Aguas Zarcas meteorite.’ *Nature Astronomy,* 6, pp. 1051-1058.

Yokoyama, T., Nagashima, K., Nakai, I., Young, E.D., Are, Y., Aléone, J., Alexander, C.M.O’D., Amari, S. et al. (2022) ‘Samples returned from the

asteroid Ryugu are similar to Ivuna-type carbonaceous meteorites.' *Science,* 379, eabn7850.

Zanetta, P-M., Leroux, H., Le Guillou, C., Zanda, B., & Hewins, R.H. (2021) 'Nebular thermal processing of accretionary fine-grained rims in the Paris CM chondrite.' *Geochimica et Cosmochimica Acta,* 295, pp. 135-154.

Zhang, M., Bonato, E., King, A.J., Russell, S.S., Tang, G., & Lin, Y. (2020) 'Petrology and oxygen isotopic compositions of calcium-aluminum-rich inclusions in primitive CO3.0-3.1 chondrites.' *Meteoritics & Planetary Science,* 55, pp. 911-935.

Zolensky, M., Mikouchi, T., Hagiya, K., Ohsumi, K., Komatsu, M., Cheng, A., & Le, L. (2022) 'Evidence for impact shock and regolith transportation on CM, CI, and CV, parent asteroids.' *Meteoritics & Planetary Science,* 57, pp. 1902-1919.

Zolensky, M., Mikouchi, T., Fries, M., Bodnar, R., Jenniskens, P., Yin, Q-Z., Hagiya, K., Ohsumi, K. et al. (2014) 'Mineralogy and petrography of C asteroid regolith: The Sutter's Mill CM meteorite.' *Meteoritics & Planetary Science,* 49, pp. 1997-2016.

Zolensky, M.E., Mittlefehldt, D.W., Lipschutz, M.E., Wang, M-S., Clayton, R.N., Mayeda, T.K., Grady, M.M., Pillinger, C., & Barber, D. (1997) 'CM chondrites exhibit the complete petrologic range from type 2 to 1.' *Geochimica et Cosmochimica Acta*, 61, pp. 5099-5115.

Zurfluh, F.J., Hofmann, B.A., Gnos, E., & Eggenberger, U. (2013) ''Sweating meteorites' – Water-soluble salts and temperature variation in ordinary chondrites and soil from the hot desert of Oman.' *Meteoritics & Planetary Science,* 48, pp. 1958-1980.